Caractérisation transcutanée non invasive du contenu sanguin en dioxyde de carbone (CO2)

Emmanuel Dervieux

Emmanuel Dervieux. Caractérisation transcutanée non invasive du contenu sanguin en dioxyde de carbone (CO2). Human health and pathology. Université de Strasbourg, 2024. English. NNT : 2024STRAD043 . tel-04960702

HAL Id: tel-04960702
https://theses.hal.science/tel-04960702v1
Submitted on 21 Feb 2025

UNIVERSITY OF STRASBOURG

ÉCOLE DOCTORALE Mathématiques, Sciences de l'Information et de l'Ingénieur (MSII)

UMR7357

PhD Thesis by

Emmanuel DERVIEUX

Defended on **DECEMBER 19, 2024**

To obtain the degree of: **Doctor from the University of Strasbourg**

In the field of: Electronics, microelectronics, optics and lasers, optoelectronics, microwave, robotics

Non-Invasive Transcutaneous Characterisation of Blood Carbon Dioxide (CO_2) Content

SUPERVISORS:

Mr UHRING Wilfried	Professor, Université de Strasbourg	*(Director)*
Mr THÉRON Michaël	Professor, Université de Bretagne Occidentale	*(Co-Director)*

REVIEWERS:

Mr PERCHOUX Julien	Professor, Université de Toulouse
Mr BOUIT Pierre-Antoine	Research Habilitation, Rennes Institute of Chemical Sciences

COMITTEE PRESIDENT:

Mrs GIROUX-METGÈS Marie-Agnès	Professor, Université de Bretagne Occidentale M.D., Hôpital Morvan

OTHER COMITTEE MEMBERS:

Mr VERGÈS Samuel	Research Director, HP2 Grenoble Laboratory
Mr LE GUILLOU Yann	PhD, Biosency

February 13, 2025

Foreword

TL;DR

Each chapter of this PhD thesis has a Too Long; Didn't Read (TL;DR) header that summarises the key points of the said chapter. You are **strongly encouraged** to read those, especially when skim-reading this document. You may also use the clickable links below to quickly navigate between chapters. Have a nice journey.

Main Table Of Content (TOC) Next chapter

> "The most merciful thing in the world, I think, is the inability of the human mind to correlate all its contents. We live on a placid island of ignorance in the midst of black seas of infinity, and it was not meant that we should voyage far. The sciences, each straining in its own direction, have hitherto harmed us little; but some day the piecing together of dissociated knowledge will open up such terrifying vistas of reality, and of our frightful position therein, that we shall either go mad from the revelation or flee from the deadly light into the peace and safety of a new dark age."
>
> — Howard Phillips Lovecraft, *The Call of Cthulhu* (1928)

Despite Lovecraft's fair warning, humanity has always endeavoured to push back the frontiers of its knowledge, further lifting the veil that used to cover the unfathomable abysses of ignorance whence it emerged. Just as the navigators of yore once outlined the contours of new, strange, and beautiful worlds, today's scientists are tirelessly exploring and meticulously mapping out the seemingly infinite expanse of scientific knowledge. As one of them, I took great pleasure in venturing into the different fields of research that my works required me to explore, and in trying to build bridges between the knowledge of old, and tomorrow's findings. Fortunately, while doing so, I managed to evade the crawling madness which often seals the destiny of Lovecraft's protagonists.

It may be seen from the many citations that sprinkle this thesis that I very much enjoy reading papers, thereby making mine the wisdom of elders. This foot in the past allowed me—at least hopefully to some extent—to derive a comprehensive view of the problem at hand, and it is my fervent wish to provide the reader with an overview of the ins and outs of the issues addressed. As for the future, in addition to the several novelties that this thesis brings to light, I also strived to clearly indicate the limitations of the presented work, as well as the future research avenues that could be explored.

When this happens, the "further research is needed" magnifying glass icon that can be seen on the right hand side of the present text will be used. As you shall see, I tried to use the many possibilities offered by LaTeX in order to offer what I intend to be an enjoyable reading experience. Of note, this thesis is **not** meant to be printed on paper: not only for ecological reasons, but also due to the many clickable links that strew it. Turquoise links are web links, green links[1] concern citations that will lead you to the corresponding bibliography entries, and red links are for other numbered elements, such as chapters, equations, figures, tables, *etc.* Do not fear clicking on a citation link, as citations are back-referenced, meaning that there is also a link in the reference list to jump back to whence you came from, thanks to `biblatex`'s package `backref` option.

further research is needed

A great deal of efforts have been put into being as educational as possible, especially because of the intrinsic multi-disciplinarity of the presented works. It is not expected from the reader to be an expert in all the covered fields(1), and a brief context is often provided, along with a reasonable amount of literature references to dig into, if need be. If I truly hope that this educational nature—as well as the extended discussions proposed—make this thesis more than a proof-of-work in the academic system, *i.e.* by making it a useful resource for those who may come after me, I am well-aware of the lengthy result that ensues. Consequently, I have included a TL;DR text box at the beginning of each chapter to provide the reader with the pith and marrow of the said chapter's content.

Finally, I hope that you will enjoy reading this thesis as much as I enjoyed conducting the corresponding research and writing the present manuscript. A GitHub repository containing all the source files is available here (including raw data and TikZ / PGFPlots plotting codes). Commit e199a7b corresponds to the final version, as validated by the doctoral committee whose members are given in the front page. If you spot any misinterpretation, typo, or error of any sort, please report it by writing me here, and always consult the afore-mentioned repository for the latest version available.

Tools that were used to write this thesis

This thesis was written using LaTeX, for which I highly recommend reading *The Not So Short Introduction to LaTeX*, by Tobi Oetiker[1]. Data plots were mostly composed using TikZ / PGFPlots, and Python programmers may find the `tikzplotlib` library particularly helpful for transitioning from Matplotlib to Tikz. Schematics were edited using Inkscape, with Gimp used for preprocessing raster images. WebPlotDigitizer was also seldom used to retrieve raw data from old figures. Most vector symbols are sourced from The Noun Project, which offers a comprehensive collection of icons with permissive licensing (CC BY 3.0, corresponding acknowledgments are provided in back matter). 3D designs were modelled using Onshape, a web-based, free, Solidworks-like software, while Printed Circuit Board (PCB) designs were achieved thanks to KiCad. Python was predominantly used for programming, data analysis, and statistical hypothesis testing, with occasional use of R for specific statistical explorations. Of note, while ChatGPT 3.5 / 4-o / 4-mini was used when redacting this manuscript, its use was limited to translation or re-wording purposes, **not** for redacting entire paragraphs / sections.

---

(1) Although being initiated with some of the presented arcana, I do not pretend being one myself. It would be presumptuous after only five years working on multiple topics at the same time to compare myself with scholars who devoted their lives to a single one.

Acknowledgements

TL;DR

I was (not) alone.

Previous chapter Main Table Of Content (TOC) Next chapter

This thesis is the result of a tripartite collaboration spanning a thousand kilometers, between Biosency (Rennes), the Orphy laboratory (Brest), and the ICube laboratory (Strasbourg), which would never have been possible without the active support of numerous individuals who deserve recognition.

First and foremost, I would like to express my sincere gratitude to Marie Pirotais, Yann Le Guillou, and Quentin Bodinier, who trusted me when I knocked at Biosency's door in late 2018, looking for a subject for my doctoral thesis. They placed their full confidence in me, granting me carte blanche and complete freedom to carry out my research, for which I am extremely grateful. I also extend my thanks to the entire Biosency team, many of whom are both friends and colleagues, each contributing to the hard-working yet convivial atmosphere of this young start-up.

Second, I would like to warmly thank Michaël Théron for welcoming me during my weeks of experimentation in Brest; not only in his laboratory, but also in his home, where I readily felt as part of his family. I also want to express my thanks to Marie-Agnès Girous-Metgès and François Guerrero for their dynamic contributions to my works, as well as for their redacting advices. More generally, I cannot emphasise enough the very positive atmosphere that prevails in the Orphy laboratory, and I warmly thank its members both for their friendly welcome (and cookies), and for their participation as guinea pigs in the rate-based study detailed in Chapter 3.

Third, I am grateful to Wilfried Uhring who—in addition to supervising my work and giving me lots of valuable advice—gave me a foothold in teaching, by entrusting me to design a lecture course on computer architecture from scratch. I am also particularly thankful to the people at ICube who strove to make my experiments feasible despite an erratic scheduling on my side and unending asbestos removal works. Of note, I want to express my warmest feelings for my fellow travellers in ICube Cronenbourg's laboratory—Lilas and Lucas—for their politically incorrect, saucy humour. They provided a much-needed respite and prevented me from losing what remained of my sanity while redacting this manuscript.

My profound thanks also go to the many teachers and scholars that gave me a strong taste for science and engineering throughout my school years. Foremost among them are my parents, who—as biology and physics teachers—instilled in me a passion for understanding and trying to explain the laws of the physical world. Their contribution is obviously not limited to that, and their ongoing support has been a great help to me throughout my whole (scientific) life.

Finally, I would like to say a few words of thanks to my friends and family, whose fellowship and affection always pushed me forward, and encouraged me to embark on numerous projects, both personal and professional. In particular, I would like to salute Joffrey for our everlasting DIY projects, and Raphaël for the already released and forthcoming music.

Of course, the support I received during my doctoral years was not limited to the few people mentioned above. I can readily think of dozens of names and faces who contributed to this work one way or another. Even if I cannot name each and every one of them here, I acknowledge their work, and deeply thank them for their contribution, however small.

Contents

List of Figures

List of Tables

Glossary

2,3-BPG 2,3-BisPhosphoGlyceric acid. 12–15, 162

AC Alternative Current (by extension, anything time varying). 17–20

ADC Analog to Digital Converter. 97, 102, 146

API Application Programming Interface. 15

BTB BromoThymol Blue. 95, 100

CIL Carbamate Ionic Liquid. 85

CO Carbon monoxide. 11, 82, 85, 158

CO$_2$ Carbon dioxide. 1–7, 9–15, 21, 22, 25, 26, 28, 30, 31, 33–35, 38, 39, 41–106, 108, 110, 112, 114, 116, 118, 120, 122, 124–128, 130, 132, 134–136, 138–144, 146–150, 152, 154–165, 175, 180, 195

CO$_2$Hb Carbamino-Haemoglobin. 1, 3, 6, 7, 9–14, 16–18, 20–26, 28–32, 34–36, 38–40, 88, 156, 158, 162, 167

COHb Carboxy-Haemoglobin. 11, 15–17, 20, 31, 33, 39, 158

COPD Chronic Obstructive Pulmonary Disease. 2, 4

CRLB Cramér-Rao Lower Bound. 119, 123

CTAH Cetyltrimethyl ammonium hydroxide. 80

CVC Cutaneous Vascular Conductance. 60

DABCO 1,4-diazabicyclo[2.2.2]octane. 151, 159

DAC Digital to Analog Converter. 97, 102

DC Direct Current (by extension, anything constant). 17–20, 191

DF-DLR Dual Frequency Dual Lifetime Referencing. 105

DFT Discrete Fourier Transform. 107, 108, 113, 150

DLR Dual Lifetime Referencing. 7, 71, 79, 80, 94, 98, 100–102, 104–107, 109, 111, 113, 115, 117, 119, 121, 123, 127, 129, 132, 148, 153, 159

DMF Dimethylformamide. 134, 136–138, 140, 144–146, 151, 160, 193

DMSO Dimethyl sulfoxide. 134, 136–138, 140

DRS Diffuse Reflectance Spectometry. 91–93, 164

DSP Digital Signal Processor. 102

EDTA Ethylene Diamine Tetraacetic Acid. 21, 22, 27–29, 31

EVOH Ethylene-vinyl alcohol. 137

f-DLR frequency-based Dual Lifetime Referencing. 71, 102, 103, 106, 107, 124–127, 129, 142, 143, 148, 150, 157, 159–161, 165

FDA Food and Drug Administration. 61, 176

FET Field-Effect Transistor. 83

FRET Fluorescent Resonance Energy Transfer. 79, 99–101, 126

FWHM Full Width at Half Maximum. 31

H_2O Water. 86

H_2S Hydrogen sulfide. 69

HHb Deoxy-Haemoglobin. 7, 9, 11, 15–17, 19–26, 28–36, 38, 39, 88, 156, 158

HiCN Cyan-Met-Haemoglobin. 158

HOPSA Trisodium salt of 8-hydroxyl-1,3,6-pyridine trisulfonic acid. 133

HPMC Hydroxy propyl methylcellulose. 79, 138–140, 143–146, 148–154, 160

HPTA Hydroxypyrenetrisulfonic acid. 133

HPTS 1-hydroxy-pyrene-3,6,8-trisulfonate. 78, 79, 95, 101, 102, 104, 129–136, 139, 141, 143, 144, 146–154, 157–161, 192

IFE Inner Filter Effect. 79, 99–102, 127, 128

IPA Isopropyl alcohol. 134

ISFET Ion-Selective Field-Effect Transistor. 75, 77, 78, 89, 91

L-CLT Lyapunov's Central Limit Theorem. 111

LDF Laser Doppler Flowmetry. 50, 60, 61

LED Light Emitting Diode. 17, 19, 20, 31, 74, 79, 91, 93, 96–98, 101, 102, 124, 130, 132, 133, 141, 142, 146–148, 150, 160, 164, 180–185, 191, 195

LOTUS Law Of The Unconscious Statistician. 109, 113

MANOVA Multivariate ANalysis Of VAriance. 164

MAP Mean Arterial Pressure. 60

MEMS Micro Electro-Mechanical Systems. 74, 75

MetHb Met-Haemoglobin. 11, 15–17, 20, 29, 31, 39

MOF Metal Organic Framework. 159

MOSFET Metal Oxyde Semiconductor Field-Effect Transistor. 77

N_2 Di-nitrogen. 7, 22, 25, 26, 28–31, 33–35, 55, 79, 86–88, 97, 102, 106, 142, 146, 147, 149, 152, 153, 158

$Na_2S_2O_4$ Sodium dithionite. 29

$Na_2S_2O_5$ Sodium metabisulfite. 22, 29

NADH Oxydised Nicotinamide Adenine Dinucleotide. 38

NAF α-naphtolphtalein. 99

NDIR Non Dispersive Infra-Red. 5, 42, 47, 55, 72–74, 81, 87–93, 159

NH Non-Heated. 46, 51, 54, 57–59, 64, 163, 177

NIR Near Infra-Red. 39, 157, 158

O_2 Di-oxygen. 1, 2, 9–12, 15, 26, 38, 41, 68, 80, 82, 85–87, 90, 91, 100, 105, 125–127, 129, 135, 150, 152, 153, 156, 157

O_2Hb Oxy-Haemoglobin. 9, 11, 15–17, 19, 20, 22–26, 28–31, 33–36, 38, 39, 156, 158, 173

$p_{Se}CO_2$ Inner sensor carbon dioxide partial pressure. 43–45, 49–51, 55, 56, 58

$p_{v\text{-}a}CO_2$ Carbon dioxide venous-to-arterial pressure difference. 4

P.U. Perfusion Units. 50, 60

$paCO_2$ Arterial carbon dioxide partial pressure. 1–6, 8, 11–14, 25, 41, 46, 58, 61, 64, 69, 88, 90, 93, 156–158, 161, 162, 165

PAN Polyacrylonitrile. 128, 135, 137, 138, 140, 143–146, 148, 151–154, 160, 193

paO_2 Arterial dioxygen partial pressure. 2, 6, 10, 11

PCB Printed Circuit Board. ii, 47, 48, 175

pCO_2 Carbon dioxide partial pressure. 3–6, 43, 48, 57–59, 61, 76, 77, 79, 81–84, 87, 90–92, 94–98, 100, 101, 104–106, 133, 148, 158, 161, 162, 164, 165

PDF Probability Density Function. 107–110, 123, 124

PDMS Polydimethylsiloxane. 140

PEG Polyethylene glycol. 148, 149

PEN Polyethylene naphthalate. 79, 160

PET Polyethylene terephthalate. 66, 79, 91, 128, 138, 160

$petCO_2$ End-tidal carbon dioxide partial pressure. 4–6, 58

PI Perfusion Index. 20

PLA Poly-lactic acid. 47, 48, 191

PMMA Poly(methyl methacrylate). 137

pO_2 Dioxygen partial pressure. 10, 11, 64, 68, 69, 106

PPG Photoplethysmography. 18, 21, 92, 93, 148, 164

PPTA Poly(p-phenylene terephthalamide). 137

PTFE Polytetrafluoroethylene. 76–79, 91, 145, 193

PVA Polyvinyl alcohol. 139

PVC Polyvinyl chloride. 36, 135

PVCD Poly(vinylidene chloride-co-vinyl chloride). 128, 137

PVDF Polyvinylidene fluoride. 65

RH Relative Humidity. 41, 65–69, 76, 137, 139, 140, 142, 148–150

RMSE Root Mean Square Error. 107, 113, 115–120, 123, 124, 146–148

ROS Reactive oxygen species. 127

Ru-bpy Tris(2,2'-bipyridyl) ruthenium (II) dichloride. 130–133

Ru-dpp Tris(4,7-diphenyl-1,10 phenanthroline) ruthenium (II) dichloride. 102, 104, 127, 128, 130–136, 138, 141, 143, 144, 146–148, 150–154, 159–161, 192, 193

Ru-pn Tris(1,10 phenanthroline) ruthenium (II) dichloride. 130–133

saCO$_2$ arterial Carbon dioxide saturation. 25, 28, 31

saO$_2$ arterial Di-oxygen saturation. 2, 11, 14, 16, 19, 24, 31

SD Standard Deviation. 12, 52, 62

SMD Surface Mount Device. 145, 193

SNR Signal to Noise Ratio. 108, 117–120, 122–124, 146, 147

SNR$_{dB}$ Signal to Noise Ratio in dB. 113, 115, 117, 118, 120–123

spO$_2$ Pulsed di-oxygen saturation. 2, 19–21, 24

STP Standard Temperature and Pressure. 47

SulfHb Sulf-Haemoglobin. 15–17

t-DLR time-based Dual Lifetime Referencing. 159

TB Thymol Blue. 99, 100

TBP Tributyl phosphate. 80

tcpCO$_2$ Transcutaneous carbon dioxide partial pressure. 5–8, 41–46, 49–51, 55, 57, 58, 61, 63, 64, 67, 69, 88, 90, 92, 93, 148, 151, 156–160, 162, 164, 165, 176, 177

tcpO$_2$ Transcutaneous dioxygen partial pressure. 68

TEAH Tetraethyl ammonium hydroxide. 144, 146

TEDA Triethylenediamine. 151

TEWL Transepidermal Water Loss. 65–67

THF Tetrahydrofuran. 134

TIA TransImpedance Amplifier. 97, 142, 153, 160

TL;DR Too Long; Didn't Read. i–iii, 1, 9, 41, 71, 125, 155, 194, 195

TMAH Tetramethyl ammonium hydroxide. 80, 149

TOAH Tetraoctyl ammonium hydroxide. 96

UART Universal Asynchronous Receiver Transmitter. 47, 48, 175

USB Universal Serial Bus. 47, 142, 175, 195

WHO World Health Organisation. 2

Chapter 1

Introduction

TL;DR

Monitoring the arterial carbon dioxide (CO_2) partial pressure—paCO_2—is of paramount importance in clinical practice. The latter can be measured directly (arterial puncture) or through proxies (tracheal intubation and transcutaneous monitoring). However, current monitors suffer from a variety of drawbacks which hamper their wider use. Thus, there is an urging need for a new kind of non-invasive, low-cost, and portable—if not wearable—biomedical CO_2 monitor.
Two main research avenues were identified to address this issue. The first one extrapolates the principle of pulse oximetry to the non-invasive determination of the arterial Carbamino-Haemoglobin (CO_2Hb) content. This approach mainly focused on spectrophotometric considerations but ultimately proved to be a dead-end—it is the object of Chapter 2. The second approach relies on transcutaneous CO_2 diffusion. It is further divided into: studying the transcutaneous CO_2 diffusion phenomenon itself—Chapter 3—finding a CO_2 sensing technology compatible with it—Chapter 4—and putting this knowledge into practice by actually designing such a transcutaneous sensor—Chapter 5.

Previous chapter Main Table Of Content (TOC) Next chapter

1.1 Carbon Dioxide as a Vital Sign

As Thomas Henry Huxley argued during his 1874 lecture to the British Association[2] “We are conscious automata”(1). And if we are but machines—although highly sophisticated ones—the question that arises next when it comes to our survival is that of maintaining our operating conditions—what biologists calls homeostasis. Maintaining this homeostasis throughout the human body requires energy and generates wasteful by-products, and just as a petrol engine needs:

1. some fuel (petrol) and
2. an oxidizing agent (di-oxygen (O_2)) to produce
3. a useful work (mechanical motion) as well as
4. unwanted by-products that have to be disposed of (heat and exhaust gases),

our body needs:

1. an energetic substrate (such as carbohydrates, lipids or proteins) and
2. an oxidizing agent (also O_2) to produce
3. a useful work (*e.g.* maintaining homeostasis, moving, breeding) as well as

---

(1) Actually the exact wording comes from one of his essays, published the same year[3]. Over a century of scientific research have gone by, and further nails have been added to the coffins of free will and soul, Anthony Cashmore further adding that “Neither religious beliefs, nor a belief in free will, comply with the laws of the physical world”[4].

4. unwanted by-products that have to be disposed of (heat, carbon dioxide (CO_2), and various excreta)

Medicine, which may be defined as "the process of enabling people to increase control over, and to improve their health"[5], aims at maintaining homeostasis as long as possible. To this end, the monitoring of so-called *vital signs*—blood pressure, temperature, pulse rate and respiratory rate[6]—is of crucial importance to ensure that no illness or injury impedes the normal functioning of the body. In addition to these four traditional vital signs, pulse oximetry[7], end-tidal CO_2[8, 9], walking speed[10] or pain[11] have all been proposed as supplementary fifth (or sixth) vital sign by a number of authors. These auxiliary variables, along with others—*e.g.* arterial blood glucose level or bicarbonate ion concentration—make up the set of *physiological parameters*, whose monitoring can give the clinician valuable clues about their patient's state.

The choice of which parameter to monitor heavily depends on the patient's physiology, and the provided information varies considerably from one parameter to another, some parameters being very sensitive but not very specific—*e.g.* heart rate—while others are very specific, but harder to monitor—*e.g.* secretin plasma concentration. Among them, blood gases—namely O_2 and CO_2—and their arterial partial pressures (paO_2 and $paCO_2$) give respiratory as well as circulatory clues on the state of a patient[12]. This latter characteristic is particularly valuable given that, according to the World Health Organisation (WHO), three of the six leading causes of death worldwide are related to respiratory diseases, as illustrated in Figure 1.1. As an example, Chronic Obstructive Pulmonary Disease (COPD) has been shown to entail a significant increase in $paCO_2$ combined with a decrease in pulsed di-oxygen saturation (spO_2)(2) along the course of its progression[17, 18]. It has further been shown that $paCO_2$ is a good predictor of survival and hospitalisation rates in COPD patients[19–21], as well as in other pathologies—*e.g.* tuberculosis[22] or pulmonary embolism[23]. Besides, the chronic accumulation of CO_2 in the organism—a condition termed chronic hypercapnia—also has several detrimental health effects related to the messaging role of CO_2 in the body[24–26]. Thus, the continuous monitoring of $paCO_2$ is of paramount importance in medical practice, especially for patients presenting severe respiratory disorders.

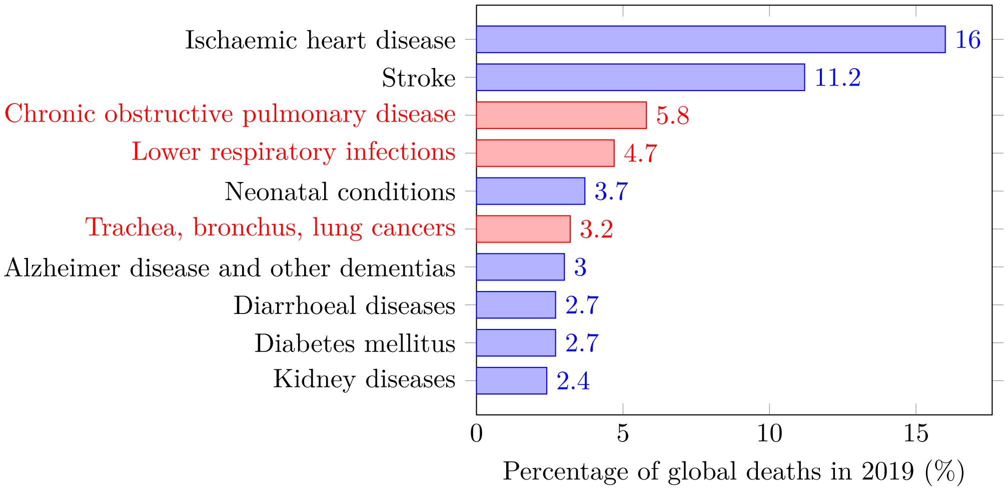

Figure 1.1: The ten leading causes of death worldwide, according to the latest WHO report (2019)[27]. Three out of ten—in red—concern respiratory-related diseases, which accounted for 13.7% of deaths worldwide in 2019.

1.2 CO_2 Sensing in Medical Practice

As a by-product of aerobic metabolism, CO_2 is ubiquitous in human body, and its influence on pH makes its regulation in the organism a key parameter to maintain homeostasis[28]. In particular, CO_2 equilibrium is controlled by several mechanisms governing the efficiency of gas exchange[29,

---

(2) spO_2 is the name given to the arterial di-oxygen saturation (saO_2) when measured by pulse oximetry—Section 2.2.2. saO_2 and paO_2 are linked together by the oxygen–haemoglobin dissociation curve *a.k.a.* "Barcroft curve" from the name of Joseph Barcroft, the British physiologist that discovered it[13]. spO_2 is thus often used as a proxy for paO_2 in a clinical setting, given its ease of measurement compared to an arterial puncture[14–16], as discussed below—see Section 2.1.1.

30] and by renal regulation of plasma bicarbonate ions[31]. Both the excess or deficiency of CO_2 in the organism—termed hyper- and hypocapnia, respectively—can have either beneficial or deleterious effects on a patient's outcome, depending on their condition[32]. As a consequence, CO_2 monitoring is of major importance in clinical care. Its measurement can be performed in three locations, presented in order of decreasing invasiveness:

1. inside the body with blood or tissues sampling—Section 1.2.1,
2. in the exhaled air with airway capnometry—Section 1.2.2,
3. on the skin with transcutaneous capnometry—Section 1.2.3.

An illustration of these locations is provided in Figure 1.2. For each one of them, the clinical significance of the corresponding pCO_2 measurement is first presented, and its probing modalities in practice are then described. One should bear in mind through the remainder of this section that CO_2 transport in the human body takes three distinct forms: dissolved CO_2, bicarbonate ions, and carbamate compounds$^{(3)}$. Those are in constant equilibrium for a given blood pH, and could give rise to as many measurements—blood pCO_2, $[HCO_3^-]$, Carbamino-Haemoglobin (CO_2Hb) concentration and pH[33, 34]. Yet, for both practical and physiological reasons, pCO_2 measurements have been predominantly adopted from a clinical perspective.

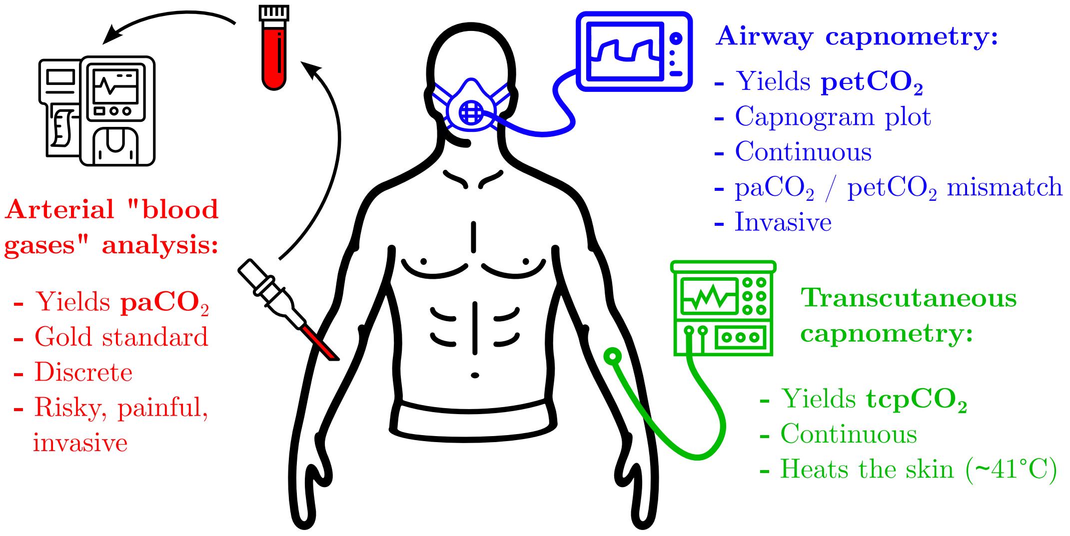

Figure 1.2: The three *in vivo* CO_2 probing modalities and their key features.

1.2.1 Blood Gas Analysis

1.2.1.1 Clinical Significance

Arterial blood sampling is considered to be the gold standard for the assessment of whole-body CO_2 content. Arterial blood exits the lungs without perfusing any organ. Contrary to capillary or venous blood, it is thus fully oxygenated with a low CO_2 content, and is not impacted by the activity of the organ that it perfuses[35, 36]—see Section 3.2.6.4.3. Consequently, the arterial partial pressure in CO_2—$paCO_2$—best represents the global haemodynamic status of patients, and gives important clues about their metabolism and homeostasis[12, 37]. There is an extremely large panel of clinical applications for $paCO_2$ measurements, including acute and chronic respiratory failures[17, 38], mechanical ventilation assessment[19, 22], general anaesthesia—but also sedation in patients at risk of hypoventilation—monitoring[39], or resuscitation procedures[40]. Due to the painful and potentially risky aspects of arterial blood puncture[41], other blood sampling techniques have been explored. In particular, arterialised capillary blood sampling was reported to be an acceptable surrogate for arterial blood sampling[42]. In contrast, peripheral venous blood cannot be used to this end[43], nor can central venous blood[44–46], even if both may be used for trend analysis. Venous blood pCO_2 measurement is nevertheless interesting in

---

(3) This aspect is further detailed in the next chapter.

critically ill patients, for whom measuring the venous-to-arterial carbon dioxide partial pressure difference ($p_{\text{v-a}}CO_2$)—or calculating the venous-to-arterial carbon dioxide content difference—makes it possible to detect organ hypo-perfusion[47].

More localised pCO_2 measurements have also been performed with intra-tissue probing—in particular into the brain[48], liver[49] or skeletal muscles[50]—yielding crucial information about the perfusion of the organ under study. Gastric tonometry and sublingual capnometry have also been explored, but their clinical interest have yet to be fully demonstrated[51, 52].

1.2.1.2 Probing Modalities

In vivo CO_2 probing can be achieved under two distinct modalities. Either pCO_2 is measured *in situ* or a biological sample is collected to be further analysed.

In the first case, the sensor is brought to the analyte. This is notably what happens for intra-tissue pCO_2 monitoring. In such cases, the sensor is inserted directly into the organ or blood vessel that is to be probed by means of a catheter, for instance. This setting allows for continuous monitoring with a low latency, which is only dictated by the response time of the chosen pCO_2 sensor[53].

In the second case, often used for blood pCO_2 measurements, the analyte is brought to an external analyser and an arterial or venous line placement may be performed to facilitate repeated blood sampling. However, this setting allows only discrete monitoring since a blood sampling must be performed every single time a pCO_2 is desired. In addition, the blood samples must be analysed quickly upon collection, which may lead to additional logistic difficulties compared to *in situ* sensing[54], even if recent hand-held blood gas analysers tend to mitigate this issue[55].

In practice, two main technologies have been used to perform blood gas analysis: optodes using dye-based CO_2 sensing—as described in Section 4.1.2.4[53, 56]—and electrochemical sensors such as the Stow-Severinghaus electrode—described in Section 4.1.2.2[57].

1.2.2 Airway Capnometry

1.2.2.1 Clinical Significance

Airway capnometry—from Greek *capnos* ($\kappa\alpha\pi\nu o\varsigma$), smoke, vapour—is the measurement of the amount of CO_2 in exhaled air. Please note that there is a semantic distinction between capno*metry*—which consists in the measurement of $petCO_2$, the end-tidal pCO_2—and capno*graphy*—which usually refers to the plot of a capnogram: pCO_2 in the exhaled air as a function of time, or volume. The distinction between capnometry and capnography is made clear in Figure 1.3.

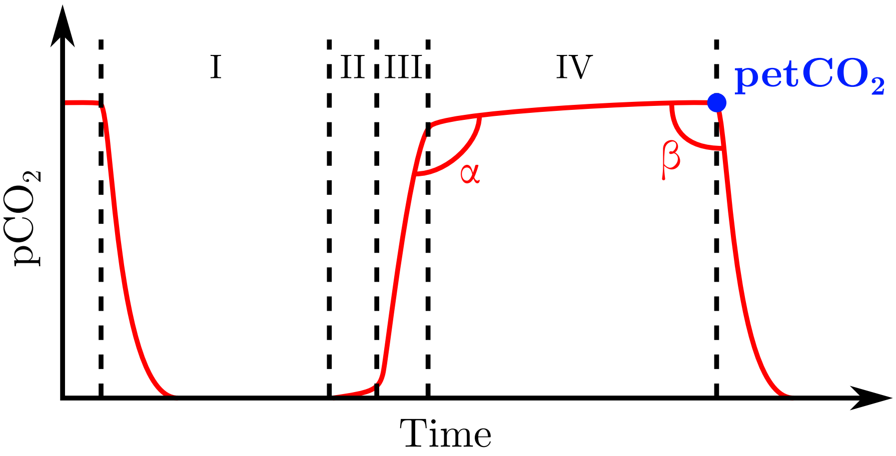

Figure 1.3: A capnogram yields important clinical clues on the state of the patient or quality of their intubation by analysing the different breathing phases—inspiration (I), and expiration: dead-space volume (II), mixed dead-space and alveolar air (III) and alveolar air (IV)—and the two α and β angles[58, 59]. More narrowly, capnometry is only interested in knowing the more concise end-tidal pCO_2 value reached at the end of the plateau (IV): $petCO_2$.

Capnography is particularly useful in medical practice since it gives information about respiratory airflow, CO_2 production and elimination, respiratory quotient, or the quality of endotracheal intubation. It can also be used to detect ventilation / perfusion inadequacy, apnea, COPD or heart failures[60, 61]. For its part, $petCO_2$ has proven to be a reliable proxy for $paCO_2$ under stable haemodynamic conditions, with $petCO_2$ being usually 2–5 mmHg lower than $paCO_2$[60]. However, the correlation between $petCO_2$ and $paCO_2$ vanishes in case of elevated physiological dead space or ventilation perfusion mismatch[12, 62]. It can also be difficult to use capnometry on neonates due to the small volume of exhaled air that they produce[63].

Interestingly, Siobal *et al.*[60] pointed out that, while airway capnometry is often criticised for its inaccuracy as a $paCO_2$ proxy—*e.g.* in case of ventilation / perfusion mismatch, elevated dead space, or poor endotracheal placement—the very root causes of this inaccuracy may be characterised by performing a simultaneous $paCO_2$ measurement. In other words, if simultaneous $paCO_2$ and $petCO_2$ measurements are performed in the same patient, discrepancies between the two values may reveal one of the afore-mentioned issues.

1.2.2.2 Probing Modalities

Two distinct probing modalities exist for airway capnometry: mainstream or sidestream measurements. In mainstream capnometry, the CO_2 sensor is positioned on the main airway of the intubated patient, so that the whole breathed air flow is forced through it. This technique yields instantaneous $petCO_2$ measurement and real-time capnogram plot. Historically, mainstream capnometry has long been criticised because the additional sensor on the patient's airway was bulky, fragile, and led to an additional respiratory dead space. In particular, the bulkiness of mainstream sensors may dislodge the endotracheal tube in young patients[60, 63]. In response, recent designs have been improved to become more rugged, compact, and with minimal sampling volume, partially mitigating these drawbacks[64, 65].

In contrast, sidestream capnometers consist in a small diameter sampling tube, which continuously aspirates a fraction of the patient's breathed air. The air is then conveyed to an external monitor wherein both the analysis and display functions are performed. Contrary to the mainstream technique, a delay is present between air sampling and the monitoring of its CO_2 content[58]. Additionally, distortions of the measured capnogram may occur, especially on its more rapidly changing portions, and sidestream-measured $petCO_2$ may be slightly underestimated compared to the mainstream-measured one[66].

In practice, airway capnometry is more often than not measured using the infrared absorption of CO_2, either using Non Dispersive Infra-Red (NDIR) sensors—see Section 4.1.1.1—or photoacoustic sensors—see Section 4.1.1.2[58, 60]. Additionally, colorimetric dye-based sensors—see Section 4.1.2.4—are also routinely used to assess the correct positioning of endotracheal intubation, although they only provide a qualitative information about the latter, and not a quantitative $tcpCO_2$ reading[67].

1.2.3 Transcutaneous CO_2 Sensing

1.2.3.1 Clinical Significance

Transcutaneous pCO_2—$tcpCO_2$—measurements are clinically relevant in two different situations: either as a surrogate for $paCO_2$ in patients with a normal tissue perfusion or as an evaluation tool to measure the $paCO_2$–$tcpCO_2$ gap in patients with an abnormal perfusion[68].

In patients with normal circulation and peripheral perfusion, $tcpCO_2$ correlates well with $paCO_2$ and, as such, may be used in all situations where $paCO_2$ is required[69]. This correlation is particularly influenced by the choice of the measuring site, and by the probe temperature, as disclosed in the next section.

Alternatively, measurements of the $paCO_2$–$tcpCO_2$ gap proved to be a reliable predicator of mortality in case of shock[70]. In such a view however, a simultaneous measurement of $paCO_2$ is required in addition to $tcpCO_2$ monitoring. One may notice the similarity between this technique, and the proposal of Siobal *et al.* for $petCO_2$ mentioned earlier—see Section 1.2.2.1.

1.2.3.2 Probing Modalities

$tcpCO_2$ measurements can be performed with the attachment of a transcutaneous probe on the skin by means of a disposable, adhesive mounting ring. The measuring site and sensor temperature depend on what is to be measured: for instance, when searching for a $paCO_2$ surrogate, it is recommended to place the $tcpCO_2$ probe at the earlobe with a setpoint temperature above 42 °C for the best results[69]. However, an elevated skin temperature can be a source of skin burn or thermal injury, especially in the neonates, requiring a frequent change of the probe site[71]. A compromise may then be found between skin temperature—and thus site change frequency—and accuracy of the tcpCO_2 measurement[72]. When assessing local perfusion or shock condition—on the contrary—a temperature as low as 37 °C may be used at the site of interest[73]. Different temperatures can also be used to assess changes in perfusion as a function of temperature[70].

Technically speaking, the tcpCO_2 is measured by means of a miniaturised Stow-Severinghaus electrode—mainly a pH-meter bathing in a bicarbonate solution, see Section 4.1.2.2—which can be heated anywhere in the 37–45 °C range[68].

1.3 The Need for a Better Alternative

While the above-mentioned monitors are routinely used in clinical practice, they are not only expensive and invasive, but also bulky and unpractical—for they require frequent external interventions for calibration or sampling purposes. These drawbacks, in addition to turning pCO_2 monitors into a coveted resource used sparingly in the hospital, make them unusable outside the clinical setting.

Yet, bringing pCO_2 monitors in homes would be highly desirable in a telemonitoring context for home use, reducing the need for hospital visits, and thus the risk of contracting a nosocomial disease. Indeed, if the positive impact of tcpCO_2 telemonitoring is yet to be demonstrated—for the obvious reason that the corresponding wearable tcpCO_2 monitor does not exist at the time being—several clinical trials demonstrate the beneficial contribution of telemedicine—*a.k.a.* telehealth—on both patient's outcome and costs of admission in a variety of conditions[74–76]. Additionally, the outbreak of contagious pandemics—such as COVID-19[77]—and the rapid development of the health wearable market[78–81] may also promote the use of telemonitoring in medical practice. Non-invasive paO_2 and paCO_2 monitoring techniques have been an active research field for decades[82–84], but while pulse oximetry proved to be a reliable proxy for paO_2[14, 15], no satisfactory equivalent exists for paCO_2.

In this context, the development of a non-invasive, low-cost, and portable—if not wearable—biomedical pCO_2 monitor appears highly desirable.

To this end, two main research avenues were explored in the course of this doctoral work: the first one focuses on CO_2Hb and proved to be but a dead end, while the second one focuses on transcutaneous CO_2 diffusion and led to some successes.

1.3.1 The Carbamino-Haemoglobin (CO_2Hb) Avenue

The idea behind the CO_2Hb avenue was the following: since *(i)* the oxygenation state of haemoglobin influences its absorption spectrum[85] and *(ii)* this change in absorption can be detected optically transcutaneously *via* pulse oximetry[14, 15], if *(iii)* a similar change in haemoglobin absorption spectrum can be triggered by the formation of haemoglobin carbamate compounds—*i.e.* CO_2Hb—then *(iv)* the theory behind pulse oximetry could be applied to the optical transcutaneous determination of the arterial CO_2Hb concentration. Then, since an equilibrium exists between this concentration and paCO_2[33], the latter could be measured non-invasively.

Of course, this train of thought could only succeed if hypothesis *(iii)* were valid. Due to the absence of information on the absorption spectrum of CO_2Hb in the literature in 2019, the first part of this doctoral work focused on the spectrophotometry of haemoglobin derivatives—this is the object of Chapter 2. In brief, I literally gave my blood for Science: human haemoglobin was equilibrated with three gases—ambient air, di-nitrogen (N_2), and CO_2—and the corresponding absorption spectra were subsequently measured over the 235–1000 nm range. These measurements were published in the Journal of Biomedical Optics in 2020[86], but revealed no differences between Deoxy-Haemoglobin (HHb) and CO_2Hb absorption spectra. Additional fluorescence measurements were also performed, searching for differences in either the excitation or emission spectra of haemoglobin upon CO_2 exposition. There again, no major variations could be observed between the fluorescence properties of HHb and CO_2Hb.

In light of the above, hopes of using a technique akin to pulse oximetry for determining the arterial blood CO_2Hb concentration shattered. Subsequently, I reoriented my studies towards transcutaneous CO_2 diffusion.

1.3.2 The Transcutaneous CO_2 Diffusion Avenue

1.3.2.1 Skin Permeability Towards CO_2

The transcutaneous diffusion of CO_2 is at the very core of current tcpCO_2 monitors. Yet, this phenomenon was poorly documented in the literature, with only a few ageing studies available, which were often performed on a limited number of subjects, and without skin temperature regulation. Since skin permeability towards CO_2 is expected to have a major influence on the response time of tcpCO_2 sensors, I first aimed at better characterising it. In particular, the influence of skin temperature on the latter permeability was vastly unknown. Yet, this temperature / permeability relationship is of crucial importance in the design of a sensor: **not** heating the skin—or heating it as little as possible—is highly desirable from an energy consumption point-of-view, thus favouring the integration of the said sensor into a wearable. To fill this knowledge gap, a custom sensor was developed and a clinical study was conducted, allowing the measurement of transcutaneous CO_2 diffusion rates at the arm and wrist on 40 healthy subjects at five different temperatures. These works are summarised in a 2023 Frontiers in Physiology article[87], and are the object of Chapter 3.

1.3.2.2 Choosing a CO_2 Sensing Technique

Once the rate of diffusion of CO_2 through the skin was better known, the next logical step was to choose a CO_2 sensing technique for the tcpCO_2 sensor-to-be. To this end, a comprehensive review of CO_2 sensing techniques was performed and published in MDPI's Sensors journal[88]. From this review, I concluded that CO_2-responsive fluorescent thin film sensors were a promising avenue. Further research on this sensing modality brought into light the Dual Lifetime Referencing (DLR) sensing scheme—a phase-based approach with sinusoidal illumination power[89]—for which extensive mathematical derivation were performed. Briefly, those derivations aimed at knowing the reachable accuracy on a CO_2 measurement, given the illumination power, measurement duration, and noise levels—they were published in the APSIPA Transactions on Signal and Information Processing[90]. Finally, the chemistry of fluorescence-based CO_2 sensing was also modelled, although corresponding experimentations confirming or infirming the presented influence of the different chemicals' concentration are lacking. These different works are compiled in Chapter 4.

1.3.2.3 CO_2-Sensitive Fluorescent Thin Films

The theoretical aspects of the issue at hand having been sufficiently delineated to allow for initial *in vitro* experiments, the next step was the fabrication of CO_2-sensitive fluorescent thin films, probed through a DLR sensing scheme. To this end, the luminescence properties of the selected luminophores were characterised at different temperatures and in the presence / absence of humidity and CO_2. Early bi-layer films showed promising results, having the ability to measure CO_2 levels in the 0–10% range with a response time below 1 min. These results were the object of a short communication at the NEWCAS 2024 conference[91]—4-pages paper and lecture—and are reviewed in much more details in Chapter 5.

1.3.3 Further Research is Needed

In spite of the relentless years of meticulous work that were dedicated to this doctoral thesis, many an aspect of the presented research have been left in the shadows. Those are explicitly indicated by the "further research is needed symbol"—as mentioned in the foreword—and are reviewed in the concluding chapter—Chapter 6. Among them, the study of the influence of skin temperature on the tcpCO_2 / paCO_2 correlation is probably the strongest remaining lock to the development of wearable tcpCO_2 sensors, as we shall see...

further research is needed

Chapter 2

Carbamino-Haemoglobin (CO_2Hb) Optical Properties

TL;DR

CO_2 blood transport follows three different pathways: as a dissolved gas, as bicarbonate ions, or as CO_2Hb (and other carbamate compounds). An equilibrium exists between these three quantities and blood pH. Thus, determining blood CO_2Hb concentration would give valuable insights for total blood CO_2 content estimation. The non-invasive determination of the concentration of certain haemoglobin species can already be achieved by pulse oximetry, which leverages the oxidation dependence of haemoglobin's absorption spectrum to estimate the relative fractions of HHb and Oxy-Haemoglobin (O_2Hb). Thus, it was expected that a similar technique, termed pulse *carbametry*, could be envisioned for transcutaneous CO_2Hb concentration measurement, given that HHb and CO_2Hb absorption spectra would be different.
Alas, CO_2Hb spectrophotometry revealed no exploitable difference between the latter spectra, even if those results still have the merit of being the first report of CO_2Hb absorption spectrum. Additional research was conducted to assess the feasibility of transcutaneous haemoglobin fluorescence measurements but also yielded negative results. Consequently, this research avenue was abandoned, and further chapters focus on transcutaneous gaseous CO_2 diffusion and sensing.

Previous chapter Main Table Of Content (TOC) Next chapter

2.1 Blood Gases Transport in the Body

Before delving into the intricacies of CO_2Hb optical properties, some basic knowledge of gaseous transport throughout the body is necessary, and is the object of the present section. As mentioned in the previous chapter, cellular respiration consumes O_2—which needs to be brought from the outer air to the cells that need it—and produces CO_2—which in turns need to be drained away from the cells that produce it so as to be exhaled in the outer air. These gaseous exchanges are predominantly performed by the lungs(1), which act as a large exchange membrane between the diaphragm-ventilated air and the capillary blood that perfuses them.

In a nutshell, O_2-rich and CO_2-poor arterial blood is first pumped by the heart throughout the body, where it goes from arteries to arterioles and finally capillaries to perfuse all organs. There, O_2 is released from the red blood cells—*a.k.a.* erythrocytes—of the capillary blood to the surrounding cells that will consume it and release CO_2 as a result. This CO_2 is then carried away by the exiting capillary blood, which is subsequently collected by venules and drained by veins, carrying the O_2-depleted, CO_2-rich venous blood back to the heart. The latter then pumps it through the lungs, wherein it will replenish in O_2 from—and release some of its CO_2 into—the alveolar air. This O_2-rich and CO_2-poor blood then enters the heart again, to be pumped throughout the whole body, and the cycle goes on. This is, of course, a somewhat

---

(1) The skin is also involved in human respiration, accounting for about 1–3% of total exchanges in adults[92], and up to 6–9% in newborns[93]; cutaneous CO_2 diffusion will be discussed in greater detail in Chapter 3.

simplified view of what actually happens, and I can only recommend the curious reader to dig into Michael Levitzky's *Pulmonary Physiology*[94], or Andrew Lumb's *Nunn's Applied Respiratory Physiology*[34] for a much more complete overview of the subtleties of the respiratory function in humans.

This crude outline of respiratory physiology emphasises the crucial role of blood for gas transport, as it must be able to convey large quantities of O_2 and CO_2 between the lungs and the perfused organs. This is achieved by various mechanisms, which are presented in Figure 2.1 with their relative contributions to gas transport, and described in the following sections.

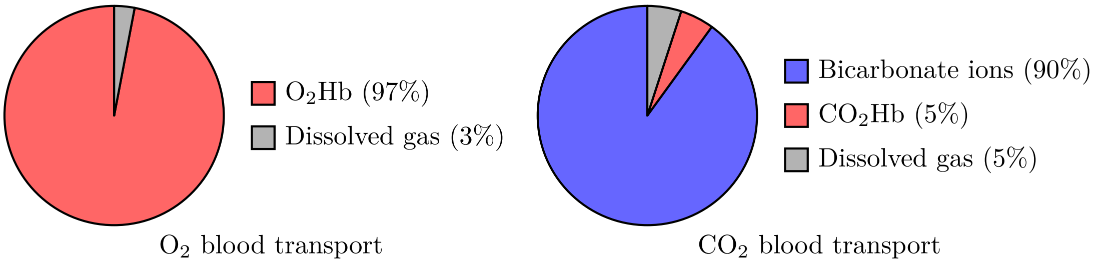

Figure 2.1: Blood gases transport for O_2 and CO_2.

2.1.1 O_2 Transport

O_2 is present in human blood in two different forms: as dissolved gas (only 3% of the total amount of O_2 in blood) and combined with haemoglobin (the remaining 97%). Although O_2 is not at the heart of this thesis, the following developments are relevant to introduce the notions of solubility, dissociation curves, and haemoglobin (oxygen) binding. This short digression on O_2 transport is also mandatory to understand the pulse oximetry principle—presented in Section 2.2.2—that is extrapolated to CO_2 with the concept of pulse carbametry—introduced in Section 2.3.

2.1.1.1 As dissolved gas

O_2 is present in blood as a dissolved gas according to Henry's law—named after the English chemist William Henry (1774-1836)—which states that the amount of dissolved gas in a liquid is proportional to its partial pressure in the gas phase[95]. The coefficient linking the partial pressure of the gas phase to the amount of gas dissolved in the liquid is known as the *solubility*. The latter is function of the nature of the considered gas and liquid, as well as the temperature. For instance, O_2 solubility in human blood at 37°C is known to be equal to 0.023 mL of O_2 per mL of blood and per 1 atm (760 mmHg)⁽²⁾ of pO_2[96]. Given a normal paO_2 of 100 mmHg[97], the concentration of O_2 dissolved in human arterial blood is⁽³⁾

$$[O_{2(\text{gas})}] = 3\ \text{mL}_{O_2}.\text{L}^{-1} = 1.2\ \text{mM} \tag{2.1}$$

As pointed out by Lewitzky[94, p. 143], if dissolved O_2 were the only oxygen source in blood, the required cardiac output to match the body consumption in O_2 should be around 83 L.min^{-1}. Knowing that the maximum cardiac output is about 25 L.min^{-1}, dissolved oxygen is clearly not sufficient for the needs of human metabolism.

2.1.1.2 Combined with haemoglobin

Indeed, dissolved oxygen is only the top of the iceberg, and most blood-carried O_2 is in fact bound to haemoglobin in the erythrocytes. Haemoglobin is an iron-containing metalloporphyrin that is composed of four subunits called haems. The latter act as fixation sites for O_2, each haem being able to bind to one O_2 molecule[98]. Haemoglobin concentration in healthy human blood is about 14 g.dL^{-1}, and given that 1 g of haemoglobin can carry up to 1.39 mL_{O_2}, human blood can theoretically carry up to about 200 $\text{mL}_{O_2}.\text{L}^{-1}$[34, Chap. 11] (*i.e.* ≈ 80 mM). Compared to the 3 $\text{mL}_{O_2}.\text{L}^{-1}$ of dissolved O_2, this explains the 98%–2% repartition for O_2 transport in blood presented in Figure 2.1. Since the overwhelming majority of blood O_2 is transported bound to haemoglobin, only the latter mechanism is considered in the next paragraph.

---

(2) Although I tried to stick with SI units throughout this thesis, pressures are conventionally expressed in mmHg in medical practice. The reader should bear in mind that 1 atm = 1.01325 bar = 101 325 Pa = 760 mmHg. Also volumes of gases are noted with the gas name in subscript, *e.g.* mL_{O_2} or mL_{CO_2}.

(3) The symbol "M" stands for 1 molar, *i.e.* 1 mol.L^{-1}.

2.1.1.3 The oxygen-haemoglobin dissociation curve

The binding of haemoglobin with O_2 can be described by the oxygen-haemoglobin dissociation curve, represented in Figure 2.2. First evidenced by Joseph Barcroft in 1909[13]—hence its alternate designation as the “Barcroft curve”—it represents the percentage of O_2-carrying haemoglobin—*i.e.* O_2Hb—over the total *active* haemoglobin concentration—*i.e.* O_2Hb and HHb. This quantity—referred to as the oxygen saturation—is defined as follows:

$$\text{oxygen saturation} = \frac{[O_2Hb]}{[O_2Hb] + [HHb]} \tag{2.2}$$

When measured in arterial blood, the latter quantity becomes the saO_2. Of note, there has been some confusion in the definition of the oxygen saturation in the past decades, with the denominator in Equation 2.2 being replaced by the *total* haemoglobin concentration instead of the *active* one. Although those two quantities are close enough in the absence of dishaemoglobins—such as Met-Haemoglobin (MetHb) or Carboxy-Haemoglobin (COHb)—the gap between them widens as their concentration in blood increases[99]—*e.g.* in case of methaemoglobinemia[100] or carbon monoxide (CO) poisoning[101], for instance.

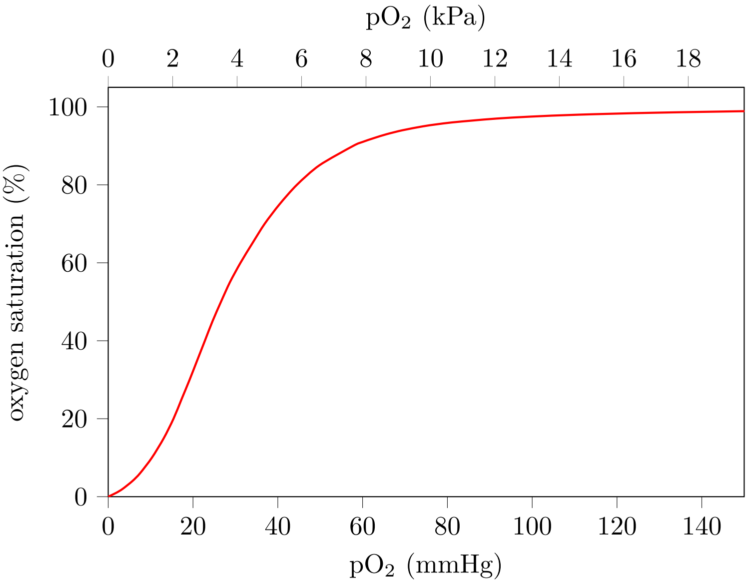

Figure 2.2: The standard oxygen-haemoglobin dissociation curve, as given by Severinghaus at pH = 7.40 and T = 37°C[102]. For reference, the arterial pO_2 is about 100 mmHg while the venous one is about 40 mmHg. However, the corresponding points were not indicated on the curve since *(i)* pH is slightly lower in venous than in arterial blood, and *(ii)* the oxygen dissociation curve is pH-sensitive, shifting to the right as pH decreases[94, Chap. 7].

Yet, granted that the total haemoglobin concentration is known and there are neither significant dishaemoglobins concentrations nor arterial pH changes, the oxygen-haemoglobin dissociation curve can be used to directly convert between a given saO_2 and the corresponding paO_2 and O_2 concentration[34, Chap. 11]. This explains why measuring saO_2 non-invasively has gathered significant efforts for decades, leading to the advent of pulse oximetry—as we shall see in Section 2.2.2.

2.1.2 CO_2 Transport

Blood conveys CO_2 under three different forms: *(i)* as a dissolved gas, *(ii)* bound to proteins—mainly haemoglobin—in the form of carbamate compounds, and *(iii)* as bicarbonate ions HCO_3^-. This section briefly details the three corresponding mechanisms before discussing the equilibria that take place between them, explaining why the determination of blood CO_2Hb concentration may be relevant to $paCO_2$ estimation.

2.1.2.1 As dissolved gas

Similarly to O_2, CO_2 can also dissolve in blood according to Henry’s law, the solubility coefficient of CO_2 in plasma at 37°C being 0.231 $mM.kPa^{-1}$ (0.0308 $mM.mmHg^{-1}$)[34, Table 10.1]. A normal paCO_2 in arterial blood(4) of 5.3 kPa (40 mmHg) thus leads to a dissolved CO_2 concentration equal to

$$[\text{CO}_{2(\text{gas})}] = 1.2\ \text{mM}(= 3.1\ \text{mL}_{\text{CO}_2}.\text{L}^{-1}) \tag{2.3}$$

2.1.2.2 Combined with haemoglobin

CO_2 can also combine chemically with the terminal amine groups of blood proteins—*i.e.* plasma proteins and haemoglobin—according to the following scheme:

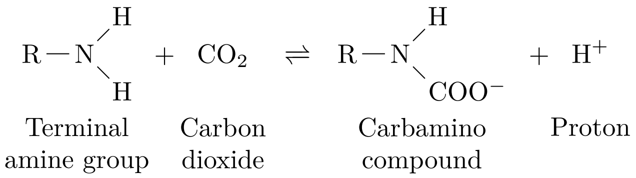

$$\text{R}-\text{N}\begin{smallmatrix}\text{H}\\ \text{H}\end{smallmatrix} + \text{CO}_2 \rightleftharpoons \text{R}-\text{N}\begin{smallmatrix}\text{H}\\ \text{COO}^-\end{smallmatrix} + \text{H}^+ \tag{2.4}$$

When CO_2 binds to haemoglobin, the so-obtained molecule is called Carbamino-Haemoglobin (CO_2Hb), while for other proteins the more general terms *carbamate compound* or *carbamino carriage* are generally used. For reference, plasma total protein levels are normally in the 6–8 g.dL^{-1} range[103, 104]—which would translate into whole blood concentration of 13–18 g.dL^{-1} assuming a 45% haematocrit—while normal haemoglobin concentration in blood is about 13.2±1.1♀ / 14.7±1.4♂ g.dL^{-1} (mean value ± Standard Deviation (SD))[105]. Nevertheless, despite plasma proteins and haemoglobin concentrations being relatively close, the latter accounts for over twice as much CO_2 transport as the former, owing to the greater capacity of haemoglobin for binding to CO_2 molecules. Indeed, under a 5.3 kPa (40 mmHg) paCO_2, CO_2Hb accounts for a concentration of CO_2 in arterial blood of 0.75 mM, while the carbamate compounds of plasma proteins account only for 0.30 mM[33]. Overall, the carbamate-bound CO_2 content of whole arterial blood is thus about 1.05 mM (or 2.7 $\text{mL}_{\text{CO}_2}.\text{dL}^{-1}$).

Of note, certain textbooks—*e.g. Nunn's [...]*[34, Chap. 10]—completely neglect plasma protein carbamates, presenting only CO_2Hb when mentioning carbamino carriage. Given the orders of magnitude involved, this may be acceptable in first approximation for educational reasons, and also explains why only CO_2Hb was mentioned in Figure 2.1. For further information about CO_2Hb formation mechanisms, the curious reader may refer to the works of Van Kampen[106], Gros *et al.*[107], and Blake *et al.*[108].

Regarding modelling the formation mechanism of carbamino compounds, while the following formula appears to be valid for plasma proteins carbamates[109]

$$[\text{R–NHCOO}^-] = \sum_{i=\alpha,\varepsilon} \frac{n_i\cdot[\text{proteins}]\cdot[\text{CO}_{2(\text{gas})}]}{[\text{CO}_{2(\text{gas})}] + \frac{[\text{H}^+]}{K_{c_i}} + \frac{[\text{H}^+]^2}{K_{c_i}\cdot K_{z_i}}} \tag{2.5}$$

no equivalent formula exists for haemoglobin binding. Indeed, although attempts have been made to obtain a similar formula for CO_2Hb concentration, these were not successful because most of them ignored the crucial role of 2,3-BisPhosphoGlyceric acid (2,3-BPG)—*a.k.a.* 2,3-DPG—in haemoglobin CO_2 binding[107, 109]. To the best of my knowledge, a single exception resides in the work of Perrella, who suggests a rational function of $[\text{CO}_{2(\text{gas})}]$ and [2,3-BPG] in his short 1975 letter[110], although *(i)* this function holds only for a pH of 7.4—which is slightly above that of inner erythrocytes (7.2, as mentioned above)—and *(ii)* Perrella might have just fitted an equation with enough degrees of freedom to his data, which could result into a poor generalisation of his approach.

2.1.2.3 As bicarbonate ions

The total CO_2 concentration in arterial blood being around 21.50 mM (or 55 $\text{mL}_{\text{CO}_2}.\text{dL}^{-1}$), the dissolved CO_2 (1.2 mM) and carbamate-bound CO_2 (1.05 mmol.L^{-1}) only account for roughly 10% of the overall amount of CO_2[33]. The 90% left are indeed present in the form of bicarbonate ions which are created through the hydration and dissociation of CO_2, which is a di-acid:

$$\text{CO}_2 + \text{H}_2\text{O} \xrightleftharpoons[\text{anhydrase}]{\text{carbonic}} \text{H}_2\text{CO}_3 \rightleftharpoons \text{H}^+ + \text{HCO}_3^- \ (\rightleftharpoons 2\,\text{H}^+ + \text{CO}_3^{2-}\ ) \tag{2.6}$$

---

(4) It seems to be common practice to use the solubility of CO_2 in plasma for both the erythrocytes and the whole arterial blood[33]. I could not find appropriate justifications for this in the literature, although the root cause may be that *(i)* erythrocyte are mainly bags of haemoglobin-rich salty water, and that *(ii)* CO_2 plasma solubility is also close to that of water, so that *(iii)* what really matters for CO_2 solubility is only the presence of water.

Of note, the second dissociation of CO_2 into carbonate ions (CO_3^{2-}) has a pK_a above 9(5), and carbonate ions are thus present in negligible concentration in human blood, hence the parentheses around the corresponding reaction. The creation of carbonic acid (H_2CO_3) from dissolved CO_2 is normally very slow in water, however the presence of carbonic anhydrase—an enzyme vastly present inside the erythrocytes—speeds up the reaction by a factor of 13 000 up to 25 000[94][33]. Thus, carbonic acid accounts for a negligible part of CO_2 in blood (only 0.0017 mmol.L^{-1}[34, Table 10.2]) and the equilibrium actually takes place between dissolved CO_2 and bicarbonate ions. In other words Equation 2.6 is virtually equivalent to:

$$\mathrm{CO_2 + H_2O \rightleftharpoons H^+ + HCO_3^-} \tag{2.7}$$

in human blood. This equilibrium is described by the following Henderson-Hasselbach equation

$$\mathrm{pH} = \mathrm{p}K_\mathrm{a} + \log_{10}\left(\frac{[\mathrm{HCO_3^-}]}{[\mathrm{CO_{2(gas)}}]}\right) = \mathrm{p}K_\mathrm{a} + \log_{10}\left(\frac{[\mathrm{HCO_3^-}]}{s{\cdot}\mathrm{P_{CO_2}}}\right) \tag{2.8}$$

wherein pK_a = 6.10 in human body at 37°C[33, 113], $s \approx 30$ µM.mmHg^{-1} is the solubility coefficient of CO_2 in plasma[34, Table 10.1] and P_{CO_2} its partial pressure. A normal pH value for human blood is considered to be between 7.35 and 7.45[114]. Taking a pH value of 7.4 and a paCO_2 of 5.3 kPa (40 mmHg) thus leads to a bicarbonate concentration $[HCO_3^-]$ of about 24 mM in plasma. Given that the erythrocytes have an intracellular pH of 7.2[115, 116], this leads to a lower erythrocytic $[HCO_3^-]$ of about 15 mM. Taking into account the relative proportions of plasma and erythrocytes in blood—*i.e.* the haematocrit—the total bicarbonate concentration in arterial blood is about 19 mM. There again, this value—when compared with the respective concentrations of dissolved CO_2 and carbamate-bound CO_2—explains the 90%-5%-5% repartition for CO_2 transport in blood presented in Figure 2.1.

2.1.2.4 $\mathbf{CO_2}$ repartition and equilibria

To wrap it all up, CO_2 is present in the body in three distinct forms(6):

1. Dissolved as a gas, according to Henry's law:

$$\underset{1.2\text{ mM}}{[\mathrm{CO_{2(gas)}}]} = \underset{0.231\text{ mM.kPa}^{-1}}{\alpha} \cdot \underset{5.3\text{ kPa (40 mmHg)}}{\mathrm{paCO_2}} \tag{2.9}$$

2. Bound to proteins, forming carbamate compounds with both haemoglobin (CO_2Hb) and plasma proteins ($R{-}NHCOO^-$). No mathematical model describes whole blood haemoglobin carriage in the literature, although the following kind of relation can reasonably be assumed:

$$\underset{1.05\text{ mM}}{[\mathrm{Carb}]} = f\Big(\underset{\substack{7.4\text{ extra}\\7.2\text{ intra}}}{\mathrm{pH}}, \underset{6\text{–}8\text{ g.dL}^{-1}}{[\mathrm{proteins}]}, \underset{13\text{–}15\text{ g.dL}^{-1}}{[\mathrm{Hb}]}, \underset{4\text{–}5\text{ mM}}{[\text{2,3-BPG}]_\mathrm{intra}}, \underset{1.2\text{ mM}}{[\mathrm{CO_{2(gas)}}]}\Big) \tag{2.10}$$

   wherein f is a rational function and [Carb] denotes the concentration of CO_2 bound to carbamates (*i.e.* $[\mathrm{Carb}] = [\mathrm{R{-}NHCOO^-}] + [\mathrm{CO_2Hb}]$).

3. As bicarbonate ions (HCO_3^-) accounting for the vast majority of blood CO_2 transport:

$$\underset{\substack{24\text{ mM extra}\\15\text{ mM intra}}}{[\mathrm{HCO_3}^-]} = \underset{1.2\text{ mM}}{[\mathrm{CO_{2(gas)}}]}\cdot 10^{\overset{\substack{7.4\text{ extra}\\7.2\text{ intra}}}{\mathrm{pH}} - \overset{6.1}{\mathrm{p}K_\mathrm{a}}} \tag{2.11}$$

Alas, the task of deriving a global equilibrium for whole blood CO_2 content from these three equations is by no means a trivial one. Indeed, variations in paCO_2 usually entail pH changes both in the plasma and the erythrocytes which are not necessarily of the same order of magnitude. Thus, in practice, many more equilibria take place between paCO_2, pH, $[HCO_3{}^-]$, [proteins], and [Hb] than the few above-described ones, not to mention other species such as 2,3-BPG, plasma phosphates, and extra- and intra-erythrocytic ions—*i.e.* Na^+, Mg^{2+}, *etc.* Navigating through

---

(5) The pK_a of the CO_3^{2-} / HCO_3^- pair is 10.25 in water at 25°C, but decreases markedly with increasing temperature and ionic strength[111, 112].

(6) Indicative values for arterial blood are given as undersets (or oversets when needed), all numerical values come from above-cited references, except for [2,3-BPG] which comes from Meen *et al.*[117]. The "extra" and "intra" terms refer to extra-cellular—*i.e.* plasmatic—and intra-cellular—*i.e.* erythrocytic—values, respectively.

this chemical hell has generated significant research efforts for decades, resulting into the creation of several whole blood acido-basic models, with major contributions from Siggaard-Andersen[118] and Stewart[119] in the seventies and early eighties. Recent improvements were added within the last two decades, which provided faithful modelling of blood acid-base equilibria, taking into account $paCO_2$ and saO_2 (cross-)influences[120–122]. Yet, the resulting models are not easily usable by common mortals due to the large number of equations and parameters they involve, and they often gain in accuracy what they lose in readability.

Consequently, I will limit myself here to presenting the simple cases of respiratory acidosis and alkalosis along with their influences on the total CO_2 content of whole arterial blood, but the reader is now warned that this is a gross simplification of a much more complex and nuanced picture. To do so, the following two equations from the well-known Davenport diagram were used[123, Fig. 17]:

$$\begin{array}{ll} [\mathrm{HCO_3}^-] = \alpha{\cdot}\mathrm{paCO_2}{\cdot}10^{\mathrm{pH}-\mathrm{p}K_\mathrm{a}} & \alpha = 0.231\ \mathrm{mM.kPa}^{-1} \\ [\mathrm{HCO_3}^-] = m - s{\cdot}(\mathrm{pH} - 7.40) & m = 24\ \mathrm{mM} \\ & s = 31.6\ \mathrm{mM}(.\mathrm{pH}^{-1}) \end{array} \tag{2.12}$$

Then, the following hypotheses were made:

$\mathcal{H}_1$: pH changes occur with the same magnitude in plasma and erythrocytes, *i.e.* if plasma pH decreases from 7.4 to 7.3, erythrocytic pH also goes down from 7.2 to 7.1.

$\mathcal{H}_2$: the proportion of intra- / extra-erythrocytic $[\mathrm{HCO_3}^-]$ remains constant, *i.e.* 27% / 73% (using Geers's data[33]).

Doing so made it feasible to derive single $[\mathrm{HCO_3}^-]$ and pH values for any given $paCO_2$. Then, using Mochizuki's data for total CO_2 blood content[124]$^{(7)}$, Figure 2.3 could be plotted considering fully oxygenated arterial blood with a plasmatic pH of 7.4 at equilibrium. The latter figure represents the so-called CO_2 dissociation curve—by analogy with the oxygen-haemoglobin dissociation curve—along with carbamate and dissolved CO_2 contributions to the total blood CO_2 content.

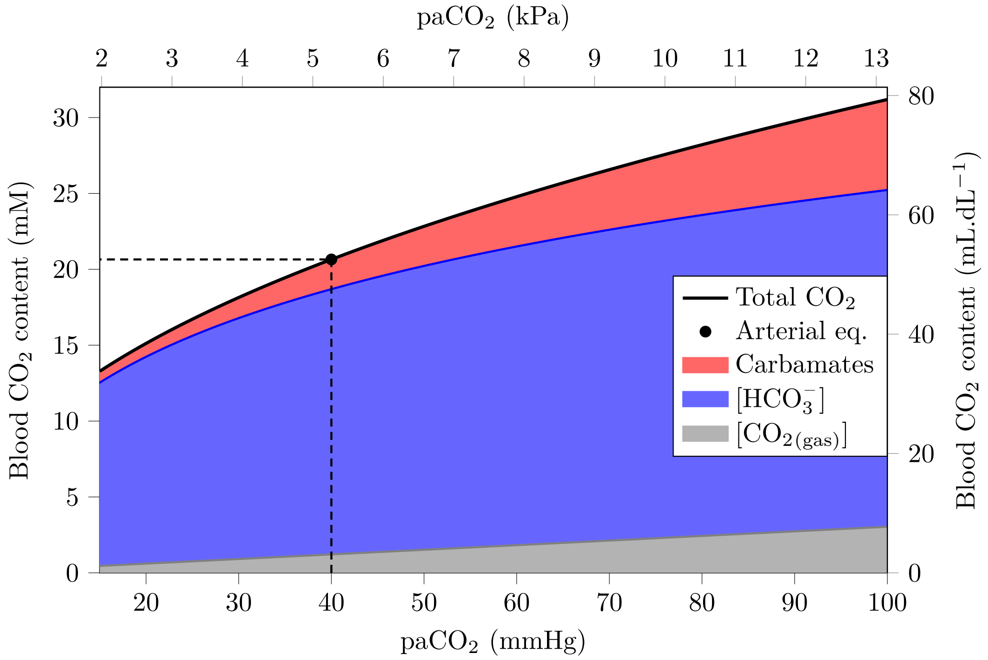

Figure 2.3: Stack plot of the respective contributions of dissolved CO_2, carbamate compounds, and bicarbonate ions to the total arterial whole-blood CO_2 content. The upper curve in black is the so-called CO_2 dissociation curve, with the normal arterial blood equilibrium marked with a black dot. Again, this curve was obtained using strong hypotheses and is given here for information only.

---

(7) First equation, using B=0.45. This equation was chosen because it yielded results in-between those of Tazawa *et al.*[125] and those of Loeppky *et al.*[126], short of a better heuristic.

This figure illustrates what happens in case of respiratory acidosis, for instance: a decrease in ventilation entails an increase in $paCO_2$, which translates into higher concentrations of carbamates, bicarbonate ions, and dissolved CO_2, while the opposite happens in case of respiratory alkalosis. Of particular interest (point (2.) of the box below), Figure 2.3 depicts the positive effect of $paCO_2$ on blood carbamates content—and thus on $[CO_2Hb]$—already reported in the literature[110, 127, 128].

The idea at the very heart of the present chapter was thus the following:

1. if we can find a non-invasive method to measure $[CO_2Hb]$ and
2. if we can uncover a satisfactory relation between $[CO_2Hb]$ and $paCO_2$,
3. then we should be able to perform non-invasive $paCO_2$ measurements.

To this end, I began my research with (1.): finding a non-invasive measurement technique for $[CO_2Hb]$. By analogy, this led me to investigate the basic principles of pulse oximetry.

2.1.3 Disclaimer on the Above Considerations

As mentioned above, the afore developments are of course a gross simplification of the equilibria involved in blood gas transport, and many well-known mechanisms have not been detailed here. In particular the O_2 and CO_2 binding properties of the haemoglobin molecule depend on its oxygenation and carbamation states, as well as on the surrounding pH and 2,3-BPG concentrations. This translates in practice into the notorious Bohr and Haldane Effect—first described in 1904 by the Danish physiologist Christian Bohr (1855-1911)[129], and in 1917 by the Scottish physiologist John Scott Haldane (1860-1936)[130], respectively. The curious reader may refer to Chapter 10 and 11 of *Nunn's ...*[34] for a more wide-angled, educational view of the situation, or may read the excellent reviews by Geers *et al.* on CO_2[33] and by Mairbaürl *et al.* on O_2[131], for more technical and profound insights.

Of note, some of the above-discussed aspects are still in need for further clarification. In particular, a better model for the formation-dissociation of carbamate compounds would be welcome, and is still an open research avenue[108]. Thorough modelling of the whole blood acid-base equilibrium including respiratory and metabolic influences is also still an open research field, and the creation of an open-source, easily implementable—*i.e.* by means of a fully sourced (in terms of literature references used to derive its parameters) Application Programming Interface (API) implemented using a popular programming language such as Python—appears to be highly desirable. In this direction, the recent works of O'Neill and Ježek appear quite promising[121, 122], although they chose closed (Matlab) or confidential (Modelica) programming languages, and only Ježek provided what is closer to a script than to a proper API.

further research is needed

2.2 Haemoglobin Optical Properties and Their Application to Pulse Oximetry

2.2.1 Spectrophotometry of Human Haemoglobin Derivatives

One noticeable property of the haemoglobin molecule is its strong optical absorption in the visible spectrum, which gives blood its characteristic red taint. Even better, the haemoglobin absorption spectrum depends on its oxygenation state—*i.e.* HHb and O_2Hb absorption spectra differ markedly—and other haemoglobin species such as COHb, MetHb or Sulf-Haemoglobin (SulfHb) also have their specific spectral features, see Figure 2.4.

Spectrophotometry of human haemoglobin derivatives began as far back as the 17th century, with the pioneering works of Fracassiti[133] and Mayow[134], who both observed a change in the colour of blood depending on its exposure to ambient air(8). However, it took no less than three centuries to translate these early qualitative observations into accurate quantitative measurements. In particular, we must salute the many contributions from van Assendelft, van Kampen

---

(8) See Engelhart for an interesting early history of haemoglobin studies[135]. Further historical considerations can be found in the introduction of Assendelft's monograph[136, Chap. 1].

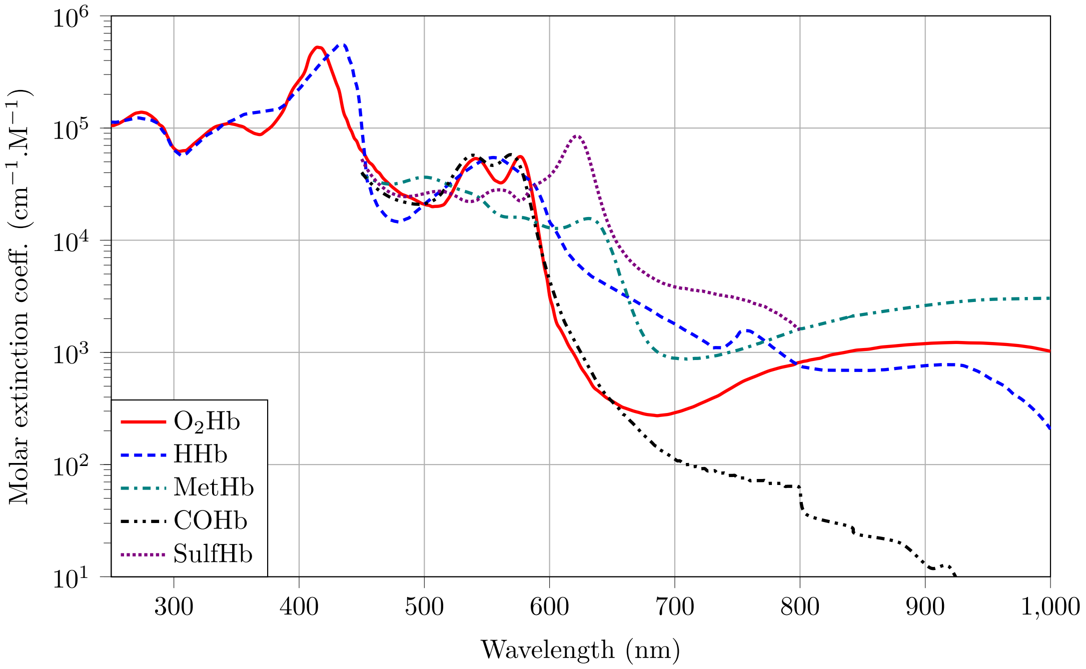

Figure 2.4: Haemoblobin absorption spectra. Data compiled from various sources: O$_2$Hb and HHb spectra come from Prahl[85], while MetHb, COHb, and SulfHb spectra come from Zijlstra *et al.*[132].
Note: Zijlstra's coefficients were converted to molar extinction coefficients according to Prahl's recommendations. Indeed, they were initially reported as *equivalents—a.k.a. quarter millimolar absorptivities—i.e.* using haem concentration instead of haemoglobin concentration. The reader eager to indulge in haemoglobin spectrophotometry should be aware of the factor of four existing between the two quantities, one haemoglobin molecule being composed of four haems.

and Zijlstra, from the University of Groningen, Netherlands. They worked relentlessly on haemoglobin spectrophotometry from the early fifties to the late nineties with two major monographs on the topic[132, 136]. In particular, their 2000 book *Visible and Near Infrared Spectra of Human and Animal Haemoglobin* condenses fifty years of research on the topic, and is an essential reading for anyone interested in haemoglobin spectrophotometry. Additional references are also given in Table 2.1 with indications of covered spectral ranges and measured haemoglobin species.

Haemoglobin spectrophotometry drew the attention of many a researcher for two main reasons. First, because it allows the total haemoglobin concentration to be determined from a blood sample using the photometric cyanmethaemoglobin method[145], which is particularly interesting from a medical viewpoint—*e.g.* when focusing on anaemia[154]. Second, because the differences in absorption spectra between O$_2$Hb and HHb can be used to non-invasively estimate a patient's saO$_2$: this is the goal of pulse oximetry.

2.2.2 Pulse Oximetry

Photometric oximetry—*i.e.* optically measuring the oxygen saturation of a blood sample—emerged in the early 20th century, following the afore-mentioned discovery that O$_2$Hb and HHb had different absorption spectra. From then, it took over half a century before Aoyagi's major breakthrough, with the invention of pulse oximetry in 1974[155]. For a thorough history of the development of both classic oximetry and pulse oximetry, I kindly redirect the curious reader to the excellent historical reviews written by Severinghaus *et al.*[83, 156](9). For more recent developments, current medical practice, and challenges, I would rather orient them towards several publications by Jubran[15], Nitzan *et al.*[14], and Tamura[16]. In the remainder of this section, I will briefly outline the core principles of pulse oximetry from a more technical point of view. Further reading on the topic include Urpalainen's work, which—despite being only a master's thesis—is extremely clear and educational, making her work quite valuable for a

---

(9) Make sure to read both papers—and not just the first one—as the second primarily serves as an erratum to the first. As a side note, those two papers are part of an heptalogy on the topic of blood gas analysis by one of the leading experts on the subject, and are worth reading from a historical viewpoint.

Year	Author	Ref.	Measurement window (nm) $\lambda_{\min}$	$\lambda_{\max}$	O_2Hb	HHb	COHb	MetHb	CNMetHb	SulfHb	CO_2Hb	Notes
1919	Newcomer	[137]	241	700	✓		✓	✓				
1938	Sidwell	[138]	230	780	✓	✓						
1943	Horecker	[139]	600	1000	✓	✓		✓	✓			
1962	Barlow	[140]	600	1900	✓	✓						
1970	Assendelft	[136]	390	1000	✓	✓	✓	✓	✓	✓		(a)
1971	Sugita	[141]	200	660	✓	✓		✓				
1977	Dijkhuizen	[142]	450	700				✓		✓		
1978	Waterman	[143]	370	650	✓	✓	✓	✓	✓			
1979	Mook	[144]	600	1000	✓	✓						
1983	Van Kampen	[145]	380	1000	✓	✓	✓	✓	✓	✓		(a)
1988	Wray	[146]	650	1050	✓	✓						
1989	Mendelson	[147]	600	1000	✓	✓						(b)
1991	Cope	[148]	650	1050	✓	✓						
1991	Zijlstra	[149]	450	1000	✓	✓	✓	✓				(b)
1994	Kuenstner	[150]	620	2500	✓	✓	✓	✓				
1997	Grosenbaugh	[151]	600	1000	✓	✓						
1997	Kuenstner	[150]	2500	11800	✓	✓	✓	✓				
1998	Prahl	[85]	250	1000	✓	✓						(c)
2000	Zijlstra	[132]	450	1000	✓	✓	✓	✓	✓	✓		(a),(b)
2006	Friebel	[152]	250	1100		✓						(d)
2012	Kolyva	[153]	650	1000	✓	✓						
2020	Dervieux	[86]	235	1000	✓	✓					✓	

Table 2.1: Selected works on the spectrophotometry of human haemoglobin derivatives. (a): additional dyshaemoglobins species reported†, (b): foetal haemoglobin also reported, (c): compiled from various data sources, (d): measurement performed on unlysed erythrocytes.
†: MetHb is sometimes called haemiglobin and noted Hi, while CNMetHb refers to cyanmethaemoglobin, also called haemiglobincyanide and noted HiCN. Many more haemoglobin species exist combining the sulf-, meth- and cyan- prefixes, as detailed by Zijlstra[132, p. 11 and Figure 2.2].

newcomer to the field[157, Chap. 2].

To understand the basic idea behind pulse oximetry, let us consider Figure 2.5, which illustrates the following. Light is shone onto a limb—*e.g.* a finger or earlobe—by means of a Light Emitting Diode (LED), with an initial incident intensity I_0. The light entering the skin is then partially absorbed inside the tissues before it eventually exits them with an intensity I, which may finally be measured with a photodiode. The absorption of light by the tissues may then be quantified by plotting the absorbance—*i.e.* $A = \log_{10}(I/I_0)$—of the tissues with respect to time. When doing so, the absorbance can be decomposed into two parts: *(i)* a *constant* signal—termed DC from the electrical engineering / signal processing analogy—due to the absorbance of tissues, venous blood, and the volume of arterial blood that remains constant throughout a cardiac cycle, and *(ii)* a *pulsatile* signal—termed AC—which corresponds to the change in arterial blood volume with each heartbeat.

Indeed, during diastole—the relaxed phase of the cardiac cycle—the arterial blood pressure is minimal, and the arteries thus occupy their minimum volume. On the contrary, when systole occurs—*i.e.* when the heart contracts and ejects its blood content into the arteries—the arterial blood pressure is maximal and the arterial volume increases—it is this volume variation that can be felt when taking the pulse of a person. This volume change is in fact a change in the volume of blood contained in the said arteries, and since blood is one of the most absorbing substances within human tissues[158], this change in blood volume in turns translates into a measurable change in tissues absorbance. This ability of measuring changes in (blood) volume by optical means is called photoplethysmography (PPG), derived from Greek *photo-* light, *-plethysmo-* increasing, enlarging (relative to volume changes), and *-graphy* writing.

Mathematically speaking, the absorbance of the perfused limb at a given wavelength λ may

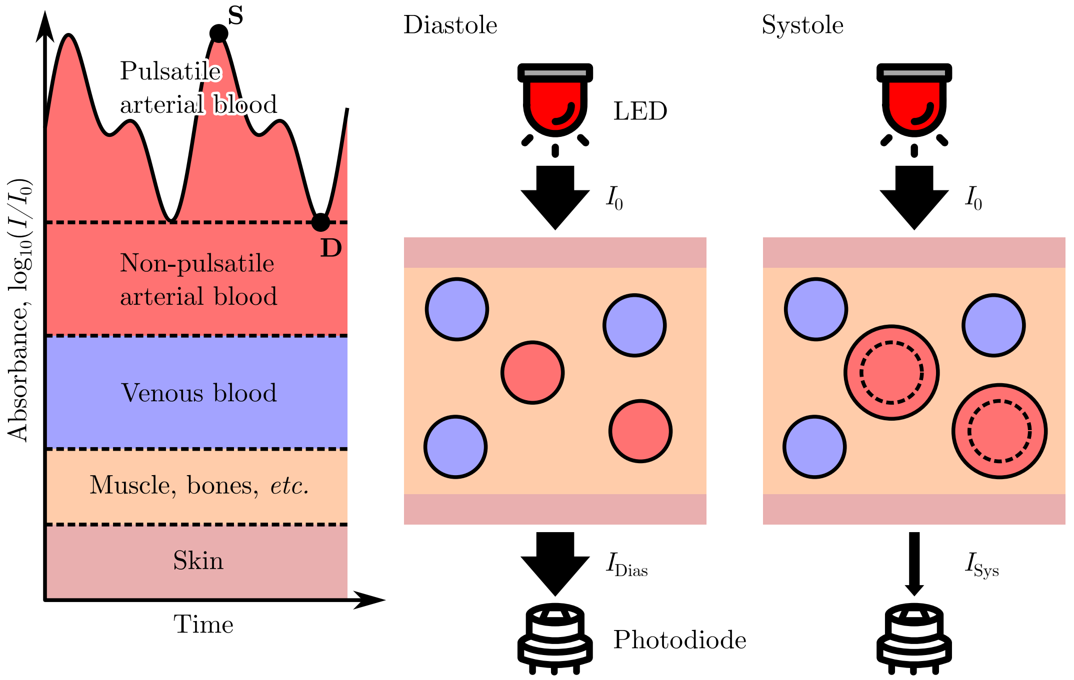

Figure 2.5: The pulse oximetry principle. **Left:** time-varying absorbance of perfused tissues, with decomposition of the said absorbance between different compartments (not to scale). Of note, the arterial blood is divided into a non-pulsatile and a pulsatile components, with the systole and diastole indicated with the "S" and "D" letters. **Center and Right:** schematised cut-views of perfused tissues during the diastole and systole. Skin, muscle, veins, and arteries are represented using the same colours as in the left-hand side diagram. Note the change in arteries diameter between the systole and the diastole, which accounts for the change in the amplitudes of I_{Sys} and I_{Dias} between the two phases of the cardiac cycle.

be written

$$A_\lambda(t) = -\log_{10}\left(\frac{I(t)}{I_0}\right) = A_{\lambda,\text{DC}} + \underbrace{A_{\lambda,\text{AC}}(t)}_{\substack{\text{pulsatile}\\\text{arterial blood}}} \tag{2.13}$$

where the total absorbance A_λ is decomposed into its DC and AC components. $A_{\lambda,\text{DC}}$ represents the sum of the respective absorbances of the non-varying afore-mentioned compartments—*i.e.* skin, muscle and bones, venous blood, and non-pulsatile arterial blood—while $A_{\lambda,\text{AC}}$ specifically represents the absorbance of pulsatile arterial blood, *i.e.*

$$A_{\lambda,\text{AC}}(t) = \sum_i \varepsilon_{\lambda,i} \cdot \mathcal{C}_i \cdot \ell_{\lambda,i}(t) \tag{2.14}$$

wherein i represents the different absorbing species in blood (mainly haemoglobin species), ε are their molar extinction coefficients, $\mathcal{C}$ their concentration, and ℓ the optical path taken by the illuminating light—*i.e.* the length of blood that would produce the same absorbance as the sum of all the optical paths actually taken through the many arteries of the perfused limb. Note that this path length ℓ is time-varying, being zero during diastole, and reaching its maximal value when the systole occurs. We can study the difference between the maximum (systolic) and minimum (diastolic) absorbance value:

$$\begin{aligned} A_{\lambda,\max} - A_{\lambda,\min} &= -\log_{10}\left(\frac{I_{\text{Sys}}}{I_0}\right) + \log_{10}\left(\frac{I_{\text{Dias}}}{I_0}\right) \\ &= \log_{10}\left(\frac{I_{\text{Dias}}}{I_{\text{Sys}}}\right) \end{aligned} \tag{2.15}$$

On the other hand we also have

$$A_{\lambda,\max} - A_{\lambda,\min} = \sum_i \varepsilon_{\lambda,i} \cdot \mathcal{C}_i \cdot \Delta\ell_{\lambda,i} \tag{2.16}$$

wherein $\Delta\ell_{\lambda,i}$ is the amplitude of $\ell_{\lambda,i}(t)$, *i.e.* $\Delta\ell_{\lambda,i} = \ell_{\lambda,i,\text{Sys}} - \ell_{\lambda,i,\text{Dias}}$. Using two different LEDs of wavelengths λ_1 and λ_2, the following ratio can then be computed:

$$\begin{aligned} R &= \frac{A_{\lambda_1,\max} - A_{\lambda_1,\min}}{A_{\lambda_2,\max} - A_{\lambda_2,\min}} = \frac{\log_{10}\left(\frac{I_{\lambda_1,\text{Dias}}}{I_{\lambda_1,\text{Sys}}}\right)}{\log_{10}\left(\frac{I_{\lambda_2,\text{Dias}}}{I_{\lambda_2,\text{Sys}}}\right)} \\ R &= \frac{\sum_i \varepsilon_{\lambda_1,i} \cdot \mathcal{C}_i \cdot \Delta\ell_{\lambda_1,i}}{\sum_i \varepsilon_{\lambda_2,i} \cdot \mathcal{C}_i \cdot \Delta\ell_{\lambda_2,i}} \end{aligned} \tag{2.17}$$

Then, the following hypotheses are made—they will be discussed later on:

$\mathcal{H}_1$: $\Delta\ell_{\lambda_1,i} = \Delta\ell_{\lambda_2,i}$, *i.e.* the light path inside the tissues is independent of the wavelength.

$\mathcal{H}_2$: $i \in$ [HHb, O$_2$Hb], *i.e.* the only two light-absorbing substances in arterial blood are the oxy- and deoxygenated haemoglobin species.

$\mathcal{H}_3$: $\mathcal{C}_{\text{Hb,TOT}} = \mathcal{C}_{\text{HHb}} + \mathcal{C}_{\text{O}_2\text{Hb}}$, wherein $\mathcal{C}_{\text{Hb,TOT}}$, $\mathcal{C}_{\text{HHb}}$, and $\mathcal{C}_{\text{O}_2\text{Hb}}$ are the total haemoglobin, HHb, and O$_2$Hb arterial blood concentration, respectively, *i.e.* haemoglobin is either present in the form of HHb or O$_2$Hb, and no dishaemoglobin is present. In particular, $\mathcal{H}_3$ leads to:

$$\mathcal{C}_{\text{O}_2\text{Hb}} = \text{saO}_2 \cdot \mathcal{C}_{\text{Hb,TOT}} \qquad \text{and} \qquad \mathcal{C}_{\text{HHb}} = (1 - \text{saO}_2) \cdot \mathcal{C}_{\text{Hb,TOT}} \tag{2.18}$$

Those three hypotheses then lead to

$$R = \frac{\text{saO}_2 \cdot \varepsilon_{\lambda_1,\text{O}_2\text{Hb}} + (1 - \text{saO}_2) \cdot \varepsilon_{\lambda_1,\text{HHb}}}{\text{saO}_2 \cdot \varepsilon_{\lambda_2,\text{O}_2\text{Hb}} + (1 - \text{saO}_2) \cdot \varepsilon_{\lambda_2,\text{HHb}}} \tag{2.19}$$

from which saO$_2$ can be expressed as:

$$\boxed{\text{saO}_2 = \frac{\varepsilon_{\lambda_1,\text{HHb}} - R \cdot \varepsilon_{\lambda_2,\text{HHb}}}{(\varepsilon_{\lambda_1,\text{HHb}} - \varepsilon_{\lambda_1,\text{O}_2\text{Hb}}) - R \cdot (\varepsilon_{\lambda_2,\text{HHb}} - \varepsilon_{\lambda_2,\text{O}_2\text{Hb}})}} \tag{2.20}$$

This latter relation is fundamental in pulse oximetry, as it allows to compute the saO$_2$ from R, which can itself be calculated using the right-hand-side of Equation 2.17 and the measured diastolic and systolic light intensities—represented in Figure 2.5—at two different wavelengths. Of note, when the saO$_2$ is computed by pulsed oximetry it is termed “peripheral oxygen saturation”, and noted spO$_2$.

2.2.2.1 Alternative calculus

There are two alternative ways of calculating spO$_2$ which are sometimes encountered in the literature. The first one generalises Equations 2.15 and 2.17 by using the derivative of the absorbance instead of its amplitude, *i.e.* turning the latter equations into

$$\begin{aligned} \frac{dA_\lambda}{dt}(t) &= \overbrace{\frac{A_{\lambda,\text{DC}}}{dt}(t)}^{=0} + \frac{A_{\lambda,\text{AC}}}{dt}(t) = \sum_i \varepsilon_{\lambda,i} \cdot \mathcal{C}_i \cdot \frac{d\ell_{\lambda,i}}{dt}(t) \\ &= -\frac{d \log_{10}\left(\frac{I(t)}{I_0}\right)}{dt} = -\frac{1}{I(t)} \cdot \frac{dI}{dt}(t) \end{aligned} \qquad \text{and} \qquad R = \frac{\frac{dA_{\lambda_1}}{dt}(t)}{\frac{dA_{\lambda_2}}{dt}(t)} \tag{2.21}$$

This can lead to instantaneous spO$_2$ values, without the need to wait for the end of a complete cardiac cycle[159]. The second alternative relies on the decomposition of light intensity into its AC and DC parts, *i.e.* using the notations

$$\text{DC} = I_{\text{Sys}} \quad \text{AC} = I_{\text{Dias}} - I_{\text{Sys}} \tag{2.22}$$

Then, equation 2.15 becomes

$$\begin{aligned} A_{\lambda,\max} - A_{\lambda,\min} &= \log_{10}\left(\frac{I_{\text{Dias}}}{I_{\text{Sys}}}\right) = \log_{10}\left(\frac{\text{DC} + \text{AC}}{\text{DC}}\right) = \log_{10}\left(1 + \frac{\text{AC}}{\text{DC}}\right) \\ &\approx \frac{\text{AC}}{\text{DC}} \end{aligned} \tag{2.23}$$

using an equivalent of $\log_{10}$ in zero(10), because AC is small with respect to DC in practice. Indeed the AC/DC ratio—referred to as the Perfusion Index (PI)—is about 4.5% when measured at the finger on healthy adults[160, 161], but this latter figure varies widely depending on the subject's position[160, 162] or state of health[163], for instance. This simplification gave R the name of *ratio-of-ratios*[14] because it thus becomes the ratio of two AC/DC ratios at wavelengths λ_1 and λ_2, *i.e.*:

$$R = \frac{\mathrm{AC}_{\lambda_1}/\mathrm{DC}_{\lambda_1}}{\mathrm{AC}_{\lambda_2}/\mathrm{DC}_{\lambda_2}} \tag{2.24}$$

2.2.2.2 Hypotheses validity and the calibration curve

Hypotheses $\mathcal{H}_1$ through $\mathcal{H}_3$, although allowing the derivation of a closed-form for spO_2—and thereby possessing significant explanatory power—are in fact wildly optimistic, as detailed below.

Regarding $\mathcal{H}_1$: $\Delta\ell_{\lambda_1,i} = \Delta\ell_{\lambda_2,i}$, significant research efforts have been put into modelling light propagation throughout the tissues. In particular, Monte-Carlo simulations conducted by Chatterjee *et al.* in a series of publications[164–167] clearly demonstrate the wavelength dependency of path lengths.

$\mathcal{H}_2$—stating that HHb and O_2Hb are the only light-absorbing substances in the arterial blood—and $\mathcal{H}_3$—stating that haemoglobin is either present as HHb or O_2Hb—are linked together in the sense that $\mathcal{H}_2$ requires $\mathcal{H}_3$ to be true. Alas, $\mathcal{H}_3$ is not quite true, since even non-smoking healthy adults have small percentages of haemoglobin present as COHb and MetHb—about 1–2% of COHb and 1% of MetHb, and the latter figures can be as high as 6–8% of COHb for heavy smokers, or over 40% of MetHb in case of methaemoglobinaemia[168–170]. Worse still regarding $\mathcal{H}_2$ veracity, haemoglobin is not the only light-absorbing substance in blood, with bilirubin presenting significant absorbance below 600 nm, for instance, although the latter should not be problematic except in case of severe hyperbilirubinemia[171–173].

Last, but not least, all the afore-mentioned considerations—and in particular Equation 2.14—assume that light propagation inside the blood and tissues obeys the Beer-Lambert law of absorption, *i.e.* only absorption was considered, not scattering events. In actuality, human tissues—and even blood alone, for that matter—are highly scattering media[158, 174]. This, in conjunction with the inexactitude of hypotheses $\mathcal{H}_{1\text{–}3}$ likely explains the observed differences between the theoretical spO_2=f(R) curve and the empirical one. Indeed, in practice, pulse oximetry manufacturers derive an empirical spO_2=f(R) curve based on real-life hypoxia sessions on a large number of subjects instead of using Equation 2.20[175, Chap. 10]. Of note, taking into account light scattering allows for the derivation of accurate calibration curves, at the expense of much more complex calculations than the above-presented ones[176], and the so-obtained curves are still influenced by total haematocrit[177].

2.2.2.3 Wavelengths selection and the multi-wavelength approach

A crucial step when building a pulse oximeter, which is also key to understanding the pulse carbametry-related considerations of the next section, is that of appropriate wavelength selection. Just as bygone researchers wondered about the optimal wavelength pair to use in static oximetry[178, 179], the advent of pulse oximetry sparked similarly intense discussions on the very same topic[159, 177, 180, Chap. 4]. Usually, λ_1 and λ_2 are chosen in the red and infra-red regions of the spectrum—*e.g.* 660 and 940 nm—although other combinations have been proposed relatively close to those—*e.g.* 660 and 805, or 735 and 890 nm[177, 181].

One of the limitations of the above-presented two-wavelengths approach is its inability to quantify haemoglobin species other than HHb and O_2Hb—*e.g.* COHb and MetHb. Even worse, high concentrations of the latter dyshaemoglobins could distort spO_2 measurements[182, 183]. To mitigate this issue, multi-wavelength pulse oximetry was developed, extending the principles of CO-oximetry—see Brunelle *et al.*[184]—to pulse oximetry. This allowed the detection and quantification of both COHb, MetHb, and total haemoglobin concentration, in addition to the classic spO_2, using between seven and sixteen LEDs[157, 185, 186].

In light of the above, I thought at the beginning of this doctoral work that multi-wavelength pulse oximetry would be an interesting research avenue for the development of a new family of non-invasive blood CO_2 monitors. Indeed, since various haemoglobin species could be determined this way, why not CO_2Hb? Since the latter is in equilibrium with total blood CO_2 content, estimating it could lead to an estimation of total blood CO_2 content. **I thus coined the term**

---

(10) More rigorously, $\log_{10}(1+x) \sim_0 x/\log(10)$, but the log(10) factor was omitted for the sake of simplicity since it disappears in R.

"pulse carbametry" to designate such an hypothetical technique, by analogy with "pulse oximetry", and owing to the *carba*mino-haemoglobin. However, developing such a technology would require CO_2Hb absorption spectra to be somewhat different from those of the already known haemoglobin species presented in Figure 2.4, above. Yet, to the best of my 2018's knowledge, CO_2Hb absorption spectrum had never been reported in the literature—despite my strong conviction that many separate teams had measured it over the centuries. They might not have reported it, however, due to both *(i)* its similarity to the HHb spectrum—as we shall see in the next section—and *(ii)* the lack of academic enthusiasm for—as well as the difficulty of—publishing negative results.

2.2.2.4 Final words on pulse oximetry and PPG

As exposed in Section 2.1.3 with respect to blood gases, the above considerations on pulse oximetry are of course only a quick glance at this complex topic, and the reader willing to embark on a photoplethysmographic journey should probably delve into the following references. As mentioned above, a good starting point would be reading Chapter 2 of Urpalainen's master thesis[157], which outlines some of the main caveats of static pulse oximetry—*e.g.* skin pigmentation[187, 188], administered dyes[189], or dyshaemoglobinemias[182, 183]. Subsequent considerations regarding the general design of pulse oximeters may also be found in the—unfortunately quite ageing—Webster's book *Design of Pulse Oximeters*[175], which is rather complete although by no means up-to-date.

Recent developments in PPG have mainly followed two research avenues: the first one is the ever-going strive for miniaturisation which allowed the advent of battery-ran wearable pulse oximeters—*e.g.* wristbands[190], in-ear[191], and even rings[192]—while the second one focuses on advanced signal processing and machine learning techniques to extract more information than spO_2 from the PPG signal—*e.g.* blood glucose levels[193], atrial fibrillation[194] or arterial blood pressure[195]—or be more robust to motions artefacts[196]. A summary of these aspects may be found in Kyriacou's *Photoplethysmography*[197], and a white paper roadmap on the topic has also been recently published by a collective of over fifty experts, reviewing possible future directions for photoplethysmographic research[198].

further research is needed

2.3 Pulse Carbametry

At this point of the discussions, it should be clear to the reader that the obtention of the CO_2Hb absorption spectrum is essential to assess the feasibility of pulse carbametry. What follows is thus essentially an introduction-less version of the article entitled *Measuring hemoglobin spectra: searching for carbamino-hemoglobin* and published in 2020 in the Journal of Biomedical Optics[86], which focuses primarily onto haemoglobin spectrophotometry with the aim of measuring the CO_2Hb absorption spectrum. As several scientists have contributed to this article, I used the first person plural for this section.

2.3.1 Material and Methods

2.3.1.1 Haemoglobin preparation and measurement

To measure the CO_2Hb absorption spectrum, the following experimental protocol was developed, strongly inspired by the afore-praised work of Zijlstra *et al.*[132]:

- Human blood was diluted at 1:10 or 1:1000 (HEPES 20mM, KCl 150 mM, pH 7.20, Ethylene Diamine Tetraacetic Acid (EDTA) 0.61 mM for the 1:10 dilution only, to prevent coagulation).

- Blood cells were lysed with ultrasound (Sonicator W-10, Heat Systems Ultrasonics, USA)

- The obtained haemolysates were equilibrated using rotating spherical glass tonometers—see Appendix A—during at least 30 min with either pure N_2—to obtain HHb—or pure CO_2—to obtain CO_2Hb. Alternatively, they were let in ambient air so as to obtain O_2Hb.

- The equilibrated haemolysates were carefully handled so as not to spoil them with ambient air. Syringes and cuvettes were rinsed three times with the tonometry gas, and the solutions were collected from the tonometers through a septum.

- Equilibrated solutions were poured in airtight quartz cuvettes (CV10Q1400FS, Thorlabs, USA, 10 mm path length), which were subsequently placed inside a spectrophotometer (Carry 5000, Agilent technologies, USA).
- Measurements were performed on the 235–600 nm range (hereafter referred to as the Ultra-Violet / Visible (UV-Vis) range) for the 1:1000 dilution and on the 600–1000 nm range (Visible / Infrared (Vis-IR) range) for the 1:10 dilution for N_2- and CO_2-equilibrated solutions (235–590 nm and 590–1000 nm for air-equilibrated solutions).

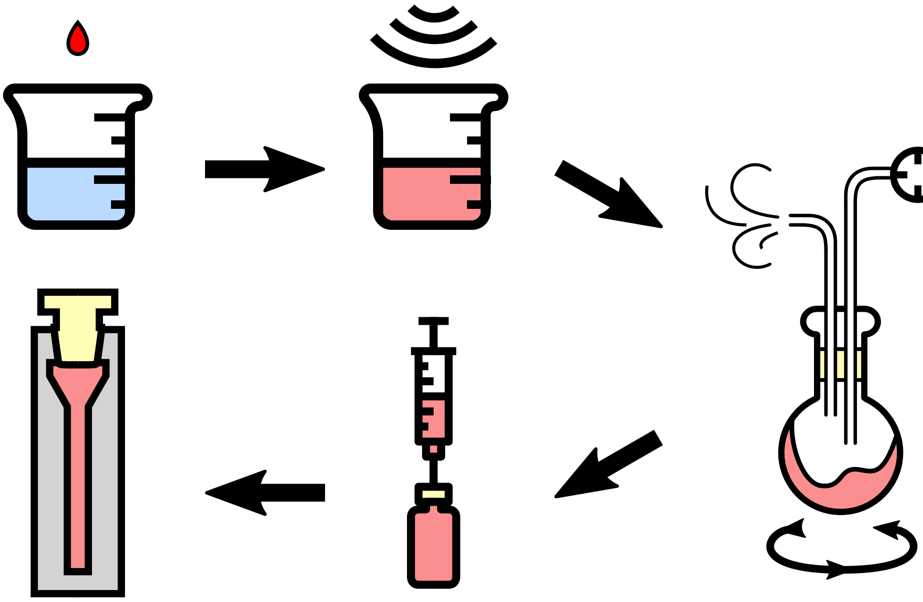

Figure 2.6: Haemolysate preparation, from the vein to the spectrophotometer. The different steps are (from top left to bottom left): venous sampling and dilution, ultrasound lysis, tonometry with CO_2 or N_2, careful anaerobic handling, and pouring into airtight glass cuvettes for spectrophotometric measurements.

Figure 2.6 summarises the above-described steps, which led to six different mixtures: diluted lysed blood at 1:10 or 1:1000 ratio, equilibrated with CO_2, N_2, or ambient air. In addition to these six mixtures, the absorption spectra of the dilution medium were also measured: pure—for baseline correction—and with EDTA and sodium metabisulfite ($Na_2S_2O_5$) separately, to assess the influence of these substances on the haemolysates measurements. Indeed, no information about the absorption spectra of sodium metabisulfite or EDTA in solution could be found in the literature. An analysis of the relative variations of the absorption spectrum of the dilution medium with and without sodium metabisulfite and EDTA was thus performed. Concentrations in the intra medium were 6.1 mM for EDTA and 2.0 mM for sodium metabisulfite.

Finally, the influence of the tonometry duration on the obtained spectra was also investigated. Equilibration durations were varied between 30 and 45 min in 3 min steps, all the while measuring the absorbance value of the 759 nm peak of the CO_2Hb and HHb absorption spectra. A Pearson correlation coefficient test was then performed, searching for an influence of the tonometry duration on the so-obtained absorbance values.

2.3.1.2 Assessment of pulse carbametry feasibility

For pulse carbametry to be achievable, one needs that the absorption spectra of CO_2Hb and HHb exhibit *sufficient* differences at accessible wavelengths(11). Assessing how much is *sufficient* is a complex task, which may be answered by addressing the following questions in order.

(a) Are the measured average spectra computed for HHb and CO_2Hb different?

(b) If they are, is this difference statistically significant?

(c) Does this difference—observed in the laboratory—translate into something actually exploitable in real life setups, where absorption measurements would be affected by:

---

(11) What is meant by “accessible wavelength” is further discussed in Section 2.4.2.4 and is not developed here.

- additional absorption caused by tissues surrounding the blood vessels,
- light reflection and scattering in the said tissues,
- inter-subject variations in physiology,
- noises related to ambulatory measurement setups (ambient light, motion),
- the accuracy of embedded sensors, which is bound to be lower than that of laboratory spectrophotometers.

Different methods were developed to answer each of these questions, as detailed below.

(a) Comparison of average spectra for Hb and CO_2Hb

After offset correction and outlier removal, a set of spectra for each haemoglobin species was obtained. Each of these sets was then averaged to obtain the final absorption spectrum of the corresponding haemoglobin species. Resulting average spectra were then plotted for visual comparison (see Figure 2.8).

(b) Statistical significance of the difference between spectra

The problem of assessing whether two absorption spectra are statistically different is non trivial. Indeed, one has to deal with limitations of two kinds:

1. The estimated absorption spectrum of each haemoglobin species is a vector of dependent random variables $\hat{A}_{\text{species}}(\lambda)$ such that

$$\forall\lambda,\ \hat{A}_{\text{species}}(\lambda) \sim \mathcal{N}\left(A_{\text{species}}(\lambda), \sigma_{\text{species}}(\lambda)^2\right) \tag{2.25}$$

   where $\sigma_{\text{species}}(\lambda)$ is the standard deviation of the noise on the measurement of the absorption of the haemoglobin species under consideration at wavelength λ. Thus, deciding whether the difference in the measured spectra of HHb and CO_2Hb is statistically significant is actually a multivariate analysis problem. Solving the latter would require one to perform at least as many measurements as there are wavelengths in the measured spectra (i.e. several hundreds)[199].

2. Variations in the measured spectrum of each species are bound to be induced by the slight differences in the manipulations specific to each species; thus, a statistically significant difference between measured spectra could actually reveal a difference in the haemoglobin species obtention protocol and not in the absorption spectra themselves.

To address such difficulties, the following analysis was performed on the measured haemoglobin spectra: for both the (HHb,CO_2Hb) and (HHb,O_2Hb) pairs of haemoglobin species, we computed the average, minimum, and maximum relative difference of their absorption spectra. This difference, computed for each wavelength, allows one to assess whether there is an exploitable discrepancy between the spectra of HHb and CO_2Hb in the same order of magnitude as that between HHb and O_2Hb.

(c) Applicability in real life setups

In order to estimate how much difference should be measured between the spectra of HHb and CO_2Hb for it to be exploitable in a pulse carbametry context, parallels were drawn with pulse oximetry. Specifically, it was proposed to:

(i) use the literature available on pulse oximetry to obtain an estimation of the accuracy of photoplethysmographic measurements on human skin,

(ii) derive a theoretical background for pulse carbametry, and

(iii) use the afore-mentioned accuracy in such background along with the results of our measurements, to conclude on the feasibility of pulse carbametry.

Note that the analysis presented in the remainder of this chapter is based on a two-wavelengths approach. Even though we acknowledge that multi-wavelengths approaches can improve the performance of photoplethysmographic systems—as above-mentioned in Section 2.2.2.3—the goal of this study was to evaluate whether there are couples of wavelengths for which the HHb and CO_2Hb absorption spectra exhibit exploitable differences. The optimisation of the exploitation of these pairs of wavelengths—should they exist—using a multi-wavelengths approach is thus out of the scope of this study.

(i) Accuracy in pulse oximetry

Our goal here is not to dive deeply into the theoretical foundations of pulse oximetry—as it has already been done in Section 2.2.2—but to estimate the sources of inaccuracy of this technique. In pulse oximetry, as mentioned above, the spO_2 is derived from the so-called *ratio of ratios*, R, which in turns utilises absorbance of light by human tissues at two different wavelengths. R is given by (Equation 2.19):

$$R = \frac{\text{saO}_2 \cdot \varepsilon_{\lambda_1,\text{O}_2\text{Hb}} + (1 - \text{saO}_2) \cdot \varepsilon_{\lambda_1,\text{HHb}}}{\text{saO}_2 \cdot \varepsilon_{\lambda_2,\text{O}_2\text{Hb}} + (1 - \text{saO}_2) \cdot \varepsilon_{\lambda_2,\text{HHb}}} \tag{2.26}$$

where λ_1 and λ_2 are the two measurement wavelengths, often 660 nm and 940 nm, and $\varepsilon_{\lambda_i,X}$ are the haemoglobin extinction coefficients of the X haemoglobin species at wavelength λ_i.

The question at stake for addressing *(i)* is then: what accuracy on R is achievable in practice by common photoplethysmographic sensors? As can be seen from Equation 2.26, such an accuracy on R can be estimated based on the accuracy on the saO_2 that is reported in the literature. The latter has been studied in many clinical trials—themselves reviewed[14, 15]—and a mean standard deviation of 2% on the 70%–100% saO_2 range can be considered to be achievable under good measurement conditions—that is, mainly no movement from the subject and a good perfusion index. Figure 2.7 represents the results obtained when taking such a standard deviation for saO_2 and computing the corresponding R measurement inaccuracies at the 660 nm and 940 nm wavelengths—the two most-used wavelengths in pulse oximetry—using Zijlstra *et al.*[132] absorption coefficient for O_2Hb and HHb.

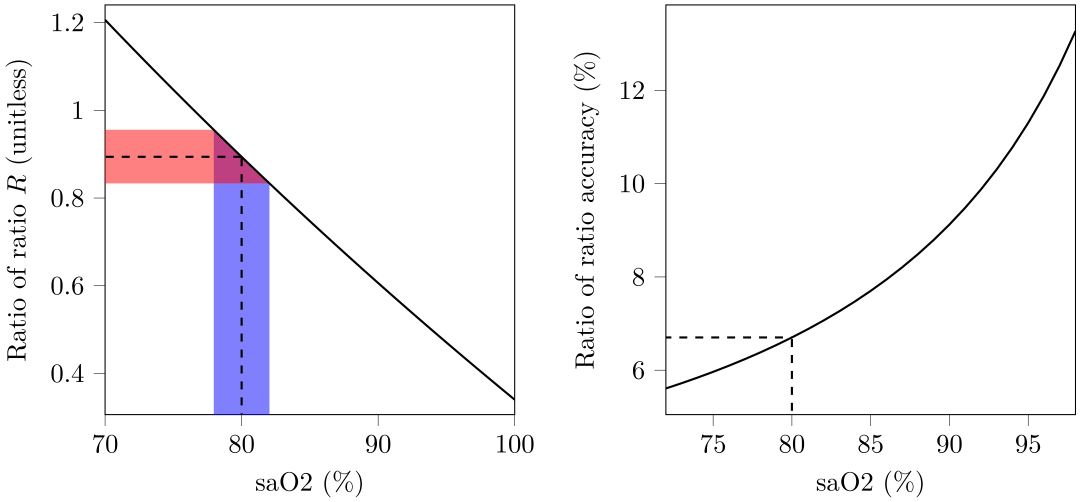

Figure 2.7: **Left**: an error of 2% on the saO_2 reading at 80% of saO_2 (in blue), is the result of an inaccuracy of 6.7% on the measurement of R (in red). **Right:** conversely, if we impose a 2% error on the saO_2 reading, we can compute the relative variation of R which generated such an error. Again, at 80% saO_2, the latter is 6.7% (dashed black lines).

One can see that the lower the oxygen saturation is, the more accurate the measurement of R needs to be to guarantee a given accuracy on saO_2. Indeed, while the accuracy on R measurement must be as low as 5.6 % at 70 % of saO_2, it can be as high as 13.3% at 98 % of saO_2. Of note, those calculations were made with the hypothesis that all errors were following Gaussian distributions.

***(ii)* Accuracy in pulse carbametry** This minimum error—5.6%—derived in the case of pulse oximetry gives a best-case—hence optimistic—value of the achievable accuracy on R measurement using transcutaneous ratiometric techniques. When applying a similar method to obtain the concentration of CO_2Hb in arterial blood using pulse carbametry, one may thus expect—at best—a similar accuracy on R estimation. The pulse carbametry context considered in this study is detailed in the remainder of this paragraph.

Let us consider a binary system composed solely of HHb and CO_2Hb and define the arterial carbon dioxide saturation (saCO_2) as:

$$\text{saCO}_2 = \frac{[\text{CO}_2\text{Hb}]}{[\text{CO}_2\text{Hb}] + [\text{HHb}]} \tag{2.27}$$

Wherein [HHb] and [CO_2Hb] are the HHb and CO_2Hb concentrations, respectively. Using the pulse oximetry theoretical background—see Section 2.2.2—saCO_2 can be derived from a measured ratio of ratio R as:

$$\mathrm{saCO_2}(\lambda_1, \lambda_2) = \frac{\varepsilon_{\lambda_1,\mathrm{HHb}} - R{\cdot}\varepsilon_{\lambda_2,\mathrm{HHb}}}{(\varepsilon_{\lambda_1,\mathrm{HHb}} - \varepsilon_{\lambda_1,\mathrm{CO_2Hb}}) - R{\cdot}(\varepsilon_{\lambda_2,\mathrm{HHb}} - \varepsilon_{\lambda_2,\mathrm{CO_2Hb}})} \tag{2.28}$$

The feasibility of pulse carbametry will be assessed as follow: considering the extinction coefficients $\varepsilon_{\mathrm{CO_2Hb}}$ and $\varepsilon_{\mathrm{HHb}}$ derived from our spectrophotometric measurements, and the aforementioned standard deviation on R, the standard deviation on saCO_2 will be computed for each (λ_1,λ_2) couple on the 235–1000 nm range. Then, finding the minimum value of this deviation with respect to (λ_1,λ_2) will provide the best achievable accuracy using pulse carbametry. More explicitly, the minimum saCO_2 accuracy reachable with pulse carbametry is given by:

$$\delta\mathrm{saCO_2} = \min_{(\lambda_1,\lambda_2)} \sigma\mathrm{saCO_2}(\lambda_1, \lambda_2) \tag{2.29}$$

Wherein $\sigma\mathrm{saCO_2}(\lambda_1, \lambda_2)$ is the relative standard deviation of $\mathrm{saCO_2}(\lambda_1, \lambda_2)$, computed from the R standard deviation in the case of pulse oximetry (5.6%). Judging whether a given minimal accuracy δsaCO_2 is *small enough* is essentially an arbitrary choice. Still, one can rely on the clinically accepted range for paCO_2, which is ±7.5 mmHg (95% limits of agreement, corresponding to ±2 S.D.)[200]. This latter range translates into a standard deviation of 9% on paCO_2 reading, at a standard paCO_2 level of 40 mmHg. Thus, the decision threshold on δsaCO_2 was set to this value as a first approximation, *i.e.* if δsaCO_2 is below 9%, pulse carbametry will be considered feasible.

2.3.2 Results

2.3.2.1 Haemoglobin spectra

The spectra of diluted lysed blood obtained once equilibrated with ambient air, pure N_2 and pure CO_2 are presented in Figure 2.8 after baseline correction and outlier removal. Each spectrum was averaged over (UV-Vis/Vis-IR spectra number): 24/13 (CO_2), 10/17 (N_2) and 32/38 (air) measurements. The variations in the number of trials between the different gases are explained by several factors. At first, there were two different measurement campaigns for the UV-Vis and Vis-IR range, leading to less measurements in the Vis-IR (some fluorescence measurements were performed instead, see Section 2.4). Then, there were twice as much measurements made with O_2Hb as with N_2 or CO_2, only because O_2Hb was readily available and measured while waiting for HHb and CO_2Hb to be obtained by tonometry. Finally, an outlier removal algorithm based on the standard deviation of the measurements was used, removing measurements diverging more than roughly ±2.5 standard deviations from the mean, using an adaptative threshold and a recursive algorithm inspired by the work of Hadi *et al.*[201]—see Appendix B. This choice of threshold was arbitrary, as is that of outlier detection and removal in the general case[202]. Given the important number of wavelengths in each measurement and the limited number of measurements performed, a power calculation was not feasible.

The absorption spectra of HHb and CO_2Hb appear to be extremely close, especially compared to O_2Hb. The standard deviations in absorption for O_2Hb, CO_2Hb and HHb were (mean standard deviation, mininum, maximum) $1.20^{7.55}_{0.38}$ mAbs, $3.16^{36.34}_{0.51}$ mAbs and $2.43^{21.02}_{0.40}$ mAbs, corresponding to relative variations of $0.53^{2.24}_{0.14}\%$, $1.08^{5.74}_{0.05}\%$ and $0.81^{4.59}_{0.07}\%$, respectively.

Figure 2.9 gives a more quantitative analysis to the difference between O_2Hb, CO_2Hb and HHb spectra. While the relative differences between O_2Hb and HHb spectra—clearly visible in Figure 2.8—can reach several tens of percent, those between CO_2Hb and HHb are much more tenuous. The differences between mean O_2Hb and HHb spectra on the one hand and CO_2Hb and HHb spectra on the other hand were (mean absolute difference, maximum) $0.18^{(1.99)}$ Abs and $0.08^{(0.11)}$ Abs, corresponding to relative variations of $36^{(153)}\%$ and $2^{(13)}\%$, respectively.

2.3.2.2 Intra medium

Figure 2.10 presents absorption spectra of the dilution medium with and without sodium metabisulfite. Results with EDTA are not shown since they were indistinguishable from pure dilution medium on a full scale view. More subtle effects of these substances are shown in Figure 2.11, which focuses on the relative deviations of the prepared EDTA or sodium metabisulfite solutions

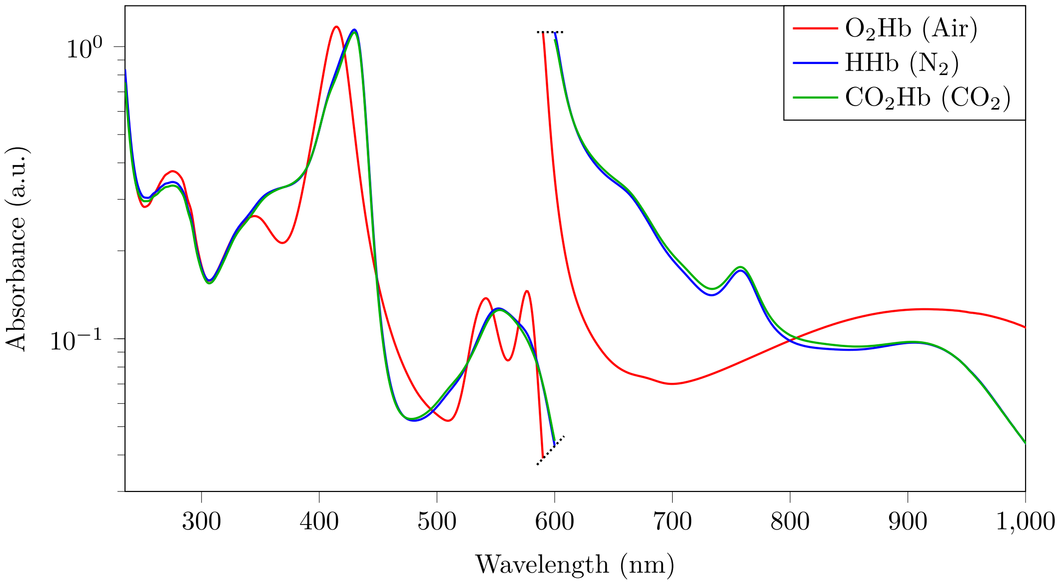

Figure 2.8: Measured absorption spectra of diluted lysed blood tonometered with O_2, N_2 or CO_2. The vertical scale is arbitrary, data were scaled for representation and correspond to two different dilution ratios of 1:1000 for the UV-Vis 235–600 nm range (left) and 1:10 for the Vis-IR 600–1000 nm range (right) (ranges are 235–590 nm and 590–1000 nm for air–equilibrated solutions). The black dashed line separates the UV-Vis from the Vis-IR measurements.

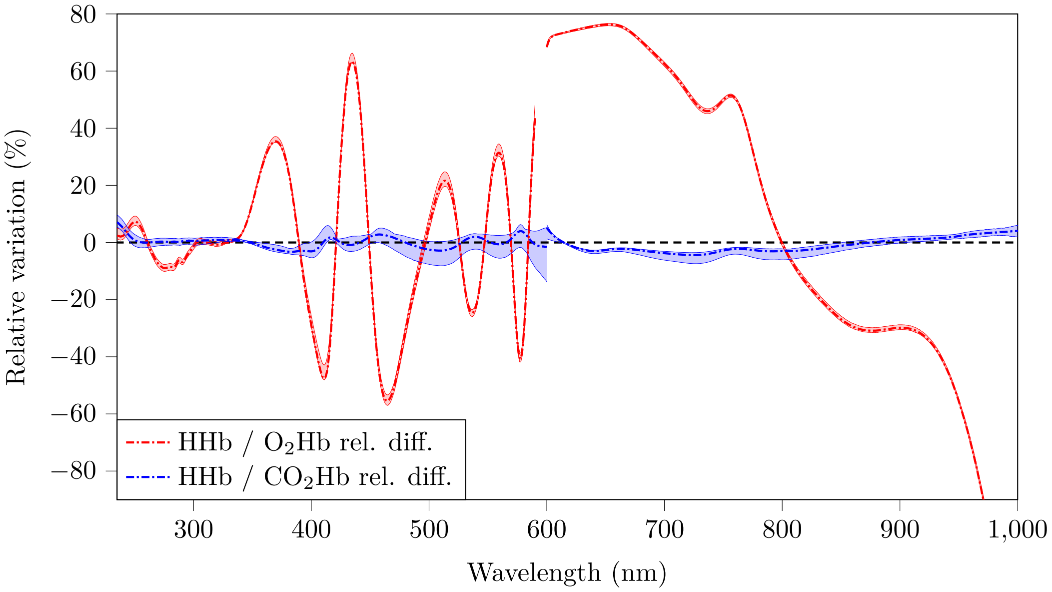

Figure 2.9: Relative differences between HHb and CO_2Hb (in blue) and between HHb and O_2Hb (in red) absorption spectra. The two thin lines for each comparison represent the maximum and minimum values along all measurements. For instance, for the HHb / CO_2Hb comparison at a given wavelength, the upper line represents HHb maximum value minus CO_2Hb minimum value, while the lower line represents HHb minimum value minus CO_2Hb maximum value (both normalised by CO_2Hb mean value).

with respect to pure dilution medium. Again, each spectrum is averaged over several measurements: 28/34 (pure) and 12/11 (sodium metabisulfite) measurements for the UV-Vis/Vis-IR range, and 5 (EDTA) measurements for the Vis-IR only range.

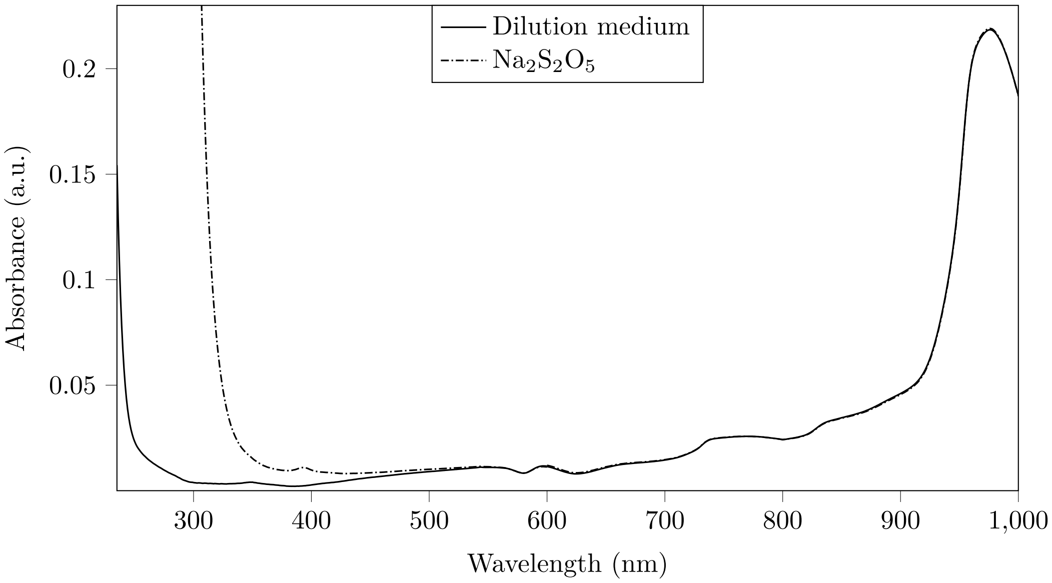

Figure 2.10: Absorption spectra of the dilution medium with and without the addition of sodium metabisulfite (2.0 mM). Note the marked absorption of sodium metabisulfite in the ultraviolet, up to almost 500 nm.

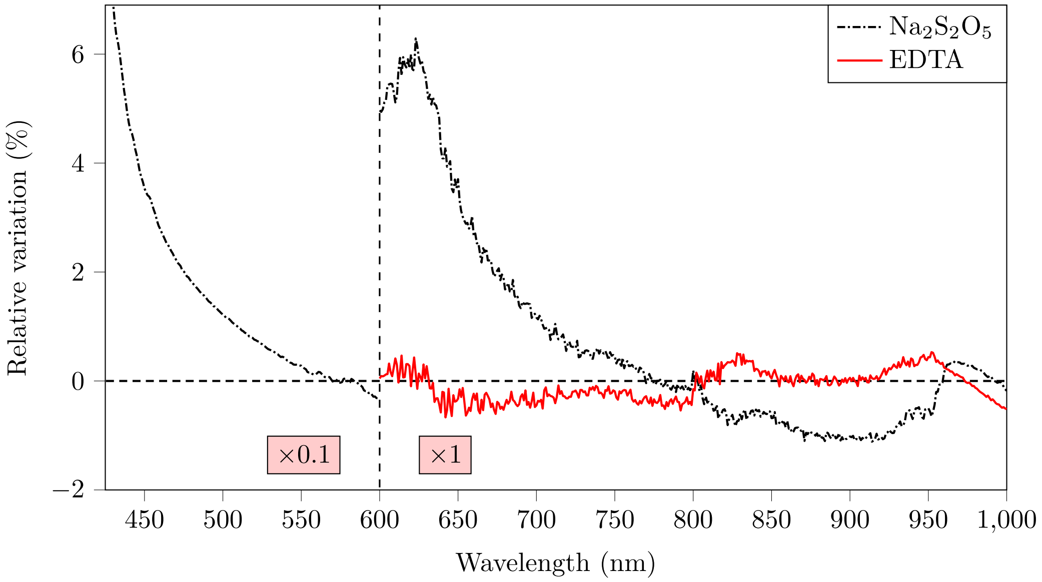

Figure 2.11: Relative variations of the dilution medium absorption spectrum upon the addition of EDTA (0.61 mM) or sodium metabisulfite (2.0 mM). The left side is multiplied by 0.1 (∼10% of relative variation for sodium metabisulfite at 500 nm). Of note, the slightly negative values in the 575–600 nm range are likely to be measurement artefacts due to measurements in the lower sensitivity limit of the spectrophotometer, given the measurements presented in Figure 2.10 and the relative variation above 4% just above 600 nm.

2.3.2.3 Tonometry duration

The influence of tonometry duration on the measured absorbances was found to be insignificant for durations between 30 and 45 min, with test results being ρ=-0.13, p=0.62, on 17 samples for N_2 tonometry and ρ=-0.04, p=0.91, on 13 samples for CO_2 tonometry (ρ being the Pearson correlation coefficient). It was thus concluded that 30 min of equilibration time were enough to obtain either CO_2Hb or HHb.

2.3.2.4 Pulse carbametry

The CO_2Hb and HHb absorption spectra presented in Figure 2.8—and obtained through CO_2 and N_2 tonometry, respectively—were then used to perform the analysis presented in Section 2.3.1.2. The value of $\sigma saCO_2$ as a function of the two wavelengths (λ_1, λ_2) are shown in Figure 2.12.

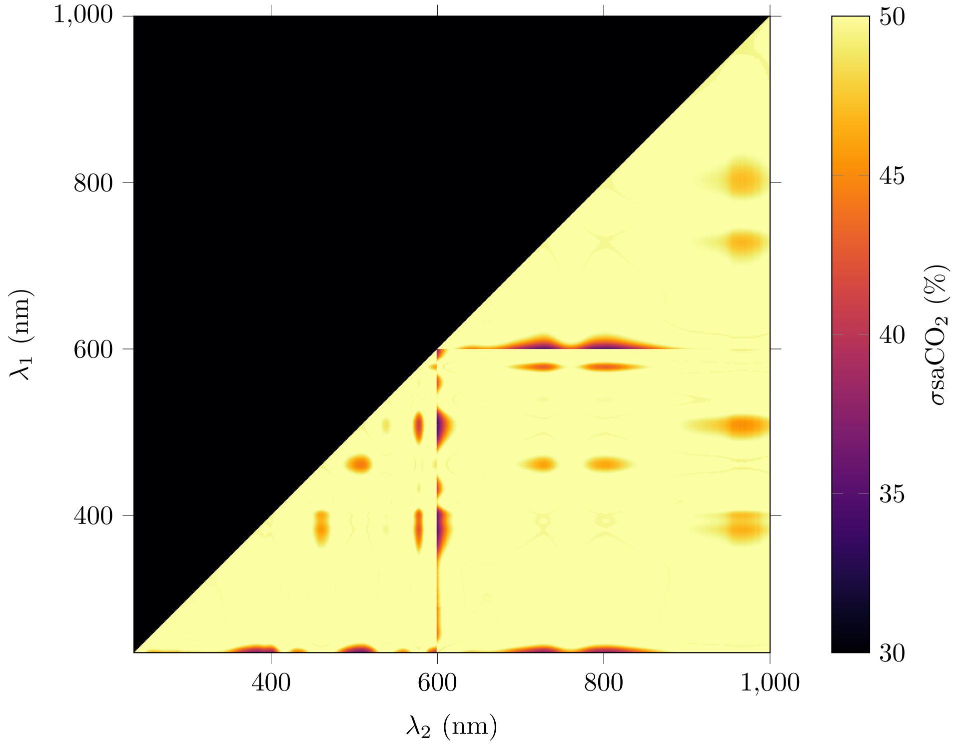

Figure 2.12: $\sigma saCO_2$ as a function of (λ_1, λ_2) on the 235–1000 nm range.

The minimal value taken by $\sigma saCO_2$, is $\delta saCO_2 = 34.2\%$ at $\lambda_1 = 508$ nm and $\lambda_2 = 600$ nm. However, as can be seen from the asymmetry of the spots on the λ_1=600 nm or λ_2=600 nm lines, these values likely originate from limitations of the measurement system that was used. Indeed, when using a 1:1000 dilution ratio, the lysed blood absorbance was below 1.2 Abs on the full 235–600 nm range, which is acceptable. By contrast, when a 1:10 dilution ratio was used, the latter absorbance topped at 2.8 Abs near 600 nm, which is close to the saturation value of 3.0 Abs of the used spectrophotometer. Ideally, to circumvent this flaw of the measurement setup, three dilutions at 1:10, 1:100 and 1:1000 should have been performed on the 235–450 nm, 450–650 nm and 650–1000 nm ranges respectively.

Still, even with these flaws, which—in the worst case—could increase the spectral differences between HHb and CO_2Hb and thus lower the error on $saCO_2$ measurements, the reached accuracy is still far above the 9% target established previously. If $\sigma saCO_2$ values near the 600 nm lines are discarded and focus is made on other spots—such as the (λ_1=510 nm, λ_2=580 nm) area—values above 41% are to be found for $\delta saCO_2$.

2.3.3 Discussion

At first, the chosen method for obtaining CO_2Hb, HHb and O_2Hb is discussed. Then the haemoglobin spectra are compared with those available in the literature, the influence of EDTA and sodium metabisulfite is also discussed. Finally, the feasibility of pulse carbametry is assessed.

2.3.3.1 On the chosen method

Among the several authors who measured haemoglobin absorption spectra, some used freshly drawn blood[132, 136, 139, 140, 144, 146–149, 203] whereas others preferred lyophilised haemoglobin[204–206]. Lyophilised blood, despite its convenience, has several drawbacks. First, it is composed merely of MetHb[203, 207] and thus needs an oxidation procedure to convert it back into O_2Hb, a step which involves chemicals that might interfere with the haemoglobin spectrum. Second, a better affinity of haemoglobin has been reported for haemoglobin extracted from freshly drawn blood[139, 203]. These considerations drove our choice towards fresh blood as a haemoglobin source.

However, fresh blood requires the lysis of erythrocytes and other blood cells to yield a limpid solution. Despite the common use of a surfactant such as Sterox SE[136, 144, 149] or equivalent[139, 146, 148], we preferred an ultrasound lysis, which adds no foreign chemical in blood for the same effect[147]. Fresh blood sampling could also require centrifugation in order to keep only the erythrocytes and avoid spectral interferences from other blood components, namely leucocytes and lipids. Yet, since haemoglobin is the main absorbing compound in blood by two up to three orders of magnitude[173], we did not consider the centrifugation step mandatory. Lastly, fresh blood sampling requires the addition of an anticoagulant if it is not largely diluted. Consequently, for the 1:10 dilution ratio—in the 600–1000 nm range—we considered the addition of EDTA to the collected blood. The spectral influence of the latter was measured, and found to be negligible over the studied range—as shown in Figure 2.11—with relative absorption variations in the ±1% range, corresponding to absolute variations in the ±1 mAbs range, well below the standard deviation measured for the absorption spectrum of the dilution medium ($1.24^{+14.1}_{-9.3}$ mAbs for the dilution medium alone, for instance, and similar values were found for the dilution medium with 2.0 mM EDTA). We concluded that EDTA did not have any influence on the measured spectra in the quantity used in our experiments.

Concerning measurements of haemoglobin in its reduced form, the use of sodium dithionite ($Na_2S_2O_4$) has been reported as a means to quickly obtain HHb[136, 140, 147, 203, 206]. Alas, it has also been reported to alter the absorption spectrum of the latter[132, 205, 208]. We conducted investigations on the possible use of sodium metabisulfite ($Na_2S_2O_5$) which—like sodium dithionite—leads in aqueous solution to the production of bisulfite anions ($HSO_3{}^-$), the strong reducing agent converting O_2Hb into HHb. Our results—see Figure 2.10 and 2.11—confirm earlier observations and extend them with quantitative measurements over the 235–1000 nm range. Because of this, we would not recommend the use of bisulfite anions for their strong absorption, particularly at short wavelengths up to 500 nm.

Tonometry was thus chosen for the obtention of HHb and CO_2Hb to avoid using the aforementioned reducing agents. Concerning its duration, 30 min were found to be sufficient in spherical glass tonometers filled with 6 mL of diluted lysed blood, as demonstrated in Section 2.3.2.3. However, one should bear in mind that this duration is strongly dependant on several parameters, such as the shape of the tonometer used for equilibration, its filling level, or the gas flow rate, for instance.

The dilution medium was chosen in order to correspond to an intracellular medium (with high K^+ concentration). pH was also set to an erythrocyte intracellular value of 7.2 since it has been reported to be that of the inner erythrocytes[115, 116]. It has also been reported that pH has an impact—although relatively small—on the measured haemoglobin spectra[205, 209, 210]. Concerning the choice of HEPES as a buffer, a better preservation of the haemoglobin oxygenation function was reported with HEPES over Tris/Bis-Tris[211]. Finally, the chosen dilution ratios are justified since haemoglobin has been reported to follow the Beer-Lambert law of absorption, whether for extremely diluted or concentrated solutions[204].

2.3.3.2 Haemoglobin spectra

The measured spectra of diluted lysed blood, either equilibrated with N_2 or ambient air, are extremely close to those of the literature for HHb and O_2Hb, as can be seen in Figure 2.13. This comforts us in the method that we employed and the above-mentioned choices. The small discrepancies observed between our spectra and those of the literature may be explained by a number of methodological differences. For instance, several authors[136, 144, 149] used a surfactant such as Sterox SE to perform the erythrocyte lysis, while we chose to use ultrasounds. The surfactant may have a spectral impact, which—to the best of our knowledge—has never been quantified. Other authors, even when choosing tonometry, added some small amount of sodium dithionite before measuring[132]. Yet, sodium dithionite, like sodium metabisulfite, is known to have a marked spectral influence[205]. Zijlstra *et al.*[132] also mentioned that in case of too long tonometry, supernatant residues sometimes appeared in the diluted blood, the nature of which was not determined. Although we did not observe such behaviour, a small turbidity might have been present in their measurements, or ours. Among the literature spectra presented in Figure 2.13, while Assendelft, and Zijlstra detailed their protocol, Prahl and Kolyva only offer raw coefficients. It is therefore difficult to analyse the potential sources of differences between their spectra, or between their spectra and ours.

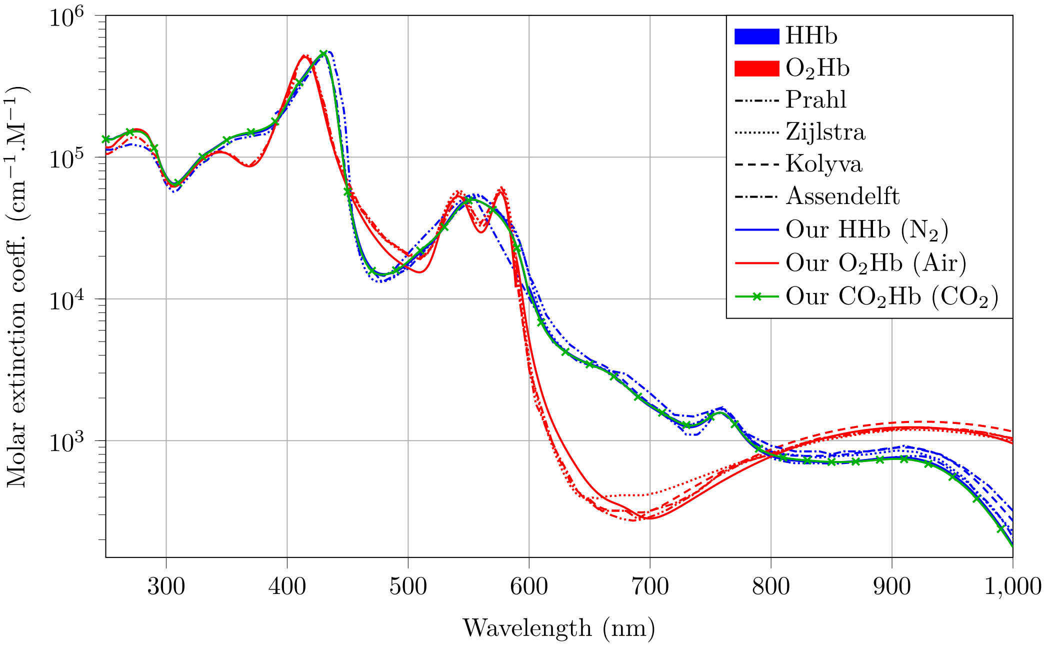

Figure 2.13: Our measurements (plain line) compared to those of Prahl[85], Zijlstra *et al.*[132], Kolyva *et al.*[153] and Assendelft[136]. Our measurements are consistent with those of the literature for O_2Hb (Air) and HHb (N_2).

Overall, the repeatability of the measurements was fairly good, with mean standard deviation of 0.53%, 1.08% and 0.81%, for O_2Hb, CO_2Hb and HHb measurements, respectively, which can be compared to values between 0.4% and 2.1% reported by Zijlstra *et al.* for various haemoglobin species[132, Table 8.3]. The rather high maximum standard deviations reported in Section 2.3.2.1 (2.24%, 5.74% and 4.59% for O_2Hb, CO_2Hb and HHb, respectively) are mainly due to the measurement limits of the spectrophotometer near 600 nm, corresponding to either too low ($\leq$0.05 Abs) absorbance below 600 nm, or too high ($\geq$2.5 Abs) absorbance above 600 nm. When computing the mean standard deviation without the 580–620 nm range for O_2Hb, CO_2Hb and HHb, maximum standard deviation values drop to 7.25 mAbs, 12.60 mAbs and 21.02 mAbs, corresponding to relative variations of 1.31%, 2.78% and 2.54%, respectively. The mean absorption spectra that we measured for O_2Hb, CO_2Hb and HHb were published as a supplementary material with this original publication[86].

Unfortunately for the future of pulse carbametry, Figure 2.8 also reveals that the absorption spectra of HHb and CO_2Hb are extremely close, their differences being more than one order of magnitude below the ones between the O_2Hb and HHb absorption spectra, as can be seen in Figure 2.9. Moreover, the measured HHb and CO_2Hb spectra are similar to the HHb spectra already available in the literature, as can be seen in Figure 2.13. Such observations tend to make one believe that the formation of carbamate compounds between CO_2 and haemoglobin terminal amine groups does not change the haemoglobin molecule conformation significantly, hence bringing no spectral alteration. However, such intuition shall not have the value of evidence, this is why the possible use of slight differences between HHb and CO_2Hb will now be discussed.

2.3.3.3 Pulse carbametry

Given the 9% accuracy threshold that was fixed for $\delta saCO_2$, and the observed value of 34.2%—or even more if the values close to the spectrophotometer saturation limit are discarded—we could readily conclude that pulse carbametry—as it was presented—is not feasible. However, several additional aspects of this technique need to be further discussed.

At first sight, the consideration of a binary system composed solely of HHb and CO_2Hb can seem surprising. Indeed, in practice, human arterial blood is composed at least of O_2Hb, HHb and CO_2Hb—and even COHb[212, 213] and MetHb[214, 215] in small amounts. That being said, it should be clear that the demonstrated inability to distinguish between CO_2Hb and HHb, even when they are the only absorbing compounds involved, would be worsened by the addition of any other perturbing absorbing species—*e.g.* O_2Hb. An in-depth analysis of the tertiary system O_2Hb–HHb–CO_2Hb would have been necessary only if pulse carbametry had been found to be possible in a binary system.

Then, we made the hypothesis that all studied errors were Gaussian. It is most often considered to be the case in the literature[14, 15] and we also stuck to this hypothesis in the absence of evidence to the contrary. Thus, the main remaining question is to know whether the mathematical functions giving $R = f(\mathrm{saO_2})$ and $\mathrm{saCO_2} = g(R)$ can be reasonably linearly approximated. The latter assumption has to be checked for f at the 660/940 nm couple, and for g across the full 235–1000 nm range. The calculation of the derivative of these two functions is straightforward and allows one to conclude that the relative variation of the slope of f stays below 3.8% in the 70–100% $\mathrm{saO_2}$ range at 660/940 nm, whereas the slope of g stays below 2.2% in the 0–100% $\mathrm{saCO_2}$ range at 340/600 nm (maximal value across the 235–1000 nm range). We can thus safely conclude that approximating f and g with linear functions is reasonable and that our hypothesis concerning Gaussian errors is justified.

Next, all the calculations leading to Figure 2.12 were made considering a monochromatic skin illumination. In a typical pulse carbametry application, the light source is more likely to be a laser, laser diode, or LED. In such cases—and especially when using an LED—the effect of a non monochromatic light source will be a degradation of $\delta\mathrm{saCO_2}$ caused by the spectral spread of the source. Such spread will basically smooth the HHb and CO_2Hb absorption spectra by convolving them with the emission spectrum of the source. The latter can in turn be regarded as a roughly Gaussian window of Full Width at Half Maximum (FWHM) of a few (laser sources) or a few tens (LED) of nanometres. For instance, a source with a FWHM of 5 nm leads to a $\delta\mathrm{saCO_2}$ of 36.8%; with an FWHM of 20 nm this value reaches 42.1%, to be compared with the 34.2% of the afore-mentioned ideal monochromatic case.

Finally, the last assumption that we made concerns the extrapolation to pulse carbametry of the accuracy on R measurement in the $\mathrm{saO_2}$ case. Such an assumption was made considering that the 660 nm and 940 nm wavelengths were not chosen randomly but to maximize pulse oximetry sensitivity. In other words, they were chosen such that a small change in $\mathrm{saO_2}$ translates into a huge change in measured light intensity at certain wavelengths[136, 179], but also such that they were in the tissues *optical window*—the 700–1000 nm range[216–218]. Such considerations make the $\mathrm{saO_2}$ 660/940 nm situation a best case, and we would expect other wavelengths couples to give equally or less accurate R measurements. This remains, however, a supposition since—to the best of our knowledge—there appears to be only a few studies on the measurement accuracy on $\mathrm{saO_2}$—and thus R—at wavelengths different from the usual 660/940 nm pair (see Section 2.2.2.3). Still, it is worth noticing that our conclusions would remain unchanged, even if we managed somehow to drastically improve the measuring accuracy on R—say by a factor two or three, we would still have a $\delta\mathrm{saCO_2}$ value above 9%.

2.3.4 Conclusion

In the afore-presented study, the CO_2Hb absorption spectrum was measured for the first time. O_2Hb, HHb and CO_2Hb were obtained from diluted lysed blood equilibrated with ambient air, pure N_2 and pure CO_2 respectively. The methodology leading to their obtention and isolation was discussed thoroughly, including the possible use of EDTA or sodium metabisulfite.

The absorption spectra of O_2Hb and HHb were close to those of the literature, while the absorption spectrum of CO_2Hb was extremely close to that of HHb. No influence of EDTA was found, whereas sodium metabisulfite—on the contrary—strongly absorbs in the ultraviolet and visible range up to 500 nm. Therefore, the latter should not be used in this spectral range for haemoglobin reduction.

A theoretical variant of pulse oximetry applied to the determination of CO_2Hb fraction was presented, which we called pulse carbametry. This theoretical framework was applied to the afore-mentioned measurements to conclude whether the slight variations observed between the HHb and CO_2Hb absorption spectra could be used in such a context. Our observations show that such an approach seems extremely challenging since these spectra are almost identical. In particular, on the basis of current knowledge, pulse carbametry may not be used in medical practice.

Yet, the present work may benefit from further investigations to consolidate its conclusions. In particular, only two wavelengths were considered for pulse carbametry. It would be interesting to use more sophisticated multi-wavelengths approaches, since they usually give better results in the case of pulse oximetry[157], although the question of wavelengths selection becomes more complex[184, 219].

2.4 Additional Fluorescence Measurement

2.4.1 Introduction

Following the negative results of the previous section, I decided to also investigate haemoglobin fluorescence properties to be on the safe side. Fluorescence is a long-known optical method for the characterization of chemicals. Its basic principle is to illuminate an analyte at a given wavelength, and to measure the light re-emitted by the sample under study. A fluorescent material will absorb photons at the excitation wavelength and re-emit photons at the same wavelength (Rayleigh scattering), at a greater wavelength (Stokes shift or Stokes Raman scattering), or at a smaller wavelength (anti-Stokes shift, anti-Stokes Raman scattering). For more information on the fluorescence phenomenon itself, I kindly redirect the curious reader towards the first chapters of the excellent book *Molecular Fluorescence: Principles and Applications*, by Bernard Valeur *et al.*[220].

The aim of this section is to evaluate the feasibility of using conventional fluorescence techniques on the human skin, in order to gather information about the oxidation or carbamation status of the haemoglobin contained in the subcutaneous blood. Indeed, haemoglobin has been shown to fluoresce slightly between 300 nm and 400 nm when excited at 280 nm or 296 nm. More interestingly, this fluorescence has been reported to depend on the oxygenation status of the haemoglobin protein[221, 222]. In a first part, bibliographic resources of previous work found in the literature about the fluorescence of human haemoglobin, tissues, and more specifically different skin layers, are presented. The feasibility of the afore-mentioned approach is then discussed in a second part.

2.4.2 Previous work

The feasibility of haemoglobin fluorescence measurements through the human skin relies mainly on three requirements. First, the haemoglobin molecule must exhibit a measurable fluorescence. Second, the surrounding medium—predominantly blood and tissues—must not disturb the measurements with the presence of other surrounding endogenous fluorophores. Third, the probed tissues—namely the external layers of the skin in the case of transcutaneous measurements—must be transparent to both the excitation wavelength and the emission wavelength of haemoglobin. These three key points will be discussed in the following subsections.

2.4.2.1 A Brief History of Haemoglobin Fluorescence

The story begins in 1957 with the discovery by Teale *et al.* of the fluorescence of several aromatic amino acids—namely phenylalanine, tryptophan and tyrosine[223]. These three species exhibit a main excitation peak between 200 and 225 nm and a secondary one between 250 and 290 nm, for fluorescence maxima at 282 (phenylalanine), 303 (tyrosine) and 348 nm (tryptophan). Those three amino acids are of particular interest since they are all present in haemoglobin(12). The early work of Teale on amino acid was extended in the eighties by several teams—mentioned below—with fluorescence measurements of complete haemoglobin molecules. The difficulty to produce fluorescence spectra for haemoglobin lies in the fact that the molecule itself is a pigment with a very strong absorption in the emission spectrum of its tryptophan constituents. This self-absorbing phenomenon is sometimes improperly referred to as *self-quenching*, whereas it is, in reality, an *inner filter effect*[226].

Hirsch *et al.* exhibited the existence of a haemoglobin fluorescence attributed to tryptophan in 1980[227]. Interestingly, Hirsch noted that above a concentration of 0.16 mM haemoglobin, no further increase in the measured fluorescence could be observed. The given explanation was that above this threshold, more haemoglobin generates more light but also absorbs more of the re-emitted light, which leads to an observed fluorescence intensity independent of the haemoglobin concentration above 0.16 mM. Such observations were made possible by the use of front-face optics. Had they used conventional right-angle optics, they would have observed a decreasing fluorescence intensity for higher haemoglobin concentrations due to the above-mentioned inner filter effect—the interested reader may refer to Appendix C for further explanations on the latter phenomenon. Hirsch's team extended this work in 1981[228], exhibiting a difference of fluorescence between O_2Hb and HHb. This difference is presented as a consequence of the

---

(12) For more information on the haemoglobin structure, see the extensive work of Mitchel Weissbluth on the topic[224, Table 1.1], itself based on the discovery of haemoglobin structure using X-rays in the fifties by Nobel prize Max Ferdinand Perutz[225].

conformational modification of the haemoglobin from its R (relaxed) to its T (tense) shape$^{(13)}$; the corresponding fluorescence spectra are reproduced in Figure 2.14.

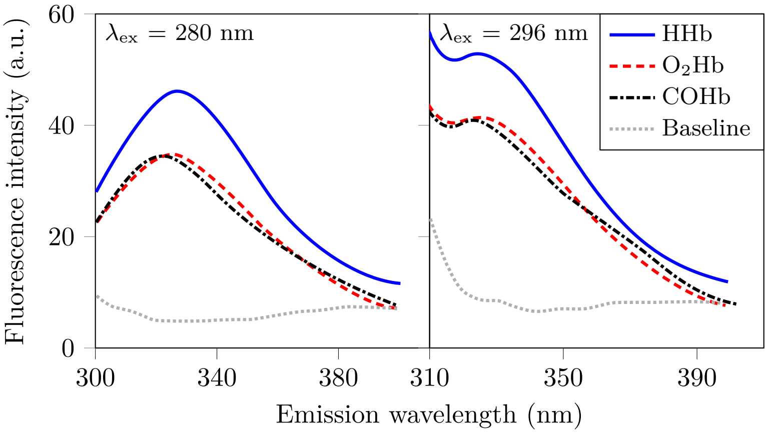

Figure 2.14: Fluorescence emission spectra of adult human haemoglobin in various liganded states—*i.e.* HHb, O_2Hb and COHb—uncorrected for baseline. Haemoglobin concentration was 155 µM. All measurements were taken in pH 7.35, 50 mM potassium phosphate buffer, at 25°C. (a): 280 nm excitation; (b): 296 nm excitation. The lower dotted lines are the baselines obtained with the buffer solution alone. Drawn using data from [228].

Still in 1980, Alpert *et al.* also used a right-angled fluorometer with extremely diluted haemoglobin solutions (2 µM)[230]. They showed that haemoglobin exhibits a fluorescence similar to that of apohaemoglobin (the polypeptidic chain of haemoglobin without any haem site) or tryptophan solutions. This attribution of the haemoglobin fluorescence to tryptophan was yet again proposed by Itoh *et al.* in 1981[221] while measuring fluorescence spectra of O_2Hb and HHb. Indeed, they found the decay time of haemoglobin fluorescence to be very similar to that of tryptophan.

More recently (2011), Zheng *et al.*[231] provided evidence of haemoglobin fluorescence when excited with two-photon. A fluorescence peak exists at 438 nm for an excitation wavelength between 600 nm and 750 nm. Their work was extended in another publication from 2015[232] on more excitation wavelengths. The two-photon absorption technique can be useful to relax the constraint on the tissues transparency at the excitation wavelength. Indeed, a two-photon absorption at 600 nm produces the same excitation as a one-photon absorption at 300 nm but can be performed even in a medium opaque at 300 nm but transparent at 600 nm. As a side note though, two-photon absorption usually requires expensive equipment such as a femtosecond laser and complex optics, bringing the cost of a complete measurement system in the ~10 k€ ballpark[233, 234].

2.4.2.2 Personal Measurements

In light of the above, we decided to perform additional haemoglobin fluorescence measurements of haemoglobin solutions equilibrated with ambient air, N_2, and CO_2. Fluorescence matrices were obtained from freshly drawn human blood, lysed with ultrasound and diluted at 1:500 in intracellular medium (150 mM KCl, 20 mM HEPES, pH 7.2) leading to an haemoglobin concentration estimated to be ~20 µM. The obtained solutions were then either tonometered for 30 min using pure N_2 or pure CO_2, yielding HHb, or left in room air for complete oxygenation, yielding O_2Hb. Measurements were performed using right-angle optics (Cary Eclipse Fluorescence Spectrophotometer, Agilent, USA). We performed coarse-grained scans across the 200–500 nm excitation window / 200–800 nm emission window, and more accurate ones across the 200–350 nm excitation / 250–450 nm emission windows. Corresponding fluorescence matrices are presented in Figures 2.15 and 2.16. Emission and excitation spectra of O_2Hb are also given in Figure 2.17.

Two excitation maxima were identified at 228 nm and 278 nm, leading to a single emission peak at 336 nm. Those results are in good agreement with those of the afore-mentioned literature[227, 230]. However, we did not perform enough measurements to be able to conclude on a difference between O_2Hb and HHb fluorescence spectra, due to a measurement error on our side

---

(13) This is a simplified view of what actually happens, see Yuan *et al.* for more details on the haemoglobin molecule conformational changes[229].

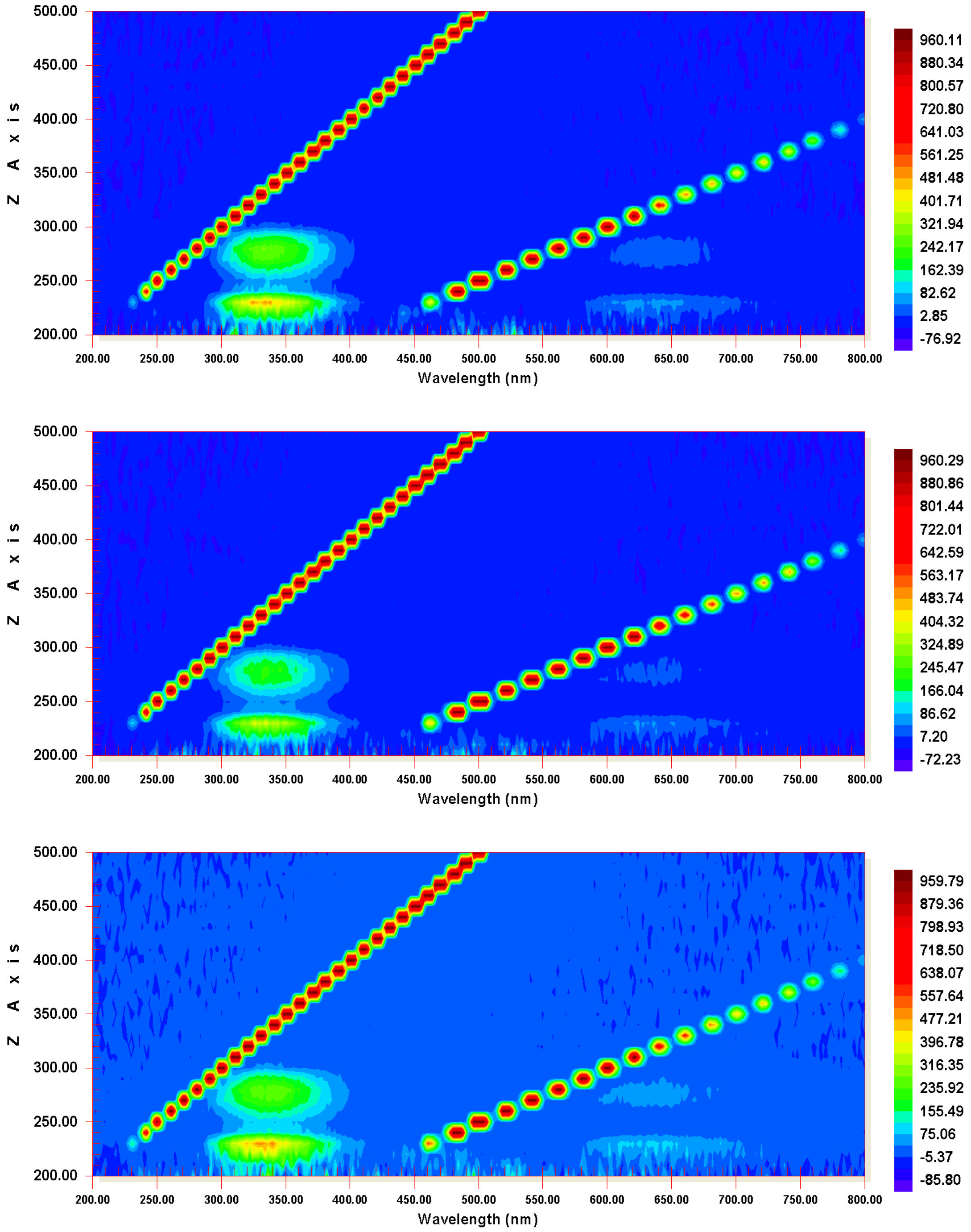

Figure 2.15: Coarse-grained (10 nm excitation step) fluorescence matrices measured on 1:500 diluted lysed blood tonometered with three different gases. The area of interest is that located between the two diagonal lines that correspond to the excitation and its second harmonic. The emission wavelength is in abscissa and the excitation wavelength is in ordinate. **Top:** O_2Hb (air). **Middle:** HHb (N_2). **Bottom:** CO_2Hb (CO_2).

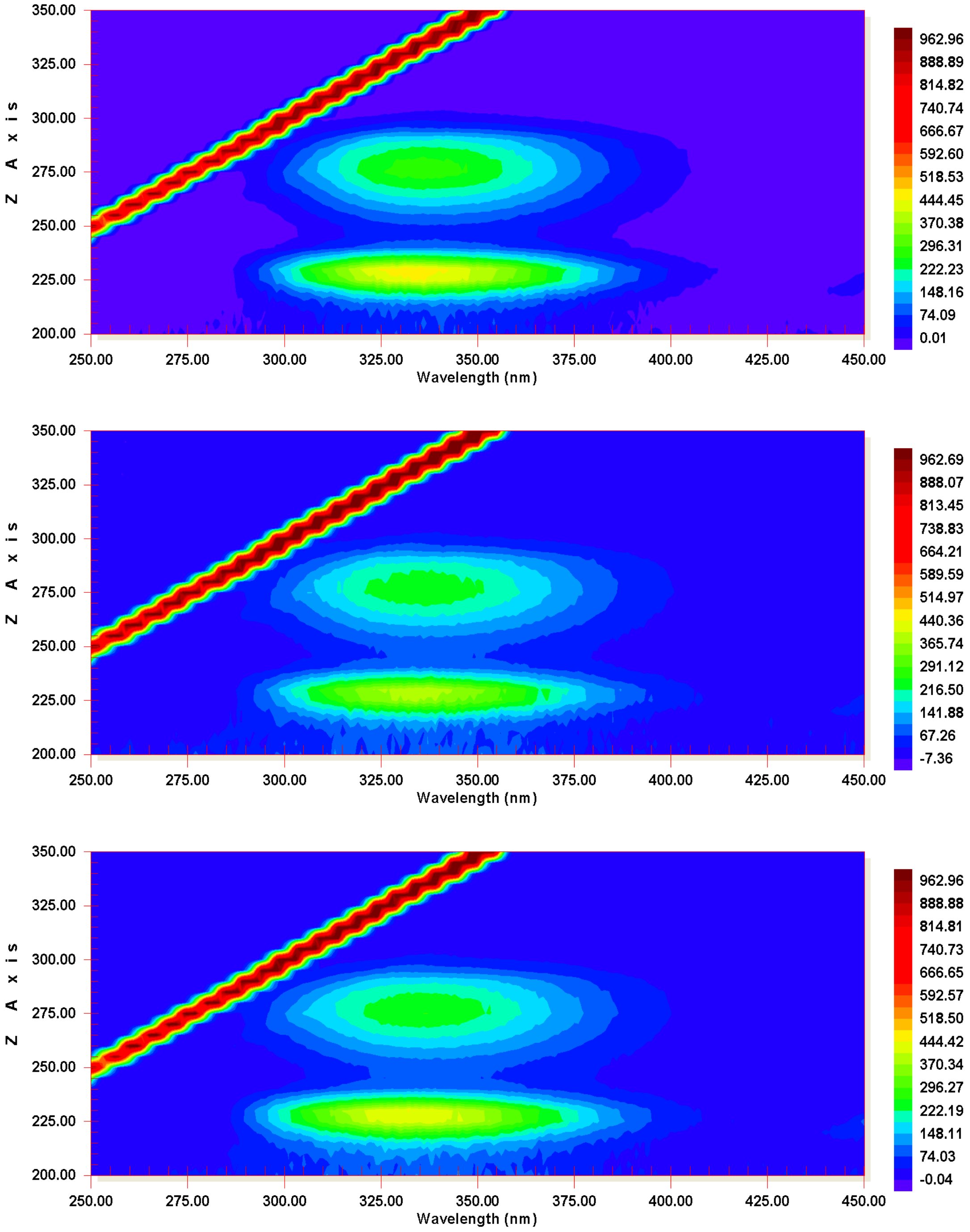

Figure 2.16: Fine grained (2 nm excitation step) fluorescence matrices measured on 1:500 diluted lysed blood tonometered with three different gases. **Top:** O_2Hb (air). **Middle:** HHb (N_2). **Bottom:** CO_2Hb (CO_2).

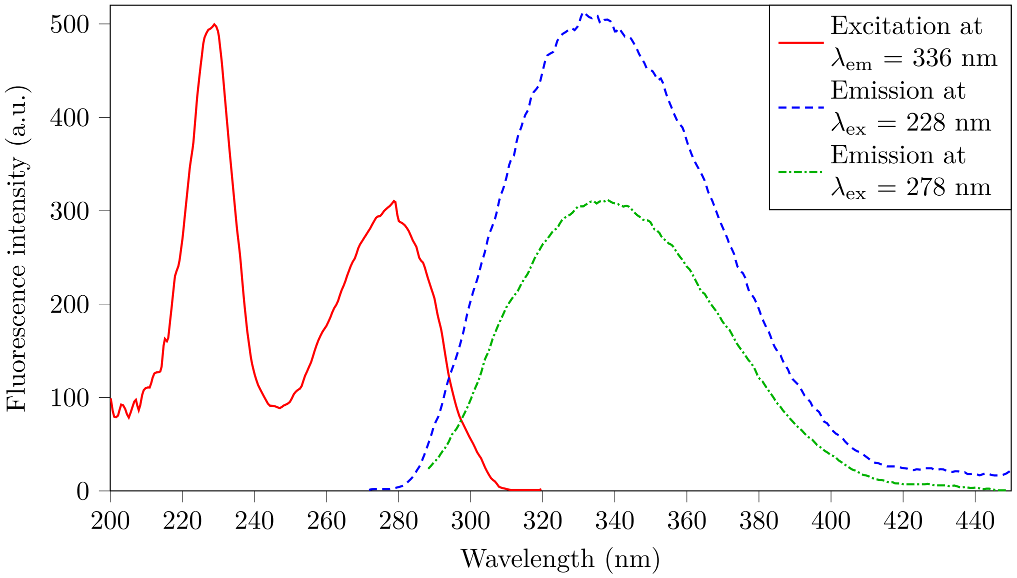

Figure 2.17: O_2Hb excitation and emission spectra. The excitation spectrum at λ_{em} = 336 nm exhibits two maxima at 228 and 278 nm, at which the corresponding emission spectra were measured.

in the same order of magnitude as the difference reported by Itoh *et al.*[221] or Hirsch *et al.*[228]. By performing such measurement, our aim was mainly to be sure that no other haemoglobin fluorescence existed apart from that already reported elsewhere.

2.4.2.3 Other Endogenous Fluorophore

When performing optical measurements *in vivo*, one should also take into account the presence of other endogenous fluorophores. Several reviews have been written on the topic[235, 236] and it appears than many fluorescent compounds are naturally present in human tissues. These fluorophores are most likely to interfere with haemoglobin fluorescence measurements, as can be seen in Figure 2.18. Of particular interest, haemoglobin is only considered as an absorber—and not as a potential source of fluorescence—in most fluorescence studies using endogenous fluorophores. One might thus expect its emission to be much lower than that of most other endogenous fluorophores[237].

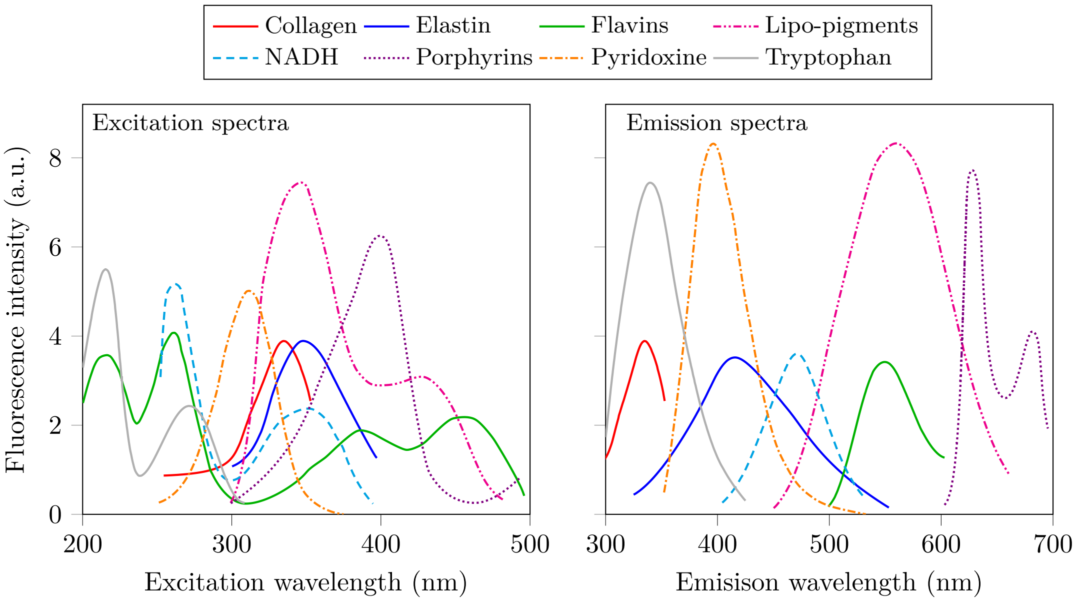

Figure 2.18: Fluorescence excitation (left) and emission (right) spectra of various endogenous tissues fluorophores. Drawn using data from [235].

Other studies focused on more specific media such as blood, erythrocyte, or serum. Wolfbeis *et al.*, for instance, measured the fluorescence spectrum of human serum, which exhibits a strong fluorescence corresponding to that of tryptophan, but otherwise weakly fluoresces[238]. Gao *et al.*[239], for their part, wrote a brief letter indicating the strong fluorescence of mouse blood—and especially erythrocytes—under a 457.9 nm excitation from Ar^+ laser. Alas, the authors did not specify the state of oxygenation of the blood that they used.

On the same topic, Saytashev *et al.*[240] used two-photon excitation fluorescence on one hand, and third harmonic generation(14) on the other hand, to study the fluorescence of erythrocytes through transfusion blood bag membranes made out of polyvinyl chloride (PVC). They used a Ti-Sapphire 800 nm laser for two-photon excitation fluorescence and a Yb-Fiber 1060 nm laser for third harmonic excitation. They also used a combination of both to equate to a 430 nm excitation. The authors performed imaging of the erythrocytes through the plastic bag membrane but could only "see" through one layer of erythrocytes because of their strong optical absorption.

Finally, from a more clinical point of view, fluorescence can also be used to probe suspicious tissues for the presence of cancerous cells. As soon as 1987, Yuanlong *et al.*[241] noticed that variations in fluorescence intensity—probably due to local variations in tryptophan content—exist between tumorous and healthy tissues. These differences were confirmed in acetone extracts and relate well to those caused by variations in porphyrin concentration. Masilamani *et al.* also studied the effect of cancer on fluorescence spectra of acetone-extracts of tumorous blood in 2004[242], and their results were later confirmed by Lualdi *et al.* in 2007[243], and by themselves in 2012[244].

2.4.2.4 Light Penetration in Tissues

Transcutaneous optical measurements have been widely used over the past decades to gain insights into the physiological or clinical state of a subject—*e.g.* in the context of pulse oximetry, as exposed in Section 2.2.2. However, such measurements always take place within the so-called "optical-window" of the tissues—*i.e.* in the 600–1000 nm range—wherein the absorptions of haemoglobin, water, and melanin are low enough to allow for light at these wavelengths to penetrate several millimetres deep inside the tissues. Indeed, from infrared wavelengths up to 630 nm, one can expect a light penetration depth in the 2–6 mm range for an attenuation factor from(15) $1/e$ to 1/100, depending on the authors[216–218].

Alas, things turn sour as the excitation wavelength shortens. For instance, when Bruls *et al.*[245] published their measurements of light transmission in human stratum corneum and epidermis, they reported an exceedingly low transmission of human skin upper layers in the ultraviolet range, with less than 5% of transmitted light at a 60 µm depth, using a 297 nm wavelength. These 5% can be compared with 53% of transmitted light at the same depth for a 546 nm incident radiation. Similar studies reported penetration depths(16) of less than 200 µm for excitation wavelengths of 400–450 nm[246–248]. These results might be explained by the strong absorbance in the ultraviolet region of the spectrum exhibited by most skin chromophores[249].

Yet, other authors such as Sinichkin *et al.* are less pessimistic: in a study on the fluorescence and attenuation of light in the upper layers of human skin—including the influence of an external pressure on the tissues—the authors concluded that no light penetration can occur deeper than 800 µm at 337 nm and 1500 µm at 460 nm[250].

Finally, on a more visual scale, Stamatas *et al.*[251] performed hyperspectral imaging on a volunteer's cheek. One can see in Figure 2.19 that at 580 nm the veins and capillary underneath the skin are clearly visible, demonstrating that light penetrates the tissues quite deep at this wavelength. However, the latter capillary bed becomes invisible at 450 nm—even if the haemoglobin optical density at this wavelength is extremely high—the upper layers of the skin preventing all the incident light from penetrating into the tissues.

2.4.3 Discussion

We stated earlier in Section 2.4.2 that three main requirements needed to be fulfilled in order to make transcutaneous haemoglobin fluorescence measurements feasible. Those three arguments are reconsidered below in light of the afore-presented bibliography:

---

(14) A non-linear optic propagation phenomenon, which generates several harmonics of a fundamental excitation frequency.

(15) $e = \exp(1) \approx 2.71$, the Napier's constant.

(16) Defined in this very example as the depth required to reach a tenfold attenuation. Various authors tend to use the expression "penetration depth" for quite different attenuation factors—*e.g.* $1/e$, 1/3, 1/10, 1/100, *etc.*

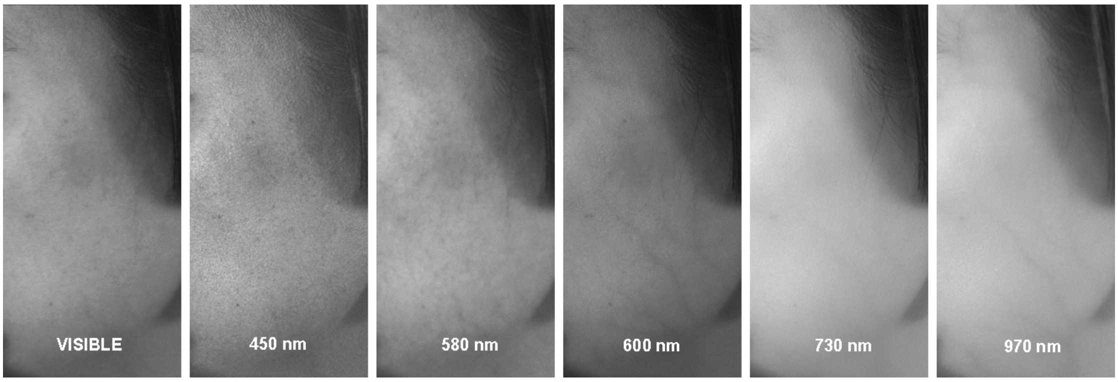

Figure 2.19: Hyperspectral image of a volunteer's face at different wavelengths. Private communication from Georgios Stamatas, a modified version of this picture was previously published in [251].

- **the haemoglobin fluorescence** is extremely weak, which likely explains why it has not been measured until the nineteen eighties, either using front-face optics with relatively dilute solutions (~0.1 mM)[227], or using an extremely dilute solution (2 µM) with more conventional right-angled optics[230]. This fluorescence weakness is justified by the above-mentioned inner filter effect, which makes fluorescence hardly detectable in concentrated haemoglobin solutions such as blood. In particular, the saturation of haemoglobin fluorescence for concentration above 0.16 mM observed by Hirsch *et al.*[227] reveals that—at high concentration—any fluorescence measured from a haemoglobin solution predominantly emanates from the thin layer of the solution present at the surface of its container. For reference, taking a normal haemoglobin concentration in blood of 13–15 $g.dL^{-1}$[105] translates into about 2 mM—more than tenfold the upper limit given by Hirsch.

- **the surrounding medium**—for instance blood serum or other tissues—contains many other fluorophores or chromophores—*e.g.* porphyrins, Oxydised Nicotinamide Adenine Dinucleotide (NADH), collagen or elastin. In all the available studies which listed such compounds and characterised their fluorescence, haemoglobin was always considered only as a purely absorbing species, showing no measurable fluorescence compared to that of other fluorophores[235–238].

- **the probed tissues** and especially the upper layers of the skin, are translucent in the 600–1000 nm optical window. However they become more and more opaque as the wavelength shortens and most authors reported a depth of penetration of at most 60–200 µm on the 300–450 nm range[245–249]. Even if Sinichkin *et al.* argue for higher values up to 1500 µm[250], such values are still way below those reported for the lower wavelengths usually selected for pulse oximetry.

2.4.3.0.1 Conclusion: facing such facts, we concluded that haemoglobin transcutaneous fluorescence measurements are but a lost cause. Thus, we did not push our experimentations any further to determine whether the fluorescence spectra of HHb, O_2Hb, or CO_2Hb do actually differ or not.

2.5 Conclusion

In humans, blood gases are transported through several pathways: O_2 is carried both as a dissolved gas and bound to haemoglobin, while CO_2 is transported in these same forms as well as in the form of bicarbonate ions and carbamates—Section 2.1. One interesting feature of haemoglobin is its strong optical absorption—the latter gives blood its vivid red colour—which depends on the oxidation state of the molecule—Section 2.2.1. This latter difference in the absorption spectra of HHb and O_2Hb gave rise to blood oximetry in the forties, followed by pulse oximetry in the seventies—Section 2.2.2. Owing to the global success of the latter technique, and to the recent possibility of embedding it into ubiquitous wearables, I thought that having an equivalent for CO_2Hb would be a convenient means to address my doctoral thesis' problematic. However, putting this naive idea into practice would require the absorption spectrum of CO_2Hb to be significantly different from that of other haemoglobin species. The above-presented experimentations demonstrated that this is unfortunately not the case, thus sealing the coffin of pulse carbametry—Section 2.3. Out of curiosity, additional research was performed on haemoglobin fluorescence, but the latter proved to be unusable for *in vivo* transcutaneous measurements—Section 2.4.

Retrospectively, with hindsight, the chances that CO_2Hb and HHb absorption spectra differed significantly were rather tenuous from the outset. Indeed, changes in the absorption spectra of haemoglobin with its ligation state are the result of conformational changes in the haemoglobin molecule itself[98]. Details on these changes have been well documented by a number of authors[225, 252–254] and Yuan *et al.* recently wrote a thorough review on this very topic[229]. However, no change of the same order of magnitude seems to happen when CO_2 binds to haemoglobin's amino groups. To the best of my knowledge, only Arnone *et al.* studied the tenuous structural changes of HHb upon CO_2 binding, concluding that "CO_2 binding does not result in major changes in β chain tertiary structure"[255]—knowing that α chains CO_2-binding is even weaker than that of β chains. This lack of major structural change of haemoglobin upon CO_2 binding in turns likely explains why HHb and CO_2Hb absorption spectra are so close to each other(17).

Following this conclusion, I decided to reorient my research towards transcutaneous CO_2 diffusion, as discussed in the following chapters. Of note, I recently conducted Near Infra-Red (NIR) measurements of O_2Hb, HHb, COHb, CO_2Hb and MetHb spectra across the 600–2350 nm range. Due to the shortness of time and the non-trivial extraction of haemoglobin absorption spectra from raw measurements—mainly caused by the significant absorption of water above 1300 nm—these measurements are not included in this doctoral work. From a very qualitative point of view, these measurements yielded HHb and CO_2Hb absorption spectra that were identical to the naked eye—as strongly expected. A more rigorous and quantitative analysis should be published soon—*i.e.* by early 2025 approximately—so stay tuned.

---

(17) As the compassionate reader can imagine, I was not aware of the state of affair described in this latter paragraph until years after having performed my original CO_2Hb spectrum measurements.

Chapter 3

Transcutaneous CO_2 Sensing

TL;DR

Given the failure of the spectrophotometric approach envisioned in the previous chapter, the remainder of this doctoral work focuses solely on transcutaneous CO_2 sensing. To perfect this latter approach, it was necessary to better understand the specificities of transcutaneous CO2 measurement. More specifically, this chapter delves into the following processes:

1. Constructing a mathematical model to determine the factors influencing the response time of such a sensor. This response time is ultimately dependent on two elements: the skin's conductivity towards CO_2 and the sensor's equivalent height—*i.e.* its internal volume divided by its contact surface with the skin.
2. Characterising the latter conductivity, and its dependence on skin temperature in particular. A clinical study was performed on 40 subjects, showing that *not* heating the skin would be acceptable from a response time point of view. This study also provided evidence that doing so might lead to $tcpCO_2$ values that are close enough to $paCO_2$.
3. Pinpointing the environmental conditions of cutaneous sensing. The latter involves a temperature in the 32–34°C range without external clothing—35° with—and humidity levels above 80–100% Relative Humidity (RH). The skin itself is highly hypoxic—but O_2 is still present—and acidic.

Taken together, this knowledge provides a framework for the development of future $tcpCO_2$ sensors, as described in the following chapters.

Previous chapter Main Table Of Content (TOC) Next chapter

As mentioned in the introduction, the many limitations of current $tcpCO_2$ monitors—combined with the unfeasibility of pulse carbametry—both call for a new generation of transcutaneous CO_2 sensors to be developed. To this end, it is necessary to better understand the specificities of transcutaneous CO_2 sensing, in particular by addressing the following questions:

1. How can the working principles of equilibrium-based $tcpCO_2$ sensors be modelled? And what key figures of merit are important to consider when designing such a sensor?
2. What are the specificities of transcutaneous CO_2 diffusion? In particular, what is the influence of skin temperature on the skin conductivity towards CO_2?
3. What factors are influencing the final $tcpCO_2$ value at equilibrium? In particular, what is the influence of skin temperature on the $paCO_2$ / $tcpCO_2$ correlation?
4. What conditions—temperature, humidity, acidity or ionic content—can be expected at the skin?

This first aspect is addressed in Section 3.1, which is strongly inspired by the Section 4.2 and

Supplementary Materials of our(1) 2022 Sensors review article[88]. The second and third aspects are then discussed in Section 3.2, based on our 2023 Frontiers in Physiology paper[87]. Finally, the fourth aspect is treated in Section 3.3.

3.1 Modelling Equilibrium-Based tcpCO_2 Sensing

This first section focuses on studying the transcutaneous diffusion of CO_2 using a simple skin and equilibrium-based sensor model. After presenting the said model in Section 3.1.1 and briefly discussing the influence of the sensor's chamber nature in Section 3.1.2, the dynamic of tcpCO_2 measurements is derived in Section 3.1.3. Finally, the existing literature is reviewed to estimate the achievable response times for future tcpCO_2 sensors in Section 3.1.4. Of note, the perceptive reader may wonder why the emphasis is placed on *equilibrium-based* sensing in the present work. This is to distinguish it from another modality of tcpCO_2 sensing, called *rate-based* sensing, which has been investigated by some authors. Although largely beyond the scope of my research, this alternative sensing technique is briefly mentioned in Section 4.2.4.1.

3.1.1 The Model

The model of transcutaneous CO_2 sensing that is considered in all subsequent developments is presented in Figure 3.1. In this model, the subcutaneous tissues are considered as a homogeneous, semi-infinite medium occupying the $x \leq 0$ space volume. The subcutaneous tissues can be thought of as a CO_2 reservoir with a constant partial CO_2 pressure equal to tcpCO_2. Between $x = 0$ and $x = w$ is the skin membrane, of thickness w and diffusivity D ($m^2.s^{-1}$) towards CO_2. In this skin model, the sub-cutaneous tissues and skin barrier are only used as a representation, and the skin barrier does **not** represent literally the stratum corneum. Consequently, the w and D parameters can hardly be measured experimentally since they are mere model parameters—see Section 3.2.6.2.1 for a more detailed discussion on this topic.

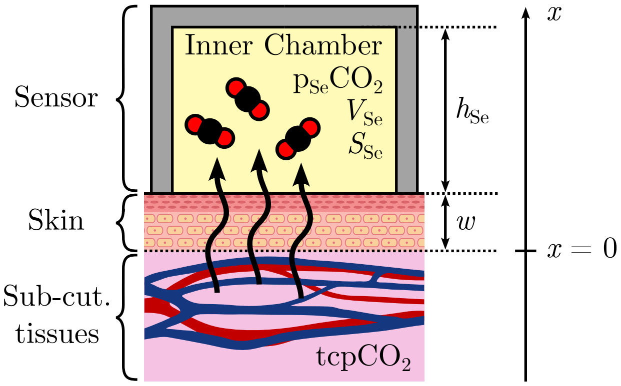

Figure 3.1: Simplified model of CO_2 diffusion through the skin inside a closed sensor.

On top of these two layers is positioned a sensor consisting in an inner sensing medium of volume V_{Se}, surface in contact with the skin S_{Se} and height $h_{Se} = V_{Se}/S_{Se}$. This sensor is in turn surrounded by a gas-tight enclosure, preventing gaseous exchanges between the sensing medium and the outside—except for those with the skin surface, of course.

3.1.2 Inner Sensing Medium

In the calculations conducted throughout the next sections, the inner sensing medium is always considered as an homogenous air volume. While this assumption is more than justified in the case of NDIR or (photo-)acoustic sensors, it seems more debatable in the case of conductometric or dye-based sensors—these different types of sensor are reviewed in Chapter 4. Yet, every sensing medium can be viewed as a potential CO_2 reservoir through Henry's law, and thus be considered as an equivalent air volume.

For instance, if the sensing medium is water—*e.g.* in the case of a wet conductometric sensor—with a water volume V_{water} of height h_{water}, this latter water volume is equivalent to an

---

(1) There again, and in the corresponding sections, the first person plural was chosen since those are collective works, whose authorship I share with my co-authors.

air volume $V_{\text{air,eq}}$ of height $h_{\text{air,eq}}$ such that the amount of CO$_2$ dissolved in the water volume $n_{\text{CO}_2\text{,water}}$ (mol) is the same as that in an equivalent air volume $n_{\text{CO}_2\text{,air,eq}}$ for a given pCO$_2$, *i.e.*

$$n_{\text{CO}_2\text{,air,eq}}(\text{pCO}_2) = n_{\text{CO}_2\text{,water}}(\text{pCO}_2) \tag{3.1}$$

with

$$\begin{aligned} & n_{\text{CO}_2\text{,air,eq}}(\text{pCO}_2) = \frac{\text{pCO}_2 \cdot V_{\text{air,eq}}}{R \cdot \text{T}} \quad \text{(ideal gas law)} \\ & [\text{CO}_{2\text{, water}}] = K_s \cdot \text{pCO}_2 \quad \text{(Henry's law)} \\ & n_{\text{CO}_2\text{,water}}(\text{pCO}_2) \triangleq V_{\text{water}} \cdot [\text{CO}_{2\text{, water}}] \\ & V_{\text{water}} = S_{Se} \cdot h_{\text{water}} \quad \text{and} \quad V_{\text{air,eq}} = S_{Se} \cdot h_{\text{air,eq}} \end{aligned} \tag{3.2}$$

wherein R is the ideal gas constant (J.K^{-1}.mol^{-1}), T the temperature (K) and K_s is the solubility of CO$_2$ in water (mol.m^{-3}.Pa^{-1})—as reported by Weiss[256], for instance. Combining the above equations yields

$$h_{\text{air,eq}} = h_{\text{water}} \cdot R \cdot \text{T} \cdot K_s \tag{3.3}$$

Taking Weiss' value for K_s in pure water at 293 K under 1 atm yields

$$h_{\text{air,eq}} \approx 0.952 \cdot h_{\text{water}} \tag{3.4}$$

and a similar train of thought can be applied to other media. Thanks to Henry's law, it is thus theoretically always possible to convert from a given sensing medium into an equivalent air volume as is done above for water.

Of note, one should bear in mind that the afore considerations are especially true if the CO$_2$ diffusion process into the sensing medium is also neglected. Indeed, it is assumed in the remainder of this chapter that as soon as CO$_2$ crosses the skin barrier and reaches the sensing medium itself, it readily diffuses into it. Thus the pCO$_2$ inside the sensing medium is considered to be homogenous and only a function of the amount of CO$_2$ having diffused through the skin. This assumption is more than justified in first approximation when considering the response times of the different sensing techniques presented in Chapter 4. Indeed, most of them easily reach response times below 1 min, which is far below the response times of the simple model presented in Section 3.1.4 for thicknesses h_{Se} in the order of 100 µm, or above.

3.1.3 Diffusion Through the Skin

The CO$_2$ diffusion across the skin barrier can be studied using Fick's first law of diffusion:

$$J_S = -D \cdot \frac{d[\text{CO}_2](x)}{dx} \tag{3.5}$$

wherein J_S is the CO$_2$ diffusion flux per unit area (mol.m^{-2}.s^{-1}), D the diffusivity of skin toward CO$_2$ (m^2.s^{-1}), and [CO$_2$] the CO$_2$ concentration (mol.m^{-3}) inside the skin membrane itself. With the hypothesis ($\mathcal{H}_1$) that there is no CO$_2$ accumulation inside the skin itself—*i.e.* that the capacitive effect of the skin is negligible compared to that of the sensing medium—J_S can be considered constant along the x axis, leading to:

$$J_S = \frac{D}{w} \cdot ([\text{CO}_2](x=0) - [\text{CO}_2](x=w)) \tag{3.6}$$

Since $x = 0$ corresponds to the subcutaneous tissues—wherein pCO$_2$ = tcpCO$_2$—and $x = w$ corresponds to the inner sensing medium—wherein pCO$_2$ = p$_{\text{Se}}$CO$_2$—we have

$$\begin{cases} [\text{CO}_2](x=0) = K_{\text{skin,CO}_2} \cdot \text{tcpCO}_2 \\ [\text{CO}_2](x=w) = K_{\text{skin,CO}_2} \cdot \text{p}_{\text{Se}}\text{CO}_2 \end{cases} \tag{3.7}$$

wherein $K_{\text{skin,CO}_2}$ is the solubility of CO$_2$ into the skin (mol.m^{-3}.Pa^{-1}). Besides, under ($\mathcal{H}_1$):

$$\frac{dn_{\text{CO}_2\text{, Se}}}{dt} = S_{\text{Se}} \cdot J_S \tag{3.8}$$

wherein $n_{\text{CO}_2\text{, Se}}$ is the amount of CO$_2$ in the inner sensing medium (mol), given by:

$$n_{\text{CO}_2\text{, Se}} = \frac{\text{p}_{\text{Se}}\text{CO}_2 \cdot V_{\text{Se}}}{R \cdot \text{T}} \quad \text{(ideal gas law)} \tag{3.9}$$

Equations 3.6–3.9 then yield:

$$\frac{d\mathrm{p_{Se}CO_2}}{dt} = \frac{D}{w{\cdot}h_{\mathrm{Se}}}{\cdot}R{\cdot}\mathrm{T}{\cdot}K_{\mathrm{skin,CO_2}}{\cdot}\left(\mathrm{tcpCO_2} - \mathrm{p_{Se}CO_2}\right) \tag{3.10}$$

Additionally, $K_{\mathrm{skin,CO_2}}$ can be estimated from the solubility of CO_2 in various biological tissues[257–260] leading to an $R{\cdot}\mathrm{T}{\cdot}K_{\mathrm{skin,CO_2}}$ factor in the 0.6–1.0 range. Close to these values, Scheuplein *et al.*[259] present an $R{\cdot}\mathrm{T}{\cdot}K_{\mathrm{skin,CO_2}}$ product near 1.5 for the stratum corneum. Again though, the skin membrane of the afore-presented model does not necessarily represent the stratum corneum alone, but is only a model for the different skin layers that may hinder CO_2 diffusion. Consequently, I chose to take the $R{\cdot}\mathrm{T}{\cdot}K_{\mathrm{skin,CO_2}}$ product equal to 1 in the following developments. Another possibility would be to simply integrate its value inside the w/D ratio, leading to identical conclusions in the end, at the cost of an additional complexity in the writing. Discarding it yields the following simplified differential equation

$$\frac{d\mathrm{p_{Se}CO_2}}{dt} = \frac{D}{w{\cdot}h_{\mathrm{Se}}}{\cdot}\left(\mathrm{tcpCO_2} - \mathrm{p_{Se}CO_2}\right) \tag{3.11}$$

which—considering the initial condition $\mathrm{p_{Se}CO_2}(t = 0) = 0$—has a unique solution:

$$\mathrm{p_{Se}CO_2}(t) = \mathrm{tcpCO_2}{\cdot}\left(1 - e^{-\frac{t}{\tau}}\right), \quad \text{with } \tau = h_{Se}{\cdot}\frac{w}{D} \tag{3.12}$$

This formulation is essentially the same as that derived by Chatterjee *et al.*[261], although they used a more sophisticated model taking into account the CO_2 production inside the skin, leading to an additional β/α factor in Equation 6 of their work. Equation 3.12 describes a classical first-order response, as can be seen in Figure 3.2, Left, with a 95% response time $\mathrm{Tr_{95\%}} \approx 3{\cdot}\tau = 3{\cdot}h_{\mathrm{Se}}{\cdot}w/D$. It is important to note at this point that only the equivalent height h_{Se} of the sensor really matters from a response time point of view. The actual inner volume of the sensor may indeed be convoluted—*i.e.* have a non-prismatic shape—only its volume to surface ratio h_{Se} comes into play in the above considerations.

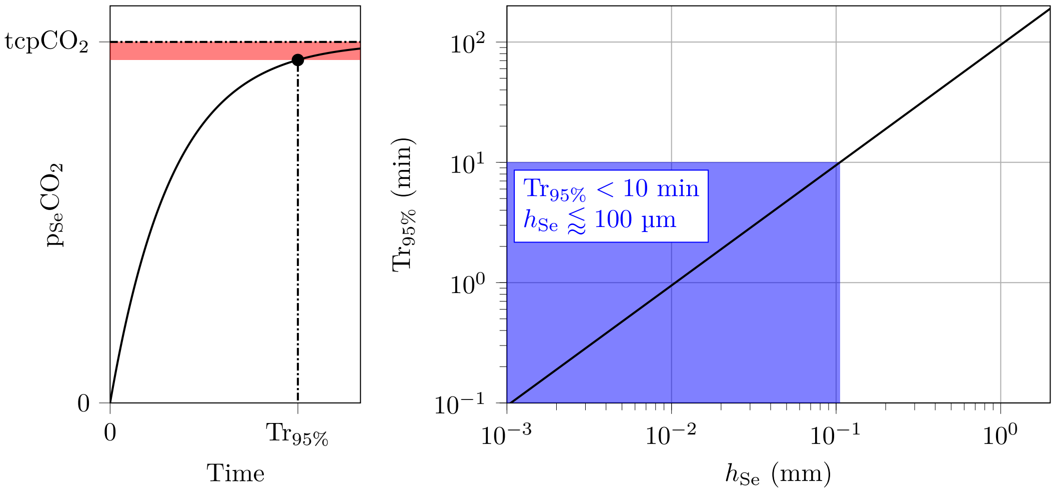

Figure 3.2: 95% response time ($Tr_{95\%} \approx 3{\cdot}\tau$) for a sensor of height h_{Se}. The blue area underlines the portion of the line with a response time below 10 min, which corresponds to a sensor height below approximately 100 µm.

3.1.4 Response Time

As mentioned in Section 3.1.1, the w and D parameters cannot be measured experimentally since they are only model parameters. However, the w/D fraction can be estimated from the CO_2 exhalation rate through the skin per unit area—Q ($\mathrm{m^3.m^{-2}.s^{-1}}$)—defined as

$$Q = \frac{1}{S_{\mathrm{Se}}}{\cdot}\frac{dV_{\mathrm{CO_2,Se}}}{dt} \tag{3.13}$$

wherein $V_{\mathrm{CO_2,Se}}$ is the volume that would occupy the CO_2 contained inside the sensing medium if considered as pure CO_2 under a total ambient pressure $\mathrm{p_0}$, and given by

$$\frac{V_{\mathrm{CO_2,Se}}}{V_{\mathrm{Se}}} = \frac{\mathrm{p_{Se}CO_2}}{\mathrm{p_0}} \tag{3.14}$$

yielding:

$$Q = \frac{h_{\mathrm{Se}}}{\mathrm{p}_0} \cdot \frac{d\mathrm{p}_{\mathrm{Se}}\mathrm{CO}_2}{dt} \tag{3.15}$$

Taking the first derivative of $\mathrm{p}_{\mathrm{Se}}\mathrm{CO}_2$—see Equation 3.12—with respect to time, and evaluating it at $t = 0$ leads to

$$\tau = \frac{h_{\mathrm{Se}}}{Q} \cdot \frac{\mathrm{tcpCO}_2}{\mathrm{p}_0} \quad \text{or} \quad \frac{w}{D} = \frac{\mathrm{tcpCO}_2}{Q \cdot \mathrm{p}_0} \tag{3.16}$$

Several works on the determination of Q for CO_2 across human skin can be found in the literature—see Table 3.3, below—and a value of 100 $\mathrm{cm}^3.\mathrm{m}^{-2}.\mathrm{h}^{-1}$ can reasonably be assumed. Since the afore-mentioned works concern healthy subjects, we can also assume a normal capnia of 5.3 kPa (or 40 mmHg)[33]. In these conditions, and $\mathrm{p}_0 = 1$ atm:

$$\frac{w}{D} \approx 1.90 \times 10^6 \ \mathrm{s.m}^{-1} \tag{3.17}$$

In other words, if the sensor has a height of 1 mm, τ will be near 1900 s, or about 32 min, and a 95% response will be achieved after 1 h 35 min—or $3{\cdot}\tau$. A more realistic response time—and above all one that can be used in clinical practice—of below 10 minutes requires for its part a thickness of less than 100 µm, as can be seen in Figure 3.2, Right.

Note: Q is of course time-dependent, especially during transcutaneous monitoring with the presented closed-chamber sensor model—as it will decrease with a diminishing tcpCO_2 / $\mathrm{p}_{\mathrm{Se}}\mathrm{CO}_2$ gradient. However, since only its value at $t = 0$ has been used in the end in the above development, and since it is also the only Q value reported in the literature, the $Q(t)$ notation was neglected.

3.1.5 Consequences for the Design of Future tcpCO_2 Sensors

The response time of the sensor introduced in the above model is thus only function of two elements:

1. the dimensions of the sensor itself, and more specifically the equivalent height h_{Se} of its sensing chamber, *i.e.* the $V_{\mathrm{Se}}/S_{\mathrm{Se}}$ ratio—as mentioned in Section 3.1.3—and

2. the properties of the skin membrane, and more specifically its thickness and diffusivity towards CO_2—*i.e.* the w/D ratio.

Quite intuitively, a large surface to volume ratio for the sensing chamber, a thin skin membrane and an elevated skin diffusivity towards CO_2 all lead to a faster sensor. Consequently, in order to decrease the response time of a transcutaneous CO_2 sensor, one can either act on the sensor's form factor—by designing a thinner sensor—or on the skin diffusivity and thickness. While choosing a CO_2 sensing technique with a compact form factor is at the very heart of Chapter 4, the next section focuses on the skin diffusivity towards CO_2. More specifically, several authors reported an increasing transcutaneous CO_2 exhalation rate with an increasing temperature[262–264]. However, the latter temperature was often that of the ambient air surrounding the skin, and not that of the skin itself. I thus decided to lead a thorough clinical study on this very topic, which is the object of the next section. As a side note, this study also led me to take an interest in skin stripping—*i.e.* thinning the skin—and its impact on the transcutaneous CO_2 exhalation rate—see Section 3.2.6.3.1.

3.2 Skin Temperature Influence on Transcutaneous CO_2 Conductivity and Skin Blood Flow

Of note, this section is essentially a slightly revised(2) version of the article entitled *Skin temperature influence on transcutaneous carbon dioxide (CO_2) conductivity and skin blood flow in healthy human subjects at the arm and wrist*, and published in the Frontiers in Physiology journal in late 2023[87].

---

(2) In particular, a large part of the introduction of the original article has been omitted.

3.2.1 Introduction

It stems from the above that developing a new generation of tcpCO_2 sensors requires to address the two following issues:

1. First, in order to dimension the sensor-to-be, it is essential to accurately know the CO_2 *exhalation rate* through the skin, as the latter directly influences the response time of the sensor.

2. Then, it is mandatory that the tcpCO_2 and paCO_2 are in good agreement at the skin temperature considered for measurement. *Id est*, that the *correlation* between tcpCO_2 and paCO_2 is satisfactory at the latter temperature.

Starting with the exhalation rate, the main issue with data available in the literature—see Table 3.3—is that the skin temperature is only mentioned once—by Eöry[265]—and never accurately regulated when this parameter is measured[92]. Even though Levshankov *et al.*[266] crafted a heating device, they do not report the temperature setpoint that they used. Thus, **the below-presented study aims at filling this gap by measuring the influence of skin temperature on the transcutaneous CO_2 exhalation rate**.

While the tcpCO_2 / paCO_2 correlation is excellent at—or above—42°C[69], scarce are the authors who investigated lower skin temperatures, with none but Wimberley *et al.*[267] experimenting with temperatures as low as 38°C. The reason for heating the skin in the first place is to trigger a local reactive hyperaemia[268]. By doing so, the subcutaneous tissues are flushed with fresh arterial blood, and their gaseous content thus gets closer to the arterial one[42, 269, 270]. While temperatures in the 42–44°C range have often been used to trigger maximal hyperaemia, lower temperatures have been seldom explored[271], and **we thus took advantage of our exhalation rate measurements to measure the skin blood flow at lower temperatures simultaneously**.

Then, the reader should bear in mind the importance of skin temperature for designing a new kind of tcpCO_2 sensor. Indeed—ideally—such a sensor should heat the skin as little as possible for two main reasons: *(i)* heating the skin is uncomfortable for the patient and can wake them up in the case of night time monitoring, and *(ii)* it consumes a significant amount of power, which precludes using such sensor in a wearable, as mentioned above. Yet, such an unnoticeable and wearable tcpCO_2 sensor would be highly desirable in a telemonitoring context for home use, reducing the need for hospital visits. Indeed, if the positive impact of tcpCO_2 telemonitoring is yet to be demonstrated—for the obvious reason that the corresponding wearable tcpCO_2 monitor does not exist at the time being—several clinical trials demonstrate the beneficial contribution of telemedicine—*a.k.a.* telehealth—on both patient's outcome and costs of admission in a variety of conditions[74–76]. Additionally, the outbreak of contagious pandemics—such as COVID-19[77]—and the rapid development of the health wearable market[78–81] may also promote the use of telemonitoring in medical practice. For these reasons, *not* heating the skin while measuring tcpCO_2 would be highly desirable.

The following study focuses on measuring the transcutaneous CO_2 exhalation rate and cutaneous micro-circulation on the full Non-Heated (NH)–44°C skin temperature range. Two measurement sites were investigated: the dorsal side of the wrist and the lateral aspect of the upper arm, while the skin blood flow was only measured at the upper arm. Additionally, a strong emphasis was placed on the transcutaneous CO_2 *conductivity*, which may be preferred to the well-known exhalation rate because of its more intrinsic nature—in particular, the latter conductivity does not depend on the ambient CO_2 level, nor on the subject's paCO_2, as opposed to the exhalation rate, which is influenced by both.

3.2.2 Materials

3.2.2.1 The Transcutaneous CO_2 Rate Sensor

A custom transcutaneous CO_2 diffusion rate sensor—hereafter simply denoted as "the sensor"—was developed for the needs of this study. Its basic working principle is close to that evoked in Section 3.1—and will be further detailed in Section 3.2.3.1.1—while its design is inspired by the early works of Eletr, Greenspan, *et al.*[272, 273]. The general outline of the sensor and its peripherals can be seen in Figure 3.3.

The sensor, designed to be placed against the subject's skin by mean of a double-sided adhesive, is connected to three main apparatuses: *(i)* a calibrated, reference thermometer (Testo 735, Testo, Germany) equipped with a type K thermocouple (110-4482, RS Pro, UK), *(ii)* a

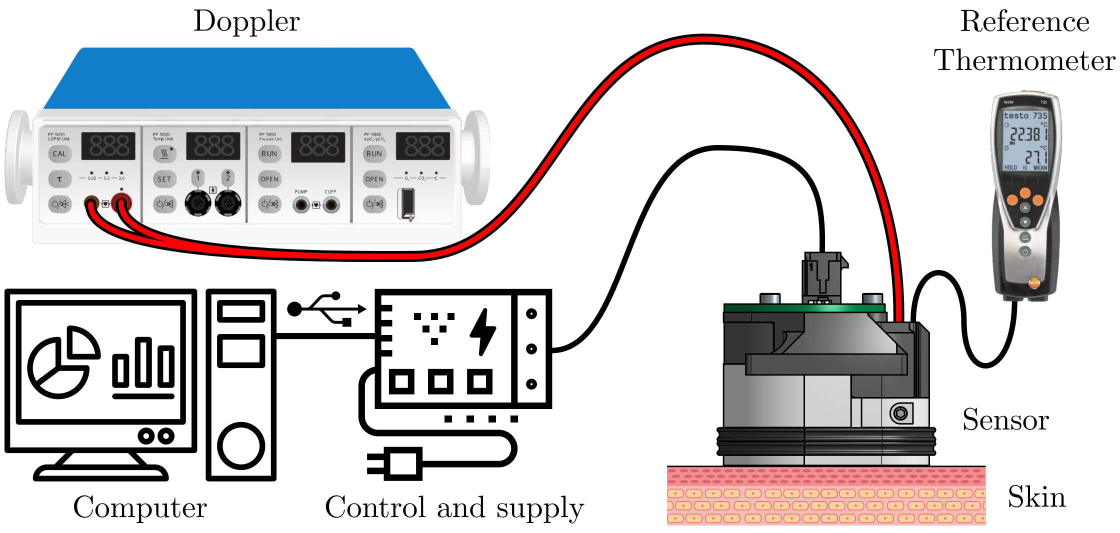

Figure 3.3: General outline of the rate sensor and its peripherals. See the text for further explanations.

Doppler perfusion monitor (Periflux 5000, Perimed, Sweden) equipped with a 407 probe, and *(iii)* a control and supply block, consisting in a thermostat, a power supply unit, and a Universal Serial Bus (USB) to Universal Asynchronous Receiver Transmitter (UART) converter, embedded in a 3D-printed case. For the sake of conciseness though, the control and supply block is only detailed in Appendix D, which also contains a thorough analysis of the safety issues that may arise when using this sensor. The sensor itself can be seen in great details in Figure 3.4. It consists in an aluminium (2017A) body, which serves as a support for the following elements: a CO_2 sensor, a heating resistive wire, a thermistor, a thermocouple, the Doppler probe, a polylactic acid (PLA) 3D-printed cover, and an interfacing Printed Circuit Board (PCB). Complete drawings of the sensor's body are provided in Appendix D.

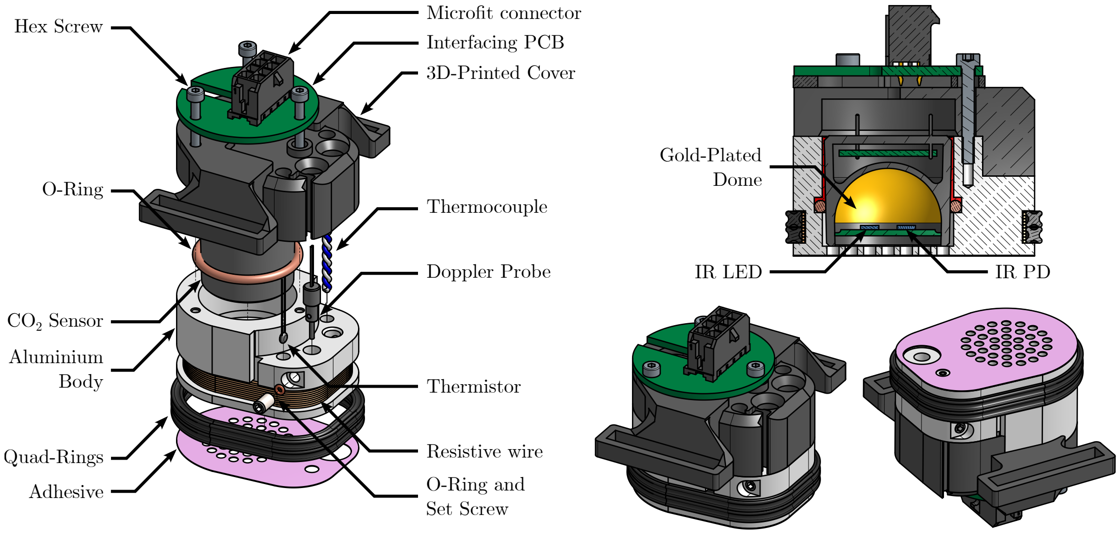

Figure 3.4: Detailed views of the sensor. **Left:** exploded view, detailing its different parts. **Top right:** cut view, showing the inner functioning principle of the CO_2 sensor. Note the epoxy resin sealing, in red. **Bottom right:** isometric views from above, and below, of the fully assembled sensor, illustrating the grid-shaped sensor's sole.

The CO_2 sensor is a MinIR (ExplorIR - M5%, CO2Meter, USA), an off-the shelf, compact, NDIR CO_2 sensor, with a full range of 5% and an accuracy of 70 ppm ±5% of reading at Standard Temperature and Pressure (STP)—see Hodgkinson *et al.*[274] for further details on the operating principle of such sensors. Its internals—a pair of IR Light Emitting Diode (LED) and photodiode (PD) facing a spherical, gold-plated mirror—may be seen in the cut view of Figure 3.4. The pCO_2 inside the sensor was recorded with a sampling frequency of 2 Hz.

As the gas-tightness of the measuring chamber is a critical aspect of the sensor's operating principle—see Section 3.2.6.1.3—a two-stage sealing was implemented: *(i)* a silicone-grease coated (515520, GEB, France), soft—60 Shore A hardness—silicone O-ring was placed between the aluminium body and the CO_2 sensor itself and *(ii)* liquid epoxy resin (Résine Cristal, Gédéo, France) was cast in the remaining interstice between the latter two elements—illustrated in the cut view of Figure 3.4 in vivid red.

The thermoregulation of the sensor is performed by mean of a resistive wire for heating, coupled to a thermistor for temperature measurement and regulation. For verification purposes, an additional thermocouple was also added, as stated above. The heating wire consists in 2×15 turns of 28 $\Omega.m^{-1}$, 0.15 mm in diameter, enamelled, resistive, constantan wire (Isotan, Thomsen), connected in parallel. The wire delivers a total heating power of 6.1 W under 12 V, and is coiled around the aluminium body, in a dedicated groove. The bottom of the groove is covered with a layer of 0.25 mm thermally conductive double sided tape (8810, 3M, USA) prior to coiling the wire, and the latter is finally covered with two nitrile quad rings, as can be seen in Figure 3.4. This covered layout prevents burns caused by direct contact with the heating wires. The thermistor (151-237, RS Pro, UK) and thermocouple were glued in two dedicated flat-bottom mounting holes which were pre-filled with a thermally conductive, electrically non-conductive, epoxy resin (8329TFM, MG Chemicals, Canada). Care was taken that *(i)* the distance between the bottom of the mounting holes and the heating wire and *(ii)* that between the sole of the sensor's body and the heating wire were equal, in order to ensure that the temperature measured by the thermistor and thermocouple is as close as possible to that of the skin.

The Doppler probe is housed in a dedicated hole, and can slide vertically, in such a way that it can be adjusted to outcrop the sole of the sensor, coming in direct contact with the skin. It holds in place by mean of a cup-pointed, headless, set screw which compresses it radially via an O-ring, so as not to damage the probe. The raw Doppler perfusion signal—originally sampled at 62.5 Hz—was downsampled to 0.625 Hz and low-pass filtered using a tenth-order Butterworth filter prior to further analysis—see Section 3.2.3.1.2.

The 3D-printed cover and interfacing PCB were added for usability purposes: the 3D-printed PLA cover allows to attach a strap (HTH 833 with H83 hooks, Velcro, UK) to the sensor in order to maintain it against a subject's skin, as illustrated in Figure 3.5, Right, while the interfacing PCB gathers the four UART pins from the CO_2 sensor, the two ends of the thermistor, and those of the heating wire into a single eight-pins Microfit connector (0430450812, Molex, USA).

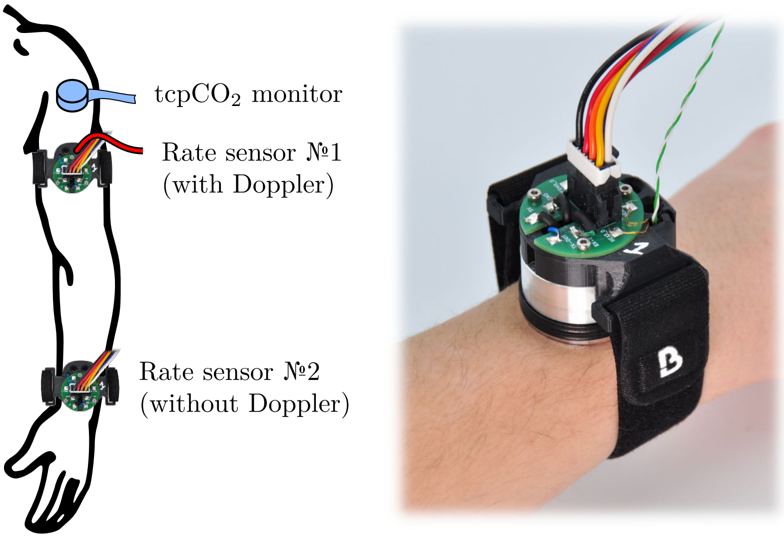

Figure 3.5: **Left:** outline of the sensors used in this study, and their location. **Right:** a picture of the sensor with its connection cable assembly and strap, attached on a wrist.

The adhesive itself consists in a disposable laser-cut, double-sided, clinical-grade tape (1567, 3M, USA). For ease of application, a special tooling was developed to accurately align the sensor and the adhesive together—see Appendix D.

3.2.2.2 Reference tcpCO_2 Monitor

In addition to the above-detailed custom-made sensor, a clinical-grade tcpCO_2 monitor (TCM4, Radiometer, Denmark) was also used on the upper deltoid—one of the recommended sites for tcpCO_2 monitoring[275]—yielding a continuous reference tcpCO_2 reading. The tcpCO_2 sensor itself (tc Sensor 54) was affixed to the skin using an appropriate attachment ring and contact gel, and it was re-membraned and re-calibrated when needed, as per the manufacturer's guidelines. All the accessories used to this end were Radiometer's[276].

3.2.2.3 Sensors Positioning

The different sensors and measurement sites chosen in the study are illustrated in Figure 3.5, Left. All sensors were placed on the subject's left arm: the reference tcpCO_2 monitor was placed on the upper deltoid, as mentioned above, while two custom rate sensors were positioned as follows. The first one was equipped with the Doppler probe, and was attached on the distal side of the upper arm, immediately below the deltoid, at the junction point between the upper part of the biceps, the lower end of the deltoid, and the triceps. The second rate sensor was placed on the dorsal side of the wrist, and did not include a Doppler probe. Both sensors were affixed to the subject's skin by mean of the above-mentioned double-sided adhesive, and secured in place with a Velcro strap. Additionally, the subject's arm laid comfortably onto an arm gutter so that it remains still and relaxed for the whole duration of the experiments.

3.2.3 Methods

3.2.3.1 Measured Metrics

3.2.3.1.1 Skin CO_2 Conductivity and Exhalation Rate

The rate of diffusion—*a.k.a.* the exhalation rate—of CO_2 through the skin per unit of area—hereafter noted Q, of dimension $L^3\ L^{-2}\ T^{-1}$—can be measured by affixing to the skin a cup-like device, which entraps the skin-exhaled CO_2. In this situation, the CO_2 diffusion through the skin can be modelled as already presented in Figure 3.1 and Section 3.1. Briefly, the skin is considered as a CO_2-permeable membrane of thickness w and diffusivity D towards CO_2 (unit of $m^2.s^{-1}$). The partial CO_2 pressure inside the sub-cutaneous tissues and inner chamber are tcpCO_2 and $\mathrm{p_{Se}CO_2}$, respectively, and the sensor area in contact with the skin is S_{Se}, while its equivalent height and volume are h_{Se} and V_{Se}. It can be shown under certain hypotheses—see Section 3.1—that

$$\frac{d\mathrm{p_{Se}CO_2}}{dt} = \frac{D}{w \cdot h_{\mathrm{Se}}} \cdot (\mathrm{tcpCO_2} - \mathrm{p_{Se}CO_2}) \tag{3.18}$$

leading to a first-order behaviour for $\mathrm{p_{Se}CO_2}$, given by

$$\mathrm{p_{Se}CO_2}(t) = \mathrm{tcpCO_2} \cdot \left(1 - e^{-\frac{t}{\tau}}\right) + \mathrm{p_{Se}CO_2}(t=0) \cdot e^{-\frac{t}{\tau}}, \quad \text{with } \tau = \frac{h_{\mathrm{Se}} \cdot w}{D} \tag{3.19}$$

and Q is then equal to

$$Q(t) = \frac{D}{w \cdot \mathrm{p_0}} \cdot (\mathrm{tcpCO_2} - \mathrm{p_{Se}CO_2}(t=0)) \cdot e^{-\frac{t}{\tau}} \tag{3.20}$$

wherein $\mathrm{p_0}$ is the total atmospheric pressure at measurement site. However, since Q depends on both the ambient level of CO_2—*via* $\mathrm{p_{Se}CO_2}(t=0)$—and the subject's capnia—*via* tcpCO_2—we introduced the skin *conductivity*—from the thermodynamic or electrical analogy—expressed in $m.s^{-1}$, and defined as

$$\boxed{K = \frac{D}{w}} = \frac{P_0 \cdot Q(t=0)}{\mathrm{tcpCO_2} - \mathrm{p_{Se}CO_2}(t=0)} \tag{3.21}$$

Contrary to Q, K is an intrinsic property of the skin and is independent of the tcpCO_2 / $\mathrm{p_{Se}CO_2}$ gradient. Additionally, deriving Equation 3.19 and evaluating it at $t = 0$ yield

$$K = \frac{h_{\mathrm{Se}}}{\mathrm{tcpCO_2} - \mathrm{p_{Se}CO_2}(t=0)} \cdot \left.\frac{d\mathrm{p_{Se}CO_2}}{dt}\right|_{t=0} \tag{3.22}$$

In practice, K was thus measured as follows, choosing arbitrarily $t = 0$ at each temperature change:

- h_{Se} is known by dividing V_{Se} by S_{Se}. The latter is known by construction of the sensor's aluminium body, while V_{Se} was estimated by filling a clone of the sensor with a low viscosity fluid—pure ethanol—and weighting it.

- the subject's $\mathrm{tcpCO_2}$ was measured using the above-mentioned reference medical grade monitor. The extraction of a single $\mathrm{tcpCO_2}$ reading for each temperature set-point is detailed in Appendix D.

- $\mathrm{p_{Se}CO_2}(t=0)$ could be measured with a simple reading of the CO_2 sensor.

- $\left.\frac{d\mathrm{p_{Se}CO_2}}{dt}\right|_{t=0}$ was estimated by fitting a linear regression on the measured $\mathrm{p_{Se}CO_2}$. The latter regression was performed on the $\mathrm{p_{Se}CO_2}$ data starting 3 min after a temperature change—to allow for temperature homogenisation of the different inner parts of the sensor—and up to 18 min after, for a total of 15 min of data. This duration was chosen following a preliminary study performed on ten subjects, which yielded R^2 regression scores above 0.95 for a regression duration above 700 s (about 12 min).

In summary, **the diffusion of $\mathbf{CO_2}$ through the skin was quantified by the skin $\mathbf{CO_2}$ conductivity $\boldsymbol{K}$**, which was measured at five different temperatures, each temperature corresponding to a 18 min measurement window for a total of 90 min of acquisition per subject, as detailed in Section 3.2.3.2, below. Additionally, Equation 3.21 was used to compute the corresponding equivalent $Q(t=0)$ with $\mathrm{p_{Se}CO_2}(t=0) \approx 0$—*i.e.* the skin CO_2 exhalation rate in free air as commonly referred to in the literature. Of note, this $Q(t=0)$ was **not** observed in practice, since the sensor was left in place—and thus $\mathrm{p_{Se}CO_2}(t=0) \neq 0$ for most temperatures. For the sake of conciseness, in the remainder of this chapter, the letter Q alone or the mention of "skin CO_2 exhalation rate" without further indications always designate the above-mentioned $Q(t=0)$. Finally, it should be noted that these Q values were derived mainly as a mean to compare with the existing literature, and that the actual statistical analyses were performed on K—see Section, 3.2.4.

3.2.3.1.2 Skin Blood Flow

The skin blood flow—*a.k.a.* (sub)cutaneous micro-circulation or perfusion—was measured using Laser Doppler Flowmetry (LDF), and expressed in Perfusion Units (P.U.), a dimensionless arbitrary unit that reflects both the amount and the speed of moving elements—mainly erythrocytes—seen by the Doppler probe[277]. When the skin temperature rises, perfusion increases, a phenomenon known as heat-triggered—or thermal—reactive hyperaemia[278], whose dynamics is illustrated in Figure 3.6, Left. The respective durations of phases ①–③ were not specified in abscissa since they may vary markedly depending on the heating rate and temperature[279, 280]. To give the reader an order of magnitude, phase ① usually lasts a few minutes, phase ② from 5 up to 10 min, and phase ③ from 30 up to 60 min[268, 278, 281–283].

Such a behaviour calls for some kind of data processing to yield a single representative perfusion metric for the initial bump, after-bump nadir, and final plateau. In this paper, $\mathrm{SkBF_{90}(T)}$ was defined as the 90^{th} percentile of the measured skin blood flow—SkBF—on a 18 min window at temperature T. This choice was made following preliminary measurements at the arm, an example of which is plotted in Figure 3.6, Right. The latter clearly exhibits five perfusion plateaux corresponding to the five temperature set points, and one can also distinguish a small initial bump at the onset of a new temperature, which is especially visible at 35, 38 and 41°C. Due to *(i)* the high variability exhibited by the measured perfusion, especially at high temperature, *(ii)* the fact that the nitric-oxide phase can take up to 30–40 min to establish[280, 282–285], and *(iii)* the fact that each temperature window lasts 18 min, it seemed a good strategy to choose a metric which was more robust than the mean—*e.g.* the n-th percentile—and focused on the very end of the observation window. In this regard, $\mathrm{SkBF_{90}(T)}$ seemed to meet the latter requirements and was therefore chosen as perfusion metric. It was additionally normed by the maximal perfusion measured on a given subject—*i.e.* the $\mathrm{SkBF_{90}}$ value measured at 44°C. Finally, the LDF metric used throughout this study is thus

$$\boxed{\mathrm{nSkBF_{90}(T)} = \frac{\mathrm{SkBF_{90}(T)}}{\mathrm{SkBF_{90}(44°C)}}} \tag{3.23}$$

3.2.3.2 Protocol Design

The clinical study was interventional, monocentric, and involved 40 healthy human subjects. Inclusion criteria were an age between 18 and 80, and having given a free and informed consent.

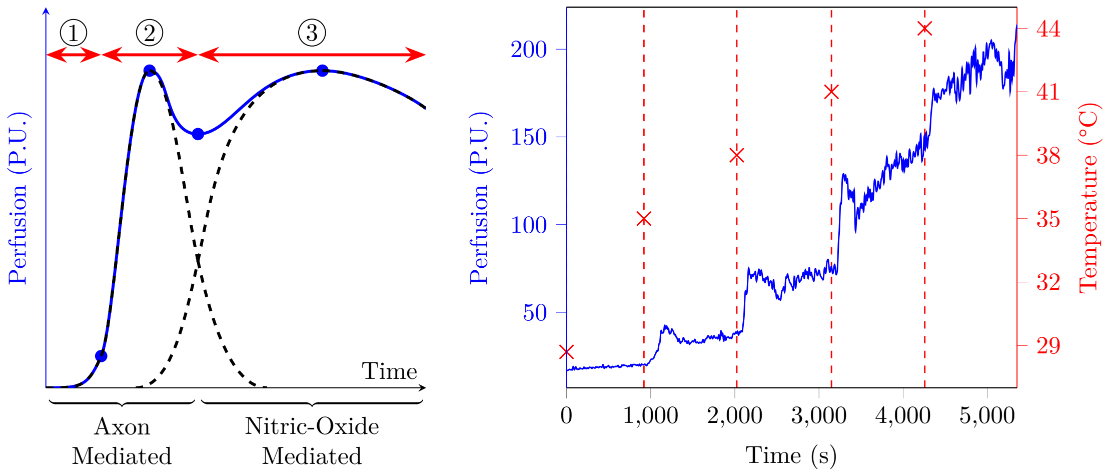

Figure 3.6: **Left:** typical skin perfusion response to local heating, schematised from different sources[268, 278, 281–283]. If we suppose the heat stress to be applied at time origin, three phases are usually observed: ① an onset lag corresponding to *(i)* the heating time required by the sensor to reach its set-point temperature and *(ii)* the time taken by the inner skin layers to reach this temperature and trigger the axon-mediated hyperaemia. ② the axon-mediated hyperaemia which rises quickly and then fades away. ③ the nitric-oxide mediated hyperaemia, whose onset is slower and which slowly fades away if the temperature set-point is not too elevated. **Right:** perfusion and skin temperature as a function of time as measured at the arm of a test subject.

Exclusion criteria were the presence of cutaneous lesions at the measurement sites or skin conditions such as dermatitis or psoriasis, and taking vasodilator therapy. The research was approved by the local ethics committee (Comité de protection des personnes Sud-Méditerrannée II, IDRCB ref.: 2020-A02185-38), registered on Clinical Trials (NCT05637138), and it was carried out in accordance with the declaration of Helsinki.

After a preliminary visit during which the subjects were informed of the study modalities and gave consent, all measurements were performed during a single visit, during which the subjects were seated. This visit began with a visual inspection of the measurement sites for detection of cutaneous lesions. The sites were then shaved if needed for a good adhesion of the sensors, using an electric trimmer in order to avoid skin inflammation. The skin was then degreased and cleaned using isopropyl alcohol, and the three above-mentioned sensors were attached to their respective measurement sites. These preliminary steps also allowed for subject acclimation and lasted about 5 min. The measurement itself then began, consisting of five 18 min periods, corresponding to five temperatures for the two rate sensors: NH, 35, 38, 41, and 44°C. At the end of the 90 min measurement period, the sensors were gently peeled off, and the skin was cleaned again. All $tcpCO_2$ and $p_{Se}CO_2$ data were recorded on computers for future analysis, and the room temperature was also recorded using a calibrated thermometer (Testo 735, Testo, Germany).

3.2.4 Data Analysis

The data analysis workflow is summarised in Figure 3.7. Raw data were collected for all 40 subjects at five different temperatures and three metrics were extracted for each i-th subject / temperature pair: K at the arm and wrist, and $nSkBF_{90}$ at the arm only. For each of those metrics, an ANOVA was performed across all subjects to determine whether their mean values differ significantly between two temperatures. If the ANOVA residuals did not significantly differ from a normal distribution—according to Shapiro-Wilk testing—and if the hypothesis of variance equality between the temperature groups was also verified—according to Bartlett testing—a Tuckey post-hoc HSD test was then performed. Otherwise, a Kruskal-Wallis test followed by a series of Mann-Whitney U-tests were performed. Additionally, Pearson and Spearman correlation tests were also carried out to study the influence of temperature on the three afore-mentioned metrics (not represented in Figure 3.7). When applicable, all tests were two-sided and a 5% alpha risk was chosen as significance threshold.

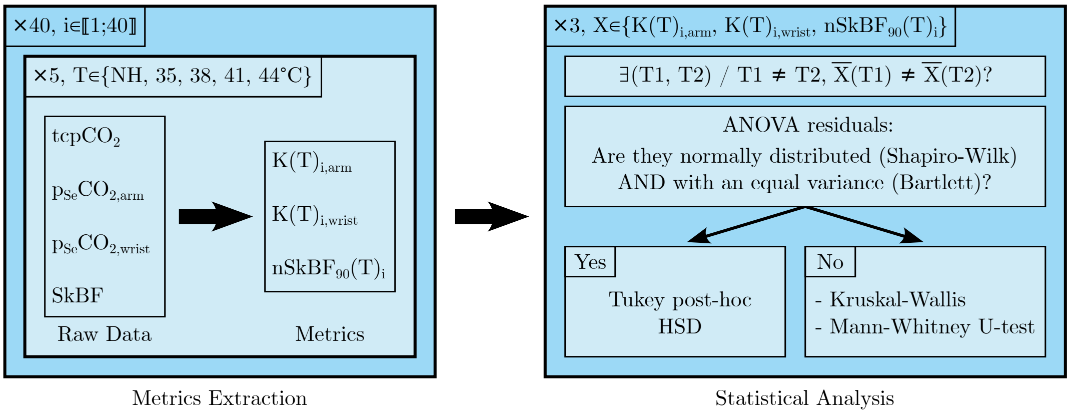

Metrics Extraction

Statistical Analysis

Figure 3.7: Graphical representation of the data analysis workflow, see the text for further details.

Arm	N.H.	35°C	38°C	41°C
35°C	$< 10^{-6}$†	-	-	-
38°C	$< 10^{-6}$†	0.72	-	-
41°C	$< 10^{-6}$†	0.05†	0.54	-
44°C	$< 10^{-6}$†	$< 10^{-3}$†	0.01†	0.44

Wrist	N.H.	35°C	38°C	41°C
35°C	$< 10^{-6}$†	-	-	-
38°C	$< 10^{-6}$†	0.35	-	-
41°C	$< 10^{-6}$†	$< 10^{-3}$†	0.14	-
44°C	$< 10^{-6}$†	$< 10^{-6}$†	$< 10^{-3}$†	0.73

Table 3.1: p-values for the Tuckey HSD post-hoc test for differences of the mean K at different temperatures. Values with a † are considered significant with a risk α=0.05. (Only the lower-left part of the tables are filled-in for the sake of clarity.)

3.2.5 Results

3.2.5.1 Demographics and Temperatures

The forty subjects consisted in 24 men and 16 women, aged between 20 and 61 years (mean / median / SD: 40 / 39 / 13 years). The laboratory temperature was in the 20.1–22.7°C range for the whole duration of the experiments (mean / median / SD: 21.3 / 21.2 / 0.7°C). The skin temperature during the non-heated 18 min phase was measured twice, at 10 and 18 min after sensor application, and these two measurements were averaged to yield a single temperature value per subject. The latter was in the 27.1–31.8°C range (mean / median / SD: 29.3 / 29.2 / 1.2°C) at the arm, and in the 24.7–33.1°C range (mean / median / SD: 28.6 / 28.5 / 1.7°C) at the wrist.

3.2.5.2 Skin CO_2 Conductivity

The linear regressions leading to K values—see Section 3.2.3.1.1—yielded excellent regression coefficients, with average R^2 values of 0.98 and 0.96 at the arm and wrist, respectively. The resulting skin conductivities are summarised in Figure 3.8, and show a sharp tendency to increase with an increasing skin temperature. Interestingly, the five upper outlying values at the arm—at all temperatures—and the four upper and below outlying values at the wrist—in the 35–44°C range—belonged each time to a single subject, who exhibited an especially high, or low skin conductivity. However, these two latter subjects were not one and the same person at the arm and at the wrist. The dispersion of skin conductivity values is also glaring with max / min ratios for a given skin temperature / location pair in the 2.9–9.0 range.

A normalisation of the variable K—using the change of variable $K \mapsto \sqrt{K}$—was carried out prior to the ANOVA, resulting in the Shapiro-Wilk and Bartlett tests to be passed (all p-values above 0.05). The ANOVA was significant (p-value below 10^{-15}) and the results of the following Tukey post-hoc HSD test are detailed in Table 3.1. The apparent increase in K with an increasing skin temperature seen in Figure 3.8 is hereby confirmed, with significantly different mean K values for most temperature differences except the closest ones—*i.e.* for the 35/38, 38/41 and 41/44°C pairs.

Pearson and Spearman correlation where both significant (p-values below 10^{-15}) with correlation coefficients of 0.60 and 0.59 at the arm, respectively, and 0.66 and 0.67 at the wrist. These coefficients indicate a moderate positive influence of the skin temperature on its diffusivity towards CO_2.

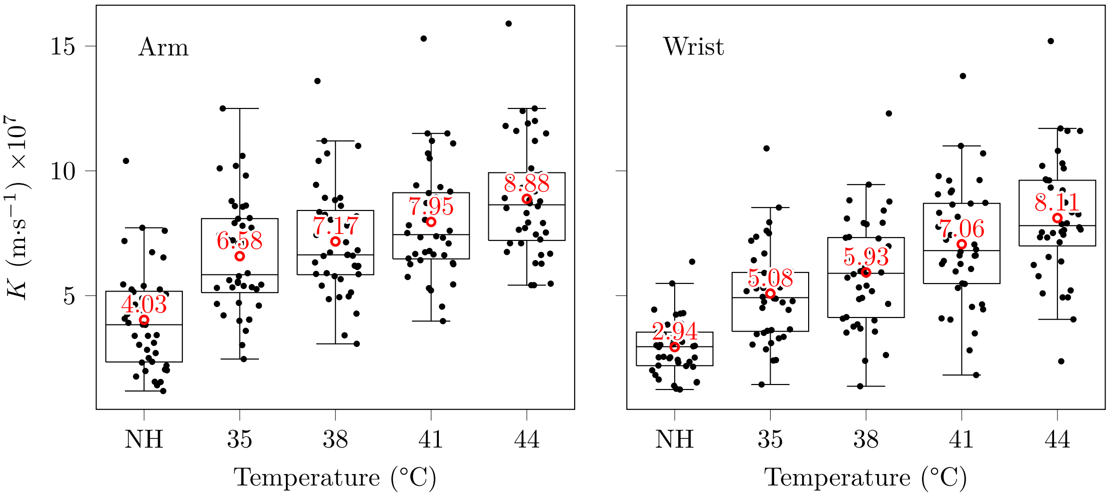

Figure 3.8: Skin conductivities at the arm and wrist. Each black mark corresponds to a subject / temperature pair, the red circles and texts indicate mean values, and some horizontal jitter was added to the black marks for legibility. The whiskers extend at most to 1.5 times the interquartile range, and descriptive statistics—range, and SD—are provided in Appendix D—two properties shared by the three box plots of the present section.

Arm	Mean	Range	S.D.
N.H.	80.4	25.1–191.7	40.3
35°C	130.3	52.4–227.4	43.5
38°C	142.7	63.0–248.1	41.4
41°C	159.9	81.9–280.2	42.8
44°C	177.5	104.6–288.4	42.5

Wrist	Mean	Range	S.D.
N.H.	58.7	24.2–141.1	22.7
35°C	100.9	27.7–220.6	38.3
38°C	118.2	27.1–248.0	42.8
41°C	141.8	36.0–282.1	47.2
44°C	162.3	46.5–300.0	45.9

Table 3.2: $Q(t = 0)$ values, as computed using Equation 3.21, expressed in cm^3.m^{-2}.h^{-1}.

3.2.5.3 Skin CO_2 Exhalation Rate

In order to provide a more accessible parameter than K for the reader, as well as to allow direct comparison with existing literature, equivalent initial exhalation rates $Q(t = 0)$ were also computed using Equation 3.21. The resulting values are presented in Table 3.2.

Although our results tend to indicate a higher CO_2 exhalation rate at the upper arm than at the wrist—a MANOVA was performed considering the measurement site as independent variable and the five Q_T as dependent variables, and yielded a p-value of 0.01 using Pillai's trace—the size of this effect is moderate, especially in view of the wide Q dispersion.

3.2.5.4 Laser Doppler Flowmetry

nSkBF$_{90}$ values were computed as described in Section 3.2.3.1.2, and are presented in Figure 3.9. Skin perfusion exhibits a strong increase with temperature, with a tenfold multiplication between the NH basal state and the maximum vasodilation 44°C stage. In particular, a mild heating to a temperature of 38°C already entails a fourfold increase in perfusion. As was the case for skin conductivity, the dispersion of the nSkBF$_{90}$ values is also considerable, with max / min ratios for a given temperature in the 2.2–9.7 range.

Regarding statistical analyses, the normality and variance homogeneity hypotheses could not be verified regardless of the changes of variable performed. A Kruskal-Wallis test was thus conducted, followed by a series of Mann-Whitney U-tests, all of which proved significant (all p-values below 10^{-10}).

Pearson and Spearman correlation where both significant (p-values below 10^{-15}) with correlation coefficients of 0.90 and 0.96, respectively. These coefficients indicate a strong positive influence of the skin temperature on its perfusion. The fact that Pearson's correlation is below Spearman's is not surprising since the relationship between skin temperature and nSkBF$_{90}$ is strongly non-linear, as emphasised by the sigmoid fit performed in Figure 3.9.

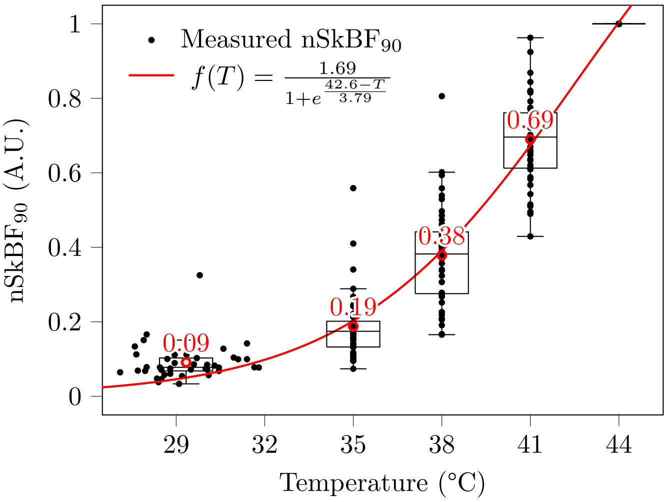

Figure 3.9: Measured $nSkBF_{90}$ at the arm. Note that since $nSkBF_{90}$ is normalised with respect to $SkBF_{90}$ at 44°C, all subjects merge into a single unitary value at this latter temperature. Each black mark corresponds to a subject / temperature pair, the red circles and texts indicate mean values, and the red curve is a least square sigmoid fit. Contrary to Figure 3.8, no horizontal jitter was added to the data, and the dispersion observed in the 27–32°C range corresponds to the inter-subject variability in non-heated skin temperatures.

3.2.6 Discussion

The main objectives of this research were to ascertain the influence of skin temperature on *(i)* its permeability towards CO_2—through the study of the skin CO_2 conductivity K, and exhalation rate Q—and *(ii)* the skin blood flow—through $nSkBF_{90}$.

3.2.6.1 Sensor Design

3.2.6.1.1 Skin Contact Surface

Although the sensor's aluminium body was precisely machined following the drawing given in Appendix D, the exact surface area in contact with the skin that participates in gaseous exchanges may slightly vary from one subject to another. Indeed, at each hole of the sensor's sole, the skin forms a small dome, whose convexity is essentially function of the mechanical properties of the skin. Yet, those mechanical properties are sex-, moisture-, age-, and temperature-dependant[286, 287], thereby introducing small intra- or inter-subject variations in skin contact surface area. Since this area is used to calculate K through S_{Se}—see Section 3.2.3.1.1—the latter is in turn influenced by these small variations.

While this would likely not change the conclusions of the present study given the order of magnitude of the above-described phenomenon reported in the literature, future research could look into replacing the grid-shaped sole that we used by a thin metal mesh, or a metallic foam. These two latter techniques were for instance implemented by Eletr, McIlroy, Hansen *et al.*[272, 288, 289]. However, it must be emphasised that the shape of the sole of a thermally-regulated transcutaneous exhalation rate sensor is essentially a compromise between: *(i)* the degree of perforation or porosity of the surface, which should be as high as possible to ensure a large diffusion surface, and *(ii)* heat transfer considerations, which call for a plain, dense, surface, with a minimum number of holes, to ensure temperature homogeneity of the skin. Additionally, while the use of a wire mesh, or metallic foam reduces the above-mentioned "dome effect", it also makes the surface estimation more tedious. Therefore, this aspect of the sensor design should be further investigated to find a satisfactory technical solution which addresses the above concerns.

further research is needed

3.2.6.1.2 CO_2 Sensor Choice

The choice of the selected NDIR CO_2 sensor was mainly motivated by its compact form factor and ease of implementation. Additionally, the 5% range was especially adapted for CO_2 diffusion rate measurement. Indeed, $tcpCO_2$ in healthy subjects is typically in the 35–45 mmHg range[290], corresponding to 4.6–5.2% of CO_2. Since the CO_2 diffusion rate measurements taking place in the present study were only limited to the first moments of CO_2 diffusion from the skin into the sensor—see Section 3.2.3.1.1—measured CO_2 fraction values stayed below 1–2%. The 5% range was thus adapted to our need.

3.2.6.1.3 Gas Tightness

As mentioned in Section 3.2.2.1, the gas tightness of the sensor's chamber with respect to ambient air was of paramount importance for the success of the study. Indeed, any leak of inner-chamber CO_2 towards the outer air would subtract from the measured rate of exhalation of CO_2 through the skin, and thus impair the resulting K values. During the sensor's design, gas tightness was assessed by sticking the sensor onto a glass plate using the same adhesive as for the human-testing part of the study. The so-obtained glass plate / sensor pair was then put inside a chamber which was successively filled with a 2.5% CO_2 / N_2 mixture and fresh air. The resulting measurements are presented in Figure 3.10, Centre, and clearly demonstrate that the greased O-ring alone was not gas tight, while the epoxy sealing was. The left part of Figure 3.10 also illustrates in a cut view how the epoxy seal complements the O-ring. In practice, the grease-coated O-ring acts as a resin-proof sealing that prevents the resin from flowing inside the sensor's chamber during its casting process.

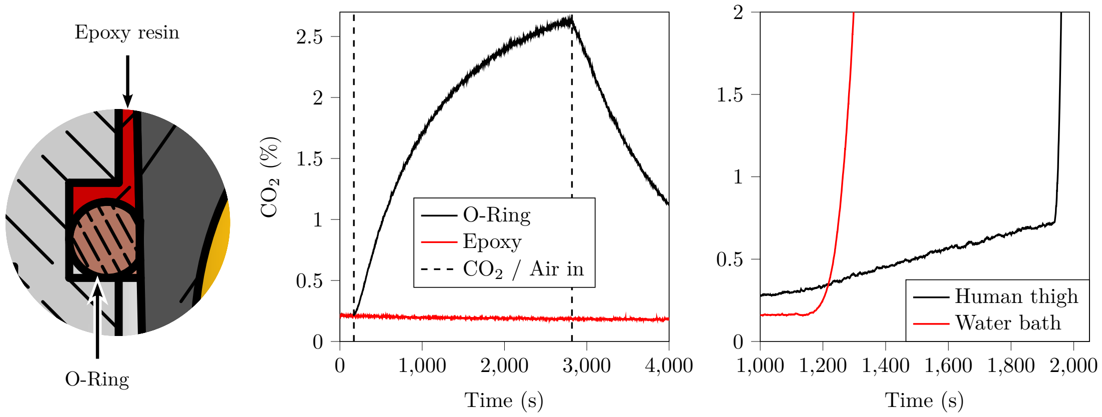

Figure 3.10: **Left:** close up of the section view of Figure 3.4, showing the two key elements of the gas tight seal: a grease-coated O-ring, and cast epoxy resin (in red). **Centre:** a sealing test comparing the greased O-ring alone with the greased O-ring and the cast epoxy resin. This test clearly indicates that the greased O-ring alone does not accomplish gas tightness, whereas the cast epoxy resin does. **Right:** sensor sensibility towards humidity, showing the onset of condensation onto the gold-plated dome. This condensation drastically reduces the quantity of light reaching the detector, effectively blinding it, which is interpreted as an exceedingly elevated CO_2 concentration.

This gas tightness allows CO_2 to accumulate into the sensor chamber until an equilibrium is reached between the subcutaneous tissue and the sensor's chamber—*i.e.* until $p_{Se}CO_2 = tcpCO_2$. While this equilibrium—although it would take several hours given the respective order of magnitudes of Q and h_{Se}—and the associated CO_2 diffusion process are at the very heart of this study, another undesirable chemical species will also accumulate into the sensor's chamber due to the combined action of diffusion and sweating: water vapour.

While the influence of water vapour on NDIR CO_2 measurements due to the infrared absorbance of water vapour is expected to be negligible given the large gap between CO_2 and water vapour infrared absorption bands[291], the onset of condensation onto the reflective part of the sensor—namely the gold-coated reflective dome—can still be an issue. Indeed, the formation of micro-droplets of condensing water onto the latter dome would drastically reduce its reflectance, fooling the sensor into believing that a large amount of CO_2 is present inside the sensor's chamber—a well-known issue in NDIR sensing[292, 293]. In order to study the influence of condensing humidity levels onto the sensor used in the present research, two experiments were carried out whose outcomes are presented in Figure 3.10, Right. The first experiment consisted in placing the sensor on a human thigh at increasing temperatures and waiting for condensation to occur, which happened after 30 min at 44°C. The second experiment consisted in bubbling ambient air (20°C) through pumice stone inside a hot water bath, yielding water-saturated hot air (40°C), which was then flowed onto the un-heated sensor. Even in these unfavourable conditions—*i.e.* a cold sensor and water-saturated hot air—it took about 20 min to detect the onset of condensation on CO_2 measurements. Given that the latter onset was particularly sudden and visible on $p_{Se}CO_2$ in both experiments, the influence of water vapour condensation on this study was deemed negligible. Indeed, it would be easily detected—were it to happen while measuring a given subject—and the corresponding measurement would be discarded, something which did not happen in practice.

Finally, the reader should bear in mind that the gas tightness of the sensor and the accumulation of humidity underneath it both create a condition called *skin occlusion*. This occlusion, while out of the scope of this section, has been studied by several authors[294–296], who reported much higher CO_2 exhalation rates for long-term—*i.e.* days—occluded skin, as compared to its basal state. This phenomenon was not investigated in the present study due to the long time scale that it involves, but further research on this topic would be welcome.

further research is needed

3.2.6.1.4 Sensors Positioning

To our knowledge, only three studies compared the influence of the measurement site on the transcutaneous CO_2 diffusion rate in humans: that of Schulze on twelve subjects[297, Table 16], that of Adamczyk *et al.*[298] on one subject, and that of Levshankov *et al.*[266] on an unspecified number of subjects. The results of the latter two authors are summarised in Figure 3.11—Schulze indications were difficult to interpret and were thus not illustrated.

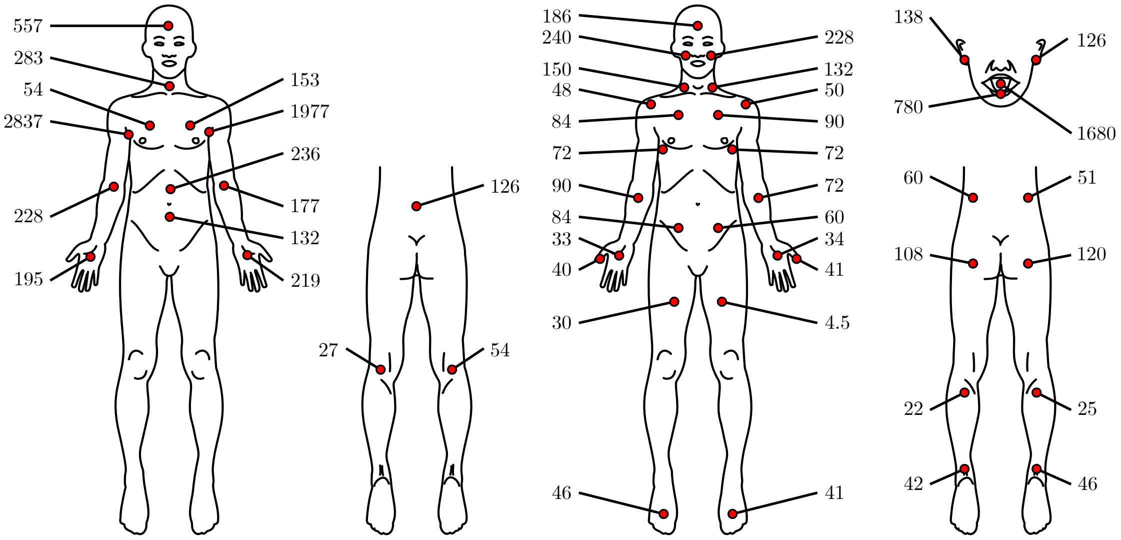

Figure 3.11: CO_2 diffusion rates through human skin at various sites, expressed in $cm^3.m^{-2}.h^{-1}$, adapted from Adamczyk *et al.*[298] (**Left**) and Levshankov *et al.*[266] (**Right**). Of note, the particularly elevated values at the axilla in Adamczyk's data (2837 and 1977 $cm^3.m^{-2}.h^{-1}$) should not be compared with the sub-mammary values in Levshankov's data (72 $cm^3.m^{-2}.h^{-1}$), since they concern two distinct locations.

The high variability in Adamczyk's data—probably caused by the inclusion of only one subject—is glaring, especially when studying left-body / right-body differences. Interesting are the extremely important values reported for the axilla. These values may be measurement artefacts, or they may be caused by a peculiar behaviour towards CO_2 diffusion of the apocrine glands, which are mainly located in the axilla—see Baker *et al.*[299]. Another possibility could be the local production of CO_2 by the axilla's bacterial flora—through either aerobic respiration or fermentation—adding to the transcutaneously-diffused CO_2[300]. However, we found no evidence in the literature for or against these hypotheses. Alternatively, those elevated values may be caused by the skin temperature, which is much higher at the axilla on resting subjects than at the extremities[301, 302], since the skin was not heated in their study. At the opposite, the results of Levshenkov *et al.* are more homogenous concerning left and right body measurements.

All in all, and apart from the extreme axilla values, the reported CO_2 diffusion rates exhibit no extreme variations and are of the same order of magnitude, regardless of the measurement site. In this aspect, **it thus seems from the limited information at our disposal that no measurement site is far better than the other** from the CO_2 diffusion rate perspective. Consequently, we chose our measurement sites mainly for their ease of access and acceptability, with a view to using these sites for a future wearable tcpCO_2 sensor. In this respect, the dorsal side of the wrist and the upper arm were found to be particularly interesting, as evidenced by the rapidly expanding and widespread use of health-related wristband and armband in the recent years[303–305].

3.2.6.2 Skin CO_2 Conductivity

3.2.6.2.1 Metric Choice

It must be emphasised here that in the simplified skin diffusion model introduced in Section 3.1 and detailed in Figure 3.1, the membrane called "skin" does *not* correspond to an actual physiological membrane. Consequently, its thickness w and diffusivity towards CO_2 does *not* correspond to any physical property that might have been measured on a specific part of the dermis or epidermis. Rather, this "skin" membrane corresponds to a physical modelling of gas transport between the subcutaneous tissue and the outer air. As such, the latter membrane models both the diffusion of CO_2 through the stratum corneum *and* the circulation of blood and diffusion of CO_2 in the dermis and subcutaneous tissues.

Moreover, this model also integrates the difference in tcpCO_2 between that measured by the reference Radiometer tcpCO_2 monitor, and that measured at the sensor's location. Indeed, since the reference tcpCO_2 monitor was set to 41°C, it is likely that the tcpCO_2 that we injected in Equation 3.21 is slightly under-estimated—as per the dilution principle presented in Figure 3.13—at temperatures below 41°C. Consequently, reported K—or Q—values below 41°C are likely to be slightly over-estimated. The amplitude of this over-estimation should be in the same order of magnitude as the arterio-venous pCO_2 gradient in resting, healthy subjects—*i.e.* about 5–15% in the NH–38°C skin temperature range[35, 40]. However, this state of fact was inevitable since, to the best of our knowledge, no clinical tcpCO_2 monitor working at a temperature below 37°C exist at the time being, and manufacturers recommend using 41–42°C—an injunction that we followed. Future research aiming at extending our work may consider the design of a tcpCO_2 sensor working at low temperature in order to be able to perform the appropriate corrections to the so-obtained K values.

further research is needed

3.2.6.2.2 Impact on the Response Time of a Future tcpCO_2 Sensor

Contrary to perfusion—which increases over elevenfold with skin heating—K only doubles from NH to 44°C, and its increase is even smaller between 35–38 and 44°C values. This latter fact is all the more interesting when having in mind the design of a future energy-efficient tcpCO_2 sensor. Indeed, internal studies measuring skin temperature under a wearable device positioned at the upper arm (Bora Band, Biosency, France) on ten healthy subjects revealed that a mean skin temperature of 33.9°C could easily be achieved at the upper arm without additional heating, and that covering the arm with an additional layer of isolation—*i.e.* shirt or jumper sleeves—makes it rise even higher to reach 35.1°C.

With such skin temperatures, there is no strong incentive—from a response time point of view—to heat the skin actively any further—*i.e.* by mean of an external electrical heating system. Indeed, the measured increase of 35% in K at the arm from 35 to 44°C—see Figure 3.8—would result in a decrease in response time of the same magnitude for a given tcpCO_2 sensor, according to the response time model presented in Section 3.1. While having a slower sensor may seem like a burning issue for critical care applications, it is not the case for telemonitoring for which long-term tendencies are to be observed over several months[306].

Additionally, it should be noted that since the Q values measured in the present study—80–178 $cm^3.m^{-2}.h^{-1}$ on average—are in line with that used in Section 3.1 for response time calculations—100 $cm^3.m^{-2}.h^{-1}$—the afore-proposed sensor thickness of 100 µm for a response time below 10 min remains credible. Of note, and to the best of our knowledge, there is a lack of clinical guidelines specifying the required response time for tcpCO_2 monitors. Nevertheless, there exists a considerable amount of literature focusing on transcutaneous monitor testing in clinical environments, from which it can be inferred that a typical *in vitro* 90% response time of about 1 min is achievable with current tcpCO_2 monitors[200, 307]. *In vivo* performance reports, on their part, mention an approximatively 10 min initial equilibration time before a first tcpCO_2 reading can be obtained[72, 308, 309]. Regarding the response time of tcpCO_2 monitors following a sudden change in paCO_2, a lag has been reported in the literature between end-tidal pCO_2—*i.e.* petCO_2—paCO_2, and tcpCO_2, inducing a higher *in vivo* response time than in the ideal *in vitro* case. Reported values for this latter lag fall within the 1–5 min range[308, 310–312].

An overall response time requirement of approximatively 5 min can thus *de facto* be assumed for a tcpCO$_2$ monitor to meet field expectations. Still, this latter assumption mainly holds for the intensive care of critically ill patients[68] and no information exists concerning long-term tcpCO$_2$ (tele-)monitoring for the obvious reason that the corresponding monitors do not exist yet.

3.2.6.3 Exhalation Rate

3.2.6.3.1 An Imperfect Metric

Considering Equation 3.18, it readily appears that the exhalation rate Q is not constant, and logically depends on the initial $\mathrm{p_{Se}CO_2}$, and of the passing of time. This issue has however been largely ignored by the literature on the topic—see Table 3.3—and Q has been considered by most authors as if it had a single constant value. The latter, which has been reported as *the* CO$_2$ diffusion rate through the skin, is actually the *initial one in free air*—*i.e.* Q(t=0) with $\mathrm{p_{Se}CO_2}(t = 0) \approx 0$—and corresponds to the slopes of the tangents to the $\mathrm{p_{Se}CO_2}$ curves at $t = 0$ in Figure 3.12, Left.

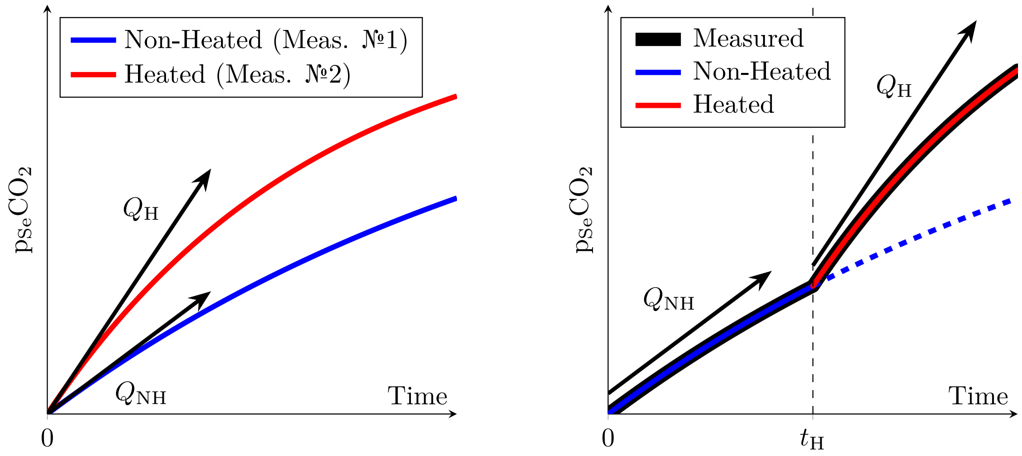

Figure 3.12: **Left:** schematic evolution of the pCO$_2$ inside the sensor's chamber when the skin is heated or not. **Right:** same as Left, but with a non-heated sensor placed onto the skin for a duration t_H before being heated. Note the difference between the two sensing schemes: the one on the left requires two successive measurements—one heated, the other one non-heated—while the one on the right consists in a single measurement during which the skin is successively non-heated and then heated. The dashed line on the right represents what would have happened without heating during the whole acquisition, which is equivalent to the solid blue line on the left.

Unfortunately, if measuring Q as illustrated in the latter figure is theoretically feasible at different temperatures, it would also require to remove the sensor at each temperature change, in order to renew the gas inside the inner chamber of the sensor with fresh air. This would in turn require to peel off the sensor from the subject's skin at each temperature change, which would distort the Q measurement, as the skin—and more specifically the *stratum corneum*, its outermost layer—would become thinner and thinner at each sensor replacement. Actually, stripping the skin with multiple tape applications and removals is a well-known technique to drastically increase Q[259, 272, 273].

Thus, the sensor was left in place in this study, while the temperature was successively changed from NH up to 35, 38, 41, and finally 44°C. This led to measured $\mathrm{p_{Se}CO_2}$ alike that represented in Figure 3.12, Right. In that case, using Q as a metric would be unpractical, since the $\mathrm{p_{Se}CO_2}$ value at t_H is not null, and Q values would no longer represent *initial* CO$_2$ diffusion rates as measured in free air. In practice, the obtained Q values at different temperatures would then not be comparable with each other, each one being measured with a slightly different $\mathrm{p_{Se}CO_2}$ initial value.

3.2.6.4 Laser Doppler Flowmetry

3.2.6.4.1 Choosing nSkBF$_{90}$ as a Metric

Exhalation Rate Q [$cm^3.m^{-2}.h^{-1}$]	Temp. [°C]	Num. of Subjects	Ref.
25–120	22–36 (air)	2	Shaw (1929)[262]
10–160	25–37 (air)	1	Shaw (1930)[263]
58–169	**26–31 (air)**	**38**	**Ernstene (1932)[313, Table 1]**
12–143	23–37 (air)	1	Whitehouse (1932)[264]
32–69	**25–28 (air)**	**13**	**Schulze (1943)[297, Table 12]**
180–2500$^{(\dagger)}$	–	1	Adamczyk (1966)[298]
25–87	–	5	Thiele (1972)[314]
11–28	25–35 (air)	3	Frame (1972)[294]
50	–	**27**	**Levshankov (1983)[266]**
140–221	**36 (skin)**	**14**	**Eöry (1984)[265]**
25–192	27–32 (skin)	40	This work, NH arm
24–141	25–33 (skin)	40	This work, NH wrist
25–288	27–44 (skin)	40	This work, all temp. arm
24–300	25–44 (skin)	40	This work, all temp. wrist

Table 3.3: CO_2 exhalation rates through the skin in the literature compared with the present studies. Past studies with more than ten participants are indicated **in bold** and were used for sample size determination. (†): Axilla measured value, possibly erroneous.

Both inter-subject and inter-site LDF variabilities have often been reported in the literature[268, 271, 278, 281, 315, 316], and appear to be inherent to this modality of skin blood flow measurement, as well as to human physiology in general. Nonetheless, certain guidelines may be followed to obtain the most reproducible results[281]. In particular, when it comes to derive a single explicit LDF metric from a given measurement period—such as a skin-site / sensor-temperature pair, for instance—several techniques have been developed to obtain meaningful results from raw LDF data.

At first, some authors—*e.g.* Hodges *et al.*[271]—prefer to express the skin blood flow as Cutaneous Vascular Conductance (CVC), which is given by the LDF in P.U. or V, divided by the Mean Arterial Pressure (MAP). The CVC is said to be more "physiological"[281], since an increase in skin blood flow could be caused by an increase in MAP but also by an increase in vascular compliance, for instance. By dividing the LDF-acquired blood flow by the MAP, the obtained CVC value is thus in theory more representative of the arteriovenous compliance, a theory supported by several works in haemodynamics[317–319]. At the same time, skin blood flow alone—often abbreviated as SkBF, and either expressed in P.U. or Volts—has been used for several decades[282, 315] and remains a good alternative to CVC when MAP is not available.

Then, once the type of measurement—SkBF or CVC—is chosen, the question that comes next is that of the extraction of a single perfusion metric from a long-lasting acquisition. Indeed, due to the peculiar dynamics of thermal hyperaemia—see Figure 3.6, above—a simple time-averaging on the whole acquisition duration would make little sense.

To circumvent this issue, several research teams used temporal averaging on manually-set periods of interest in the raw LDF data. The averaging duration that they used depended on the studied phenomenon, with durations of 1–3 min for transient phenomena—*i.e.* initial bump and after-bump nadir—up to 5–10 min for long-lasting ones—*i.e.* baseline or maximum perfusion plateau[282, 283]. Other authors, for their parts, chose to average the 2–3 last minutes of a 10–25 min measurement window at the maximal perfusion value, the obtention of which is detailed below[271, 320]. However, Barcroft, Taylor, *et al.*[284, 285] mentioned even longer durations for thermal hyperaemia to fully settle following a change in skin temperature—up to 40–60 min. Such a lengthy onset period would result in a total acquisition duration in the 3–5 h range for the five different temperatures involved in the present study. At the opposite, a total experiment duration—including informing the subjects and obtaining their consent—of about 2 h seemed to us to be an acceptable maximum for easily recruiting volunteers. This 2 h duration in turn entails that each temperature window of the present study only lasted 18 min, which may not be enough for the establishment of the nitric-oxide mediated hyperaemia detailed in Figure 3.6. Thankfully, this 18 min duration is by far long enough for the axon mediated response to take place, and the latter often yields perfusion levels comparable to that reached at the end of the nitric-oxide mediated phase[278, 282, 320]. Thus, by taking the 90-th percentile of SkBF—see Section 3.2.3.1.2—the obtained SkBF_{90} values are likely to be representative of the SkBF plateau values which would have been observed by increasing the duration of each temperature window. The latter hypothesis is further confirmed by the similarity between our results and that of the literature, as discussed in the next section.

Finally, it is also common practice to normalise the measured skin blood flow—whether expressed as SkBF or CVC—by its maximum value, often taken after a prolonged ($\geq$15 min) period at an elevated ($\geq$44°C) temperature[271, 285, 321] or by direct injection of sodium nitroprusside[320]. Although it has been seldom proposed to normalise the measured values by the baseline blood flow value instead of the maximum one[279, 322], this is considered bad practice because intra-subject baseline variations can be far from negligible, even in a temperature controlled room[281, 323].

In this study, CVC was not considered due to the invasiveness of a continuous MAP measurement, and SkBF was thus chosen as raw perfusion metric. Then, we proposed to take the 90-th percentile of a given temperature window instead of time averaging. Finally, normalisation by the maximum perfusion value—*i.e.* the one reached at the end of the 44°C window—was performed, as per literature guidelines.

3.2.6.4.2 Comparison With the Literature

The LDF measurements that were gathered in the present study are consistent with existing literature on the topic. In particular, the sigmoid behaviour observed in Figure 3.9—revealing a strong onset of hyperaemia in the 35–41°C range—is on par with the observations of Magerl, Stephens, Hodges *et al.*[271, 279, 324].

3.2.6.4.3 Impact on the Accuracy of a Future tcpCO_2 Sensor

The fact that the perfusion is doubled at 35°C and quadrupled at 38°C compared to baseline—see Figure 3.9—is especially encouraging for the development of a future energy-efficient tcpCO_2 sensor, since these temperatures can be easily achieved without—or with minimal—heating, as already discussed in Section 3.2.6.2.2 (reaching over 35°C at the upper arm under jumper sleeves). Indeed, since arterialised capillary blood—either obtained by local heating or by applying a vasoactive cream—is gaseously close to arterial blood[42], it is to be expected that partially arterialised capillary blood obtained by a mild heating—*i.e.* below 44°C—lies somewhere between venous and arterial blood, from a gaseous content point of view. More specifically, Rooth *et al.*[270] hypothesised that the subcutaneous capillary pCO_2—*i.e.* tcpCO_2—would be a barycentre between venous and arterial pCO_2, as illustrated in Figure 3.13.

This figure emphasises the fact that—especially for a resting subject—even a mild heating of the skin in the 35–38°C range could be enough to yield a tcpCO_2 only a few mmHg away from the paCO_2. The latter error may be acceptable depending on the clinical application targeted. For example, the Food and Drug Administration (FDA) requires tcpCO_2 monitors to be accurate within 5 mmHg, with an allowed drift of up to 10% of the initial reading over a one-hour period[325].

3.2.6.5 Sample size

The main objective of the present study was to estimate the mean K value as a function of temperature. The latter mean can be estimated at each temperature T by

$$\widehat{K}_T = \frac{1}{N} \cdot \sum_{i=1}^{N} K_{S,i} \tag{3.24}$$

wherein the i index stands for the i-th subject of the study, and N stands for its sample size. Contrary to hypothesis testing, for which a sample size may be derived straightforwardly from targeted alpha or beta risks and some prior knowledge of the data[326, Chap. 19][327], sample size determination in the case of an exploratory—or pilot—study is more challenging, with its share of arbitrary decision[328]. Indeed, while a 95% confidence interval can be computed for K_T as

$$C.I._{K_T}^{95\%} = [\widehat{K}_T - \varepsilon, \widehat{K}_T + \varepsilon], \quad \text{and} \quad \varepsilon = -t_{N-1}\left(\frac{0.05}{2}\right) \cdot \frac{s}{\sqrt{N}} \tag{3.25}$$

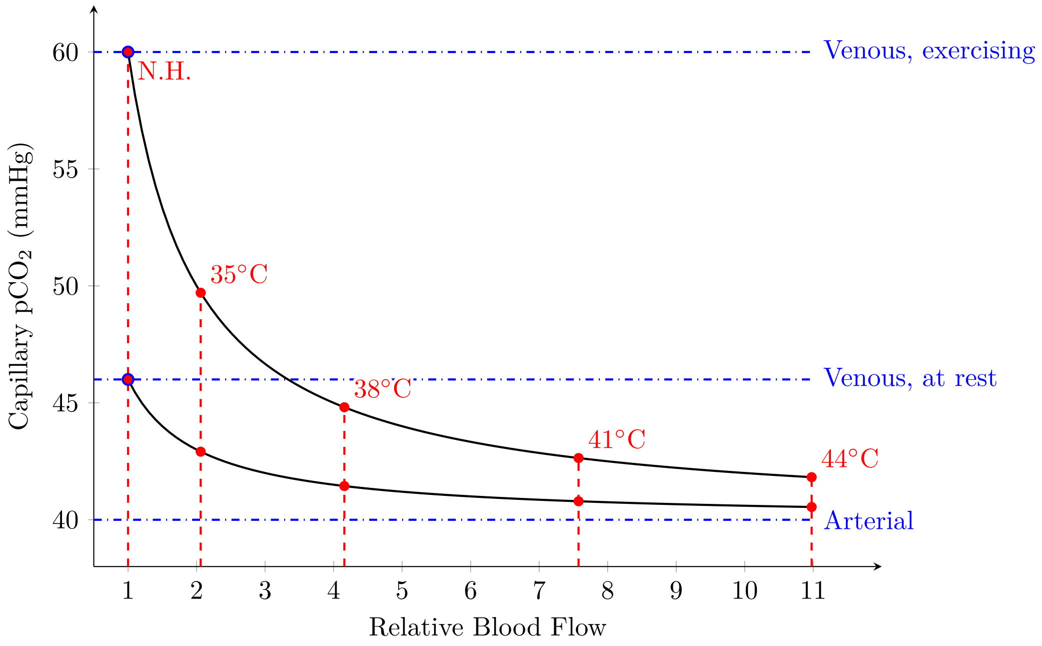

Figure 3.13: Capillary pCO_2 as a function of relative blood flow considering two venous pCO_2 levels: at rest, and while exercising. Relative blood flow values measured in the present study were also added in red with their respective temperature labels. A normal $paCO_2$ of 40 mmHg[40] was taken for arterial blood, while venous blood levels were set to 46 and 60 mmHg at rest and while exercising, respectively. Of note, while 46 mmHg at rest is generally accepted in the literature[43], the 60 mmHg exercising value was mainly chosen for legibility reasons. Indeed, exercising values may exceed 100 mmHg during heavy exercise, or in case of septic shock[35, 36]. Modified from Rooth *et al.*[270].

wherein t_{N-1} is the percentile score of a Student distribution with $N-1$ degrees of freedom, and s is the SD of the sample—*i.e.* the *estimated* standard deviation of the population—the value of the latter SD is vastly unknown. In order to estimate an adequate sample size for the study at hand—based on an *acceptable* margin of error on $\widehat{K_T}$—a prior estimation of s is thus needed, and is the object of the upcoming section. Importantly, since Q—that is $Q(t=0)$ using the above-presented notation—was studied by earlier authors instead of K, the following reasoning will be made using the former. This can be done safely since the two values are linked by a proportionality constant—see Equation 3.21. Of note, Equation 3.25 holds only if the K_T follow a normal distribution, which had neither been confirmed nor denied in the literature, to the best of our knowledge, but which was verified in the current study—see Section 3.2.6.5.3.

3.2.6.5.1 Literature Review

Among the literature studies on the topic of skin CO_2 exhalation rate measurements on human subjects detailed in Table 3.3, only four of them have been performed on more than ten subjects, and are highlighted **in bold** in the afore-mentioned table. Unfortunately, the latter studies are sometimes unclear about Q measuring conditions—measurement site and skin temperature, in particular. We did our best not to distort or misinterpret the works of their authors, but what follows is essentially our best *interpretation* of their writings. These four studies reported—or made it possible to derive from raw data—a $\widehat{Q}$ and s value for each measurement site investigated. These data can be used to compute 95% confidence intervals on Q estimation—as shown in Equation 3.25—or on s, yielding [326, Chap. 4]

$$C.I._{\sigma}^{95\%} = \left[\frac{s^2 \cdot (N-1)}{\chi^2_{N-1}\left(\frac{0.05}{2}\right)} \; ; \; \frac{s^2 \cdot (N-1)}{\chi^2_{N-1}\left(1-\frac{0.05}{2}\right)} \right] \tag{3.26}$$

wherein χ^2_{N-1} is the percentile score of a χ^2 distribution with $N-1$ degrees of freedom. The resulting confidence intervals are reported in Table 3.4 and tend to indicate a relative uncertainty on Q estimation in the order of 5–30% for relatively small sample sizes—*i.e.* 13–38 subjects.

	Lower bound	Reported	Upper bound	Relative uncertainty	Measurement site	Ref.
σ	18.7	22.9	29.6	48%	Whole arm	Ernstene (1932)[313]
	8.5	11.9	19.6	93%	Abdomen	Schulze (1943)[297]
	2.65	3.36	4.60	58%	Left forearm	Levshankov (1983)[266]
	2.41	3.06	4.19		Right forearm	Levshankov (1983)[266]
	15	21	34	89%	Acupuncture site	Eöry (1984)[265]
	13	18	28		"adj. skin area"	Eöry (1984)[265]
Q	113	120	128	13%	Whole arm	Ernstene (1932)[313]
	41	48	55	30%	Abdomen	Schulze (1943)[297]
	48.0	49.3	50.7	5.39%	Left forearm	Levshankov (1983)[266]
	48.4	49.6	50.8	4.88%	Right forearm	Levshankov (1983)[266]
	209	221	233	11%	Acupuncture site	Eöry (1984)[265]
	130	140	150	14%	"adj. skin area"	Eöry (1984)[265]

Table 3.4: Confidence intervals at the 95% level for σ and Q, computed from s and $\widehat{Q}$ values reported in the literature. Aside from the relative uncertainties—defined as $2{\cdot}\varepsilon/X$ wherein X is σ or Q—all values are given in $\mathrm{cm^3.m^{-2}.h^{-1}}$.

3.2.6.5.2 Chosen Sample Size

The reported s value, as well as the upper and lower bounds of s 95% confidence interval, were then used to compute the relative uncertainty on Q as a function of the number of subjects, using Equation 3.25. While this relative uncertainty decreases when the sample size increases, its reducing rate—as well as the associated uncertainty values—varies wildly depending on the considered data source. Indeed, while a sample size of 20–30 subjects should lead to a relative uncertainty on Q in the 5–10% range using Levshankov *et al.* data, much larger sample sizes—*i.e.* 100–150 subjects—would be needed to reach the same level of accuracy using Schulze, or Ernstene *et al.* measurements. In the end, since the works of the latter two authors were much older—1932 and 1943, respectively—than that of Eöry, Levshankov *et al.*—1983 and 1984, respectively—it was decided to put them aside. The sample size determination for the present study was thus grounded only on the works of Eöry, Levshankov *et al.*, and a sample size of 40 subjects was deemed acceptable, since it should have resulted into a relative uncertainty on Q estimation below 10%.

3.2.6.5.3 Results

Unfortunately, this initial estimation of a 40 subjects cohort proved to be rather optimistic in practice. Indeed, the relative uncertainty on measured Q values can be computed using Equation 3.25, and falls in the 15–32% range, depending on the skin temperature and measurement site. In this aspect, our results are close to those presented by Ernstene, Schulze, Eöry *et al.*[265, 297, 313] who report relative uncertainties in the 11–30% range. Yet, the latter authors used less than 40 subjects, and our uncertainty ranges were thus expected to be narrower than theirs. Moreover, the present study also exhibits a higher variability than that of Levshankov *et al.*[266]—whose results indicate a relative uncertainty of only about 5%, see Table 3.4.

The origin of these discrepancies between literature-driven expectations and the above-presented results is not fully understood at the moment. One possible explanation could be differing measurement sites between the above-mentioned studies and the ones that we chose. Indeed, the data reported by Eöry and Schulze (Table 16 *op. cit.*) tend to indicate some degree of variability in the relative uncertainty expected at different sites—in particular when comparing the abdomen and hand in Schulze's data (30 *vs.* 45%), or the two sites used by Eöry (10 *vs.* 14%). Thus, it seems plausible that Q variability at the upper arm and wrist is above that reported in earlier studies for differing sites.

Ultimately, we cannot but recommend using larger sample sizes in future studies of a similar nature, considering the significant variability that we observed. As a side note related to sample size determination, the normality of the Q distribution was ascertained using a series of Bonferroni-corrected Shapiro-Wilk tests which were non-significant, further justifying the approach presented in Section 3.2.6.5. To the best of our knowledge, this is the first report of normality for transcutaneous CO_2 exhalation rates.

3.2.7 Conclusion

As stated in Section 3.2.1, the aim of this study was twofold: measuring the influence of skin temperature on the transcutaneous diffusion of CO_2, and on the skin blood flow. To this end, a custom sensor was designed and used on 40 healthy human subjects at two measurements sites: the upper arm, and the wrist.

Our results indicate comparable behaviours at both sites, with an increasing relationship between temperature on the one hand, and CO_2 exhalation rate, CO_2 conductivity and perfusion on the other hand. These results are encouraging for the development of a future energy-efficient tcpCO_2 sensor for the following reasons:

- Skin conductivity towards CO_2 increases only moderately with an increase in skin temperature, at most doubling from NH to 44°C. Thus, if the response time of the sensor-to-be is not critical—*i.e.* if a 35% slower response is acceptable compared to the one reachable at maximum skin heating—the latter may not require additional heating. This is especially encouraging in the perspective of building a wearable, battery-operated device.
- Perfusion, for its part, increases strongly with an increase in skin temperature, already doubling from NH to 35°C, and quadrupling from NH to 38°C. This phenomenon is especially interesting since—according to Rooth *et al.*[270]—this should bring tcpCO_2 close to paCO_2 even for skin temperatures as low as 35–38°C, which are reachable at the arm without additional heating given that the latter is covered by warm clothings. However, this latter hypothesis—*i.e.* the existence of a clinically-satisfying tcpCO_2 / paCO_2 correlation in the 35–38°C skin temperature range—is yet to be demonstrated experimentally *in vivo*, which will be the subject of future research.

further research is needed

Additionally, our results highlight the significant variability of transcutaneous CO_2 exhalation rate and conductivity measurements in human subjects. Hence, we strongly advise future research on the topic to consider large sample sizes—*i.e.* more than 40 subjects—in order to ensure accurate estimates of the latter metrics. The present study also focuses only on two measurement sites—the upper arm and the wrist—and further investigations at other sites would be welcome. In particular, the remarkably high axilla values reported by some authors is intriguing, and could benefit from a special attention. Of note, the study data—demographics, K, Q, and nSkBF$_{90}$ values—were provided as Supplementary Materials in the original paper[87], and are also available in this thesis' repository.

3.3 Cutaneous Measuring Conditions

While the previous section focused solely on the transcutaneous CO_2 diffusion, this section addresses other conditions affecting cutaneous measurements. In particular, the following factors are considered:

- temperature, in Section 3.3.1,
- humidity, in Section 3.3.2,
- pO_2, in Section 3.3.3, and
- acidic compounds, in Section 3.3.4.

3.3.1 Skin Temperature

Skin temperature has been measured by several authors—including myself—on human subjects. Early studies conducted on one subject by Benedict *et al.*[329] in 1919, and on 15 subjects by Barcroft *et al.*[284] in 1943 report forearm temperatures averaging at 33.3°C and 33.0°C, respectively. A more recent work performed by Zhu *et al.*[330] in 1999 on 223 subjects (138 male, 85 female) presents mean temperatures of 32.3°C at the forearm, and 31.4°C and 31.1°C at the right and left wrists, respectively. Several studies made at the university of Murcia in Spain in 2008[331], 2012[332] and 2013[333] on 99 subject, 28 subjects and 103 subjects by the same research team report mean wrist temperatures of 34.0°C, 33.7°C and 33.5°C, respectively. These latter studies, however, used a wristband to perform their measurement. Since this wristband prevents the heat produced by the wrist from being dissipated in the ambient air, temperatures in these studies were expected to be higher than in the afore-mentioned works.

Concerning studies that I performed internally on Biosency's employee who gave their informed consent, a first work on 18 resting subjects (12 male, 6 female) revealed bare skin temperature at the wrist of $30.7^{+2.2}_{-2.5}$°C at a room temperature of $22.5^{+0.6}_{-0.9}$°C. Measurements in the same conditions but under a wristband yielded temperatures of $31.9^{+3.9}_{-4.0}$°C (mean over a ≥ 30 min duration, after a 8 min ramp-up time). This increase of about 1° is attributed to the supplementary isolation provided by the worn wristband. A second study was performed on 10 subjects (5 male, 5 female) at the upper arm under a shirt or jumper sleeve, and yielded a mean temperature of $35.1^{+1.5}_{-0.6}$°C.

To sum up, in the absence of external heating and when uncovered, mean skin temperature may lie in the 31–33°C range at the wrist. When the skin is covered by a wristband, it heats up slightly to reach temperatures in the 32–34°C range. When the latter wristband is further covered by an additional clothing layer and moving to the upper arm, 35° or above can reasonably be expected without active heating.

3.3.2 Skin Humidity

Human skin has a critical double barrier function: *(i)* from the outside to the inside in order to prevent the introduction of foreign bodies, contaminants, and potentially harmful microorganisms into the organism, and *(ii)* from the inside to the outside, mainly to prevent excessive water losses, and the dehydration of the body in a dry environment[334]. Still, the skin remains significantly permeable to a variety of substances, including for instance gases, water vapour, drugs, and solvents[259, 335]. In particular, water diffuses from the deeper layers of the skin towards its dryer outer layers, forming the so-called Transepidermal Water Loss (TEWL).

3.3.2.1 Transepidermal Water Loss

TEWL is defined as the amount of water leaving the skin per unit of time and surface, and is often expressed in $g.m^{-2}.h^{-1}$. Although it can be used as a metric to assess the proper barrier function of the skin[336], there is no such think as a "normal" TEWL level, with values reported in the 2.3–44.0 $g.m^{-2}.h^{-1}$ range, with wide variations across measurement sites[337, 338]. Additionally, several authors have noted that, strictly speaking, the TEWL should be expressed without taking into account the water added by sweating[339, 340]. Although this additional constraint has been ignored by a number of authors, some used a topical treatment—*e.g.* poldine methylsulfate—to prevent sweating during TEWL measurements[341]. Preventing sweating may however not be that much of a concern, since heat-triggered sweating rates are usually order of magnitudes higher than reported TEWL values[342]. As such, the pollution of TEWL measurements by the unwanted onset of sweating—if it occurred—could be easily detected.

3.3.2.2 Variables Affecting the TEWL

TEWL is affected by a number of variables, such as the measurement site, skin and probe temperatures, occlusion duration, presence of skin diseases, or subject's stress level, among others[340, pp. 63–76][339, 343–345]. A brief overview of these variables is given below:

- **Measurement site:** huge discrepancies exist between different body parts, with TEWL reported for the palm, forehead, and forearm about 38, 18 and 6 $g.m^{-2}.h^{-1}$[346], for instance. More detailed comparisons of many more skin sites are available in the works of Fluhr, Akdeniz, Kottner *et al.*[337, 338, 340].

- **Temperature:** the skin and probe temperatures also plays an important role in the measurement of TEWL, the higher those temperatures, the higher the measured TEWL[346–348].

- **Humidity:** the ambient RH, on its part, may play a role in TEWL, although conflicting studies exist in the literature: in the work of Grice *et al.*[341] the measured TEWL seems maximal at 25–50% RH but decreases for extremely low or high RH values, whereas Sunwoo *et al.*[349] report increasing TEWL values with a decreasing RH.

- **Occlusion:** occluding the skin greatly enhances the TEWL, with early reports of tripling of the TEWL value after five days of occlusion under a polyvinylidene fluoride (PVDF) film by Aly *et al.*[343]. Other authors have also shown similar tendencies, as reported by Golda *et al.*[350] in an overview on the topic.

- **Skin diseases:** as mentioned above, TEWL is a good indicator of the proper barrier function of the skin and, as such, may be used as a diagnostic tool for the screening of psoriasis or dermatitis[336, 351]. These diseases provoke a degradation of the skin and a decline in its barrier function, resulting in a significant increase in TEWL.
- **Stress:** psychological stress *may* induce modifications of the TEWL—conflicting sources—with a possible increase in TEWL values in case of skin disruption after an injury—*i.e.* tape stripping—in the presence of psychological stress[352, 353].

All in all, these numerous sources of variations may explain the wide range of TEWL values reported in Section 3.3.2.1. In the context of this doctoral work, TEWL should be as high as possible to provide a quick hydration of the CO_2-sensing patch introduced in the next chapter. Thus, the consequences of occlusion, skin diseases, or stress, may all be beneficial in effects. Temperature should not be an issue either, since skin temperature can easily be brought above 32°C without active heating—see Section 3.3.1—and because there is no further increase in TEWL with cutaneous temperatures above ≈30°C[346]. The measurement site, on its part, must be well-accepted by future patients, as mentioned in Section 3.2.6.1.4, and in this respect the upper arm and wrist seem particularly suitable. However—and this is especially true for the upper arm—these two sites have relatively low TEWL values, compared to other body sites[337, 338]. Thus, the results presented below for RH measurements at the upper arm, on healthy skin, and without heating or clothing, are expected to be a worst-case scenario.

3.3.2.3 Experimental Validation

3.3.2.3.1 Humidity Sensing Patch

In order to evaluate reachable humidity levels under a gas-tight impermeable layer, a custom transcutaneous humidity testing patch was designed, inspired by the early work of Masaki *et al.*[354]. The latter patch is presented in Figure 3.14 and entraps four colorimetric sensing dots—which change colour at 20, 40, 60 and 80% RH—under a gas-tight polypropylene layer.

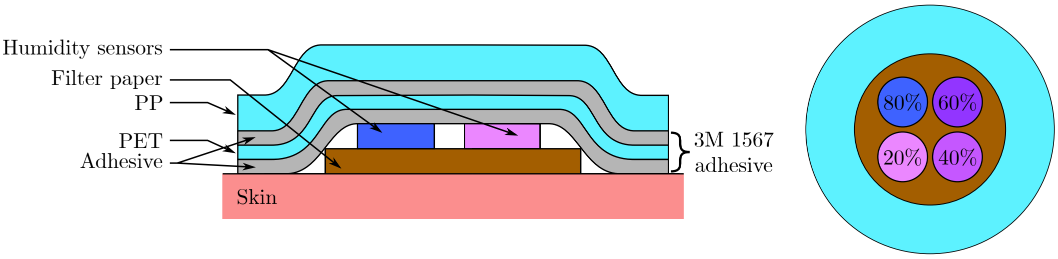

Figure 3.14: Colorimetric humidity sensing patch. **Left:** cross-sectional view of the patch. From bottom to top: a filter paper disk is covered with colorimetric sensing dots (humidity sensors), a double sided layer of adhesive and a polypropylene (PP) covering film. **Right:** top view, showing the concentric design of the patch. The four colorimetric sensing dots are placed at the centre, above a filter paper disk, itself covered with a double-layer adhesive and a polypropylene film.

All parts were hand-cut using a scalpel and a set of punches, and consist in:

- A top, gas-tight, 110 µm thick and 31 mm in diameter, polypropylene layer (3365249, Office Depot, USA).
- An intermediate, double-sided adhesive layer, also 31 mm in diameter, made out of two synthetic rubber-based pressure sensitive adhesive layers, coating a 20 µm thick polyethylene terephthalate (PET) film, for a total thickness of 130 µm (1567, 3M, USA).
- Four reversible, colorimetric, cobalt chloride-based, humidity sensing dots scavenged from humidity test strips (PGA05V50, Bartovation, USA), 200 µm thick and 3 mm in diameter, which change colour from blue to pink depending on the RH to which they are exposed. These four sensing dots switch to pink at 20, 40, 60 and 80% RH. Of note, due to the scavenging process—*i.e.* peeling off the sensing patches using a scalper—the actual thicknesses of the dots were in the 110–190 µm range (mean: 153 µm).

- A bottom layer of filter paper (100% cellulose coffee filter №4×80, Système U, France) to avoid direct skin contact with the sensing dots—as cobalt chloride is a potential allergen[355, 356]—100 µm thick and 11 mm in diameter.

Note that given the low water vapour transmission rate of PET—*i.e.* 0.98 $g.m^{-2}.h^{-1}$ for a 20 µm layer[357]—compared to reported TEWL values—2.3–44.0 $g.m^{-2}.h^{-1}$[337, 338]—it was considered in first approximation that water vapour stopped at the PET layer and diffused no further. Thus, the thickness of the volume into which the water vapour diffuses from the skin is considered to be 308 µm on average (100 µm of filter paper, 55 µm of adhesive, and 153 µm of colorimetric sensing spot, on average). This approximation leads to pessimistic estimates of the amount of water diffusing from the skin to the outer air, and is therefore conservative. Indeed, considering the PET layer as permeable would lead to a thicker equilibration volume, and thus to higher estimated water vapour diffusion rates.

3.3.2.3.2 Protocol

Once built, the patches were stored in a dry environment, so that all sensing dots were blue at the beginning of the measurements. The sensing patches were then placed on the flat area located between the biceps, the triceps, and the lower part of the deltoid, on the dorsal side of the arm, as depicted in Figure 3.15, Right. For illustration, two test strips in a dry and humid environment are also depicted in Figure 3.15, Left, as well as a fully-assembled patch before application on a test subject, Center.

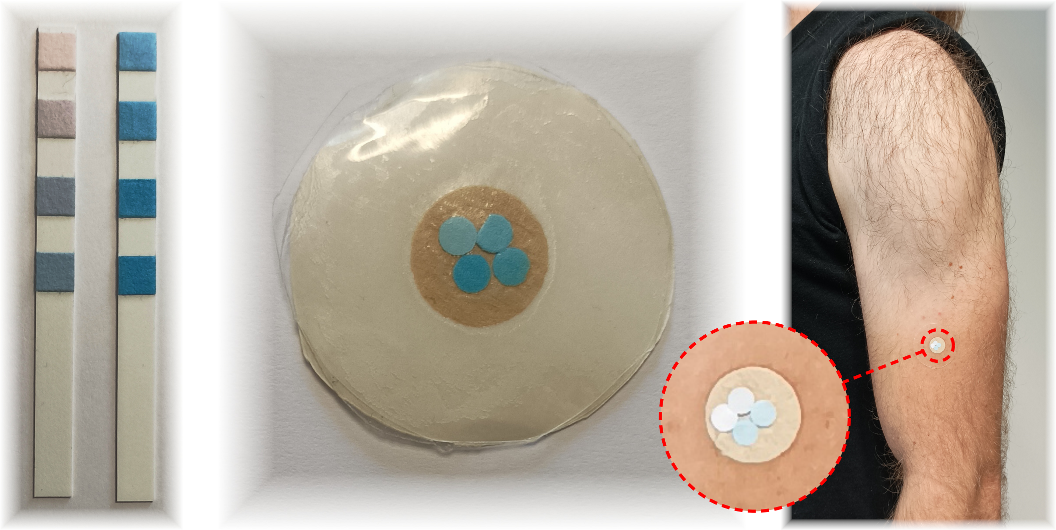

Figure 3.15: **Left:** two test strips, one equilibrated with ambient air at 59% RH (on the left) and the other one stored in a dry box (on the right). The sensing squares turn to pink (read at lavender) at 20, 40, 60 and 80% RH—from top to bottom. Note how the left strip turned to pinkier tones—in particular, its 60% square is lavender. **Center:** a fully assembled patch stored in dry air just before its application on a subject's skin. **Right:** the application site of the patch is on the flat area below the deltoid (circled in dashed red). Note how the applied patch has already partially changed colour to turn pink, lavender, and pale blue.

The studied population consisted of 10 human adults (5 male, 5 female) between 23 and 50 years of age (median age 33), all of whom signed an informed consent notice before the experimentation. The research was led indoor, with an ambient temperature in the 20.6–27.3°C range and RH levels in the 50.7–59.8% range, as measured using a calibrated Testo 174H data logger (Testo, Germany).

3.3.2.3.3 Results

The outcomes of the experiment are summarised in Figure 3.16. The 20% and 40% sensing dots all turned to pink or lavender within the first 10 min after application of the patches, and the 60% sensing dots all turned to pink or lavender after only 20 min. However, the change in colour from blue to pink for the 80% sensing dots took between 40 and 90 min, depending on the test subject, with a mean duration of 70 min. This wide range of humidity saturation times is not surprising though, considering the wide range of TEWL reported in the literature (see Section 3.3.2.1). It could also be partially explained by the discrepancies in the sensing dots thicknesses, as above-mentioned (see Section 3.3.2.3.1).

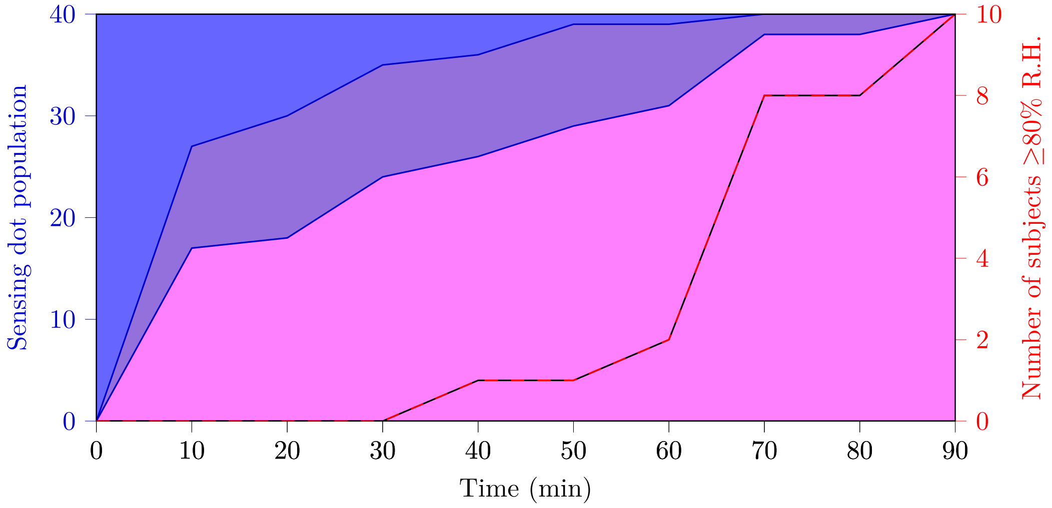

Figure 3.16: Temporal evolution of the experiment. The coloured areas represent the number of blue, lavender, and pink sensing dots in a normalised stacked area chart. The red and black dashed line represents the number of subjects for whom all four sensing dots turned to pink, *i.e.* those for whom the RH under the patch is above 80%.

Those results are particularly encouraging because the RH easily reached over 80% under the designed patch. Thus, the presence of water molecules for the hydration of CO_2 inside a fluorescent sensing patch such as that considered in the next chapter should not be a source of concern. As a result, **the design of fluorescence-based CO_2-sensing thin films for tcpCO_2 measurement can be performed considering RH levels in the 80–100% range**. The concerns expressed by several authors[358–363] about the *drying-out* of the film when used for ambient air CO_2 sensing can thus be safely ignored in the context of trans-cutaneous CO_2 sensing. These first results are also consistent with the findings of Matsumura *et al.*[364], who noticed sweat drips forming under a low water permeability polymer film occluding human skin.

Then, the *response time* of the humidity patches is also particularly interesting. Indeed, the mean time taken to reach a RH level above 80% was 70 min. Considering that the equilibration volume—*i.e.* the equivalent air volume that is entrapped between the top layers of the sensing patch and the skin—to be filled by humid air is 308 µm thick on average, a much shorter humidification time is expected for thinner patches. Indeed, a similar reasoning to that exposed in Section 3.1 about CO_2 diffusion in an enclosed chamber can be performed for water vapour. In this case, the equilibration time is essentially a linear function of the thickness of the equilibration volume. Thus, the presented measurements imply an equilibration rate—*i.e.* time taken to reach over 80% RH under a patch of given thickness—of 14 s.µm^{-1} on average(3). This means that **the RH under a CO_2 sensing patch could be over 80% in a matter of minutes for sensing films 10–50 µm thick**—*i.e.* the range of thicknesses envisioned for fluorescence-based CO_2-sensing thin films in the next chapters.

3.3.3 O_2 Diffusion

O_2 also diffuses through the skin, albeit typically in the opposite direction to CO_2—*i.e.* from the ambient air towards the tissues—since the pO_2 in tissues is necessary lower than that in the ambient air. Normal transcutaneous O_2 pressure varies strongly depending on skin temperature: for a skin heated at 37°C, values as low as 0.3–0.7 kPa have been reported[365], while at 45°C the tcpO_2 mean value can reach 10.9 kPa[267]. O_2 diffusion rates are close to—although lesser than—that of CO_2, namely in the 20–140 cm^3.m^{-2}.h^{-1} range[92, 262, 266, 366] and are also strongly impacted by skin temperature[263]. In summary, the skin is a highly hypoxic environment,

---

(3) Value computed taking the average values of the equilibration time and dot thickness. Minimum value—shortest equilibration time with thickest dot—is 7 s.µm^{-1} and maximum value—longest equilibration time with thinnest dot—of 20 s.µm^{-1}.

although oxygen remains present. This is particularly annoying in the context of fluorescence-based CO_2-sensing, as several fluorophores degrade rapidly under illumination in the presence of oxygen—a phenomenon known as *photobleaching*, and discussed in Section 5.1.1.

3.3.4 Skin pH and Acidic Vapours

The surface of human skin is slightly acidic, with a normal pH between 4 and 7[367]. This low pH is believed to originate from the presence of lactic acid and free fatty acids in the upper layers of the stratum corneum, an hypothesis confirmed by mass spectrometric measurements of the acidic vapours exhaled by the skin, those vapours being predominantly composed of pyruvic and lactic acids[368].

Additionally, since H_2S is also present in the tissues, some may permeate through the skin, although probably at a very low rate considering its low concentration in human tissues—about 0.5 μM[369]. Probably because of this very low concentration, a recent review of volatile compounds present in the human body does not mention its presence on the skin[370][Table 1], nor does it for SO_2 (*ibid.*), despite its physiological role and presence in the body[371]. Still, the same review mentions many other acidic compounds which have been detected at the skin barrier—*e.g.* acetic, lactic, and meth- through octadec-anoic acids[370][Tables 8a–9d]. Acidic poisoning of an unprotected transcutaneous CO_2 sensor is thus not excluded.

Furthermore, and especially in case of elevated skin temperatures, sweat will be secreted by eccrine, apocrine or apoeccrine glands. Although sweat consists mainly of salty water, it also contains lactate, amino acids and bicarbonate, being overall slightly acid (pH 4–7)[299], which may also influence a transcutaneous CO_2 sensor. If the latter is not protected by a membrane, the water contained in the sweat may even act as a solvent to facilitate the migration of the afore-mentioned acidic or basic compounds into the sensing film.

3.4 Conclusion

This chapter lays down the basic knowledge required to develop a new generation of transcutaneous CO_2 sensor. More specifically:

- A simple—yet efficient—modelling of equilibrium-based tcpCO_2 sensors is proposed in Section 3.1. This model gives a direct relationship between the thickness of a given sensor, the skin conductivity towards CO_2, and the expected response time of the said sensor.
- This model was then used in a clinical study—as reported in Section 3.2—to measure the skin conductivity towards CO_2 at different cutaneous temperatures. The latter study also measured the sub-cutaneous blood flow and reached the following two main conclusions:
  - From a response time point of view, it is not necessary to actively heat the skin, and a layer of clothing might be enough to yield a response time only 35% longer than that obtained when heating the skin at 44°C.
  - From an accuracy point of view, skin temperatures in the 35–38°C range might be enough to bring the measured tcpCO_2 close enough to paCO_2 for general clinical practice.
- The cutaneous environmental conditions are finally detailed in Section 3.3: the occluded skin is humid—reaching over 80% RH at a 14 $s.\mu m^{-1}$ rate—highly hypoxic—with pO_2 in the 0.3–0.7 kPa range at 37°C—and acidic—with a pH in the 4–7 range due to the secretion of various acidic compounds by the sweat glands. Its temperature is in the 32–34°C under a wristband without external clothing, and can reach over 35°C under a shirt or jumper sleeve.

Those key aspects of transcutaneous CO_2 sensing are used as inputs in the following chapter, which focuses on choosing and perfecting a CO_2 measurement technique well-suited to the above-presented cutaneous specificities.

Chapter 4

Choosing a CO_2 Sensing Technique

TL;DR

The specifics of transcutaneous CO_2 sensing revealed in the previous chapter are used to select an appropriate CO_2 sensing technique for cutaneous application. Thin-film dye-based CO_2 sensing is opted for, and both the associated chemistry and potential optical sensing schemes are presented. Frequency-based Dual Lifetime Referencing (f-DLR) is finally chosen and its mathematical intricacies are briefly exposed, outlining the need for an accurate phase shift measurement between two—potentially noisy—sinusoidal signals. This latter mathematical problem is then studied in-depth, reaching a practically-interesting solution that highlights a power consumption / accuracy compromise. This chapter lays the theoretical foundations that will be applied in practice in the next one.

Previous chapter Main Table Of Content (TOC) Next chapter

With the previous chapter outlining the main characteristics of transcutaneous CO_2 sensing, the next step is to choose a CO_2 sensing technique that aligns with these specificities. In this view, the present chapter begins with a massive literature review of CO_2 sensing techniques in Section 4.1—itself corresponding to Section 2 of our Sensors review article[88]. Then, the conclusions of the previous chapter are put in perspective with this review, in order to select what seems to be the most appropriate sensing technique in a transcutaneous sensing context. This is done in Section 4.2, itself partially inspired by Section 4 of the afore-mentioned article[88]. The chosen technique—dye-based CO_2-sensitive thin films—is then discussed in more detail in Section 4.3, outlining the possible use of an interesting sensing scheme termed DLR. The latter calls for an accurate phase measurement from a noisy sinusoidal signal, which is the very topic of Section 4.4—itself based on our APSIPA Transactions on Signal and Information Processing paper[90].

4.1 Review of CO_2 Sensing Techniques

Fortunately, since CO_2 is ubiquitous in our world, its measurement has been the goal of many researchers from very different fields, each with their own constraints and objectives. In particular, CO_2 sensing is used: in the food storage and agri-food industry[372], in medical science[82], in sea and environmental research[373], and of course in the laboratories themselves—*e.g.* analytical chemistry. Such a diversity of applications leads to different constraints in terms of operating conditions—such as temperature and pressure—cost, durability, maintenance, *etc.*

Yet, our aim is not to produce in the following pages a complete bibliographic review of each and every one of the mentioned techniques. We do so for the sake of conciseness, and because comprehensive reviews focusing on one or another of the techniques presented below are available in the literature[374–382]. While the latter perform an in-depth coverage of their respective topics—*e.g.* nanomaterials-based sensors[377, 381]—they never cover the full spectrum of CO_2 sensing possibilities. This is partly done, however, in the book *Carbon Dioxide Sensing*[383], which covers certain aspects of the present work in much more details, although letting others aside, and to which the curious reader may refer to quench their curiosity.

The present review spans the full range of CO_2 measuring techniques with the exception of the analytical ones. That is for instance (mass) spectroscopy, magnetic resonance, chromatography, or titration. We did so because such techniques are not likely to be used for biomedical monitoring in the near future, due to the bulky and expensive apparatuses they require. These methods are covered in-depth by dedicated analytical chemistry works, though[384, 385].

For each technique reviewed, the underlying physical principle enabling CO_2 measurement is exposed briefly. Such explanations are often accompanied by a clear figure or schematic to allow for a rapid comprehension of the presented technique. The main features, advantages, and drawbacks of the technique are also disclosed, with typical characteristics of commercial or research applications, when available or relevant. The aim of such summaries is to provide the reader with a basic understanding of each exploited phenomenon, while giving them references to research articles or reviews to dig further. At the end of this section, a table is also given to summarise all the presented techniques and to compare them on several merit criteria—*e.g.* lifetime, accuracy, drift, cross-sensitivities, response time, form factor, *etc.*—see Section 4.1.5.

The structure of this review is organized around the physico-chemical properties of the CO_2 molecule, namely:

- The infrared absorption of CO_2—Section 4.1.1.
- The hydration of dissolved CO_2 into carbonic acid—Section 4.1.2.
- The reduction of CO_2 into CO_2^- and CO_3^{2-}—Section 4.1.3.
- The acoustic properties of gaseous CO_2—Section 4.1.4.

4.1.1 Infrared Absorption of CO_2

4.1.1.1 NDIR Sensors

The operating principle of NDIR CO_2 sensors is that of the Beer-Lambert law of absorption, for gaseous CO_2 exhibits an absorbance peak at 4.26 µm, as can be seen in Figure 4.1. Due to the absence of other commonly encountered gases absorbing at this wavelength, NDIR sensors are very specific and can reach extremely low levels of detection if the sensing cavity is long enough. They operate as follows: an infrared source is placed on one end of a cavity containing the gaseous analyte, while an infrared receptor is placed at the other end. At a given wavelength λ, the measured light flux Φ_{mes} (W) is then a function of: the emitted light flux Φ_0 (W), the geometry of the sensor k (unit-less), the light path length l (m), the CO_2 volume fraction χ_{CO_2} (unit-less), and its absorbance $\mathcal{A}_{\text{CO}_2}$ (m^{-1}) following[386]

$$\Phi_{\text{mes}}(\lambda) = k{\cdot}\Phi_0(\lambda){\cdot}10^{-l\cdot\chi_{\text{CO}_2}\cdot\mathcal{A}_{\text{CO}_2}(\lambda)} \tag{4.1}$$

While this equation indicates a linear relationship between $\log_{10}(\Phi_{\text{mes}}/\Phi_0)$, l, and χ_{CO_2}, the actual linkage between the latter quantities is generally much more difficult to model accurately, due to a variety of light paths that contribute differently to the sensor response. Although this plurality of light paths can be studied beforehand by simulation—as did Hodgkinson, Liu *et al.*[388–390]—most sensors are calibrated empirically once manufactured.

Theoretically, only one emitter / receiver duo is needed, given that one of them is narrow-band—or bandpass filtered—around 4.26 µm, so as to avoid interferences from other gases. In practice however, a *reference* channel is often placed beside the *measurement* one[391–393]. The role of this additional reference channel is to compensate for fluctuations in the light source intensity due to temperature variations, for instance. In this case, the sensor is composed of two sensing elements, one is covered by a 4.3 µm bandpass filter, while the other one is covered by a bandpass filter in the 3.8–4.1 µm region, where no other gas absorbs. Other designs have also been proposed using a time-interleaved reference / measurement channel alternation, instead of two physically distinct light paths. In this case, a single sensing element is covered by a rotating filter wheel equipped with multiple bandpass filters at 4.2 µm and 3.8 µm[394]. The typical design of such referenced sensors is presented in Figure 4.2, Left.

NDIR sensors were often criticised because of the infrared source they used—*i.e.* a bulb with a heating filament—which both consumed much power and generated heat[395]. However, with recent advances in the domain of infrared emission and sensing, this is no longer a source of concern. In particular, recent InAsSb semi-conductors allow for reasonably cheap and energy efficient

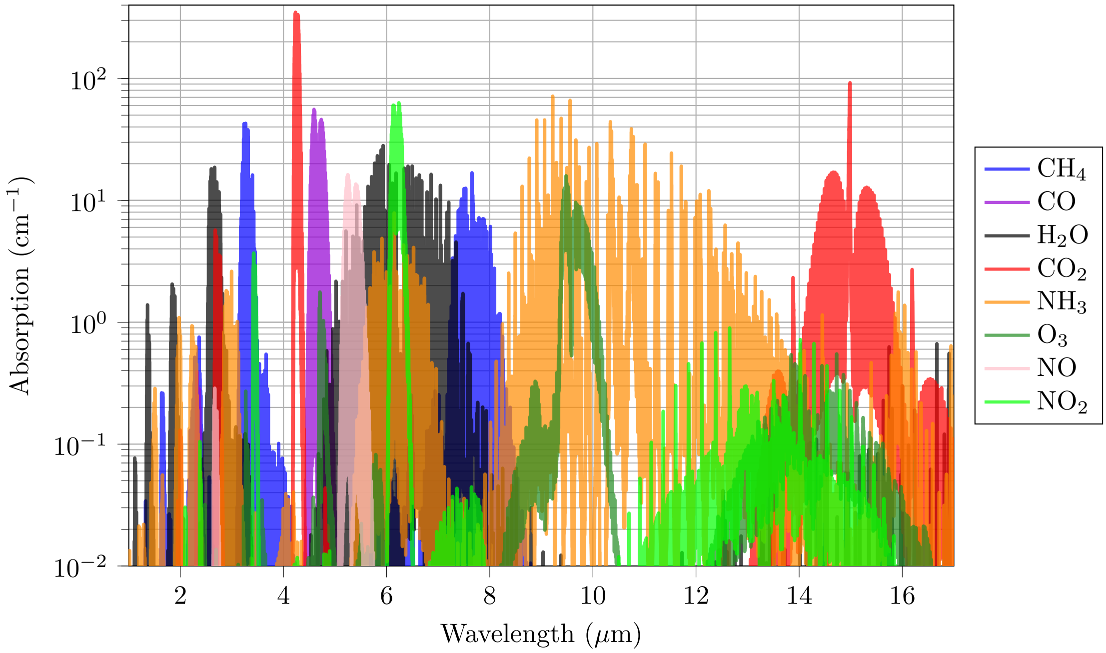

Figure 4.1: Mid infrared absorption spectra of various gases, only CO_2 absorbs at 4.26 µm. Data source: HITRAN database[387]. A Lorentzian broadening profile was considered for a dilution in air at 1 atm and 296 K.

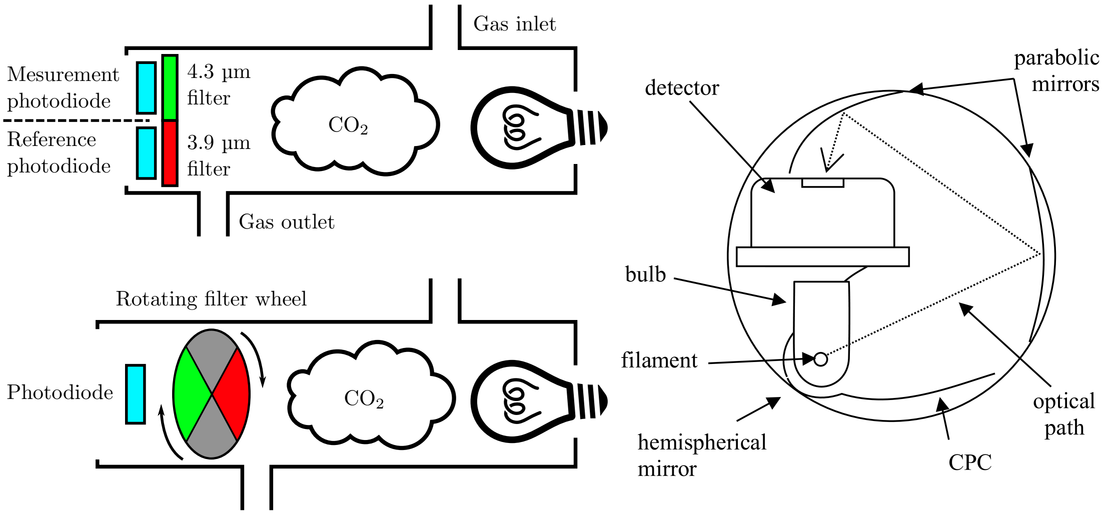

Figure 4.2: **Left:** outline schematic of a space-interleaved (top) and time-interleaved (bottom) NDIR CO_2 sensor. In the time-interleaved sensor, a rotating filter wheel acts as a chopper, with two opaque sectors, and two sectors equipped with 4.3 µm and 3.9 µm bandpass filters, respectively. **Right:** a more complex design allowing for longer light paths in a compact device. The detector has two channels, a measurement and a reference one, as in the upper left scheme. CPC stands for Compound Parabolic Collector, a type of light concentrator. Reproduced with permission from Hodgkinson *et al.*[389].

emitters and receivers, *e.g.* AK9700AE (LED) and AK9710 (sensor), AKM, Japan, or Lms43 LED and photodiode, LMSNT, Russia. Alternatively, thermopiles—possibly miniaturised as Micro Electro-Mechanical Systems (MEMS)—also offer good alternatives to the afore-mentioned photodiodes[396]. Similarly, MEMS emitters have also been developed[390, 397].

The response time of NDIR sensors is limited by the gas flow rate into the sensing chamber, while their sensing range is essentially a function of their light path. Thus, it is possible to create fast sensors with operating ranges going from a few hundreds ppm up to 100% CO_2[395, 398]. It should be noted however, that since the detection of small concentrations requires long light path—up to 80 mm for 100 ppm for instance[398]—it can lead to bulky sensors. In order to solve the latter issue, more complex sensing geometries can be envisioned to lengthen the light path while keeping a compact sensor, as can be seen in Figure 4.2, Right. Additionally, while NDIR CO_2 sensors are not sensitive to relative humidity levels below 100%[394, 395], condensation can lead to the formation of water droplets, either in the light path as fog, or on the surface of light emitters, receivers, or reflectors, thus disturbing the measurements[398, 399]⁽¹⁾. Fortunately, this latter issue may be solved by either detecting potential dew-point situations and removing potentially polluted measurements[293], or heating the sensor itself, though at the cost of a higher power consumption[292, 400].

Reviews of mid-infrared sources[401], NDIR applications for gas sensing in general[274, 391], and concrete applications to CO_2 measurement[389, 392, 398, 402] can all be found in the literature. Interestingly, even if predominantly reported in the gas phase, NDIR CO_2 measurements may also be performed onto an aqueous solution containing dissolved CO_2[403].

4.1.1.2 Photoacoustic Sensors

Photoacoustic sensors also use the afore-mentioned absorbance of CO_2 in the mid infrared (4.26 µm), and periodically illuminate the CO_2 present inside a given sensing volume. Either a mechanical chopper with a continuous source, a low-inertia pulsating source, or even a pulsed laser is used to produce a periodic infrared illumination on the gas sample to analyse. If CO_2 is present in the gas mixture, it absorbs the infrared radiation and thus heats up, dilating slightly. When the illumination is stopped, the mixture cools down and thus compresses. An alternating illumination thus causes a repetition of these dilatations and compressions, which is nothing more than an acoustic wave that can in turn be measured with a microphone[404].

This technique requires a light source that can be modulated at high frequencies—depending on the geometry of the cell and the sensor used—which is achievable using LEDs or lasers, but precludes the use of a light bulb as an infrared light source—unless a mechanical chopper is used, of course. Depending on the targeted accuracy or measurement range, several designs may be employed. The simplest one consists in a non-resonant acoustic cell with a basic microphone and light modulated in the 20 Hz–20 kHz range⁽²⁾. However, using a resonant cell design and placing the microphone at an antinode of the acoustic wave can lead to much higher output levels. Such a design is illustrated in Figure 4.3 with an organ-pipe-like resonant cell. With cells in the centimetre range, this translates into frequencies below 40 kHz. Further still, the microphone can consist in a quartz tuning fork—a piezoelectric transducer with a quality factor above 10 000.

With the use of resonant photoacoustic cells or microphones—*e.g.* quartz tuning forks—very high sensitivities of a few ppm or even ppb can be achieved[405]. Yet, quartz tuning forks are influenced by temperature and humidity—even if this cross-sensitivity is reproducible and can thus be compensated for—and may need to be frequently recalibrated[406]. Contrariwise, MEMS microphones appear to be independent of humidity—even if being temperature-sensitive—and no frequent calibration need was reported[407]. Abundant examples of photoacoustic sensors can be found in the literature[407–409] and recent research is ongoing, targeting their miniaturisation into MEMS sensors[410]. Besides, photoacoustic CO_2 sensors can be designed for the full range of CO_2 sensing—from a few ppb up to 100% CO_2—and their response time is mainly limited by the gas flow inside the sensor. It should be noted that this flow is necessarily limited, since high flow values generate turbulences, which are essentially acoustic noise[404].

---

(1) This issue was also mentioned in Section 3.2.6.1.3 regarding the onset of condensation inside the gold-plated dome of the NDIR sensor that was used for transcutaneous CO_2 conductivity measurements.

(2) Since this range corresponds to human hearing, many microphones are available off-the-shelf in this frequency band.

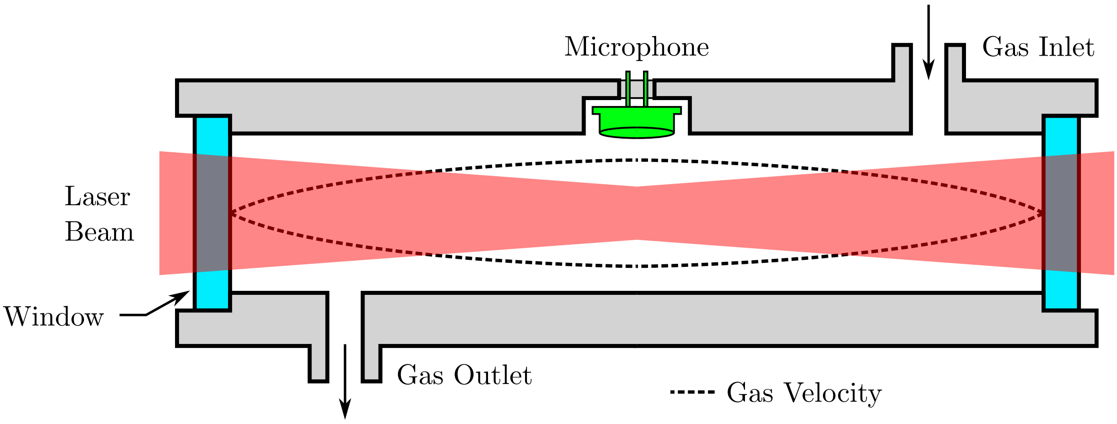

Figure 4.3: Outline schematic of an organ-pipe-like resonant acoustic cell. The cell consists in a pipe closed at its two ends with optical windows. A laser beam at 4.26 µm is then pulsed at the resonant frequency of the pipe, which forms a $\lambda/2$ resonator. For instance, if a 32,768 Hz quartz tuning fork is used as a microphone, $\lambda \approx 10$ mm and a pipe length of ~5 mm would be ideal. A velocity-sensitive microphone may be placed at half the pipe as depicted. Alternatively, a pressure-sensitive microphone would rather be placed near one of its ends.

4.1.2 Hydration of CO$_2$ into Carbonic Acid

As mentioned in Section 2.1.2.3, when presented to an aqueous medium, gaseous CO$_2$ dissolves into carbonic acid ($H_2CO_{3,(aq)}$), which further dissociates into bicarbonate ($HCO^-_{3,(aq)}$) and carbonate ($CO^{2-}_{3,(aq)}$) ions, following[411, 412]:

$$CO_{2,(aq)} + H_2O \xrightleftharpoons{K_1} H_2CO_{3,(aq)} \quad \begin{cases} K_1 = 1.5{\cdot}10^{-3} \\ pK_1 = 2.8 \end{cases} \tag{4.2}$$

$$H_2O + H_2CO_{3,(aq)} \xrightleftharpoons{K_2} H_3O^+_{(aq)} + HCO^-_{3,(aq)} \quad \begin{cases} K_2 = 4.44{\cdot}10^{-7} \\ pK_2 = 6.35 \end{cases} \tag{4.3}$$

$$H_2O + HCO^-_{3,(aq)} \xrightleftharpoons{K_3} H_3O^+_{(aq)} + CO^{2-}_{3,(aq)} \quad \begin{cases} K_3 = 4.67{\cdot}10^{-11} \\ pK_3 = 10.33 \end{cases} \tag{4.4}$$

wherein typical values of K_i can be found in the literature[413, 414] and are given here in pure water at 25°C. The consequences of such dissociations are twofold: first, CO$_2$ dissolution tends to lower the pH of the aqueous medium; second, the presence of dissolved ions induces changes in the conductance of the solution. While the first phenomenon is the basis for the functioning of the Stow-Severinghaus electrode, Ion-Selective Field-Effect Transistor (ISFET) sensors and dye-based sensors, the second one enables conductometric CO$_2$ sensors to operate.

4.1.2.1 Wet Conductometric Sensors

Wet conductometric sensors take advantage of the fact that when CO$_2$ dissolves into an aqueous solution, HCO_3^- and H_3O^+ ions are produced, which in turn modifies the conductivity of the solution[415]. A typical static conductometric sensor is composed of a chamber filled with distilled water and containing two electrodes. The chamber is then covered with a CO$_2$-permeable membrane to allow outer CO$_2$ to diffuse inside the sensor[416–418]. Alternatively, a dynamic conductometric sensor may be built, into which distilled water is circulated between a gas diffusion area and an impedance measurement area[372, 415]. A static measurement cell is depicted in Figure 4.4. Using such an apparatus, the sensing medium may be either liquid or gaseous, whereas dynamic flow-through geometries have only been reported using gaseous analytes.

Such sensors are in theory inexpensive, easy to build, and stable. In practice however, a drift is often observed whose roots are not accurately known, even if some authors suggest a contamination of the distilled water with external ions. In particular, if glues or resins are used to attach the membrane to the sensor, or to assemble the different parts of the embodiment together, they may suffer from outgassing and release ions in the distilled water[417]. If the membrane is not tightly sealed, foreign ions originating from the sensing medium may also enter the solution, and thus change its conductivity. Drift correction[419] or automatic recalibration[420] techniques

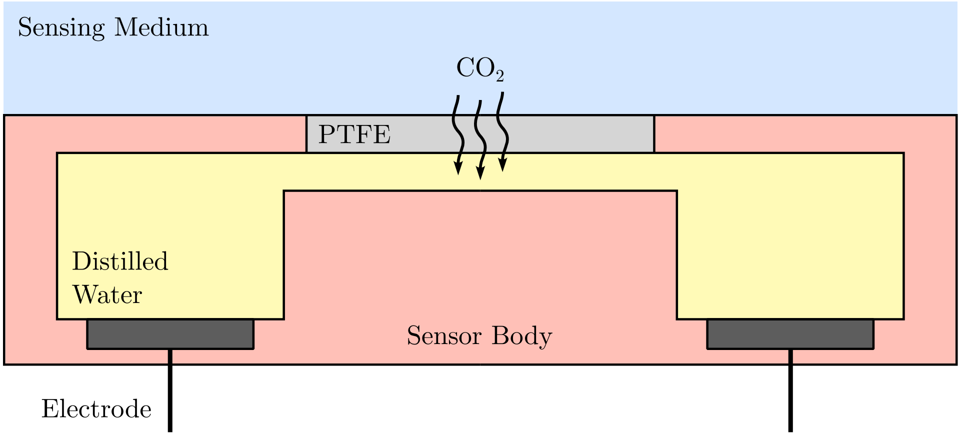

Figure 4.4: Outline of a static conductometric cell. CO_2 diffuses into distilled water, modifying the concentration of H_3O^+, HO^- and HCO_3^- and thus the conductivity of the solution, which may be measured using alternative current to avoid polarisation by means of two electrodes.

have thus been developed to compensate for this phenomenon. Alternatively, other authors immersed the body of their electrode for at least two weeks in bi-distilled water to make sure that foreign ions possibly bound to the glass surface of their sensor re-dissolve in the rinsing water and are thus eliminated[421]. The dynamic flow-through geometry also eludes this issue by forcing the water into a de-mineralizing resin while being recycled.

As is the case for other membrane-covered sensors—see Section 4.1.2.2 below, for instance—the water can still evaporate through the covering membrane depending on the ambient relative humidity, especially in the case of static sensors used on a gaseous analyte. This issue was partially addressed by Neethirajan *et al.*[422], who presented a polytetrafluoroethylene (PTFE) membrane-covered sensor using Nafion as a proton conductor over a layer of polyaniline boronic acid, which exhibits a conductivity change upon a change in its pH. Using this contraption, the authors reported a relatively stable response for RH levels in the 20–70% range. Overall, wet conductometric CO_2 sensor can be used on the full 0–100% CO_2 range, with response times below 1 min. Still, their usable lifetime has not been reported in the literature and may be seriously impacted by the afore-mentioned drift.

4.1.2.2 The Stow-Severinghaus Electrode

The Stow-Severinghaus electrode—named after its inventors Richard Stow[82] and John Severinghaus[423]—is the current state-of-the-art method for transcutaneous pCO_2 sensing[69]. Even if it has been miniaturised since its first introduction, its basic working principle remains unchanged. As one can see in Figure 4.5, it is nothing more than a pH-meter plunging in an electrolyte and covered with a thin membrane. Originally designed for *ex vivo* blood pCO_2 sensing, it was later modified to be used transcutaneously as well[424].

Dissolved CO_2 diffuses from the outer medium into the sensor's embodiment through a thin membrane, made of an ion-impermeable and CO_2-permeable material. A rubber membrane was originally proposed but was quickly replaced by a PTFE one[82, 423], although silicone rubber is still occasionally used for its ease of application and better adhesion[425]. The electrolyte was also switched from distilled water to a solution of sodium carbonate ($NaHCO_3$) and sodium chloride (NaCl) in various concentrations that influence both the sensitivity and response time of the electrode[411]. CO_2 dissociation lowers the pH of the electrolyte—as described by Equations 4.2–4.4—which is then measured using a pair of electrodes: the glass electrode, and the reference electrode. The glass electrode consists in an Ag/AgCl electrode more often than not, although a Sb/SbO_x electrode has also been occasionally reported[424], while the reference electrode can be made of Pt[423, 426] or AgCl[424]. Alternatives to the glass electrode have been explored with liquid membranes instead of the traditional glass bulb[427], or a replacement of the whole electrode by an iridium oxide film grown electrochemically on an iridium wire, yielding a higher sensitivity and being reportedly easier to manufacture than the glass electrode[428, 429].

Apart from miniaturisation and the exploration of other membrane materials, redox electrode pairs, or pH membrane material, the electrode underwent little changes compared to its original design. The response time of the Stow-Severinghaus electrode is generally reported to lie in the 1–5 min range, although the addition of carbonic anhydrase—a catalyst to the reaction 4.2—led

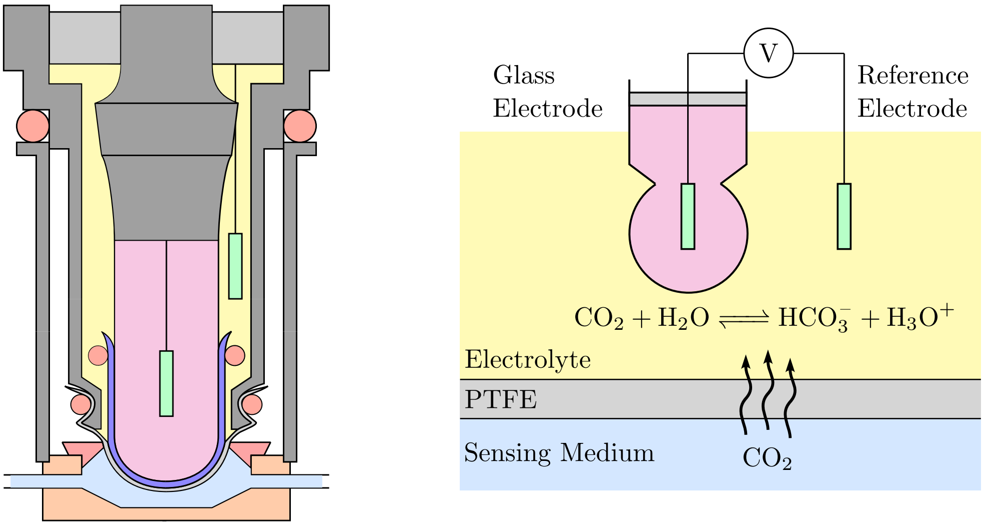

Figure 4.5: **Left:** the Severinghaus electrode, an improvement of the Stow electrode, as first described in the 1958 publication[423]. The colour of the different elements matches that of the simplified schematic on the right. **Right:** outline schematic of the Severinghaus electrode. CO_2 diffuses through a PTFE membrane into an electrolyte, causing a change in the pH of the latter. Such a change is then recorded by means of a pH-meter that consists of a glass electrode and a reference electrode.

to response times below 1 min[425, 430]. Still, the long-term stability of the electrode rarely exceeds a few months and some amount of drift is always present, making it necessary to recalibrate the electrode every few hours or days, depending on the targeted accuracy[427, 431]. The full range of the Stow-Severinghaus electrode is usually that of physiological pCO_2 levels—*i.e.* ~2.6–13.2 kPa (or ~20–100 mmHg)[69]—although applications for concentrations as low as ~0.05–0.1% (~0.5 mmHg) have also been reported[427, 432]. The temperature dependency of the electrode may be compensated for, and a mixture of water and ethylene glycol can be used as a base for the electrolyte, preventing the electrode from drying out from a loss of water vapour through the gas-permeable membrane[433].

4.1.2.3 ISFET Sensors

Due to the limited miniaturisation potential of the Stow-Severinghaus electrode, Ion-Selective Field-Effect Transistors (ISFETs) were explored as CO_2 sensing devices. ISFETs are Metal Oxyde Semiconductor Field-Effect Transistor (MOSFET) whose gate is H_3O^+ sensitive. The addition of a reference electrode can turn them into compact—yet fully functional—pH-meters. The use of ISFET for pH sensing has been reported as early as 1970[434] and was later extended to CO_2 sensing with the addition of a layer of bicarbonate solution covered with a gas-permeable, ion-impermeable, silicone rubber membrane[435].

As can be seen in Figure 4.6, the ISFET gate insulator is not metallised but rather covered with a layer of silicon oxide (SiO_2), itself optionally covered with another layer of silicon nitride (Si_3N_4), hafnium oxide (HfO_2), aluminium oxide (Al_2O_3) or tantalum pentoxide (Ta_2O_5). Once hydrated, the upper layer of the gate insulator becomes able to exchange protons with the surrounding electrolyte, thus acting as a pH electrode. Still, another electrode—the reference electrode—is needed to apply or measure a grid-source potential on the transistor. This latter potential—V_{GS}—itself a function of the pH of the electrolyte, modulates the conductance of the transistor, hence turning it into a pH sensor[436]. CO_2 detection can then be performed by covering the electrolyte with a CO_2-permeable membrane, impermeable to other ions. This basic approach has been successfully applied by a number of authors in the literature, either for pH measurements[435, 437], or direct CO_2 sensing[373, 438–440].

Among the above-mentioned gate insulators, hafnium oxide offers better performance in terms of drain current, sensitivity and body effect than silicon nitride. Hafnium oxide may even be used alone, in place of the silicon oxide layer[441]. The inner electrolyte usually consists in a bicarbonate solution, while the reference electrode is often an AgCl / Ag electrode. ISFET CO_2 sensors are subject to the same drawbacks as the Stow-Severinghaus electrode, namely the drift of the reference electrode and temperature dependency, although the latter may be

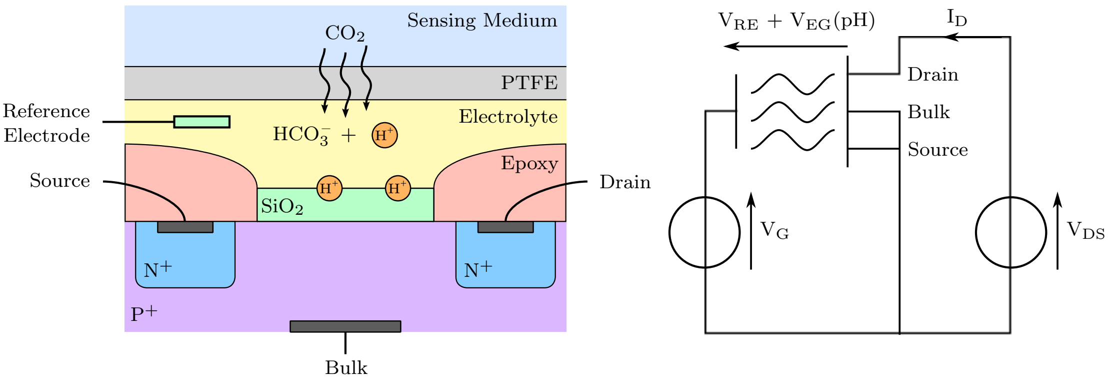

Figure 4.6: **Left:** outline schematic of an ISFET CO_2 sensor. CO_2 diffuses from the analyte inside the inner electrolyte through a PTFE membrane, changing the pH of the electrolyte and generating hydronium ions (abbreviated H^+). The ions will penetrate the upper layer of the porous SiO_2 gate insulator, influencing the P^+ substrate underneath, and thus the conductance of the transistor. **Right:** basic electrical implementation schematic of an ISFET sensor. The actual grid-source potential seen by the transistor is the sum of the applied grid voltage V_G, the voltage between the reference electrode and the electrolyte V_{RE}, and that between the electrolyte and the gate insulator V_{EG}, itself a function of the pH of the electrolyte.

compensated for. An approach for drift correction has also been proposed with good results either on restrained[437] or wide pH ranges[442]. The dry-out and humidity sensibility problems have been addressed with a dry sensor[443], even if the drift of the latter has yet to be reported. Alternatively, a low-drift design with a deported reference electrode has also been proposed with promising results[444].

4.1.2.4 Dye-Based Sensors

Dye-based CO_2 sensors also rely on the influence of CO_2 hydration and dissociation on the pH of an aqueous solution. The pH change caused by the dissociation of CO_2 translates into a change in the optical properties of a pH-sensitive dye, which can exist in either a protonated—AH—or an anionic—A^-—form. The dye is chosen so that its protonated and anionic forms differ either in their absorbance or luminescence spectra, and also for having a K_a acidity constant near that of reaction 4.3 ($pK_a = -\log_{10}(K_a) \approx 6.3$ in water at 25°C[112]). This dye can either be dissolved in an aqueous solution—which is in turn entrapped between a substrate layer and a gas-permeable, ion-impermeable membrane—or dissolved in a thin polymer film with the aid of a phase transfer agent. These two kinds of sensors are often referred to as "wet" and "dry" sensors, respectively. A typical fluorescent sensor is depicted in Figure 4.7, along with the fluorescence spectra of 1-hydroxy-pyrene-3,6,8-trisulfonate (HPTS)—a commonly encountered pH-sensitive fluorophore—at different pH values.

The most basic sensors use a single wavelength for illumination—in case of absorbance measurements—or a pair of excitation-emission wavelengths—in case of luminescence measurement. Photobleaching may be compensated for, using more wavelengths and ratiometric methods similar to those driving pulse oximetry[361, 445–451], while variations in the emitted light intensities or sensitivities toward received light can be addressed by using referencing—*i.e.* taking a measurement in pure N_2 and / or pure CO_2 prior to CO_2 measurement for sensor calibration purposes[358–360, 362, 363, 452–463].

Three other more sophisticated sensing schemes have been developed through the years, in addition to the afore-mentioned techniques, using an additional pH-independent, reference fluorescent dye: namely the Inner Filter Effect (IFE), Dual Lifetime Referencing (DLR) and Fluorescent Resonance Energy Transfer (FRET). Those techniques are presented in more detail in literature reviews or research articles focusing either on dye-based sensors in general[412, 464] or on specific applications such as the IFE[465–472], DLR measurements[89, 473–478] or FRET[479–482]. Surprisingly, none of these methods appears to be notably better than another, with some state-of-the-art works using either DLR[478], IFE[471] or simple referencing[462].

In contrast, a clear distinction exists between dry and wet sensors, with dry sensors largely outperforming wet ones, were it in terms of response time, long-term stability, or ease of manufacturing[412, 483]. Dry sensors are basically made out of a substrate layer, onto which a polymer is cast. The dye(s) of interest is prior dissolved into the polymer by means of a phase transfer agent

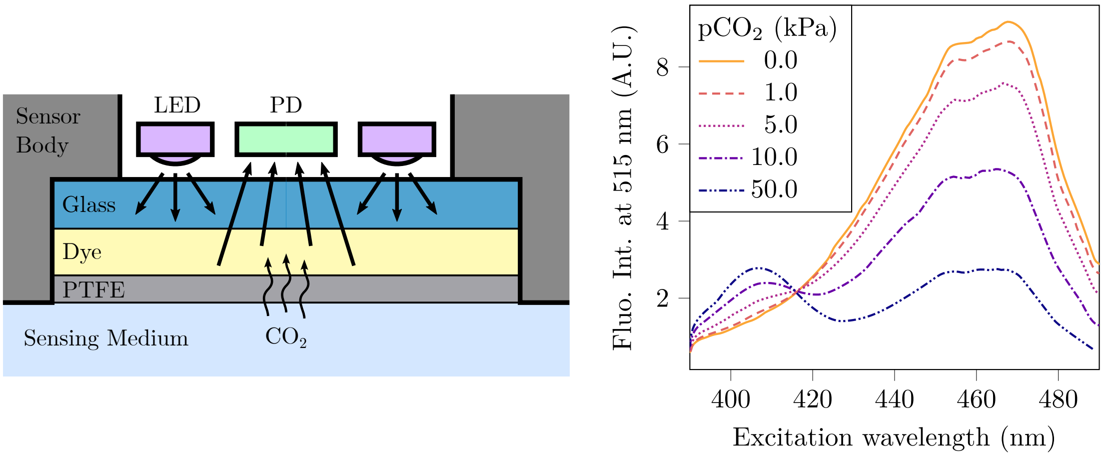

Figure 4.7: **Left:** outline schematic of a typical dye-based CO_2 sensor. The LEDs illuminate a pH-sensitive dye, either dissolved in an aqueous solution or a polymer, through a layer of transparent substrate—here a glass slide. The dye is protected from ionic contamination by a PTFE, gas-permeable, ion-impermeable membrane. The LEDs and photodiode (PD) may additionally be covered by excitation or emission filters in case of fluorescence measurement. **Right:** the fluorescence excitation spectra of 1 mM HPTS in carbonated distilled water equilibrated with different pCO_2 values. Data source: Uttamlal *et al.*[445].

before casting. A plasticiser is also often added to enhance the CO_2 diffusion inside the polymer layer. Optionally, the latter may be covered by an additional protective layer, so as to prevent ionic contamination, or destruction of the sensor by acidic vapours. Apart from the optical sensing scheme, the main differences between the many dry sensors mentioned in the literature lie in the choice of the substances used for the afore-mentioned layers. Although no exhaustive comparison can be found, several authors compared different combinations of chemicals:

1. **Substrate:** the substrate material does not seem to have any major influence on the sensing performance and is indifferently made of PET films, glass slides, or optical fibres. Nonetheless, polyethylene naphthalate (PEN) appears to be superior to PET, because its lower diffusivity towards CO_2 yields shorter response times[476]. In addition, the adhesion of the polymer film on glass substrate can be difficult without a cumbersome surface preparation[363, 475] while PEN foils may just be roughened to enhance the sensitive layer adhesion[476].

2. **Polymer:** hydroxy propyl methylcellulose (HPMC) may be a better choice than ethyl cellulose for being more hydrophilic than the latter, allowing water molecules to be entrapped with the dye and favouring the hydration of CO_2 into bicarbonate ions[470].

3. **Plasticiser:** several plasticisers were compared in the literature, tributyl phosphate (TBP) and Tween 20 appear to be the most efficient ones in terms of sensor response time[457, 470].

4. **Phase transfer agent:** cetyltrimethyl ammonium hydroxide (CTAH) tends to lead to shorter response times[473] although tetramethyl ammonium hydroxide (TMAH) may be more stable since it is less susceptible to Hofmann elimination[470].

5. **Covering membrane:** Hyflon or even Cytop may be used if a minimal response time is not mandatory, in order to limit the sensor poisoning and humidity loss[476].

Overall, dye-based sensors cover the full 0–100% CO_2 range with response times below 1 min—a few seconds have even been occasionally reported[460, 462, 468]—accuracies below 1%, lifetimes approaching one year[471, 472] and thicknesses as low as 1 µm[363]. Still, they may be destroyed quickly by acidic vapours, and often suffer from a high cross-sensitivity towards humidity, O_2—for it is a fluorescence quencher[484, 485]—and temperature. While a protective membrane may mitigate the first two drawbacks, temperature influence may be compensated for. O_2 cross-sensitivity can also be reduced, either by using polymers with a low oxygen permeability[469, 471] or by entrapping the O_2-sensitive luminophore inside polystyrene micro- or nano-beads[473, 475, 486]. Using a dual frequency DLR scheme may also be relevant to compensate for O_2 luminescence quenching[89].

4.1.2.5 Optical Fibre Sensors

Although optical fibres have been used in some of the afore-mentioned dye-based sensors to convey light back and forth between bulky bench-top equipments and compact sensing membranes or solutions[447, 448, 455], they did not consist in the CO_2-sensitive part itself. On the contrary, optical fibre-based CO_2 sensors put optical fibres at the very heart of their sensing principle, using one of the four different techniques presented in Figure 4.8. These four sensing schemes can be grouped in two categories : either *(i)* the CO_2 sensitive material changes the total light path length by shrinking or dilating in response to a change in CO_2 concentration and thus turns the optical fibre into a miniaturised Fabry-Perrot interferometer (case (b)), or *(ii)* the CO_2 sensitive material exhibits a change in its refractive index or exerts a mechanical constraint on the fibre core. In these last two cases, changes are made to the evanescent modes of the fibre, introducing a shift in the transmitted or reflected wavelengths (cases (a), (c) and (d)).

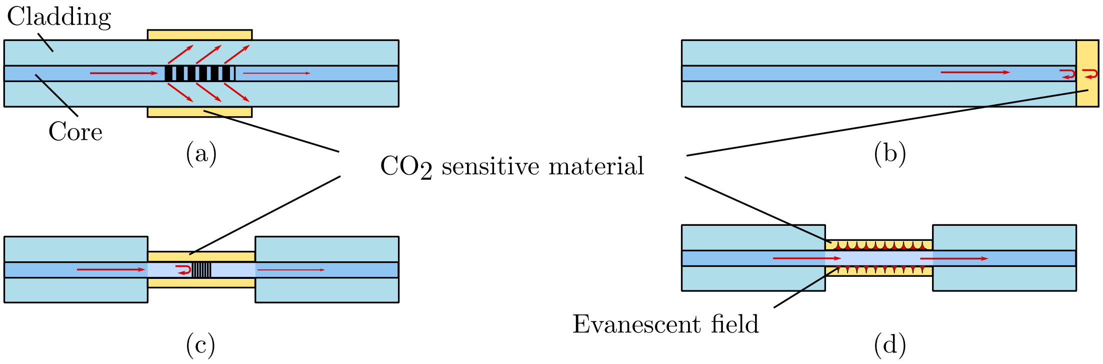

Figure 4.8: “Various techniques that have been employed in CO_2 sensors to cause light propagating in the core to interact with the surrounding environment: (a) [Long Period Grating]; (b) extrinsic Fabry-Perot cavity; (c) [Fibre Bragg Grating] and; (d) etched cladding. All the examples here use a material which demonstrates CO_2 sensitivity and the subsequent change in coating upon exposure to CO_2 is sensed by the interacting light” – Text and figure reproduced with permission from Barrington[379].

The principle behind end-of-fibre Fabry-Perrot interferometer-based sensors is to measure the interferences between the light wave reflected by the fibre-film interface and the one reflected by the film-analyte interface. Depending on the wavelength of the probing light and the thickness of the film, the interferences can be either constructive or destructive, causing notches and peaks in the observed reflected spectrum. The exact positions of those spectral features are directly linked to the thickness of the film, and the latter fluctuates with the surrounding pCO_2. Thus, accurate spectral measurements of the shift in wavelength of a given notch can yield reliable pCO_2 measurements[487, 488].

As for evanescent mode-based fibres, several sensing modalities exist. Fibre Bragg gratings may be used as a strain gauge on a block of pH-sensitive hydrogel that swells or contracts with pH changes, thus bending the fibre it is attached to[489]. Applying a mechanical strain on the optical fibre modifies its effective refractive index[490], inducing a wavelength shift in the evanescent modes of the grating. This technique does not require an optical fibre in itself, however, since a regular pressure sensor may be used instead, possibly much cheaper and more convenient to implement[491]. The pH-sensitive hydrogel can also directly coat the optical fibre optic, with similar consequences, exerting strain on it[492]. Other materials, which exhibit a direct change in their refractive index upon CO_2 adsorption, have also been explored for optical fibre coating—such as metal organic frameworks or ionic liquids—with some success[379, 493].

Alternatively, other optical fibre-based sensors have been developed relying on principles closer to NDIR absorption than CO_2 hydration. Those utilise the absorption of evanescent waves by the CO_2 present in the air surrounding the fibre at ~1.5 µm, where CO_2 absorbs electromagnetic radiations. An additional coating of the fibre was shown to greatly improve the sensitivity of such sensors towards CO_2[494, 495].

The main drawback of optical fibre-based sensors—apart from the elevated price tag of the measurement apparatuses they require—is their cross-sensitivity towards external strain, temperature, relative humidity, and possibly other chemicals which can be adsorbed by the optical fibre coating. Those sensors exhibit response times in the order of 1 min on the full 0–100% range[379, 495]. To our knowledge, the accuracy of such CO_2 sensors has never been characterised extensively, although Melo *et al.*[494] measured a 4.1% resolution on the full scale. Of note, if multiple sensors are used in the same facilities or geographical area, multiplexing can be used to share the light source and measurement apparatus between them, thus greatly reducing the cost per sensor[496]. Such a multiplexing was demonstrated for probing up to 256 sensors with the same fibre, and distances as long as 150 km were reported[497].

4.1.3 Reduction of CO_2

Sensors based on the reduction of CO_2 into CO_2^- and CO_3^{2-} radicals operate following several schemes:

- CO_2 may be reduced following its adsorption on a thin film of metal oxide, thus modifying the conductivity of the oxide layer—Section 4.1.3.1.
- A similar adsorption mechanism has also been reported between CO_2 molecules and graphene, leading to graphene-based sensors—Section 4.1.3.2.
- Alternatively, the reduction of CO_2 may be used in an electrochemical cell, whose electromotive force yields the surrounding CO_2 activity—Section 4.1.3.3.
- Lastly, ionic liquids have also been used in CO_2 sensing, either binding to CO_2 to form carbamate species in conductometric sensors, or acting as a substrate for CO_2 reduction to peroxydicarbonate ions in amperometric sensors—Section 4.1.3.4.

4.1.3.1 Adsorption by Metal Oxide Thin Film

Adsorption-based sensors use the change in conductivity of a thin layer of metal oxide caused by the adsorption of CO_2. Although the latter adsorption has been studied for a number of years[498–502], its mechanism is still not entirely understood and remains a discussed topic in the scientific community[503–506]. Indeed, both physical adsorption and chemisorption appear to take place at the metal oxide interface, and the reduction of CO_2 into CO_2^- may not be the only mechanism involved[505]. That being said, the following reaction is often considered in the absence of a more satisfactory alternative[507–509]:

$$\begin{aligned} CO_{2,(gas)} + e^- &\rightleftharpoons CO^-_{2,(ads)} \\ CO^-_{2,(ads)} + O^-_{(lat)} &\rightleftharpoons CO^{2-}_{3,(ads)} \end{aligned} \tag{4.5}$$

wherein *ads* stands for *adsorbed*, *lat* for *lattice*, and the O^- radicals and e^- are supposed to come from the MO lattice—where M may be Zn or Cu, for instance. Overall, despite the use of metal oxide CO_2 sensors by an important number of authors, few of them propose an explicit sensing scheme, and even fewer mind using equilibrated or justified schemes, which may lead to incoherences. For instance, it has been proposed that since the above-mentioned scheme consumes free electrons from the MO lattice, fewer of them remain available for conductivity[510]. The resulting expected behaviour would be an increase in the metal oxide resistance with an increase in pCO_2. While this assertion seems to hold in the simple ZnO case[508, 510, 511], opposite behaviours were observed when doping ZnO with lanthanum[512] or calcium / aluminium[513, 514]. Consequently, we believe that further research is needed to gain a deeper insight into the working principle of thin film metal oxide sensors. Concerning the present review, we are nevertheless able to mention some interesting works and put them into perspective.

further research is needed

The main drawback of most metal oxide sensors is their elevated operating temperature—in the 200–600°C range—and cross-sensitivity towards CO, O_2, H_2, and humidity. Along the years, several metals were explored, the most ubiquitous being copper, zinc and—although to a lesser extent—cadmium and tin. But chromium (Cr_2O_3)[501], barium / tungsten (Ba_xWO_y)[515], barium titanate ($BaTiO_3$)[511] and lanthanum ($La_2O_2CO_3$)[516] compounds were also studied. While the performance of chromium-based sensors were not measured, $La_2O_2CO_3$-based sensors exhibit a fairly good sensitivity towards CO_2, but a lengthy response time—over 1 hour—and Ba_xWO_y-based sensors showed an important drift. $BaTiO_3$-based sensors were loaded with different metal oxides, and promising results were obtained with zirconium and lanthanum oxides, with response times below 10 min, and almost no humidity influence near 600°C[511].

Several elements were used as doping agents for CuO or ZnO thin films, such as the above-mentioned lanthanum and calcium / aluminium, but sodium[517], germanium / neodymium / tungsten[508], manganese[518], gold[509], silver[503, 519], and indium[520] were also explored. While the manganese-, gold-, and indium-doped ZnO-based sensors reported in the literature performed worse than their pure ZnO counterpart, all the other above-mentioned doping elements greatly enhanced the sensitivity of the sensors—more than doubling it in certain cases[514].

Overall, metal oxide sensors can only work at an elevated temperature—above 100°C at least, even if 200–600°C are more usual. Rare attempts to operate at room temperature resulted in sensors which appeared to be rather unstable and highly sensitive to humidity[521, 522], or that were not thoroughly characterised[509, 517]. Sensitivity to humidity may be mitigated by the addition of silver in the metal oxide[511, 523], while some degree of CO and H_2 cross-sensitivity seems to be inevitable at first glance.

However, a temperature modulation approach—*a.k.a.* temperature cycling approach—may be used to isolate the sensor's response due to CO_2 from that of other interfering gases. This approach has been first suggested in the early 1980s[524], and was quickly demonstrated in the following years as a proof-of-concept[525–529]. In brief, temperature modulation is performed by cycling the operating temperature of a metal oxide sensor, and recording its dynamic response. Since both *(i)* the peak sensitivity as a function of temperature and *(ii)* the kinetic of adsorption / desorption onto the metal oxide layer vary from one gas to another, it is possible to discriminate between different gases using the same sensor operated at different cycling temperatures[530]. This approach has been successfully used to discriminate between organic—*e.g.* benzene, methane, ethanol[528, 529]—and inorganic—*e.g.* CO, H_2S[526]—gases, or mixtures thereof. Both qualitative—*i.e.* classification of an unknown gas mixture in pre-determined categories[531, 532]—and quantitative—*i.e.* accurately measuring the concentration of each gas in a given mixture[533, 534]—have been performed successfully. Applications to CO_2 sensing can also be envisioned, in spite of a more scarce literature on the topic[535, 536].

Measurements in the physiological range have been reported[511] and response times below 30 s are reachable[508, 519, 537]. The influence of humidity has also been discussed in detail by Gankanda *et al.*[507] and the above-mentioned hydration of CO_2 is suspected to alter the sensing properties of metal oxide sensors. Interestingly, while most works focused on the change in conductivity of metal oxide upon CO_2 adsorption, other works were based on capacitive[519, 523, 538], work function[521, 522] or optical properties[509] measurements. Thorough reviews on metal oxide-based sensors for gas sensing—although not focused on CO_2 detection alone—are also available[382, 539].

4.1.3.2 Adsorption by Graphene

More recently, a similar approach to that of the previous section has been used, replacing metal oxides with graphene as the sensing material[540, 541]. As with metal oxide-based sensors, the working principle of such graphene-based sensors is also a debated topic. Overall, graphene acts as a room-temperature p-type semiconductor that can be used either in a purely conductometric setup—measuring the bulk resistance or impedance of the graphene layer[542–544]—or in a Field-Effect Transistor (FET) setup—of which graphene is the canal[545]. However, the interaction of the CO_2 molecule with the graphene layer is not exactly known, and different competing theories have been proposed. On the one hand, CO_2 has been presented as an oxidising or reducing agent, which exchanges electrons with the graphene lattice, the direction of the charge transfer depending on the applied electric field[546]. On the other hand, it has also been proposed that the change of conductivity of the graphene layer following CO_2 adsorption could be caused by adsorption-induced impurity scattering without formal charge exchange[547].

Graphene has been used both as a pristine material[542, 548–550] and in its oxidised form[544, 551] for CO_2 sensing. Additionally, other authors even considered the fabrication of composite sensors, combining graphene with polyethyleneimine[543] or metal oxides—such as Al_2O_3[552], Sb_2O_3[553], In_2O_3 and NiO[554] with mixed results. Indeed, the performance of graphene-based devices for CO_2 sensing is hindered by a high cross-sensitivity towards a variety of other gases—*e.g.* N_2, O_2, NH_3, CO or H_2[544, 548, 549]—and humidity[549, 550, 555]. Encouragingly, however, Akther *et al.*[544] recently reported temperature and humidity correction techniques for a graphene-based CO_2 sensor, with a mean error below 3% over the full 400–4000 ppm range, and a response time of 3–5 s, despite showing some degree of cross-sensitivity towards other gases. So as to overcome the latter cross-sensitivity issue in graphene-based sensors, Rumyantsev *et al.*[556] developed a discrimination method based on the analysis of the low-frequency noise spectrum of a pristine graphene transistor. However—at least to the best of our knowledge—their method is yet to be applied to CO_2 sensing.

4.1.3.3 Electrochemical Cells

Potentiometric sensors based on electrochemical cells have been proposed for CO$_2$ sensing since the late seventies[557], and although several ameliorations have been developed in half a century of intense research, their basic working principle remains largely untouched. An extensive description of the sensing principle of such sensors for CO$_2$ can be found in the work of Maruyama *et al.*[558] and is briefly summarised here. The sensor itself consists in the following electrochemical cell

$$\mathrm{Au, CO_2, O_2|Na_2CO_3||Na_2O|O_2, Au} \tag{4.6}$$

wherein the ion bridge is made of NASICON ($Na_3Zr_2Si_2PO_{12}$)[559], which acts as a sodium-ion conductor. The anode, cathode, and global cell reactions are given by

$$\begin{aligned} 2\,\mathrm{Na}^+ + \mathrm{CO_2} + \frac{1}{2}\mathrm{O_2} + 2\,\mathrm{e}^- &= \mathrm{Na_2CO_3} && \text{(anode)} \\ 2\,\mathrm{Na}^+ + \frac{1}{2}\mathrm{O_2} + 2\,\mathrm{e}^- &= \mathrm{Na_2O} && \text{(cathode)} \\ \mathrm{CO_2} + \mathrm{Na_2O} &\rightleftharpoons \mathrm{Na_2CO_3} && \text{(global)} \end{aligned} \tag{4.7}$$

and the electromotive force of the cell appears to be proportional to log(pCO$_2$). The anode, covered in sodium carbonate (Na_2CO_3) is referred to as the *sensing electrode*, while the cathode is the *reference electrode*. The outline schematic of such a potentiometric sensor is presented in Figure 4.9.

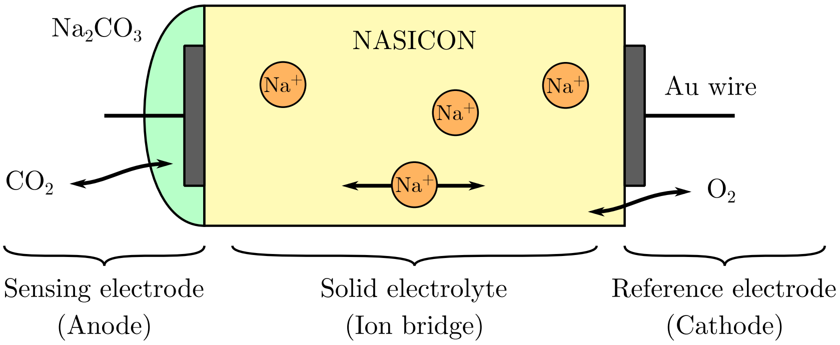

Figure 4.9: Outline schematic of a potentiometric CO$_2$ sensor as described by Maruyama *et al.*[558]. The NASICON sandwich with one end covered in sodium carbonate makes an electrochemical cell, the electromotive force of which yields pCO$_2$.

A major improvement to the stability of potentiometric sensors has been the addition of a third reference electrode[558, 560, 561], or the use of a solid reference electrode instead of the above-mentioned Na_2O / O_2 interface[562–564]. Still, even with this referencing, such sensors usually suffer from some degree of cross-sensitivity towards humidity. In addition, one of their major drawback for biomedical applications is their high operating temperature—in the 300–700°C range.

The performance of a potentiometric sensor strongly depends on the thickness of its different constituents, but also on the choice of the materials used for the electrolyte and for the sensing electrode coating. Concerning the electrodes themselves, their composition does not seem to have any significant influence on the sensing performance, since they are often made out of noble metals—such as gold[558, 560, 565] or platinum[557, 561, 566]. The electrode wires are bound to the solid electrolyte using pastes of the same metal—possibly deposited with a stencil—which are further sintered to make an electrical bond between the solid electrolyte and the wires. For a wider contact area, the use of a gold mesh has also been proposed[565]. The solid electrolyte consists more often than not in NASICON, but potassium carbonate (K_2CO_3)[557], sodium β-alumina[567], lithium phosphate (Li_3PO_4)[562–564], and more recently yttrium-doped LSBO ($La_{9.66}Si_{5.3}B_{0.7}O_{26.14}$)[568] and $Li_7La_3Zr_2O_{12}$[569] have also been used with some success. As for the coating of the sensing electrode, various carbonates were explored such as Na_2CO_3, Li_2CO_3 or $CaCO_3$, with similar performance. Reference materials such as yttrium stabilised zirconia[558], BiCuVO$_x$-perovskite-oxide[560], Li_2TiO_3 / TiO_2[562–564] and $Bi_8Nb_2O_{17}$[561] were used exhibiting good stability.

If an objective comparison between any of the chemical combinations mentioned above is made difficult by the change in form-factor and film thickness in the reported works, one can still notice some remarkable facts. At first, in an attempt to mitigate the humidity cross-sensitivity of potentiometric sensors, the addition of barium carbonate to a lithium carbonate sensing material ($BaCO_3$ / Li_2CO_3)[560, 562, 564], or the addition of lithium carbonate to an indium tin oxide sensing material (Li_2CO_3 / ITO)[565] have been successfully explored by several authors, yielding potentiometric sensors with no cross-sensitivity toward humidity. Then, room temperature operation of such sensors was also achieved with good sensitivity at 30°C on the 300–3000 ppm CO_2 range[565]. Finally, some investigations on thin-film designs yielded particularly fast responding sensors—below 1 min[563, 564, 570]. The full range of potentiometric CO_2 sensors covers the 0–100% CO_2 concentration range.

4.1.3.4 Ionic Liquids-Based Sensors

Room temperature ionic liquids have been intensively studied since the early 2000s, with targeted applications for gas sensing and CO_2 sequestration in particular[571–574]. Ionic liquids, unlike ordinary liquids, are not made out of neutral molecules but consist exclusively of ion pairs. They also exhibit a negligible vapour pressure and their electrical conductivity makes them appropriate candidates to act as liquid electrolytes. As for metal oxide sensors, the exact mechanisms underlying CO_2 sensing with ionic liquids are still partially unknown, although three main pathways have been proposed. One is the reduction of CO_2 at the anode and its further oxidation at the cathode, possibly following[575]

$$CO_{2,(\mathrm{ads})} + e^- \rightleftharpoons CO^-_{2,(\mathrm{ads})} \tag{4.8}$$

although—since there is a reasonable amount of doubt about the latter equation and the existence of $CO^-_{2,(\mathrm{ads})}$—most authors did not explicit it, or preferred the R-CO_2 notation—standing for *Reduced*-CO_2—instead of CO_2^-[576]. CO_2 reduction can be measured either by a change in the impedance of the ionic liquid[577–581], or by amperometric or cyclic voltammetry techniques[575, 576, 582].

A second sensing scheme has been proposed, in which CO_2 binds with an amine to form a Carbamate Ionic Liquid (CIL) following[583]

$$\begin{aligned} RNH + CO_2 &\rightleftharpoons RNCOOH \\ RNCOOH + RNH &\rightleftharpoons \underbrace{RNH_2^+ + RNCOO^-}_{CIL} \end{aligned} \tag{4.9}$$

Since the CIL conducts electricity, it can serve as a CO_2 probe using different sensing schemes. Although a simple impedance measurement may be performed, Chen *et al.*[583] exploited the chemoluminescence of luminol in the presence of O_2 instead. In their sensor, the presence of CO_2 in solution generated a conducting CIL as described by equation 4.9. Electric current is then passed through the CIL, reducing dissolved O_2 into O_2^- ions which oxidises luminol. Oxidised luminol in turn emits light by chemoluminescence, which can be quantified by optical measurements.

A third sensing scheme takes advantage of the irreversible reduction of CO_2 into peroxydicarbonate in the presence of oxygen, following[584, 585]

$$\begin{aligned} O_2^{\bullet-} + CO_2 &\longrightarrow CO_4^{\bullet-} \\ CO_4^{\bullet-} + CO_2 &\longrightarrow C_2O_6^{\bullet-} \\ C_2O_6^{\bullet-} + O_2^{\bullet-} &\longrightarrow C_2O_6^{2-} + O_2 \end{aligned} \tag{4.10}$$

Since it is not reversible, the latter scheme may not be used for a traditional CO_2 sensor, but rather for CO_2 detection, dosimetry or sequestration. Interestingly, this reduction of CO_2 in the presence of oxygen has been treated as an interference by several authors[575, 582], who placed an oxygen trap before their CO_2-sensitive ionic liquid layer to prevent it from happening. This reduction may also be the cause of the slight drift observed in some of the afore-mentioned, non-oxygen-protected sensors[577, 580, 581].

In most cases, ionic liquids sensors are probed by amperometric or conductimetric methods, such as cyclic voltammetry, galvanostatic or impedance measurements. However, Fabry-Perot interferometry—see Section 4.1.2.5—has also been reported[586] as well as acoustic resonant sensors using quartz micro-balances[585, 587]. The idea of such sensors is to assess the shift in frequency of a resonant element coated with an ionic liquid. When the ionic liquid adsorbs CO_2, its mass increases, lowering the resonance frequency of the micro-balance. When CO_2 desorbs, the inverse phenomenon occurs. Of note, such acoustic resonant sensors based on CO_2

solubility were also explored with silicone or amine-based polymers instead of ionic liquids[588–592], although they often exhibit significant sensitivity to humidity.

Overall, ionic liquid sensors have been used across the physiological[575] or full 0–100%[576, 587] CO_2 range. Response times in the 40–200 s range seem reachable[575, 583, 587] although much longer response times have also been reported, especially for CO_2 desorption when returning to baseline[579–581]. The accuracy of such sensors was seldom characterized, with only Chen *et al.*[583] mentioning a 2.05% accuracy measured over 10 trials. The same remark holds for the sensor lifetime, reported in only one case to be over 4 months[575]. Ionic liquids sensors also exhibit a temperature-dependent response[575, 582], and are often sensitive to CO, O_2, H_2, NO_2, N_2O, SO_2 and humidity[575, 577, 583].

4.1.4 Acoustic Properties of CO_2

4.1.4.1 Time of Flight Acoustic Sensors

Time of flight sensors are based on the difference in sound velocity between CO_2 and other gases—*e.g.* 351, 330 and 269 $m.s^{-1}$ for N_2, O_2 and CO_2 under 1 atm and 25°C, respectively[593]. Thus, a simple time of flight sensor can be constructed for CO_2 sensing, consisting in an ultrasound emitter and receiver pair, facing each other in the analyte gas mixture. Joos *et al.*[594], for instance, performed acoustic measurements using a 20 cm tube at the end of which the ultrasound transducers were attached. The authors were able to measure the CO_2 content of a CO_2 / N_2 gas mixture over the full 0–100% CO_2 range with an accuracy of 0.3%. An outline schematic representing the working principle of their experiment is depicted in Figure 4.10.

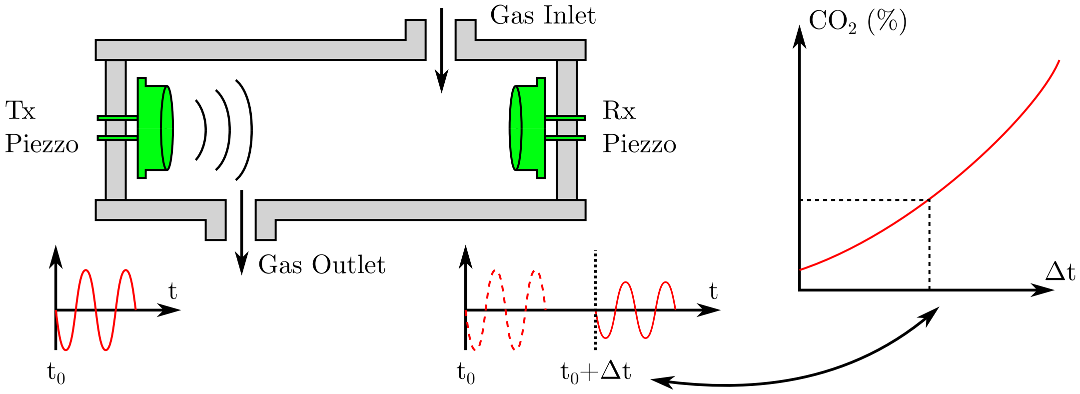

Figure 4.10: Outline schematic of a time of flight CO_2 sensor as described by Joos *et al.*[594]. Two ultrasound (40 kHz) transducers—emitter (Tx) and receiver (Rx)—are placed at both ends of an acoustic chamber which may consist of a simple tube. A burst of ultrasound is emitted at t_0 (on the left) and arrives at $t_0 + \Delta t$ at the receiver (on the right). The Δt value can then yield the percentage of CO_2 in the gas mixture using velocity-based calculations.

These sensors usually have long path lengths—20 cm in the above-mentioned work[594]—which may be difficult to embed in a portable apparatus. Still, they can provide low latency measurements, since their response time is only limited by the time taken by the analyte gas mixture to fill the acoustic chamber. Interestingly, recent research by Cicek *et al.*[595] demonstrates another exploitation of the difference in sound velocity between N_2 and CO_2, using an array of miniature Helmholtz resonators, whose resonance frequency shifts depending on the CO_2 concentration to which they are exposed. They achieved CO_2 sensing in the 0–1% range with a 70 mm radius sensing array.

However, while this technique may seem interesting at first glance for its low cost and long-term stability, it is usually limited to a mixture of two gases[596]. Consequently, it might be unusable in the context of biomedical CO_2 monitoring. Indeed, most human tissues not only produce CO_2 and consume O_2, but also evaporate water. As such, a gaseous volume equilibrated with human tissues may contain as many as four different gases—CO_2, O_2, N_2 and H_2O—whose amounts cannot be found with a single pulse velocity measurement.

4.1.4.2 Acoustic Attenuation Sensors

The acoustic attenuation sensing scheme is based on the phenomenon of vibrational relaxation, which consists in the reduction in intensity of a propagating acoustic wave in a gas. This attenuation depends on the sound frequency and the specific gas or gas mixture in which it occurs[597, 598]. Acoustic attenuation measurements performed at different frequencies allows to establish the acoustical absorption spectrum—i.e. attenuation intensity as a function of the acoustic wave frequency—of a gas mixture. Several such spectra are presented in Figure 4.11, and can be used to identify the different gases that compose an analyte gas mixture as well as their proportion in the latter. To do so, an apparatus similar to that presented in Figure 4.10 may be used, but with multiple emitter / receiver pairs placed at different distances. Then, measurements of the sound attenuation and velocity can be performed, yielding an absorption value. The latter may in turn be compared with theoretical calculations—or experimental data—for a CO_2 / N_2 gas mixture, leading to a pCO_2 value.

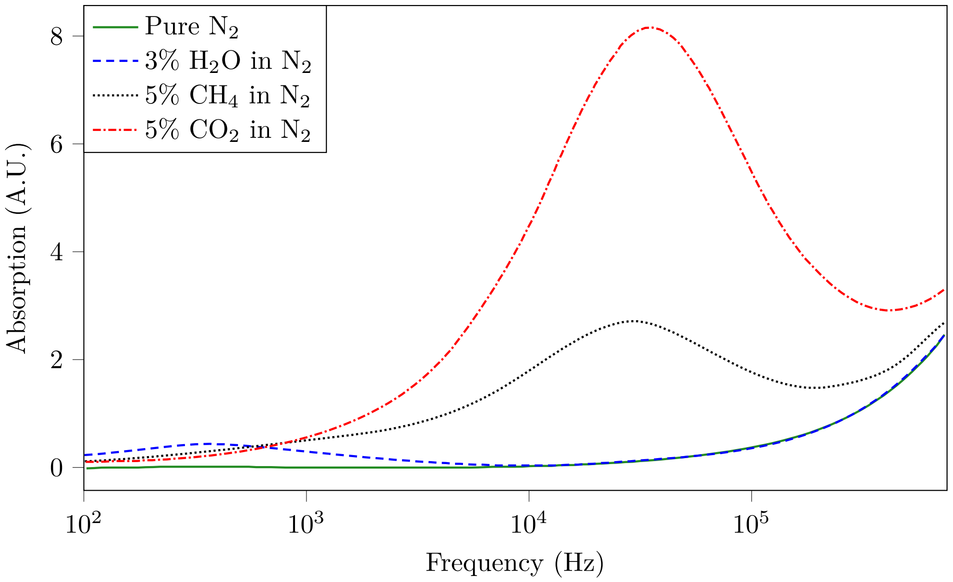

Figure 4.11: Acoustical absorption spectra of diverse nitrogen mixtures. Data source: Petculescu *et al.*[599].

Theoretical and practical applications of this phenomenon are available in the literature[599–604]. However, at least to the best of our knowledge, vibrational relaxation applied to CO_2 sensing never went further than the proof of concept presented by Petculescu *et al.*[603]. Unlike most of the other sensors presented in this review, cross-sensitivity towards O_2 should be negligible. Indeed, O_2 does not exhibit any vibrational relaxation phenomenon in the 10^3–10^7 Hz.atm^{-1} range[602]. The influence of humidity may be another source of concern, however. If the lower mode of water vibrational relaxation occurs at much lower frequencies than that of CO_2[605], higher frequency components are also present at high humidity fractions which can interfere with CO_2 measurements[602]. In addition, temperature should be measured and compensated for, as it influences sound propagation, and thus the position and amplitude of the acoustical absorption peaks[600].

4.1.5 Comparison Table

Although an objective comparison of the above-mentioned CO_2 measurement techniques is made exceedingly difficult due to the incompleteness of most of the referenced works, we tried to do our best to gather state of the art performance for the different sensing schemes presented. The pith and marrow of our literature review is thus summarised in Table 4.1.

We gently warn the reader that each column of the table contains the best performance reported in the literature for a given criterion and that no sensor may exist with all the characteristics presented in a given row. For instance, concerning ionic liquids-based sensors, Chen *et al.*[583] reported a 2.05% accuracy but with a 2 min response time, while Mineo *et al.*[587] reported a 40 s response time without reporting the accuracy of their sensor. Still the “ionic liquid” row of Table 4.1 contains both the 2.05% accuracy and 40 s response time, even if no sensor exists with such characteristics.

Finally, although most criteria are self-explanatory, a few additional comments may be necessary for a sound understanding and interpretation of this table. First, the lifetimes of several sensor families—and especially those of the (photo-)acoustical ones—are not explicitly reported in the literature. Yet, since NDIR sensors were reported to reach a lifetime of at least 15 years[395], and since acoustical building blocks—*e.g.* ultrasonic transducers—usually last for years, the infinity symbol (∞) was used, meaning that a lifetime of at least several years should be expected. Second, the calibration need refers to the need to re-calibrate a sensor frequently—*i.e.* every few hours or days—due to the presence of a significant drift in its response. This criterion does *not* refer to the initial sensor calibration that may be performed in the factory. Third, the response time of the evaluated sensors was often measured using test benches which flush the sensors with a continuous flow of a gas mixture containing a known CO_2 concentration. In such a configuration, the four sensors noted with an (a) are supposed to respond as soon as the latter gas mixture flows inside their embodiment, hence the ≤ 1 s indication. In practice, however, the response time strongly depends on the sensor housing dimensions, since CO_2 will have to diffuse from the analyte gas—or medium—inside the sensor embodiment.

4.2 Potential Application to Transcutaneous Sensing

Returning to the development of next-generation tcpCO_2 sensors, let us briefly review past attempts before choosing one of the CO_2 sensing techniques mentioned above, based on the specificities of transcutaneous CO_2 sensing.

4.2.1 Past Attempts

The Stow-Severinghaus electrode appeared in the late 1950s, underwent only minor improvements since then, and reigns supreme over the tcpCO_2 monitoring market[68, 82]. Yet, several authors have been trying to push forward other means of measuring a subject's tcpCO_2, mainly using NDIR sensing and mass spectroscopy, as disclosed in the following sections. It is also worth mentioning here that we measured the absorption spectrum of CO_2Hb while searching for a non-invasive alternative to tcpCO_2 monitoring, even if this track proved to be but a dead end, as CO_2Hb and HHb have identical absorption spectra—see Section 2.3.

4.2.1.1 Non-Dispersive Infrared and Transcutaneous Sensing

Regarding NDIR, a couple of works by Eletr, Greenspan *et al.* surfaced in the early 1980s[272, 273], describing a Hewlett-Packard capnometer that collects the CO_2 exhaled by the skin inside a small sampling chamber probed by infrared radiations. Despite the fair performance achieved—up to 48 h of continuous monitoring, an SD of 0.2 kPa (1.5 mmHg) between paCO_2 and tcpCO_2 on 3–6 h sessions and a response time about 90 s[272]—the main drawback of this sensor was the need to strip the *stratum corneum* with 20–50 successive applications of adhesive tape so as to reach a reasonable response time.

The NDIR track was then dropped until the mid 2010s and the advent of rate-based approaches by the team of Chatterjee, Ge, Iitani *et al.*[261, 612–614] at first and by the team of Grangeat *et al.*[615, 616] in a second move. If the latter work is insufficiently detailed—especially the explanations concerning the sensing part itself—the former allows for a sound understanding of the rate-based approach. This approach consists in placing a sampling cup against the skin to collect transcutaneously exhaled CO_2, but—contrary to what was done in the earlier work of Eletr, Greenspan *et al.*—no time is left for the gas in the cup to reach an equilibrium with the skin CO_2 content. Rather, the gas in the cup is flushed with fresh air or pure N_2, and its CO_2 fraction is then measured using a conventional NDIR sensor. Theoretically, the so-obtained CO_2 diffusion rate is only a function of *(i)* the patient's tcpCO_2 and *(ii)* their skin diffusivity towards CO_2[261]. However, since this latter parameter is not known accurately and fluctuates a lot depending on the skin temperature[259, 263], measurement site[266, 298] and subject at hand[313], the rate-based approach is most likely limited to trend analysis at best(3).

In the afore-mentioned works, it should also be noted that contrary to the teams of Chatterjee, Ge, Iitani, *et al.*, those of Grangeat, Eletr, Greenspan *et al.* heated the skin in the 35–43°C range, likely so as to boost the skin conductivity towards CO_2, as explained in Section 3.2.

4.2.1.2 Mass Spectroscopy and Transcutaneous Sensing

Overcoming the issue of the latter rate-based approach, a more sophisticated technique has been explored in parallel by Mc Ilroy's team in the early 1980s[288, 289, 617], using mass spectrometry

---

(3) In addition to the presented references, the mnemonist reader surely recalls the large variability of measured skin CO_2 conductivities reported in Section 3.2.

Criterion → ↓ Technique	Lifetime	Calibration need	Humidity cross-sensitivity	Accuracy	Response time	Miniaturisation potential	References
NDIR (Section 4.1.1.1)	$\geq$ 15 years	No	No	0.03%	$\leq$1 s $^{(a)}$	Moderate (down to $10 \times 10 \times 0.5$ mm^3)	[391–393, 395]
Photoacous. (Section 4.1.1.2)	? (∞)	No	No	1%	$\leq$1 s $^{(a)}$	Low (∼cm)	[407, 606, 607]
Wet Conduct. (Section 4.1.2.1)	?	Yes (0.4% drift / hour)	Yes (dries out)	?	5 s	High (down to 100 µm thickness)	[416, 418]
S-S elec. (Section 4.1.2.2)	80 days	Yes (0.03 mV/h)	Yes (dries out)	0.03% (0–100 mmHg)	30 s	High (down to 10 µm thickness)	[423, 425, 429, 608]
ISFET (Section 4.1.2.3)	$\geq$ 30 days	Yes (0.23 mV/h)	Yes	?	60 s	High (down to 100 µm thickness)	[435, 444]
Dye-based (Section 4.1.2.4)	19 months	No	Yes	0.1%	$\leq$ 1 s	Excellent (down to 1 µm thickness)	[358, 363, 412, 609] [471, 472]
Optical fibre (Section 4.1.2.5)	?	?	Yes	4.1%	40–75 s	Excellent (down to 55 nm coating thickness)	[493–495]
Metal Oxide Ads. (Section 4.1.3.1)	$\geq$5 months	No	Yes (low)	1.6%	30 s	Excellent (down to 125 nm thickness)	[511, 519, 523, 537] [503, 512, 610]
Graphene (Section 4.1.3.2)	$\geq$90 days	No	Yes	0.8%	3 s	Excellent (down to 3 nm thickness)	[542, 544, 555]
Electro. Cells (Section 4.1.3.3)	$\geq$2 years	No	No	4%	2–4 s	Excellent (down to 1 µm thickness)	[562, 563, 570, 611]
Ionic liquids (Section 4.1.3.4)	$\geq$4 months	No	No	2.05%	40 s	Excellent (down to 430 nm thickness)	[580, 583, 587] [575, 582]
Time of flight (Section 4.1.4.1)	? (∞)	No	Yes (low)	0.3% (0–10% range)	$\leq$1 s $^{(a)}$	Low (∼cm)	[594]
Acous. Att. (Section 4.1.4.2)	? (∞)	No	?	?	$\leq$1 s $^{(a)}$	Low (∼cm)	[599, 603]

Table 4.1: An overview of the presented CO_2 sensing techniques. (∞): expected to be at least several years. (a): limited primarily by the diffusion of the analyte gas inside the enclosure of the sensor. Please refer to detailed explanations in Section 4.1.5.

for CO_2 detection. The main idea behind their work is to perform a per-subject and per-site calibration to first determine the skin permeability towards CO_2 and only then access to the patient's tcpCO_2. While in its first version, their sensor required a change of membrane to perform this calibration[289], a second version with two sampling chambers and an additional valve solved this need for external intervention[617]. In their setup, the skin was also stripped with 5–10 applications of adhesive tape beforehand, and heated to 43–45°C. They achieved a correlation factor of 0.81 between paCO_2 and tcpCO_2, and a response time below 5 min. The main drawback of their technique is of course the need for a mass spectrometer, which is bulky, requires maintenance, and costs tens if not hundreds of thousands of euros. Their dual-rate technique, however, might presumably be adapted to a NDIR sensing scheme, thus compensating for the fluctuations of skin diffusivity mentioned in the previous section, and emphasised in our above-presented clinical study—Section 3.2.

4.2.2 Transcutaneous Sensing Constraints

An effective biomedical tcpCO_2 sensor should fulfil two main objectives: it must respond swiftly to a patient's haemodynamic changes, and it must measure a tcpCO_2 that reflects accurately their state. To do so, the sensor design must take into account the two main characteristics of CO_2 diffusion through the skin, which both are temperature dependent:

- The correlation between the pCO_2 measured at the skin surface—that is, tcpCO_2—and that of arterial blood—that is, paCO_2. This correlation will determine the ability of the sensor to give clues about the patient's status through a tcpCO_2 reading. This was briefly mentioned in Section 3.2.6.4.3 and is further detailed below.
- The exhalation rate of CO_2 through the skin into the sensor, which will determine the response time of the sensor. This aspect was already covered in great details in Section 3.2 and will not be discussed any further.

Additionally, the sensor design must also take into account the specificities of cutaneous sensing—*i.e.* temperature, humidity, acidity, and O_2 presence—outlined in Section 3.3.

4.2.2.1 Correlation Between paCO_2 and tcpCO_2

The paCO_2 / tcpCO_2 correlation has been demonstrated at 42°C and above[69], but heating the skin is not only uncomfortable for the patient but also energy consuming—which limits the ability of the sensor to be integrated into a wearable, battery-powered device—and potentially harmful due to the risk of thermal injury, especially above 44°C—see Appendix D.1.4.1 for a more detailed discussion on this topic.

For these reasons, working at low skin temperature seems highly desirable. To the best of our knowledge, only the work of Wimberley *et al.*[267] studied the influence of skin temperature on the correlation between paCO_2—through arterialised capillary blood, to be accurate—and tcpCO_2. Their study covers the full 37–45°C range and they show a fair—$r = 0.93$—correlation between capillary and transcutaneous pCO_2, even at a temperature as low as 37°C. Yet, further research on the topic would be valuable since other sources argue that a higher probe temperature still yields narrower limits of agreement for tcpCO_2[69].

further research is needed

4.2.3 Recommendations for a Closed-Chamber Design

Summarising the above, the following parameters should be carefully taken into account when designing a next-generation tcpCO_2 sensor using a closed-chamber—*a.k.a.* equilibrium-based—design:

1. **The skin temperature** influences both the sensor's *response time* through the CO_2 rate of diffusion and its *accuracy* through the paCO_2 / tcpCO_2 correlation. The clinical study presented in Section 3.2 revealed that a skin temperature in the 35–38°C range should yield a reasonably fast sensor—only 35% slower than when using a 44°C skin temperature. Accuracy-wise, despite a lack of data in the literature, this study also tends to indicate that heating the skin in the afore-mentioned range could be enough to yield a clinically-usable tcpCO_2 reading.
2. **The form factor of the sensor** directly influences its response time. The analyses presented in Section 3.1.4 revealed that a volume to surface ratio of 100 µm or below is required to yield response times below 10 min.

3. **The cutaneous measurement conditions** may hamper the adequate functioning of the sensor. More specifically, Section 3.3 revealed that the skin is a highly hypoxic medium, from which numerous acidic compounds may emanate, and which exhibits saturating humidity levels when occluded.

The CO_2 sensing techniques presented in Section 4.1 are reviewed below according to these latter aspects.

At first, only some of them can deal with a height limitation of only 100 µm. In that respect, NDIR, photoacoustic, time of flight, and acoustic attenuation sensors cannot be miniaturised to reach such a thickness. Second, the use of metal oxide thin films as well as electrochemical cells should be highly discouraged since both operate at several hundred degrees Celsius. As such, using them close to the skin may entail a significant safety hazard. Then, conductometric and ISFET-based sensors as well as the Stow-Severinghaus electrode all suffer from important drift issues, making them unusable for more than a few hours, or days. Optical fibre-based sensors, for their part, require an expensive and bulky measurement apparatus which seems hardly embeddable into a wearable device.

Remain the ionic liquid-, graphene- and dye-based sensors. While recent research on ionic liquid-based sensors showed definite progress, they are still extremely sensitive to O_2 and often exhibit particularly elevated recovery times[575, 581]. Similarly, recent developments pave the way for graphene-based CO_2 sensors[544], but their important cross-sensitivity towards humidity precludes their use without an additional humidity sensor for referencing, due to the skin humidity. Thus, the option of choice appears to be the more mature dry dye-based sensors, for they can yield thin enough, fast responding, and long lasting pCO_2 sensors—see Section 4.1.2.4. In addition, dye-based sensors can be dissociated into a CO_2 sensing part on the one hand, and an optical probing part on the other hand, as presented in Figure 4.12. This design is especially interesting since it makes it possible to use a disposable sensing patch that can be replaced every few days while the sensing head can be reused indefinitely. Finally, the multilayer structure of the patch seems well adapted to existing manufacturing processes—roll-to-roll in particular—for mass production[618, 619].

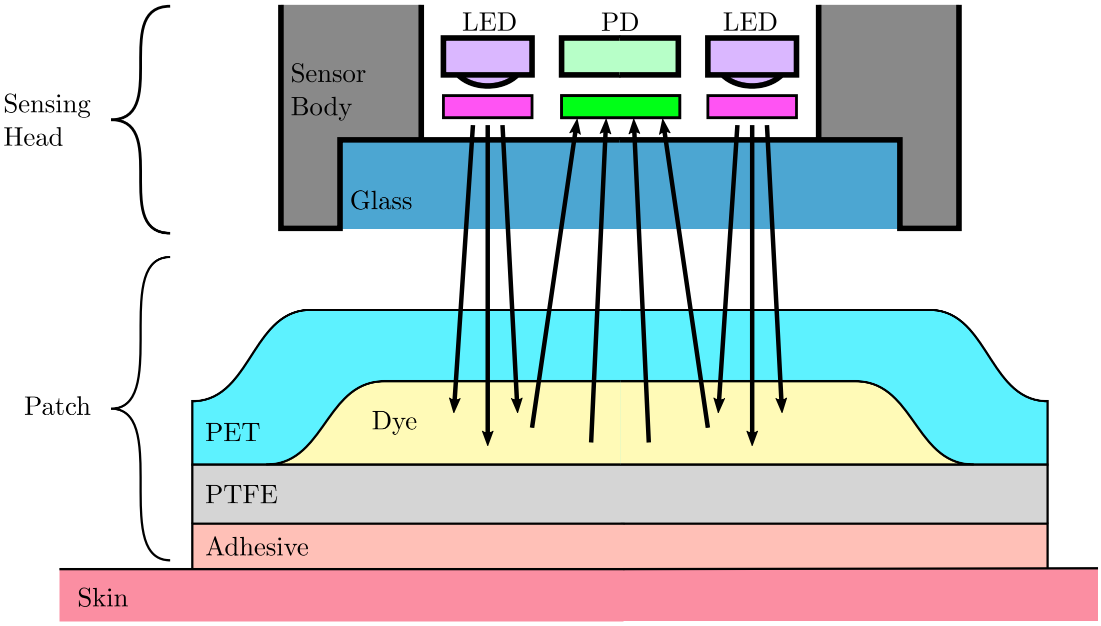

Figure 4.12: Schematic outline of a dye-based fluorescent transcutaneous sensor, consisting in two parts. **Top:** a sensing head with the LEDs and photodiode covered with their emission and reception filters (bright purple and green rectangles) and enclosed in a solid body, protected by a covering glass. **Bottom:** a multilayer sensing patch stuck on the skin, consisting in—from top to bottom—a transparent layer, impermeable towards CO_2—*e.g.* PET—a layer of CO_2 sensitive dye in a polymer matrix, a layer of ion-impermeable, CO_2-permeable material such as PTFE for CO_2 diffusion from the skin into the dye, and a thin adhesive layer to maintain the patch onto the skin. See Section 4.1.2.4 for a detailed review of material choices as well as their advantages and drawbacks when designing a dye-based CO_2 sensor.

4.2.4 Other Perspectives

Apart from a closed-chamber design—for which dye-based sensing seems to be the most appropriate sensing technique—transcutaneous CO_2 monitoring may also be envisioned using a rate-based approach, or Diffuse Reflectance Spectometry (DRS).

4.2.4.1 Rate-Based Approach

The rate-based approach has already been presented in Section 4.2.1, and corresponding theoretical developments can be found in the work of Chatterjee *et al.*[261]. The main advantage of this approach is that it relaxes the form factor constraint highlighted above in the closed-chamber case. Thus, NDIR sensing can be used instead of a dye-based thin film, with better lifetime, accuracy, and selectivity over the latter. These advantages made NDIR sensing the foremost choice of the authors who considered using a rate-based approach for transcutaneous CO_2 sensing[261, 612, 613, 615, 616].

The biggest issue with this approach is the large inter-subject variability in skin diffusivity values towards CO_2. Indeed, all studies that reported measurements of the cutaneous CO_2 exhalation rate do mention this variability—see Table 3.3—and factors in the 1.5–2 range are not unheard of, between the exhalation rates of two individuals, even at the same skin site and temperature. Our own investigations revealed even wider variabilities, with maximum-minimum ratios in the 2.8–9.2 range for a given skin site / temperature pair—see Table 3.2. This strong variability among individuals precludes the measurement of *absolute* $tcpCO_2$ by means of a rate-based approach without further improvements of the technique. This was recently demonstrated by several authors, who could only report trend analyses of skin CO_2 exhalation rate, and no rate-based absolute $tcpCO_2$ readings[613, 615, 616]. Further still, the recent work of Iitani *et al.*[614] clearly illustrates the afore-mentioned inter-subject variability with a factor of more than ten between the exhalation rates of two subjects (S2 and S6 in their Figure 4-H). An exception may exist for neonates, however, whose exceedingly thin skin could be more homogeneous than that of adults, resulting in less variability in their skin CO_2 exhalation rate. This latter *hypothesis* might explain why Chatterjee *et al.*[261] were able to demonstrate a significant correlation between skin CO_2 exhalation rate and $tcpCO_2$ in 4 preterm neonates with gestational ages ranging from 23 to 36 weeks.

To overcome this challenge, several tracks can be followed. At first, further studies on the CO_2 exhalation phenomenon through human skin would be welcome. As already mentioned, the currently available literature on this topic is ageing, and rarely includes more than a handful of subjects. In addition, the temperature dependence of the exhalation rate also needs to be carefully studied by regulating the skin temperature, and not that of the ambient air surrounding it. A better understanding of the process of CO_2 diffusion through the skin and of the different variables influencing the said process may help to better characterise—and perhaps even compensate for—the intra- and inter-subject variations in CO_2 exhalation rate with skin site, skin temperature, or time of the day. In this aspect however, the clinical study presented in Section 3.2 gives little clue—if not little hope—only confirming the wide variability mentioned above.

further research is needed

Second, dual membrane techniques—such as that presented by Targett *et al.*[617]—may be adapted to modern sensing techniques in a setup and compactness close to that of the prototype presented by Grangeat *et al.*[615], but using two different sensing channels, for instance.

Third, the need for an absolute $tcpCO_2$ reading could also be mitigated in two ways. First off, by means of a punctual per-subject calibration, following the example of non-invasive, cuffless, PPG-based, arterial blood pressure measurements[620, 621]. In this sensing scheme, the actual $tcpCO_2$ could be measured from time to time using a reference $tcpCO_2$ monitor, whose measurements would then serve to calibrate a lighter, wearable, rate-based device. This would allow to share a main—expensive—$tcpCO_2$ monitor among multiple patients, in a clinical setting. Alternatively, it could also be envisioned that rate-based devices do not provide any absolute $tcpCO_2$ reading. Rather, they may provide the user with trend analysis only, raising alarms following the crossing of certain thresholds or abrupt variations. This last approach, however, may be difficult to introduce into medical practice without further clinical studies, even though the clinical interest of similar variability metrics for other physiological variables—such as heart rate[622] or oxygen saturation[623, 624]—is encouraging in this regard.

4.2.4.2 Diffuse Reflectance Spectometry (DRS)

As stated in Section 4.1.1.1, dissolved CO_2 measurements can be performed not only in the gaseous phase, but also in aqueous solution[403]. This result was also demonstrated for whole blood samples, the pCO_2 of which could be retrieved with a standard error of about 5 mmHg, using infrared spectroscopy in the 1024–2290 nm range[625]. Further still, it has been recently suggested in a patent that transcutaneous CO_2 measurements could be performed using mid-infrared LEDs of wavelength “between about 2 µm and about 18 µm”[626]. Although patents do not constitute scientific evidence[627], the idea has been put forth, and further research would be interesting on the topic, in order to assess the feasibility of such transcutaneous CO_2 measurements. *Prima facie*, two major challenges conceivably need to be solved for DRS-based transcutaneous measurements.

further research is needed

First, contrary to pulse oximetry, the possibility to measure a pulsatile absorbance component due to CO_2 dissolved in the arterial blood by transcutaneous DRS probing in the mid-infrared is vastly unknown. If possible though, the whole theoretical background developed over the years for pulse oximetry and PPG signal processing[16] could be translated to CO_2 measurements.

Second, the penetration depth of mid-infrared light in the human tissues may also be a source of concern, especially because of the elevated infrared absorbance of water. Indeed, water absorbance becomes predominant in the tissues in the near and mid infrared[158], with values over 1 cm^{-1} above 1150 nm, and over 5 cm^{-1} above 1380 nm[628]. This may cause serious difficulties for mid-infrared tissue probing and lead to a very low signal to noise ratio, which may be the reason why Marasco *et al.* suggest the use of a lock-in amplifier for transcutaneous CO_2 measurement in their patent[626].

In both cases, heating the skin to provoke a local hyperaemia—as mentioned in Section 3.2.3.1.2—may tackle the above-mentioned probing depth issue, by bringing the CO_2 content of subcutaneous tissues close to that of arterial blood.

4.2.5 Synthesis

$tcpCO_2$ is the least invasive and the most accessible proxy for $paCO_2$—which is of major clinical significance—given that the skin temperature is at least above 37°C (Section 3.2.6.4.3). $tcpCO_2$ may be measured by two means: either exploiting the cutaneous respiration phenomenon, or by direct infrared tissue probing, using DRS.

While the feasibility of the latter technique has yet to be demonstrated for *in vivo* transcutaneous CO_2 monitoring, it seems like an appetising proposal (Section 4.2.4.2). Indeed, it would require merely a mid-infrared source and detector—which are readily available components, see Section 4.1.1.1—and conceivably the same kind of electronic as that already embedded in commercially available pulse oximeters. Yet, such an application of DRS remains vastly hypothetical at the time of writing this thesis, and further research would be needed on the topic, so as to consolidate the above-mentioned research works.

further research is needed

Cutaneous respiration, on its part, has long proven to be a reliable access route to $tcpCO_2$, by capturing the CO_2 exhaled by the skin inside the embodiment of a CO_2 sensor (Section 4.1.2.2). A simple model for such a closed-chamber sensor design has been extensively described, as well as its expected response time as a function of its form factor (Section 3.1.4). We conclude that, in such a closed-chamber design, the compactness of the CO_2 sensor is crucial in order to reach reasonable response times. Taking into account other merit criteria such as response time, long-term stability and accuracy, **we put forth the application of dye-based CO_2 sensing to serve such a purpose**.

Alternatively, a rate-based approach may be envisioned using a constant flow of air or N_2 passing over the skin, and being analysed thereafter (Section 4.2.4.1). The main advantage of this technique is that the form factor of the sensor itself is not as much a source of concern as in the closed-chamber setup. Thus, other sensing techniques can be envisioned such as NDIR CO_2 sensing. However, several challenges remain, precluding rate-based approaches to yield an absolute $tcpCO_2$ measurement. In particular, a better characterisation of human skin CO_2 exhalation rate, dual membrane approaches, or self-calibration from time to time are all interesting leads that need further exploration.

4.3 Dye-Based CO_2 Sensing

Hopefully, the reader now has a satisfactory understanding of the ins and outs of transcutaneous CO_2 measurement: why $tcpCO_2$ is clinically important—Chapters 1 and 2—what are the specificities of transcutaneous CO_2 sensing—Chapter 3—and what CO_2 sensing technique best fits these specificities—first half of the present chapter. **The remainder of this doctoral work focuses solely on the intricacies of dye-based CO_2 sensing.** While Chapter 5 details the *practical realisation* of CO_2-sensing fluorescent thin films—*i.e.* what encapsulating strategy, polymer, and fluorophores were chosen, what concentrations were actually used, and what response towards CO_2 was achieved, also giving insights on the optoelectronics setup that was used—the second half of the present chapter is devoted to the *theoretical foundations* of dye-based CO_2 sensing. More specifically:

- The chemistry of wet and dry sensors is given in Section 4.3.1.
- The available optical measurement schemes and the associated signal processing techniques are presented in Section 4.3.2.
- The DLR sensing scheme, which has been chosen among the latter schemes to fulfil the goal of this doctoral work, is then further detailed in Section 4.3.3.

4.3.1 Sensing Chemistry

The development of dye-based CO_2 sensors occurred in two main phases, corresponding to the afore-mentioned *wet* and *dry* sensor families—see Section 4.1.2.4. Briefly, a first line of works emerged in the mid eighties introducing wet-type sensors[446, 452, 453, 629], which underwent no major changes for several years until the pivotal works of Andrew Mills in the early nineties, who introduced dry-type sensors in a series of seminal papers[358, 630, 631]. The main difference between wet and dry sensors is the following. In wet sensors, the CO_2-sensitive pigment is dissolved in an aqueous solution, which makes water molecules directly available for the hydration and dissociation of CO_2 into bicarbonate ion and protons. On the contrary, in dry sensors, all chemicals are entrapped inside a solid polymer layer. Since hydration water is no longer present, additional chemicals—termed phase transfer agents—are added, whose role is to bind water molecules to make them available for the afore-mentioned dissociation. The differences and common points between these two modalities will become more evident in the next subsections.

4.3.1.1 Wet Sensors

4.3.1.1.1 The pH-pCO2 Relationship

Let us consider a solution of sodium bicarbonate in water, equilibrated with a gas mixture with a CO_2 partial pressure pCO_2. The following equilibria take place in the solution[411, 412]:

$$\mathrm{CO}_{2,(g)} \xrightleftharpoons{K_1} \mathrm{CO}_{2,(\mathrm{aq})}, \qquad \begin{cases} K_1 = 3.4\cdot 10^{-2} \\ pK_1 = 1.5 \end{cases} \tag{4.11}$$

$$\mathrm{CO}_{2,(\mathrm{aq})} + \mathrm{H_2O} \xrightleftharpoons{K_2} \mathrm{H_2CO}_{3,(\mathrm{aq})}, \qquad \begin{cases} K_2 = 1.5\cdot 10^{-3} \\ pK_2 = 2.8 \end{cases} \tag{4.12}$$

$$\mathrm{H_2O} + \mathrm{H_2CO}_{3,(\mathrm{aq})} \xrightleftharpoons{K_3} \mathrm{H_3O}^+_{(\mathrm{aq})} + \mathrm{HCO}^-_{3,(\mathrm{aq})}, \qquad \begin{cases} K_3 = 4.54\cdot 10^{-7} \\ pK_3 = 6.34 \end{cases} \tag{4.13}$$

$$\mathrm{H_2O} + \mathrm{HCO}^-_{3,(\mathrm{aq})} \xrightleftharpoons{K_4} \mathrm{H_3O}^+_{(\mathrm{aq})} + \mathrm{CO}^{2-}_{3,(\mathrm{aq})}, \qquad \begin{cases} K_4 = 5.61\cdot 10^{-11} \\ pK_4 = 10.25 \end{cases} \tag{4.14}$$

$$2\cdot\mathrm{H_2O} \xrightleftharpoons{K_\mathrm{W}} \mathrm{H_3O}^+_{(\mathrm{aq})} + \mathrm{OH}^-_{(\mathrm{aq})}, \qquad \begin{cases} K_\mathrm{W} = 1.0\cdot 10^{-14} \\ pK_\mathrm{W} = 14 \end{cases} \tag{4.15}$$

Typical values for K_1–K_4 can be found in the literature[112, 412]. In the following development, all species will be aqueous, unless otherwise specified. Additionally the neutrality of the solution can be written as:

$$[\mathrm{H_3O^+}] + [\mathrm{Na^+}] = [\mathrm{HCO_3^-}] + 2\cdot[\mathrm{CO_3^{2-}}] + [\mathrm{OH^-}] \tag{4.16}$$

which combines with the above-described equilibria, leading to:

$$[\mathrm{H_3O^+}]^3 + [\mathrm{Na^+}]\cdot[\mathrm{H_3O^+}]^2 = ([\mathrm{H_3O^+}] + 2\cdot K_4)\cdot K_2\cdot K_3\cdot[\mathrm{CO_2}] + K_\mathrm{W}\cdot[\mathrm{H_3O^+}] \tag{4.17}$$

The latter equation can be simplified under certain hypotheses. In particular, if *(i)* the pH of the solution is near neutral (pH range 6–9), *(ii)* the sodium ion concentration is above 1 mM—which is often the case[452, 453]—and (iii) $[CO_2]$ is above 1 mM—which is typically the case for a physiological pCO_2 of 40 mmHg, for instance, see Section 2.1.2—the following approximations can be performed on Equation 4.17:

$$\underbrace{[H_3O^+]^3 + [Na^+]\cdot[H_3O^+]^2 - K_W\cdot[H_3O^+]}_{\approx[Na^+]\cdot[H_3O^+]^2} = \underbrace{\big([H_3O^+] + 2\cdot K_4\big)}_{\approx[H_3O^+]}\cdot K_2\cdot K_3\cdot[CO_2] \tag{4.18}$$

Knowing that $[CO_2] = K_1\cdot pCO_2$ finally leads to

$$pCO_2 = \frac{[Na^+]\cdot[H_3O^+]}{K_{13}} = k\cdot 10^{-pH}, \text{ where } \begin{cases} k = \frac{[Na^+]}{K_{13}} \\ K_{13} = K_1\cdot K_2\cdot K_3 \end{cases} \tag{4.19}$$

which gives a direct relationship between a bicarbonate solution's pH, and the pCO_2 it is equilibrated with. Although the equations differ, a similar reasoning can be made with trisodium phosphate (Na_3PO_4) or other similar salts. The general idea is always the same: given that the sensor's medium is permeable to CO_2 and contains available water molecules for CO_2 hydration, the diffusion of CO_2 inside this medium will change its pH. Of note, these derivations are similar to those presented by Jensen *et al.* in the case of the Stow-Severinghaus electrode[411].

4.3.1.1.2 Adding a Dye

Dye-based CO_2 sensing involves the use of a dye—*e.g.* phenol red, BromoThymol Blue (BTB) or HPTS, to name a few[445–448]—which is nothing more than a molecule that can exist in either an acidic (AH) or basic (A^-) form. Changes in pCO_2 levels induce changes in the sensing solution's pH as emphasised in Equation 4.19. These latter changes in pH in turn entail changes in the relative proportion of the A^- and AH species. Since these two species have differing absorbance or luminance properties, optical pH—and thus pCO_2—sensing may thereby be achieved. Chemically speaking, the dye obeys the following equilibrium (typical numerical values for HPTS were used, see Section 5.2.2):

$$AH \xrightleftharpoons{K_A} A^- + H_3O^+, \quad \begin{cases} K_A = 5.0\cdot 10^{-8} \\ pK_A = 7.3 \end{cases} \tag{4.20}$$

The simplified neutrality equation then becomes

$$[Na^+] = \frac{K_{13}\cdot pCO_2}{[H_3O^+]} + [A^-] \tag{4.21}$$

We also have

$$[H_3O^+] = K_A\cdot\frac{\mathcal{C}_A - [A^-]}{[A^-]} \tag{4.22}$$

wherein $\mathcal{C}_A$ is the total dye concentration ($\mathcal{C}_A = [A^-] + [AH]$), supposed to be above 1 mM. Leading to

$$pCO_2 = \frac{K_A}{K_{13}}\cdot\frac{\big([Na^+] - [A^-]\big)\cdot\big(\mathcal{C}_A - [A^-]\big)}{[A^-]} \tag{4.23}$$

Additionally, if the solution is sufficiently *buffered*—*i.e.* if $[Na^+] \gg \mathcal{C}_A(\overset{\Delta}{>} [A^-])$—the latter equation becomes

$$pCO_2 = k\cdot\frac{\mathcal{C}_A - [A^-]}{[A^-]} = k\frac{[AH]}{[A^-]}, \quad \text{with} \quad k = \frac{K_A\cdot[Na^+]}{K_{13}} \tag{4.24}$$

which—even being a crude approximation—allows a facile understanding of the basic working principle of dye-based sensors: having a way to determine either the A^- concentration or the relative quantities of A^- and AH means that the solution's pCO_2 can be derived. The fact that the protonated and anionic forms of the dye differ in their absorbance or luminescence properties makes the optical determination of the latter quantities all the more doable, as detailed in Section 4.3.2.

4.3.1.2 Dry Sensors

Dry sensors were introduced to circumvent the difficulty in manufacturing exceedingly thin films of solutions—which prevented wet sensors to reach response times of a few seconds—as well as to tackle the drying-out issue that plagued them[412, 483]. The basic idea behind dry sensors is to replace the aqueous solution by a polymer thin film. However, solely dispersing a pH-sensitive dye inside a polymer matrix would not work because of the mandatory presence of water molecules for reactions 4.12–4.15. To address this issue, a phase transfer agent is added, whose role is not only to bind with the hydrophilic dye and allow it to dissolve in an organic solvent along with a potentially hydrophobic polymer, but also to bind several water molecules that thus become available for the above-mentioned reactions[412]. To this end, a quaternary ammonium ion is often chosen—such as tetraoctyl ammonium hydroxide (TOAH), for instance[466]—noted $Q^+AH \cdot x\,H_2O$ when bound to the protonated form of the dye, which obeys the following equilibrium, instead of Equation 4.20:

$$Q^+AH \cdot x\,H_2O \overset{K_A}{\rightleftharpoons} Q^+A^- \cdot (x{-}1)H_2O + H_3O^+ \tag{4.25}$$

Considering this latter equation, and under the hypothesis that enough water molecules are available to regard the so-obtained polymer matrix as *aqueous*, a similar reasoning to that of the previous section may lead to an equation very close to Equation 4.23, replacing $[Na^+]$ with $[Q^+]$, the total concentration of added phase transfer agent:

$$pCO_2 = \frac{K_A}{K_{13}} \cdot \frac{\big([Q^+] - [Q^+A^- \cdot (x{-}1)H_2O]\big) \cdot \big(\mathcal{C}_A - [Q^+A^- \cdot (x{-}1)H_2O]\big)}{[Q^+A^- \cdot (x{-}1)H_2O]} \tag{4.26}$$

Which also simplifies in case of strong buffering into

$$pCO_2 = k \cdot \frac{[Q^+AH \cdot x\,H_2O]}{[Q^+A^- \cdot (x{-}1)H_2O]}, \quad \text{with} \quad k = \frac{K_A \cdot [Q^+]}{K_{13}} \tag{4.27}$$

which is very similar to the equations proposed by Mills, Neurauter, Amao, and others[468, 480, 630]. Again, even bound to phase transfer agents, the protonated and anionic forms of the dye still differ in their optical properties, enabling a variety of optical sensing schemes to be implemented in order to measure the pCO_2 to which the dyed thin film is exposed.

4.3.2 Optical Measurement Schemes

4.3.2.1 Basic Schemes

This section will cover the case of a monolayer, transparent sensing film, entrapping a pH-sensitive absorbing—*i.e.* non-luminescent—dye and the appropriate buffer, such that the molecular extinction coefficient of the entrapped dye depends on the surrounding CO_2 partial pressure. The following hypotheses will also be adopted:

$\mathcal{H}_1$: The dye is diluted enough, and the film transparent enough, so that the Beer-Lambert law applies.

$\mathcal{H}_2$: All the partially absorbed light is collected by the photodetector.

4.3.2.1.1 The Issue with Single-Wavelength Direct Probing

In the remainder of this section, a simple absorbance sensing scheme will be considered. The corresponding optical setup consists in: *(i)* a mono-chromatic light source—*e.g.* LED—illuminating the thin film with a light intensity I_{ex} at wavelength λ, *(ii)* a transparent absorbing CO_2-sensitive thin film, and *(iii)* a photodetector—*e.g.* photodiode—receiving a light intensity I_{mes}. The latter can then be written as

$$I_{mes}(\lambda) = I_{ex}(\lambda) \cdot 10^{-A_{film}} \cdot \mathcal{S}_{PD}(\lambda) \tag{4.28}$$

wherein $\mathcal{S}_{PD}(\lambda)$ is the photodiode's sensitivity at wavelength λ, and A_{film} is the thin film's absorbance, given by

$$A_{film} = (\alpha \cdot \varepsilon_{AH} + (1-\alpha) \cdot \varepsilon_{A^-}) \cdot w_{film} \cdot \mathcal{C}_A \tag{4.29}$$

wherein $\varepsilon_{\mathrm{AH}}$ and $\varepsilon_{\mathrm{A}^-}$ are the molar extinction coefficients of the dye in its protonated and anionic states, respectively, $\mathcal{C}_A$ is the total dye concentration, w_{film} is the film's thickness, and α is the proportion of the dye in its protonated state:

$$\alpha \triangleq \frac{[\mathrm{AH}]}{[\mathrm{AH}] + [\mathrm{A}^-]} \tag{4.30}$$

In the case of a wet dye-based sensor—Equation 4.24—this definition of α leads to

$$\mathrm{pCO_2} = k{\cdot}\frac{\alpha}{1-\alpha} \tag{4.31}$$

Combining Equations 4.28–4.31 then leads to

$$\mathrm{pCO_2} = -k{\cdot}\frac{\mathcal{L} + w_{\mathrm{film}}{\cdot}\mathcal{C}_A{\cdot}\varepsilon_{\mathrm{A}^-}}{\mathcal{L} + w_{\mathrm{film}}{\cdot}\mathcal{C}_A{\cdot}\varepsilon_{\mathrm{AH}}}, \quad \text{wherein} \quad \mathcal{L} = \log_{10}\left(\frac{I_{\mathrm{mes}}}{I_{\mathrm{ex}}{\cdot}\mathcal{S}_{\mathrm{PD}}}\right) \tag{4.32}$$

which could theoretically be used to derive a $\mathrm{pCO_2}$ from a simple absorbance measurement. The main issue with such a sensing scheme, however, is that while $\varepsilon_{\mathrm{AH}}$ and $\varepsilon_{\mathrm{A}^-}$ are known optical constants depending on the chosen dye, I_{ex} and $\mathcal{S}_{\mathrm{PD}}$ can rarely be known accurately. Worse, their value might change during the lifetime of the sensor, and with the temperature of the light source[632] or photodetector[633]. Worse still, while the swelling of the dyed film may be neglected and w_{film} can be considered as a constant during the lifespan of the sensor, $\mathcal{C}_A$, on the contrary, is most likely to decrease due to photobleaching—see Section 5.1.1.

Note: $\mathcal{S}_{\mathrm{PD}}$ was introduced to keep things simple while still providing the reader with an overview of the unpredictable variabilities induced by the acquisition toolchain in the calculations. In actuality, much more complex modelling than a simple coefficient should be introduced, since one might drive the LED and read the photodiode's output as voltages—themselves read and written by means of a Digital to Analog Converter (DAC) / Analog to Digital Converter (ADC) pair. A whole transfer function should thus be applied in order to model the latter pair, the LED driver, the LED itself, the photodiode's sensitivity, and the photodiode's TransImpedance Amplifier (TIA). This is largely out of the scope of this doctoral work, however, and the reader only needs to know that both the intensity of the LED and the photodiode's sensitivity may be strongly influenced by temperature or may differ from one part to the next. Further information on this topic and appropriate deign approaches may be found in the work of Bigio and Fantini[634, Chap. 13], or Cenni[635].

4.3.2.1.2 Single Wavelength Referencing

As a result, no author used the above-mentioned scheme as is. Instead, many of them[359, 363, 452–457, 460–462] implemented some sort of referencing with one or two supplementary I_{mes} values taken in pure N_2 and / or pure CO_2 atmospheres. For instance, if a first I_0 measurement is taken at 0% CO_2 in an atmosphere of pure N_2 on the one hand, and a second *blank* light intensity without film I_{blk} is also taken on the other hand, the following quantity may be considered:

$$r = \frac{\log_{10}\left(\frac{I_0}{I_{\mathrm{mes}}}\right)}{\log_{10}\left(\frac{I_{\mathrm{mes}}}{I_{\mathrm{blk}}}\right)} = \frac{A_{\mathrm{film},0} - A_{\mathrm{film}}}{A_{\mathrm{film}} - \underbrace{A_{\mathrm{blk}}}_{\triangleq 0}} \tag{4.33}$$

During I_0 measurement, $\mathrm{pCO_2}$ is null, and thus $\alpha = 0$ leading to

$$r = \frac{\alpha{\cdot}(\varepsilon_{\mathrm{A}^-} - \varepsilon_{\mathrm{AH}})}{(1-\alpha){\cdot}\varepsilon_{\mathrm{A}^-} + \alpha{\cdot}\varepsilon_{\mathrm{AH}}} \tag{4.34}$$

Under the further hypothesis that $\varepsilon_{\mathrm{A}^-} \gg \varepsilon_{\mathrm{AH}}$ at the considered wavelength, which is usually the case[360, 412], the latter equation yields

$$r = \frac{\alpha}{1-\alpha} \tag{4.35}$$

Thus, the $\mathrm{pCO_2}$ may now be derived as

$$\mathrm{pCO_2} = k{\cdot}\frac{\alpha}{1-\alpha} = k{\cdot}\frac{\log_{10}\left(\frac{I_0}{I_{\mathrm{mes}}}\right)}{\log_{10}\left(\frac{I_{\mathrm{mes}}}{I_{\mathrm{blk}}}\right)} \tag{4.36}$$

Given that such zero-blank referencing is made frequently enough, the light source intensity and photodetector sensibility does not matter anymore, nor does the dye concentration. The effect of photobleaching is thus also cancelled. However, such referencing supposes that the temperature remains constant throughout the different measurements. Otherwise, it would need to be compensated for using specific calibration methods, since temperature influences both the LED and photodiodes performance, as reported above. Additionally, temperature may also change the optical properties of the involved dye, a phenomenon known as *thermochromism*—see Day and El-Ayaan for an introduction on this topic[636, 637].

4.3.2.1.3 The Ratiometric Scheme

To address the latter limitations, the ratiometric scheme introduces a second wavelength and probes the dye simultaneously at the two (or more) wavelengths (λ_1, λ_2). This scheme also requires to take blank measurements to be able to compute the value

$$A_{\lambda_i} = -\log_{10}\left(\frac{I_{\text{mes}}(\lambda_i)}{I_{\text{blk}}(\lambda_i)}\right) \iff A_{\lambda_i} = \mathcal{C}_A \cdot \left(\alpha \cdot \varepsilon_{\text{A}^-,\lambda_i} + (1-\alpha) \cdot \varepsilon_{\text{AH},\lambda_i}\right),\ i \in [\![1,2]\!] \tag{4.37}$$

yielding an explicit form for α

$$\alpha = \frac{A_{\lambda_2} \cdot \varepsilon_{\text{AH},\lambda_1} - A_{\lambda_1} \cdot \varepsilon_{\text{AH},\lambda_2}}{A_{\lambda_2}(\varepsilon_{\text{AH},\lambda_1} - \varepsilon_{\text{A}^-,\lambda_1}) - A_{\lambda_1}(\varepsilon_{\text{AH},\lambda_2} - \varepsilon_{\text{A}^-,\lambda_2})} \tag{4.38}$$

from which pCO$_2$ can be computed as in the above-described schemes. This approach completely eliminates the effect of photobleaching or film swelling. However, it still requires blank measurements to compensate for the variations in the emitted light or in the photodetector sensibility. A typical way to satisfy such a need is to add a reference light path inside the sensor to compensate for the variations in emitted light intensity[450]. Additionally, it should be noted that the use of isobestic points to perform simplifications—equalling $\varepsilon_{Dye,RH}(\lambda_{iso})$ with $\varepsilon_{Dye,R^-}(\lambda_{iso})$[479]—should be discouraged. Indeed, isobestics are rarely perfect—as some degree of blurring often occurs[360, 412]—and reliable molar extinction coefficients at specified wavelengths should be employed instead.

4.3.2.1.4 Extension to Luminescence Measurements

Although the above developments concern only absorbance-based sensors, the presented measurement schemes have also been applied successfully to fluorescence- or phosphorescence-based sensors[361, 445, 450, 451]. The reasoning is essentially the same, replacing Equation 4.28 by

$$I_{\text{mes}}(\lambda_{\text{em}}) = I_{\text{ex}}(\lambda_{\text{ex}}) \cdot \Phi(\lambda_{\text{ex}}, \lambda_{\text{em}}) \cdot 10^{-A_{\text{film}}(\lambda_{\text{ex}})} \cdot \mathcal{S}_{\text{PD}}(\lambda_{\text{em}}) \tag{4.39}$$

wherein λ_{ex} and λ_{em} are the excitation and emission wavelengths, respectively, and $\Phi(\lambda_{\text{ex}}, \lambda_{\text{em}})$ is the quantum yield of the used luminophore at the considered wavelengths. The curious reader may additionally refer to the work of Bernard Valeur[638, p. 338] for an elegant demonstration of the same results as those presented above in the case of pH measurements, but using fluorophores instead of solely absorbing dyes.

4.3.2.2 Advanced Schemes

In parallel to direct, referenced, or ratiometric probing techniques, more advanced sensing schemes have also been developed along the years, involving pH-*in*sensitive dyes in addition to the pH-sensitive ones. The above sections are not superfluous, however, since they hopefully gave the reader a satisfying understanding of how the chemical equilibria presented in Section 4.3.1—linking pCO$_2$, pH and the A$^-$ / AH ratio—can be exploited using simple optical techniques to yield a pCO$_2$ reading from luminous intensity measurements. The upcoming sections deal with more advanced techniques, one of which was ultimately chosen and implemented in the course of this doctoral work—namely DLR.

4.3.2.2.1 Inner Filter Effect

Sensors based on the inner filter effect can be obtained by mixing a pH-sensitive colorimetric dye with a pH-insensitive luminescent dye—also referred to as the *reference* dye. The two dyes are chosen such that the absorption spectrum of at least one of the two forms—protonated or anionic—of the pH-sensitive dye overlaps with the emission spectrum of the luminescent dye. A typical example of a dye pair meeting this requirement can be seen in Figure 4.13.

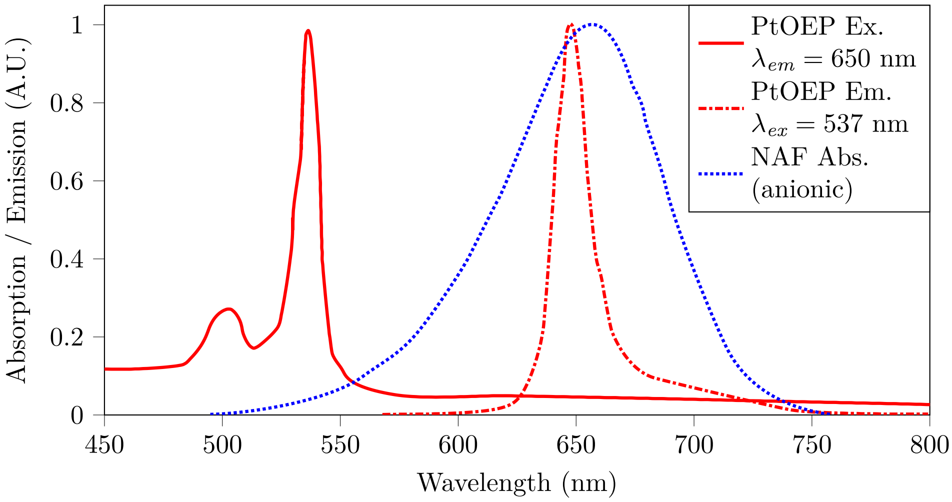

Figure 4.13: Excitation and emission spectra of a Platinum(II) complex—namely PtOEP—the luminophore, and absorption spectrum of the anionic form of α-naphtolphtalein (NAF)—the pH-sensitive dye. Note how the PtOEP's emission spectrum overlaps with the absorption of NAF. Data source: Perez *et al.*[469].

Under this condition, the luminescence of the reference dye is modulated by the absorbance of the pH-sensitive dye, itself a function of the sensor's pH. The pH-sensitive dye thus effectively acts as a filter, absorbing a fraction of the light emitted by the reference luminophore, hence the name of this technique. As the perceptive reader might have noticed, IFE suffers from the same limitations as the above-presented techniques—*i.e.* the need for some form of referencing[466]—but their main advantage lies in the fact that there exist very few fluorescent pH indicators, while absorbing pH indicators are legion[465].

Several dye pairs have been proposed in the literature such as Thymol Blue (TB), phenol red or cresol red with a Europium(III) complex[465], NAF with a Platinium(II) complex[469–471] or azaBODIPYs with Chromium(III)-doped gadolinium aluminium borate. As can be seen, the pH-sensitive dye is often a well-known pH indicator, while the pH-insensitive luminophore is a metallic complex exhibiting long fluorescence lifetimes—in the microsecond range.

It should be noted that the inner filter effect finds its roots in radiative energy transfer, which means that incident light at the excitation wavelength is first absorbed by the reference luminophore, which in turn emits another radiation at its emission wavelength. The latter is then—partially—quenched by the pH-sensitive dye. Consequently, the pH-sensitive dye only needs to be nearby the luminophore, but not necessarily in the same solution. For instance, the luminophore can be placed on one side of a glass slide, and the pH-sensitive dye on the other side[465–467], which can be useful to limit poisoning and contamination by external reagents, since only the pH-sensitive dye needs to be exposed to the external environment.

4.3.2.2.2 Fluorescent Resonance Energy Transfer (FRET)

By contrast, FRET(4) is based on radiationless energy transfer between a pH-insensitive luminescent donor and a pH-sensitive acceptor dye. Usually FRET takes place between a luminophore L, and the anionic form of a pH-sensitive dye A^-, according to

$$L^* + R^- \xrightarrow{\text{FRET}} L + R^{-*} \tag{4.40}$$

wherein the '*' symbol denotes an excited state. In this scheme the so-obtained excited R^{-*} then returns to its de-excited state through non-radiative thermal relaxation. The more CO_2 is present, the lower the pH and the less R^- available for FRET, leading to a higher fluorescence intensity. Contrariwise, the less CO_2 is present, the higher the pH. More pH-sensitive dye will then be present in its R^- form, effectively quenching the luminophore fluorescence *via* FRET.

---

(4) Also known as Förster Resonance Energy Transfer after the German scientist Theodor Förster[639].

Interestingly, this quenching decreases both the luminescence intensity *and* its decay time. A measurement of one of these two parameters can thus yield the pCO_2 value inside the sensor. FRET has two major constraints though, namely:

1. the absorption spectrum of R^- and the emission spectrum of L must overlap, as can be seen in Figure 4.14, and as was the case for IFE-based sensing.
2. the two dyes must be present in relatively high concentration (1–10 mM), so that the distance between two R^- and L molecules is below the Förster distance for this couple. They must also be present in the same location, or medium, which may expose the luminophore to unwanted chemical species, such as O_2. By comparison, this latter condition is not mandatory in the case of IFE- or DLR-based sensing.

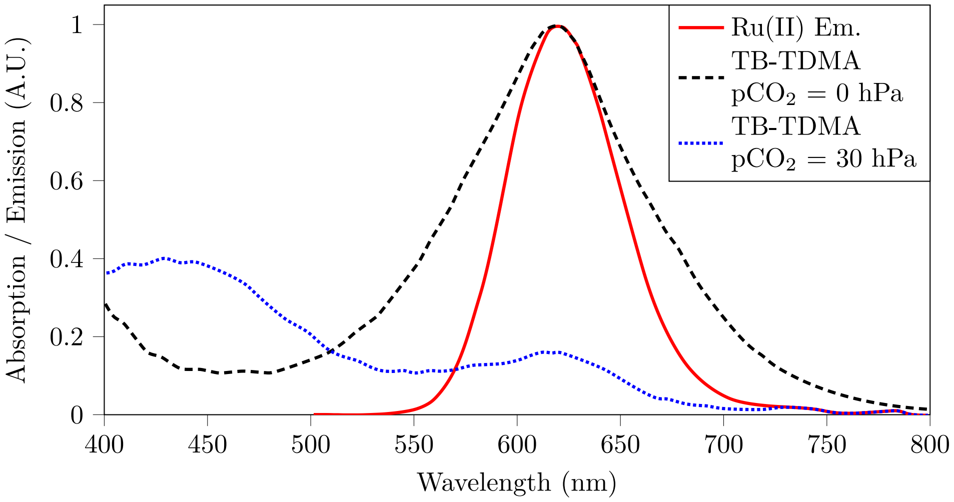

Figure 4.14: Absorption spectra of the protonated ($pCO_2 = 30$ hPa) and anionic ($pCO_2 = 0$ hPa) forms of TB bound to tridodecylmethylammonium (TB-TDMA) and emission spectrum of a Ruthenium(II) complex (Ru(dph-bpy)$_3$-(TMS)$_2$). Data source: Neurauter *et al.*[480].

More information on FRET in general may be found in the literature[412, 481] and concrete applications to CO_2 sensing were also published using phenol red or BTB (pH-sensitive acceptor) with Eosin, Rhodamine 6G or Texas Red Hydrazide (fluorescent donor)[479], Sudan III with a Ruthenium(II) complex[482] or TB with a Ruthenium(II) complex[480], for instance.

Usually, because the dye concentrations are rather elevated—generating adverse inner-filter effects or turbidity in the samples—an approach based on the luminescence decay time is favoured over one based on the luminescence intensity. Such measurements can either take place in the frequency domain—measuring phase shifts[479, 482]—or in the time domain—measuring effective decay times[480]. In both cases, long luminophore lifetimes are especially interesting since they allow for lower frequency—and thus slower and less expensive—detection electronics. Typically 20–75 kHz for long-lifetime Ruthenium(II) complexes[480, 482] compared to over 100 MHz for shorter lifetime fluorophores[479]. The modification of the decay time of the luminophore does not occur with the other techniques presented hitherto and may be the main advantage of FRET, since time- or frequency-based approaches ignore the fluctuations of the light source intensity or photodetector sensitivity.

4.3.2.2.3 Dual Lifetime Referencing (DLR)

Contrary to the IFE and FRET sensing schemes, which both rely on one luminescent and one absorbing dye, DLR uses two luminescent dyes: *(i)* a short-lived (~ns(5)) pH-sensitive fluorophore (noted A), and *(ii)* a long-lived (~µs) reference, pH-insensitive luminophore (noted R). At this point of the discussion, the reader only needs to know that the fluorescence intensity of A is influenced by the sensor's pH. As for IFE-based sensors—see Section 4.3.2.2.1—the dyes need not be close to each other and may be entrapped in stacked films[470]. However, the excitation spectra

---

(5) The order of magnitude of the luminescence decay time, when modelling it with a mono-exponential decrease. This is a commonly used approximation, although real-world luminescence decays are generally not following a purely mono-exponential model—this is especially true for large and complex molecules such as proteins[640].

of the two dyes must overlap so that a single excitation wavelength triggers the luminescence of both dyes. pCO_2 measurement can then be performed in two modalities, either with time-based of frequency-based methods.

The time-based DLR principle is illustrated in Figure 4.15, Left. When the illumination LED is turned on, the rise in fluorescence of the pH-sensitive dye $A_{\mathrm{A,rise}}$ is almost instantaneous compared to that ot the pH-insensitive reference dye $A_{\mathrm{R,rise}}$. Similarly, when the light is turned off, fluorescence decay of pH-sensitive dye is also instantaneous, leaving only the slow decaying $A_{\mathrm{R,fall}}$ signal of the reference indicator. The pCO_2 can then be directly calculated from the I_{A} / I_{R} ratio[89].

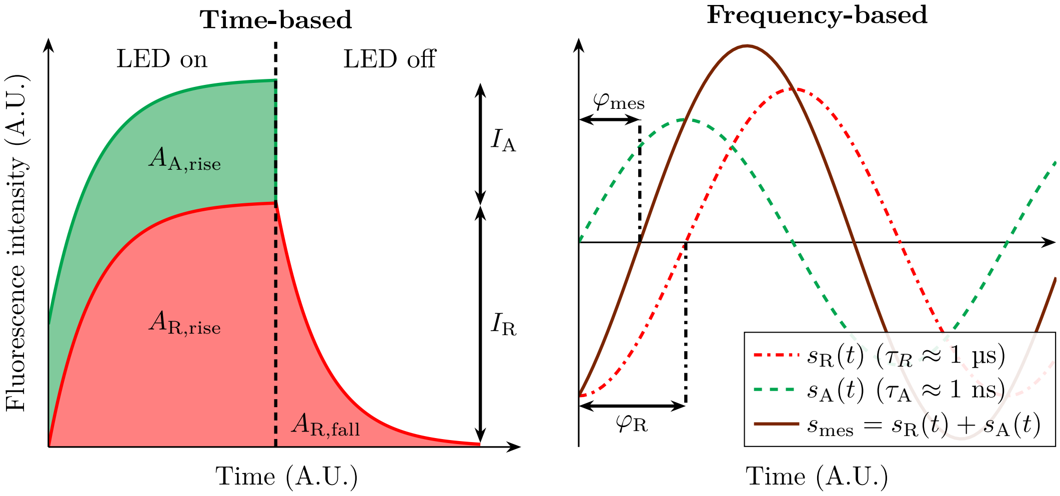

Figure 4.15: The DLR sensing scheme: time-based (Left) and frequency-based (Right). Adapted from Klimant *et al.*[89].

Alternatively, a frequency-based scheme can be used, as illustrated in Figure 4.15, Right. When illuminating the two dyes with a light source of sinusoidally-modulated intensity, the signal s_{mes} is measured with a photodetector and its phase shift φ_{mes} with respect to the illuminating signal is evaluated. The signal s_{mes} is itself the sum of two luminescence signals that are emitted by:

1. the reference dye s_{R}, which possesses a constant phase shift φ_{R} and intensity, and
2. the pH-sensitive fluorescent indicator s_{A}, whose phase shift is null, but whose intensity depends on pCO_2[89].

The main advantage of DLR lies in its independence towards light source / photodetector fluctuations. Applied to pCO_2 sensing, DLR was studied by a number of authors in the literature, using HPTS and a Ruthenium (II) complex[473–475] or BODIPYs and Egyptian Blue[476–478] as pH-sensitive dye / reference dye pairs.

4.3.2.3 Choosing a Sensing Scheme

To the newcomer, choosing a single sensing scheme among the above-presented ones may appear a daunting endeavour. Indeed, a not-so-quick dive into the above-cited works reveals that all of them manage to decently measure a pCO_2 *in the laboratory*. However, implementing those techniques *in the field* is a whole different can of worms.

As mentioned in Section 4.3.2.1.1, single wavelength direct probing is plagued by fluctuations of the photodiode sensitivity and LED intensity with temperature, or from part to part—not to mention the dye photobleaching issue—and the same flaws exist with IFE or intensity-based FRET. Then, single wavelength referencing implies regularly exposing the sensors to a pure N_2 or CO_2 atmosphere, which is hardly feasible outside the laboratory. The most promising sensing schemes are thus those of dual wavelength ratiometric measurements—Section 4.3.2.1.3—time- or frequency-based IFE—Section 4.3.2.2.1—and DLR—Section 4.3.2.2.3—for a real-world, calibration-free implementation.

Then, absorbance-based methods seem difficult to implement in a transcutaneous sensor without the addition of a reflective layer between the sensing film and the skin—especially in case of dark skin colour. Indeed, an optical transcutaneous measurement setup such as that depicted in Figure 4.12 is essentially a reflectance-based design. Without the latter additional reflective layer, the non-absorbed light would continue its route towards the skin, and be absorbed or partly reflected by the latter differently for each patient. The above-mentioned reflective layer may be a real additional layer—although it would have to be permeable to CO_2—or may consist in titanium dioxide (TiO_2) particles dispersed either *(i)* in the protective membrane or *(ii)* in the sensing film containing the dye itself, rendering either of them diffusive and reflective[363, 478, 641]. Considering fluorescence sensing schemes, it then appears that while ratiometric measurements require two LEDs, DLR-based ones, or time- or frequency-based IFE would only require one. However, DLR and IFE require the use of two dyes, when ratiometric measurements only need one.

Overall, the choice thus boils down to selecting one of the following six techniques:

1. ratiometric absorbance with a reflective compound,
2. ratiometric fluorescence,
3. time-based IFE,
4. frequency-based IFE,
5. time-based DLR, or
6. frequency-based DLR.

However, this choice strongly depends on the price of the following elements, which are used to implement the latter schemes:

- The optical parts: LEDs, fluorescence filters, lenses.
- The chemicals: absorbing dyes or luminophores.
- The electronics: especially for the DLR or IFE schemes, which may require relatively high-speed DAC, ADC, and Digital Signal Processor (DSP)

Since thoroughly analysing the latter parameters in terms of costs, ease of implementation, and performance would be the work of a lifetime, I had to choose boldly one of these six options. I finally settled on frequency-based Dual Lifetime Referencing (f-DLR), for it seemed to me that a phase-based approach would be more robust than an intensity-based one, as reported by Klimant *et al.*[89]. The remainder of the present chapter details the f-DLR theory of operation in Section 4.3.3, before focusing on the accuracy of phase estimation from a noisy sinusoidal signal in Section 4.4.

4.3.3 DLR Theory of Operation

Complete DLR theoretical developments can be found in the work of Klimant, Neureuter *et al.*[89, 642]—in particular, DLR was the subject of Gerhard Neurauter's PhD thesis. The basic idea behind frequency-based DLR applied to pH sensing is presented in Figure 4.16. As mentioned above, two luminophores are used: a reference one, noted R in the following developments, and an indicator one, sensitive to the analyte of interest—*i.e.* pH, or CO_2 in our case. This latter indicator can exist in two forms, the above-mentioned protonated—AH—and anionic—A^-—forms, and it is assumed for the sake of simplicity that only the anionic form A^- fluoresces. R, on its part, is chosen so that its luminescence lifetime is much longer than that of A^-, and so that its luminescence intensity remains constant with respect to the analyte. A^- is chosen so that its luminescence lifetime is much shorter than that of R, and so that its luminescence intensity depends on the analyte. In the remainder of this section, in order to have numbers to work with, A^- refers to the strongly fluorescent anionic form of HPTS, while R refers to tris(4,7-diphenyl-1,10 phenanthroline) ruthenium (II) dichloride (Ru-dpp), a commonly used ruthenium(II) complex—more information on these two dyes are given in Sections 5.2.2 and 5.2.3, respectively.

4.3.3.1 General Framework

Hypotheses: The studied system is a mixture of luminophores R and A^-. Their concentration is supposed to be low enough to prevent non-radiative energy transfer between them. The inner filter effect and the solvent influence are also neglected. The luminescence decay model for the two luminophores is a single exponential decay model.

Argument: Under a sinusoidal excitation of intensity I_0 at a pulsation ω (frequency $f = \frac{\omega}{2\cdot\pi}$),

$$s_{\mathrm{ex}}(t) = I_0\cdot \sin(\omega\cdot t) \tag{4.41}$$

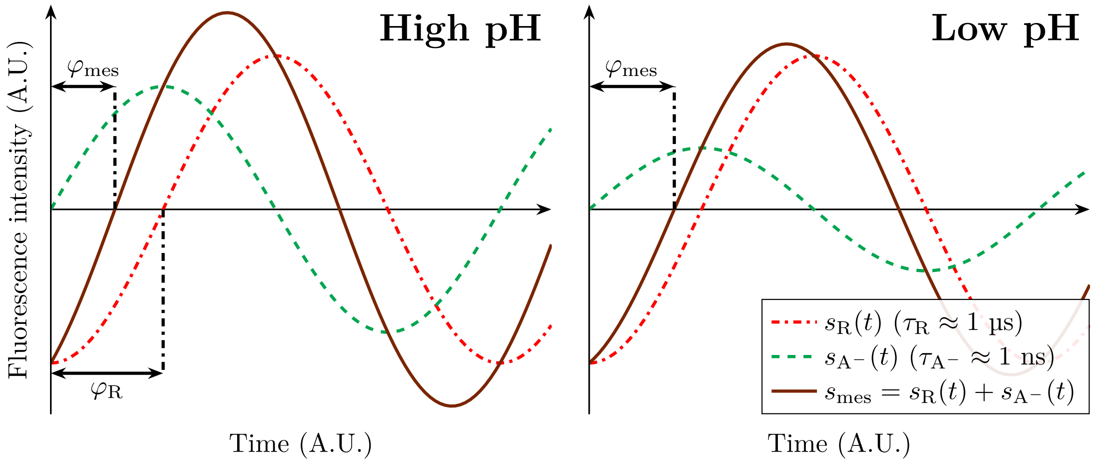

Figure 4.16: Basic principle of f-DLR pH sensing. When excited by a zero-phase sinusoidal signal, the reference and anionic forms of the pH-sensitive luminophores produce the s_{R} and $s_{\mathrm{A^-}}$ luminescence signals, respectively. s_{mes}—their sum—is the signal measured *in fine* by the photodetector, while φ_{mes} is the phase shift of s_{mes} with respect to the zero-phase exciting signal. At high pH values (left side of the figure), the pH-sensitive fluorophore is in its anionic form A$^-$, exhibiting a strong fluorescence, and φ_{mes} is low. Conversely, when the pH decreases (right side of the figure), A$^-$ converts into its non-luminescent protonated form AH, and the amplitude of $s_{\mathrm{A^-}}$ decreases, increasing φ_{mes}.

both luminophores re-emit light at the same frequency with a phase shift φ and a gain G in reference to s_{ex} which are given by (first order system response, consequence of the mono-exponential decay model)

$$\begin{cases} G_{\mathrm{L}} = \varepsilon_{\mathrm{L},\lambda}\cdot\Phi_{\mathrm{L}}\cdot\frac{k\cdot[\mathrm{L}]}{\sqrt{1+(\omega\tau_{\mathrm{L}})^2}} \\ \varphi_{\mathrm{L}} = -\arctan(\omega\cdot\tau_{\mathrm{L}}) \end{cases} , \quad \mathrm{L} \in \{\mathrm{R}, \mathrm{A}^-\} \tag{4.42}$$

wherein τ_{L} is the decay time of a given luminophore L, Φ_{L} its quantum yield, $\varepsilon_{\mathrm{L},\lambda}$ its molar absorption coefficient at the probing wavelength λ, [L] its concentration, and k a geometrical constant function of the optical setup used. The signal emitted by each luminophore may then be written

$$s_{\mathrm{L}}(t) = I_{\mathrm{L}}\cdot\sin(\omega\cdot t + \varphi_{\mathrm{L}}), \quad \text{wherein} \quad I_{\mathrm{L}} = G_{\mathrm{L}}\cdot I_0 \tag{4.43}$$

The overall response of a mixture of A$^-$ and R will thus be a signal of the shape

$$\begin{aligned} s_{mes}(t) &= I_{mes}\cdot\sin(\omega\cdot t + \varphi_{\mathrm{mes}}) \\ s_{\mathrm{mes}}(t) &= s_{\mathrm{R}}(t) + s_{\mathrm{A^-}}(t) \\ s_{\mathrm{mes}}(t) &= I_{\mathrm{R}}\cdot\sin(\omega\cdot t + \varphi_{\mathrm{R}}) + I_{\mathrm{A^-}}\cdot\sin(\omega\cdot t + \varphi_{\mathrm{A^-}}) \end{aligned} \tag{4.44}$$

wherein s_{mes} is the measured signal and I_{mes} and φ_{mes} are its amplitude and phase shift with respect to I_{ex}, respectively. This principle is represented in Figure 4.16. Evaluating the latter equation at $t = 0$ and $t = \frac{\pi}{2\cdot\omega}$ leads to:

$$\begin{cases} I_{mes}\cdot\sin(\varphi_{mes}) = I_R\cdot\sin(\varphi_R) + I_H\cdot\sin(\varphi_H) \\ I_{mes}\cdot\cos(\varphi_{mes}) = I_R\cdot\cos(\varphi_R) + I_H\cdot\cos(\varphi_H) \end{cases} \tag{4.45}$$

In practical DLR applications, R and A$^-$ are often chosen so that $\tau_{\mathrm{A^-}} \ll \tau_{\mathrm{R}}$. For instance, the use of Ru-dpp for R ($\tau_{\mathrm{R}} \approx$ 1–6 µs(6)) and HPTS for A$^-$ / AH ($\tau_{\mathrm{A^-}} \approx$ 5 ns(7)) has been reported multiple times in the literature[473–475]. The several orders of magnitude between τ_R and $\tau_{\mathrm{A^-}}$ allows for mathematical simplifications that are exposed in the next section (Section 4.3.3.2), while the general case is also treated in Section 4.3.3.3.

---

(6) Ru-dpp and HPTS are presented in great detail in Section 5.2, along with appropriate references regarding their luminescence properties.

(7) See footnote (6).

4.3.3.2 Simplified Scheme

Under the hypothesis that the luminescence decay time constant of A$^-$ is orders of magnitude lower than that of R—*i.e.* $\tau_{\mathrm{A}^-} \ll \tau_{\mathrm{R}}$—and if working at a sufficiently low frequency—$\omega \ll 1/\tau_{\mathrm{A}^-}$—$\varphi_{\mathrm{A}^-}$ may be safely neglected compared to φ_{R}. In this case, and if I_{R} is not orders of magnitude below I_{A^-}, Equation 4.45 translates into

$$\begin{cases} I_{\mathrm{mes}} \cdot \sin(\varphi_{\mathrm{mes}}) = I_{\mathrm{R}} \cdot \sin(\varphi_{\mathrm{R}}) \\ I_{\mathrm{mes}} \cdot \cos(\varphi_{\mathrm{mes}}) = I_{\mathrm{R}} \cdot \cos(\varphi_{\mathrm{R}}) + I_{\mathrm{A}^-} \end{cases} \tag{4.46}$$

and dividing the lower line by the upper one yields

$$\operatorname{cotan}(\varphi_{\mathrm{mes}}) = \operatorname{cotan}(\varphi_{\mathrm{R}}) + \frac{1}{\sin(\varphi_{\mathrm{R}})} \cdot \frac{I_{\mathrm{A}^-}}{I_{\mathrm{R}}} \tag{4.47}$$

From equations 4.43 and 4.47, **it becomes clear that $\boldsymbol{\varphi_{\mathrm{mes}}}$ is independent of the incident light beam intensity $\boldsymbol{I_0}$**. Rather, φ_{mes} depends on the intrinsic properties of the luminophores and of the ratio of their concentrations. Using Equation 4.42, $\operatorname{cotan}(\varphi_{\mathrm{mes}})$ can be further developed into

$$\operatorname{cotan}(\varphi_{\mathrm{mes}}) = -\frac{1}{\omega \cdot \tau_{\mathrm{R}}} - \frac{1}{\sin(\arctan(\omega \cdot \tau_{\mathrm{R}}))} \cdot \sqrt{\frac{1 + (\omega \cdot \tau_{\mathrm{R}})^2}{1 + (\omega \cdot \tau_{\mathrm{A}^-})^2}} \cdot \frac{\varepsilon_{\mathrm{A}^-,\lambda}}{\varepsilon_{\mathrm{R},\lambda}} \cdot \frac{\Phi_{\mathrm{A}^-}}{\Phi_{\mathrm{R}}} \cdot \frac{[\mathrm{A}^-]}{[\mathrm{R}]} \tag{4.48}$$

which is in line with what can be found in the literature about DLR[475, 642]. It can also be noted that since

$$\sin(\arctan(x)) = \frac{x}{\sqrt{1 + x^2}} \tag{4.49}$$

the above equation can be simplified into:

$$\operatorname{cotan}(\varphi_{\mathrm{mes}}) = -\frac{1}{\omega \cdot \tau_{\mathrm{R}}} \cdot \left(1 + \frac{1 + (\omega \cdot \tau_{\mathrm{R}})^2}{\sqrt{1 + (\omega \cdot \tau_{\mathrm{A}^-})^2}} \cdot \frac{\varepsilon_{\mathrm{A}^-,\lambda}}{\varepsilon_{R,\lambda}} \cdot \frac{\Phi_{\mathrm{A}^-}}{\Phi_{\mathrm{R}}} \cdot \frac{[\mathrm{A}^-]}{[\mathrm{R}]} \right) \tag{4.50}$$

In normal operation, [R] and ω are constants. Additionally, τ_{L}, $\varepsilon_{\mathrm{L},\lambda}$ and Φ_{L} are intrinsic properties of the fluorophores and—as such—are also constants. [A$^-$] remains the only variable, and since it is the concentration of pH-sensitive dye—*e.g.* HPTS—in its anionic state, it is directly related to pCO$_2$ as per Equations 4.24 or 4.27. Equation 4.50 can thus be rewritten

$$[A^-] = -\alpha \cdot (\operatorname{cotan}(\varphi_{\mathrm{mes}}) + \beta) \quad \text{wherein} \quad \begin{cases} \alpha = \omega \cdot \tau_{\mathrm{R}} \cdot \frac{\sqrt{1 + (\omega \cdot \tau_{\mathrm{A}^-})^2}}{1 + (\omega \cdot \tau_{\mathrm{R}})^2} \cdot \frac{\varepsilon_{\mathrm{A}^-,\lambda}}{\varepsilon_{\mathrm{R},\lambda}} \cdot \frac{\Phi_{\mathrm{R}}}{\Phi_{\mathrm{A}^-}} \cdot [\mathrm{R}] \\ \beta = \frac{1}{\omega \cdot \tau_{\mathrm{R}}} \end{cases} \tag{4.51}$$

By combining equations 4.24—which gives pCO$_2$ as a function of $[A^-]$—and 4.51—which gives $[A^-]$ as a function of φ_{mes}—we finally have a relation in the form(8)

$$\mathrm{pCO}_2 = f(\varphi_{\mathrm{mes}}) \tag{4.52}$$

Further remarks: the choice of the probing frequency f is a compromise between the accuracy of φ_{mes} measurements and the total signal strength, I_{mes}. Indeed, choosing an exceedingly low frequency maximises the amplitude of the measured signal I_{mes}, but leads to almost no phase shift of the reference signal s_{R}. In this case, φ_{mes} decreases towards zero and a small error in its measurement results in a huge error in $\operatorname{cotan}(\varphi_{\mathrm{mes}})$ estimation, and thus in pCO$_2$ estimation.

Contrariwise, very high frequencies lead to a phase shift of s_{R} close to $\pi/2$ (see Equation 4.42). In such a configuration, s_{R} and s_{A^-} are in phase quadrature and φ_{mes} is maximal. However, the more f increases, the lower I_{R} gets. Additionally, if f gets too high, φ_{A^-} can no longer be neglected (see Section 4.3.3.3). In practice, an ω value above $1/\tau_{\mathrm{R}}$ should yield $\varphi_{\mathrm{R}} \geq \pi/4$, which translates into frequencies in the 26–160 kHz for τ_{R} in the 1–6 µs range ($f = 1/(2 \cdot \pi \cdot \tau_{\mathrm{R}})$).

Of note, the influence of f, $\mathcal{C}_A$, [R], [Q$^+$], and pCO$_2$ and their interactions are briefly mentioned as a future research avenue in the last chapter of this thesis—see Section 6.2.10.

---

(8) In this manuscript notations such as $x = f(y)$ are sometimes used to denote an anonymous function f (also sometimes g, h, *etc.*) linking variables x and y, not to be confused with the letter 'f' alone, which stands for the *frequency* of periodic signals.

4.3.3.3 General Case

Due to constraints on the excitation and emission spectra, lifetimes, or availability of the two luminophores involved, it might not be always feasible to have $\tau_{\mathrm{R}} \gg \tau_{\mathrm{A}^-}$. The general case without the simplification performed in the previous section is thus studied below. Starting back with the results of Section 4.3.3.1, Equations 4.42 and 4.44 yield

$$s_{\mathrm{mes}}(t) = I_0 \cdot k \cdot \left(A_{\mathrm{R}} \cdot \sin(\omega \cdot t + \varphi_{\mathrm{R}}) + A_{\mathrm{A}^-} \cdot \sin(\omega \cdot t + \varphi_{\mathrm{R,A}^-}) \right) \tag{4.53}$$

wherein A_{L} is solely a function of the properties of the luminophores, defined as

$$A_{\mathrm{L}} = \frac{\Phi_{\mathrm{L}}}{\sqrt{1 + \omega^2 \tau_{\mathrm{L}}^2}}, \tag{4.54}$$

When considering φ_{mes}, we thus have

$$\tan(\varphi_{\mathrm{mes}}) = \frac{A_{\mathrm{R}} \cdot [\mathrm{R}] \cdot \sin(\varphi_{\mathrm{R}}) + A_{\mathrm{A}^-} \cdot [\mathrm{A}^-] \cdot \sin(\varphi_{\mathrm{A}^-})}{A_{\mathrm{R}} \cdot [\mathrm{R}] \cdot \cos(\varphi_{\mathrm{R}}) + A_{\mathrm{A}^-} \cdot [\mathrm{A}^-] \cdot \cos(\varphi_{\mathrm{A}^-})} \tag{4.55}$$

which can be rewritten

$$\tan(\varphi_{\mathrm{mes}}) = \frac{a + b \cdot [\mathrm{A}^-]}{c + d \cdot [\mathrm{A}^-]} \quad \text{wherein} \quad \begin{cases} a = [\mathrm{R}] \cdot A_{\mathrm{R}} \cdot \sin(\varphi_{\mathrm{R}}), & b = A_{\mathrm{A}^-} \cdot \sin(\varphi_{\mathrm{A}^-}) \\ c = [\mathrm{R}] \cdot A_{\mathrm{R}} \cdot \cos(\varphi_{\mathrm{R}}), & d = A_{\mathrm{A}^-} \cdot \cos(\varphi_{\mathrm{A}^-}) \end{cases} \tag{4.56}$$

$[\mathrm{A}^-]$ can thus be expressed as

$$[\mathrm{A}^-] = \frac{c \cdot \tan(\varphi_{\mathrm{mes}}) - a}{b - d \cdot \tan(\varphi_{\mathrm{mes}})} \tag{4.57}$$

Since $[\mathrm{A}^-]$ is a function of pCO_2, we can thus again establish a relation—although more complicated—of the form

$$\varphi_{\mathrm{mes}} = f(pCO_2) \tag{4.58}$$

And this relation is also independent of I_0 and k but only depends on $[\mathrm{Q}^+]$, $[\mathrm{R}]$, $\mathcal{C}_{\mathrm{A}}$, f, and the properties of the chosen luminophores—*i.e.* τ_{L}, $\varepsilon_{\mathrm{L},\lambda}$ and Φ_{L}.

4.3.3.4 Dual Frequency Dual Lifetime Referencing (DF-DLR)

While the above-presented schemes assume that τ_{R} remains constant, the latter can actually be influenced by external perturbations, namely *(i)* the presence of a luminescence quencher such as O_2 and *(ii)* temperature fluctuations[643]. Thus, having a means to monitor τ_{R} would allow either to compensate for quenching, or to monitor the temperature of the sensor optically. To this end, DF-DLR was developed by Gerhard Neurauter in the course of his PhD thesis[642] and barely used ever since[644–646]. Although I did not use this dual-frequency scheme in my experiments, it may be an interesting avenue to consider for future improvements, and it is thus presented here briefly for the sake of completeness.

The following developments only consider the simplified DLR scheme, but the same train of thought could also be followed with the general DLR scheme, although leading to much more complex calculations. Starting with Equation 4.50,

$$\omega_i \cdot \tau_{\mathrm{R}} \cdot \mathrm{cotan}(\varphi_{\mathrm{mes},i}) + 1 = -\frac{1 + (\omega_i \cdot \tau_{\mathrm{R}})^2}{\sqrt{1 + (\omega_i \cdot \tau_{\mathrm{A}^-})^2}} \cdot \frac{\Phi_{\mathrm{A}^-}}{\Phi_{\mathrm{R}}} \cdot \frac{[\mathrm{A}^-]}{[\mathrm{R}]} \tag{4.59}$$

wherein i is either 1 or 2 for the two probing frequencies of the scheme, f_1 and f_2. If the latter are chosen sufficiently low, we thus have $1 + (\omega_i \cdot \tau_{\mathrm{A}^-})^2 \approx 1$, that is,

$$\omega_i \cdot \tau_{\mathrm{R}} \cdot \mathrm{cotan}(\varphi_{\mathrm{mes},i}) + 1 = -\left(1 + (\omega_i \cdot \tau_{\mathrm{R}})^2\right) \cdot \frac{\Phi_{\mathrm{A}^-}}{\Phi_{\mathrm{R}}} \cdot \frac{[\mathrm{A}^-]}{[\mathrm{R}]} \tag{4.60}$$

Dividing the latter equation written for f_2 by the same one for f_1 leads to the quadratic form

$$A \cdot \tau_{\mathrm{R}}^2 + B \cdot \tau_{\mathrm{R}} + C = 0 \tag{4.61}$$

with

$$\begin{cases} A = \omega_1^2 \cdot \omega_2 \cdot \mathrm{cotan}(\varphi_{\mathrm{mes},2}) - \omega_2^2 \cdot \omega_1 \cdot \mathrm{cotan}(\varphi_{\mathrm{mes},1}) \\ B = \omega_1^2 - \omega_2^2 \\ C = \omega_2 \cdot \mathrm{cotan}(\varphi_{\mathrm{mes},2}) - \omega_1 \cdot \mathrm{cotan}(\varphi_{\mathrm{mes},1}) \end{cases} \tag{4.62}$$

leading to

$$\tau_{\mathrm{R}} = \frac{-B \pm \sqrt{B^2 - 4{\cdot}A{\cdot}C}}{2{\cdot}A} \tag{4.63}$$

The sign of the root that should be kept can be deduced by considering the limit case wherein only R is present. In this situation, $\mathrm{cotan}(\varphi_{\mathrm{mes},i}) = -1/(\omega_i{\cdot}\tau_{\mathrm{R}})$, assuming $\omega_2 > \omega_1$, $C = 0$, $A > 0$ and $B < 0$. Since $\tau_{\mathrm{R}} \neq 0$,

$$\tau_{\mathrm{R}} = \frac{-B + \sqrt{B^2 - 4{\cdot}A{\cdot}C}}{2{\cdot}A} \tag{4.64}$$

τ_{R} knowledge can then be used for temperature or quenching (pO_2) probing and / or corrections[642, 647].

4.3.4 Synthesis

This Section 4.3 focused on dye-based CO_2 sensing, first presenting the link between pCO_2 and pH in both wet and dry media—Section 4.3.1. Adding an acid-base indicator exhibiting differing optical properties between its protonated and anionic forms then allows for an optical determination of the sensor's pH—Section 4.3.2.1. However, most of the classical sensing schemes call for some kind of referencing, which brings its own constraints—*e.g.* measuring in a pure N_2 / CO_2 atmosphere, or adding other optical components to form a reference light-path. Among the different sensing schemes reviewed—Section 4.3.2.2—f-DLR was chosen and further developed in Section 4.3.3, finally reaching an equation of the form

$$\mathrm{pCO_2} = f(\varphi_{\mathrm{mes}}) \tag{4.65}$$

wherein φ_{mes} is the phase shift between an excitation signal s_{ex}, and the fluorescence signal re-emitted by the luminophores s_{mes}. Thus, this latter scheme demands accurate phase measurements in order to yield an accurate pCO_2 measurement. Since s_{mes} is a potentially noisy sinusoidal signal, I thus wondered how to accurately measure its phase, which is at the very heart of the upcoming section.

4.4 Accurate Phase Estimation for DLR

What follows is essentially a slightly formatted and edited version of the article entitled *On the Accuracy of Phase Extraction from a Known-Frequency Noisy Sinusoidal Signal*, and published in 2024 in the APSIPA Transactions on Signal and Information Processing[90]. However, the reader probably does not need to understand all the mathematical subtleties presented in the following pages, and might only be interested in the concluding remarks presented in Section 4.4.6. Those conclusions are also briefly outlined in the conclusion of the present chapter—Section 4.5. Again, the first person plural is used in the following subsections, as this was a collective work.

4.4.1 Introduction

Spectral estimation plays a critical role in signal processing by characterising a signal's spectral attributes, including amplitudes and phase shifts. This topic has gathered considerable research interest for decades due to its numerous applications in various fields, such as telecommunications, radar, seismology, and power grid analysis[648–651]. In the general case, the frequencies of interest f_i of the signal under study are *a priori* unknown. Thus, it is exceedingly unlikely that given a sampling frequency f_s and a sampling length N, the numbers $f_i{\cdot}N/f_s$ are integers. This condition—known as "asynchronous sampling"—leads to the infamous picket fence and spectral leaking effects[652], which may be mitigated by an appropriate windowing function choice[653], the use of all-phase Discrete Fourier Transform (DFT)[654, 655], or both[656], for example.

There are certain cases, however, for which the signal under study is purely sinusoidal with a known frequency. This scenario arises when characterising linear systems, which may be fed a sinusoidal excitation signal of known frequency, amplitude, and phase, while recording their output. The analysis of the attenuation and phase shift induced by the system at hand can then yield useful information. For instance, in the context of f-DLR[89], the phase shift between a fluorescence excitation signal of known frequency and the re-emitted one can be used to accurately measure the concentration of a variety of analytes[473, 477, 609, 657]. In this situation—known as "synchronous sampling"—the number of samples taken, as well as the sampling and excitation frequencies f and f_s, can be chosen so that $f{\cdot}N/f_s$ is an integer, which suppresses the above-mentioned deleterious effects[652, 658].

Yet, as far as we were aware when performing the following developments, no comprehensive study had been conducted to characterise the achievable accuracy of phase estimation in such a synchronous sampling scenario. In the next sections, we present theoretical developments leading to a closed-form expression of the asymptotic Probability Density Function (PDF) of the phase estimate of a noisy sinusoidal signal in the presence of both phase and additive noises. The presented derivations are supported by simulations results, showing the resulting phase Root Mean Square Error (RMSE) at different noise levels. We then show that the derived phase estimator is asymptotically efficient with a fast convergence. Finally, we discuss its asymptotic behaviour in the case of very high or very low noise levels and sample numbers.

4.4.2 Problem Formulation

In the remainder of this document, the objective is always to retrieve the phase φ of a real discrete signal of length N defined as

$$s_n = A_s\cdot \cos\left(\frac{2\cdot\pi\cdot f_0\cdot n}{f_s} + \varphi + p_n\right) + x_n,\ \text{with}\ \begin{cases} x_n \overset{iid}{\sim} \mathcal{N}(0,\sigma_x^2) \\ p_n \overset{iid}{\sim} \mathcal{N}(0,\sigma_p^2) \\ n \in \llbracket 0; N-1 \rrbracket \end{cases} \tag{4.66}$$

with f_0 the frequency of the signal itself, f_s its sampling frequency—always chosen such that $f_s > 2\cdot f_0$, the Nyquist frequency—and A_s its amplitude. The x_n and p_n random variables—of variances σ_x^2 and σ_p^2—represent additive measurement noise and sampling-induced phase noise, respectively. Of note, it is also considered that A_s and φ, though unknown, remain constant throughout the acquisition duration N/f_s. A representative illustration of the issue at hand, involving most of the parameters introduced above, may be seen in Figure 4.17.

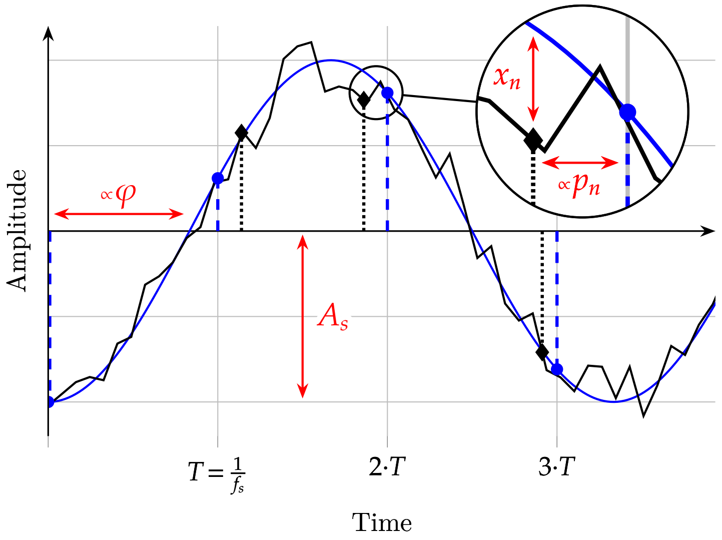

Figure 4.17: Temporal representation of the problem: the objective is to estimate the phase φ of an idealised sinusoidal signal of amplitude A_s (—●—) from a noisy measurement of the latter (—◆—). The noise originates from two distinct sources: *(i)* an additive noise x_n which makes the sampled signal depart from its ideal counterpart, and *(ii)* a phase noise p_n, which randomly shifts the sampling times (···) in comparison to an ideal sampling at frequency f_s (- -). The symbol $\propto$ denotes proportionality, not to be confused with the Greek letter *alpha* (α), used later on in this section.

Typically, in an f-DLR sensing scheme, A_s and φ would correspond to:

1. the intensity of the collected light: a function of the quantum yield of the involved luminophores, of their concentrations, and of the illumination and light collection parameters, and
2. the phase shift: function of the ratio of the different luminophores species, conveying the concentration of the analyte of interest—see Section 4.3.3.

Hence, it is of particular importance to accurately estimate φ, and to characterise the influence of σ_p, σ_x, and N on its RMSE, since it will directly influence the reachable accuracy on the measurement of a given analyte's concentration.

In the remainder of this article, we adopt the following notations: x_n refers to the n-th element of a given vector X, $\square^\intercal$ is the transpose operator, $\mathbb{0}_N$ and $\mathbb{1}_N$ stand for the zero and unit vector in $\mathbb{R}^N$, respectively, $\Re(z)$ and $\Im(z)$ stand for the real and imaginary parts of a given complex number z, while $|z|$ and $\arg(z)$ stand for its modulus and argument. $\triangleq$ means "per definition", $\overline{\square}$ is the complex conjugate operator, $\mathcal{N}$ and $\mathcal{CN}$ stand for the normal and complex normal distributions, respectively, and $x \perp\!\!\!\perp y$ denotes the independence between two random variable x and y. Finally, the Signal to Noise Ratio (SNR) of the measurement is defined as

$$\mathrm{SNR} = \frac{A_s^2}{2\cdot\sigma_x^2} \quad \text{and} \quad \mathrm{SNR}_{\mathrm{dB}} = 10\cdot\log_{10}(\mathrm{SNR}) \tag{4.67}$$

4.4.3 Characterisation of the DFT Distribution

This study focuses on φ estimation through the study of the DFT of the above-presented noisy signal. Indeed, we demonstrate in Section 4.4.4 that an unbiased and efficient estimator of φ—denoted as $\widehat{\varphi}$—can be derived by taking the argument of the signal's DFT at frequency f_0. In order to derive the PDF of $\widehat{\varphi}$, the PDF of this DFT must thus be known first.

To this end, let us first consider the k-th index of the N-points DFT of the above-mentioned signal[659], *i.e.* its DFT at frequency f_0:

$$D_N = \sum_{n=0}^{N-1} s_n\cdot \mathrm{e}^{-i\cdot\frac{2\cdot\pi\cdot k\cdot n}{N}} \tag{4.68}$$

with k, N, f_0 and f_s chosen such that $\frac{k}{N} = \frac{f_0}{f_s}$ (synchronous sampling hypothesis). Let $\alpha = \frac{2\cdot\pi\cdot f_0}{f_s}$ and

$$S = \begin{pmatrix} s_0 \\ s_1 \\ \vdots \\ s_{N-1} \end{pmatrix},\ X = \begin{pmatrix} x_0 \\ x_1 \\ \vdots \\ x_{N-1} \end{pmatrix},\ Z = \begin{pmatrix} \mathrm{e}^{i\cdot p_0} \\ \mathrm{e}^{i\cdot p_1} \\ \vdots \\ \mathrm{e}^{i\cdot p_{N-1}} \end{pmatrix},\ \mathcal{U}_\alpha = \begin{pmatrix} 1 \\ \mathrm{e}^{-i\cdot\alpha} \\ \vdots \\ \mathrm{e}^{-i\cdot\alpha\cdot(N-1)} \end{pmatrix} \tag{4.69}$$

Then D_N may be rewritten as

$$D_N = \sum_{n=0}^{N-1} s_n\cdot \mathrm{e}^{-i\cdot\alpha\cdot n} = \mathcal{U}_\alpha^\intercal\cdot S \tag{4.70}$$

Let also define $\widetilde{S}$ as $S = \widetilde{S} + X$. Using Euler's formula, each element $\widetilde{s}_n$ of $\widetilde{S}$ may then be expressed as

$$\begin{aligned} \widetilde{s}_n &= A_s\cdot\frac{\mathrm{e}^{i\cdot\left(\frac{2\cdot\pi\cdot f_0\cdot n}{f_s}+\varphi+p_n\right)} + \mathrm{e}^{-i\cdot\left(\frac{2\cdot\pi\cdot f_0\cdot n}{f_s}+\varphi+p_n\right)}}{2} \\ &= \frac{A_s}{2}\cdot\left(\mathrm{e}^{i\cdot(\alpha\cdot n+\varphi+p_n)} + \mathrm{e}^{-i\cdot(\alpha\cdot n+\varphi+p_n)}\right) \end{aligned} \tag{4.71}$$

The remainder of this section is organised as follows: the expected value and variance of D_N are computed in Sections 4.4.3.1 and 4.4.3.2, respectively, while its asymptotic PDF is derived in Section 4.4.3.3.

4.4.3.1 Expected Value of D_N

The expected value of D_N is given by

$$\mathbf{E}[D_N] = \mathbf{E}[\mathcal{U}_\alpha^\intercal\cdot\widetilde{S}] + \mathbf{E}\left[\mathcal{U}_\alpha^\intercal\cdot X\right] \tag{4.72}$$

Regarding $\mathbf{E}[\mathcal{U}_\alpha^\intercal\cdot\widetilde{S}]$,

$$\begin{aligned} \mathcal{U}_\alpha^\intercal\cdot\widetilde{S} &= \frac{A_s}{2}\left(\mathrm{e}^{i\cdot\varphi}\sum_{n=0}^{N-1}\mathrm{e}^{i\cdot p_n} + \mathrm{e}^{-i\cdot\varphi}\cdot\sum_{n=0}^{N-1}\mathrm{e}^{-2\cdot i\cdot\alpha\cdot n}\cdot\mathrm{e}^{-i\cdot p_n}\right) \\ &= \frac{A_s}{2}\cdot\left(\mathrm{e}^{i\cdot\varphi}\cdot\mathbb{1}_N^\intercal\cdot Z + \mathrm{e}^{-i\cdot\varphi}\cdot\left(\mathcal{U}_\alpha^2\right)^\intercal\cdot\overline{Z}\right) \end{aligned} \tag{4.73}$$

hence

$$\mathbf{E}[\mathcal{U}_\alpha^\intercal\cdot\widetilde{S}] = \frac{A_s}{2}\cdot\left(\mathrm{e}^{i\cdot\varphi}\cdot\mathbb{1}_N^\intercal\cdot\mathbf{E}[Z] + \mathrm{e}^{-i\cdot\varphi}\cdot\left(\mathcal{U}_\alpha^2\right)^\intercal\cdot\mathbf{E}[\overline{Z}]\right) \tag{4.74}$$

We thus need to compute $\mathbf{E}[Z]$. For a given p amongst p_n, let us consider $\mathbf{E}[\mathrm{e}^{i\cdot p}]$ first, and let $\left[g : v \mapsto \mathrm{e}^{i\cdot v}\right]$. Then

$$\mathbf{E}[\mathrm{e}^{i\cdot p}] = \mathbf{E}[g(p)] = \int_{-\infty}^{+\infty} g(v)\cdot f_p(v)dv \tag{4.75}$$

thanks to the Law Of The Unconscious Statistician (LOTUS)[660], wherein f_p is the probability density function of p—namely a centred normal distribution of variance σ_p^2, see Equation 4.66—given by

$$\left[f_p : v \mapsto \frac{1}{\sigma_p\cdot\sqrt{2\cdot\pi}}\cdot\mathrm{e}^{-\frac{v^2}{2\cdot\sigma_p^2}}\right] \tag{4.76}$$

We thus have

$$\mathbf{E}[\mathrm{e}^{i\cdot p}] = \int_{-\infty}^{+\infty} \frac{1}{\sigma_p\cdot\sqrt{2\cdot\pi}}\cdot\mathrm{e}^{-\frac{v^2}{2\cdot\sigma_p^2}+i\cdot v}dv = \frac{\mathrm{e}^{-\frac{\sigma_p^2}{2}}}{\sigma_p\cdot\sqrt{2\cdot\pi}}\int_{-\infty}^{+\infty} \mathrm{e}^{\left(\frac{i\cdot v}{\sigma_p\cdot\sqrt{2}}+\frac{\sigma_p}{\sqrt{2}}\right)^2}dv \tag{4.77}$$

Using the change of variable $u = h(v)$ with

$$\left[h : v \mapsto \frac{i\cdot v}{\sigma_p\cdot\sqrt{2}} + \frac{\sigma_p}{\sqrt{2}}\right] \tag{4.78}$$

we thus have $du = \frac{i\cdot dv}{\sigma_p\cdot\sqrt{2}}$, with erfi being the imaginary error function,

$$\begin{aligned}\mathbf{E}[\mathrm{e}^{i\cdot p}] &= \frac{\mathrm{e}^{-\frac{\sigma_p^2}{2}}}{\sigma_p\cdot\sqrt{2\cdot\pi}}\cdot\lim_{v\to+\infty}\int_{-h(v)}^{+h(v)} \mathrm{e}^{u^2}\cdot\frac{\sigma_p\cdot\sqrt{2}}{i}du \\ &= \frac{\mathrm{e}^{-\frac{\sigma_p^2}{2}}}{2\cdot i}\cdot\underbrace{\lim_{v\to+\infty}\underbrace{\frac{2}{\sqrt{\pi}}\int_{-h(v)}^{+h(v)} \mathrm{e}^{u^2}du}_{=[\mathrm{erfi}(u)]_{-h(v)}^{+h(v)}}}_{=2\cdot i} = \mathrm{e}^{-\frac{\sigma_p^2}{2}}\end{aligned} \tag{4.79}$$

Back to $\mathbf{E}[\mathcal{U}_\alpha^\intercal\cdot\widetilde{S}]$, since

$$\mathbf{E}[\overline{Z}] = \overline{\mathbf{E}[Z]} = \mathbf{E}[Z] = \mathbb{1}_N\cdot\mathrm{e}^{-\frac{\sigma_p^2}{2}} \tag{4.80}$$

we thus have

$$\mathbf{E}[\mathcal{U}_\alpha^\intercal\cdot\widetilde{S}] = \frac{A_s}{2}\cdot\left(\mathrm{e}^{i\cdot\varphi}\cdot N\cdot\mathrm{e}^{-\frac{\sigma_p^2}{2}} + \mathrm{e}^{-i\cdot\varphi}\cdot\mathrm{e}^{-\frac{\sigma_p^2}{2}}\cdot\sum_{n=0}^{N-1} u_{\alpha,n}^2\right) \tag{4.81}$$

Noting that $\sum_{n=0}^{N-1} u_{\alpha,n}^2 = 0$ because $\mathrm{e}^{-2\cdot i\cdot\alpha}$ is an N-th root of unity, comes

$$\mathbf{E}[\mathcal{U}_\alpha^\intercal\cdot\widetilde{S}] = \frac{A_s\cdot N}{2}\cdot\mathrm{e}^{i\cdot\varphi}\cdot\mathrm{e}^{-\frac{\sigma_p^2}{2}} \tag{4.82}$$

Regarding $\mathbf{E}[\mathcal{U}_\alpha^\intercal\cdot X]$,

$$\mathbf{E}[\mathcal{U}_\alpha^\intercal\cdot X] = \mathcal{U}_\alpha^\intercal\cdot\underbrace{\mathbf{E}[X]}_{=\mathbb{0}_N} = 0 \tag{4.83}$$

Finally, the expected value of D_N comes to be

$$\boxed{\mathbf{E}[D_N] = \frac{A_s\cdot N}{2}\cdot\mathrm{e}^{i\cdot\varphi}\cdot\mathrm{e}^{-\frac{\sigma_p^2}{2}}} \tag{4.84}$$

4.4.3.2 Variance of D_N

The variance of D_N may also be calculated in a similar manner, starting with

$$\mathbf{Var}(D_N) = \mathbf{Var}(\mathcal{U}_\alpha^\intercal \cdot \widetilde{S}) + \mathbf{Var}\left(\mathcal{U}_\alpha^\intercal \cdot X\right) \tag{4.85}$$

Regarding $\mathbf{Var}(\mathcal{U}_\alpha^\intercal \cdot \widetilde{S})$,

$$\begin{aligned}\mathbf{Var}(\mathcal{U}_\alpha^\intercal \cdot \widetilde{S}) &= \mathbf{Var}\left[\frac{A_s}{2} \cdot \left(\mathrm{e}^{i\cdot\varphi} \cdot \mathbb{1}_N^\intercal \cdot Z + \mathrm{e}^{-i\cdot\varphi} \cdot \left(\mathcal{U}_\alpha^2\right)^\intercal \cdot \overline{Z}\right)\right] \\ &= \frac{A_s^2}{4} \cdot \left(\sum_{n=0}^{N-1} \mathbf{Var}(z_n) + \mathbf{Var}\left(\overline{z_n}\right)\right)\end{aligned} \tag{4.86}$$

We thus need to compute $\mathbf{Var}(z_n)$, *i.e.* $\mathbf{Var}(\mathrm{e}^{i\cdot p_n})$.

$$\mathbf{Var}(\mathrm{e}^{i\cdot p}) = \mathbf{E}\left[\left|\mathrm{e}^{i\cdot p}\right|^2\right] - \left|\mathbf{E}\left[\mathrm{e}^{i\cdot p}\right]\right|^2 = 1 - \mathrm{e}^{-\sigma_p^2} = \mathbf{Var}(\mathrm{e}^{-i\cdot p}) \tag{4.87}$$

as $\mathbf{E}[e^{-i\cdot p}] = \overline{\mathbf{E}[e^{i\cdot p}]}$. Thus

$$\mathbf{Var}(\mathcal{U}_\alpha^\intercal \cdot \widetilde{S}) = \frac{N \cdot A_s^2}{2} \cdot \left(1 - \mathrm{e}^{-\sigma_p^2}\right) \tag{4.88}$$

Regarding $\mathbf{Var}\left(\mathcal{U}_\alpha^\intercal \cdot X\right)$,

$$\begin{aligned}\mathbf{Var}\left(\mathcal{U}_\alpha^\intercal \cdot X\right) &= \sum_{n=0}^{N-1} \mathbf{Var}\left(u_{\alpha,n} x_n\right) = \sum_{n=0}^{N-1} \left(\mathbf{E}\left[\left|u_{\alpha,n} x_n\right|^2\right] - \left|\mathbf{E}\left[u_{\alpha,n} x_n\right]\right|^2\right) \\ &= \sum_{n=0}^{N-1} \mathbf{E}[x_n^2] = N \cdot \sigma_x^2\end{aligned} \tag{4.89}$$

Finally, the variance of D_N comes to be

$$\boxed{\mathbf{Var}(D_N) = N \cdot \left(\frac{A_s^2}{2} \cdot \left(1 - \mathrm{e}^{-\sigma_p^2}\right) + \sigma_x^2\right)} \tag{4.90}$$

4.4.3.3 Distribution of D_N

Now that the expected value and variance of D_N are known, the next step is to study its PDF. To do so, we focus on a reduced version of D_N—$\widetilde{D}_N$—defined as $\widetilde{D}_N = \frac{2 \cdot D_N}{A_s \cdot N}$, with

$$\beta_p = \mathrm{e}^{-\frac{\sigma_p^2}{2}} \qquad \begin{aligned}&\mathbf{E}[\widetilde{D}_N] = \beta_p \cdot \mathrm{e}^{i\cdot\varphi} \\ &\mathbf{Var}(\widetilde{D}_N) = \tfrac{2}{N} \cdot \left(1 - \beta_p^2 + \tfrac{1}{\mathrm{SNR}}\right)\end{aligned} \tag{4.91}$$

We then proceed in two steps: at first, the convergence in law of $\Re(\widetilde{D}_N)$ and $\Im(\widetilde{D}_N)$ towards normal distributions is demonstrated. Then, the asymptotic independence of the latter two quantities is shown. These two demonstrations establish that $\widetilde{D}_N$ converges in law(9) towards a complex normal distribution[662, pp. 540–559], which is a crucial requirement for the forthcoming developments (see Section 4.4.4). However, before delving any deeper into this two-step demonstration, we can further simplify the issue at hand, observing that

$$\widetilde{D}_N = \underbrace{\frac{2 \cdot \mathcal{U}_\alpha^\intercal \cdot \widetilde{S}}{A_s \cdot N}}_{\widetilde{D}_s} + \underbrace{\frac{2 \cdot \mathcal{U}_\alpha^\intercal \cdot X}{A_s \cdot N}}_{\widetilde{D}_x} \tag{4.92}$$

Since X is stationary and ergodic, it readily follows that $\widetilde{D}_x$ converges in distribution toward a complex normal distribution[663, 664]. Since $\widetilde{D}_s$ and $\widetilde{D}_x$ are independent, the two abovementioned steps thus only have to be performed for $\widetilde{D}_s$.

---

(9) Of note, convergence in law is sometimes also referred to as "convergence in distribution" or "weak convergence"[661, p. 18].

4.4.3.3.1 Convergence in Law Towards a Normal Distribution

Let us consider the real part of $\widetilde{D}_s$

$$\begin{aligned}\Re(\widetilde{D}_s) &= \frac{2}{N}\cdot\sum_{n=0}^{N-1}\cos(\alpha\cdot n)\cdot\cos(\alpha\cdot n+\varphi+p_n)\\ &= \frac{2}{N}\cdot\sum_{n=0}^{N-1}V_n, \quad \text{with} \quad V_n=\cos(\alpha\cdot n)\cdot\cos(\alpha\cdot n+\varphi+p_n)\end{aligned} \tag{4.93}$$

We will use Lyapunov's Central Limit Theorem (L-CLT) to demonstrate the convergence of $\sum V_n$ towards a normal distribution. To do so, we will first show that there exists a positive δ such that

$$\lim_{N\to+\infty}\underbrace{\frac{1}{s_N^{2+\delta}}\sum_{n=0}^{N-1}\mathbf{E}\left[\left|V_n-\mathbf{E}[V_n]\right|^{2+\delta}\right]}_{\gamma_N}=0 \tag{4.94}$$

wherein $s_{\mathrm{N}}^2=\sum_{n=0}^{N-1}\mathbf{Var}(V_n)$, and $\mathbf{Var}(V_n)=\cos^2(\alpha\cdot n)\cdot\underbrace{\mathbf{Var}(\cos(t_{\mathrm{n}}+p_n))}_{=\mathbf{E}(\ldots^2)-\mathbf{E}(\ldots)^2}$, with $t_n=\alpha\cdot n+\varphi$.

Where

$$\mathbf{E}(\ldots^2)=\frac{1}{2}+\frac{e^{-2\cdot\sigma_p^2}}{2}\cdot\cos(2\cdot t_n), \quad \text{and} \quad \mathbf{E}(\ldots)^2=e^{-\sigma_p^2}\cdot\frac{1+\cos(2\cdot t_n)}{2} \tag{4.95}$$

and thus

$$\begin{aligned}\mathbf{Var}(V_n) &= \cos^2(\alpha\cdot n)\cdot\left[\frac{1}{2}+e^{-\sigma_p^2}\cdot\left(\frac{\cos(2\cdot t_n)}{2}\cdot e^{-\sigma_p^2}-\frac{1+\cos(2\cdot t_n)}{2}\right)\right]\\ &= \frac{\cos^2(\alpha\cdot n)}{2}\cdot\left(1-e^{-\sigma_p^2}\right)\cdot\left(1-e^{-\sigma_p^2}\cdot\cos(2\cdot t_n)\right)\\ &\geq \frac{\cos^2(\alpha\cdot n)}{2}\cdot\left(1-e^{-\sigma_p^2}\right)^2\end{aligned} \tag{4.96}$$

Back to s_n,

$$s_n^2\geq\frac{\left(1-e^{-\sigma_p^2}\right)^2}{2}\overbrace{\sum_{n=0}^{N-1}\cos^2(\alpha\cdot n)}^{=N/2^{(\ddagger)}}\geq\frac{N\cdot\left(1-e^{-\sigma_p^2}\right)^2}{4} \tag{4.97}$$

wherein (‡) comes from the facts that $\cos^2 x=\frac{1+\cos(2\cdot x)}{2}$, and that $e^{-2\cdot i\cdot\alpha}$ is an N-th root of unity (see Equations 4.81–4.82). Then, $\forall\delta>0$

$$\gamma_N=\frac{1}{s_N^{2+\delta}}\sum_{n=0}^{N-1}\overbrace{\mathbf{E}\left[\left|V_n-\mathbf{E}[V_n]\right|^{2+\delta}\right]}^{\leq 2^{2+\delta}}\leq\frac{N\cdot 2^{2+\delta}}{\left(\frac{N}{4}\cdot\left(1-e^{-\sigma_p^2}\right)^2\right)^{1+\frac{\delta}{2}}}\xrightarrow[N\to+\infty]{}0 \tag{4.98}$$

Since V_n are independent and of finite variance, according to L-CLT, we thus have

$$\frac{1}{s_N}\sum_{n=0}^{N-1}(V_n-\mathbf{E}[V_n])\xrightarrow[N\to+\infty]{d}\mathcal{N}(0,1) \tag{4.99}$$

wherein $\xrightarrow{d}$ denotes convergence in distribution.

Hence, since $\Re(\widetilde{D}_s)=\frac{2}{N}\cdot\sum_{n=0}^{N-1}V_n$,

$$\Re(\widetilde{D}_s)\xrightarrow[N\to+\infty]{d}\mathcal{N}\left(\frac{2}{N}\cdot\sum_{n=0}^{N-1}\mathbf{E}[V_n],\left(\frac{2\cdot s_N}{N}\right)^2\right) \tag{4.100}$$

A similar train of thought can be followed to also demonstrate the asymptotic normality of $\Im(\widetilde{D}_s)$.

4.4.3.3.2 Asymptotic Independence

Demonstrating the complex normality of $\widetilde{D}_s$ then only requires to demonstrate that $\Re(\widetilde{D}_s) \perp\!\!\!\perp \Im(\widetilde{D}_s)$. To do so, it suffices to show that[665, Th. 4.5-1]:

(i) $\Re(\widetilde{D}_s)$ and $\Im(\widetilde{D}_s)$ follow a bivariate normal distribution, and that

(ii) $\mathbf{Cov}(\Re(\widetilde{D}_s), \Im(\widetilde{D}_s)) = 0$.

Bivariate normality

$\forall (a, b) \in \mathbb{R}^2$ let

$$\begin{aligned} T &= a{\cdot}\Re(\widetilde{D}_s) + b{\cdot}\Im(\widetilde{D}_s) \\ &= \sum_{n=0}^{N-1} \frac{a{\cdot}\cos(\alpha{\cdot}n) + b{\cdot}\sin(\alpha{\cdot}n)}{N}{\cdot}\cos(\alpha{\cdot}n + \varphi + p_n) \end{aligned} \tag{4.101}$$

It can be shown—as was done in the previous section with $\Re(\widetilde{D}_s)$—that T also converges in law towards a normal distribution. Thus, by definition, $\Re(\widetilde{D}_s)$ and $\Im(\widetilde{D}_s)$ follow a bivariate normal distribution.

Covariance

Let

$$C = \mathbf{Cov}(\Re(\widetilde{D}_s), \Im(\widetilde{D}_s)) = \underbrace{\mathbf{E}[\Re(\widetilde{D}_s){\cdot}\Im(\widetilde{D}_s)]}_{C_L} - \underbrace{\mathbf{E}[\Re(\widetilde{D}_s)]{\cdot}\mathbf{E}[\Im(\widetilde{D}_s)]}_{C_R} \tag{4.102}$$

and $\forall n$, $\Phi_n = \varphi + p_n$. Then

$$\begin{aligned} C_L &= \mathbf{E}\left[\left(\sum_{l=0}^{N-1} \frac{\cos(\alpha{\cdot}l)\cdot\cos(\alpha{\cdot}l + \Phi_l)}{N}\right){\cdot}\left(\sum_{l=0}^{N-1} \frac{\sin(\alpha{\cdot}m)\cdot\cos(\alpha{\cdot}m + \Phi_m)}{N}\right)\right] \\ &= \sum_{l,m=0}^{N-1}\left(\frac{\cos(\alpha{\cdot}l){\cdot}\sin(\alpha{\cdot}m)}{N^2}{\cdot}\mathbf{E}\left[\cos(\alpha{\cdot}l + \Phi_l){\cdot}\cos(\alpha{\cdot}m + \Phi_m)\right]\right) \end{aligned} \tag{4.103}$$

while

$$C_R = \sum_{l,m=0}^{N-1}\left(\frac{\cos(\alpha{\cdot}l){\cdot}\sin(\alpha{\cdot}m)}{N^2}{\cdot}\mathbf{E}\left[\cos(\alpha{\cdot}l + \Phi_l)\right]{\cdot}\mathbf{E}\left[\cos(\alpha{\cdot}m + \Phi_m)\right]\right) \tag{4.104}$$

Since (p_n) are independent, (Φ_n) are also independent and $\forall l \neq m$

$$\mathbf{E}\left[\cos(\alpha{\cdot}l + \Phi_l){\cdot}\cos(\alpha{\cdot}m + \Phi_m)\right] = \mathbf{E}\left[\cos(\alpha{\cdot}l + \Phi_l)\right]{\cdot}\mathbf{E}\left[\cos(\alpha{\cdot}m + \Phi_m)\right] \tag{4.105}$$

The corresponding terms in C_L and C_R thus cancel out and

$$C = \frac{1}{N^2}\sum_{n=0}^{N-1}\cos(\alpha{\cdot}n){\cdot}\sin(\alpha{\cdot}n){\cdot}\underbrace{\left[\mathbf{E}\left[\cos^2(\alpha{\cdot}n + \Phi_n)\right] - \mathbf{E}\left[\cos(\alpha{\cdot}n + \Phi_n)\right]^2\right]}_{=\mathbf{Var}(\cos(\alpha{\cdot}n + \Phi_n))} \tag{4.106}$$

Using Popoviciu's inequality on variances to bound $\mathbf{Var}(\cos(...))$ yields

$$C \leq \frac{1}{N^2}\sum_{n=0}^{N-1}\underbrace{|\cos(\alpha{\cdot}n)|}_{\leq 1}\cdot\underbrace{|\sin(\alpha{\cdot}n)|}_{\leq 1}\cdot\underbrace{\mathbf{Var}(\cos(...))}_{\leq 1} \leq \frac{1}{N} \xrightarrow[N\to+\infty]{} 0 \tag{4.107}$$

Thus $\Re(\widetilde{D}_s) \perp\!\!\!\perp \Im(\widetilde{D}_s)$ asymptotically, and we finally demonstrated that $\widetilde{D}_s$—and thus $\widetilde{D}_N$—converges in law towards a complex normal distribution with increasing values of N. This can be rephrased as

$$\begin{cases} \widetilde{D}_N = x + i{\cdot}y \\ x \sim \mathcal{N}\left(\mu_x = \beta_p{\cdot}\cos(\varphi), \sigma^2\right) \\ y \sim \mathcal{N}\left(\mu_y = \beta_p{\cdot}\sin(\varphi), \sigma^2\right) \\ x \perp\!\!\!\perp y \end{cases} \quad \text{wherein } \sigma^2 = \frac{1}{N}{\cdot}\left(1 - \beta_p^2 + \frac{1}{\mathrm{SNR}}\right) \tag{4.108}$$

4.4.3.3.3 Convergence in Practice

While this convergence is theoretically proven for $N \to +\infty$, its practical validity was studied for relatively small values of N. To do so, simulations were performed for Signal to Noise Ratio in dB ($\mathrm{SNR_{dB}}$)= 0..30 dB, $\sigma_p = 0.1..10°$, $N = 10..100$. The multivariate normality of $\Re(\widetilde{D}_N)$ and $\Im(\widetilde{D}_N)$ was tested using Henze-Zirkler test[667] on 2.10^3 $\widetilde{D}_N$ outcomes. Their independence, was asserted using Hoeffding's D measures[668] between $\Re(\widetilde{D}_N)$ and $\Im(\widetilde{D}_N)$ using 10^5 $\widetilde{D}_N$ outcomes. In the case of the Henze-Zirkler test, simulations were repeated ten times, and their p-values—adjusted using the Benjamini-Hochberg correction[669] and combined with Fisher's method. The outcomes of these simulations were as follows. Henze-Zirkler multivariate test revealed no deviation from normality for N values above 20 using a significance level of 0.05. Hoeffding's D measures between $\Re(\widetilde{D}_N)$ and $\Im(\widetilde{D}_N)$, on their part, were found to be below 10^{-4} for as little as $N = 20$ measurement points, clearly demonstrating the practical independence of the two random variables. These two tests confirm that the convergence of $\widetilde{D}_N$) towards a complex normal distribution is observed in practice across a wide range of conditions, even for relatively small N values. Of note, this fast convergence is again demonstrated in Figure 4.19, further below, for as little as 20 samples.

4.4.4 Phase Estimation from the DFT

The phase φ of the signal S may be estimated by $\widehat{\varphi} = \arg(\widetilde{D}_N)$. Of paramount importance are thus the mean bias and RMSE of this estimator, *i.e.* the two quantities

$$\mathbf{E}[\varphi - \widehat{\varphi}] \quad \text{and} \quad \sqrt{\mathbf{E}\left[(\varphi - \widehat{\varphi})^2\right]} \tag{4.109}$$

In order to derive them, we can notice that $\widehat{\varphi} = \arg(x + i\cdot y)$, and focus on the joint probability function of (x, y), given by

$$f(x,y) = \frac{1}{2\cdot\pi\cdot\sigma^2}\cdot \mathrm{e}^{-\frac{1}{2\cdot\sigma^2}\cdot\left((x-\mu_x)^2+(y-\mu_y)^2\right)} \tag{4.110}$$

Then—thanks to the LOTUS—$\widehat{\varphi}$'s mean bias ($a = 1$) and RMSE ($a = 2$) may be computed using

$$\mathbf{E}\left[(\varphi - \widehat{\varphi})^a\right] = \iint_{\mathbb{R}^2} \arg\left(x + i\cdot y\right)^a \cdot f(x,y)\ dxdy \tag{4.111}$$

While direct numerical calculations are presented in Section 4.4.4.3, another approach involving a switch to polar coordinates is first presented in the next section, allowing an in-depth comprehension of the influence of noises by means of meaningful illustrations.

4.4.4.1 Marginalisation in Polar Coordinates

A representation of the estimation of φ in the complex plane can be seen in Figure 4.18. Naturally, different realisations of S would lead to different $\widetilde{D}_N$ values. Since $\widetilde{D}_N$ follows a complex normal distribution, this translates into the small black dots ($\cdot$) whose repartition is characteristic of a bivariate normal law, in the complex plane. This distribution is centred around its mean—$\mathbf{E}[\widetilde{D}_N]$—of Cartesian coordinates $(\mu_x, \mu_y)_c$, represented as a large black dot (●). Interestingly, this centre is distinct from its position in the noiseless case, represented as a large blue dot (●), due to the $\mathrm{e}^{-\sigma_p^2}$ term in $\mathbf{E}[\widetilde{D}_N]$, which is dragging the $\widetilde{D}_N$ distribution towards the origin. A given $\widetilde{D}_N$ realisation—depicted as a large red dot (●)—yields an estimation of φ, namely $\widehat{\varphi}$.

Formally, the following change of variable from Cartesian to polar coordinates may be performed:

$$\left[\begin{array}{cc} & \mathbb{R}^+ \times [0; 2\cdot\pi[\;\to \mathbb{R}^2 \\ \mathbf{F}: & \begin{pmatrix} r \\ \theta \end{pmatrix} \mapsto \begin{pmatrix} r\cdot\cos\ \theta \\ r\cdot\sin\ \theta \end{pmatrix} \end{array}\right] \quad \text{and} \quad \mathbf{J_F}(r,\theta) = r \tag{4.112}$$

wherein $\mathbf{J_F}$ is the Jacobian of $\mathbf{F}$. Expressing f as a function of r and θ yields

$$\begin{aligned} f(r,\theta) &= \frac{1}{2\cdot\pi\cdot\sigma^2}\cdot \mathrm{e}^{-\frac{1}{2\cdot\sigma^2}\cdot\left(r^2 - 2\cdot r\cdot\beta_p\cdot\cos(\theta-\varphi) + \beta_p^2\right)} \\ &= \frac{1}{2\cdot\pi\cdot\sigma^2}\cdot \mathrm{e}^{-\frac{(r-\beta_p\cdot\cos(\theta-\varphi))^2 + \beta_p^2\cdot\sin^2(\theta-\varphi)}{2\cdot\sigma^2}} \\ &= \frac{\mathrm{e}^{-\beta_p^2\cdot\frac{\sin^2(\theta-\varphi)}{2\cdot\sigma^2}}}{2\cdot\pi\cdot\sigma^2}\cdot \mathrm{e}^{-\frac{1}{2\cdot\sigma^2}\cdot(r-\beta_p\cdot\cos(\theta-\varphi))^2} \end{aligned} \tag{4.113}$$

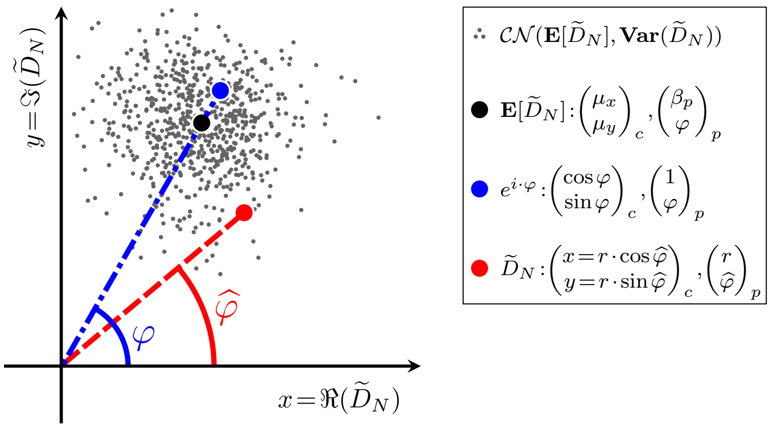

Figure 4.18: A representation of the estimation issue at hand in the complex plane. The $(\square)_c$ and $(\square)_p$ subscripts denote Cartesian and polar coordinates, respectively. See the text for further explanations.

Applying the above-mentioned change of variables, taking care to replace $dxdy$ by $\mathbf{J_F}(r,\theta)drd\theta$ in the integrand leads to the following expression for the marginal density probability of θ under φ:

$$\iint\limits_{(x,y)\in\mathbb{R}^2} f(x,y)dxdy = \iint\limits_{\substack{r\in\mathbb{R}^+\\ \theta\in[0;2\cdot\pi[}} f(r,\theta)\cdot r\ drd\theta \tag{4.114}$$

and f can be marginalised with respect to r alone, leading to

$$g_\varphi(\theta) \triangleq \int_0^{+\infty} f(\theta,r)\cdot r\ dr = \frac{\mathrm{e}^{-\beta_p^2\cdot\frac{\sin^2(\theta-\varphi)}{2\cdot\sigma^2}}}{2\cdot\pi\cdot\sigma^2}\cdot \underbrace{\int\limits_0^{+\infty} r\cdot\mathrm{e}^{-\frac{(r-\beta_p\cdot\cos(\theta-\varphi))^2}{2\cdot\sigma^2}}dr}_{\mathcal{G}_\theta} \tag{4.115}$$

$\mathcal{G}_\theta$ can be further decomposed into $\mathcal{H}_\theta$ and $\mathcal{K}_\theta$, following

$$\begin{aligned}\mathcal{G}_\theta = & \overbrace{\int\limits_0^{+\infty} (r-\beta_p\cdot\cos(\theta-\varphi))\cdot\mathrm{e}^{-\frac{(r-\beta_p\cdot\cos(\theta-\varphi))^2}{2\cdot\sigma^2}}dr}^{\mathcal{H}_\theta}\\ & +\beta_p\cdot\cos(\theta-\varphi)\cdot\underbrace{\int\limits_0^{+\infty}\mathrm{e}^{-\frac{1}{2\cdot\sigma^2}\cdot(r-\beta_p\cdot\cos(\theta-\varphi))^2}dr}_{\mathcal{K}_\theta}\end{aligned} \tag{4.116}$$

And $\mathcal{H}_\theta$ and $\mathcal{K}_\theta$ can be explicitly calculated using appropriate change of variables as

$$\mathcal{H}_\theta = \int\limits_{-\beta_p\cdot\cos(\theta-\varphi)}^{+\infty} t\cdot\mathrm{e}^{-\frac{t^2}{2\cdot\sigma^2}}dt = -\sigma^2\cdot\int\limits_{-\beta_p\cdot\cos(\theta-\varphi)}^{+\infty}\frac{d}{dt}\left(\mathrm{e}^{-\frac{t^2}{2\cdot\sigma^2}}\right)dt = \sigma^2\cdot\mathrm{e}^{-\beta_p^2\cdot\frac{\cos^2(\theta-\varphi)}{2\cdot\sigma^2}} \tag{4.117}$$

and

$$\begin{aligned}\mathcal{K}_\theta &= \int\limits_{-\beta_p\cdot\cos(\theta-\varphi)}^{+\infty}\mathrm{e}^{-\frac{t^2}{2\cdot\sigma^2}}dt = \int\limits_{-\beta_p\cdot\cos(\theta-\varphi)}^{+\infty}\mathrm{e}^{-\left(\frac{t}{\sqrt{2}\cdot\sigma}\right)^2}dt = \sigma\cdot\sqrt{2}\cdot\int\limits_{-\beta_p\cdot\frac{\cos(\theta-\varphi)}{\sigma\cdot\sqrt{2}}}^{+\infty}\mathrm{e}^{-u^2}du\\ &= \sigma\cdot\sqrt{\frac{\pi}{2}}\cdot\underbrace{\frac{2}{\sqrt{\pi}}\cdot\int\limits_{-\beta_p\cdot\frac{\cos(\theta-\varphi)}{\sigma\cdot\sqrt{2}}}^{+\infty}\mathrm{e}^{-u^2}du}_{\mathrm{erfc}(\ldots)} = \sigma\cdot\sqrt{\frac{\pi}{2}}\cdot\mathrm{erfc}\left(-\beta_p\cdot\frac{\cos(\theta-\varphi)}{\sigma\cdot\sqrt{2}}\right)\end{aligned} \tag{4.118}$$

and thus:

$$\mathcal{G}_\theta = \sigma^2 \cdot \mathrm{e}^{-\beta_p^2 \frac{\cos^2(\theta-\varphi)}{2\cdot\sigma^2}} + \sigma\cdot\beta_p\cdot\sqrt{\frac{\pi}{2}}\cdot\cos(\theta-\varphi)\cdot\mathrm{erfc}\left(-\beta_p\cdot\frac{\cos(\theta-\varphi)}{\sigma\cdot\sqrt{2}}\right) \tag{4.119}$$

Finally, putting it all together leads to

$$\boxed{g_\varphi(\theta) = \frac{\mathrm{e}^{-\frac{\beta_p^2}{2\sigma^2}}}{2\cdot\pi} + \frac{\beta_p\cdot\cos(\theta-\varphi)\cdot\mathrm{e}^{-\beta_p^2\cdot\frac{\sin^2(\theta-\varphi)}{2\cdot\sigma^2}}}{2\cdot\sqrt{2\cdot\pi}\cdot\sigma}\cdot\mathrm{erfc}\left(-\beta_p\cdot\frac{\cos(\theta-\varphi)}{\sigma\cdot\sqrt{2}}\right)} \tag{4.120}$$

$g_\varphi(\theta)$ is represented in Figure 4.19, along with the histogram of simulated $\widehat{\varphi}$ values—*i.e.* $\arg(\widetilde{D}_N)$ values, $\widetilde{D}_N$ being computed from simulated S vectors. $g_\varphi(\theta)$ resembles a normal distribution which would have been wrapped around the $[0, 2\cdot\pi]$ interval—although it is not a wrapped normal distribution nor a von Mises distribution strictly speaking (for further information on these distributions, see Collett, Mardia, Ley *et al.*[670–672]). As could have been expected intuitively, the shape of $g_\varphi(\theta)$ narrows as N or $\mathrm{SNR_{dB}}$ increase, or as σ_p decreases, as emphasised in the inset of Figure 4.19.

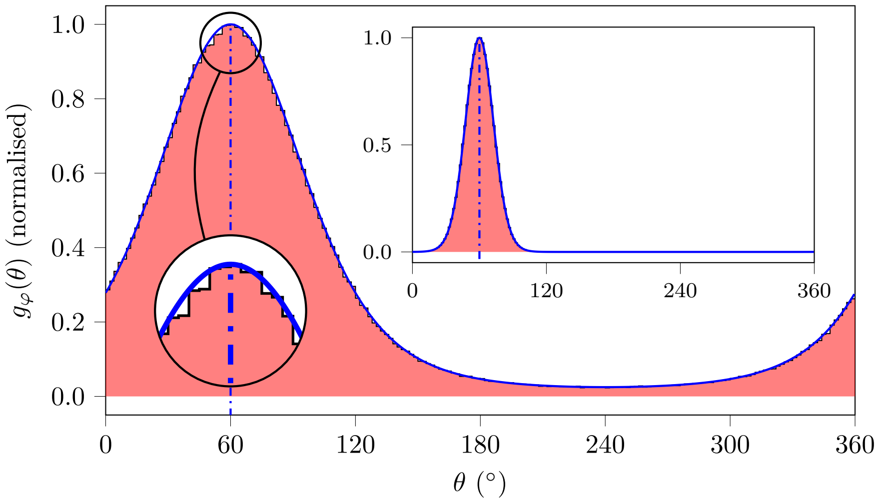

Figure 4.19: Normalised representations of $g_\varphi(\theta)$ and of the histogram of simulated $\widehat{\varphi}$ values (10^6 draws, φ=60°). **Main picture:** $N = 20$, $\mathrm{SNR_{dB}}$=-10 dB and $\sigma_p = 5°$. The magnifying glass clearly shows how the histogram of simulated $\widehat{\varphi}$ is close to the analytic expression of $g_\varphi(\theta)$. **Inset:** $N = 20$, $\mathrm{SNR_{dB}}$=0 dB and $\sigma_p = 1°$.

4.4.4.2 Expressing the Error in the Polar Case

Since $g_\varphi(\theta)$ is the probability density function to measure a phase shift $\widehat{\varphi} = \theta$ given a true phase shift φ, the mean bias and RMSE of the $\widehat{\varphi}$ estimator, may be expressed as

$$\begin{aligned} \underset{\text{(bias)}}{\mathbf{E}[\varphi - \widehat{\varphi}]} &= \int_0^{2\cdot\pi} err_\varphi(\theta)\cdot g_\varphi(\theta) d\theta, \text{ and} \\ \mathrm{RMSE} &= \sqrt{\int_0^{2\cdot\pi} err_\varphi^2(\theta)\cdot g_\varphi(\theta) d\theta} \end{aligned} \tag{4.121}$$

wherein $err_\varphi(\theta)$ is the estimation error at a given polar angle θ, as represented in Figure 4.20, and is defined as

$$err_\varphi(\theta) = \min\left(d, 2\cdot\pi - d\right) \tag{4.122}$$

with $d \equiv \theta - \varphi \pmod{2\cdot\pi}$, that is

$$err_\varphi(\theta) = \pi - |\pi - \theta| \tag{4.123}$$

It can also be demonstrated that the RMSE and bias are independent of φ, as could have been expected intuitively. Only the RMSE case is detailed below, but a similar train of thought

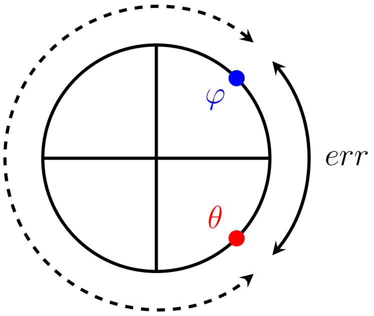

Figure 4.20: Illustration of err on the trigonometric circle: err always represent the minimum angular distance between the true φ value and an angle θ.

can be followed for the bias. Since the square root function is bijective on $\mathbb{R}^+$, we only have to demonstrate that $\forall(\varphi,\varphi') \in [0, 2\cdot\pi[^2$

$$\underbrace{\int_0^{2\cdot\pi} err_\varphi^2(\theta)\cdot g_\varphi(\theta)d\theta}_{\mathcal{J}_\varphi} = \underbrace{\int_0^{2\cdot\pi} err_{\varphi'}^2(\theta)\cdot g_{\varphi'}(\theta)d\theta}_{\mathcal{J}_{\varphi'}} \tag{4.124}$$

Then, with the change of variable $t = \theta - \varphi + \varphi'$,

$$\mathcal{J}_\varphi = \int_{-\varphi+\varphi'}^{2\cdot\pi-\varphi+\varphi'} err_\varphi^2(t+\varphi-\varphi')\cdot g_\varphi(t+\varphi-\varphi')d\theta \tag{4.125}$$

Using the definitions of err and g comes

$$\begin{aligned}\mathcal{J}_\varphi &= \int_{-\varphi+\varphi'}^{2\cdot\pi-\varphi+\varphi'} err_{\varphi'}^2(t)\cdot g_{\varphi'}(t)dt \\ &= \underbrace{\int_{-\varphi+\varphi'}^{0} err_{\varphi'}^2(t)\cdot g_{\varphi'}(t)dt}_{\mathcal{M}_\varphi} + \int_0^{2\cdot\pi-\varphi+\varphi'} err_{\varphi'}^2(t)\cdot g_{\varphi'}(t)dt\end{aligned} \tag{4.126}$$

Using the change of variable $u = t + 2\cdot\pi$, and since err and g are $2\cdot\pi$-periodic,

$$\mathcal{M}_\varphi = \int_{2\cdot\pi-\varphi+\varphi'}^{2\cdot\pi} err_{\varphi'}^2(u-2\cdot\pi)\cdot g_{\varphi'}(u-2\cdot\pi)du = \int_{2\cdot\pi-\varphi+\varphi'}^{2\cdot\pi} err_{\varphi'}^2(u)\cdot g_{\varphi'}(u)du \tag{4.127}$$

Leading to

$$\begin{aligned}\mathcal{J}_\varphi &= \int_0^{2\cdot\pi-\varphi+\varphi'} err_{\varphi'}^2(t)\cdot g_{\varphi'}(t)dt + \int_{2\cdot\pi-\varphi+\varphi'}^{2\cdot\pi} err_{\varphi'}^2(u)\cdot g_{\varphi'}(u)du \\ &= \int_0^{2\cdot\pi} err_{\varphi'}^2(t)\cdot g_{\varphi'}(t)dt = \mathcal{J}_{\varphi'}\end{aligned} \tag{4.128}$$

The RMSE is thus independent of φ, and taking $\varphi = 0$ leads to $err(\theta) = |\theta|\ \forall\theta \in [-\pi,\pi]$, yielding finally

$$\boxed{\text{RMSE} = \sqrt{\int_{-\pi}^{+\pi} \theta^2\cdot g_0(\theta)d\theta}} \tag{4.129}$$

However, due to the complexity of $g_0(\theta)$, we did not manage to derive a closed-form expression of the RMSE in the general case, and used numerical simulations to compute the latter as a function of σ_x—or, equivalently, the SNR—σ_p, and N.

The bias, on the other hand, can be readily computed since it can be shown similarly that:

$$\mathbf{E}(\widehat{\varphi} - \varphi) = \int_{-\pi}^{+\pi} \theta\cdot g_0(\theta)d\theta \tag{4.130}$$

and since $[\theta \mapsto \theta\cdot g_0(\theta)]$ is an odd function, it follows that the bias is null and that **$\widehat{\varphi}$ is an unbiased estimator of φ**, which further justifies its choice as φ estimator in the first place.

4.4.4.3 Numerical Calculation of the RMSE

Despite giving a better understanding of the issue at hand, and allowing one to clearly visualize the influence of N, σ_p or σ_x on the probability density function of $\widehat{\varphi}$—as demonstrated by Figures 4.18 and 4.19—the polar coordinates considerations did not give a closed form expression for the RMSE of $\widehat{\varphi}$. The latter may thus be calculated numerically using either Equation 4.111 (Cartesian case) or Equation 4.129 (polar case):

$$\text{RMSE} = \sqrt{\iint_{\mathbb{R}^2} \arg\left(x + i{\cdot}y\right)^2 \cdot f(x, y)\ dxdy} = \sqrt{\int_{-\pi}^{+\pi} \theta^2{\cdot}g_0(\theta)d\theta} \tag{4.131}$$

While these two expression of the RMSE obviously yield the same quantity, the Cartesian approach is much more computationally expensive than the polar one, due to the double integration over the discretised, truncated $\mathbb{R}^2$ plane. Thus, all the results below were obtained using the polar approach. The influence of both the SNR_dB—and thus σ_x—and the phase noise σ_p on the RMSE is depicted in Figure 4.21. Simulated RMSE values were also added to the latter figure, computed in a similar fashion to Figure 4.19. The closeness between these simulated values and the theoretical predictions consolidates the above-presented approach.

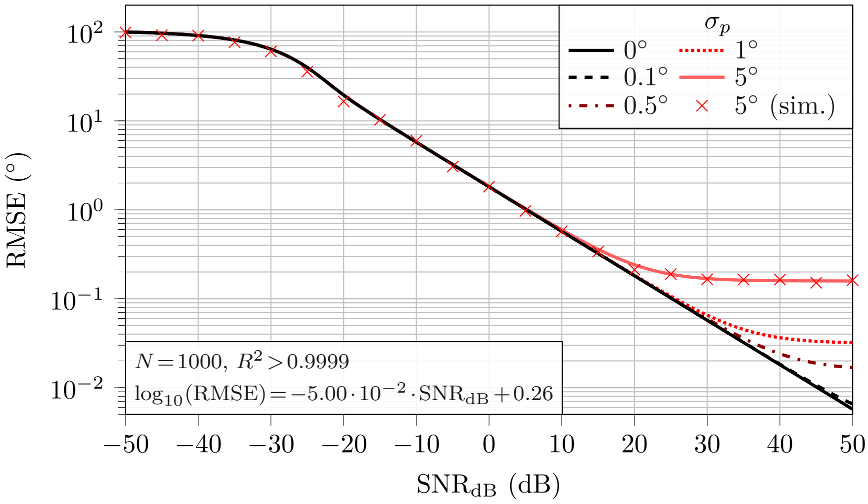

Figure 4.21: The RMSE on φ estimation as a function of SNR_dB for various σ_p values. In the absence of phase noise—*i.e.* the black, continuous line (—)—a linear regression can be performed for $\text{SNR}_\text{dB} \geq -20$ dB, yielding the displayed equation and associated determination coefficient. As indicated, all calculations were performed taking N=1000 points. Simulated values were computed using only 10^2 realisations so that some dispersion is perceivable. Indeed, using 10^6 realisations as was done in Figure 4.19 led to marks indistinguishable from the plain red line.

The evolution of the RMSE as a function of the SNR_dB can be split into three behaviours:

- At very low SNR_dB values—*i.e.* below −30 dB—the RMSE saturates, to reach approximately 100°. This corresponds to an exceedingly noisy case, for which $\widehat{\varphi}$ is basically no more than a random guess on $[0; 2{\cdot}\pi[$. In this case, $g_\varphi(\theta)$ converges towards a uniform distribution, and the RMSE tends towards $\pi/\sqrt{3}$ rad (≈104°), as shown in Section 4.4.5.1.
- At higher SNR_dB value and in the absence of phase noise—*i.e.* when $\text{SNR}_\text{dB} > -20$ dB and σ_p=0—the RMSE follows a linear relationship with the SNR (or a log-linear relationship with SNR_dB, as indicates the equation on the graphic). In this case, $g_\varphi(\theta)$ converges towards a normal distribution centred around φ, and the RMSE tends towards $1/\sqrt{N{\cdot}\text{SNR}}$, as demonstrated in Section 4.4.5.2.
- Finally, when $\text{SNR}_\text{dB} \geq -20$ dB but the phase noise is significant—typically above 0.5° in Figure 4.21—the RMSE becomes independent of SNR_dB at some point as SNR_dB increases, and becomes a function of σ_p alone. This latter case is developed in Section 4.4.5.3.

The influence of N on $\widehat{\varphi}$ RMSE is presented in Figure 4.22. Starting with the left part of the figure, while the three above-mentioned behaviours can be observed irrespective of N value, increasing N by a factor m has two main effects. First, it shifts the saturation threshold in case of extreme noise—*i.e.* for SNR_{dB} values in the [-50,-20] dB range—by a factor $10 \cdot \log_{10}(m)$ (in dB) to the left. Then, it divides the RMSE at higher SNRs—*i.e.* for SNR_{dB} values in the [-20,50] dB range—by a factor $\sqrt{m}$. Looking at the right part of Figure 4.22, $\widehat{\varphi}$ RMSE appears to decrease linearly with increasing N values, while increasing the SNR shifts the RMSE lines downwards.

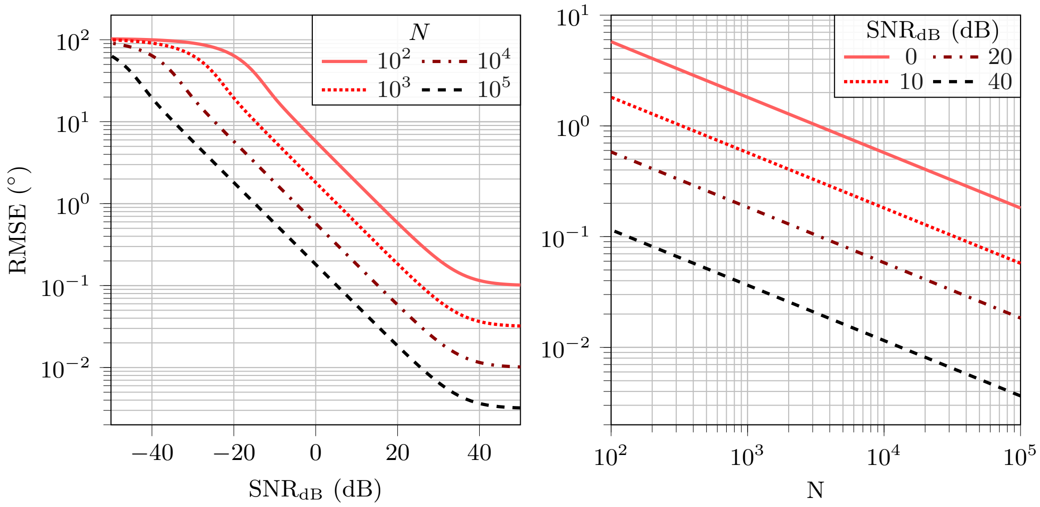

Figure 4.22: The RMSE on φ estimation as a function of SNR_{dB} and N, with σ_p=1°.

Of note, the reader should bear in mind that the SNR_{dB} thresholds given above, as well as the numerical values given below, are of course dependent on N and A_s. As a general rule, A_s is considered unitary in all our simulations, and N=1000 unless otherwise stated. Still, the same above-described behaviours would be observed with different N and A_s values, only the numerical values stated in our developments would be altered. Of note, σ_p values were also deliberately chosen relatively high for the sake of illustration. In practice, modern analogue-to-digital converters can feature phase noises in the $[10^{-2}$–$10^{-3}]$° range[673, 674].

Finally, Figure 4.23 depicts the evolution of $\widehat{\varphi}$ RMSE with σ_p. Here, the behaviour observed in Figure 4.21 can be examined from another perspective: at low enough phase noise levels—*i.e.* when σ_p is below approximately 0.01°—the RMSE is solely function of N and the SNR. However, as soon as σ_p increases, it starts to act as a noise floor, and increases the RMSE progressively. This effect is particularly pronounced at relatively high N and SNR values, potentially ruining an otherwise excellent accuracy, as can be seen in the left part of the figure for $N = 10^5$ and $\text{SNR}_{\text{dB}} = 50$ dB.

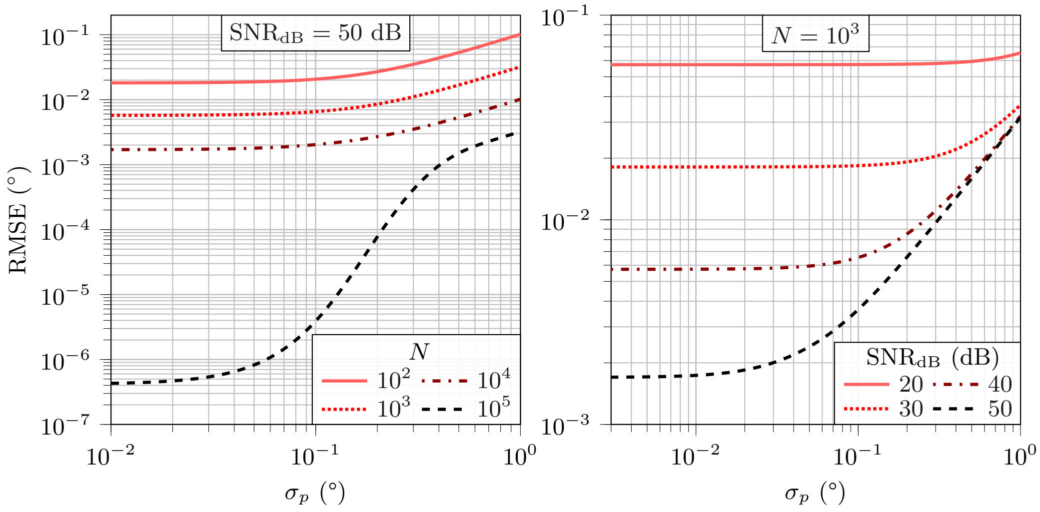

Figure 4.23: The RMSE on φ estimation as a function of σ_p, for various N and SNR values.

4.4.4.4 Estimation Efficiency

The efficiency of the performed estimation can be found by computing the Cramér-Rao Lower Bound (CRLB) of $\widehat{\varphi}$. The likelihood $\mathcal{L}\left(\widehat{\varphi}|\widetilde{D}_N\right)$ of observing $\widetilde{D}_N$ under a given $\widehat{\varphi}$—hereafter noted $\mathcal{L}$ for the sake of conciseness—is given by

$$\mathcal{L} = \prod_{z=\{x,y\}} \frac{1}{\sqrt{2{\cdot}\pi{\cdot}\sigma^2}}{\cdot}\mathrm{e}^{-\frac{(z-\mu_z)^2}{2\cdot\sigma^2}} \tag{4.132}$$

The log-likelihood is then

$$\log\left(\mathcal{L}\right) = -\log\left(2{\cdot}\pi{\cdot}\sigma^2\right) - \sum_{z=\{x,y\}} \frac{\left(z-\mu_z\right)^2}{2{\cdot}\sigma^2} \tag{4.133}$$

and its first and second derivatives are given by

$$\frac{\partial \log\left(\mathcal{L}\right)}{\partial\widehat{\varphi}} = \frac{1}{\sigma^2}\sum_{z=\{x,y\}}\left(z-\mu_z\right)\cdot\frac{\partial\mu_z}{\partial\widehat{\varphi}} \tag{4.134}$$

and

$$\frac{\partial^2 \log\left(\mathcal{L}\right)}{\partial\widehat{\varphi}^2} = \frac{1}{\sigma^2}\sum_{z=\{x,y\}}\left[\left(z-\mu_z\right)\cdot\frac{\partial^2\mu_z}{\partial\widehat{\varphi}^2} - \left(\frac{\partial\mu_z}{\partial\widehat{\varphi}}\right)^2\right] \tag{4.135}$$

The Fisher information $\mathcal{I}\left(\widehat{\varphi}\right)$ may then be derived as

$$\begin{aligned}\mathcal{I}\left(\widehat{\varphi}\right) = -\mathbf{E}\left[\frac{\partial^2\log\left(\mathcal{L}\right)}{\partial\widehat{\varphi}^2}\right] &= \frac{1}{\sigma^2}\sum_{z=\{x,y\}}\left[\left(\frac{\partial\mu_z}{\partial\widehat{\varphi}}\right)^2 - \mathbf{E}\underbrace{\left[z-\mu_z\right]}_{=0}\cdot\frac{\partial^2\mu_z}{\partial\widehat{\varphi}^2}\right] \\ &= \frac{\beta_p^2}{\sigma^2}\end{aligned} \tag{4.136}$$

Finally leading to

$$\boxed{\mathrm{CRLB} = \frac{1}{\mathcal{I}\left(\widehat{\varphi}\right)} = \frac{\sigma^2}{\beta_p^2}} \tag{4.137}$$

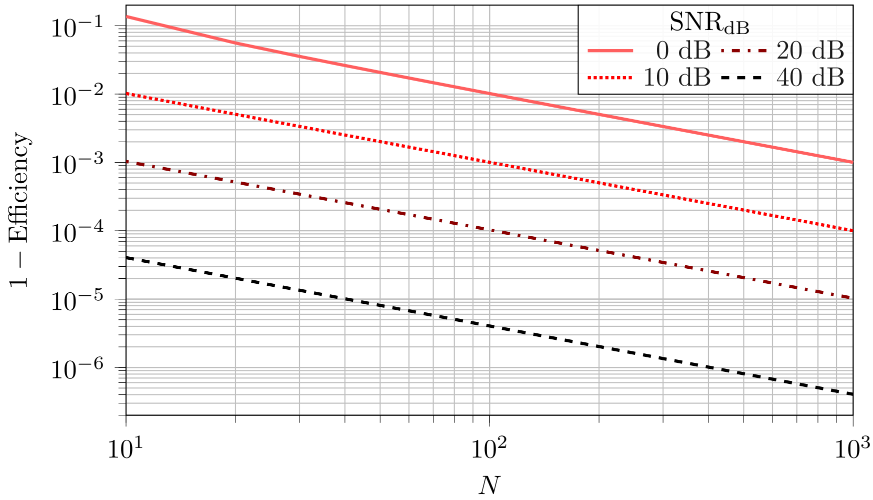

Figure 4.24: Asymptotical efficiency of $\widehat{\varphi}$. σ_p was set to 1°.

The convergence of $\widehat{\varphi}$ towards its CRLB is illustrated in Figure 4.24. $\widehat{\varphi}$ appears to be an asymptotically efficient estimator of φ with a fast convergence rate, exhibiting $1-$Efficiency values below 10^{-3} for as little as 1000 samples even in the presence of strong noise (SNR=0 dB). As a remainder, the efficiency of an unbiased estimator—which is the case for $\widehat{\varphi}$—is defined as[665, p. 279]

$$\mathrm{Efficiency} = \frac{\mathrm{CRLB}}{\mathbf{Var}(\widehat{\varphi})} = \frac{\mathrm{CRLB}}{\mathrm{RMSE}^2} \tag{4.138}$$

4.4.5 Asymptotical Behaviours of the RMSE

4.4.5.1 Saturation in Case of Excessive Additive Noise

For $\mathrm{SNR}_{\mathrm{dB}}$ values below approximately -30 dB, the RMSE appears to be converging towards approximately 100°—see Figure 4.21. This phenomenon corresponds to an extremely noisy case, wherein the estimated φ value is no better than a random guess on the $[0; 2\cdot\pi[$ interval. In this case, $g_0(\theta)$ converges toward a uniform distribution as $\mathrm{SNR}_{\mathrm{dB}}$ decreases, as illustrated in Figure 4.25.

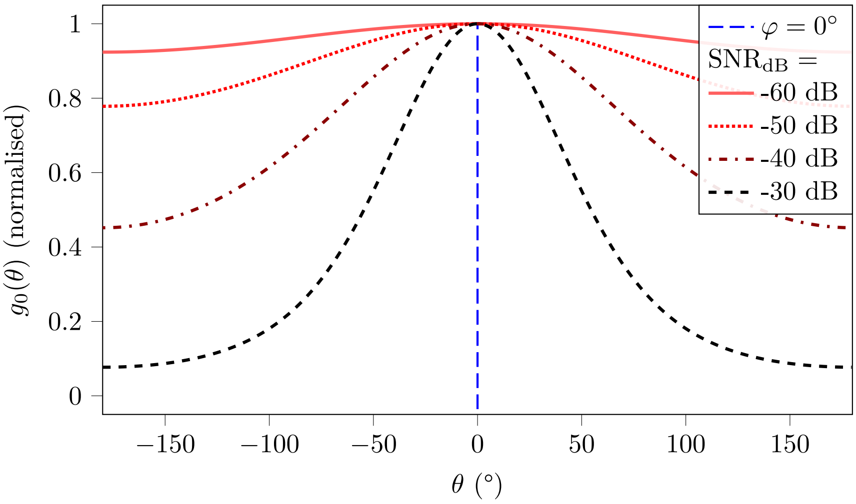

Figure 4.25: $g_0(\theta)$ for different $\mathrm{SNR}_{\mathrm{dB}}$ values. For increasing $\mathrm{SNR}_{\mathrm{dB}}$ values, $g_0(\theta)$ converges towards a uniform distribution. N=1000, σ_p=0.

Indeed, as $\mathrm{SNR}_{\mathrm{dB}}$ decreases, σ increases and we can make the following approximation

$$g_0(\theta) = \frac{1}{2\cdot\pi}\cdot \underbrace{\mathrm{e}^{-\frac{\beta_p^2}{2\sigma^2}}}_{\xrightarrow[\sigma\to+\infty]{}1} + \overbrace{\underbrace{\frac{\overbrace{\beta_p\cdot\cos(\theta)}^{|\ldots|\leq 1}}{2\cdot\sqrt{2\cdot\pi}\cdot\sigma}}_{\xrightarrow[\sigma\to+\infty]{}0} \cdot \underbrace{\mathrm{e}^{-\beta_p^2\cdot\frac{\sin^2(\theta)}{2\cdot\sigma^2}}}_{<1} \cdot \underbrace{\mathrm{erfc}\left(\underbrace{-\beta_p\cdot\frac{\cos(\theta)}{\sigma\cdot\sqrt{2}}}_{\approx 0}\right)}_{\xrightarrow[\sigma\to+\infty]{}1}}^{\xrightarrow[\sigma\to+\infty]{}0} \tag{4.139}$$

$$g_0(\theta) \xrightarrow[\sigma\to+\infty]{} \frac{1}{2\cdot\pi}$$

In other words, $g_0(\theta)$ can be approximated by a uniform distribution on the $[-\pi, \pi[$ interval. The Kullback-Leibler divergence between $g_0(\theta)$ and a uniform distribution can also be computed, and is presented in Figure 4.26. As expected, the divergence decreases steeply with a decreasing $\mathrm{SNR}_{\mathrm{dB}}$, further confirming the above-mentioned convergence phenomenon.

Subsequently the RMSE becomes

$$\mathrm{RMSE} = \sqrt{\int_{-\pi}^{\pi} \theta^2\cdot\frac{1}{2\cdot\pi} d\theta} = \frac{\pi}{\sqrt{3}} \tag{4.140}$$

hence the saturation behaviour observed for the RMSE at high σ_c values in Figure 4.21. The 100° plateau value noted above simply comes from the radian to degree conversion ($\pi/\sqrt{3}$ rad$\approx$104°). That being said, contrary to the linear case given in the next section, this saturation phenomenon is of little practical interest since it corresponds to an extremely noisy case, which only yields random guesses as phase estimation. It was thus only presented here for the sake of completeness.

4.4.5.2 Linear Relationship With the SNR

The observed linear relationship between the RMSE and the SNR can be explained by the fact that, for increasing SNR values, $g_0(\theta)$ converges towards a normal distribution, as illustrated in Figure 4.27.

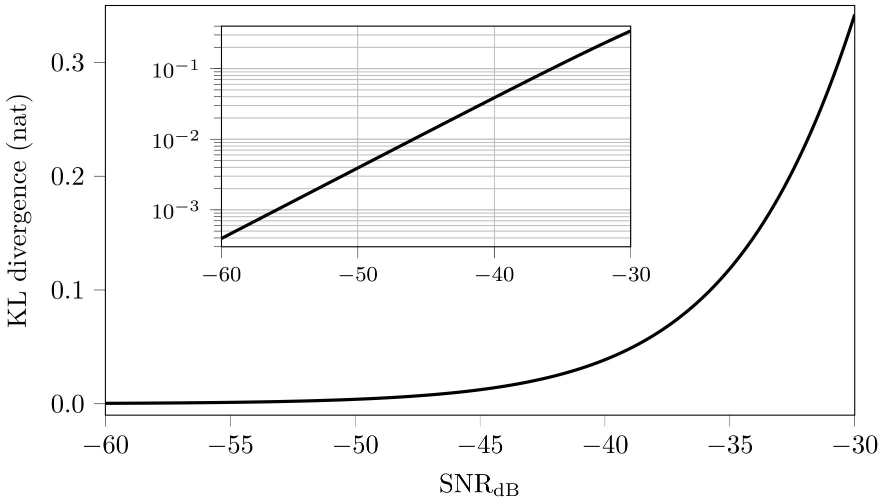

Figure 4.26: The Kullback-Leibler divergence between $g_0(\theta)$ and a uniform distribution as a function of $\mathrm{SNR_{dB}}$. The inset shows the same data on a logarithmic scale. N=1000, σ_p=0.

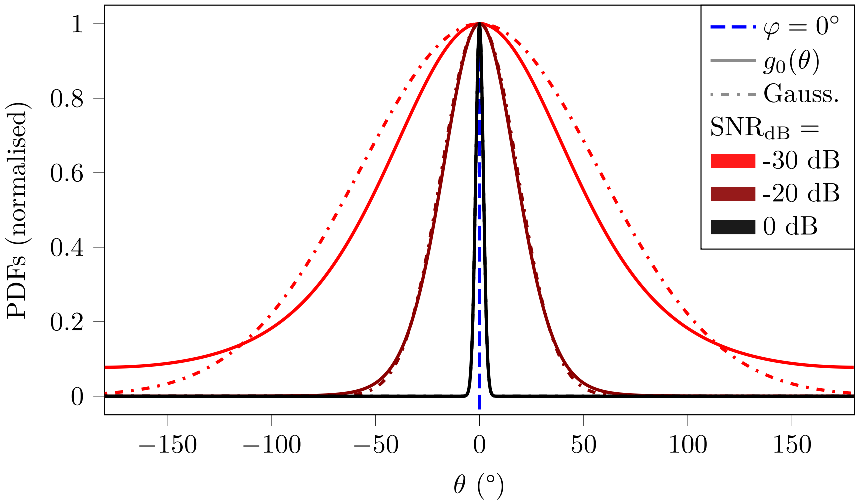

Figure 4.27: Normalised probability density functions: $g_0(\theta)$ is plotted with its associated simplified Gaussian model. For $\mathrm{SNR_{dB}}$ above −10 dB, $g_0(\theta)$ becomes indistinguishable from its Gaussian approximation. N=1000, σ_p=0.

Indeed, taking $\varphi = 0$ and high $\mathrm{SNR_{dB}}$ values leads to an extremely narrow $g_0(\theta)$ function—as was already noted above in Figure 4.19—which is non-negligible only for very small θ deviations from zero. More formally:

$$\begin{gathered}
\mathbf{Var}(\widetilde{D}_N) \xrightarrow[\mathrm{SNR_{dB}} \to +\infty]{} 0 \quad (*) \\
(*) \implies \widetilde{D}_N \xrightarrow[\mathrm{SNR_{dB}} \to +\infty]{L_2} \mathbf{E}[\widetilde{D}_N] \\
(*) \implies \theta = \arg(\widetilde{D}_N) - \varphi \xrightarrow[\mathrm{SNR_{dB}} \to +\infty]{P} 0
\end{gathered} \tag{4.141}$$

wherein $\xrightarrow{L_2}$ and $\xrightarrow{P}$ denote convergence in mean square and convergence in probability, respectively. By definition of the latter convergence, $g_0(\theta)$ is thus non-negligible only for very small deviations from zero with a non-null probability. Under these conditions, and in the absence of phase noise, $\beta_p = 1$ and σ tends towards zero as $\mathrm{SNR_{dB}}$ tends towards infinity. We can then make the following approximation:

$$\begin{aligned}
g_0(\theta) &= \underbrace{\frac{\mathrm{e}^{-\frac{\beta_p^2}{2\sigma^2}}}{2{\cdot}\pi}}_{\approx 0} + \frac{\beta_p}{2{\cdot}\sqrt{2{\cdot}\pi}{\cdot}\sigma} \cdot \underbrace{\cos(\theta)}_{\approx 1} \cdot \mathrm{e}^{-\beta_p^2 \cdot \frac{\overbrace{\sin^2(\theta)}^{\approx \theta^2}}{2\cdot\sigma^2}} \cdot \underbrace{\mathrm{erfc}\left(\underbrace{-\beta_p {\cdot} \frac{\overbrace{\cos(\theta)}^{\approx 1}}{\sigma{\cdot}\sqrt{2}}}_{\ll -1} \right)}_{\approx 2} \\
&\approx \frac{1}{\sqrt{2{\cdot}\pi}{\cdot}\sigma} {\cdot} \mathrm{e}^{-\frac{\theta^2}{2\cdot\sigma^2}}
\end{aligned} \tag{4.142}$$

Thus, for high enough SNR values, $g_0(\theta)$ can be reasonably well approximated by a simple normal distribution of null mean, and variance σ^2. The fast convergence towards this approximation is further illustrated in Figure 4.28, wherein the Kullback-Leibler divergence and Bhattacharyya distance between $g_0(\theta)$ and its Gaussian approximation are represented as a function of $\mathrm{SNR_{dB}}$. It appears that for $\mathrm{SNR_{dB}}$ values above -10 dB, this distance becomes virtually null ($\approx 10^{-5}$).

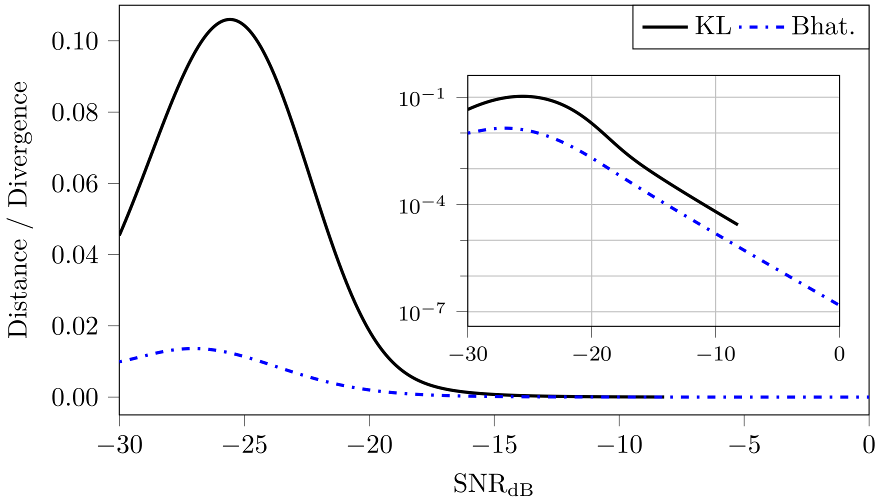

Figure 4.28: The Kullback-Leibler divergence (KL) and Bhattacharyya distance (Bhat.) between $g_0(\theta)$ and its Gaussian approximation as a function of $\mathrm{SNR_{dB}}$. The inset shows the same data on a logarithmic scale. N=1000, σ_p=0.

As a reminder, the Bhattacharya distance quantifies the *closeness* between two distributions. Given two random variables P and Q with probability density function $p(x)$ and $q(x)$ the Bhattacharya distance and Kullback-Leibler divergence are defined as follows[675]:

(i) Bhattacharya distance:

$$d_B(P \| Q) = -\log\left(\int p(x){\cdot}q(x)\; dx \right) \tag{4.143}$$

(ii) Kullback-Leibler divergence:

$$d_{KL}(P \| Q) = \int p(x){\cdot} \log\left(\frac{p(x)}{q(x)} \right) dx \tag{4.144}$$

One may notice that the division by $q(x)$ in d_{KL} may be problematic in case of numerical applications if $q(x)$ is near zero. Such an issue can be observed in Figure 4.28 for $\mathrm{SNR}_{\mathrm{dB}}$ values above roughly -8 dB: d_{KL} cannot be computed even using 64-bits double-precision floats, because the Gaussian probability density function tends towards zero extremely fast as soon as θ deviates from zero. This is the reason why the Bhattacharya distance was introduced in the first place, so as to better cover the case of high $\mathrm{SNR}_{\mathrm{dB}}$ values.

Subsequently the RMSE becomes

$$\mathrm{RMSE} = \sqrt{\int_{-\pi}^{\pi} \theta^2 \cdot \frac{1}{\sqrt{2 \cdot \pi} \cdot \sigma} \cdot \mathrm{e}^{-\frac{\theta^2}{2 \cdot \sigma^2}} d\theta} = \sigma = \frac{1}{\sqrt{N \cdot \mathrm{SNR}}} \tag{4.145}$$

hence the linear relationship observed in Figure 4.22 between $\log_{10}(\mathrm{RMSE})$ on the one hand, and $\mathrm{SNR}_{\mathrm{dB}}$ and N on the other hand. This result is especially interesting for practical applications. Indeed, a $\mathrm{SNR}_{\mathrm{dB}}$ above -10 dB can easily be reached in practice, ensuring the validity of the above-mentioned Gaussian approximation for $g_0(\theta)$, and the ensuing conclusions on the RMSE. Of particular interest, if this condition is fulfilled, **the expected RMSE on the phase estimation can be directly inferred from N and the SNR**, using Equation 4.145. Still, one should bear in mind that this conclusions holds only if $\beta_p \approx 1$, otherwise the developments presented in the next section should apply.

4.4.5.3 Saturation in the Presence of Phase Noise

When some amount of phase noise is present—*i.e.* $\beta_p \in]0;1[$—and for high enough SNR, the following approximation can be made, as was done in Equation 4.142:

$$g_0(\theta) \approx \frac{\beta_p}{\sqrt{2 \cdot \pi} \cdot \sigma} \cdot \mathrm{e}^{-\frac{\beta_p^2 \cdot \theta^2}{2 \cdot \sigma^2}} \tag{4.146}$$

Again, $g_0(\theta)$ can be approximated by a simple normal distribution, but of variance σ^2/β_p^2, instead of σ^2 alone in the previous section. The convergence towards a Gaussian is nearly identical with that presented in Section 4.4.5.2 and thus Figures 4.27 and 4.28 were not reproduced for the sake of conciseness. Similarly to Equation 4.145 comes

$$\mathrm{RMSE} = \frac{\sigma}{\beta_p} = \sqrt{\frac{1}{\beta_p^2 \cdot N} \cdot \left(1 - \beta_p^2 + \frac{1}{\mathrm{SNR}}\right)} \tag{4.147}$$

which, in case of high enough SNR—*i.e.* $1 - \beta_p^2 \gg 1/\mathrm{SNR}$—becomes

$$\mathrm{RMSE} \approx \sqrt{\frac{1}{N} \cdot \left(\frac{1}{\beta_p^2} - 1\right)} \tag{4.148}$$

This result is also interesting because it provides a lower limit for the RMSE, even at exceedingly large SNR values: **the RMSE is ultimately limited by the phase noise, which acts as a noise floor**. This explains the saturations observed on the right part of Figure 4.21 and 4.22: the lower limits reached by the different curves with non-zero phase noises directly depend on their respective σ_p values, following Equation 4.148. Most interestingly, Equation 4.147 gives a generic expression for the RMSE at reasonably high SNR values taking into account the joint influences of: *(i)* the number of points N, *(ii)* the amplitude of the phase noise—through β_p—and *(iii)* that of the additive noise—through the SNR.

4.4.6 Concluding Remarks on Phase Estimation Accuracy

This study presents a thorough analysis of the influence of additive and phase noises on the accuracy of the phase measurement of a known-frequency sinusoidal signal. More specifically, we focused on synchronous detection, a measurement scheme for which the number of collected samples N on the one hand, and the sampling and probing frequency f_s and f_0 on the other hand can be chosen so that $f_0 \cdot N/f_s$ is an integer. In this particular case, a closed-form expression of the PDF of the phase estimate $\widehat{\varphi}$ could be derived, depending on N and on the levels of additive and phase noises—σ_x and σ_p, respectively. $\widehat{\varphi}$ was also shown to be asymptotically efficient, with a fast convergence towards its CRLB, even using a limited number of samples in the presence of substantial noise levels.

When using the above-mentioned PDF to compute $\widehat{\varphi}$ RMSE, three main behaviours could be identified: *(i)* in case of excessive noise, the RMSE saturates towards the random guess situation, *(ii)* as the SNR increases, the RMSE decreases linearly with the square roots of the SNR and N, and *(iii)* as the SNR further decreases, the RMSE saturates again, reaching a noise floor caused by phase noise. While *(i)* is of little practical interest, *(ii)* and *(iii)* are of major importance in practical scenarios, since they can tell the experimenter whether lowering the RMSE should be achieved by taking more samples or by increasing the SNR—*e.g.* by increasing the emission power. Indeed, in case *(iii)*, increasing the SNR is no use once the phase noise floor is reached, and only taking more samples can yield lower RMSE values.

In addition to its theoretical significance, this study is thus also of practical value, allowing for informed decision-making when designing a phase-measuring apparatus. In particular, in the context of f-DLR mentioned in Section 4.3.3, a compromise often has to be made between reducing the number of samples and the illumination power—which preserves the involved dyes from photobleaching, and saves power in case of battery-powered devices—and reducing the RMSE by increasing the two latter parameters—at the expense of power consumption, computing costs, and dye photobleaching. Of particular importance, we recently published a short communication demonstrating a real-world implementation of f-DLR applied to CO_2 sensing[91], whose main outcomes are presented in Section 5.5.3. In this communication, we validated the theoretical results derived in the present study in the case of a low phase noise and a relatively high SNR—*i.e.* Equation 4.145.

Finally, one possible limitation of this work resides in its simplified modelling of phase noise. Indeed, phase noise—studied through its influence on the power spectral density of a clock signal in the frequency domain[676], or by the distribution of the jitter it induces in the time domain[677]—can result from several phenomena that can be either purely random or partially deterministic[678, Chap. 2–4]. While a thorough review on the origins and statistical properties of phase noise is clearly out of the scope of this thesis, and although some oscillators do exhibit Gaussian phase jitters in practice[679–681], this may not be the case in general[677]. As a result, future research could focus on extending our work to address non-Gaussian and/or non-*i.i.d.* phase noise.

4.5 Conclusion

The full range of CO_2 sensing techniques was first reviewed, extracting key figures of merit for each of the presented techniques—Section 4.1. Those techniques were then confronted to the requirements of transcutaneous CO_2 sensing that were outlined in the previous chapter—Section 4.2. In particular, *(i)* the constraints for a small volume to surface ratio, *(ii)* for a low drift, and *(iii)* the presence of humidity at the skin oriented my choice towards dye-based CO_2 sensing. This sensing technique was then presented in great details in Section 4.3, by introducing both the sensing chemistry taking place inside the sensor and the optical sensing schemes that may be used to probe the latter. To this end, f-DLR was selected because of its inherent referencing—and thus independence towards fluctuations in LED intensity or photodiode sensitivity—and its reduced number of optical elements compared to ratiometric measurements, although at the cost of an increased complexity in signal processing. The subtleties of f-DLR were then discussed in Section 4.3.3, concluding that an accurate phase measurement of the fluorescence signal was essential to its proper functioning.

This led me to conduct a thorough mathematical analysis of the influences of both additive and phase noise on the accuracy of the phase measurement of a sinusoidal signal—4.4. This analysis resulted in a particularly interesting result in case the phase noise is not excessive, with the RMSE of the phase measurement following

$$\mathrm{RMSE}(\varphi_{\mathrm{mes}}) = \frac{1}{\sqrt{N \cdot \mathrm{SNR}}} \tag{4.149}$$

The latter relation can then be used in real-world situations to adjust the illuminating power—which influences the SNR—or the duration of an acquisition—which changes N—to dynamically make a compromise between power consumption and photobleaching on the one hand, and phase measurement accuracy on the other hand. With these theoretical foundations in place, we are now well prepared to tackle the next chapter, which covers the concrete implementation of the afore-mentioned principles into an f-DLR CO_2 sensor fit for transcutaneous sensing.

Chapter 5

CO_2 Sensing Using Fluorescent Thin Films

TL;DR

This chapter primarily contains chemical considerations about the practical implementation of an f-DLR, dye-based, thin film CO_2 sensor. In particular, the photobleaching and quenching issues generally plaguing luminescence measurements are briefly presented, along with strategies to mitigate their effect. Candidate dyes and polymers are then benchmarked to select the most suitable dye / polymer pairs for CO_2 sensing. The optoelectronics used to probe the manufactured thin films are also briefly presented. Finally, experimental results demonstrating accurate *in vitro* CO_2 sensing are reported. Photobleaching, quenching, and humidity cross-sensitivity are also studied, leaving open research avenues for the future.

Previous chapter Main Table Of Content (TOC) Next chapter

While the previous chapters of this doctoral work are mainly focused on

1. the motivations behind transcutaneous CO_2 sensing (Chapter 1),
2. the feasibility of the latter given the properties of
   (a) haemoglobin (Chapter 2) and
   (b) skin CO_2 exhalation (Chapter 3),
3. the choice of a given CO_2 measurement technique, and
4. the theoretical developments surrounding its implementation (Chapter 4),

the present chapter focuses on the practical implementation of the said technique into a fully functional sensor. More specifically, the pH-sensitive and reference luminophores need to be dispersed and immobilised into a polymer matrix, which should ideally maintain satisfying humidity levels while limiting the photobleaching of the luminophores.

Section 5.1 thus discusses different encapsulation strategies, presenting the photobleaching and quenching phenomena, as well as the deleterious influence of O_2 on the latter. Sections 5.2 and 5.3 are then dedicated to the choice of the two luminophores and polymers that will be used in the final sensors, respectively. Subsequently, Section 5.4 presents briefly the optoelectronics that were used to probe the luminescent sensing films, while the complete design study of the optical setup is relegated to Appendix E. Finally, Section 5.5 showcases the actual realisation of CO_2-sensing thin films using the above-mentioned luminophores, polymers, and optoelectronics. Basic sensing properties are demonstrated, some theoretical predictions are validated experimentally, and several caveats are also briefly exposed, opening new research avenues that are detailed in the next—and final—chapter. Of note, the impatient reader interested only in a minimalist summary of these practical works might be interested in reading our short—four pages—2024 NEWCAS article entitled *Dual Lifetime Referencing for Accurate CO_2 Sensing: An Experimental in vitro Validation*[91].

5.1 Encapsulation Strategies

As mentioned in Section 4.3.2—and contrary to FRET—f-DLR does not require both luminophores to be in close contact with each other. This is fortunate, since both luminophores call for very different encapsulations: while the pH-sensitive fluorophore needs a strongly hygroscopic medium with a good CO_2 permeability—see Section 5.3.2—the reference phosphor needs a gas-tight encapsulation to prevent its exposure to O_2, which would likely worsen its photobleaching. Section 5.1.1 details the latter issue, while Section 5.1.2 presents resulting encapsulation strategies.

5.1.1 Photobleaching and O_2 Influence

Not to be confused with the luminescence *decay* phenomenon—which is defined as the decreasing luminescence intensity following a pulsed illumination, and characterised by a luminescence lifetime τ, as mentioned in Section 4.3.2.2.3—the *photobleaching* phenomenon—*a.k.a.* photoinduced or photochemical degradation, fading, or photodegradation—corresponds to the irreversible destruction of luminophore molecules under illumination. This fundamental difference is illustrated in Figure 5.1, Left.

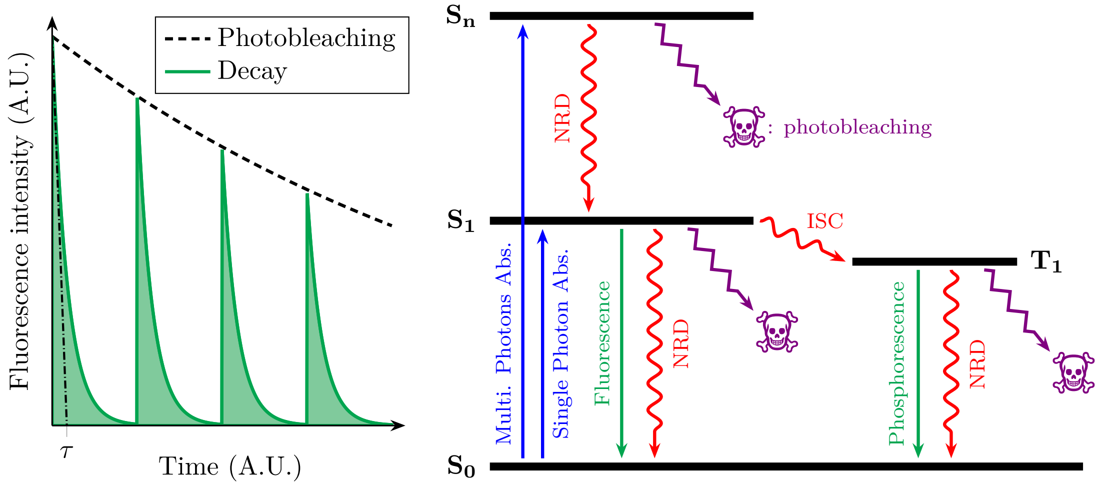

Figure 5.1: **Left:** difference between photobleaching and luminescence decay. In green is the luminescence intensity of a luminophore excited by a train of pulses. Each pulse causes a reproducible luminescence decay of lifetime τ (considering a mono-exponential decay, which is not necessarily the most accurate model, although being widely spread[640]). Meanwhile, the repetition of pulses progressively destroys dye molecules, causing a slow but irreversible decrease in overall luminescence intensity: photobleaching is observed. Adapted from Song *et al.*[682]. **Right:** simplified Perrin-Jablonski diagram of a luminophore, illustrating single and multiple photon absorption(1), non radiative decays (NRD), intersystem crossing (ISC), fluorescence, phosphorescence, and possible photobleaching pathways. See the text for further explanations. Elaborated from Demchenko[683] and Valeur[220, Chap. 3].

Photobleaching has been a long known phenomenon, but—despite intense research efforts—its intricacies remain relatively obscure, even by the admission of recently published reviews on the topic[683, 686]. While a thorough discussion on photobleaching is beyond the scope of this thesis, the curious reader may refer to the works of Diaspro *et al.*[687], Zheng *et al.*[686] and Demchenko[683], which, taken together, constitute an excellent introduction that covers the main aspects of the subject. Briefly, photobleaching describes photoinduced chemical reactions that lead to the conversion of the luminescent molecule into a by-product which is non-luminescent, hence decreasing the overall luminescence intensity of a given sample with time and illumination intensity. The photoinduced part comes from the fact that excited singlet or triplet states tend

---

(1) These single photon and multiple photon absorption paths are presented for illustration purposes only. In particular, the energy of a multiple photon absorption is not necessarily an integer multiple of the energy of a single photon absorption. See He *et al.*[684] and Rumi *et al.*[685] for a thorough introduction to multiple photon absorption.

to be more chemically reactive than the basal S_0 state[(2)], leading to photobleaching pathways alike those depicted in Figure 5.1, Right. While O_2 and other reactive oxygen species (ROS) are often cited as being the main culprits for photobleaching, their deleterious influence seems to be especially significant for the T_1 photobleaching pathway, and other pathways may originate from dye-dye, or dye-solvent reactions taking the S_1 photobleaching pathway, for instance[688].

The main difficulty in studying the photobleaching phenomenon comes from the fact that every dye is subjected to different photobleaching mechanisms, which also depend on:

1. its concentration, with higher concentrations favouring dye-dye interactions[689],
2. the illumination intensity, with higher intensities favouring multiple photon absorption and thus excitation to higher S_n states and subsequent photobleaching from there[690],
3. its surrounding medium, with marked differences between in-solution and *in vitro* photobleaching behaviours[690],
4. the solvent used[691].

As a result, accurate photobleaching pathways are known only for a limited number of intensively studied luminophores—*e.g.* erythrosine, as well as various fluorescein, rhodamine, and coumarin derivatives[682, 686, 692]—and remain to be brought into light for the vast majority of luminophores.

Despite exhibiting some degree of usefulness in characterising the transport of luminescent molecules in cells[693], photobleaching is more often than not considered to be a bane plaguing luminescence measurements, and its existence alone fully justifies the development of the ratiometric technique presented in Section 4.3.2.1.3 to mitigate dye concentration decrease with time. More generally, fighting against photobleaching is no easy task, since the means for combatting it must be adapted to the photobleaching pathways involved. For instance, higher order S_n pathways may be avoided by keeping the illumination power low, thereby limiting multiple photon absorption[687, 690]. Targeting the same objective, using multiple low-intensity pulses instead of rarer high-intensity ones also results in less photobleaching[694, 695]. Molecular engineering is another trail to follow to derive more stable compounds from already-known luminophores[696], and lowering dye concentration may also reduce photobleaching rate[689]. Then, so-called anti-fading agents may be added, which have different modes of operation: they may prevent either oxidation or reduction of the dyes following their ionisation in S_n states, or quench their long-lived triplet state to favour a quick return to S_0 and thereby decrease the probability of a dye molecule to react with singlet oxygen or other ROS[687]. Finally, removing oxygen or ROS from the medium is one obvious solution since it often greatly reduces photobleaching, especially if the latter originates from long-lived triplet states[682, 690].

In this thesis, I solely focused on this last aspect, leaving the use of anti-fading agents as a potential avenue for future improvements—see Chapter 6. This was done primarily because it was thought that photobleaching issues would predominantly concern the long-lived luminophore that was used—Ru-dpp. Indeed, the latter remains in its long-lived triplet state for several microseconds—see Section 5.2.3—thus being particularly sensitive to photodegradation by molecular oxygen. Of note, there was a second reason that pushed me to focus on reducing Ru-dpp exposure to oxygen, which is oxygen luminescence *quenching.* This phenomenon is characterised by a *reversible* decrease in luminescence intensity and lifetime caused by the presence of O_2[697], which has even been used as the basic working principle to elaborate O_2 sensors using luminescent dyes[698]. Since *(i)* the decrease in luminescence intensity caused by both the irreversible photobleaching and reversible quenching phenomena, and *(ii)* the decrease in luminescence lifetime caused by the quenching phenomenon would influence the outcome of f-DLR measurements, sustained efforts have been made to limit Ru-dpp exposure to oxygen as much as possible, mainly by encapsulating it into a low oxygen permeability polymer.

5.1.2 Resulting Encapsulation Strategies

In the literature of thin film CO_2 sensors, efforts have been focused on reducing the exposure of phosphors to O_2, whether in the case of DLR- or IFE-based sensors[469, 471, 473–475]. This is understandable, since phosphors remain in the triplet state for a long time, which favours both the quenching of their luminescence *and* their photobleaching. Popular polymers for the

---

[(2)] If the reader is not familiar with Perrin-Jablonski diagrams nor the notion of singlet / triplet states, they might refer to the first three chapters of Bernard Valeur's *Molecular Fluorescence*[220].

encapsulation of these sensitive dyes are poly(vinylidene chloride-co-vinyl chloride) (PVCD)[469, 471], polyacrylonitrile (PAN)[475, 699] and polystyrene[478]. Various encapsulation strategies have been explored, a representative example of which can be seen in Figure 5.2. To the best of my knowledge, the only authors to compare different encapsulation strategies in the same study are Perez *et al.*[469]. Their investigations led them to conclude that sandwiching the substrate layer between the two dye layers—scheme *(iv)*, top row in Figure 5.2—is preferable to the other schemes presented since *(a)* it prevents diffusion of the base buffer into the PtOEP particles, which would otherwise degrade them, and *(b)* it reduces oxygen quenching compared to the lower row schemes (only 1.2% of quenching when using plain membrane compared to 7% when using microparticles). Consequently, it is the strategy that I also applied in my experimentations—see Section 5.5.

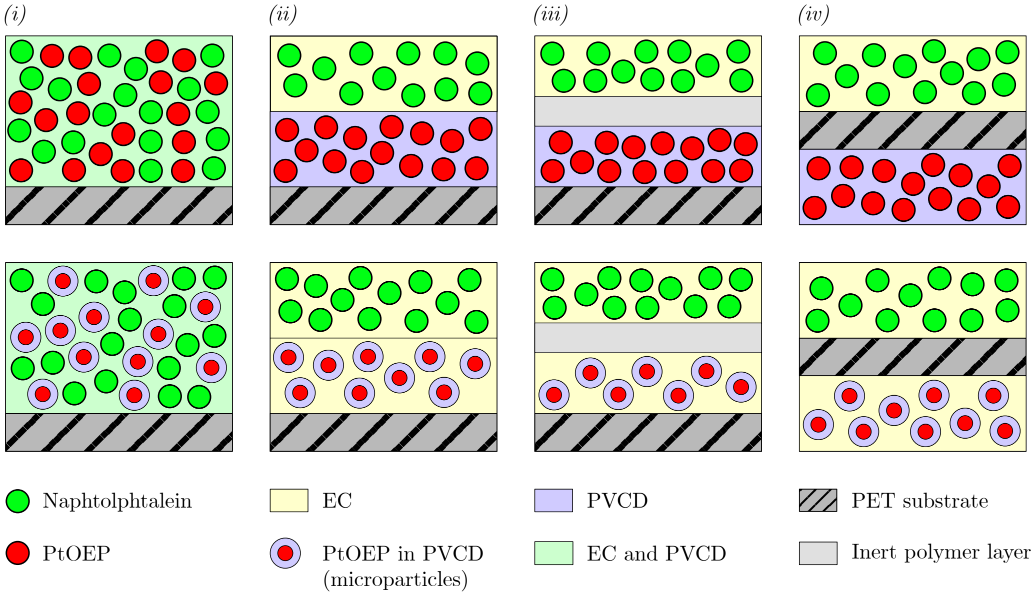

Figure 5.2: Different PtOEP encapsulation strategies for an IFE-based sensor. α-naphtolphtalein is used as pH-sensitive dye while PtOEP acts as reference phosphor. **Top row:** *(i)*: a solution of α-naphtolphtalein in ethyl cellulose (EC) is mixed with a solution of PtOEP in PVCD and then cast onto a PET substrate, *(ii)*: the two solutions are cast successively on top of each other, *(iii)*: same as *(ii)* but with an intermediate inert polymer layer, *(iv)*: the two solutions are cast on different sides of the PET substrate. **Bottom row:** same as top row, except that the solution of PtOEP in PVCD is replaced with a suspension of microparticles of PtOEP encapsulated in PVCD into an ethyl cellulose solution. Adapted from Perez *et al.*[469].

Still, despite the latter observation that microparticles seem to perform worse than plain polymer films, significant research efforts have also been deployed to manufacture micro- or nanoparticles for phosphors encapsulation[642, 700–703]. This apparent contradiction can be explained by the need for luminescent microparticles in medical imaging[704, 705], or by the need for encapsulated ruthenium complexes for drug delivery[706]. Additionally, the results of Perez with PVCD[469] may not be extrapolated to other luminophore / polymer pairs[701, Chap. 5].

As a side note, we tried to synthesise Ru-dpp-doped PAN nanobeads with Jeanne Beyrle—an intern who worked on the manufacturing of fluorescent thin films for six months during my thesis—following the routes described by Edwards[702, Chap. 2] and Ye *et al.*[703], but without success. In the first case, non-spherical aggregates were obtained that did not encapsulate Ru-dpp adequately—the latter redissolved when ethanol was added to the obtained particles. In the second case, polymerisation of acrylonitrile into PAN could not be achieved, likely due to the presence of inhibitors, although this matter could not be investigated any further due to a lack of time. Ultimately, I stuck with the encapsulation strategy advised by Perez *et al.* in the remainder of this work—*i.e.* casting separately the pH-sensitive dye in a hydrophilic permeable polymer and the reference dye in an O_2-impermeable one.

Name	Substance number	Spectra	Φ_f	τ_f	Sourced	Ref.	
PhotochemCAD	339	Yes	Yes	No	Yes	[708, 709]	Scholars
Mol. fluo. Appendix	84	No[1]	Yes	Yes	Yes	[710]	
TU Graz	955	Yes	Yes[2]	Yes[2]	Yes[2]	[711]	
Max-Planck Institute	637	Yes	Yes[2]	Yes[2]	Yes	[712]	
McNamara	1627	Yes	Yes[2]	No	Yes	[713]	
Thermo Fisher	470	Yes	No	No	No	[714]	Industrials
Leica	257	No[1]	No	No	No	[715]	
Zeiss	276	Yes	No	No	No	[716]	
FluoroFinder	823	Yes	No	No	No	[717]	

Table 5.1: Main luminophore databases and resources available. (1): principal excitation and emission wavelengths provided. (2): not available for all substances.

5.2 Selecting the Luminophores

To be usable in an f-DLR sensing scheme, the two luminophores must meet two main criteria: their excitation spectra must overlap, and τ_{R} should be several orders of magnitude higher than τ_{A^-}. Additionally, the A^- / AH pH-sensitive fluorophore must have a pK_A in the 6–8 range, while R should remain as unaffected by external factors as possible. Ideally, both luminophores must exhibit a good photostability, be reasonably cheap, and possibly available off-the-shelf.

5.2.1 Luminophore Review

A brief literature and internet search was conducted to find luminophores that might meet the above criteria. However, given the vast amount of research available on the topic—a Google Scholar query on "`phosphorescence OR fluorescence OR luminescence`" returns over four million entries—and the limited time that was available, the search for luminophore candidates had to be narrowed down to a select few, in a manner that was not strictly objective.

Nevertheless, this research brought into light several luminophore databases, which are summarised in Table 5.1. These databases may be helpful for anyone eager to continue this work with other luminophores than those selected in the present work. In addition to these databases, one may also refer to the extensive review written by Benezin *et al.*[707] on the topic of lifetime fluorescence measurements. Going even further, one may also read through several recent publications on the topic of available collections of luminophores, written by the team of Lindsey, Taniguchi, *et al.*[708, 709], the very creators and maintainers of the PhotochemCAD database.

5.2.1.1 Short-Lived pH-Sensitive Fluorophore

Many pH-sensitive fluorophores have been developed and deeply studied, both for pH sensors in general[718], and for *in vivo* (intra-)cellular imaging in particular[719]. Commonly used substances include for instance BCECF, SNARF, BODIPY, and fluorescein derivatives[719–721]. However, most of the substances reviewed in the afore-mentioned references are either unavailable off-the-shelf, or extremely expensive—*i.e.* often over 1 k€/g. Two notable exceptions are pure fluorescein and HPTS, which are both cheap, pH-sensitive, and easily available off-the-shelf. Their absorption and emission spectra are presented in Figure 5.3. Both fluorophores have quantum yields near unity, but the absorption of fluorescein is almost four times that of HPTS, hence its markedly higher fluorescence intensity. However, the pK_A of fluorescein is 6.30[722], while that of HPTS is at or above 7.3 depending on the solvent[723–725] which might make the latter a better candidate for DLR applications (see Section 6.2.10). Consequently, HPTS was chosen as pH-sensitive fluorophore in my experimentations.

5.2.1.2 Long-Lived Reference luminophore

The choice of the long-lived reference luminophore is much more limited than that of the pH-sensitive short-lived one, because most fluorescence imaging applications use short-lived fluorophores with τ_{L} in the 1–50 ns range[707, 720, 727]. Consequently, when the three databases

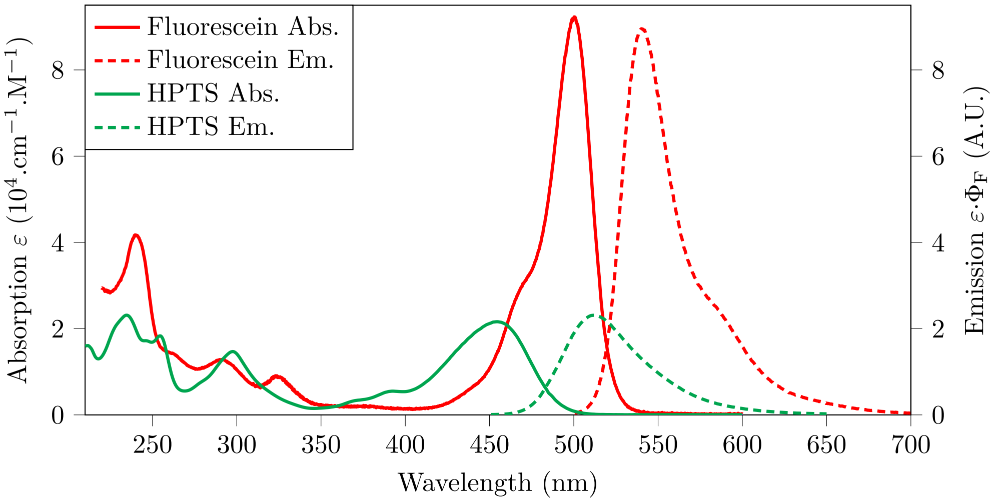

Figure 5.3: Absorption and emission spectra of the anionic—*i.e.* basic—form of HPTS and fluorescein. The emission intensity is computed as the peak absorbance times the fluorescence quantum yield. HPTS was measured in water at a pH of 10 (NaOH solution), fluorescein was measured in ethanol. More information on the pH-dependence of fluorescein may be found in the work of Martin *et al.*[726], while the case of HPTS is treated in Section 5.2.2. Data source: PhotoChemCAD database[709].

presented in Table 5.1 were searched for luminophores with lifetime exceeding 100 ns, only a few molecules were identified: ref. [710] yielded pyrene, ref. [712] yielded nothing, and ref. [711] yielded eight compounds: four iridium, one palladium, and three platinum complexes, with lifetimes in the 8.5–195 µs range. To this list of ten compounds, we added Ru-dpp, tris(1,10 phenanthroline) ruthenium (II) dichloride (Ru-pn) and tris(2,2'-bipyridyl) ruthenium (II) dichloride (Ru-bpy), three popular long-lived ruthenium complexes. These substances are summarised in Table 5.2. It should be stressed once again that this selection—although grounded in an in-depth database search—is by no means exhaustive, as exemplified by the many more luminophores compiled by Wang and Wolfbeis in their impressive review of oxygen-sensing materials[728]—some of which have long lifetimes and acceptable quantum yields for our application. Their work might therefore serve as a future source of inspiration, in order to try out other luminophores than the one that I ended up working with.

As one may notice, iridium-based luminophores are not readily available off the shelf, and most palladium and platinum complexes are extremely expensive, with the exception of PtOEP. Thus, we can narrow down our investigations to the following five remaining compounds: PtOEP, Ru-dpp, Ru-pn, Ru-bpy and pyrene. The absorption and emission spectra of these compounds are plotted in Figure 5.4 along with those of HPTS.

Choosing the optimal long-lived luminophore in these conditions may prove to be a difficult task. Indeed, both the long- and short-lived luminophores must exhibit spectral overlaps—as mentioned in Section 4.3.2.2.3—and the long-lived one must also be reasonably cheap. To address this issue, the following approach was used:

- For each of the long-lived fluorophores, a basic sensing scheme was considered. This sensing scheme consists in: an ideal monochromatic light source for excitation, an ideal low-pass reception filter tuned $\delta_{\mathrm{LP}} = 50$ nm above the wavelength of the light source, and located in front of a typical UV-enhanced Si photodiode (*e.g.* FDS010, Thorlabs, USA, 5% of peak sensitivity at 200 nm). The 50 nm difference between the light source and the low-pass filter was set arbitrarily to ensure that—even if the light source is a regular LED in reality—no light it emits may reach the detector[(3)].
- For a given excitation wavelength λ_{ex}, the emission spectra of the luminophore under study—$\mathcal{S}_{\mathrm{L,em}}(\lambda_{\mathrm{ex}})$—is multiplied by its relative absorbance at the excitation wavelength—$\varepsilon_{\mathrm{L},\lambda_{\mathrm{ex}}}/\varepsilon_{\mathrm{L},\lambda_{\mathrm{abs,max}}}$—its quantum yield—$\Phi_{\mathrm{L}}$—and the so-obtained spectrum is then multiplied by that of the sensitivity of the photodiode—$\mathcal{S}_{\mathrm{PD}}$. Finally, the resulting spectrum

---

[(3)] This is an ideal case, as actual LEDs may bleed quite significantly even at wavelengths up to 50 nm away from their peak. Here, "significantly" refers to values as low as 10^{-3}–10^{-4} times their maximum luminosity, since fluorescence signals are typically quite weak compared to the excitation signals that trigger them. See Section E.4 for further details on this topic.

Name	CAS	$\lambda_{abs}/\lambda_{em}$ (nm)	$\Phi_L \cdot \varepsilon_{H,\lambda_{abs}}$ (A.U.)	τ_L (µs)	Price	Ref.	
$(C_S)_2Ir(\mu\text{-}Cl)_2Ir(C_S)_2$	N/A	457 / 587	$0.21 \cdot 136900$	13.1	N/A	[647, 711]	Ir(III)
$(C_N)_2Ir(\mu\text{-}Cl)_2Ir(C_N)_2$	N/A	433 / 567	$0.30 \cdot 133600$	9.7	N/A	[647, 711]	
$Ir(C_N)_2$(acac)	952584-93-9	421 / 545	$0.53 \cdot 86900$	8.5	N/A	[647, 711]	
$Ir(C_S)_2$(acac)	N/A	472 / 563	$0.54 \cdot 92800$	11.3	N/A	[647, 711]	
Ir-OEP-CO-Cl	N/A	404 / 672	$0.14 \cdot 165000$	97	N/A	[711]	
PdTPTBP	119654-64-7	444 / 797	$0.17 \cdot 264000$	195	238 € / 25 mg	[711, 729]	Pd(II)
PtTPTBP	166174-05-6	430 / 770	$0.7 \cdot 203000$	53	411 € / 50 mg	[730]	Pt(II)
PtOEP	31248-39-2	382 / 647	$0.41 \cdot 264000$	90	550 € / 1 g	[731, 732]	
PtOEPK	172617-46-8	398 / 760	$0.12 \cdot 86200$	61	439 € / 10 mg	[731, 733]	
Ru-dpp	36309-88-3	463 / 618	$0.37 \cdot 28600$	6.4	635 € / 2 g	[734](1)	Ru(II)
Ru-pn	304695-79-2	445 / 595	$0.02 \cdot 20000$	0.45	154 € / 1 g	[734]	
Ru-bpy	14323-06-9	286 / 625	$0.04 \cdot 86100$	0.64	21 € / 1 g	[711, 735, 736]	
Pyrene	129-00-0	241 / 381	$0.65 \cdot 80000$	0.45	95 € / 500 g	[710, 712]	

Table 5.2: A selection of long-lived organo-metallic luminophores. CAS: Chemical Abstracts Service identification number. (1): the given values are sourced from Alford *et al.*[734]. However, it should be noted that a much wider range of values can be found in the literature—see Section 5.2.3. This variability applies to most of the chemicals listed here, so the provided numerical values are indicative only, as they may differ between publications—*e.g.* depending on the solvent used, reference standard used for Φ_L measurement, buffer or additive added, *etc.* Prices are given as of February 2022.

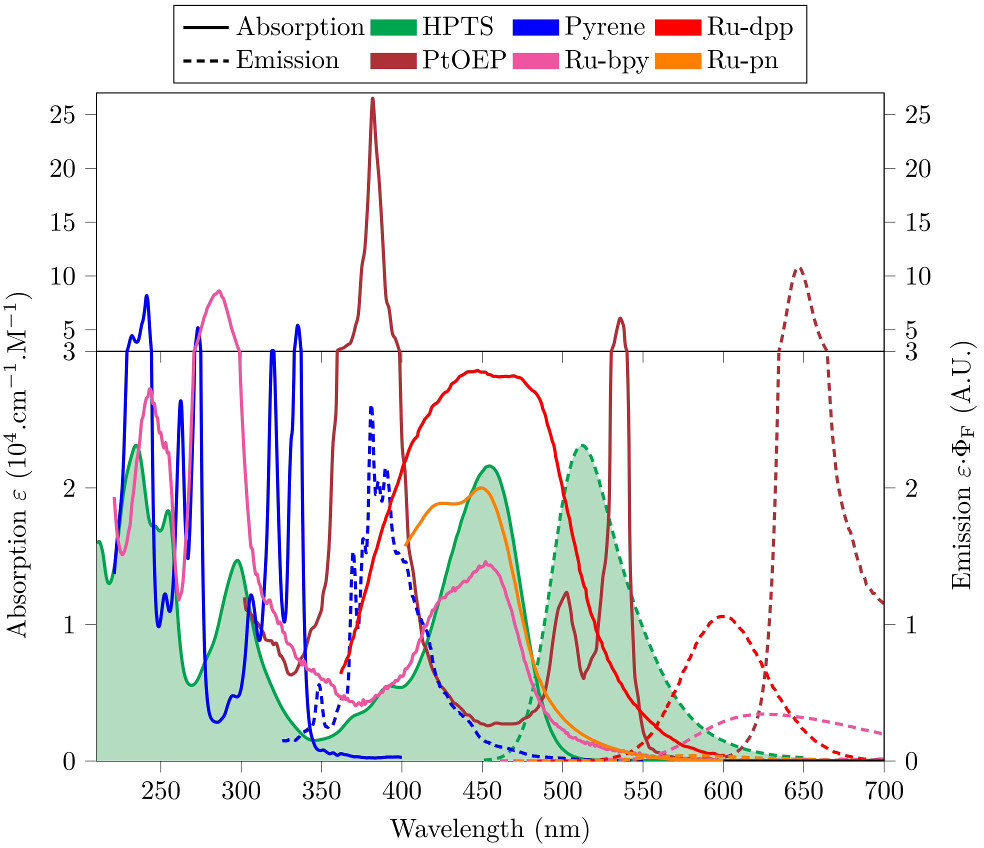

Figure 5.4: Absorption and emission spectra of selected luminophores. Data source: PhotochemCAD (HPTS and pyrene), TU Graz (PtOEP, Ru-pn, Ru-bpy, with quantum yields and extinction coefficients from Table 5.2), and Bultzingslöwen *et al.*[473] (Ru-dpp). The area under the absorption and emission spectra of HPTS *in its anionic form* is coloured in green. Note the difference in vertical scale between the upper and lower part of the figure.

is integrated over $[\lambda_{\mathrm{ex}} + \delta_{\mathrm{LP}}; +\infty]$ to yield a unique real value representing the amount of collected light at the photodiode for a given excitation wavelength λ_{ex}:

$$\mathcal{S}_{\mathrm{L,PD}}(\lambda_{ex}) = \frac{\varepsilon_{\mathrm{L},\lambda_{\mathrm{ex}}}}{\varepsilon_{\mathrm{L},\lambda_{\mathrm{abs,max}}}} \cdot \Phi_L \int_{\lambda=\lambda_{\mathrm{ex}}+\delta_{LP}}^{+\infty} \mathcal{S}_{\mathrm{L,em}}(\lambda_{\mathrm{ex}}) \cdot \mathcal{S}_{\mathrm{PD}}(\lambda_{\mathrm{ex}}) \tag{5.1}$$

- By repeating this procedure for λ_{ex} values in the 220–500 nm range, we obtain for each luminophore an excitation spectrum $\mathcal{S}_{\mathrm{L,PD}}$ that takes into account the above-described sensing scheme. The lower bound of this range was limited by the available spectroscopic data, while the upper bound corresponds to the highest bound on HPTS excitation spectrum (see Section 5.2.2). So-obtained excitation spectra are presented in Figure 5.5.

Of note, these $\mathcal{S}_{\mathrm{L,PD}}$ spectra are an ideal case wherein *(i)* all the LED-emitted light would be absorbed by the considered luminophores, *(ii)* no inner filter effect between the luminophores and HPTS is considered and *(iii)* all the luminophore-emitted light reaches the photodiode.

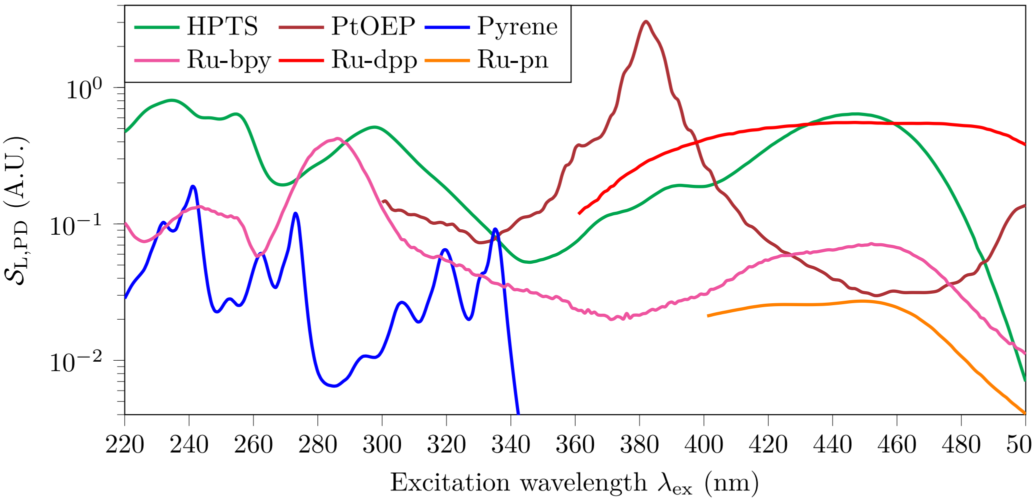

Figure 5.5: Collected light for selected long-lived luminophore and HPTS. Data source: same as Figure 5.4.

At first sight, it seems that PtOEP, Ru-bpy and Ru-dpp may be good candidates to use as long-lived luminophores in a DLR sensing scheme. However, the *cost* of the long-lived luminophores at hand was not taken into account in the above considerations, neither was the availability of affordable light sources in the afore-mentioned 220–500 nm range, nor the fact that—due to the conversion of HPTS between its acid and basic forms—not all wavelength ranges are suitable for HPTS-based pH sensing. To overcome these issues, $\mathcal{S}_{\mathrm{L,PD}}$ was divided by the price per gram of the different luminophores under study. LEDs having short emission wavelengths and a reasonable price were also searched for, and some were found at—or above—275 nm$^{(4)}$, but not below. Finally, the spectral properties of HPTS require to work either around 380 nm or—better—above 430 nm, *i.e.* in spectral ranges wherein the absorption and emission spectra of the protonated and anionic forms of HPTS differ the most (see Section 5.2.2). These different considerations are summarised in Figure 5.6.

Here, pyrene is greatly advantaged by the fact that it is—one, up to three—orders of magnitude cheaper than its competitors. However, it is also the worst compound of the five in terms of luminescence lifetime, having the shortest one, a place that it shares with Ru-pn. Additionally, pyrene's luminosity drops significantly in the HPTS-usable range (green areas in Figure 5.6), making it no better than PtOEP, Ru-dpp, and Ru-bpy, which all outperform it in terms of luminescence lifetime. While Ru-pn is clearly out of the race for both intensity *and* lifetime reasons, either PtOEP, Ru-dpp, or Ru-bpy could be used, since all three of them appear to be good candidates with respect to these latter two criteria. Therefore, a compromise had to be made between luminescence lifetime—for which PtOEP is clearly advantaged before Ru-dpp first, and Ru-bpy second—and maximum HPTS fluorescence intensity—for which Ru-dpp and

---

(4) For instance the CUD7QF1A LED (275 nm of peak wavelength, Seoul Viosys, South Korea), which sells below 3€ per unit if ordered in large quantities.

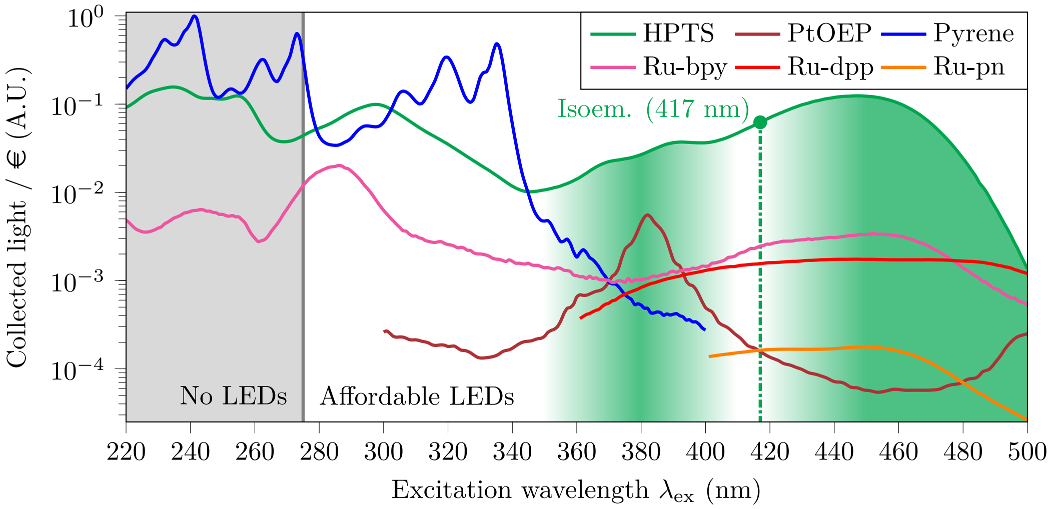

Figure 5.6: Collected light per euro for selected long-lived luminophore and HPTS. The domain of LED non-availability is shaded in light grey. The optimal measurement domains with respect to HPTS spectral properties are shaded in green. The isoemissive point of HPTS must be avoided at all costs since it makes HPTS-based pH sensing unfeasible. Data source: same as Figure 5.4.

Property	Notation	Value		References
		AH	A^-	
Acidity constant	pK_A	7.3		[473, 475, 629, 738]
Quantum yield	Φ	∼1		[724, 738, 739]
Decay time	τ	4.8±0.5 ns	5.3±0.1 ns	[724]
Absorption peak	λ_{abs}	∼404 nm	∼460 nm	[361, 445, 449, 450, 457, 629, 724]
Molar extinction coefficient at λ_{abs}	$\varepsilon_{\lambda_{abs}}$	2.0×10^4 $M^{-1}.cm^{-1}$	2.4×10^4 $M^{-1}.cm^{-1}$	[725]
Emission peak	λ_{em}	∼430 nm	∼515 nm	[449, 455, 458, 460, 461, 724]

Table 5.3: Main properties of HPTS. The '∼' symbol is used: *(i)* for the quantum yield, since it has never been reported accurately, and *(ii)* for the wavelengths to allow for a few nanometres of variation from one publication / solvent to another.

Ru-bpy are equally advantaged ahead of PtOEP—and **I finally chose to use Ru-dpp in my experiments**, probed above ∼430 nm. Now that both the short-lived fluorophore—HPTS—and long-lived phosphor—Ru-dpp—have been selected, they will be briefly presented in the following subsections.

5.2.2 HPTS

HPTS—also known as trisodium salt of 8-hydroxyl-1,3,6-pyridine trisulfonic acid (HOPSA), hydroxypyrenetrisulfonic acid (HPTA), solvent green 7, or simply pyranine (CAS 6358-69-6, M = 524.39 $g.mol^{-1}$)—is a green, fluorescent, pH-sensitive dye, which has been used in many a pH or pCO_2 sensor[412, 483, 737]. Its main properties are summarised in Table 5.3, and its molecular structure is given in Equation 5.2. Contrary to the more simple pyrene from which it is derived—which exhibits a much longer decay time, in the 200 ns range[723]—its decay time is independent of oxygen quenching[723, 738] and its fluorescence is pH-sensitive, thanks to its hydroxyl group.

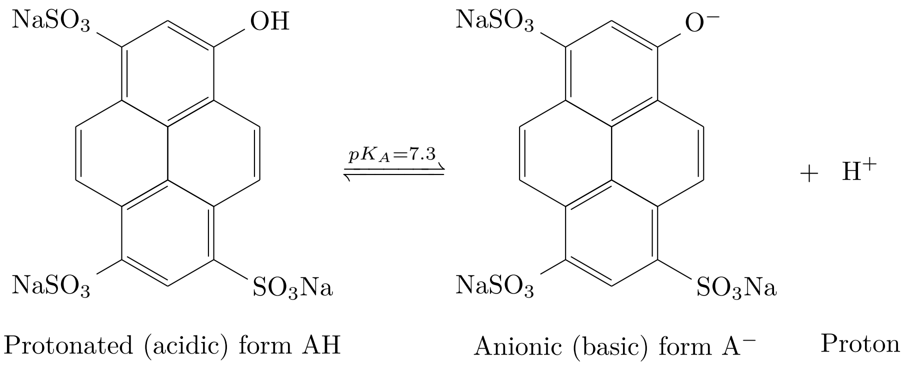

(5.2)

pK_A, the acidity constant of HPTS, has often been reported to be about 7.3 at 20°C. However, the latter value is especially true *in water*. When HPTS is immobilised in a thin polymer film, pK_A appears to shift slightly, ending up lying in the 6.55–8.50 range[449, 738]. Similarly, if HPTS is dissolved in room temperature ionic liquids, its pK_A may reach values as high as 9.5–11.2[458]. Further considerations on the effect of ionic strength on the pK_A of HPTS can also be found in Valeur *et al.*[220, p. 414].

The quantum yield of HPTS is often reported to be high, justifying its use, and only a few publications mention it to be near unity, without being overly precise[724, 738, 739].

The decay time of HPTS has not been measured thoroughly, at least to the best of my knowledge. In the work of Tran-Thi *et al.*[724], values were reported to differ for the protonated (4.8±0.5 ns) and anionic (5.3±0.1 ns) forms of HPTS, although the reported differences lie in the error bars of their measurement. On their part, Wolfbeis *et al.*[723] reported a constant 5.3 ns decay time, over the full 2–13 pH range. On the contrary, Schulman *et al.*[738] found decay times of 3.7±0.1 ns and 5.0±0.1 ns in immobilised HPTS equilibrated with 1 M HCl and 1 mM NaOH, respectively. Overall, it is thus unclear whether there is a difference in fluorescence decay time between the protonated and anionic forms of HPTS. Should such a difference exist in deed, it is nevertheless likely to be quite small—*i.e.* below 1–2 ns.

The spectral properties of HPTS have been reported to a greater or lesser extent by a number of authors—see Table 5.3—and the excitation and emission spectra of HPTS in water can be seen in Figure 5.7. The protonated form of HPTS absorbs at ∼404 nm and fluoresces at ∼430 nm, while its anionic form is excited at ∼460 nm and fluoresces at ∼515 nm, and an isoemissive point is to be found at ∼417 nm[445, 459]. However, it has been reported that the polarity of the solvent influences these wavelengths with a red-shift occurring with more polar solvents[724, 740]. Furthermore, the use of ionic liquids[458, 459], or the interactions between the dye and its substrate in case of polymer-based, thin film sensors[359, 460, 461] may also shift the absorption and emission peaks of HPTS.

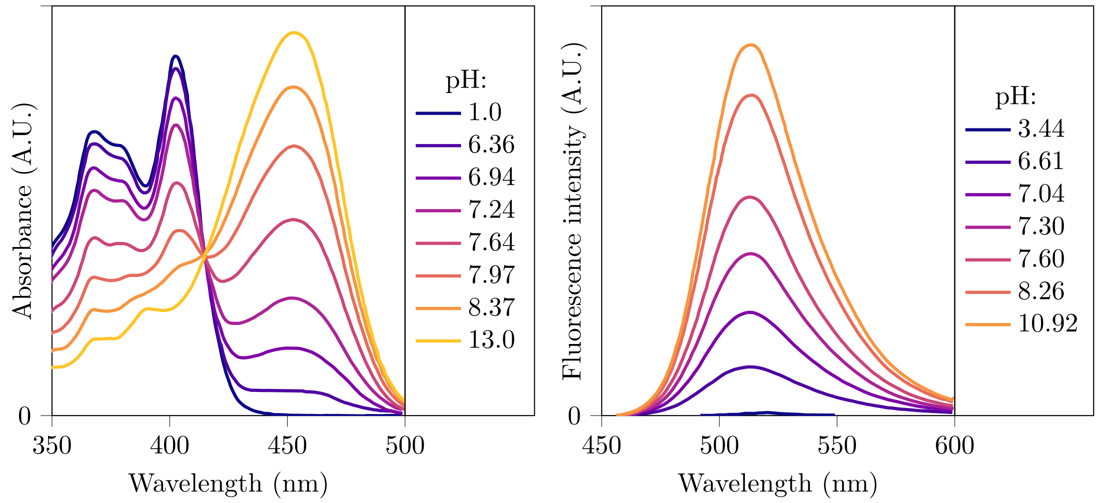

Figure 5.7: Absorption and emission spectra of HPTS in the 1–13 pH range. **Left:** absorption spectra of 22.2 µM HPTS in aqueous 1/15M phosphate buffer. **Right:** emission spectra of 3.82 µM HPTS when excited at 454 nm. Data source: Wolfbeis *et al.*[723].

Ageing and photobleaching of HPTS have seldom been reported in the literature for

Property	Notation	Value	References
Quantum yield	Φ	0.2–0.75	[734, 744]
Decay time	τ	0.8–6.40 µs	[734, 744–747]
Absorption peak	λ_{abs}	∼430–467 nm	[734, 745, 747, 748]
Molar extinction coefficient at λ_{abs}	$\varepsilon_{\lambda_{\text{abs}}}$	2.86×10^4 $M^{-1}.cm^{-1}$	[734]
Emission peak	λ_{em}	∼604–618 nm	[734, 745, 747, 748]

Table 5.4: Main properties of Ru-dpp.

CO_2 sensing[641]. Recent work by Nairn *et al.*[741] aiming at characterising HPTS photobleaching revealed that—although HPTS is considered a fairly stable compound by a number of authors[457, 473, 475]—it is nonetheless subject to photobleaching to some extent. Nairn *et al.* indeed reported degradation time constants of only a few hours upon continuous exposure to sunlight.

Solubility of HPTS has been reported in a wide range of solvents, although quantitative data are sparsely available. For instance, Bobe *et al.* reported HPTS solubility constants of at least 3 µM in dimethylformamide (DMF), dimethyl sulfoxide (DMSO), ethanol, and methanol[742] (∼1.6 $mg.L^{-1}$). Other sources report up to 300 $g.L^{-1}$ in water, and 100 $g.L^{-1}$ in methanol[743]. An extensive list of solvents—among which isopropyl alcohol (IPA), acetone, acetonitrile, ethylene glycol, and tetrahydrofuran (THF)—can also be found in the work of Barrash *et al.*[740], although no precise solubility figures are given.

5.2.3 The Ruthenium(II) Complex

The Ruthenium(II) complex that will be used as a reference luminophore is tris(4,7-diphenyl-1,10 phenanthroline) ruthenium (II) dichloride (Ru-dpp) (CAS 36309-88-3, M = 1169.17 $g.mol^{-1}$). Ru-dpp is an organometallic phosphorescent dye with a long lifetime, and whose luminescence is strongly quenched by O_2. Its main properties are summarised in Table 5.4 and its molecular structure as well as excitation and emission spectra are given in Figure 5.8.

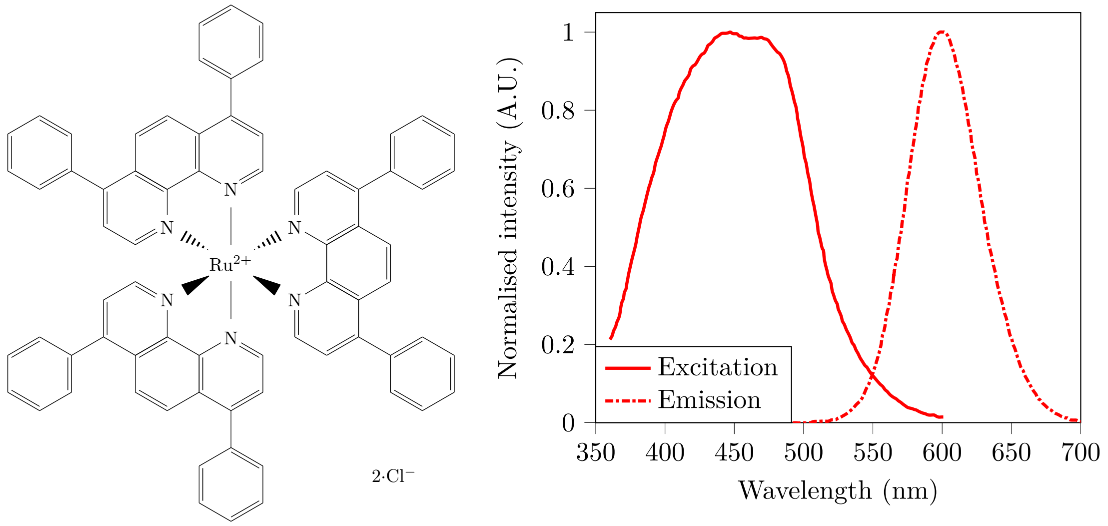

Figure 5.8: **Left:** Ru-dpp molecular structure. **Right:** excitation and emission spectra of Ru-dpp immobilised in polymer nano-beads. Redrawn from Bultzingslöwen *et al.*[473].

The O_2 fluorescence quenching of Ru-dpp has been a long known phenomenon, which has been exploited to elaborate O_2 probes and sensors since the nineteen eighties[744, 745, 747, 748]. However, this quenching becomes an unwanted cross-sensitivity when developing a CO_2 sensor. Consequently, several authors proposed dye encapsulation techniques—notably into PAN films or micro-beads[473–475, 746]—to avoid the influence of O_2 on Ru-dpp fluorescence. Of note, some of the latter references—*e.g.* Liebsch *et al.*[746]—did not study Ru-dpp di*chloride* strictly speaking, but Ru-dpp di*hexafluorophosphate* or other anionic variants instead.

The quantum yield of Ru-dpp has seldom been reported and depends both on the solvent in- and on the temperature at which it is measured. Values reported in ethanol[734] or butyronitrile[749] are rather low—0.2 and 0.366, respectively—while entrapment in polymers can raise it to as much as 0.75[734]. Xu *et al.*[744] reported a more laconic value of 0.5, although their primary source—Nakamaru *et al.*[750]—could not be retrieved, seemingly lost in the sands of time. Again, O_2 quenching plays its role in the quenching of the emission intensity of Ru-dpp[748].

The decay time of Ru-dpp—as its quantum yield—also strongly depends on the solvent with values near 5.34 µs in deoxygenated methanol[751], 6.9 µs in PVC[734] but closer to 0.8 µs in aqueous solution[746]. This lifetime was also reported to decrease notably with temperature[745, 746], and—of course—with oxygen quenching[745].

The luminescence properties of Ru-dpp consist in a broad excitation spectrum in the blue end of the visible spectrum (∼400–500 nm) and a narrower emission peak in the yellow-red (∼550–650 nm). The emission spectrum of Ru-dpp has been reported to blue-shift once entrapped into a polymer film[734] and to red-shift with an increase in temperature[747](5).

Solubility of Ru-dpp has been reported in a 4:1 ethanol / methanol mixture[734] and in methanol[751] without specific numerical values, and up to 400 µM (∼0.47 $g.L^{-1}$) in ethanol[747], 40 $g.L^{-1}$ in chloroform[704] or approximately 33 $mg.L^{-1}$ in dichloromethane[744]. In the course of my experimentations, I observed a fast—*i.e.* below one minute—dissolution at 9.0 mM (∼10.5 $g.L^{-1}$) in both DMF and DMSO, and a slower one—*i.e.* several hours—in a 3:1 ethanol / water mixture at 4.5 mM (∼5.2 $g.L^{-1}$). These indicative durations and solubility values were observed during the preparation of 5–10 mL of solutions stirred at 60°C—see Section 5.5.1 for chemicals origin.

5.3 Selecting the Polymers

The use of two luminophores with very distinct purposes calls for two corresponding polymers with very distinct properties: one of them must act as an oxygen barrier in order to encapsulate the oxygen-sensitive Ru-dpp, hence it should have a very low gaseous solubility and diffusivity. On the contrary, the other one must be highly hydrophilic / hygroscopic, and facilitate the diffusion of CO_2, in order to allow for a good acid-basic conversion of HPTS and a fast detection of the latter gas. Additionally, those two polymers must be optically clear, reasonably cheap, and solvent-compatible with the involved luminophores as well as with one another—*i.e.* the solvent used to dissolve one polymer must not dissolve the other, and *vice versa*.

Note that considerations relative to the thermal, oxidative, (photo)chemical, or physical degradation of the said polymers—while relevant in the general case of polymer benchmarking—were set aside in the following developments since the obtained thin films will operate at room-temperature and without excessive mechanical load. Furthermore, the involved luminophores are orders of magnitude more sensitive to (photo)chemical and oxidative degradations than the polymers that will embed them—see Sections 5.1.1 and 5.5.5. Consequently, the luminophores in the polymer films will have completely photobleached long before the polymers which encapsulate them begin to suffer from the ravages of time and radiation. Still, the curious reader may refer to Korotcenkov for further discussions on polymer (long-term) stability[752, Chap. 9].

5.3.1 Ru-dpp Encapsulating Polymer

5.3.1.1 Polymer Selection

In choosing the Ru-dpp encapsulating polymer, I focused on having the lowest permeability as possible towards oxygen. A compilation of various bibliographic resources on the topic of polymer permeability towards oxygen can be found in Table 5.5.

Of note, this table should be taken with a pinch of salt, because several authors reported widely varying values for the same substance—*e.g.* depending of the considered nuance(6), EVOH permeability can be multiplied more than tenfold[761, p. 185]. As such, it is not rare to see reports of permeability values spanning more than one order of magnitude for a given polymer, even at a single given temperature[762, App. II]. It should also be noted that both temperature

---

(5) Here “blue-shift” and “red-shift” were used instead of the more literary *hypsochromic* and *bathochromic* shift denomination, so as to remain comprehensible to a novice reader.

(6) The word *nuance* is loosely used here to denote constitutive variations in commercial grades of polymers. These variations can correspond to different amounts of additives, degrees of polymerisation, of proportions of the different monomers involved (in case of a copolymer). The curious reader may refer to McKeen for further information on this topic[761, Chap. 2].

Nb. of polymers reviewed	Lowest P (barrer$^{(a)}$)	Corresponding Polymer	Ref.
6	2.34	polyethylene (low density)	Yasuda *et al.*[753]
10	0.43	poly(butylene adipate) polyester-based polyurethane	Wang *et al.*[754]
5	0.16	poly(methyl methacrylate) (PMMA)	Yang *et al.*[755]
22	3.28×10^{-2}	polyvinyl fluoride (PVF)	Aiba *et al.*[756]
19	4.0×10^{-3}	PVCD	Surgi *et al.*[757]
84	2.8×10^{-3}	BTDA-p,p'-DAS	Koros *et al.*[758]
11	5.61×10^{-4}	poly(p-phenylene terephthalamide) (PPTA)	Kanehashi *et al.*[759]
57	2.0×10^{-4}	polyacrylonitrile (PAN)	Sangaj *et al.*[760]
~400	$3.7\times10^{-5\ (b)}$	ethylene-vinyl alcohol (EVOH)	McKeen [761, p. 187]

Table 5.5: Bibliographic review of the permeability P of polymers towards oxygen. (a): 1 barrer is equal to $10^{-10}\times\mathrm{cm}^3_{\mathrm{STP}}\cdot\mathrm{cm}\cdot\mathrm{cm}^{-2}\cdot\mathrm{s}^{-1}\cdot\mathrm{cmHg}^{-1}$. (b) an even lower value of 3.1×10^{-6} have been reported by Massey[762, p. 267] for 140°C heat-treated EVOH.

and humidity greatly influence polymers' permeability—*e.g.* EVOH oxygen permeability can be multiplied by up to 63 from 0% RH to 100% [762, pp. 264–5], similar orders of magnitude are also observed when increasing the temperature from room temperature (20–25°C) to the 25–50°C range[762, App. II]. Most of the time, the values reported in 5.5 are given in dry air and at room temperature, although this is not always the case due to the multiplicity of sources. The reader is therefore highly encouraged to delve into the afore-mentioned references for precise comparisons. From this crude bibliographic research, PPTA, PAN and EVOH were considered for further investigations due to their outstandingly low permeability values.

At first, PPTA—better known to the general audience under DuPont's commercial name *Kevlar*—was discarded for two main reasons:

1. It is insoluble in almost all solvents but sulphuric acid[763, 764](7), hence it is a polymer especially difficult to work with, requiring multiple steps to turn it into a film[766, 767].
2. PPTA films, if transparent when thin enough, are not optically clear—having been reported as gold or yellow in colour[767–769]. This yellowish colouring—which is similar to that of the well-known Kevlar fabric—prevents their use in the envisioned fluorescence setup, since it indicates a strong light absorption in the blue wavelengths. Although absorption spectra of micrometer-thick PPTA thin films could not be found in the literature, the work of Yang *et al.* indeed indicates significant light absorption for DMSO / Kevlar nanofibres dispersion in the 300–500 nm wavelength range[770]. Furthermore, Kevlar also fluoresces when excited in the 300-500 nm range, re-emitting light in the 450–700 nm region[771].

Then, PAN was preferred over EVOH for its better tolerance towards humidity. Indeed, while PAN permeability only increases by 10–20% at high humidity levels[772], that of EVOH increases dramatically, as stated above. Ultimately, this results in EVOH having a far higher permeability than PAN in water-saturated air[773], a condition that is met at occluded human skin—see Section 3.3.2.

5.3.1.2 PAN

PAN comes in the form of a white powder, which is highly soluble in a variety of solvents, notably DMF, DMSO, nitric and sulphurous acid, as well as aqueous solutions of sodium thiocyanate (NaSCN) and zinc chloride ($ZnCl_2$). Various reports indicate solubilities of at least 5–6m%(8) for all the afore-mentioned solvents[775, 776], and much higher figures have even been reported for DMF, with solubilities in the 20–25m% range[777, 778]. Further still, it has been suggested that there was no upper limit to the solubility of PAN in DMF, apart from the difficulty of thoroughly homogenising the polymer / solvent mixture—especially for PAN concentrations above 25m%[778, 779]. Indeed, PAN powder tends to swell when exposed to DMF, forming a gel layer which prevents the solvent from reaching the remaining undissolved powder[780], a

---

(7) For the sake of completeness, some organic solvents—such as dimethylacetamide or (m)ethylformamide—may also work in conjunction with a variety of salts[765].

(8) The 'm%' notation is used for mass percentage, *a.k.a.* mass fraction or percentage by weight, and sometimes also noted 'wt.%' or '%w/w'—although this can be seen as a misuse of the term weight[774].

behaviour that I also observed in the lab (PAN powder, 99.5% acrylonitrile, $M \approx 230$ kg.mol^{-1}, AN316010, Goodfellow, UK). Thus, PAN concentrations above 20m% are difficult to come by in practice, and hardly workable because of their extreme viscosity. Interestingly, Eom *et al.* reported that this swollen gel layer phenomenon is far less marked when using DMSO instead of DMF[780]. Therefore, even if—for historical reasons—all my experimentations were conducted with DMF as a solvent for the Ru-dpp / PAN mixture, DMSO could have probably also been envisioned(9).

The curious reader may have a look to references [782, pp. 393–443] and [783, Chap. 4] for further considerations about *e.g.* PAN history, polymerisation process, mechanical properties, thermal stability, or morphology, to name a few.

5.3.2 Breathable Polymer

5.3.2.1 Polymer Selection

A priori, the choice of the polymer used to embed the pH-sensitive dye should be guided by the fact that this polymer has both a good CO_2 permeability—so that CO_2 can easily dissolve from the skin into the polymer matrix—and hygroscopy—so that water molecules entrapped in its bulk may contribute to the hydration of collected CO_2 molecules. This breathable polymer should in addition have decent optical transparency and mechanical properties, for optical probing and cutaneous application, respectively. Yet, despite the fact that Aguayo-López *et al.* mention that choosing a more hydrophilic polymer for the preparation of dye-based thin film sensors should yield a better stability, their results show satisfying performance using either ethyl cellulose or HPMC with no major difference between the two, in spite of the fact that the latter is more hydrophilic than the former[470]. Additionally, McMurray put forth as far back as 1992 that the water molecules available for CO_2 hydration may predominantly originate from the quaternary ammonium cation used as phase transfer agent, rather than from the encapsulating polymer matrix[784], a hypothesis grounded in the work of Landini *et al.*, although the authors indicate that it may be the complementary cation and not the quaternary ammonium anion by itself that interacts with water molecules[785].

That being said, since McMurray's hypothesis has—to the best of my knowledge—neither been confirmed nor infirmed to date, I considered that the hygroscopy of the encapsulating polymer *may* influence the behaviour of thin film CO_2 sensors. In order to better understand the phenomena of hydrophily and hygroscopy of polymers, a quick bibliographic search about those phenomena was performed. However, this research is mainly presented here for reference, as well as to hopefully provide the reader with a few insights on this broad topic. Indeed, I ended up making my choice between the narrow range of polymers which had been already successfully tried out by other authors for CO_2 sensing to stay on the safe side—see Section 5.3.2.1.2—though further research on this topic is definitely needed—notably to investigate the validity of McMurray's hypothesis.

further research is needed

5.3.2.1.1 Of Polymers and Water

Polymers, in addition to the concepts of water solubility—*i.e.* the ability to dissolve into water, characterised by the solubility coefficient or solubility parameter[786]—or water (vapour) permeability—*i.e.* the ability to let water molecules diffuse through it, characterised by various physical quantities such as water vapour transmission rate, permeability, solubility and diffusivity[787]—can also be defined by their hydrophilic or hygroscopic nature. These two notions, however, may have different meanings depending on the authors and research fields. Indeed, *hydrophilicity* can be used to describe distinct properties: as a synonym for hygroscopy or solubility, but also to describe the surface-wetting properties of water onto a given material—often characterised by the contact angle of water droplets at its surface[788, 789]. On its part, the meaning of *hygroscopy* is relatively consensual, and relates to the ability of a polymer to embed water molecules into its bulk. It is often characterised by the influence of RH on mass change—often simply denoted as "water uptake" or "moisture content", and expressed as a percentage of the dry polymer mass[790, 791]—swelling[792], or glass transition temperature shift[793–795].

---

(9) In practice, this may not be that simple: several tests were performed in this direction and, while dissolving Ru-dpp (9.0 mM) and PAN (10m%) in DMSO proved relatively straightforward (<8 h at 70°C), the resulting films curled in on themselves while drying, delaminated from the glass substrate they were cast onto, and developped a whitish opaque tint. A quick assessment of photobleaching led to results similar to those obtained with DMF. Finally, it should be noted that PET is soluble in DMSO[781, p 13-9], which further refrained me from using the latter in the end, since PET was a candidate substrate for the final thin films instead of glass—see Section 6.2.8.

Those phenomena have been extensively studied, either theoretically by means of diffusion models[787, 796] and—more recently—molecular simulations[797, 798], or practically *via* myriads of specific studies on the water uptake, swelling, or wettability of polymers—a simple Google Scholar request on "`polymer AND ("water uptake" OR (water AND swelling) OR hygroscopy OR hydrophilic) AND review`" yields over one million results. This vast literature corpus originates from the ubiquitous presence of water on earth coupled to the ever-growing polymer use in industrial applications[799, Fig. S1], and recent research interests on water-polymer interactions include for instance food packaging[800], edible coating[801], microencapsulation for ink printing or drug delivery[802], water-soluble capsules for clinical use[803], anti-fouling coatings[804], or water harvesting in dry environments[805], to name a few.

Yet, this diversity of applications and research perspectives makes it exceedingly difficult for the novice to provide a comprehensive and usable picture of water-polymer interactions. Even specialised textbooks dedicated to polymer permeability such as Massey's 2003 *Permeability Properties of Plastics and Elastomers*[762] or McKeen's update of the latter[761] largely ignore cellulose derivatives, for instance(10). Worse still, any attempt to paint such a picture seems doomed to failure, for there is no such thing as "a polymer", from a water-interaction perspective. Indeed, while there are of course major differences in hygroscopy based on a polymer's monomer unit—*e.g.* between ethyl cellulose, hydroxypropyl cellulose, or HPMC[794]—there are also considerable variations depending on the polymer's degree of polymerisation[793, 806] or crystallinity[807], temperature[793–795], or presence of additives[801, 808, 809]—*e.g.* plasticisers(11)—not to mention the measurement variability from one publication to the other, which can be induced by inappropriate protocols[790]. Facing this growing number of parameters and the factorial explosion of possible combinations that ensues, taking into account my relative ignorance on this complex topic, and because of the limited time I had to complete this doctoral work, I chose to stay on the safe side, and to select a polymer / plasticiser combination among those used in the literature for thin film CO_2 sensing specifically.

5.3.2.1.2 In the CO_2-Sensing Literature

Table 5.6 presents a literature review of breathable polymers used for dry dye-based thin film CO_2 sensing. Because of its moderate sensitivity towards humidity, plurality of reporting works, and affordability, HPMC was finally chosen to act as a breathable polymer for HPTS encapsulation, plasticised by Tween 20. Again, it must be emphasised that this choice has its share of arbitrariness, and other solutions could prove to be better alternatives. In particular, cellulose acetate and cellulose acetate butyrate, or polyvinyl alcohol (PVA) may be interesting alternatives to HPMC given their high CO_2 permeability and water vapour transmission rate[357].

5.3.2.2 HPMC

HPMC—*a.k.a.* hypromellose, or under the trade name *Methocel*—has a cellulosic backbone from which several hydroxyl groups have been substituted by either methoxy or hydroxypropyl groups[812, Fig. 1]. As such, it is often characterised by both its degree of polymerisation—or molar mass—and by the percentage of its hydroxyl groups that have been substituted by methoxy or hydroxypropyl groups[813, Table I]. HPMC comes in the form of a white powder that is extensively soluble in water—*i.e.* up to at least 60m%[814]—but also in water-ethanol mixtures[472], DMSO, benzyl alcohol and formamide[813]. However, just as with PAN dissolution in DMF, HPMC also tends to form a gel when dissolving into water[812], making it particularly difficult to reach concentrations above a few tens of percent. Additionally, HPMC is reputed to be poorly soluble in hot water, exhibiting thermoreversible gelation—*i.e.* forming a gel at high temperature which dissolves upon cooling—a phenomenon which depends on both the HPMC concentration and degree of hydroxypropyl substitution[815]. Cloud points are usually reported to lie in the 37–70°C range, depending on the type—*i.e.* percentage of methoxy and hydroxypropyl groups—and concentration of HPMC used. In the lab, no cloud point nor gelation were observed with a 20m% concentration at 55°C in a 1:1 water / ethanol mixture or with a 10m% concentration at 60°C in a 2:1 water / ethanol mixture (HPMC powder, 29m% methoxy,

---

(10) Massey only mentions the oxygen permeability of methyl cellulose and HPMC without much detail on the materials (molar mass, methoxy content, *etc*), while McKeen focuses solely on raw, nitro, and ethyl cellulose, as well as cellulose acetate, but without mentioning HPMC.

(11) As well as the degree of polymerisation of the considered polymer[810].

Polymer	Plasticiser	Humidity influence on CO_2 readings	Ref.
Cellulose fibres	None	Yes, strong	[451]
EG / PEG	TBP	Yes, moderate	[475]
Ethyl cellulose	DOP TBP TOP Tween 20	Yes, strong	[462, 466, 467, 470, 482] [358, 449, 465, 472, 476] [459, 469, 478, 480] [454, 457, 477]
Hydroxyethyl cellulose	Glycerol	Yes, moderate	[475]
HPMC	Tween 20	Yes, moderate	[470–472]
Ormosil	None	Yes, strong	[359, 360, 363, 460, 461, 473]
PolyIBM	TBP	N/A	[468]
PMMA / MOF	DOP	N/A	[811]
metal-loaded PVA	None	None for RH > 25–50%	[362]
PVCD	TBP	Yes (stability?)	[469]
Silicone	None	Conflicting sources[a]	[361, 474, 641]

Table 5.6: Bibliographic review of breathable polymers that were used for CO_2 sensing. EG: Eudragit. PEG: polyethylene glycol. TBP: tributylphosphate. DOP: dioctylphtalate (*a.k.a.* bis(2-ethylhexyl) phthalate). TOP: tris(ethyl-hexyl) phosphate. PolyIBM: poly(isobutyl methacrylate). PMMA: poly(methyl methacrylate). MOF: metal organic framework. PVA: polyvinyl alcohol. PVCD: polyvinylidene chloride. Silicone: polydimethylsiloxane (PDMS) and derivatives thereof. (a): two authors reported a marked influence of water while Borisov *et al.* report that one of their sensors "still responds to carbon dioxide at relative humidities close to 0 and shows sensitivity similar to that in humidified gas."[641].

$M \approx 10$ kg.mol^{-1}, 423238, Sigma-Aldrich, USA). Dissolution was always quick—less than 2 h—but 20m% solutions were exceedingly thick(12), making them difficult to work with.

5.4 Optoelectronics

A synoptic view of the opto-electronic system that was used to probe the manufactured CO_2-sensing thin films can be seen in Figure 5.9. The following sections detail separately the optical and electronic aspects of this setup.

5.4.1 Optical Setup

5.4.1.1 Spectral Configuration

The 450 nm blue LED (LED450L, Thorlabs, USA) is focused through a 450 nm cut-off, shortpass, OD5, excitation filter (FES0450, Thorlabs) onto the CO_2-sensitive fluorescent thin film. The re-emitted light is passed through a 500 nm cut-off, longpass, OD5, emission filter (FEL0500, Thorlabs), and collected onto a silicon photodiode (SM05PD1A, Thorlabs). The fluorescence excitation and emission filters, LED, and photodiode were chosen such that *(i)* the excitation spectra of the two luminophores embedded in the film—HPTS and Ru-dpp—match that of the LED, *(ii)* that the excitation and emission filters block the excitation signal while letting through the light re-emitted by the film, and *(iii)* that the photodiode is sensitive to the filtered, re-emitted wavelengths. The fulfilment of these conditions can be observed in Figure 5.10.

5.4.1.2 Geometrical Configuration

A custom optical setup was designed, using the afore-mentioned optical elements—*i.e.* LED, photodiode, filters and lenses—embedded within a 3D-printed mount. While the thorough design study relative to this particular configuration has been relegated to Appendix E, Figure 5.11

---

(12) No viscometer was available in the lab, but 20m% HPMC solution in 1:1 water / ethanol mixture were estimated to be in the 10,000-50,000 cP range using visual scales—*i.e.* akin to molten chocolate just before solidifying, very thick honey, or ketchup, for instance—flowing with great difficulty and immobilising the magnetic stirrer.

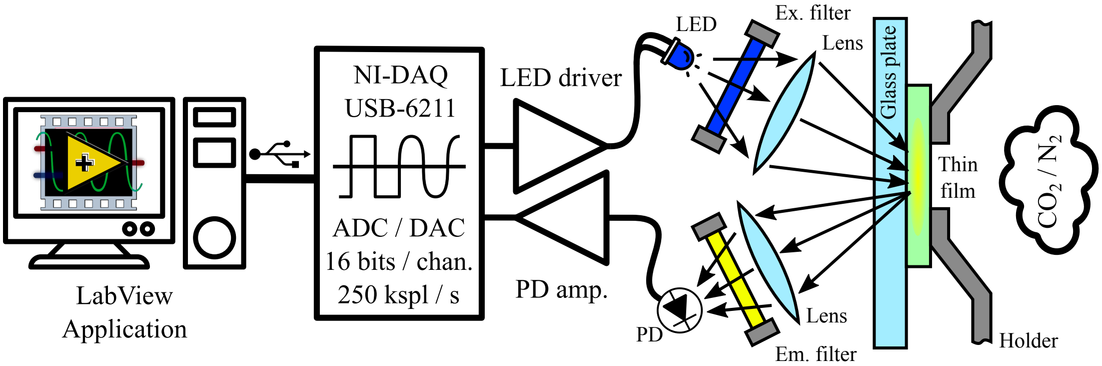

Figure 5.9: Synoptic view of the acquisition system. The computer runs a LabView application which communicates with the acquisition board. The latter in turn sends an excitation signal to the LED through the LED driver. The emitted light is focused through a shortpass excitation filter onto the fluorescent thin film that is placed inside a gas-tight box, into which the CO_2 concentration, temperature and humidity levels can be regulated. The re-emitted light is then collected and passed through a longpass emission filter to reach the photodiode (PD). The photodiode's signal is then amplified and read back by the acquisition board.

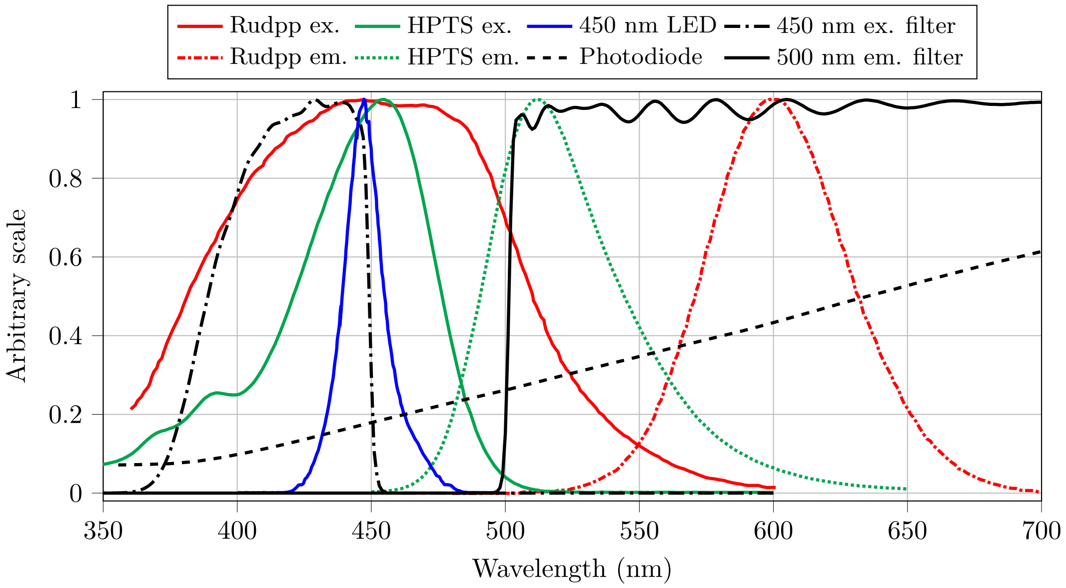

Figure 5.10: Optical spectra of the components and chemicals involved. Note that these spectra were normalised and are of different natures: excitation and emission spectra for HPTS (anionic form) and Ru-dpp, transmission spectra for the excitation and emission filters, emission spectrum for the LED, and sensitivity spectrum for the photodiode. Spectral data gathered from [723] (HPTS), [473] (Ru-dpp), and Thorlabs (others).

showcases the resulting optical assembly. It is composed of two 1 inch mounting tubes that form the illuminating and collecting assemblies. The illuminating assembly contains the LED, excitation filter, and a first condensing lens (ACL25416U, Thorlabs), which focuses the filtered LED light onto a spot of approximately 1 cm in diameter on the sensing thin film. The collecting assembly, on its part, collects the re-emitted light by means of a second condensing lens, filters out the LED-generated parasitic stray light, and focuses the resulting flux through a third condensing lens onto the photodiode's light-sensitive area. Of note, the glass window is part of a larger atmospheric chamber that allows control over the CO_2 / N_2 ratio, RH, and temperature to which the thin film is exposed. This chamber is of standard design and is not detailed here for the sake of conciseness.

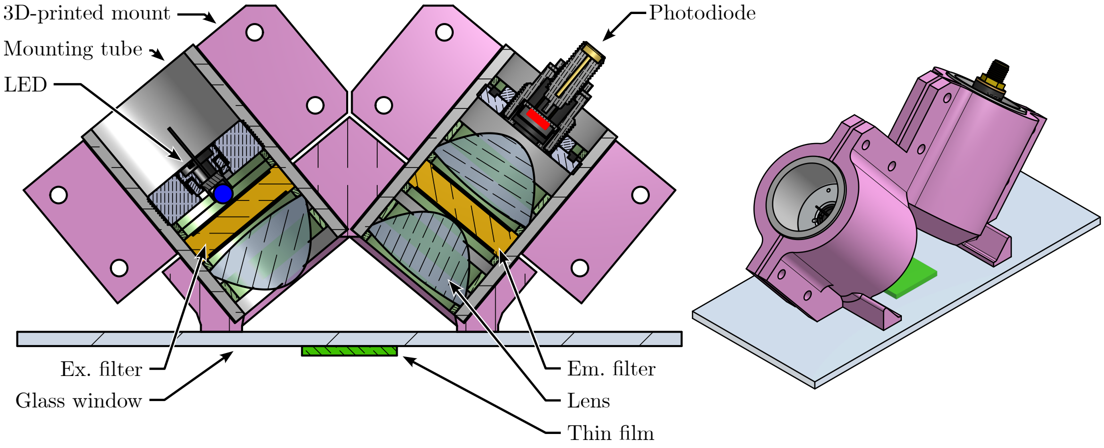

Figure 5.11: Real-world implementation of the afore-mentioned optical parts. Cut view (Left) and isometric view (Right) of the optical assembly. Note the blue and red areas on the Left side of the figure, representing the LED's ball lens and photodiode's sensitive area, respectively. See the text for further explanations

Briefly, Appendix E details how this setup was optimised in order to maximise the amount of collected light at the photodiode. In particular, all the LED light is theoretically focused onto the thin film, and approximately 5.9% of the re-emitted light reaches the photodiode. Using relatively pessimistic figures for the absorbance and quantum yield of the film, this results in a photocurrent in the order of 1–2 µA for an optical LED power of 10 mW. In order to reach a voltage in the range of 100–500 mV at the photodiode amplifier's output, a transimpedance gain in the order of 10^5 V.A^{-1} is thus needed.

5.4.2 Electronic Setup

The electronic setup used to drive the LED and amplify the photodiode's current is represented in Figure 5.12. It was built on top of the acquisition board (NI-DAQ USB-6211, National Instruments, USA) that communicates with the computer through a USB link. This board is further connected to the LED driver (LDP-2023, Roithner Lasertechnik, Austria) and, to the photodiode's TIA (AMP102, Thorlabs), whose gain was set to 10^5 V.A^{-1}. The LabView application, on its part, can perform f-DLR acquisitions with various excitation intensities and recording lengths—*i.e.* sample count N. Please refer to Section 4.3.3 for further details on f-DLR sensing, and Section 4.4 on phase measurements.

5.5 Thin Film Characterisation

Up till now, this doctoral work has:

- presented the specificities of transcutaneous CO_2 sensing—Chapter 3
- reviewed the existing CO_2 sensing techniques 4.1
- chosen one CO_2 sensing technique according to the latter specificities: **dye-based thin film sensing**—Section 4.2

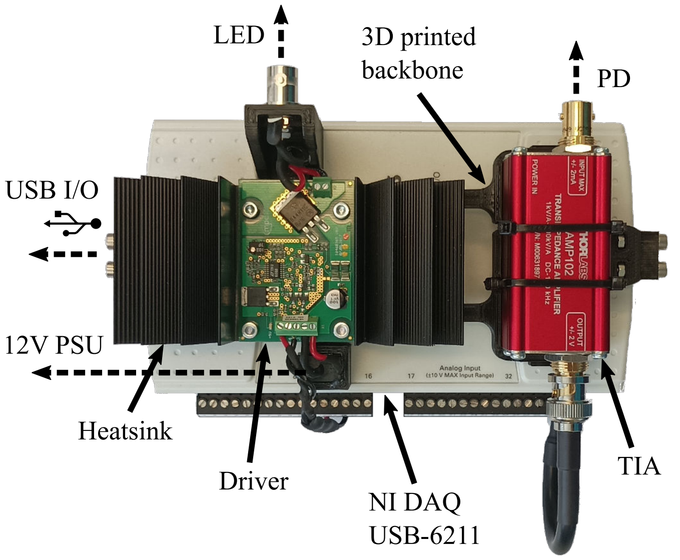

Figure 5.12: The main active electronic components that were used, assembled together on a 3D-printed backbone. Dashed arrows represent external electrical connexions.

- reviewed the chemical and optical sensing schemes associated with dye-based thin film CO_2 sensing—Section 4.3—and chosen one of them: **dry thin films with an f-DLR sensing scheme**

- presented the maximal theoretical accuracy reachable using this scheme—Section 4.4

- outlined the caveats of using humidity and oxygen-sensitive luminophores and the associated workaround strategies—Section 5.1—selecting a bilayer structure for appropriate luminophore encapsulation

- reviewed potential candidates for the luminophores and polymers used to build the said thin films—Sections 5.2 and 5.3—finally choosing **HPTS, Ru-dpp, PAN, and HPMC** as the short- and long-lived luminophores, and Ru-dpp- and HPTS-encapsulating polymers, respectively

- presented the optoelectronics that was used to probe the manufactured thin film prototypes—Section 5.4

This was done with a twofold objective in mind: first, to establish a hopefully reasonable starting point for the experimentations presented below; second, to offer a comprehensive view of the motivations behind what often seems to be arbitrary choices in the literature(13), as well as alternative paths for those interested in continuing this work.

The current section differs from those encountered previously in this thesis in that it adopts a more narrative style, as opposed to the conventional structure of materials and methods / results / discussion / conclusion that was used to report the experimental investigation conducted so far—*e.g.* measuring haemoglobin absorption spectra, skin conductivity towards CO_2, or humidity levels of occluded skin. This shift is primarily due to the still-ongoing nature of the presented research, as well as to the lack of hindsight on my part, preventing me from presenting as in-depth an analysis as I would wish to. As the reader would have surely understood by now, the optimisation of fluorescent CO_2-sensing thin films is a complex matter, and the fine tuning of the numerous above-mentioned parameters is a very time-consuming process—a time I did not have. As a result, I was faced with the bitter choice of either trying to optimise a single parameter very thoroughly, or to explore superficially a few. I chose the second option, trying to do my best to at least highlight the several directions into which further work will be needed in order to achieve industry-ready, consumer-grade, f-DLR thin film-based, transcutaneous CO_2 sensors.

---

(13) Without placing blame, the paper-driven research model we are accustomed to demands a conciseness that precludes the lengthy discussions found in the preceding chapters.

5.5.1 Materials

The following chemicals were used in the next sections: Ru-dpp (044123.04, Thermo Fisher Scientific, USA), PAN with a mean particle size of 50µm, copolymer with 99.5m% acrylonitrile / 0.5m% methyl acrylate, molecular weight: 230 kg.mol^{-1} (AN316010, Goodfellow, Canada), HPTS (H1529, Sigma-Aldrich, USA), HPMC with 29m% methoxy and 7m% propylene oxide groups, molecular weight: 10 kg.mol^{-1} (423238, Sigma Aldrich), 25% tetraethyl ammonium hydroxide (TEAH) solution in methanol (∼1.5 M, 86631, Sigma Aldrich), Tween 20 (P1379, Sigma Aldrich). DMF and ethanol were of analytical grade. Wet film thicknesses were assessed with a wet film gauge, while dry film thicknesses were measured using a surface profiler (Dektak 150, Bruker, USA).

5.5.2 Making Homogeneous (Not So)(14) Thin Films

In order to make multilayer thin film CO_2 sensors, luminophore-loaded polymer thin films of the required thickness must be reproducibly manufactured, allowing the assessment of different luminophore loadings or concentrations of other chemicals—*e.g.* phase transfer agent or plasticiser. Among the variety of existing polymer coating techniques—see Krebs[817] and Butt[818]—blade coating was selected for its ability to create relatively thick—*i.e.* up to tens of micrometers if needed—films while being adaptable to roll-to-roll processes for scalability. However, due to my lack of experience with this technique combined to the absence of technical expert on this matter in my laboratory, quite some time was spent to reach an acceptable reproducibility level.

5.5.2.1 Polymer Solubility Assays

Before experimenting with blade coating, solubility assays were performed to evaluate the ease of dissolution of PAN and HPMC in DMF and water / ethanol mixtures, respectively. A secondary objective was also to assess the viscosity and workability of the so-obtained solutions. Briefly, as some of these observations were already mentioned in Section 5.3, both polymers were found to be infinitely soluble in their solvents—*i.e.* pure DMF for PAN, and 1:1 or 2:1 ethanol / water mixtures for HPMC. However, due to *(i)* the formation of a gel preventing further dissolution and *(ii)* the viscosity increase that prevented magnetic mechanical stirring, polymer concentrations above 15–20m% were difficult to come by in practice.

Temperature greatly influenced the solubility of PAN in DMF: while three hours at 80°C led to a complete dissolution of 15m% PAN, three days at 30°C were completely insufficient, with large lumps and aggregates still present. Of note, cooling the so-obtained 80°C / 15m% solution down to ambient temperature did not result in any PAN precipitation, allowing one to conclude that the influence of temperature is indeed on the kinetics of dissolution rather than on the solubility itself. Regarding HPMC, no thermoreversible gelation was observed, as mentioned above—see Section 5.3.2.2. When using 10m% polymer concentrations, complete dissolution was observed within 4 h using 80°C for PAN in DMF and 55° for HPMC in 1:1 ethanol / water mixture.

Of note, a first batch of PAN in DMF dissolution assays completely failed, producing turbid solutions even at PAN concentration as low as 5m%. This was attributed to the use of an old bottle of DMF in lack of a better alternative hypothesis, since a freshly opened DMF bottle did not exhibit this behaviour. This possible explanation is not really satisfactory, however, since DMF is a reputedly stable compound when stored in gas-tight, opaque, containers. Nevertheless, the faulty bottle might have picked up some humidity, which may have caused hydrolysis of DMF into dimethylamine and formic acid[819]. These compounds—or the presence of water—may in turn have hampered PAN dissolution.

5.5.2.2 Doctor-Blading and Screen Printing

A first series of experiments was conducted with HPMC solutions in a 1:1 water / ethanol mixture, but what follows was also observed with PAN solutions in DMF, and likely depends only on the mechanical properties—*i.e.* viscosity, density, surface tension, *etc.*—of the fluids considered. A K Control Coater (Erichsen, Germany) was used, whose basic working principle is depicted in Figure 5.13, Left.

---

(14) The term “thin film” is often used in the literature to denote film thicknesses in the nanometre range, up to 1 µm[816, Sect. 523-05-02]. In contrast, our focus is on films approximately 10 µm thick, hence the “(Not So) Thin” heading. Of note, this 10 µm film thickness target was set arbitrarily, based on dye-based sensing films found in the literature[468, 472, 476].

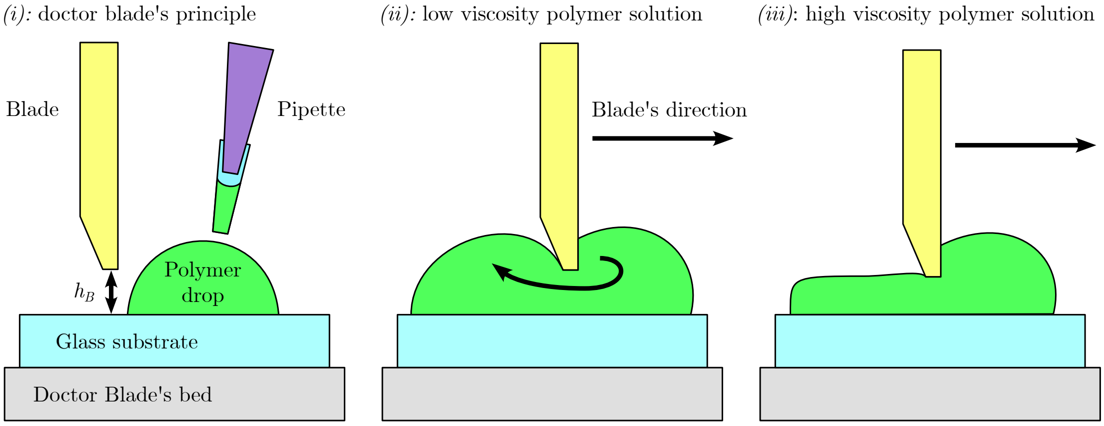

Figure 5.13: Doctor blade working principle: A blade can be adjusted vertically to a height h_B above the substrate. A drop of polymer is then deposited in front of the blade using a pipette *(i)*. The blade then spreads the polymer drop onto the surface. However, the resulting wet film thickness is strongly dependent on the viscosity of the polymer solution. If the solution is too fluid *(ii)*, it flows under the blade and bulges behind it, forming a wet film much thicker than h_B. Conversely, if the solution is sufficiently viscous, the bulging is minimal, and the wet film achieves the desired thickness.

At first, it was readily observed that—due to the limited amount of polymer solution that could practically be deposited at a time—h_B was limited to approximately 250 µm. Indeed, using larger substrate / blade gaps resulted in wet thin films that were thick at the beginning—*i.e.* close to the blade—but which became thinner and thinner after less than 1 cm of blade travel, due to polymer depletion. Then, it was also observed that h_B values in the 150–250 µm range yielded dry film thicknesses of very similar values—0.91 µm (SD 0.16 µm) for h_B = 150 µm and 1.22 µm (SD 0.14 µm) for h_B = 225 µm when using 2m% HPMC solution (averages and SD computed on three measurements on three different films, 9 measurements in total for each h_B value). This was ascribed to the phenomenon depicted in Figure 5.13, Centre and Right panels, *i.e.* back-flow of polymer solution under the blade leading to wet thin films far thicker than h_B. Luckily, this behaviour disappeared when using more viscous solutions—*e.g.* 10% polymer in solution, which has a viscosity akin to that of honey, or chocolate syrup (approximately 2–10,000 cP). For instance, 10m% PAN in DMF yielded dry thin films of 7.87 µm (SD 0.85 µm) and 16.0 µm (SD 1.3 µm) for h_B values of 100 and 200 µm, respectively (between 7 and 12 measurements per film, on three different films, 21 and 36 measurements in total for each configuration). This 10m% concentration was found to be a satisfactory intermediate between *(i)* having a quickly dissolving solution but back-flow issues—which happened for concentrations below approximately 5m%—and *(ii)* having a solution too thick to be dissolved in a reasonable time, mixed magnetically, or practical to handle—which happened for concentrations above approximately 15m%. For these reasons, **this 10m% value was selected and used in the remainder of this doctoral work**, be it for PAN in HPMC or for HPMC in water / ethanol mixtures.

Then, a better alternative to the K Control Coater was sought: the blade must be removed for cleaning after each thin film is deposited—otherwise, gooey, partially dried polymer builds up, contaminating and scratching the next thin film—and the h_B adjustment must be redone afterward using a micrometric screw and shims. This is a time-consuming process, which additionally introduces a source of variability with h_B adjustment, and it was thus decided to switch to screen printing instead. To this end, a large PTFE blade was machined, and used in combination with a framed Surface Mount Device (SMD) stainless steel stencil—see Appendix F for detailed drawings. PTFE was selected because of its ease of cleaning, while framed SMD stencils were found convenient to work with. They can furthermore be ordered with arbitrary and accurate cuts to accommodate any screen printing need, while being available in various thicknesses in the 80–300 µm range. Moving the blade was done by hand, and resulted in thin films of mean thickness 9.26 µ (SD 0.81 µm, 6 measurements on six films, 36 measurements in total) when using a 100 µm thick stencil and 10m% PAN solution in DMF. Seeing no degradation in reproducibility with using the K Control Coater—*i.e.* approximately a SD of 10% the film thickness—and being much more convenient to work with in the lab, this screen printing technique was thus adopted for the remainder of my work.

Of note, the use of coating rods—*a.k.a.* spiral rods, coating bars, wire(-wound) bars, grooved (metering) rod, or a combination thereof—was also considered, but this trail was not explored due to a lack of time. Additionally, there was no strong incentive to try and polish the thin film fabrication technique: in case of industrial mass-production, roll-to-roll processes—fine-tuned by experts—are likely to be used. The added value of this doctoral work is thus more on the formulation of the thin film chemistry and the implementation of the sensing technique than on manufacturing thin polymer films of highly reproducible thickness.

5.5.3 Successful Proof of Concept

A first successful proof of concept was developed and presented at the NEWCAS 2024 conference[91] using the afore-presented optical sensing scheme, opto-electronics, screen printing setup, and polymers / solvents / dyes combinations. The main objective of this early prototype was to validate all the components of the resulting CO_2-sensing acquisition chain. Additionally, this was an ideal opportunity to also validate the theoretical considerations on the accuracy of phase measurements developed in Section 4.4. Indeed, it has been demonstrated that, given that the phase noise of the sampling ADC can be neglected—see Equation 4.145:

$$\mathrm{RMSE} \approx \frac{1}{\sqrt{N}\cdot\mathrm{SNR}}, \tag{5.3}$$

wherein N is the number of samples, and SNR is the signal-to-noise ratio of the measured signal (see Section 4.4 for further information). Thus, by increasing either N or the SNR, one should in theory be able to lower the RMSE on φ_{mes} at will—a theory that I aimed to validate with the following experimentations.

5.5.3.1 Material and Methods

Fluorescent thin films were fabricated using 25×25 mm polished soda lime glass substrates, onto which two polymer layers were successively screen printed on top of each other. The first layer consisted of a 100 µm-thick wet film of the following solution: 52.4 mg Ru-dpp and 524 mg PAN in 5 mL DMF (1m% of Ru-dpp added to a 10m% PAN solution in DMF). After complete solvent evaporation at room temperature, the second layer was applied, which consisted of a 100 µm-thick wet film of the following solution: 47.0 mg HPTS, 993 mg HPMC, 47 mg Tween 20, and 60 µL of a 25% TEAH solution in methanol, in 10 mL of a 50:50 ethanol / distilled water mixture (1m% of HPTS added to a 10m% HPMC solution in ethanol / water). The total thickness of the two stacked films was measured to be 10.9 µm.

5.5.3.2 Measurement Protocol

Two distinct measurement sessions were performed. At first, the films were submitted to water-saturated 0, 5, 10 and back to 0% CO_2 in N_2 at 25°C, while measuring φ_{mes} every second. A 50 kHz excitation frequency was used with a 15 mA amplitude / 20 mA offset LED driving signal, while taking $N = 10$k samples per measurement at 250 kspl.s^{-1}.

Then, the CO_2 concentration was fixed to 5% while the sample count was varied from 50 to 50k with a 15 mA fixed excitation signal amplitude in a first set of measurements. In a second phase, the amplitude of the driving signal was varied from 1 up to 24 mA with a fixed $N = 10$k sample count and 24 mA offset. In these two configurations, 300 phase measurements were taken and their RMSE was computed.

The excitation frequency and sampling rate were the same in all measurements. Most importantly, the excitation frequency f_0, sampling frequency f_{s}, and sample count N, were chosen such that $N\cdot f_0/f_{\mathrm{s}}$ is an integer, in order to ensure a synchronous sampling situation—see Section 4.4. Finally, all experiments were performed under 100% relative humidity, consistently with expected levels under occluded skin—see Section 3.3.2.

5.5.3.3 Results

5.5.3.3.1 Response to CO_2

The typical thin film response to different CO_2 levels may be seen in Figure 5.14, Left. Initially, in pure N_2, all the HPTS is present in its strongly fluorescent anionic form. Since the fluorescence time of HPTS is only of a few nanoseconds—as opposed to that of Ru-dpp which is in the microsecond range—the measured phase φ_{mes} is maximal, being “lifted” upwards by HPTS. On the contrary, when the percentage of CO_2 inside the enclosure rises, the HPTS gradually turns into its non-fluorescing protonated form. Thus, φ_{mes} shifts towards lower values, being “dragged” downward by the long fluorescence time of Ru-dpp.

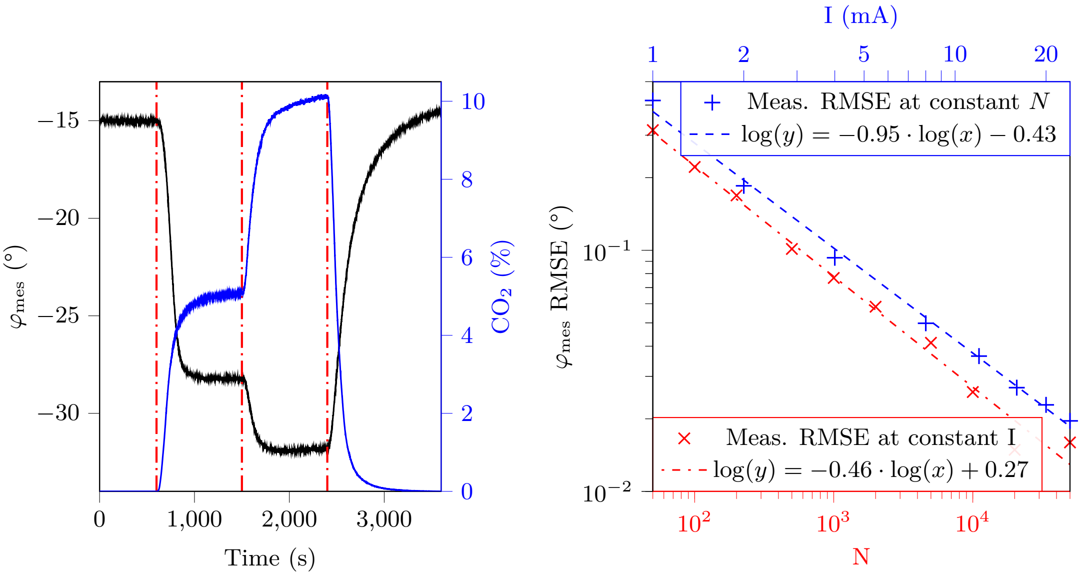

Figure 5.14: **Left:** phase response of the fluorescent thin film (in black) upon exposure to different CO_2 levels (in blue). The red, dash-dotted, vertical lines correspond to the times at which the gaseous mixture in the enclosure was changed from pure N_2 to 5% CO_2, 10% CO_2, and pure N_2 again. **Right:** RMSE of the phase measurements. Each data point is computed from 300 phase measurements. The associated (log-log) linear regressions are least-square fitted ($R^2 \geq 0.99$).

Unfortunately, while Figure 5.14, Left, indicates no major time lag between changes in CO_2 levels and the associated phase shifts of the thin film, measuring the response time of the latter proved challenging due to the slow response time of the enclosure. In other words, it takes a considerable amount of time for the system to reach a specific CO_2 level. Addressing this limitation is currently under investigation to shorten the equilibrium time of the measurement setup, thus enabling the characterization of the thin film’s response time. Still, making the approximation that *(i)* the sensor is a first-order system, and that *(ii)* it responds to a ramp of CO_2—which holds relatively true at the beginning of the CO_2 exponential response where it is almost linear—leads to a response time estimation of about 47 s, which is on par with the existing literature of thin film dye-based CO_2 sensing—see Section 4.1.2.4 and references therein.

5.5.3.3.2 Theoretical Results Validation

Figure 5.14, Right, presents on a logarithmic scale the experimental validation of former theoretical results describing the decline of the phase measurement RMSE with an increase in N or SNR—see Section 4.4.5.2. In this case, Equation 5.3 becomes:

$$\log(\text{RMSE}) = -\frac{1}{2} \cdot \log(N) - \frac{1}{2} \log(\text{SNR}) \tag{5.4}$$

Since $\text{SNR} = \frac{A^2}{2 \cdot \sigma_x^2}$, wherein A is the amplitude of the excitation signal and σ_x the variance of the additive Gaussian noise added, Equation 5.4 further becomes:

$$\log(\text{RMSE}) = -\frac{1}{2} \cdot \log(N) - \log(A) + \log(\sqrt{2} \cdot \sigma_x) \tag{5.5}$$

This equation explains the slopes of the two linear regressions performed in Figure 5.14, Right. Indeed, when N is varied with a constant illumination intensity (Figure 5.14, Right, in red), the observed slope of -0.46 is close to the theoretical value of $-1/2$. Similarly, when the LED intensity is varied while keeping a constant sample count (Figure 5.14, Right, in blue), the observed slope of -0.95 is close to the theoretical value of -1, which is expected since the optical power A of an LED is directly proportional to its driving current.

Those two results thus validate the theory presented in Section 4.4, and allow for a better comprehension of the reachable accuracy in an f-DLR sensing scheme. In particular, they show that even with a moderate number of samples and a relatively low intensity—*i.e.* 10k samples (40 ms at 250kspl/s) and 15 mA—an RMSE below 0.03° can be reached. This RMSE would in turn translate into errors in CO_2 concentration estimation of roughly 0.05% (≈0.4 mmHg), according to the results presented in Figure 5.14, Left, which may be acceptable for tcpCO_2 monitoring in clinical practice[69].

5.5.3.4 Conclusion

This first proof of concept gives promising clues for the use of an f-DLR sensing scheme for accurate CO_2 sensing in general, and hopefully to tcpCO_2 monitoring applications in particular. Of note, the results presented in Figure 5.14 are in good agreement with existing literature on the topic of thin film, fluorescence-based, CO_2 sensing[646], as well as with the theoretical considerations on the accuracy of f-DLR measurements presented in Section 4.4. In particular, these results indicate that a shorter acquisition with a higher emission power—*i.e.* decreasing N and increasing A—may be desirable from an RMSE and power consumption point of view. This paves the way for power consumption analyses similar to that recently presented by Ebrahimi *et al.* in the case of PPG sensors[820], but for DLR-, fluorescent-based CO_2 sensors.

The obtained fluorescent thin film exhibited a clear correlation between its phase shift and the surrounding CO_2 concentration, even if its response time could unfortunately not be measured accurately, a limitation that should be addressed in future works. Experimental validation of theoretical findings regarding the decline of φ_{mes} RMSE with increased sample count or signal-to-noise ratio also demonstrated that—even with a modest number of samples and limited illumination power—an accuracy below 0.03° on φ_{mes} may be reached. This value in turn leads to pCO_2 estimation accuracy well below medical expectations.

Despite these encouraging results, two significant issues remain: a strong influence of humidity on the intensity of HPTS fluorescence was observed, and some amount of photobleaching also affected both HPTS and Ru-dpp.

5.5.4 Humidity Influence

5.5.4.1 The Issue

Glass slides were prepared as described in Section 5.5.3.1, but with only one of the two luminescent thin films—*i.e.* with only a film of HPTS in HPMC or with only a film of Ru-dpp in PAN. While no humidity influence was observed for the Ru-dpp / PAN films, HPTS / HPMC films were on the contrary exceedingly sensitive to it, as illustrated in Figure 5.15, Left. Two compatible hypotheses may explain this observation, and are discussed below.

5.5.4.2 First Hypothesis

($\mathcal{H}_1$): there is not enough hydration water in the HPMC matrix at ambient humidity levels—*i.e.* in the 40–60% RH range—and only by reaching very high RH values can sufficient amounts of water be available for HPTS to fluoresce strongly(15). This first hypothesis is comforted by the fact that water uptake curves for HPMC follow the same exponential aspect as in Figure 5.15, Left. This exponential aspect is indeed shared by a variety of hygroscopic polymers, as can be seen in Figure 5.15, Right—let us ignore silica data, which are discussed below—but also in the works of Thijs *et al.*[806], Patel *et al.*[793–795] and Yang *et al.*[803], to cite a few.

If ($\mathcal{H}_1$) is true, this humidity sensitivity issue may be mitigated by choosing a more hygroscopic polymer than HPMC, such as gelatin, pullulan[803], hydroxypropyl cellulose[794], polyvinylpyrrolidone[795], PAA-Na[806], PEG, sorbitol, or carboxymethyl cellulose sodium salt[821], for instance. Additionally, adding more significant amounts of some hygroscopic plasticisers—*e.g.* glycerol or PEG—might also be beneficial to increase HPMC water uptake[822]. Indeed, the quantity of Tween 20 that we added was mainly a guesstimate based on the work of Fernandez-Ramos *et al.*[471], and amounts to about 4m% of the dry film. By contrast, other authors—not attempting at manufacturing CO_2 sensing films, but rather studying the water uptake properties of polymer / plasticisers pairs—used plasticiser contents in the 20–50m% range[808, 822–824], *i.e.* ten times more than we did.

---

(15) Dry HPTS crystals do not fluoresce strongly, as opposed to their solution in water. When films dry out, they turn from a bright fluorescent yellow-green to a pale non-fluorescent yellow. Personal observations.

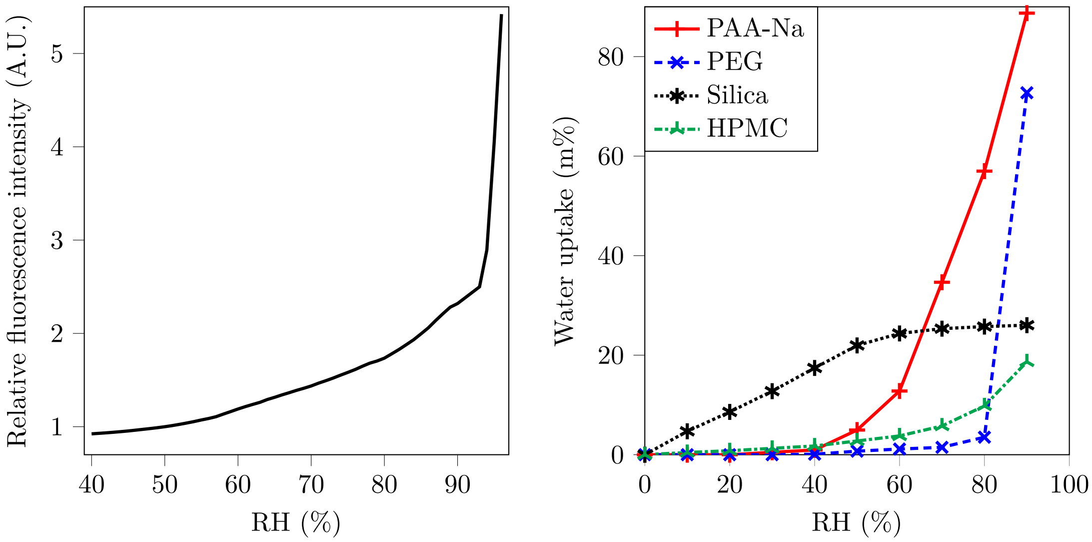

Figure 5.15: **Left:** humidity influence on the fluorescence intensity of HPTS thin films measured at 27° in pure N_2. The breaks in the curve observed at 90 and 93% are due to a lack of data on the 90–93% RH range, a linear interpolation was thus used to fill the resulting gap. The intensity was normalised with respect to its value at 50% RH. **Right:** water uptake of different compounds as a function of RH. Data sources: polyacrylic acid sodium salt (PAA-Na), polyethylene glycol (PEG), and silica data come from Thijs *et al.*[806] and were measured at 30°C, while HPMC data are those of 100cp Affinisol from Patel *et al.*[794], and were measured at 25°C.

Alternatively, no amount of uptaken water might be *enough* to completely eliminate the humidity dependence of the fluorescence intensity of HPTS-containing thin films. In other words, the issue may lie not in the water uptake of HPMC being too low, but in its increase with humidity—*i.e.* the slope of HPMC's water uptake isotherm—being too large. In this latter case, it might be a better choice to move to a not-so-hygroscopic material that has an almost flat water uptake isotherm, such as silica—see Figure 5.15, Right. Indeed, it has almost the same water uptake across the full 60–90% RH range. A film-forming polymer with this kind of behaviour might thus be an interesting alternative to HPMC.

Finally, since it has been suggested that hydration water might be bound to the phase transfer agent—TMAH, in our case—rather than to the polymer itself, as mentioned in Section 5.3.2.1, maybe solely increasing the TMAH concentration could reduce humidity cross-sensitivity. In the same line of thought, several authors also mentioned increasing the phase transfer agent concentration for stability purposes[361, 470, 475, 480]. This trail thus deserves particular attention for upcoming developments on the presented work.

further research is needed

5.5.4.3 Second Hypothesis

($\mathcal{H}_2$): water uptake changes the optical properties of the HPMC thin films. Indeed, swelling usually accompanies water uptake in hygroscopic polymers to some extent[792], which may change how light propagates throughout thin films. Water uptake can also influence the refractive index[825] or the transparency of polymer layers[826]. In the particular case of HPMC, Trezza *et al.*[827] reported a decrease in gloss and an increase in whiteness index with increasing humidity levels, while Laksmana *et al.*[828] reported a significant swelling of HPMC with increasing RH values. Both these phenomena may in turn influence light propagation inside the HPMC thin films, and thus their resulting fluorescence intensity. For instance, a strong haziness of the films may induce strong scattering within the films and increase the resulting fluorescence signal, in a similar way to when TiO_2 particles are added[363].

However, this second hypothesis does not seem extremely likely given the magnitudes of the above-mentioned phenomena, and was mainly mentioned here for the sake of not neglecting any potential research avenue. Of note, while there exists an extensive literature(16) on the swelling mechanisms of (potentially doped with numerous types of plasticisers, nanoparticles, pigments, and the like) HPMC *matrices*—*i.e.* HPMC powder pressed into tablets—almost no studies were available on the swelling and change in optical properties of HPMC-based *thin films*.

---

(16) See *e.g.* Gao *et al.*[829] which is a good stereotype of the said literature.

5.5.4.4 Is This Even a Problem?

At first glance, the fact that a 5–10% RH increase can more than double the HPTS fluorescence intensity when the latter is entrapped in HPMC thin films—as shown in Figure 5.15, Left—may seem devastating for the future of dye-based CO_2 sensing as presented in the second half of this doctoral work. However, things may in fact not be as desperate as they appear: as discussed in Section 3.3.2, occluded skin is likely to be humidity-saturated, meaning a constant 100% RH value. If this holds true, humidity cross-sensitivity will not be an issue in real-world transcutaneous applications. Yet, this cross-sensitivity remains an issue for the in-lab thin film characterisation—and formulation optimisation—processes. Indeed, achieving humidity levels above approximately 95% proved to be exceedingly difficult in practice: if any single part of the gas piping after the humidification stage—or any part of the enclosure containing the film under test—is below the gas temperature, condensation occurs at the culprit cold spot, thus lowering the humidity content of the gas below 100%. Of note, while adding heating elements inside the enclosure and a heated sleeve around gas pipes mitigates the issue, it remained unfeasible to reach humidity levels in the 95–100% range. Alas, this latter range is that of highest humidity cross-sensitivity—Figure 5.15, Left. This makes the difficulty of reaching humidity saturation particularly troublesome in practice. Therefore, eliminating the humidity cross-sensitivity of HPTS thin films still seems essential, and should be the subject of future research. Additionally, 100% RH does not translate into the same water chemical activity depending on the temperature[830]. Thus, if it is this activity that impacts HPTS fluorescence and not the RH level *per se*, even saturated humidity conditions would be particularly cross-sensitive towards temperature.

further research is needed

Of note, while the above-mentioned difficulty in reaching very high humidity levels holds for the main gas mixing and equilibration setup that was used for the majority of my experiments—*i.e.* a modified Bell Flow setup(17) which achieves accurate regulation of both humidity and temperature (±0.3°C, ±0.5% RH)—a secondary enclosure was built using means at hand. The latter could not achieve as good temperature and humidity regulation accuracies (±0.5°C, ±1.5% RH), but made it possible to reach $\leq$99% RH, at the cost of condensation inside the enclosure. This secondary enclosure was used for the HPTS photobleaching measurements presented below.

5.5.5 Photobleaching and Quenching

As mentioned in Section 5.1.1, both photobleaching and O_2 luminescence quenching were expected to be major issues, especially concerning Ru-dpp phosphorescence. Thus, investigations were conducted on both luminophores in the presence and absence of oxygen.

5.5.5.1 HPTS Photobleaching

Starting with HPTS, the photobleaching of thin films entrapping it in HPMC is shown in Figure 5.16. The film composition is identical to that described in Section 5.5.3.1, and the films were exposed to $\geq$99% RH and 25.4±0.2°C for over one hour. Probing was achieved using the same above-presented f-DLR setup, but looking at the modulus of the DFT of the measured signal, instead of its phase. Optical probing was performed each second, using a 50 kHz modulated sine wave, having a 15 mA amplitude and 20 mA offset, recording 10 k samples at 250 kspl.s^{-1}—*i.e.* 40 ms probing pulses. Between the pulses, the blue LED was lit up with a 40 mA current to speed up photobleaching. To give an idea of the scale, this translates into an illumination power of about 180 W.m^{-2}(18).

It appears that HPTS is quite sensitive to photobleaching, consistently with the above-mentioned observation of Nairn *et al.*[741]. A first-order time constant of approximately 8.37 h was observed, corresponding to a loss in fluorescence intensity of 11.7%.h^{-1}. However, this may not pose a problem for practical tcpCO_2 sensing applications: as presented in Section 5.5.3, using a number of samples N = 10 k and a 24 mA offset / 15 mA amplitude probing signal results in an already very satisfying accuracy. These conditions translate into a signal of 24 mA average value (9–39 mA peak to peak) and 40 ms duration. If the final tcpCO_2 sensor takes

---

(17) Unfortunately, due to the age of the setup, no further information is available about this apparatus, since no model name or serial number could be found. It is identified only as a humidity regulation system manufactured by Bell Flow (Japan) in the late 1990s / early 2000s, equipped with an additional temperature regulation system (PR-59, Laird Technologies).

(18) Value computed for a 1 cm spot diameter, assuming no losses in the illumination block, and using Thorlabs LED450L's efficiency and intensity / voltage characteristics.

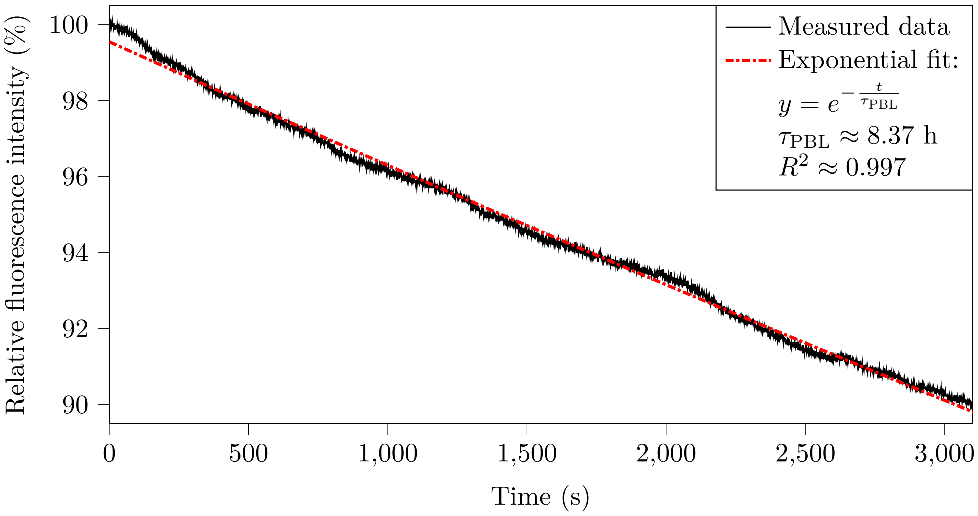

Figure 5.16: Temporal evolution of the fluorescence intensity of HPTS thin films under heavy illumination, normalised with respect to time origin. Although photobleaching is not necessarily a first-order reaction[683], an exponential fit led to a slightly higher R^2 than a linear one in this particular case ($R^2 \approx 0.995$). Using a linear model led to a photobleaching rate of 11.3%.h^{-1}.

one measurement per minute during two weeks of patch wearing(19), this results in 806 s of total illumination. Using a linear dependency of photobleaching on light intensity—which is likely to be a worst case(20)—the resulting HPTS fluorescence intensity decrease would be of only 1.85%. Still, this phenomenon could be further minimised by two different means.

At first, the measurement conditions could be fine-tuned towards lower intensities: keeping a 15 mA amplitude, the offset could be lowered down to 15 mA without loss in accuracy, resulting in a 15 mA average value (0–30 mA peak to peak). Additionally, both the amplitude and length of the signal could be decreased, leading in a predictable—using Equation 5.5—loss in accuracy at the expense of much less photobleaching. In particular, if the HPTS photobleaching phenomenon—and especially its (non-)linearity towards illumination power—were accurately known, it would be possible to choose between increasing or decreasing the sample number and illumination power while minimising photobleaching. Further research on the HPTS photobleaching should thus be conducted if its occurrence proves to be an issue in practice.

further research is needed

Second, as mentioned in Section 5.1.1, anti-fading agents can be added to reduce the photobleaching of luminophores. In the particular case of HPTS, 1,4-diazabicyclo[2.2.2]octane (DABCO)—*a.k.a.* triethylenediamine (TEDA)—has been reported by a number of authors to greatly reduce photobleaching, resulting in extremely photostable sensing films[831, 832]. Alas, time was running short to try and add some DABCO to my HPTS thin films. This second trail therefore remains a future path to explore to further reduce HPTS photobleaching.

further research is needed

5.5.5.2 Ru-dpp Photobleaching and Quenching

Ru-dpp photobleaching was assessed using the same probing scheme as HPTS—*i.e.* one short probing pulse per second with heavy illumination in between—in eight configurations, which correspond to two modalities of three different parameters ($2^3 = 8$).

1. Two different **film formulations** were tested, changing the Ru-dpp encapsulation polymer: using PAN (10 mL DMF, 1.05 g PAN, 17.5 mg Ru-dpp), and using HPMC (10 mL ethanol, 5 mL water, 1.29 g HPMC, 21.5 mg Ru-dpp(21)). The idea was to validate our polymer choice by comparing a highly O_2-impermeable polymer (PAN) with a highly O_2-permeable one (HPMC). It was expected that photobleaching should be less pronounced in PAN than in HPMC, especially in ambient air ($\mathcal{E}_1$).

---

(19) This duration was chosen based on the practical lifetime of transcutaneous blood glucose monitors—*e.g.* Freestyle Libre (Abbott, USA).

(20) Photobleaching is often non-linearly dependent on illumination power, and higher power levels lead to significantly faster photobleaching[687, 690].

(21) Contrary to HPTS / HPMC films, the ethanol / water ratio was increased to 2:1 due to the poor solubility of Ru-dpp in water which led to incomplete dissolution otherwise.

2. Two different **film drying methods** were evaluated: drying the films in ambient air, or in vacuum for 10 min. Vacuum drying was expected to remove the small air bubbles that may otherwise be present inside the films, and thus decrease the presence of O_2 within them. Photobleaching was thus expected to be less marked in vacuum dried films, ($\mathcal{E}_2$).
3. Two different **atmospheres** were tested, both at 25°C: dry N_2, and ambient air (38% RH). Due to the harmful role of O_2 in photobleaching, it was expected that dry N_2 would lead to less photobleaching than ambient air, ($\mathcal{E}_3$).

The resulting reductions in phosphorescence intensity are illustrated in Figure 5.17.

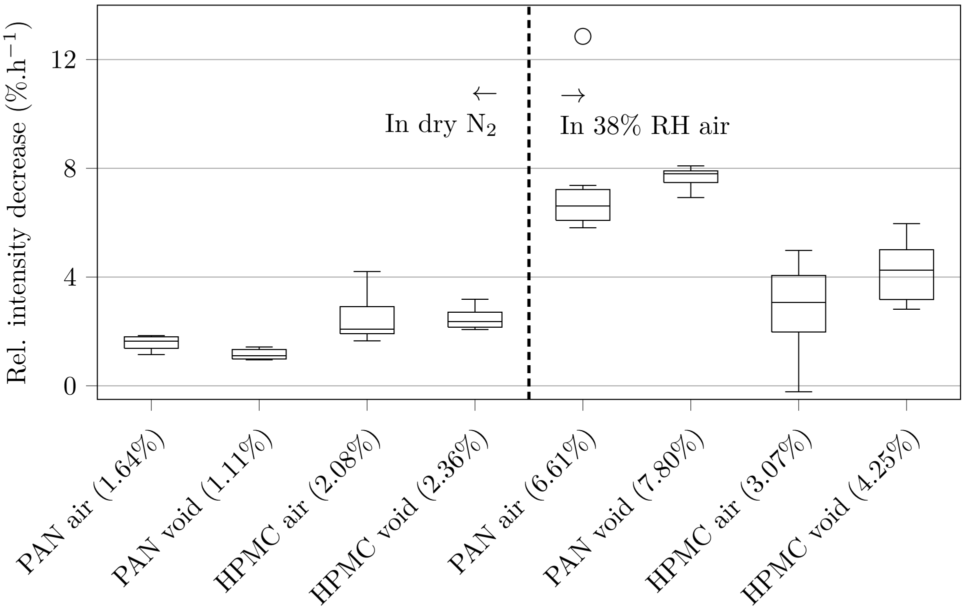

Figure 5.17: Ru-dpp photobleaching expressed as relative intensity decrease under different conditions. Each box-plot corresponds to six different films whose photobleaching was measured during 3000 s, and whiskers extend at most to 1.5 times the interquartile range. Median values are indicated in parentheses in the x-axis ticks' labelling.

At first, it is reassuring to note that Ru-dpp photobleaching is relatively low for all the conditions tested. With median values in the 1–8%.h^{-1} range$^{(22)}$, this translates into a real-world phosphorescence intensity decrease in the 0.2–1.8% range over two weeks of measurements, taking one measurement per minute. It also appears that photobleaching is lower in N_2 than in ambient air, as expected ($\mathcal{E}_3$). However, the other results reported in Figure 5.17 are quite surprising, deceiving some of the above-presented expectations. Indeed, vacuum drying the films does not seem to have any major impact on photobleaching, apart perhaps from slightly reducing the dispersion of the measurements$^{(23)}$, so ($\mathcal{E}_2$) is not verified. In the meantime, while PAN encapsulation does reduce photobleaching in N_2 as compared to HPMC this is no longer the case in ambient air, whereas the opposite behaviour was expected—*i.e.* no major difference in N_2 but a major photobleaching decrease in ambient air, ($\mathcal{E}_1$). More shockingly, air dried HPMC exhibits a negative value in ambient air!

To better understand what happened, some additional measurements were taken using much longer recording durations (26 000 s / 7.2 h). Corresponding representative temporal plots can be observed in Figure 5.18: while PAN films exhibit an exponential decrease from early on, HPMC films first exhibit some strange behaviour before settling to reach a steady-state photobleaching rate after some three hours. The reason for this is still unclear at the moment, with no plausible candidate hypotheses at hand. Maybe some impurities initially present in HPMC can promote Ru-dpp phosphorescence before being photobleached, but this seems quite unlikely, and the mystery remains. Besides this first anomaly, observing Figure 5.18 in the 3–7 h range still gives

---

(22) No exponential fit was performed for Ru-dpp due to the unexpected shapes of the photobleaching curves—see Figure 5.18. Thus, those photobleaching rates were measured on 3000 s acquisitions and scaled to get a "per hour" value.

(23) This would require more tests to confirm, although a Bartlett test comparing the variances of N_2 and ambient air populations (N=24 in each population) led to a p-value below 10^{-4} (normality was tested using Shapiro-Wilk test, after $x \mapsto \sqrt{x}$ transformation).

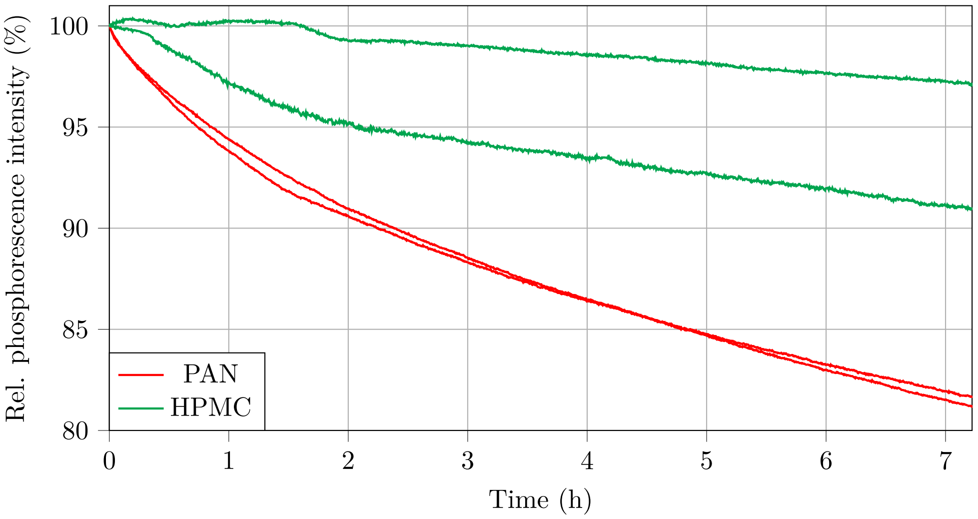

Figure 5.18: Temporal evolution of Ru-dpp photobleaching. Films were air dried and photobleached in ambient air.

a much higher photobleaching rate for PAN than for HPMC (~2.4 *vs* 0.7%.h^{-1}). This is against all odds, and in contradiction with the afore-mentioned existing literature on photobleaching, O_2 permeability, and encapsulation—see Sections 5.1 and 5.3.1. Again, the reason for this is still unclear. One possible trail to follow would be to study more thoroughly the photobleaching of Ru-dpp in a variety of media—*i.e.* in several polymers and solvents—to try and identify a pattern or degradation pathway for this photobleaching.

further research is needed

Lastly, Ru-dpp phosphorescence quenching was also assessed by observing the phase shifts of Ru-dpp phosphorescence signals, which are represented in Figure 5.19. Again, it seems that vacuum drying reduces the variability of measurements, especially in the case of PAN films. However, contrary to the photobleaching case, the encapsulating effect of PAN seems to be effective, since φ_{mes} changes of less than 0.5° for PAN films between N_2 and ambient air, whereas it shifts by almost 3° for HPMC in the meantime. That being said, the reader should take these last results with a *shaker* of salt, as it was observed that phase measurements tended to be influenced by the fluorescence intensity as well. This is a flaw of the photodiode's TIA, which appears to have led to phase measurement errors in the ±1° range(24). This latter observation triggered the development of a double-stage, op-amp based, low-noise and high-gain TIA to try and mitigate this issue. However, this amplifier has not been tested yet, and thus remains beyond the scope of this thesis.

5.6 Conclusion

This chapter begins—Section 5.1—with the presentation of two photochemical mechanisms that make luminescence measurement practically challenging: namely photobleaching and quenching. Those phenomena tend to affect particularly long-lived luminophores—*i.e.* phosphors—and call for some kind of mitigation strategy. To this end, it was decided to select an O_2 impermeable polymer for the phosphor that ended up being used, and a multilayer thin film architecture.

A second part—Sections 5.2 and 5.3—focuses on the selection of appropriate chemicals, based on the different criteria that the previous chapter established: fluorescence lifetime, permeability, availability, cost, ease of implementation, stability, *etc.* This benchmarking work led to the selection of two dye / polymer pairs: Ru-dpp in PAN, and HPTS in HPMC.

A third part—Section 5.4—briefly presents the electronics that were used for practical DLR measurements, while the detailed design study associated with the optical design and electronics dimensioning is relegated to Appendix E.

Finally, a fourth part—Section 5.5—concentrates on an experimental validation of the theory presented and choices made throughout all the above sections and chapters. While an initial proof of concept yielded encouraging results, many research questions remain open, particularly regarding dye photobleaching and humidity influence on HPTS-containing thin films.

---

(24) This error should be thought of as an offset—*i.e.* a constant value added to φ_{mes}—being dependent on both the amplitude and offset of the signal that the TIA sees.

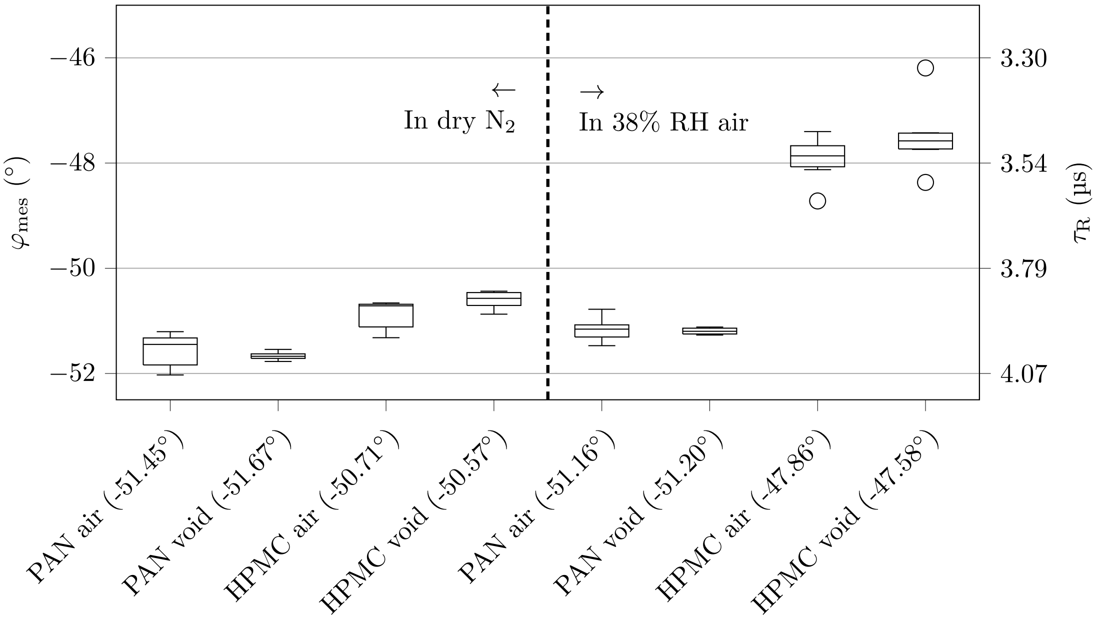

Figure 5.19: Phase shifts of PAN and HPMC thin films containing Ru-dpp under various conditions. Each box-plot corresponds to six different films, and whiskers extend at most to 1.5 times the interquartile range. Median values are indicated in parentheses in the x-axis ticks' labelling. Corresponding decay times assuming a first order decay phenomenon are given on the right axis ($\tau_R = -\frac{\tan(\varphi_{\mathrm{mes}})}{2\cdot\pi\cdot f}$, $f = 50$ kHz). Be cautious that the right axis scale is thus non-linear.

These observations conclude the present chapter, which is the last to report the contributions of this doctoral work and the penultimate chapter of this thesis. Unlike the previous chapters, this one is much more experimental in nature, and since time was running short, several drastic, arbitrary choices had to be made. Similarly, several questions remain unanswered. Fortunately, to ensure the reader is not left wanting more, a final chapter explores the future research prospects envisioned to continue this work.

Chapter 6

Conclusion and Perspectives

TL;DR

This last chapter is divided into four parts. The first part briefly summarises the main contributions of this thesis. The second part then outlines the key points that need to be addressed for the future of dye-based thin film transcutaneous CO_2 sensing. The third part explores other potential research avenues not directly related to the subject of this doctoral work. Finally, the fourth part concludes this manuscript with a concise bullet-point list of the core ideas of this thesis, along with channels to follow my likely future endeavours.

Previous chapter Main Table Of Content (TOC) Next chapter

All good things must come to an end, and this doctoral journey is no exception. This final chapter has the delicate task of bringing this thesis to a close, with a dual purpose: briefly summarizing the key contributions made throughout, and highlighting promising research directions for future work. Indeed, as the reader who loves figures would have noticed, the

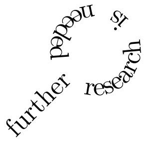

symbol appears 17 times throughout this manuscript—excluding its introductory and current occurrences, of course—which translates into at least as many open research avenues. Yet, while some of those avenues must be explored to achieve real-word non-invasive transcutaneous CO_2 sensing using dye-based thin films, others consist in more fundamental research questions that are only loosely related to the subject of this thesis, or whose answers are not critical to the development of the said sensing scheme. As a result, the perspectives-related part of the present chapter is divided in two—Sections 6.2 and 6.3—so as to accommodate for this state of affairs.

6.1 Main Contributions

This thesis resulted in four journal articles and one shorter conference communication[86–88, 90, 91], to which the hasty reader is redirected for a rapid overview of the work done. A short glance at the table of contents of this manuscript also gives a good idea of the key aspects of this doctoral thesis. For a brief synopsis, please carry on reading.

6.1.1 Context and Early Spectrophotometric Work

This doctoral work is grounded in a robust clinical and physiological context—Chapter 1 and Section 2.1—which offers clear motivations—and even a pressing need—to develop a new generation of transcutaneous CO_2 monitors. To do so, two main research avenues were initially envisioned: either *(i)* using a hypothetical change in the absorption spectrum of haemoglobin upon CO_2 capture, or *(ii)* measuring the transcutaneous partial pressure of CO_2—$tcpCO_2$—directly, thanks to the diffusion of CO_2 through the skin. Haemoglobin spectrophotometry was first investigated—Chapter 2—with the initial intention of giving birth to *pulse carbametry*, *i.e.* the equivalent of pulse oximetry, but for CO_2 instead of O_2. However, **the optical properties of CO_2Hb—both in absorbance and fluorescence—appeared to be identical to that of HHb for all practical purposes**. This nevertheless led to a first publication in the Journal of Biomedical Optics to report the absorbance spectra of O_2Hb, HHb, and CO_2Hb in the 235–1000 nm range[86]. This spectrophotometric research avenue was then abandoned, and the remainder of the time allocated to this thesis was devoted to the transcutaneous CO_2 diffusion pathway.

6.1.2 Transcutaneous CO_2 Sensing

With this ultimate goal in mind, a lot of work remained to be done in order to yield a next-generation, clinically usable, tcpCO_2 sensor:

1. The transcutaneous diffusion of CO_2 needed to be accurately characterised, in particular with respect to skin temperature. It was also necessary to get a clear picture of the other environmental conditions present at the skin.
2. These two pieces of information could then be used as guiding factors in choosing an appropriate CO_2 sensing technique for transcutaneous measurements.
3. Having chosen that technique—*i.e.* dye-based thin film sensing—several theoretical considerations needed to be put out of the way, and optimising the chemistry of the thin films remained to be done.
4. Finally, the correlation between tcpCO_2 and paCO_2 also needed to be accurately characterised with respect to skin temperature.

This doctoral work satisfyingly addressed the first two aspects of the above to-do list, partially investigated the third one, and did not have the time to even scratch the surface of the last one—except for indices related to micro-circulation measurements.

6.1.2.1 Sensing at the Skin

Starting with skin properties, a simple model based on Fick's first law was proposed to describe transcutaneous CO_2 diffusion—Section 3.1. This model led to the definition of a metric called skin *conductivity* towards CO_2, whose primary interest is that it does not depend on the ambient CO_2 level nor on the test subject's tcpCO_2, as opposed to the transcutaneous CO_2 *diffusion rate* used up till now in the literature. A custom skin conductivity sensor allowing for cutaneous temperature regulation was then designed, and later used in a clinical study involving forty participants—Section 3.2.

Briefly, this study showed that skin conductivity at most doubles from 35 to 44°C at the wrist and upper arm. This first result is encouraging for the development of next-generation tcpCO_2 sensors, since it means that **heating the skin is not mandatory from a response time point of view**, thus potentially enabling wearable sensors. This clinical study also included micro-circulation measurements at the upper arm, showing a doubling of perfusion from non-heated to 35°C, and a quadrupling from non-heated to 38°C. This second result is also encouraging, as it gives clues indicating that **heating the skin is probably not mandatory to guarantee a good tcpCO_2 / paCO_2 correlation either**. This clinical study and the above results led to a publication in the Frontiers in Physiology journal[87]. Further research was also conducted on cutaneous environmental conditions—Section 3.3—and revealed that occluded human skin is a humidity-saturated medium, slightly hypoxic, whose temperature can reach over 35°C under light clothing, and which can exudate a variety of acidic compounds.

6.1.2.2 Choosing a CO_2 Sensing Scheme

A massive bibliographic effort was then undertaken to map out the landscape of CO_2 sensing, and resulted in the publication of a review journal article in Sensors[88]. **This work, combined with the afore-described cutaneous specificities, led to the selection of dry, dye-based, thin film sensors** among the many state-of-the-art solutions suitable for CO_2 sensing—Section 4.2. The basic chemistry of these thin films was then presented, and optical sensing schemes were also reviewed—Section 4.3—leading to the selection of an f-DLR sensing scheme.

6.1.2.3 Fine-Tuning the Sensing Scheme and Thin-Film Formulation

While the theoretical foundations for (even dual-frequency) f-DLR were laid in the late 1990s by a pioneering team at the University of Regensburg[89, 642], the relationship between noise levels—*e.g.* additive or phase noises—and error in the estimation of the analyte concentration remained to be demonstrated. What initially appeared to be a simple question about accurate phase estimation from a noisy sinusoidal signal actually took several months to answer, filling over ten pages of equations—Section 4.4. These relentless efforts were not in vain, however, since **a formula was finally derived, linking noise levels, sample count, and phase estimation accuracy**—and thus CO_2 concentration accuracy in the case of f-DLR CO_2 sensing. The resulting analysis—valuable not only within the specific context of f-DLR sensing, but in the more general framework of spectral estimation whenever synchronous sampling is possible—has been published in the APSIPA Transactions on Signal and Information Processing[90].

Time was then devoted to selecting suitable chemicals for the thin film formulation, both in terms of choosing appropriate polymers and luminophores—Sections 5.1–5.3. In particular, the detrimental influence of O_2 on photobleaching and luminescence quenching was given significant attention, as was the expected impact of water uptake on HPTS fluorescence intensity, especially regarding its encapsulation into a breathable polymer. A sensing optoelectronics assembly was then designed to probe the thin films that were manufactured using the selected chemicals, demonstrating the *in vitro* feasibility of the technique for CO_2 sensing at physiological levels. **This enabled the validation of the theoretical developments mentioned above regarding phase estimation accuracy**, and led to a short communication at the 2024 NEWCAS conference[91]. Additionally, the photobleaching, quenching, and humidity influence phenomena were briefly investigated. While photobleaching should not pose a significant issue in practice, the use of anti-fading agents seems to be an interesting avenue to explore so as to strengthen the resulting thin films. It remains unclear whether the influence of humidity would be an actual problem in real-life transcutaneous applications; however, it is indeed challenging in the lab, where achieving saturating humidity levels has proven relatively difficult.

6.2 Short-Term Research Avenues for CO_2 Sensing

This section and the next focus on potential directions for future research, which were split into two categories. In the current section, the emphasis is placed on short-term research avenues that may have a direct—and potentially strong—impact on the development of next-generation tcpCO_2 sensors. In the next section, by contrast, the focus shifts to other research avenues which may not be critical to explore from a tcpCO_2 sensing point-of-view, but whose investigation is of a certain scientific interest. Of note, the issues raised in the following subsections were arranged in the same order as they appeared in the main manuscript, **not** in their order of criticality. Regarding the latter, the aspects of utmost importance for the translation of this doctoral work into an industry-ready tcpCO_2 sensor are the following:

1. finding out if a 35–37°C skin temperature would be high enough to guarantee a clinically-usable correlation between paCO_2 and tcpCO_2—Section 6.2.2,

2. improving the chemistry of the thin films in order to reduce photobleaching—Section 6.2.5—and humidity cross-sensitivity—Section 6.2.7, and

3. miniaturising the optoelectronics—Section 6.2.9—and moving from a glass to a polymer substrate—Section 6.2.8—to perform early *in vivo* tests.

6.2.1 NIR Haemoglobin Spectrophotometry

As mentioned in the conclusion of the second chapter—Section 2.5—some additional haemoglobin absorption spectra were measured in the NIR. Briefly, the protocol used was the same as that detailed in Section 2.3, with the exception that blood was not diluted, but rather *concentrated*. Indeed, due to the exceedingly low absorbance of haemoglobin species in the NIR—see Section 2.3.2.1—and in order to achieve reliable spectrophotometric measurements, it has proved necessary to reach haemoglobin concentrations at least as high as that of human blood. To do so, venous blood was centrifuged and rinsed thrice upon collection to finally keep only the erythrocytes, which were then lysed with ultrasounds, and equilibrated with different gases—CO_2, N_2, CO, and ambient air. The absorption spectra of the so-obtained O_2Hb, HHb, CO_2Hb, and COHb solutions were then recorded across the full 600-2350 nm range, and the total haemoglobin concentrations of the samples were also measured using a Cyan-Met-Haemoglobin (HiCN) standard.

Unfortunately, due to the significant water absorption in the NIR and the dilution effects that ensue—also due to a lack of time—the resulting haemoglobin spectra could not be presented in this thesis. It is envisioned to remedy this situation and publish a short paper on the NIR absorbance of haemoglobin by early 2025. **Although—and this should be stressed out—a thorough analysis is yet to be done to confirm or refute this early observation, there seems to be no perceivable difference between the absorbance spectra of HHb and O_2Hb in the NIR.** Again, this would be expected for the conformational reasons already-mentioned in Section 2.5, and would bring yet another nail to the coffin of pulse carbametry. Still, to the best of my knowledge, this would at the same time be one of the few reports of human haemoglobin in the NIR—see Table 2.1—and the first one providing tabulated coefficients.

6.2.2 paCO_2 / tcpCO_2 Correlation at Low Skin Temperature

Although *(i)* there is empirical proof that subcutaneous micro-circulation at the upper arm doubles at 35°C and quadruples at 38°C compared to baseline—see Section 3.2.5—and *(ii)* there is a sound theoretical framework to explain why this should translate into a good correlation between paCO_2 and tcpCO_2 at those temperatures—see Section 3.2.6.4.3—this correlation remains to be demonstrated experimentally. More specifically, there is—to the best of my knowledge—no report of such correlation below 37°C, and only Wimberley *et al.* did experiment at this temperature back in 1985[267]. In their study, the authors demonstrated a good agreement between paCO_2⁽¹⁾ and tcpCO_2 on a sample of only ten human subjects, making it a relatively fragile piece of evidence. **This paCO_2 / tcpCO_2 correlation issue at low temperature is, in my humble opinion, one of the strongest remaining locks to the development of wearable tcpCO_2 sensors.** Indeed, wearable battery-powered sensors cannot afford actively heating the skin for obvious power-consumption reasons, and only the existence of the latter correlation at low temperatures—*i.e.* temperatures achievable without active heating—would make their materialisation conceivable, as discussed in Section 3.2. Removing this lock to make non-invasive tcpCO_2 sensing a reality would in turn require a clinical study specifically targeting the characterisation of the paCO_2 / tcpCO_2 correlation at low cutaneous temperatures.

More specifically, this study should use a custom temperature-regulated tcpCO_2 sensor to measure the tcpCO_2 of test subjects at cutaneous temperatures in the 35–41°C range. Alongside, *(i)* clinical-grade tcpCO_2 sensors worn at the earlobe and set to their highest temperature—in order to have the closest value possible to paCO_2[69]—or even *(ii)* arterial blood gases analysers directly measuring the subjects' paCO_2 should be used as references. Ideally, the subjects should also include non-healthy individuals—which would tend to exhibit paCO_2 in the 35–45 mmHg range (4.7–6.0 kPa)—to ensure a wide dispersion of paCO_2 and tcpCO_2 values.

6.2.3 CO_2 Sensing Review Update

This section is more of a short note—as well as a disclaimer—regarding the technological review presented in Section 4.1. Indeed, this review is largely adapted from our 2022 Sensors article[88], which was itself based on literature researches from early 2020. It might thus benefit from an update including recently published works on the topic, some of which use novel sensing mechanisms that were not identified in the original review.

Firstly, several publications improved some of the afore-mentioned CO_2 sensing mechanisms—*i.e.* hydration, reduction, *etc.*—which may lead to interesting alternatives to the dye-based thin film approach that is at the heart of this doctoral work. In particular, a team from the University of Eylul published a series of papers on the improvement of HPTS-based sensors[833–836]. Other works include improvements of conductometric[837, 838], dye-based[839, 840] or carbamate formation-based[841, 842] sensors. Another interesting CO_2-sensing route has been proposed using optical probes that exhibit a change in their molecular structure upon reaction with CO_2 that differs from a simple carbamation[843, 844]. Lastly, it seems that a great deal of research effort is being devoted to Metal Organic Framework (MOF) for gas or pH measurement purposes[845, 846].

Secondly, there has also been a renewed interest for the development of novel tcpCO_2 sensing modalities in the past few years, following almost forty years of dormancy. With this respect,

---

(1) Actually, they used arterialised capillary blood punctured from the earlobe, which exhibits excellent agreement with arterial blood in terms of pCO_2[42].

two strategies emerged: *(i)* that of Grangeat *et al.*[847] or Persson *et al.*[848], using a rate-based approach[2], and *(ii)* the one proposed in this doctoral work, based on an equilibrium between the subcutaneous tissues and a thin film sensitive to CO_2. This thin film can be dye-based—as proposed by the teams of Cascales *et al.*[849, 850], Tufan *et al.*[657, 851, 852], and Cui *et al.*[853]—redox[854], or potentiometric[855], for instance. Of note, although other authors proposed equilibrium-based NDIR sensors—*i.e.* similar to that used in Section 3.2, but waiting for an equilibrium between the tissues and the sensor's chamber—the sensing volumes involved are likely to induce clinically unacceptable lags[856–858]. Finally, it is also worth mentioning two recent reviews by Tufan *et al.*[859] and Bernasconi *et al.*[860] both compiling recent works on the topic of transcutaneous CO_2 sensing.

6.2.4 Temporal Alternative to DLR

Upon discussions with Wilfried Uhring—the director of this doctoral work—he returned to his old flame for time-resolved ultrafast optical sensing, and put forth the idea that a variant of time-based Dual Lifetime Referencing (t-DLR) might be used instead of f-DLR. Accurate sensing could be achieved by using multiple low intensity pulses—to reduce photobleaching—and then measuring the decay times of the two luminophores involved. The main advantage of doing so is that the emission and reception optical filters may thus be omitted. This may be of particular interest from a large-scale industrialisation point-of-view, since the optical filters are by far the costliest pieces of equipment of the whole sensing optoelectronics. However, this sensing scheme might require more expensive acquisition electronics and should thus be carefully studied from a cost perspective.

6.2.5 Photobleaching Investigations

Although the photobleaching of Ru-dpp and HPTS is already relatively low—below 2% for two weeks of service, taking one measurement per minute—further reducing its magnitude may still prove beneficial in order to improve the sensor's accuracy. In particular, the use of anti-fading agents such as DABCO seems promising, especially for HPTS—see Section 5.5.5.1. Studying the photobleaching mechanisms and pathways for both luminophores more deeply is also mandatory to devise appropriate measures to mitigate the said phenomenon. **Most critically, knowing the dynamics of the phenomenon, as well as its dependence on the luminophores' concentrations and illumination power would allow a compromise to be made between these parameters and the illumination duration**—through the sample count N—as evoked in Section 5.5.3. Since polymer-dye interactions can also influence photobleaching—see Section 5.5.5.2—it could also be interesting to further investigate the use of different polymers for both luminophores.

6.2.6 Alternative Luminophores

Despite the significant research efforts that were put into selecting suitable luminophores for the envisioned f-DLR application—see Section 5.2—HPTS and Ru-dpp may not be the absolute optimal choice. Indeed, their selection was performed on a subset of the myriad of available off-the-shelf luminophores, and other dyes might have been benchmarked. In particular two main directions could be followed: *(i)* other long-lived organometallic complexes could be envisioned to replace Ru-dpp among those proposed by Wang *et al.*[728, Sect. 6.2], taking care to keep only the ones that exhibit a relatively low sensitivity towards oxygen, *(ii)* in line with the previous section, photobleaching could also be taken into account for luminophore selection—in addition to the cost / luminance / pH-sensitivity analysis already performed. The main issue with this latter option, however, is that photobleaching data are scarcely available in the literature for the said fluorophores. This state of affairs—combined with the photobleaching dependency towards encapsulating polymer, concentration, *etc.*—unfortunately makes objective comparisons between one luminophore and the next exceedingly difficult, if not impossible, potentially requiring thorough experimentations to yield meaningful, exploitable figures.

---

(2) This approach in its simplest form seems doomed to failure, however, as mentioned briefly in the introduction of the above-mentioned NEWCAS article[91], due to the wide variability in skin permeabilities towards CO_2 from one subject to another (see Section 3.2.5). One possible solution to overcome this issue could be to implement a per-patient calibration or to use a dual-membrane scheme—as suggested in the early work of Hansen *et al.*[289], or more recently by Persson *et al.*[848].

6.2.7 Humidity Cross-Sensitivity

The manufactured thin films demonstrated a major cross-sensitivity towards humidity—see Section 5.5.4. While it is not certain at the time of writing whether this would translate into an actual issue for real-world $tcpCO_2$ sensing, it is definitely an issue in the lab, wherein reaching humidity levels close to saturation proved to be exceedingly difficult. The reasons for this cross-sensitivity are also unclear at the time being, with two mutually compatible hypotheses put forth: *(i)* there are not enough water molecules available in the HPMC thin film at below-saturation humidity levels, or *(ii)* the humidity level has a strong impact on the optical properties of the HPMC thin film. This issue should definitely be addressed swiftly, in order to devise appropriate mitigation strategies. In particular, changing the polymer, adding more plasticisers, phase transfer agent, and investigating the McMurray hypothesis all seem possible avenues for future research.

6.2.8 Changing the Substrate

For *in vivo* use, **the manufactured sensing thin films need to switch from a rigid glass substrate to a more flexible one, to conform to the curved organic shapes of the human body**. In contrast with most of the other difficulties encountered in this doctoral work, this issue should be relatively straightforward to address. As mentioned in Section 4.1.2.4, both PEN and PET make good candidates for replacing glass: they exhibit a good barrier function towards CO_2 when used in thicknesses of about 100 µm, are optically clear, flexible, inexpensive, and do not exhibit any significant fluorescence upon 450 nm excitation when compared to the added luminophores[861]. Additionally, some tests were already performed in the lab, demonstrating good wettability and film-forming ability of both PEN and PET with respect to Ru-dpp / DMF / PAN and HPTS / HPMC / water / ethanol mixtures, and good adhesion of the films upon drying.

6.2.9 Miniaturising the Optoelectronics

With the same *in vivo* sensing objective in mind, **miniaturising the optoelectronics presented in Section 5.4 will be mandatory to make it wearable-embeddable**. This aspect is currently being investigated, and is closer to an engineering work than to an open research question, even if achieving an optical design of about 1 cm^3 is still challenging. The envisioned optical design uses smaller LED and photodiode as the above-presented ones, two interferometric excitation and emission filters, and two ball lenses(3). Including a protective glass cover, the overall dimensions of this optical setup is about $13 \times 7 \times 6$ mm. In a first *in vivo*-ready prototype, it is envisioned to use it with the legacy electronics presented in Section 5.4, potentially replacing Thorlabs' TIA by a custom one offering better performance.

6.2.10 Develop a Solid Chemical Background

This last point involves substantial work, aiming at developing a consistent theoretical chemical framework for the design of dry dye-based thin films. Indeed, although the chemistry of wet dye-based thin films relies on the classical theory of aqueous solutions and works relatively well in practice[446, 447, 455], there is currently no satisfactory equivalent for dry polymer thin films, in particular with respect to phase transfer agent concentration, or dye-polymer interactions. Admittedly, the approach usually adopted in the literature—*i.e.* considering that wet chemistry also takes place in dry thin films, as presented in Section 4.3.1—fits remarkably well with experimental data, resulting in a linear relationship between the CO_2 concentration and the ratio of fluorescence intensities I_0/I in a ratiometric scheme[460, 461, 641], or in a rational relationship between the CO_2 concentration and the measured phase shift in an f-DLR scheme[474, 699]. Yet, there is to date no theoretical background to satisfactorily explain the influence of phase transfer agent concentration nor embedding polymer choice on the response of dry thin films sensors. To the best of my knowledge, only three papers tried to investigate the influence of the concentration in quaternary ammonium anion[359, 362, 471], and all of them settle for experimental observations without theory to quantitatively back them up.

To try and make up for this lack of understanding, I started from Equation 4.26, *i.e.*

$$\mathrm{pCO_2} = \frac{K_A}{K_{13}} \cdot \frac{\big([\mathrm{Q^+}] - [\mathrm{Q^+A^-} \cdot (x{-}1)\mathrm{H_2O}]\big) \cdot \big(\mathcal{C}_A - [\mathrm{Q^+A^-} \cdot (x{-}1)\mathrm{H_2O}]\big)}{[\mathrm{Q^+A^-} \cdot (x{-}1)\mathrm{H_2O}]} \tag{6.1}$$

---

(3) Precise references are not given since developments are still ongoing.

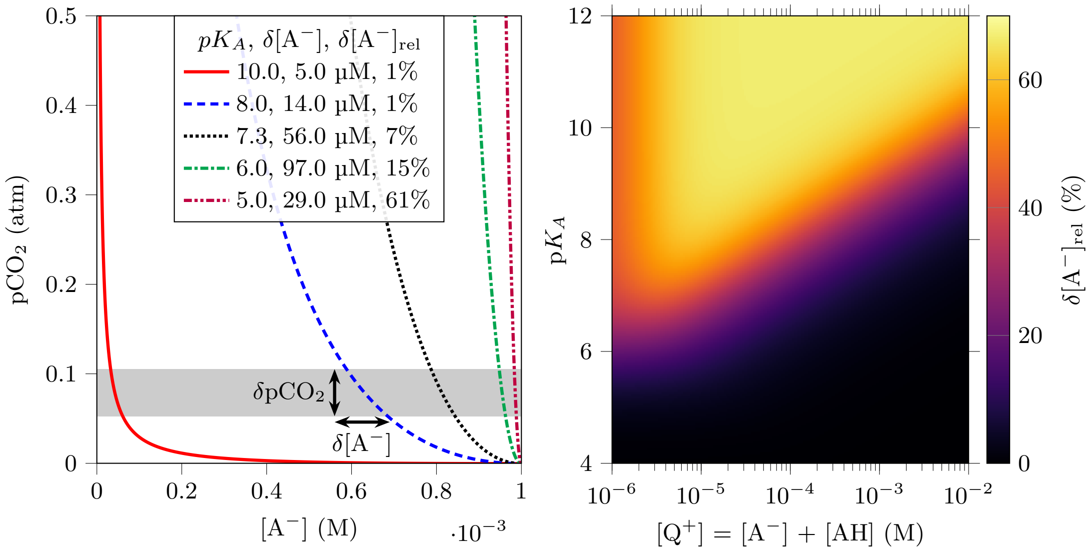

Figure 6.1: Influence of the pK_A of the pH-sensitive dye A$^-$ / AH on the sensor's response towards CO$_2$. **Left:** relationship between pCO$_2$ and the concentration in the anionic form of the pH sensitive dye, A$^-$. The grey area corresponds to the physiological 40–80 mmHg paCO$_2$ range, while δ[A$^-$] and its relative variant $\delta[\text{A}^-]_{\text{rel}}$ correspond to [A$^-$] variations across it. In this case [Q$^+$] = [A$^-$] + [AH] was set to 1 mM. **Right:** influence ot the total dye / phase transfer agent concentration and pK_A on the relative A$^-$ concentration across the 40–80 mmHg range.

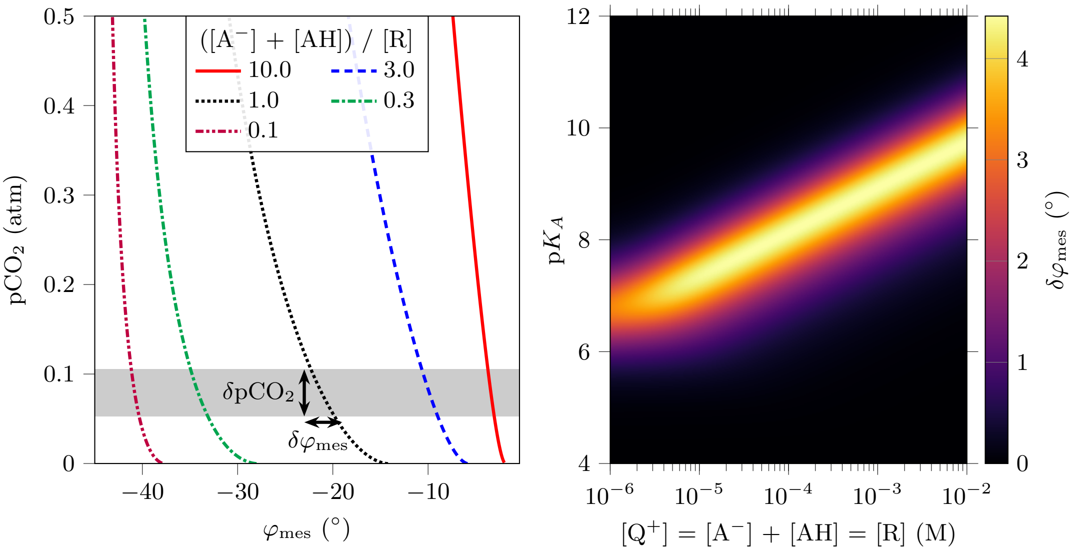

Figure 6.2: Influence of the pH-sensitive / reference dyes ratio and of the pK_A of the pH-sensitive dye on the sensor's response towards CO$_2$. **Left:** relationship between pCO$_2$ and the measured phase shift as a function of the pH-sensitive / reference dyes ratio. In this case [Q$^+$] = [A$^-$] + [AH] was set to 100 µM, the probing frequency (f-DLR scheme) was set to 80 kHz and typical literature values were taken for the optical properties of HPTS for the pH-sensitive dye, and Ru-dpp for the reference dye. **Right:** influence ot the total dye / phase transfer agent concentration and pK_A on the φ_{mes} variation across the 40–80 mmHg range.

and strived to link the concentrations in Q^+, pH-sensitive and reference dyes, the pCO_2, and the pK_A of the pH-sensitive dye, with the relative variation in the concentration of the anionic form of the pH-sensitive and—more importantly—the resulting phase shift caused by a variation of pCO_2. This analysis led to simulation results akin to those presented in Figures 6.1 and 6.2, but it was not included in this thesis for two main reasons: at first, this manuscript is already quite substantial, and this analysis would have made it even longer, not to mention the amount of time necessary to properly typeset it, a time I was running short of. Secondly, I do not have any piece of experimental evidence to back up this work, making it little more than a pipe dream at the time of writing. That being said, the upside of the coin is that **there is room for a future research program aiming at building an experimentally-supported theoretical framework, which would make designing dry thin film sensors somewhat less like walking in the dark.**

6.3 Other Open Avenues

The other research avenues presented in the following sections are clearly not essential for the improvement of the dye-based thin film CO_2 sensors on which this thesis focuses. Still, they constitute interesting research questions, whose answer might bring further insights and a better understanding of the phenomena underlying the above-presented work.

6.3.1 Blood Carbamate Formation

As mentioned in Section 2.1.2.2, there seems to be a lack of a satisfactory model to quantitatively relate the blood pCO_2 with its CO_2Hb concentration—*i.e.* with the amount of CO_2 present as carbamate haemoglobin compounds. The existence of such a model would allow for the expression of the whole blood carbamate CO_2 content as a function of its pCO_2, potentially also including the 2,3-BPG, bicarbonate ions, and haemoglobin concentrations, as well as blood pH. Although deriving such a model might not be vital from a clinical point-of-view, it might still be interesting to better understand haemoglobin CO_2 binding, and more generally blood gases transport, therefore providing valuable insights from a physiological viewpoint.

6.3.2 CO_2 Diffusion Model

The diffusion model that was introduced in Section 3.1—while allowing for useful derivations and relatively easy skin conductivity measurements—is rather simplistic, modelling the skin as a single membrane, and the tissues as an ideal pCO_2 source. As a result, this model does not correspond to any physical reality. In particular, as first mentioned in Section 3.1.1 and later emphasised in Section 3.2.6.2.1, the thickness of the model's skin membrane does not correspond to the real-world thickness of the *stratum corneum*. It might thus be interesting—in order to yield a more interpretable model closer to the histological reality of skin structure—to separately study the skin conductivities of different skin layers. In particular, such modelling could allow for the prediction of skin conductivity from a given subject's age, since age strongly influences the *stratum corneum*'s thickness[862], and this thickness strongly influences skin permeability[259].

However, to develop such a model, it would be mandatory to have the ability to measure the actual subcutaneous pCO_2 at the chosen conductivity measurement site and temperature. Indeed, as noted in Section 3.2.6.2.1, the reference $tcpCO_2$ monitor that we used could not be set at temperatures lower than 41°C. This led to conductivity values slightly over-estimated, and is thus not satisfactory from a metrological point-of-view. In particular, in order to develop the afore-mentioned model *in vivo*—*i.e.* without having to skin the subjects, but rather by gently peeling their skin with tape, for instance—it would be necessary to have a temperature-regulated $tcpCO_2$ monitor capable of low temperature measurement. Of note, in this latter case, the aim of this $tcpCO_2$ monitor would be to measure the true subcutaneous pCO_2, and not a proxy for the $paCO_2$—as is usually done by heating the skin above 41°C.

6.3.3 Sole of the Transcutaneous CO_2 Conductivity Sensor

As noted in Section 3.2.6.1.1, both *(i)* the shape of the sole of the sensor that was used to measure skin conductivity towards CO_2, and *(ii)* the skin elasticity can affect the exchange surface between the sensor and the skin. This is illustrated sketchily in Figure 6.3, Left. Each circular hole in the sensor's sole will create a small dome of skin, which will have a surface S that deviates from its ideal value of $\pi \cdot R^2$ with increasing skin curvature. This curvature itself depends on the radius of the hole—R—on the mechanical properties of the skin, and on the sensor's application force. As can be seen in the a–c parts of the figure, the change in cutaneous exchange surface between an ideal—*i.e.* perfectly flat–and worst—*i.e.* perfect half-sphere—cases can result in up to a twofold variation. Since S is then used directly to compute the skin conductivity towards CO_2 K—see Equation 3.22—this variation on S directly affects the latter$^{(4)}$.

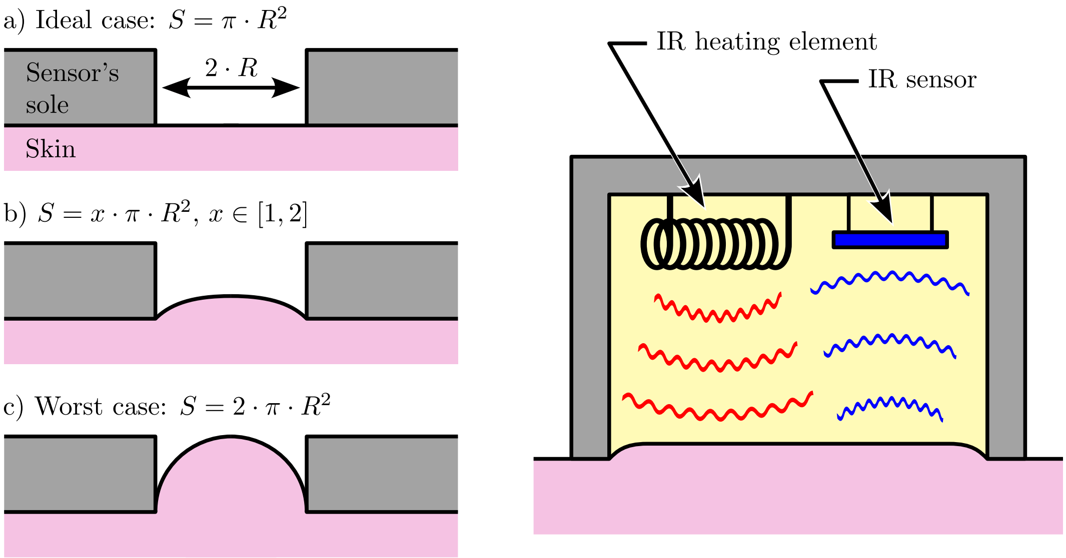

Figure 6.3: **Left:** cross-section view of the dome formation effect. Depending on several factors such as the skin elasticity or temperature, the hole radius value R, and the sensor's contact force, the dome can be more or less convex. The two extreme situations a and c correspond to a perfectly flat, or a hemispheric shape of the skin surface underneath the hole. **Right:** an alternative heating method, using a radiative heating system and a single big hole in the sensor's sole, instead of a conductive heating system and multiple holes, as was the case in Section 3.2.

Yet, as discussed in Section 3.2.6.1.1, this is no easy problem to remedy: there is a compromise to be made between the shape of the sensor's sole and its thermal efficiency. More specifically, using a single very large hole is likely to mitigate the dome formation effect, as illustrated in Figure 6.3, Right. However, without adapting the heating system—*i.e.* if the heat is brought *conductively* by the sensor's sole itself, as presented in Section 3.2.2.1—the skin at the centre of the hole would likely be cooler than the sole—*i.e.* it would be cooled at the NH temperature by the subcutaneous blood flow. One possible way to address this would be to implement a *radiative* heating system coupled to an infrared remote sensor for accurate thermoregulation of the skin surface, as presented in Figure 6.3, Right. Such a design could therefore be envisioned for future quantitative studies of skin conductivity towards *e.g.* CO_2 as a function of the skin temperature.

6.3.4 Influence of Occlusion on Skin CO_2 Conductivity

Observed if only through the whitening and swelling of the skin under a plaster, occlusion does have an impact on the properties of human skin. More specifically, occlusion and the hydration that ensues have long been known to strongly influence the skin barrier properties[863]. In the case of CO_2, the influence of skin occlusion on the transcutaneous diffusion rate has been studied by several authors[294–296]—see Section 3.2.6.1.3—and these early works demonstrated much higher CO_2 exhalation rates for long-term—*i.e.* days—occluded skin, as compared to its basal state. It could therefore be interesting to extend the study performed in Section 3.2 to occluded skin. Of note, since the sensor presented in Section 3.2.2.1 is relatively unpractical to keep for several hours—not to mention days—it could be envisioned to first place an occlusive dressing on the skin of human subjects, and only then—*i.e.* after several hours or days—remove it and replace it with the above-mentioned sensor for conductivity measurements.

---

(4) In actuality, there is no reason why the shape of the skin dome should be spherical, it could be closer to the surface generated by rotating a catenary around its axis for relatively small—*i.e.* a few millimetres—holes. Enlarging the hole leads to a flattening of the dome, as represented in Figure 6.3, Right, because the bond between the skin and the underlying tissues prevents the former from bulging out too much in the centre of the hole.

6.3.5 Conductivity Variability Factors

Another aspect that could deserve further attention is the wide variability—*i.e.* about threefold variations, see Section 3.2.5.2—observed in measured skin conductivities towards CO_2. Age- and sex-based analyses were conducted using a Multivariate ANalysis Of VAriance (MANOVA) but yielded non-significant results (p-values above 0.05, even without Bonferroni correction). The source of variability from one subject to another thus remains unclear: at low temperature, it could be related to the afore-mentioned gap between the actual subcutaneous pCO_2 and that measured by the $tcpCO_2$ monitor. However, this gap should no longer exist at 41°C, for instance, whereas the wide variability observed persists at this temperature. Perhaps conducting further studies including more participants could clarify this, or perhaps the observed variability is inherent to this metric.

6.3.6 Working Principle of Metal Oxide Sensors

Discussed in Section 4.1.3.1, the working principle of metal oxide thin film gas sensors remains relatively obscure. Indeed, several mechanisms seem to take place concurrently in such films: a purely conductive effect due to the depletion of lattice electrons upon CO_2 adsorption—which may itself be mono-, bi-, or tridentate[506], and also depends on which adsorption plane is considered[505]—and a semi-conductive effect depending on the dopant used[864–866]. These two phenomena, combined with the virtually infinite possibilities of doping elements and their mass fractions, make any prediction regarding the sensing performance of any given sensor formulation quite adventurous, at best. Additionally, most *ab initio* simulations available in the literature considered only a uniform lattice—*i.e.* without the addition of doping elements. It would therefore be interesting to see further research aiming at aggregating the existing studies on metal oxide sensing into a single theoretical framework, taking into account the many possible planes, adsorption modalities, doping substances, and grain boundaries effects. Such a framework would in turn be exceedingly useful for the development of more sensitive / selective pCO_2 sensors, and any step in this direction—however small—would be relevant in moving away from the trial-and-error approach used to date.

6.3.7 DRS for $tcpCO_2$ Sensing

Briefly mentioned in Section 4.2.4.2, DRS seems to be an interesting avenue for investigation, as it could potentially allow direct transcutaneous CO_2 measurements—*i.e.* without having to resort to an approach based on equilibrium with an external detection medium, as is the case with dye-based thin film sensors. However, two major challenges still hinder the application of DRS to $tcpCO_2$ monitoring. First, DRS-based CO_2 sensing uses wavelengths in the 1–4.3 µm range[403, 625]. Water's very high absorbance at these wavelengths—*i.e.* over 5cm^{-1} above 1380nm, and over 10cm^{-1} above 1850nm[628]—would likely attenuate any DRS signal by orders of magnitude, making their detection significantly more difficult than in a classic pulse oximetry setup(5). Second—and this comes as a direct consequence of the limited penetration depth of not-so-near infrared radiations into human tissues—it is not known at the time being whether a pulse signal could be retrieved when using DRS on living tissues in the above-mentioned wavelengths range. Would it be the case, however, the whole theoretical background developed for pulse oximetry would likely be usable for DRS-based $tcpCO_2$ sensing. Encouragingly, one clue that DRS *could* work is the fact that whole blood absorbance in the 1000–2500 nm range is comparable to that in the 500–600 nm range[174], which yields an exploitable green PPG signal(6). Yet, one remaining challenge for DRS $tcpCO_2$ sensing is the lack of low-cost available optical sources and detectors in the 1–4.3 µm range(7), which could hamper its industrialisation. Overall, the DRS research avenue appears promising, and continued efforts in this direction could unlock new transcutaneous sensing modalities.

---

(5) For the record, whole blood absorbance is below 10 cm^{-1} in the 650–1000 nm range usually used for pulse oximetry measurements[174].

(6) Even if—as always—things may not be that simple, since the pulsatile waveform of green PPG signals is thought to originate from *venous* blood put into motion by more deeper arteries, and not by arterial blood *per se*[867].

(7) For instance, infrared LEDs references above 1300 nm available at Thorlabs, Radiospare, and Roithner easily cost several (tens of) euros. For comparison, ordinary (infra)red LEDs can cost as low as a few cents—*e.g.* LTST-C170EKT (Lite-On, Taiwan), ∼3 ct€/pc.

6.4 Epilogue

The time has now come to bring this long journey through the lands of transcutaneous CO_2 sensing to an end, and I sincerely hope that you enjoyed reading this manuscript as much as I enjoyed conducting the associated research. You are now hopefully well aware of the nuts and bolts underlying practical transcutaneous CO_2 sensing, and of the limitations that still hinder its large-scale commercial development. In particular, I trust that my efforts to provide you with detailed insights throughout these dense pages, while trying to maintain an educational tone and including appropriate references for further exploration, have not been in vain: this was mandatory to ensure you could navigate the multi-disciplinary nature of this doctoral work.

In a nutshell, the key takeaways of this thesis are the following:

- The transcutaneous diffusion of CO_2 through human skin and the measurement of the resulting tcpCO_2 appears to be a promising approach for having a proxy for paCO_2.
- However, current monitors are expensive, bulky, non battery-powered, and drifting. Dye-based thin film sensors could alleviate most of these issues, but battery-powered sensors still require two conditions to be fulfilled:
  - skin permeability must be sufficiently high at low temperature to ensure a reasonably fast sensor response, this was proven to be the case.
  - there should be a good correlation between paCO_2 and tcpCO_2 at low temperature, this is yet to be demonstrated.
- Using an f-DLR sensing scheme with dye-based sensors enables reaching an arbitrarily good accuracy on pCO_2 measurements.
- The dye-based sensors manufactured in this thesis still suffer from several shortcomings—humidity cross-sensitivity and photobleaching, in particular—that require further investigation.

As a final note, I have no intention of stopping there, if only to publish the above-mentioned infrared absorption spectra of various haemoglobin species. After years of dedication to this doctoral work, I am indeed more than ever motivated to bring dye-based thin film transcutaneous CO_2 sensing from the lab to the field. If you are interested in following my future works, feel free to follow me on ResearchGate or Google Scholar. You are also more than welcome to contact me directly for further discussions.

Appendix A

Spherical Glass Tonometer

Back to Section 2.3.1.1 Main Table Of Content (TOC)

The spherical glass tonometer used for the CO_2Hb spectrophotometry measurements related in Chapter 2 is depicted in Figure A.1, right. When used with the setup shown on the left-hand side of the figure, the rotation of the upper electric motor and the eccentric wheel agitates the tonometer in a manner similar to how one aerates red wine. This homogenises the haemolysate while maximising its exchange surface with the equilibration gas that flows over it, as depicted in the section view of the picture.

Of note, this piece of equipment has no specific name or serial number; it is a purely handcrafted contraption that has always belonged to the Orphy laboratory. As such, it may be compared with the tonometers used by Assendelft or Zijlstra, which are of a similar homemade nature[136, Fig. 3.1][132, Fig. 6.1].

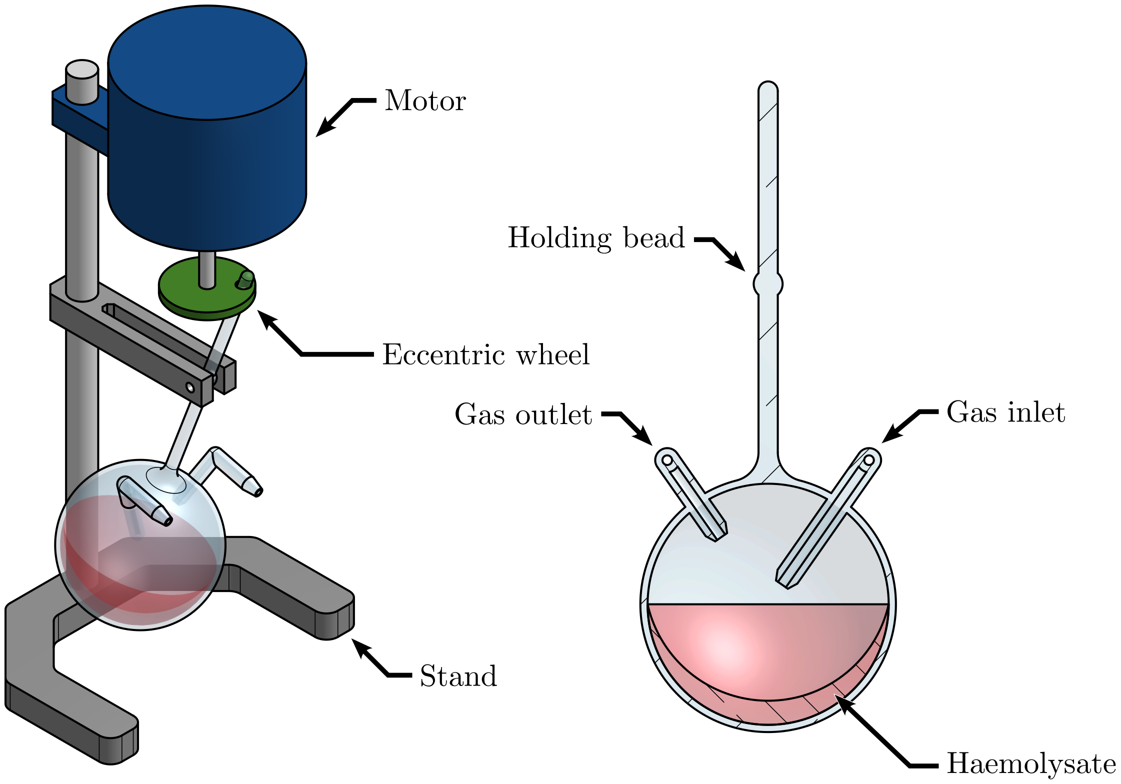

Figure A.1: **Left:** the whole tonometer assembly (inlet and outlet tubing not represented). **Right:** a section view of the spherical glass tonometer.

Appendix B

Spectrophotometric Outlier Removal Algorithm

Back to Section 2.3.2.1 Main Table Of Content (TOC)

The outlier removal technique that was used on haemoglobin absorption spectra was partly inspired by Hadi's recursive algorithm[201]. I also tried to take into account several remarks made by Aguinis *et al.*[202] on the different existing approaches for outlier handling. Of note, what follows focuses on the example of intra medium spectra measurement because the variance in these spectra was expected to be especially low, making it a relatively conservative case—*i.e.* there should be only a limited number of outliers. The same approach was also applied to haemoglobin absorption spectra, which are further subjected to daily haemoglobin concentration variations[868] and, as such, were first scaled to their median before outlier pruning.

B.1 Ethical Considerations

At first, outlier detection and removal is often criticised because it is performed on measurements *a posteriori*, and aims at supporting an already formulated hypothesis. As such, one may be tempted to keep only the data in accordance with their theory, and thus reach erroneous conclusions[869]. In the intra medium case, the solution was prepared once and for all, and it was poured from the same bottle inside one of the six quartz cuvettes at my disposal. The cuvettes were carefully cleaned and dried before each measurement, and all measurements are thus expected to be extremely similar, exhibiting discrepancies close to that of a Gaussian distribution. Any measurement exhibiting large deviations from the average—or median, if a more robust location estimator is sought—spectrum should thus be considered as an outlier. Additionally, all measurements on the intra medium were performed on the same day, but were it not the case, we should not observe any spectral drift. Indeed, the intra medium is composed of distilled water, KCl and HEPES buffer which makes it a stable solution (the shelf life of HEPES solutions is of at least two years[870]).

Second, concerning the handling of the so-obtained outliers, the logical way to treat them would be to remove them from the dataset. Indeed, the aim of the study at hand was to measure the most accurate intra medium spectrum as possible, and the latter should not be polluted by undesirable, presumably erroneous measurements. However, these outliers can still reveal valuable insights about the measurement protocol that was used, and they will need to be investigated. The possible origins of these outliers are further discussed in paragraph B.3.

B.2 Outlier Identification and Removal

As can be seen in Figure B.1, on 30 measured intra medium spectra plotted with a dashed line—five measurements for each of the six cuvettes at our disposal—at least two of them—the two upper curves—appear to be quite suspicious, exhibiting large deviations compared to the other spectra. The first one is far above all the others, and the second one exhibits a strong drift in the

250–300 nm range. To investigate this issue with a more objective point-of-view, the following algorithm was set up.

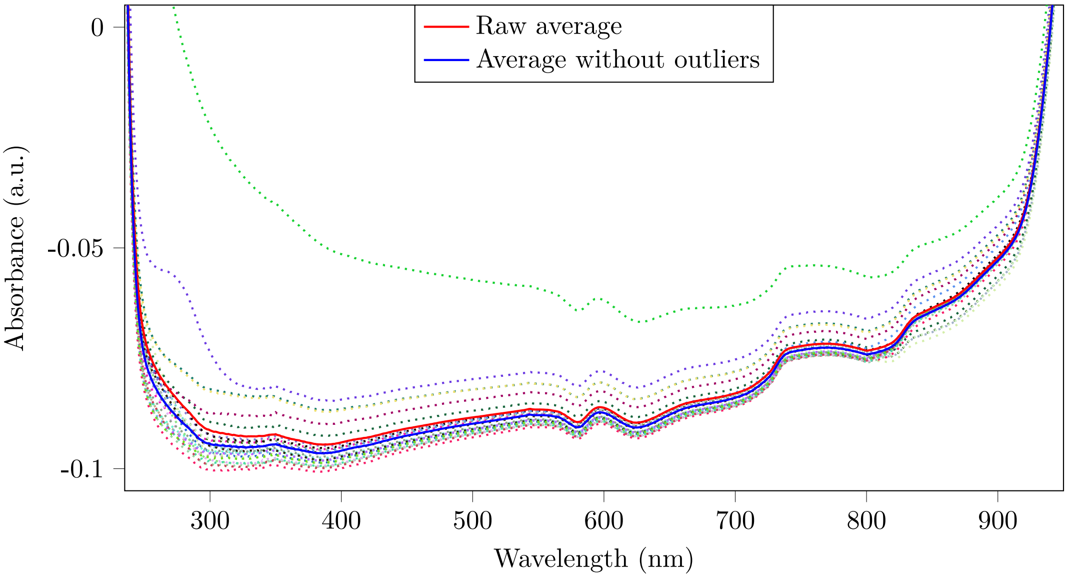

Figure B.1: All the intra medium measurements and the mean intra medium spectra before and after outlier removal. The removed outliers are the two upper curves.

First, the spectral data are centred and normalised, that is

$$\forall\lambda,\ \widetilde{\mathcal{S}}(\lambda) = \frac{\mathcal{S}(\lambda) - \overline{\mathcal{S}}(\lambda)}{\sigma(\lambda)} \quad \text{where} \quad \begin{cases} \overline{\mathcal{S}}(\lambda) & = \frac{1}{N}\sum_{i=1}^{N}\mathcal{S}(\lambda) \\ \sigma(\lambda) & = \sqrt{\frac{1}{N-1}\sum_{i=1}^{N}(\mathcal{S}_i(\lambda) - \overline{\mathcal{S}}(\lambda))^2} \end{cases} \tag{B.1}$$

Then, for each spectrum, the maximum deviation of $\widetilde{\mathcal{S}}$ is compared to a given threshold, in order to decide whether this spectrum is an outlier or not:

$$\max_{\lambda} \widetilde{\mathcal{S}}(\lambda) \begin{cases} \leq \text{threshold} \implies \text{Nothing to report} \\ \geq \text{threshold} \implies \text{Outlier} \end{cases} \tag{B.2}$$

Once this simple two-step process has been run on all spectra, the detected outliers are removed from the available dataset and the algorithm—*i.e.* normalising and thresholding—is re-run for a new epoch. It stops either if no supplementary outlier is detected at the end of an epoch, or if there is only one spectrum left in the dataset⁽¹⁾. The idea behind this iterative process is that, in the presence of an extreme outlier, the resulting estimated standard deviation $\sigma(\lambda)$ will be much higher than it would have been without the said outlier. Thus, some spectra might have been considered normal while they were in fact quite deviant. The iterative nature of the algorithm then guarantees that the latter spectra will be removed by subsequent runs.

In Figure B.2, different scenarios of evolution of the algorithm are shown, depending on different threshold values. One can see that the first outlier gets rejected even with a threshold value as high as 5 S.D., while the second one is rejected at roughly 3.85 S.D. (more threshold values were tested for accuracy purposes but are not shown here for readability reasons).

We arbitrarily chose to take a final threshold value of 3 S.D., which allowed 28 out of 30 intra medium spectra to be kept. The resulting mean spectrum is plotted in blue in Figure B.1, whereas the mean spectrum computed on all the 30 available spectra is shown in red. The gain of the outlier removal is especially pronounced in the shorter wavelengths region. In more quantitative terms, the mean m of the distances between all intra medium spectra and the mean spectra can be used:

$$m = \frac{1}{N_s} \cdot \sum_{i=1}^{N_s} \left(\frac{1}{N_\lambda} \sum_{\lambda} \left(\mathcal{S}_i(\lambda) - \overline{\mathcal{S}}(\lambda) \right)^2 \right) \tag{B.3}$$

wherein N_s is the number of intra medium spectra (30 in total, 28 without the two detected outliers) and N_λ it the number of measured wavelengths. When computing this metric on the

---

(1) This case should never be reached in practice, but is mentioned here for the sake of completeness.

whole population of intra medium spectra and when removing the outliers, m decreases from 5.19×10^{-5} down to 8.24×10^{-6}. Concerning the maximum deviation from the mean, the latter decreases from ${}^{+0.122}_{-0.015}$ Abs (range: 0.137 Abs) to ${}^{+0.013}_{-0.010}$ Abs (range: 0.023 Abs), hence the interest of the presented technique.

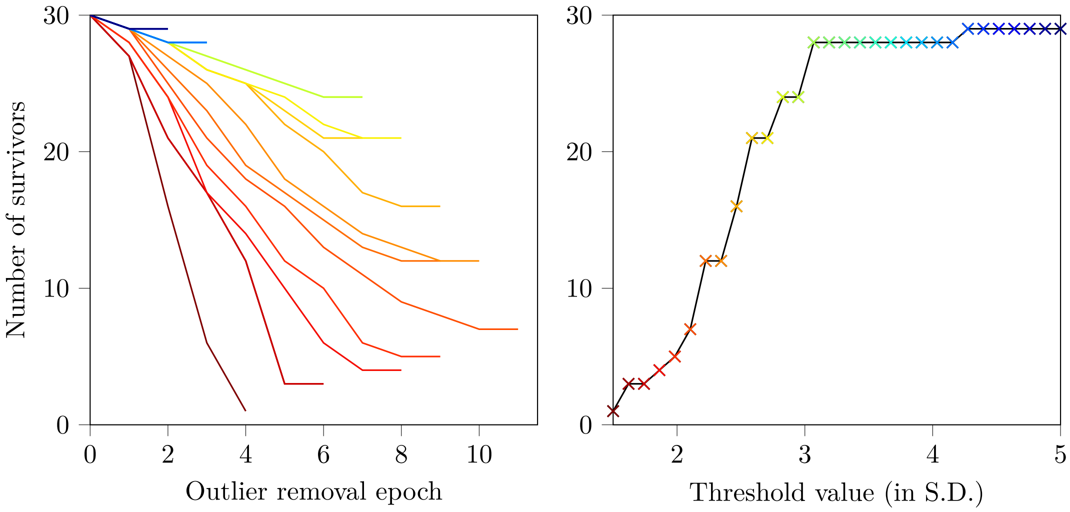

Figure B.2: **Left:** several runs of the algorithm with different threshold values. The number of remaining spectra (survivors) is plotted as a function of the number of steps made by the algorithm. Threshold values are colour-coded in the right part of the figure. **Right:** number of remaining spectra as a function of the threshold value chosen. Each point corresponds to a scenario in the left part of the figure.

B.3 On the Detected Outliers

The two outliers removed by the above-mentioned method were the first and second acquisitions performed on the 2^{nd} quartz cuvette. While it was tempting to incriminate the cuvette itself, the other three measurements performed with it passed the algorithm successfully. It thus seems that the cause of these outlying measurements lies elsewhere.

Most likely, the spectrum that is far above the others in Figure B.1 corresponds to a cuvette which was placed in the wrong orientation. In such a configuration, the light path-length in the intra medium is reduced while that in the quartz of the cuvette is increased. Considering the second outlier—which only diverges in the 250–300 nm range—it might result from a soiled cuvette, possibly from greasy fingers. Indeed, human skin lipids can have important absorption in this spectral region[871].

B.4 Obtained Spectrum After Outlier Removal

As mentioned above, the chosen outlier removal technique pruned 2 spectra out of the 30 intra medium spectra measured. With the remaining 28 spectra, an average spectrum could be computed that was later used as a baseline in subsequent spectrophotometric analyses—*i.e.* this average spectrum was subtracted from the haemoglobin absorption spectra to remove the influence of the quartz cuvette and intra medium from them. The outlier removal technique was also used on the haemoglobin absorption spectra themselves, as mentioned in Section 2.3.2.1, above. In all cases, the number of survivors *versus* the threshold value always presented a shape similar to that of Figure B.2, right—*i.e.* a few outliers are removed for a high threshold value, before a steep decrease at a threshold value of about 3 S.D. Consequently this latter value was always chosen in all subsequent spectra pruning operations.

Back to Section 2.3.2.1 Main Table Of Content (TOC)

Appendix C

Haemoglobin Inner Filter Effect

Back to Section 2.4.2.1 Main Table Of Content (TOC)

When measuring the fluorescence of a solution, one might expect to measure more fluorescence signal when increasing the fluorophore concentration. However, this is not the case if the fluorophore also absorbs at the wavelength of the re-emitted fluorescent light—a phenomenon sometimes improperly referred to as *self-quenching*, but which is, in reality, an *inner filter effect*[226]. The following developments present two simplified models of right-angle and front-face geometry fluorometers to emphasise this latter phenomenon.

C.1 Right-Angle Optics

The geometry of right-angle fluorometers has emerged against classical spectrometers' construction, in order to avoid blinding the detector with the exciting beam[872]. In a theoretical study however, we are unimpeded by such practical considerations, since an ideal detector can be assumed, sensitive only to the wavelength of the re-emitted light, and not to that of the exciting beam. The right-angle optics can thus be "unfolded" into a geometry aligning the light source, cuvette, and detector. Such an unfolded spectrofluorometer is depicted in Figure C.1 wherein $\Phi_\mathrm{X}(x)$ is the excitation flux at the abscissa x (W.m^{-2}), $\Phi_\mathrm{M}(x)$ the re-emitted flux (W.m^{-2}), c the solution concentration in fluorophore (M), and L the length of the solution path (m).

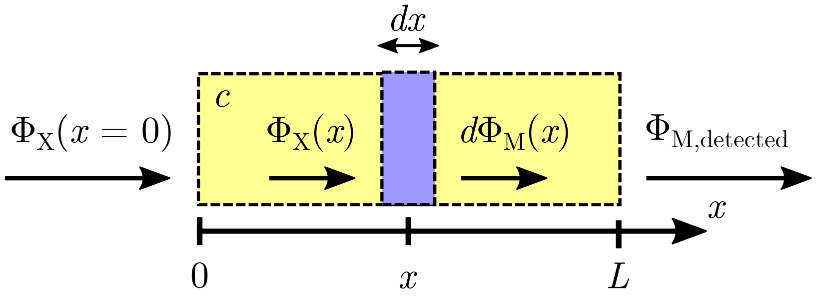

Figure C.1: Simplified representation of a right-angle optics fluorometer. The input exciting beam—intensity $\Phi_\mathrm{X}(x=0)$—comes from the left of the figure. The output flux to be detected at the emission wavelength exits the cuvette on the right. The solution—concentration in fluorophore c—is depicted in yellow. A slice of solution of thickness dx is also represented in light blue. It receives the flux $\Phi_\mathrm{X}(x)$ attenuated by a layer of thickness x of solution. This slice in turns emits fluorescent light in the detector's direction with intensity $d\Phi_\mathrm{M}(x)$. The light re-emitted by all the cuvette's slices in the $0..L$ abscissa forms the overall detected light at the detector, $\Phi_\mathrm{M,detected}$.

This simple model is considered as a one dimensional problem—along the x axis—and the hypothesis that the solution is purely absorbing—*i.e.* without scattering—is also made. This hypothesis holds for diluted lysed blood, which, from being originally translucent but opaque, becomes transparent with haemolysis. Regarding the direction of propagation of the fluorescent re-emitted light, isotropic emission results in half of the emitted light being back-scattered, while half is transmitted in the forward direction (increasing x axis). We can thus write for a small slice of solution

$$d\Phi_{\mathrm{M}}(x) = {}^1\!/\!_2{\cdot}\eta_{\mathrm{Q}}{\cdot}d\Phi_{\mathrm{X}}(x) \tag{C.1}$$

using the definition of the quantum yield η_{Q} of a fluorophore[634], where $d\Phi_{\mathrm{M}}(x)$ is the flux emitted by the slice of solution of thickness dx in the detector's direction when absorbing an exciting flux $d\Phi_{\mathrm{X}}(x)$. Using Beer-Lambert law leads to

$$d\Phi_{\mathrm{M}}(x) = {}^1\!/\!_2{\cdot}\eta_{\mathrm{Q}}{\cdot}\mu_{\mathrm{X}}{\cdot}\Phi_{\mathrm{X}}(x=0){\cdot}e^{-x\cdot\mu_{\mathrm{X}}}{\cdot}dx \tag{C.2}$$

wherein μ_X is the attenuation coefficient of the solution at the excitation wavelength (m^{-1}), with $\mu_X = c{\cdot}\varepsilon_{\mathrm{X}}$, ε_{X} being the molar extinction coefficient of the fluorophore at the excitation wavelength(1) (L.mol^{-1}.m^{-1}). This emitted flux $d\Phi_{\mathrm{M}}(x)$ is itself absorbed by the solution—of attenuation coefficient μ_{M} at the emission wavelength—before it reaches the detector, following

$$d\Phi_{\mathrm{M,detected}}(x) = d\Phi_{\mathrm{M}}(x){\cdot}e^{-(L-x)\cdot\mu_{\mathrm{M}}} \tag{C.3}$$

To get the total flux at the detector at the emission wavelength, we need to integrate on L, leading to:

$$\begin{aligned}\Phi_{\mathrm{M,detected}} &= \int_{x=0}^{x=L} d\Phi_{\mathrm{M,detected}}(x)\\ \Phi_{\mathrm{M,detected}} &= \frac{\eta_{\mathrm{Q}}{\cdot}\Phi_{\mathrm{X}}(x=0)}{2}{\cdot}\frac{\varepsilon_{\mathrm{X}}}{\varepsilon_X-\varepsilon_{\mathrm{M}}}{\cdot}e^{-L\cdot c\cdot\varepsilon_{\mathrm{M}}}{\cdot}\left(1-e^{-L\cdot c\cdot(\varepsilon_{\mathrm{X}}-\varepsilon_{\mathrm{M}})}\right)\end{aligned} \tag{C.4}$$

Note that in the—highly unlikely—case where $\varepsilon_X = \varepsilon_{\mathrm{M}}$ the latter equation simply becomes

$$\Phi_{\mathrm{M,detected}} = \frac{\eta_{\mathrm{Q}}{\cdot}\Phi_{\mathrm{X}}(x=0)}{2}{\cdot}\varepsilon_{\mathrm{X}}{\cdot}L{\cdot}c{\cdot}e^{-L\cdot c\cdot\varepsilon_{\mathrm{M}}} \tag{C.5}$$

Figure C.2 depicts several plots of $\Phi_{\mathrm{M,detected}}$ as a function of the fluorophore concentration c for different values of ε_X and ε_M, and is useful to understand the inner filter effect phenomenon that takes place during right-angle haemoglobin fluorescence measurements.

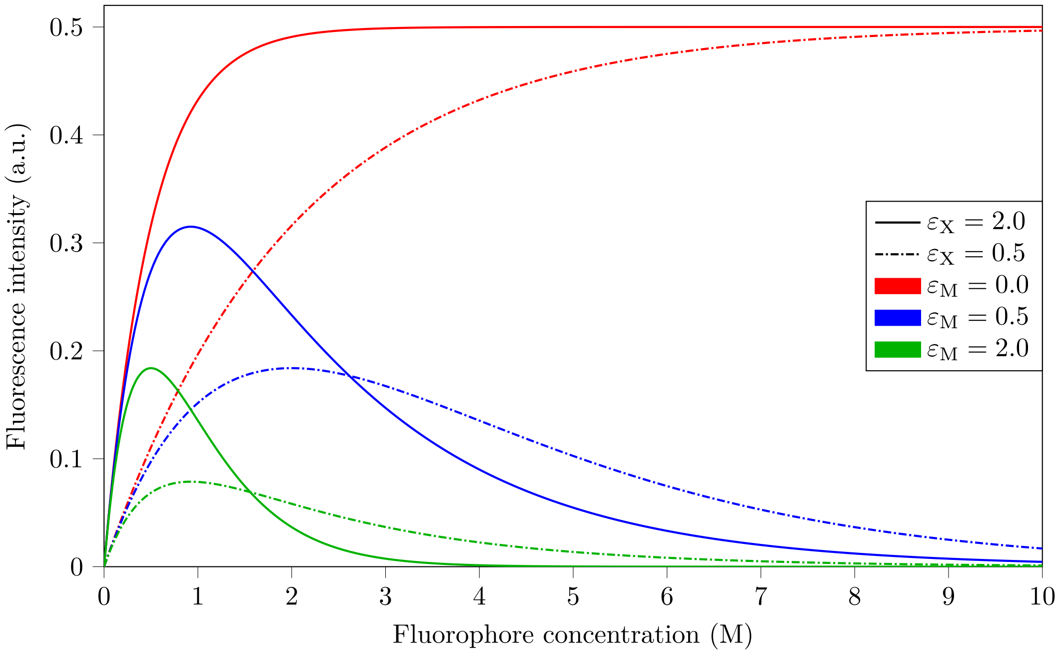

Figure C.2: Detected fluorescence intensity $\Phi_{\mathrm{M,detected}}$ as a function of the fluorophore concentration for different $(\varepsilon_{\mathrm{X}}, \varepsilon_{\mathrm{M}})$ values, taking unitary η_{Q}, L and $\Phi_{\mathrm{X}}(x=0)$.

At first, we can notice that in the absence of absorption at the emission wavelength—red curves—increasing the fluorophore concentration above a certain threshold is pointless. Indeed,

---

(1) Strictly speaking, $\mu_X = c{\cdot}\varepsilon_{\mathrm{X}}{\cdot}\log(10)$, but the log(10) was omitted for simplification purposes. Similarly, it is assumed that all the forward-propagating light is received at the detector, which is never the case in practice.

the re-emitted light—and thus detected light, since all the re-emitted light will be collected without attenuation—becomes limited by the intensity of the exciting beam $\Phi_\mathrm{X}(x=0)$. In this configuration, the collected light is directly proportional to the exciting beam intensity, given that the fluorophore concentration is at least three up to five-fold larger than $(\varepsilon_\mathrm{X}{\cdot}L)^{-1}$ (first-order exponential decay).

Then, if the fluorophore also absorbs at the emitting wavelength, as is the case for haemoglobin—green and blue curves—it appears that there is an optimal concentration to measure the highest possible fluorescence intensity, where the fluorescence intensity peaks—typically in the 0.5–3 M range in Figure C.2 depending on which blue or green curve is taken. The higher the fluorophore absorption at the re-emitted wavelength, the lower the fluorophore concentration should be to maximise $\Phi_\mathrm{M,detected}$, but also the lower the $\Phi_\mathrm{M,detected}$ value will be. This illustrates well the so-called “inner filter effect” mechanism.

As a quick application, taking the extinction coefficients of Prahl[85] for O_2Hb and an optical path length of approximately 1 cm—as is the case in commonly encountered right-angle fluorometers—leads to an optimal fluorophore concentration of 10 µM for an excitation at 280 nm and an emission at 326 nm. The measurements related in Section 2.3 were performed with $c \approx 20$ µM, and were thus well targeted, being in the corresponding fluorescence intensity peak (peak over its half-width in the 1–25 µM range).

C.1.1 Front-Face Optics

In the case of front-face optics, the geometry depicted in Figure C.3 will be considered. It is quite similar to that of Figure C.1, with the exception that the detector is now located on the same side as the exciting beam source.

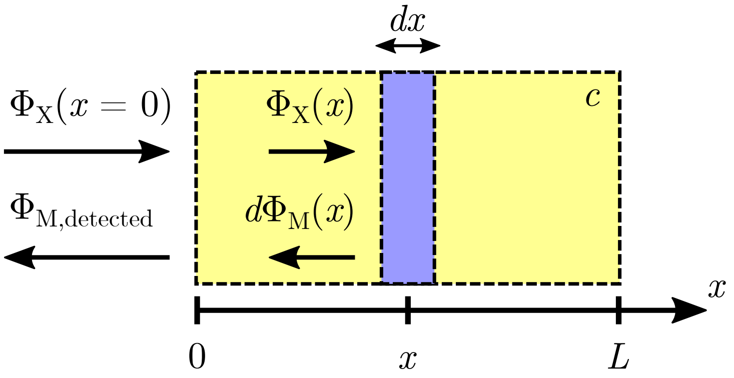

Figure C.3: On this variant of Figure C.1, the re-emitted light exits the sample from the same side as it enters it. In other words, the detector is located on the same side as the exciting beam (left side of the figure).

The same reasoning as in the previous section can be followed, now considering only the part of the emitted light that is backward-propagating towards the detector. Equations C.1 and C.2 still hold, and the re-emitted flux that reaches the detector after partial absorption is

$$d\Phi_\mathrm{M,detected} = d\Phi_\mathrm{M}(x){\cdot}e^{-x\cdot\mu_\mathrm{M}} \tag{C.6}$$

Integrating on the full length of the cuvette yields

$$\begin{aligned}\Phi_\mathrm{M,detected} &= \int_{x=0}^{x=L} d\Phi_\mathrm{M,\ detected}(x)\\ \Phi_\mathrm{M,detected} &= \frac{\eta_\mathrm{Q}{\cdot}\Phi_\mathrm{X}(x=0)}{2}\cdot\frac{\varepsilon_\mathrm{X}}{\varepsilon_\mathrm{X}+\varepsilon_\mathrm{M}}\cdot(1-e^{-L\cdot c\cdot(\varepsilon_\mathrm{X}+\varepsilon_\mathrm{M})})\end{aligned} \tag{C.7}$$

and the corresponding fluorescence intensity curves are presented in Figure C.4. Contrary to the right-angle case, an increase in the fluorophore concentration does not result into a decrease in fluorescence intensity in case of non-null ε_M—blue and green curves.

One can see that given that *(i)* the solution is sufficiently concentrated, *(ii)* the cuvette is long enough, or *(iii)* the molar absorption coefficients are high enough, the intensity of the fluorescent light measured with such a system is only a function of the $\varepsilon_\mathrm{X}/\varepsilon_\mathrm{X}+\varepsilon_\mathrm{M}$ ratio, η_Q and $\Phi_\mathrm{X}(x=0)$. In other words, if the afore-mentioned conditions are fulfilled, the fluorescence measurement only depends on the fluorophore and the fluorometer, but not on the concentration of the former nor on the cuvette's depth. This is because the exciting beam is only probing a superficial layer of the cuvette, and we could even define the value $(c{\cdot}(\varepsilon_X + \varepsilon_M))^{-1}$ as the *characteristic depth* probed by the exciting beam.

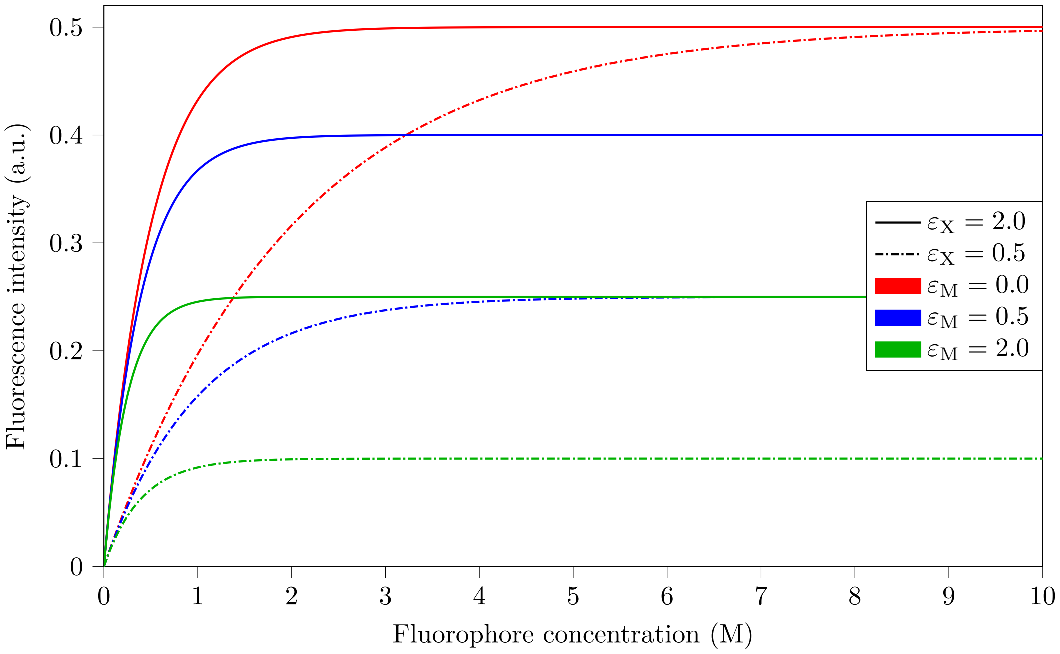

Figure C.4: Detected fluorescence intensity $\Phi_{M,\text{detected}}$ as a function of the fluorophore concentration in the case of front-face optics for different $(\varepsilon_X, \varepsilon_M)$ values, taking unitary η_Q, L and $\Phi_X(x = 0)$.

Such calculations are in good agreement with the results presented by Hirsch *et al.*[227] when using the haemoglobin extinction coefficients provided by Prahl[85]. Last detail, with such extinction coefficients and at a physiological haemoglobin concentration (that of blood for instance), the latter characteristic depth is as low as 4.2 µm. Probing tissues with fluorescence transcutaneously at the considered wavelengths is thus most certainly unfeasible.

Back to Section 2.4.2.1 Main Table Of Content (TOC)

Appendix D

Technical Information on the Transcutaneous CO_2 Conductivity Measurements

Back to Section 3.2.2.1 Main Table Of Content (TOC)

D.1 Sensor Design

D.1.1 Mechanical Drawings

Complete mechanical drawings of the sensor's aluminium body are given at the end of this appendix, in page 176. Aluminium was chosen for its high thermal conductivity—134 $W.m^{-1}.K^{-1}$—as well as its low density—2.79[873]. The choice of pure copper was also considered, as it has a higher thermal conductivity than aluminium—401 $W.m^{-1}.K^{-1}$—but it is alas also much denser—with a density of 8.9[874]. As it seemed desirable to make the sensor as lightweight as possible in order to minimise skin blood flow perturbations, aluminium was ultimately chosen. Indeed, several works indicate that even a mild—*i.e.* above 10 mmHg / 1.3 kPa—local cutaneous pressure can significantly impact local blood flow[875–877]. Besides, aluminium does not oxidise as copper does, and can be considered safe for skin contact, as further discussed in Section D.1.4.2.

D.1.2 Power and Supply Block

The power and supply block is illustrated in Figure D.1, Left. It consists in:

- an interfacing PCB similar to that used on top of the sensor, which enables connection with the latter by means of an eight-pin microfit Molex cable,
- a thermostat board (XH-W1209, Shenzhen Global Technology, China) allowing for the temperature regulation of the sensor's aluminium body,
- a USB to UART converter (CP2102, Silicon Labs, USA), which enables connection between the CO_2 sensor—through UART—and the computer—through USB,
- a 230 V-AC to 12 V-DC / 10 A switching power supply onto which the afore-mentioned elements are affixed by means of a 3D-printed contraption (black plate in Figure D.1),
- a 3D-printed cover (not shown) that prevents contact with any exposed electrical conductor, while allowing the USB and Molex cables to be plugged, and the temperature to be adjusted.

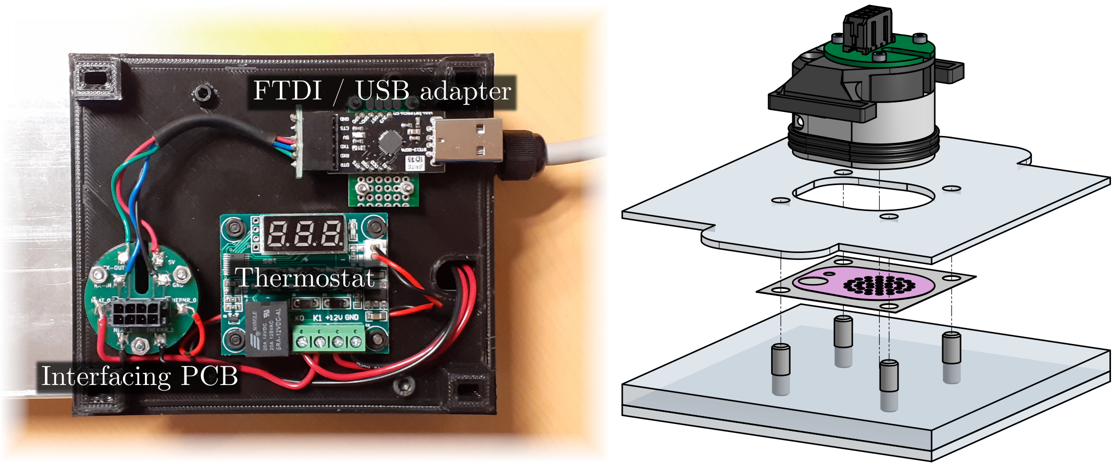

Figure D.1: **Left:** the power and supply block. **Right:** the adhesive mounting jig with—from top to bottom—the sensor, the centring layer, the adhesive stuck onto its release liner, and the chassis.

D.1.3 Adhesive Tooling

A custom mounting jig was developed to ensure an accurate and reproducible positioning of the laser-cut, double-sided, clinical-grade tape (1567, 3M, USA) onto the sensor's sole. It is represented in Figure D.1, Right, and allows the user to: ① put a release liner—with the adhesive stuck on it—onto a chassis, positioning it by means of the four steel studs integrated into the latter, ② add a centring layer above the liner, and ③ stick the sensor onto the adhesive, with the centring of the former being ensured by an appropriate cut made into the centring layer. Finally, when ④ the user removes the sensor, the adhesive remains stuck onto it, precisely aligned, and the release liner remains onto the chassis. The sensor is then ready to be applied on a subject's skin.

D.1.4 Safety Issues

Three distinct safety concerns have been identified regarding the application of the sensor on the skin of human subjects: thermal injury hazard, dermatological reaction hazard, and electric shock hazard.

D.1.4.1 Thermal Injury Hazard

Given the relatively low thermal power of the heating wire (6.1 W), the temperature of the sensor cannot reach excessive values within minutes, even in case of thermostat malfunction. Would the latter occur, both the investigator and the subject would notice it thanks to the external reference thermometer, and cutaneous sensation, respectively. In addition, the enamelled resistive wire is covered by two quad rings, guaranteeing that neither the subject nor the investigator may touch it directly during the experimentations.

The only relevant source of thermal injury is thus long term burn. Literature on the topic suggests a maximum long-term skin temperature of 42°C, but higher temperatures can be used for a limited amount of time—up to 45°C for a few minutes for instance[878], or up to several hours depending on the study[879]. In the medical practice of tcpCO$_2$ monitoring, temperatures up to 45°C were used for up to one hour[267] or 42°C for eight hours[200]. Temperatures in the 40–44°C are also often encountered, since temperatures above 42°C yield the most accurate tcpCO$_2$ measurements[69]. Legally speaking, the FDA guidance for tcpCO$_2$ monitors recommends not to exceed 44°C for more than four hours[325]. Consequently, since the sensor will not be used for more than 90 min on each subject, a maximal temperature set-point of 44°C was deemed safe.

D.1.4.2 Dermatological Reaction Hazard

The body of the sensor is made out of solid aluminium, which is vastly inert towards the skin. Indeed, most allergic reactions related to aluminium come from aluminium ions used in vaccines and not from solid metal[880, 881]. Although some rare cases of reaction to thin solid aluminium particles have been reported, they concern factory workers being exposed daily to aluminium

Arm	Mean	Range	SD
NH	4.03	1.18–10.40	2.03
35°C	6.58	2.46–12.50	2.26
38°C	7.17	3.07–13.60	2.19
41°C	7.95	3.98–15.30	2.24
44°C	8.88	5.42–15.90	2.28

Wrist	Mean	Range	SD
NH	2.94	1.24–6.36	1.11
35°C	5.08	1.44–10.90	1.89
38°C	5.93	1.37–12.30	2.15
41°C	7.06	1.82–13.80	2.39
44°C	8.11	2.37–15.20	2.37

Table D.1: Measured skin conductivities K at the arm and wrist, expressed in $\times 10^7 \text{m}\cdot\text{s}^{-1}$.

	Mean	Range	SD
NH	9.11	3.34–32.51	4.77
35°C	18.77	7.39–55.88	8.89
38°C	37.87	16.55–80.59	13.38
41°C	69.01	42.93–96.27	12.02

Table D.2: nSkBF$_{90}$ as measured at the arm, expressed in percentages (arbitrary unit).

dust for months—if not years—prior to sensitisation[882, 883]. Thus, it was considered most unlikely that the subjects exhibit any reaction to the aluminium sensor's body.

Then, the other parts of the sensor that may be in close contact with the skin are the Doppler probe and double-sided adhesive. Since they were both designed for skin application and are medical-grade products, any adversarial reaction with the skin is also highly unlikely to happen.

Finally, for hygienic reasons, the sensor was also cleaned with a disposable paper towel soaked in a 70% isopropyl alcohol / 30% water mixture prior to measurements, which is standard medical practice for disinfection.

D.1.4.3 Electric Shock Hazard

The supply block is designed so that no bare high voltage conductor is exposed. Additionally, all the electrical connections to and from the sensor itself are only raised to low voltage—12 V at most—ensuring that no electric shock can possibly happen, even if the insulation of one or several wires were to fail.

D.2 tcpCO$_2$ Extraction

The subject's capnia was monitored using a clinical grade transcutaneous capnometer (TCM4, Radiometer, Denmark), which recorded tcpCO$_2$ at a sampling rate of 1 min^{-1}. In order to get only one tcpCO$_2$ value per temperature window—as required for K calculations—the raw tcpCO$_2$ signal was processed as follows:

- the first ten minutes of the acquisition were truncated to allow the sensor to stabilise,
- the remainder of the acquisition was split in five segments, each segment corresponding to a temperature window—NH, 35, 38, 41 and 44°C,
- for each segment, the measured tcpCO$_2$ was then averaged to yield a single value, which was then used to compute K, as described in Section 3.2.3.1.1.

This approach was deemed appropriate since tcpCO$_2$ in healthy resting subjects was fairly stable (mean / median standard deviation on all acquisitions: 0.92 / 0.78 mmHg).

D.3 Box-Plot Descriptive Statistics

Mean, ranges, and SD of K and nSkBF$_{90}$ measurements are given in Tables D.1 and D.2, respectively.

Back to Section 3.2.2.1 Main Table Of Content (TOC)

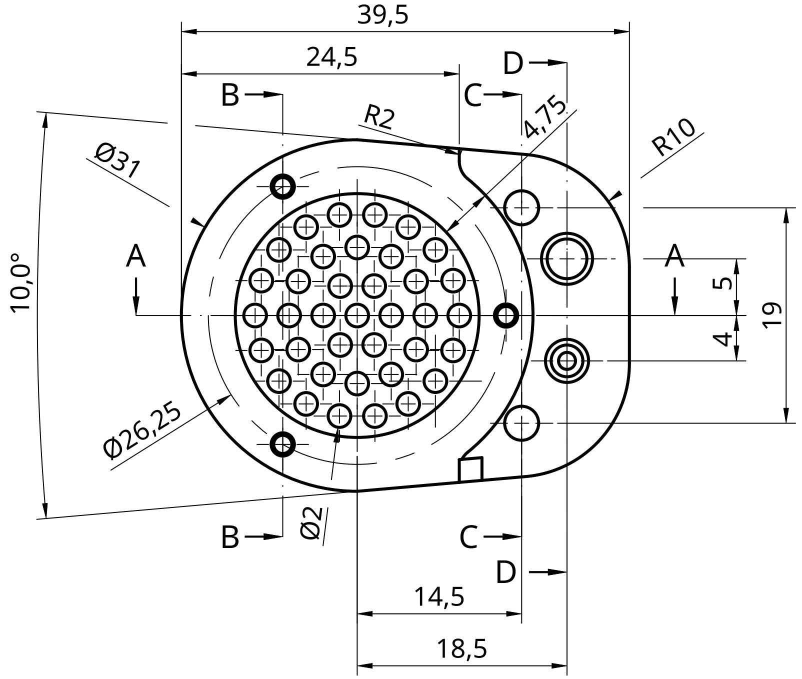

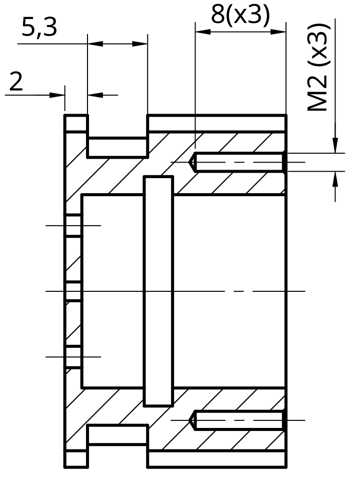

B - B

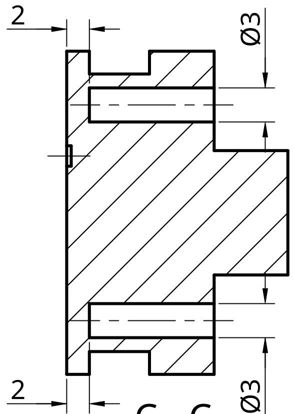

C - C

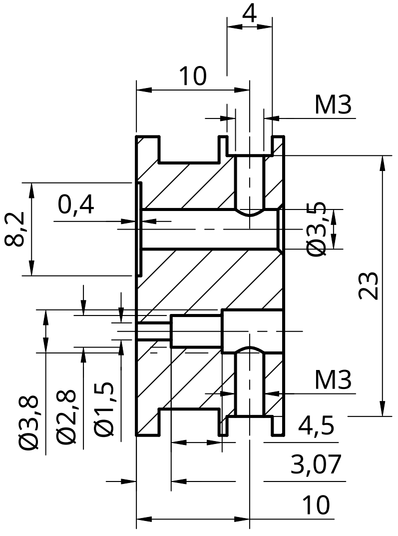

D - D

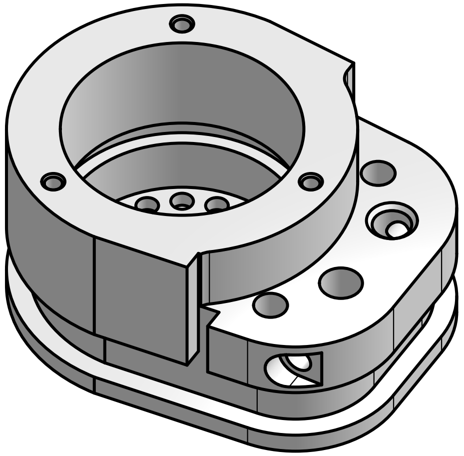

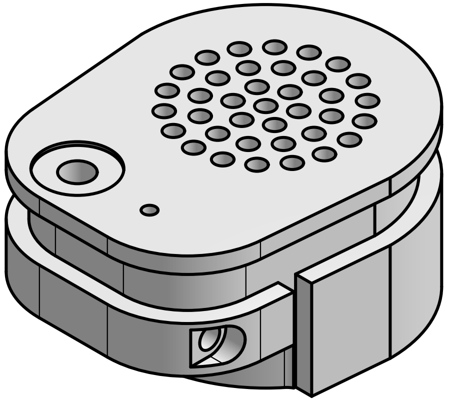

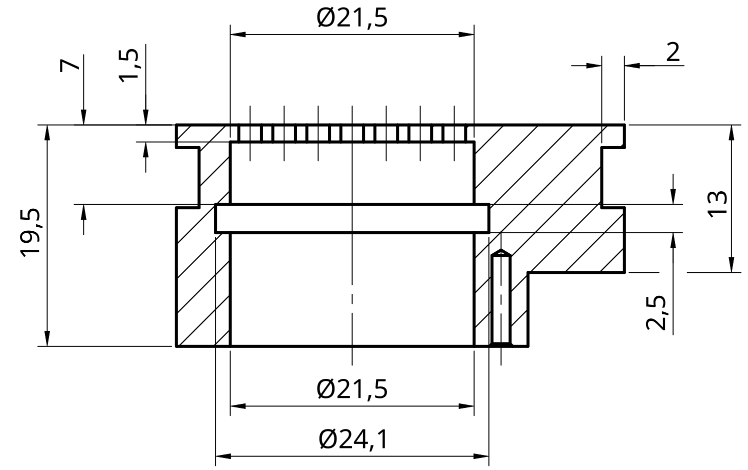

A - A

UNLESS OTHERWISE SPECIFIED, DIMENSIONS ARE IN MILLIMETERS		NAME	DATE
General Tolerance: ±0.1	DRAWN	EMMANUEL DERVIEUX	2023/07/05
Angular Tolerance: ± 0.1°	CHECKED		
SURFACE FINISH √	APPROVED		
DO NOT SCALE DRAWING			
BREAK ALL SHARP EDGES AND REMOVE BURRS			
FIRST ANGLE PROJECTION	MATERIAL Aluminium 2017A	FINISH	

TITLE

SENSOR BODY

SIZE	DWG NO.		REV.
A4	1		1
SCALE 3:2	WEIGHT 26.27 g	SHEET 1 of 1	

Appendix E

Optical Design

Back to Section 5.4.1.2 Main Table Of Content (TOC)

Ideally, the most simple and naive design that can be envisioned is that coarsely presented in Figure E.1, Left: a supposedly ideal LED—hence the absence of excitation filter—shines its monochromatic light through a glass window onto a CO_2 sensitive luminescent thin film placed against the skin. The re-emitted light then reaches a photodiode covered by an emission filter to discard the parasitic diffused LED light that may otherwise reach it.

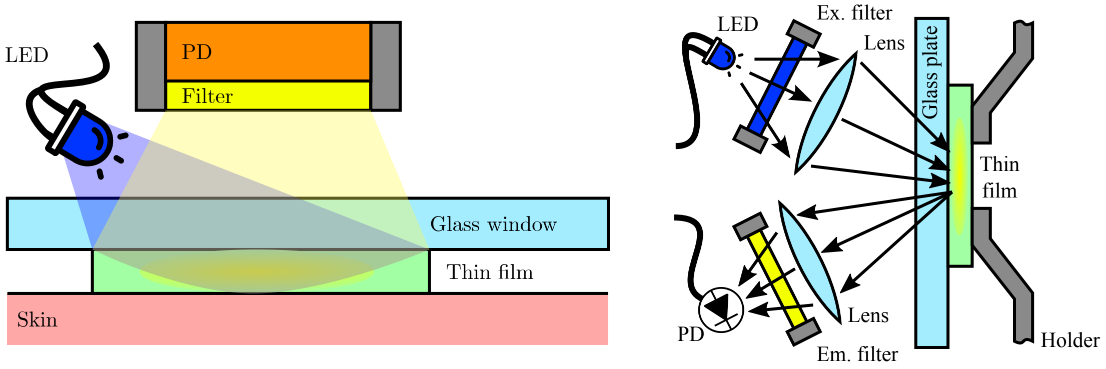

Figure E.1: **Left:** crude outline of an idealised optical setup. **Right:** a more realistic version of the same optical setup.

However, in the lab, the bulkiness of the emission filter, LED and photodiode mounts—in addition to the need for a second excitation filter—called for a larger optical setup made out of discrete optical components, since off the shelf filtered photodiodes were not available. The later setup is depicted in Figure E.1, Right, and can be seen as two distinct blocks:

- An illuminating block (Top), which purpose is to collect as much light as possible from the LED to form a spot of a given size w on the thin film.
- A collecting block (Bottom), which role is to maximise the amount of light reaching the photodiode.

These two blocks will be placed as presented in Figure E.2. At the bottom of the picture is the glass window (3 mm thick) while the two tilted blocks are the illuminating and collecting blocks, each one of them consisting of a mounting tube into which the different optical elements—*i.e.* filters, lenses, LED and photodiode—will be housed. The diameter of the optical elements is 1 inch (25.4 mm), while the outer diameter of the optomechanics holding them is 30.5 mm. For practical reasons—*i.e.* being able to mechanically integrate the two tubes into a larger assembly—two clearances were defined: one of 2 mm between the two optical blocks, and another one of 3 mm between the optical blocks and the glass window. These two clearances resulted in a 78.6° angle between the two blocks. Of note, each block is shown with a length of 10 mm for illustration purposes only, since their actual length is substantially greater in practice.

It readily appears that the distance between the first optical element—*i.e.* the lower end of the tubes—and the bottom of the glass window where the film will be placed is not constant.

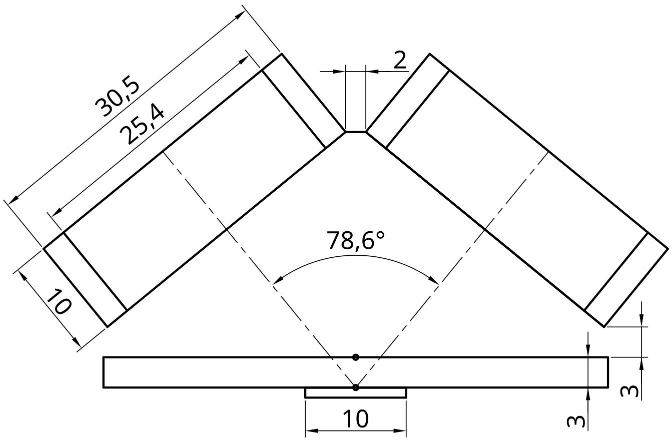

Figure E.2: Placement of the different optical blocks. Bottom is the glass window, while the two tilted blocks are the illuminating and collecting blocks. See the text for a more complete description.

Neglecting the effect of diffraction in the glass window on the optical path length, and for an illuminated spot of 10 mm in diameter for instance, this distance is between 17 and 23 mm. In the remainder of the present study, this distant will be considered to be constant and equal to 20 mm, so that we can "unfold" the optical setup into two distinct and *aligned* optical sub-assemblies—*i.e.* wherein a given block sees the illumination spot perpendicular to its optical axis. Additionally, since the different lenses and other optical elements used are mounted by means of retaining rings (SM1RR, Thorlabs) the effective optical aperture of these sub-assemblies is equal to 0.9 inch (22.9 mm) instead of 1.0 inch (25.4 mm).

E.1 Illumination block

The scheme retained for the illuminating block is depicted in Figure E.3. The LED is placed in front of a converging glass lens, which goal is to collect the light emitted by the LED and to concentrate it into a spot of the required dimension. For the sake of simplicity, the excitation filter was not considered, its optical properties and thickness being unknown—apart from its transmission, of course. This block must meet two targets: first, as much light as possible must be collected by the lens aperture, a condition which sets a maximum value for d_{LL}. Second, the rays emerging from the lens must converge onto the film and form a spot of diameter w_S, a condition which steer the choice of d_{LL} and d_{LS} values, as well as the lens focal length.

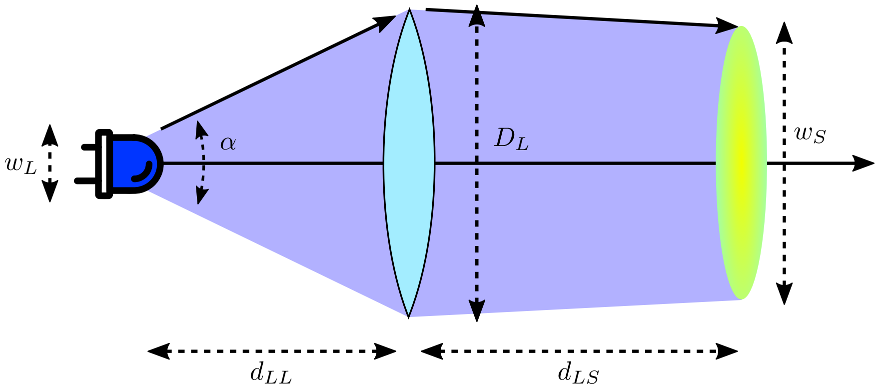

Figure E.3: Schematic drawing of the illuminating block. The light is emitted by the LED of width w_L with an maximum angle α. d_{LL} and d_{LS} are the distances between the LED and the lens, and between the lens and the film, respectively. D_L is the lens diameter, while w_S is the width of the light spot, on the film.

E.1.1 Maximum d_{LL}

The maximum d_{LL} value is reached when the most diverging rays emerging from the LED—*i.e.* those forming an angle $\alpha/2$ with the optical axis— reach the border of the lens. This condition may be written

$$\tan\left(\frac{\alpha}{2}\right) = \frac{D_L - w_L}{2\cdot d_{LL}} \iff d_{LL} = \frac{D_L - w_L}{2\cdot \tan\left(\frac{\alpha}{2}\right)} \tag{E.1}$$

Taking Thorlabs' LED450L specifications—$\alpha/2 = 22°$, $w_L = 4$ mm and $D_L = 22.9$ mm— yields a maximum value $d_{LL,\mathrm{MAX}}$ of 23.4 mm. This means that if the LED is placed further away from the lens than 23.4 mm some rays will miss the lens and be lost, as can be seen in Figure E.4, in red.

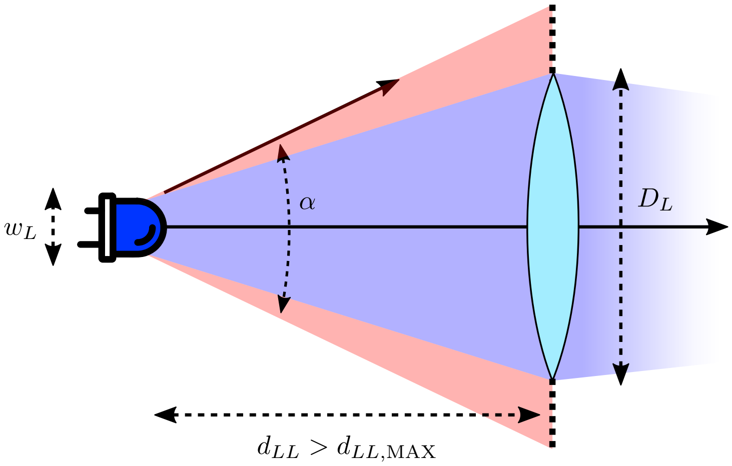

Figure E.4: If d_{LL} is greater than the maximum value $d_{LL,\mathrm{MAX}}$ of 23.4 mm, some of the light emitted by the LED with an angle α will be lost (in red). This loss in turns reduces the amount of light concentrated onto the film (in blue).

E.1.2 Light Concentration onto the Film

E.1.2.1 Lens Focal Length

Since the light emerging from the LED is already collimated, all the rays emerging from it are comprised between the two most diverging rays at $\pm\alpha/2$. So as to form a spot of diameter $w_L < D_L$, the rays emerging from the lens must converge. The borderline case is depicted in Figure E.5 and the corresponding equations are

$$\tan\left(\frac{\alpha}{2}\right) = \frac{D_e}{2\cdot f} \quad \text{with} \quad \frac{D_e}{2} = d_{LL}\cdot \tan\left(\frac{\alpha}{2}\right) + \frac{w_L}{2} \tag{E.2}$$

$$\text{hence} \quad f = d_{LL} + \frac{w_L}{2\cdot \tan\left(\frac{\alpha}{2}\right)} \tag{E.3}$$

wherein f is the lens focal length. With the same numerical values as above, we find that the maximum f value is equal to $d_{LL} + 5.0$ mm. Taking the above-calculated d_{LL} upper value of 23.4 mm for instance, this means that f must be below 28.3 mm.

E.1.2.2 Adjusting the Spot Diameter

If the two above conditions on the lens-to-LED distance d_{LL} and focal length f are met, as much light as possible is collected by the lens, and the rays emerging from it are converging. The relation between d_{LS} and the size of the spot can then be expressed with the help of Figure E.6 as

$$\tan\left(\frac{\beta}{2}\right) = \frac{D_I - D_E}{2\cdot f} = \frac{D_I - w_S}{2\cdot d_{LS}} \tag{E.4}$$

with

$$D_I = 2\cdot d_{LL}\cdot \tan\left(\frac{\alpha}{2}\right) + w_L \quad \text{and} \quad D_E = 2\cdot f\cdot \tan\left(\frac{\alpha}{2}\right) \tag{E.5}$$

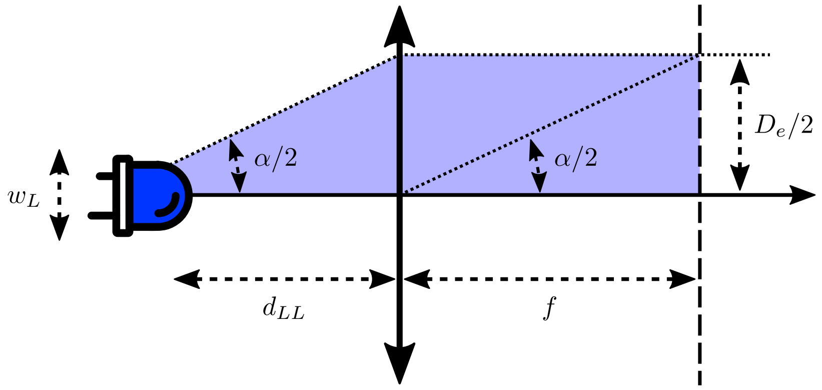

Figure E.5: In the borderline case, the emerging rays are parallel to the optical axis. The diameter of the light spot projected onto the lens by the LED is noted D_e. The focal plane of the lens is represented with long dashes, while construction rays are represented using smaller dashes or dots.

wherein D_I, D_E and β are defined in Figure E.6. These equations leads to:

$$\begin{aligned} d_{LS} &= f \cdot \frac{D_I - w_S}{D_I - D_E} \\ d_{LS} &= f \cdot \frac{2 \cdot d_{LL} \cdot \tan\left(\frac{\alpha}{2}\right) + w_L - w_S}{2 \cdot \tan\left(\frac{\alpha}{2}\right) \cdot (d_{LL} - f) + w_L} \end{aligned} \tag{E.6}$$

This latter equation is interesting because it tells us that if f and d_{LL} are chosen too close, a small inaccuracy on the LED-lens positioning—*i.e.* d_{LL}—might result in an important d_{LS} shift, and thus in an important change in the spot size w_S. Additionally, the practical considerations exposed while presenting Figure E.2 limits d_{LS} to a minimum of approximately 20.2 mm.

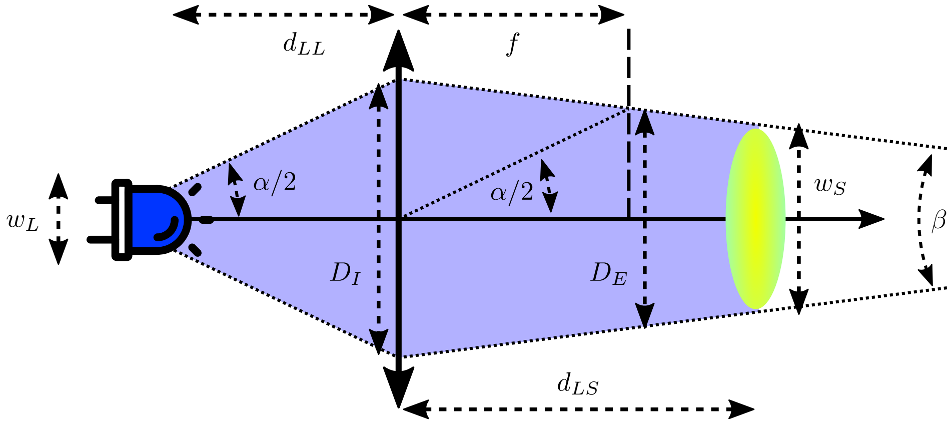

Figure E.6: Complete annotated schematic of the illuminating block. D_I is the diameter of the light spot produced by the LED onto the lens surface, and D_E is the diameter of the emerging light beam in the focal plane. β is the angle of the converging rays emerging from the lens.

E.1.2.3 Practical Realisation

To sum up the above considerations, we must meet the following conditions (using a 16 mm focal length lens, as detailed below):

(i) $d_{LL} > 19$ mm because of the presence of the excitation filter of thickness 6.3 mm, plus 8.7 mm of lens thickness (16 mm focal minus 7.3 back focal length), 2 mm of retaining ring, 1.7 mm of LED bulb, rounded to the upper value to allow for positioning error and in order to avoid crushing the LED into the filter.

(ii) $d_{LL} < 23.4$ mm not to lose any LED-emerging rays, as explained in Section E.1.1.

(iii) $f < d_{LL} + 5.0\ mm$ to allow for converging rays emerging the lens, as explained in the previous section.

(iv) $d_{LS} > 23.8\ mm$ due to the practical consideration exposed in Figure E.2.

In practice, if d_{LL} and d_{LS} can be changed continuously, there is only a limited number of focal lengths available from the manufacturer. For instance, Thorlabs' standards focal lengths are 25.4 mm or 16.0 mm for 1" lenses. Since the optical system should remain compact for practical reasons, Thorlabs' $f = 16$ mm condensing lens (ACL25416U) was finally chosen. In this configuration, the shortest possible d_{LL} of 19 mm and a spot of diameter $w_S = 10$ mm lead to a d_{LS} distance of 23.3 mm. However, the latter being slightly below the 23.8 mm of constraint *(iv)*, it was rounded up to 24 mm, which would result in practice to a spot slightly smaller than 10 mm in diameter (9.7 mm). For reference, Figure E.7 represent d_{LS} as a function of d_{LL} for a variety of spot diameters w_S. Finally, Figure E.8, presents both a schematic mechanical drawing reporting the above dimensions and a 3D-view of the resulting opto-mechanical assembly.

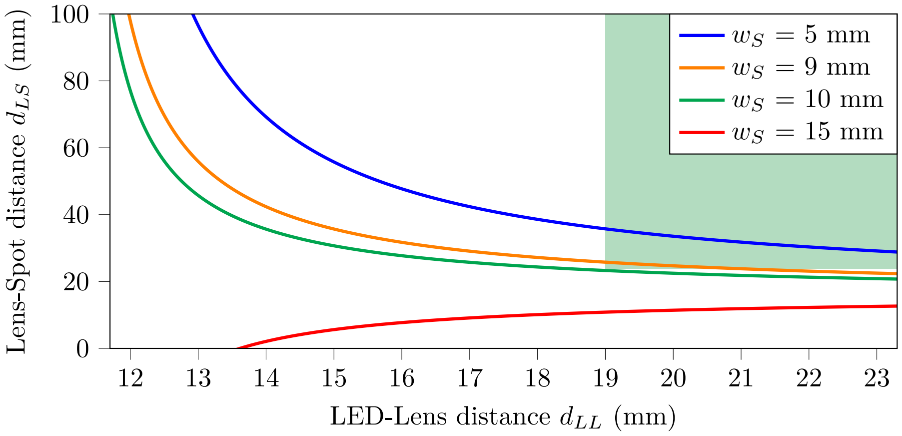

Figure E.7: Distance between the lens and the thin film as a function of the LED-lens distance for various spot sizes. Calculations were made with a 16 mm focal length lens. The green square indicates constraints *(i)* and *(iv)*.

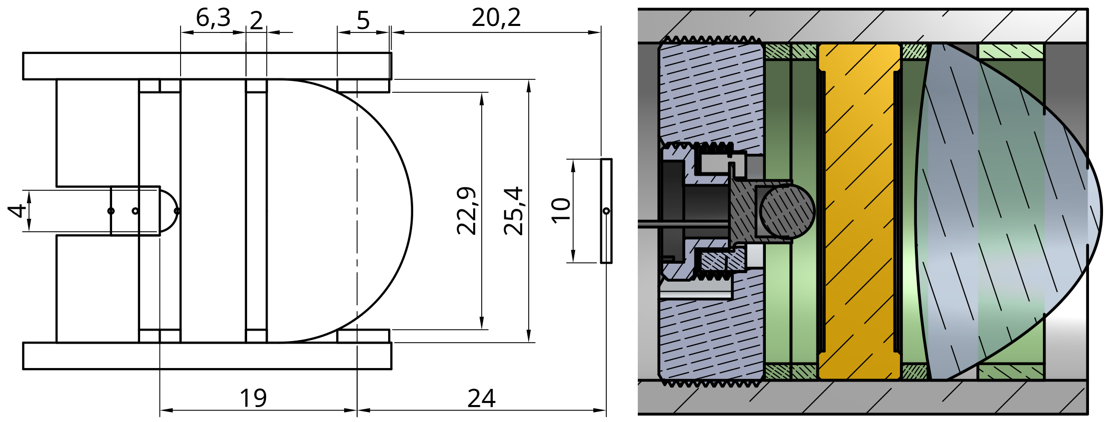

Figure E.8: Mechanical drawing (Left) and 3D section-view (right) of the final illuminating block assembly. From left to right (all parts are Thorlabs'): an LED mount (S1LEDM) holding the LED (LED450L), two retaining ring (SM1RR), the excitation shortpass filter (FES450), a third retaining ring (SM1RR), the lens (ACL25416U), and a large retaining ring (SM1RRC). All elements are mounted into a SM1 threaded tube. The rectangle element on the right part of the mechanical drawing depicts the thin film. Note that the focal plane of the lens is plotted as a dashed line.

E.2 Light Collection block

The scheme retained for the collecting block is depicted in Figure E.9. The light collection block aims at collecting as much light as possible from the fluorescent film, but contrary to the LED, the film emits light in all directions—*i.e.* it is an isotropic source. Thus, it would seem intuitive to place the first collecting lens as close as possible to the film. However, since the focal of the lens cannot be arbitrarily small, placing it too close from the film would result in rays emerging from the lens diverging from the optical axis, and therefore not collectible by the photodiode. In addition, the mechanical considerations presented in Figure E.2 prevents the first lens to be placed closer than 20.2 mm from the film. Please note that the illuminated spot also emits light opposite to the photodiode, so 50% of the light re-emitted by the film is lost anyway. Unless a mirror, or some kind of reflective or highly diffusive—*i.e.* white—coating is placed below the film, for instance. This possibility is not further explored in the present study however.

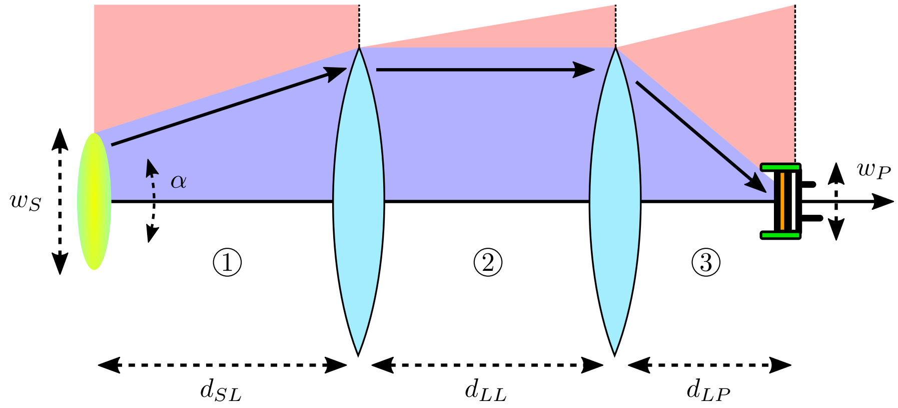

Figure E.9: Principle schematic of the collecting block. The light is emitted by the film spot of width w_S illuminated by the LED. d_{SL}, d_{LL} and d_{LP} are the distances between the spot and the first lens, between the two lenses, and between the second lens and the photodiode, respectively. w_P is the width of the photodiode. In mauve are the rays contributing to the signal measured at the photodiode, while in pink are the rays that are lost. The light-collecting surface of the photodiode is coloured in orange, while its mechanical enclosure is green.

As can be seen in Figure E.9, the path of a light ray can be decomposed into three travels, delimited by the two deviations caused by the lenses: ① between the film and the first lens, ② between the two lenses, and ③ between the second lens and the photodiode. While the amount of light reaching the first lens relative to the total amount of light emitted by the spot can be easily expressed analytically (see Section E.2.2), the calculation quickly becomes unfeasible in a more general case involving several lenses and other opto-mechanical components. Thus, it was decided to create a basic ray-tracing engine(1) that would launch rays uniformly from the spot, and measure the number of rays reaching the photodiode in the end. Then, the three parameters d_{SL}, d_{LL} and d_{LP} were optimised so as to maximise the amount of light collected at the photodiode. As in the previous section, light propagation through the emission filter was not considered, and the latter filter was only considered in terms of its physical dimensions.

E.2.1 Ray-Tracing

The main advantage of ray tracing is that it is quite simple to mathematically express the conditions that a ray must satisfy in order to reach the photodiode. These conditions are the following:

(i) A ray emitted by the spot must reach the surface of the first lens.

(ii) A ray emerging from the first lens must reach the surface of the second lens.

(iii) A ray emerging from the second lens must reach the photodiode's surface without being blocked by its mechanical enclosure.

The spot is uniformly divided into a number n_{pts} of points, and each spot point uniformly launches a number n_{rays} of rays. These three conditions are then checked sequentially for a given ray, if the condition tested is false, the considered ray is terminated and another ray is launched, if the condition is true, the ray continues its travel until the next condition. If the

---

(1) This approach was quite artisanal, and I would advise readers to use dedicated software—such as Zemax or the like—if they need to perform similar work. However, building a simple ray-tracing engine for this specific use case was a relatively quick process—*i.e.* taking only a few days of work—and may still be faster than learning to navigate Zemax, which can be somewhat labyrinthine.

three conditions are met, the ray is considered as "detected". These conditions are depicted in Figure E.10. The following paragraphs detail the different steps leading to the detection of a ray by the photodiode.

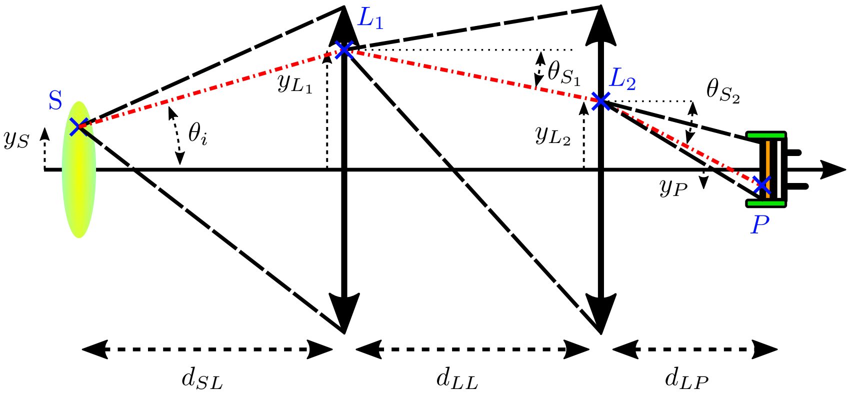

Figure E.10: Study of a ray emerging with an initial angle θ_i from a source point S (ordinate y_S). Its path is represented with a red dashed-doted line. It emerges successively from the two lenses at points L_1 and L_2 with the angles θ_{S_1} and θ_{S_2}. The conditions *(i)–(iii)* are represented with the long-dashed black lines. The red ray is valid / detected because it is always between these two lines.

E.2.1.1 Reaching the First Lens

Considering a source point S of ordinate y_S, and a light ray emitted by S at an angle θ_i with respect to the optical axis. Reaching the second lens means that y_{L_1}, the ordinate of the intersection of this ray and the first lens plane must satisfy

$$-D_L < 2{\cdot}y_{L_1} < D_L \quad \text{wherein} \quad y_{L_1} = d_{SL}{\cdot}\tan(\theta_i) + y_S \tag{E.7}$$

If the condition described by equation E.7 is satisfied, the ray travels further—*i.e.* it will exit the lens—otherwise it is terminated.

E.2.1.2 Deviation by the Lenses

Once the ray reached the first lens in L_1, its emerging angle θ_{S_1} can be computed, which value will determine whether the ray reaches the second lens or not. Considering Figure E.11, we have

$$f{\cdot}\tan(\theta_{S_1}) = f{\cdot}\tan(\theta_i) - y_{L_1} \quad \text{which leads to} \quad \theta_{S_1} = \arctan\left(\frac{f{\cdot}\tan(\theta_i) - y_{L_1}}{f}\right) \tag{E.8}$$

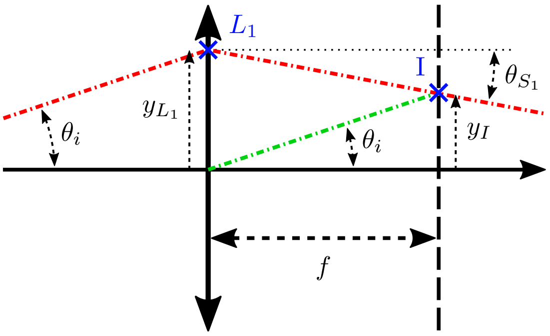

Figure E.11: Deviation of an incident ray by a converging lens of focal f. The green ray is parallel to the incident red ray coming from the left of the picture with an angle θ_i. The focal plane of the lens is represented by a long-dashed line. The point I is the intersection between the real emerging ray in red, the fictitious green ray and the focal plane.

It is clear that the same train of thought can be applied to the second lens, substituting θ_{S_1} to θ_i, θ_{S_2} to θ_{S_1} and L_2 to L_1, we have

$$f{\cdot}\tan(\theta_{S_2}) = f{\cdot}\tan(\theta_{S_1}) - y_{L_2} \quad \text{leading to} \quad \theta_{S_2} = arctan\left(\frac{f{\cdot}tan(\theta_{S_1}) - y_{L_2}}{f}\right) \tag{E.9}$$

E.2.1.3 Reaching the Second Lens

As for the first lens, we can write the condition for the ray emerging from the surface of the first lens to reach the second one as

$$-D_L < 2{\cdot}y_{L_2} < D_L \quad \text{wherein} \quad y_{L_2} = d_{LL}{\cdot}\tan(\theta_{S_1}) + y_{L_1} \tag{E.10}$$

Using equation E.8 leads to

$$y_{L_2} = d_{LL}{\cdot}\tan(\theta_i) + y_{L_1}{\cdot}\left(\frac{f - d_{LL}}{f}\right) \tag{E.11}$$

As before, if the condition described by equation E.10 is true, it means that the ray reaches the second lens and can travel further. Otherwise, it is terminated.

E.2.1.4 Reaching the Photodiode

To reach the photodiode, a ray emerging from the second lens must fulfil two criteria: *(i)* it must be directed towards the surface of the photodiode and *(ii)* it must not be blocked by the mechanical enclosure of the photodiode. These two conditions are illustrated in Figure E.12.

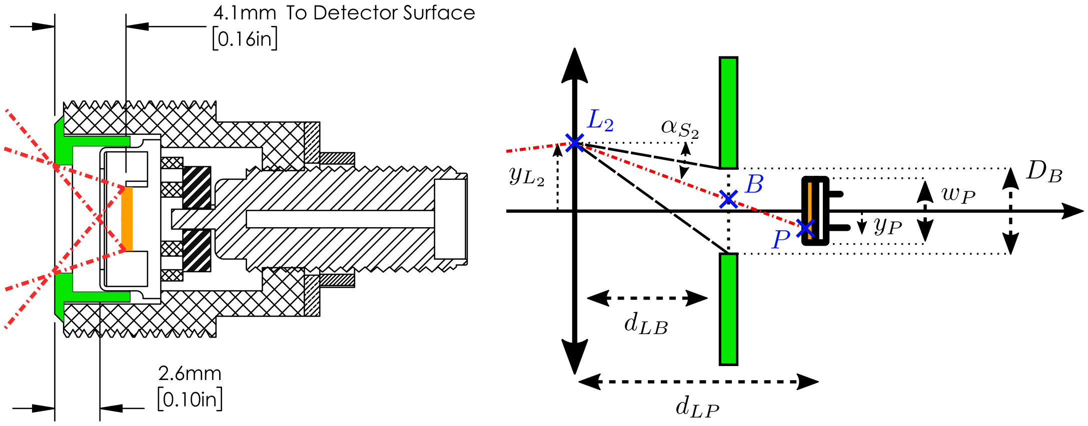

Figure E.12: **Left:** drawing of the mounted photodiode with the light-sensitive surface in orange and the potentially blocking elements in green. In red, some borderline rays are plotted: rays cannot reach the surface of the photodiode if they are more diverging than the plotted ones. **Right:** schematic view of the photodiode when placed in front of the second lens. The aperture D_B of the blocking element (in green), limits the collection of rays too diverging compared to the optical axis. This aperture is placed at a distance d_{LB} from the lens. B is the point located at the intersection between the ray and the blocker plane.

The blocking part of the photodiode can be considered as a infinitely thin plane with one circular aperture of diameter D_B located at a distance d_{LP} of the second lens. In such a case, the condition for a ray to pass through this aperture is

$$-D_B < 2{\cdot}y_B < D_B \quad \text{with} \quad y_B = d_{LB}{\cdot}\tan(\theta_{S_2}) + y_{L_2} \tag{E.12}$$

and that for a ray to reach the light-sensitive surface of the photodiode is

$$-w_P < 2{\cdot}y_P < w_P \quad \text{with} \quad y_P = d_{LP}{\cdot}\tan(\theta_{S_2}) + y_{L_2} \tag{E.13}$$

E.2.2 Accuracy Considerations

Now that the conditions for a given light ray emitted by the luminescent spot to reach the photodiode are known. The next step is to study the accuracy of the designed ray tracing engine in terms of number of rays launched *versus* prediction error. Indeed, when using a ray-tracing algorithm, one must ensure that *enough* rays are being launched, and there is always a trade-off between the reached accuracy—which increases with an increasing number of rays—and performance—with a simulation time also increasing with the number of rays. The total number of rays launched can be expressed as

$$N_{\text{rays}} = n_{\text{pts}}{\cdot}n_{\text{rays}} \tag{E.14}$$

wherein n_{pts} is the number of points into which the light source is divided, and n_{rays} is the number of rays emitted by each one of these source points. To ascertain the accuracy of the devised ray-tracing engine, it was tested on the first condition that was mentioned in the collecting block analysis, which can be translated into the following question: which amount of emitted light by the spot does reach the surface of the first lens? The latter can be expressed exactly as

$$E_L = \frac{1}{2 \cdot \pi \cdot w_S} \cdot \int_{-\frac{w_S}{2}}^{+\frac{w_S}{2}} \arctan\left(\frac{D_L/2 - y}{d_{SL}}\right) - \arctan\left(\frac{-D_L/2 - y}{d_{SL}}\right) dy \tag{E.15}$$

wherein E_L is the relative energy reaching the surface of the first lens, compared to the total energy re-emitted by the spot. E_L thus has a theoretical maximum value of 50%, which is reached when the lens is placed against the spot (d_{SL}=0), and its overall outline is represented in Figure E.13. As can be seen, E_L decreases sharply with an increase in d_{SL}. For instance, the amount of light that can be collected by a 1 inch lens (effective diameter of D_L=22.9 mm) from an isotropic 1 cm circular spot drops from 26.6% at 10 mm down to 16.4% at 20 mm and 11.5% at 30 mm. Since E_L can be exactly known in this way, its theoretical value can be compared with the ray-tracing results to ascertain the accuracy of the devised ray-tracing engine in a simple case.

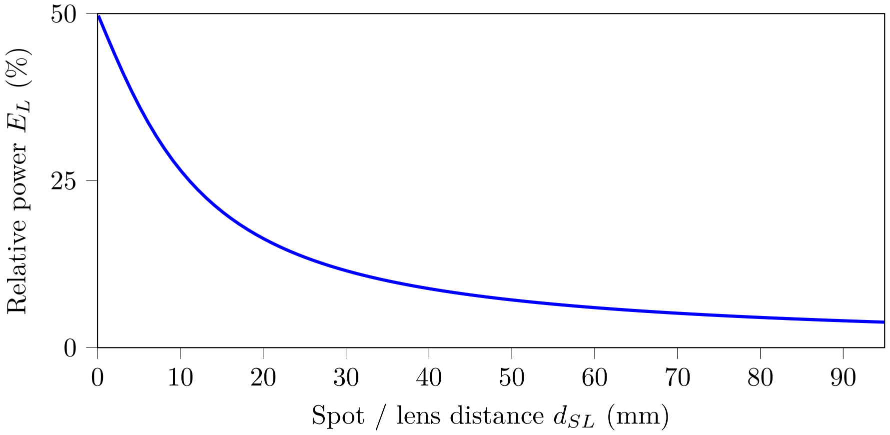

Figure E.13: Relative power E_L collected at the surface of the lens, as a function of the object / lens distance d_{SL}. E_L quickly drops from its theoretical maximum of 50% at d_{SL}=50 mm down to below 10% for a d_{SL} above 35 mm.

The influence of n_{pts} and n_{rays} were investigated separately, as can be seen in Figure E.14. Taking into account the scale difference between the two graphs, it appears that n_{rays} has a greater influence than n_{pts} on the accuracy. Indeed increasing n_{pts} above 300 source points has no further effect on the resulting accuracy, while higher n_{rays} values continue to improve it. The influence of both parameters can be seen in Figure E.15. For all three figures, d_{SL}=20 mm, w_S=10 mm, D_L=25.4 mm.

It can be concluded that an n_{pts} value above 200 is enough, while an n_{rays} of 500 is a good starting value, leading to a relative error of 0.2% and a computation time of 0.15 s. It must be stressed out that this choice is of course essentially arbitrary, and that higher figures could always be chosen, yielding even lower error values. However, given the approximations that were used—*e.g.* no influence of the filters, no backscattered rays or internal reflections inside the lenses, *etc*—the overall model accuracy is likely to be driven by the latter rather than by ray-tracing Monte-Carlo-like errors. To give an idea of the orders of magnitude involved, the underlying Python code was optimised so that up to 10^6 rays can be traced in ~1.3 s, and the simulation time is proportional to the number of rays traced.

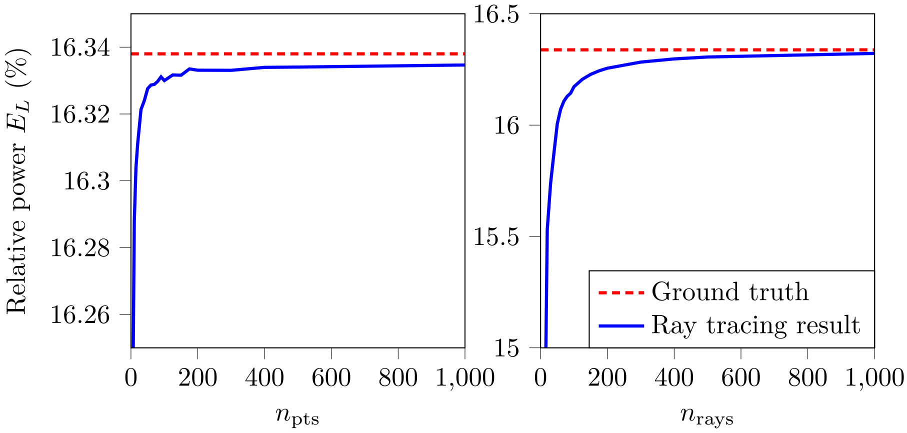

Figure E.14: **Left:** amount of light collected as a function of the number of source points used (n_{rays}=5000). **Right:** amount of light collected as a function of the number of rays per source point used (n_{pts}=5000). In both cases the ground truth corresponds to the exact calculus.

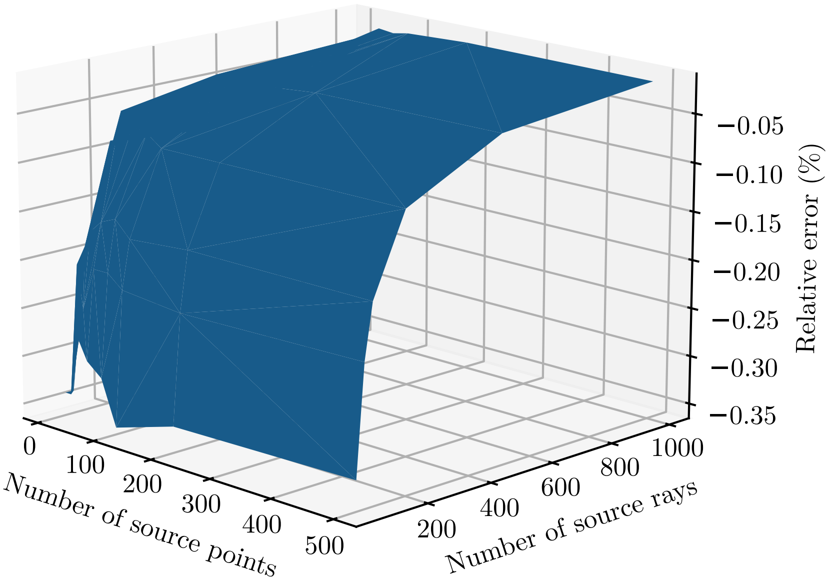

Figure E.15: 3D plot of the influence of both n_{pts} and n_{rays} on the relative error on E_L.

E.2.3 Positioning the Optical Elements

With the help of the above-described ray tracing engine, an approximation of the relative amount of light collected at the photodiode E_P can be computed as a function of d_{SL}, d_{LL} and d_{LP}. The maximum value of E_P as well as the corresponding d_{SL}, d_{LL} and d_{LP} values can thus be found using a standard optimisation algorithm. As an illustration, and since representing E_P as a function of its three parameters is unfeasible, the influence of d_{LL} on E_P for several d_{SL} and d_{LP} values was plotted in Figure E.16. Similar graphs can of course be obtained for d_{SL} and d_{LP}.

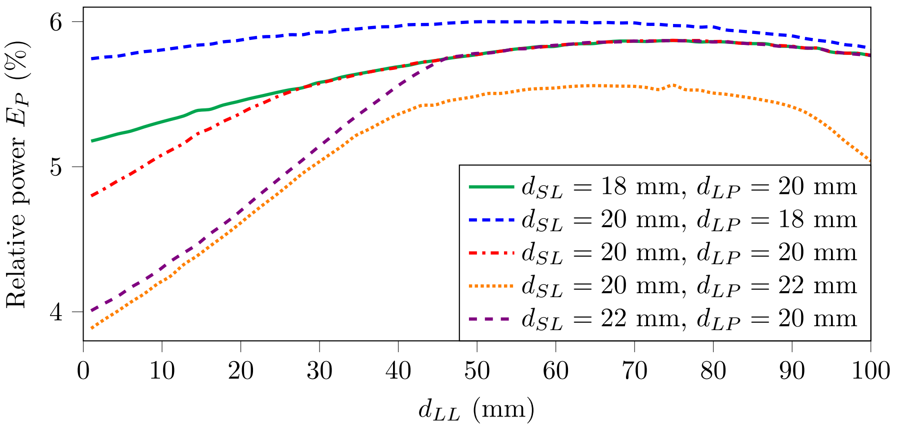

Figure E.16: Influence of d_{LL} on E_P for several d_{SL} and d_{LP} values.

E.2.3.1 Setting Boundaries

To maximise the amount of light collected at the photodiode, the following optimisation problem must be addressed, *i.e.* the (d_{SL}, d_{LL}, d_{LP}) values which fulfil the following relation must be found:

$$(d_{SL}, d_{LL}, d_{LP}) = \underset{d_{SL},d_{LL},d_{LP}}{\arg\max}(E_P) \quad \text{wherein} \quad \begin{cases} d_{SL} \in B_{SL} \\ d_{LL} \in B_{LL} \\ d_{LP} \in B_{LP} \end{cases} \tag{E.16}$$

with B_{SL}, B_{LL} and B_{LP} delimiting the boundaries for the three d_{XX} variables. At first, as earlier presented in Figure E.2, d_{SL} should be at least 20.2 mm. Alas, due to the thicknesses of the mounting ring and lens, this distance must me extended up to 30.8 mm. Then, due to the size of the lenses, d_{LL} should be at least 14.0 mm, but since the low-pass filter must also be added to the assembly, this distance is raised up to 21.4 mm. d_{LP}, on its part, is at least 9.4 mm. No upper values do exist in theory. However, to speed up the optimisation process, we set an upper bound of 50 mm for the three d_{XX} variables. To sum up (all lengths in mm):

$$\begin{cases} d_{SL} \in B_{SL} = [30.8; 50.0] \\ d_{LL} \in B_{LL} = [21.4; 50.0] \\ d_{LP} \in B_{LP} = [9.4; 50.0] \end{cases} \tag{E.17}$$

E.2.3.2 Optimisation Results

The above-given limits and optimisation problem were fed to a numerical solver—namely the `differential_evolution` program from the SciPy Python library[884], itself based on an algorithm proposed by Storn *et al.*[885]. The algorithm converged towards the following optimal distances to maximise E_L:

$$\begin{cases} d_{SL} = 30.8 \text{ mm} \\ d_{LL} = 21.5 \text{ mm} \\ d_{LP} = 11.2 \text{ mm} \end{cases} \tag{E.18}$$

which yield an E_P value at the photodiode of 5.9%. This value can be compared with the maximum value of E_L=11.3% received by the surface of the first lens for d_{SL}=30.8 mm. One may also note that d_{SL} and d_{LL} are equal—or extremely close—to their lower bounds.

Out of curiosity, we performed the same optimisation with no lower bounds for d_{SL} and without taking the filter into account—*i.e.* setting the lowest d_{SL} value to 10.6 mm and the lowest d_{LL} value to 14 mm. In such a configuration, we found a maximum amount of light collected of 6.8%, a value which is reached for d_{SL}=30.6 mm, d_{LL}=14.0 mm and d_{LP}=9.4 mm (E_L=11.3% at d_{SL}=30.6 mm)

It is also interesting to note that to reach such levels—in the 10% region—in a *proximity* configuration—that is to say with the photodiode located directly in front of the spot—a spot / photodiode distance d_{SP} below 8.6 mm would be necessary. This result is not significantly modified by the size of the spot, with a d_{SP} below 9.4 mm still required even with a spot size of only 3 mm. The calculations leading to this result are essentially the same as those presented in section E.2.2.

E.2.3.3 Practical Realisation

As was the case for the illuminating block, the above presented light collection scheme must be implemented in the real world, preferably using off-the-shelf optical components. The whole assembly fits into a 2 inches long tube, as can be seen in Figure E.17, and can be build using standard Thorlabs components.

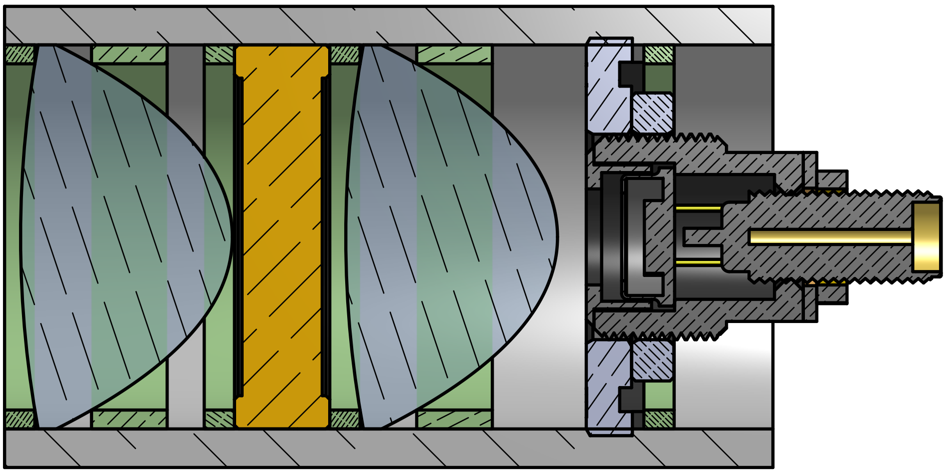

Figure E.17: Cut view of the whole collecting block assembly (all part numbers are Thorlabs'). In green are the thin (SM1RR) and thick (SM1RRC) retaining rings, in transparent blue are the two lenses (ACL25416U), and in yellow is the filter (FEL0450). Finally the block on the right is composed of the photodiode (SM05PD1A) mounted into a SM1 to SM05 thread adapter (SM1A6) and locked with a SM05 ring (SM05NT).

E.3 Complete Assembly

A PLA 3D-printed contraption was designed to hold the illumination and collection blocks altogether, and point them at the fluorescent thin film placed behind the glass window, as can be seen in Figure 5.11 of the main text.

E.4 Link Budget

To appropriately size the LED's power and photodiode transimpedance amplifier's gain, a link budget was calculated, considering the optical setup as a whole. Of note, the values given below are mainly use as orders of magnitude and should **not** be taken too literally.

Starting with the LED, an optical power of 10 mW was taken, slightly above the 7 mA of nominal DC power from the LED450L (Thorlab), but below its maximal one (~20 mW)

$$P_{\text{LED,opt}} = 10 \text{ mW} \tag{E.19}$$

The illuminating assembly was designed so that all the light emitted by the LED reaches the film. The film absorbance and conversion factor T_{film} is then function of the film absorbance A and quantum yield Φ. A value of 0.1 was deemed reasonable since the absorbance can be tuned by either changing the film thickness, dye concentration, or both, and since the quantum yields of the dyes—*i.e.* HPTS and Ru-dpp is relatively high

$$T_{\text{film}} = A{\cdot}\Phi = 0.1 \tag{E.20}$$

The collecting assembly is then able to collect 5.9% of the light re-emitted by the film, as mentioned above.

$$T_{\text{collect}} = 0.059 \tag{E.21}$$

The optical power received at the photodiode is thus

$$P_{\text{PD,opt}} = P_{\text{LED,opt}}{\cdot}T_{\text{film}}{\cdot}T_{\text{collect}} \approx 50\ \mu W \tag{E.22}$$

Ideally generating a photocurrent given by

$$\begin{aligned} E_{\text{photon}} &= h{\cdot}\nu = \frac{h{\cdot}c}{\lambda} \\ \frac{dn_{\text{photons}}}{dt} &= \frac{P_{\text{PD,opt}}}{E_{\text{photon}}} = \frac{P_{\text{PD,opt}}{\cdot}\lambda}{h{\cdot}c} \\ dQ &= dn_{\text{photons}}{\cdot}e{\cdot}\eta_{\text{PD}} \end{aligned} \tag{E.23}$$

wherein e=1.60×10^{-19} C is the elementary charge, h=6.63×10^{-34} J.s Plank's constant, c=3.00×10^{8} m.s^{-1} light's celerity, λ=450 nm, and η_{PD} the quantum yield of the photodiode, taken equal to 0.1. Finally, the photocurrent produced by the photodiode may thus be written:

$$\begin{aligned} I_{\text{PD}} &= \frac{dQ}{dt} = \frac{P_{\text{PD,opt}}{\cdot}\lambda{\cdot}e{\cdot}\eta_{\text{PD}}}{h{\cdot}c} \\ I_{\text{PD}} &\approx 1.7\ \mu A \end{aligned} \tag{E.24}$$

To reach an output voltage in the range of 100-500 mV, a trans-impedance gain of 10^5 V.A^{-1} is thus needed. The selected first-stage amplifier AMP102 (Thorlabs) can reach 10^5 V.A^{-1} and a second stage of amplification could be used if the signal is still too low. I did not expect the latter situation to happen, though, since some factors taken to establish this link budget were rather pessimistic—T_{film}, in particular.

Back to Section 5.4.1.2 Main Table Of Content (TOC)

Appendix F

Custom Screen Printing Setup

Back to Section 5.5.2.2 Main Table Of Content (TOC)

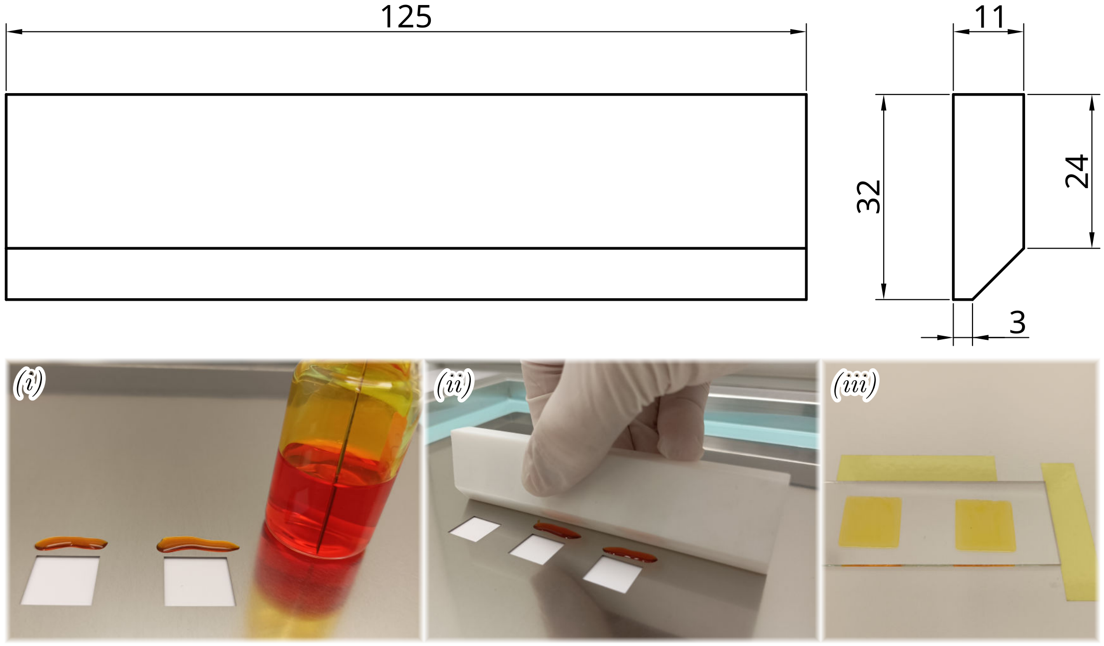

Figure F.1: **Top:** mechanical drawing of the PTFE doctor blade used for screen printing. **Bottom:** screen printing process. *(i)*, a standard 100 µm thick SMD stencil is positioned on top of a microscope glass slide and some amount of solution (here Ru-dpp and PAN in DMF) is deposited next to the stencil's openings. *(ii)*, the PTFE doctor blade is then scraped across the surface of the stencil in a single continuous motion, spreading the solution evenly on the glass substrate. *(iii)*, the resulting liquid thin-films after the stencil is removed.
Disclaimer: contrary to most other aspects of this doctoral work, the blade dimensions, the scraping speed, and the overall screen printing process were not particularly fine-tuned. It yielded results at least as good as using a dedicated doctor blade setup (K Control Coater, Erichsen) while being much easier to work with, mainly due to faster cleaning times, as exposed in Section 5.5.2.2.

Bibliography

TL;DR

Except for Nakamaru's paper[750]—which appears to be lost in the sands of time as indicated in Section 5.2.3—all the works below can be requested from the author if need be.

Previous chapter Main Table Of Content (TOC) Next chapter

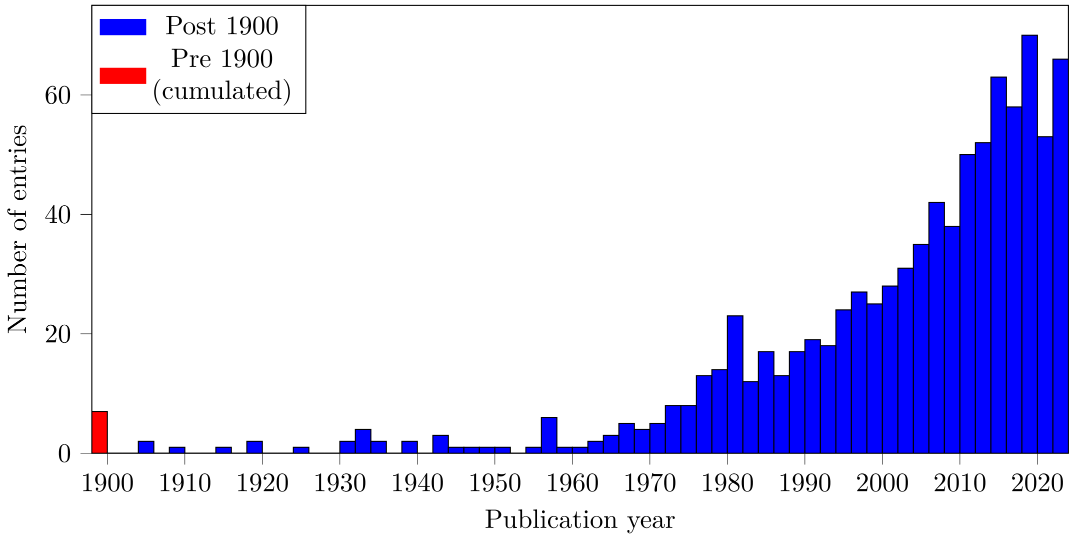

Figure F.2: Histogram of used references, covering over a century of relentless scientific efforts.

[1] Tobias Oetiker et al. *The Not So Short Introduction to LaTeX*. 2023. URL: `https://tobi.oetiker.ch/lshort/lshort.pdf` (cit. on pp. i, ii).

[2] "On the Hypothesis that Animals are Automata, and its History". In: *Nature* 10.253 (1874), pp. 362–366. ISSN: 1476-4687. DOI: `10.1038/010362a0` (cit. on p. 1).

[3] "On the Hypothesis That Animals are Automata, and its History". In: Cambridge Library Collection - Philosophy. Cambridge: Cambridge University Press, 1874, pp. 199–250. ISBN: 9781139149204. DOI: `10.1017/CBO9781139149204.007` (cit. on p. 1).

[4] Anthony R. Cashmore. "The Lucretian Swerve: The Biological Basis of Human Behavior and the Criminal Justice System". In: *Proceedings of the National Academy of Sciences* 107.10 (2010), pp. 4499–4504. DOI: `10.1073/pnas.0915161107` (cit. on p. 1).

[5] Enhanced Well-being (WEL). *Health Promotion Glossary of Terms 2021*. World Health Organisation, 2021. ISBN: 978-92-4-003834-9. URL: `https://web.archive.org/web/20231106040048/https://www.who.int/publications/i/item/9789240038349` (cit. on p. 2).

[6] Craig Lockwood, Tiffany Conroy-Hiller, and Tamara Page. "Vital Signs". In: *JBI Reports* 2.6 (July 2004), pp. 207–230. ISSN: 1479-697X. DOI: `10.1111/j.1479-6988.2004.00012.x` (cit. on p. 2).

[7] James M. Callahan. “Pulse Oximetry in Emergency Medicine”. In: *Emergency Medicine Clinics of North America* 26.4 (2008), pp. 869–879. ISSN: 0733-8627 (cit. on p. 2).

[8] Tom Ahrens. “Monitoring Carbon Dioxide in Critical Care: The Newest Vital Sign?” In: *Critical Care Nursing Clinics of North America* 16.3 (2004), pp. 445–451. ISSN: 0899-5885 (cit. on p. 2).

[9] Christopher L. Hunter et al. “The Sixth Vital Sign: Prehospital End-Tidal Carbon Dioxide Predicts In-Hospital Mortality and Metabolic Disturbances”. In: *The American Journal of Emergency Medicine* 32.2 (2014), pp. 160–165. ISSN: 0735-6757 (cit. on p. 2).

[10] Addie Middleton, Stacy L. Fritz, and Michelle Lusardi. “Walking Speed: The Functional Vital Sign”. In: *Journal of Aging and Physical Activity* 23.2 (2015), pp. 314–322. DOI: `10.1123/japa.2013-0236` (cit. on p. 2).

[11] Natalia E. Morone and Debra K. Weiner. “Pain as the Fifth Vital Sign: Exposing the Vital Need for Pain Education”. In: *Clinical Therapeutics* 35.11 (2013), pp. 1728–1732. ISSN: 0149-2918 (cit. on p. 2).

[12] Peter D. Wagner. “The Physiological Basis of Pulmonary Gas Exchange: Implications for Clinical Interpretation of Arterial Blood Gases”. In: *European Respiratory Journal* 45.1 (2015), pp. 227–243. ISSN: 0903-1936. DOI: `10.1183/09031936.00039214`. eprint: `https://erj.ersjournals.com/content/45/1/227.full.pdf`. URL: `https://erj.ersjournals.com/content/45/1/227` (cit. on pp. 2, 3, 5).

[13] Joseph Barcroft and Ff. Roberts. “The Dissociation Curve of Haemoglobin”. In: *The Journal of Physiology* 39.2 (1909), pp. 143–148. DOI: `10.1113/jphysiol.1909.sp001331`. eprint: `https://physoc.onlinelibrary.wiley.com/doi/pdf/10.1113/jphysiol.1909.sp001331`. URL: `https://physoc.onlinelibrary.wiley.com/doi/abs/10.1113/jphysiol.1909.sp001331` (cit. on pp. 2, 11).

[14] Meir Nitzan, Ayal Romem, and Robert Koppel. “Pulse Oximetry: Fundamentals and Technology Update”. In: *Medical devices: Evidence and Research* 7 (July 2014), pp. 231–239. DOI: `10.2147/MDER.S47319` (cit. on pp. 2, 6, 16, 20, 24, 31).

[15] Amal Jubran. “Pulse Oximetry”. In: *Critical Care* 19.1 (July 2015), p. 272. ISSN: 1364-8535. DOI: `10.1186/s13054-015-0984-8`. URL: `https://doi.org/10.1186/s13054-015-0984-8` (cit. on pp. 2, 6, 16, 24, 31).

[16] Toshiyo Tamura. “Current Progress of Photoplethysmography and SpO2 for Health Monitoring”. In: *Biomedical Engineering Letters* 9.1 (Feb. 2019), pp. 21–36. ISSN: 2093-985X. DOI: `10.1007/s13534-019-00097-w`. URL: `https://doi.org/10.1007/s13534-019-00097-w` (cit. on pp. 2, 16, 90).

[17] Vesna Cukic. “The Changes of Arterial Blood Gases in COPD During Four-Year Period”. In: *Medical archives (Sarajevo, Bosnia and Herzegovina)* 68.1 (2014), pp. 14–18. ISSN: 0350-199X. DOI: `10.5455/medarh.2014.68.14-18`. URL: `https://doi.org/10.5455/medarh.2014.68.14-18` (cit. on pp. 2, 3).

[18] Ahmed M. Al Rajeh and John R. Hurst. “Monitoring of Physiological Parameters to Predict Exacerbations of Chronic Obstructive Pulmonary Disease (COPD): A Systematic Review”. In: *Journal of Clinical Medicine* 5 (Nov. 2016), p. 108. DOI: `10.3390/jcm5120108` (cit. on p. 2).

[19] S Nava et al. “Survival and Prediction of Successful Ventilator Weaning in COPD Patients Requiring Mechanical Ventilation for More Than 21 Days”. In: *European Respiratory Journal* 7.9 (1994), pp. 1645–1652. ISSN: 0903-1936. eprint: `https://erj.ersjournals.com/content/7/9/1645.full.pdf`. URL: `https://erj.ersjournals.com/content/7/9/1645` (cit. on pp. 2, 3).

[20] Kessler Romain et al. “Predictive Factors of Hospitalization for Acute Exacerbation in a Series of 64 Patients with Chronic Obstructive Pulmonary Disease”. In: *American Journal of Respiratory and Critical Care Medicine* 159.1 (1999), pp. 158–164. ISSN: 1073-449X. DOI: `10.1164/ajrccm.159.1.9803117` (cit. on p. 2).

[21] Joo Hun Park et al. “Is Hypercapnea a Predictor of Better Survival in the Patients who Underwent Mechanical Ventilation for Chronic Obstructive Pulmonary Disease (COPD)?” In: *Korean J Intern Med* 21.1 (2006), pp. 1–9. ISSN: 1226-3303. DOI: `10.3904/kjim.2006.21.1.1` (cit. on p. 2).

[22] Tomomasa Tsuboi et al. “Importance of the PaCO₂ From 3 to 6 Months After Initiation of Long-Term Non-Invasive Ventilation”. In: *Respiratory Medicine* 104.12 (Dec. 2010), pp. 1850–1857. issn: 0954-6111. doi: 10.1016/j.rmed.2010.04.027. url: https://doi.org/10.1016/j.rmed.2010.04.027 (cit. on pp. 2, 3).

[23] Savas Ozsu et al. “Prognostic Significance of PaO2/PaCO2 Ratio in Normotensive Patients With Pulmonary Embolism”. In: *The Clinical Respiratory Journal* 6.2 (2012), pp. 104–111. issn: 1752-6981. doi: 10.1111/j.1752-699X.2011.00253.x (cit. on p. 2).

[24] István Vadász et al. “Hypercapnia: A Nonpermissive Environment for the Lung”. In: *American Journal of Respiratory Cell and Molecular Biology* 46.4 (2012), pp. 417–421. issn: 1044-1549. doi: 10.1165/rcmb.2011-0395PS (cit. on p. 2).

[25] D. E. Phelan et al. “Carbon Dioxide-Dependent Signal Transduction in Mammalian Systems”. In: *Interface Focus* 11.2 (2021), p. 20200033. doi: 10.1098/rsfs.2020.0033 (cit. on p. 2).

[26] Amilkar Almanza-Hurtado et al. “Hypercapnia from Physiology to Practice”. In: *International Journal of Clinical Practice* 2022.1 (2022), p. 2635616. doi: 10.1155/2022/2635616 (cit. on p. 2).

[27] World Health Organisation. *Cause-specific mortality, 2000–-2019.* 2020. url: https://web.archive.org/web/20240507143339/https://www.who.int/data/gho/data/themes/mortality-and-global-health-estimates/ghe-leading-causes-of-death (visited on 05/07/2024) (cit. on p. 2).

[28] Norman L. Jones. “An obsession with CO2”. In: *Applied Physiology, Nutrition, and Metabolism* 33.4 (2008), pp. 641–650. doi: 10.1139/H08-040. eprint: https://doi.org/10.1139/H08-040. url: https://doi.org/10.1139/H08-040 (cit. on p. 2).

[29] Patrice G. Guyenet and Douglas A. Bayliss. “Neural Control of Breathing and CO2 Homeostasis”. In: *Neuron* 87.5 (Sept. 2015), pp. 946–961. issn: 0896-6273. url: http://www.sciencedirect.com/science/article/pii/S0896627315006765 (cit. on p. 2).

[30] Andrew Lumb. “Control of Breathing”. In: *Nunn’s Applied Respiratory Physiology, 8th Edition.* Elsevier, 2016. Chap. 5, pp. 61–82. isbn: 9780702062940 (cit. on p. 2).

[31] L. Lee Hamm, Nazih Nakhoul, and Kathleen S. Hering-Smith. “Acid-Base Homeostasis”. In: *Clinical Journal of the American Society of Nephrology* 10.12 (2015), pp. 2232–2242. issn: 1555-9041. doi: 10.2215/CJN.07400715. eprint: https://cjasn.asnjournals.org/content/10/12/2232.full.pdf. url: https://cjasn.asnjournals.org/content/10/12/2232 (cit. on p. 3).

[32] Gerard Curley, John G. Laffey, and Brian P. Kavanagh. “Bench-to-Bedside Review: Carbon Dioxide”. In: *Critical Care* 14.2 (Apr. 2010), p. 220. issn: 1364-8535. doi: 10.1186/cc8926. url: https://doi.org/10.1186/cc8926 (cit. on p. 3).

[33] Cornelia Geers and Gerolf Gros. “Carbon Dioxide Transport and Carbonic Anhydrase in Blood and Muscle”. In: *Physiological reviews* 80 (May 2000), pp. 681–715. doi: 10.1152/physrev.2000.80.2.681 (cit. on pp. 3, 6, 12–15, 45).

[34] Andrew Lumb. *Nunn’s Applied Respiratory Physiology, 8th Edition.* Elsevier, 2016. isbn: 9780702062940 (cit. on pp. 3, 10–13, 15).

[35] J. M. Kowalchuk et al. “Factors Influencing Hydrogen Ion Concentration in Muscle After Intense Exercise”. In: *Journal of Applied Physiology* 65.5 (Nov. 1988), pp. 2080–2089. issn: 8750-7587. doi: 10.1152/jappl.1988.65.5.2080. url: https://doi.org/10.1152/jappl.1988.65.5.2080 (cit. on pp. 3, 57, 61).

[36] J. J. Diaztagle Fernández, J. C. Rodríguez Murcia, and J. J. Sprockel Díaz. “Venous-to-Arterial Carbon Dioxide Difference in the Resuscitation of Patients With Severe Sepsis and Septic Shock: A Systematic Review”. In: *Med Intensiva* 41.7 (May 2017), pp. 401–410. issn: 1578-6749. doi: 10.1016/j.medin.2017.03.008. url: https://doi.org/10.1016/j.medin.2017.03.008 (cit. on pp. 3, 61).

[37] Brenda G. Larkin and Robert J. Zimmanck. “Interpreting Arterial Blood Gases Successfully”. In: *AORN Journal* 102.4 (2015), pp. 343–357. doi: https://doi.org/10.1016/j.aorn.2015.08.002. eprint: https://aornjournal.onlinelibrary.wiley.com/doi/pdf/10.1016/j.aorn.2015.08.002. url: https://aornjournal.onlinelibrary.wiley.com/doi/abs/10.1016/j.aorn.2015.08.002 (cit. on p. 3).

[38] Steven Foster, Deborah Lopez, and Henry M. Thomas. "Pulmonary Rehabilitation in COPD Patients With Elevated PCO2". In: *American Review of Respiratory Disease* 138.6 (1988). PMID: 3144219, pp. 1519–1523. DOI: `10.1164/ajrccm/138.6.1519`. eprint: `https://doi.org/10.1164/ajrccm/138.6.1519`. URL: `https://doi.org/10.1164/ajrccm/138.6.1519` (cit. on p. 3).

[39] R. L. Campbell and M. A. Saxen. "Respiratory Effects of a Balanced Anesthetic Technique–Revisited Fifteen Years Later". In: *Anesthesia progress* 41.1 (1994), pp. 1–5. ISSN: 0003-3006. URL: `https://pubmed.ncbi.nlm.nih.gov/8629740` (cit. on p. 3).

[40] Antoine G. Schneider et al. "Arterial Carbon Dioxide Tension and Outcome in Patients Admitted to the Intensive Care Unit After Cardiac Arrest". In: *Resuscitation* 84.7 (July 2013), pp. 927–934. ISSN: 0300-9572. URL: `http://www.sciencedirect.com/science/article/pii/S0300957213001408` (cit. on pp. 3, 57, 61).

[41] Bernd Volker Scheer, Azriel Perel, and Ulrich J. Pfeiffer. "Clinical Review: Complications and Risk Factors of Peripheral Arterial Catheters Used for Haemodynamic Monitoring in Anaesthesia and Intensive Care Medicine". In: *Critical Care* 6.3 (Apr. 2002), p. 199. ISSN: 1364-8535. DOI: `10.1186/cc1489`. URL: `https://doi.org/10.1186/cc1489` (cit. on p. 3).

[42] Gerald S. Zavorsky et al. "Arterial Versus Capillary Blood Gases: A Meta-Analysis". In: *Respiratory Physiology & Neurobiology* 155.3 (Mar. 2007), pp. 268–279. ISSN: 1569-9048. URL: `http://www.sciencedirect.com/science/article/pii/S1569904806002175` (cit. on pp. 3, 46, 60, 156).

[43] Anthony L Byrne et al. "Peripheral Venous and Arterial Blood Gas Analysis in Adults: Are They Comparable? A Systematic Review and Meta-Analysis". In: *Respirology* 19.2 (2014), pp. 168–175. DOI: `https://doi.org/10.1111/resp.12225`. eprint: `https://onlinelibrary.wiley.com/doi/pdf/10.1111/resp.12225`. URL: `https://onlinelibrary.wiley.com/doi/abs/10.1111/resp.12225` (cit. on pp. 3, 61).

[44] Darren J. Malinoski et al. "Correlation of Central Venous and Arterial Blood Gas Measurements in Mechanically Ventilated Trauma Patients". In: *Archives of Surgery* 140.11 (Nov. 2005), pp. 1122–1125. ISSN: 0004-0010. DOI: `10.1001/archsurg.140.11.1122`. URL: `https://doi.org/10.1001/archsurg.140.11.1122` (cit. on p. 3).

[45] Richard Treger et al. "Agreement Between Central Venous and Arterial Blood Gas Measurements in the Intensive Care Unit". In: *Clinical Journal of the American Society of Nephrology* 5.3 (2010), pp. 390–394. ISSN: 1555-9041. DOI: `10.2215/CJN.00330109`. eprint: `https://cjasn.asnjournals.org/content/5/3/390.full.pdf`. URL: `https://cjasn.asnjournals.org/content/5/3/390` (cit. on p. 3).

[46] Allan J. Walkey et al. "The Accuracy of the Central Venous Blood Gas for Acid-Base Monitoring". In: *Journal of Intensive Care Medicine* 25.2 (2010). PMID: 20018607, pp. 104–110. DOI: `10.1177/0885066609356164`. eprint: `https://doi.org/10.1177/0885066609356164`. URL: `https://doi.org/10.1177/0885066609356164` (cit. on p. 3).

[47] Thomas W.L. Scheeren, Jannis N. Wicke, and Jean-Louis Teboul. "Understanding the Carbon Dioxide Gaps". In: *Current Opinion in Critical Care* 24.3 (2018). ISSN: 1070-5295. URL: `https://journals.lww.com/co-criticalcare/Fulltext/2018/06000/Understanding_the_carbon_dioxide_gaps.9.aspx` (cit. on p. 4).

[48] Fady T. Charbel et al. "Brain Tissue PO2, PCO2, and pH During Cerebral Vasospasm". In: *Surgical Neurology* 54.6 (Dec. 2000), pp. 432–437. ISSN: 0090-3019. URL: `http://www.sciencedirect.com/science/article/pii/S0090301900003402` (cit. on p. 4).

[49] Adam J. Brooks et al. "The Effect of Hepatic Vascular Inflow Occlusion on Liver Tissue pH, Carbon Dioxide, and Oxygen Partial Pressures: Defining the Optimal Clamp/Release Regime for Intermittent Portal Clamping". In: *Journal of Surgical Research* 141.2 (Aug. 2007), pp. 247–251. ISSN: 0022-4804. DOI: `10.1016/j.jss.2006.10.054`. URL: `https://doi.org/10.1016/j.jss.2006.10.054` (cit. on p. 4).

[50] Bruce A. McKinley and Bruce D. Butler. "Comparison of Skeletal Muscle PO2, PCO2, and pH With Gastric Tonometric PCO2 and pH in Hemorrhagic Shock". In: *Critical Care Medicine* 27.9 (1999). ISSN: 0090-3493. URL: `https://journals.lww.com/ccmjournal/Fulltext/1999/09000/Comparison_of_skeletal_muscle_PO2,_PCO2,_and_pH.27.aspx` (cit. on p. 4).

[51] Michael G. Mythen. “Does Gastric Tonometry-Guided Therapy Reduce Total Mortality in Critically Ill Patients?” In: *Critical Care* 19.1 (Apr. 2015), p. 172. ISSN: 1364-8535. DOI: `10.1186/s13054-015-0893-x`. URL: `https://doi.org/10.1186/s13054-015-0893-x` (cit. on p. 4).

[52] Jihad Mallat and Benoit Vallet. “Regional Capnography”. In: *Monitoring Tissue Perfusion in Shock: From Physiology to the Bedside*. Ed. by Alexandre Augusto Pinto Lima and Eliézer Silva. Springer International Publishing, 2018, pp. 181–192. ISBN: 978-3-319-43130-7. DOI: `10.1007/978-3-319-43130-7_13`. URL: `https://doi.org/10.1007/978-3-319-43130-7_13` (cit. on p. 4).

[53] M. Ganter and A. Zollinger. “Continuous Intravascular Blood Gas Monitoring: Development, Current Techniques, and Clinical Use of a Commercial Device”. In: *BJA: British Journal of Anaesthesia* 91.3 (Sept. 2003), pp. 397–407. ISSN: 0007-0912. DOI: `10.1093/bja/aeg176`. URL: `https://doi.org/10.1093/bja/aeg176` (cit. on p. 4).

[54] Amin A. Nanji and Karen J. Whitlow. “Is it Necessary to Transport Arterial Blood Samples on Ice for pH and Gas Analysis?” In: *Can Anaesth Soc J.* 31 (1984) (cit. on p. 4).

[55] Antti A.M. Luukkonen et al. “Evaluation of a Hand-Held Blood Gas Analyzer for Rapid Determination of Blood Gases, Electrolytes and Metabolites in Intensive Care Setting”. In: *Clinical Chemistry and Laboratory Medicine (CCLM)* 54.4 (2016), pp. 585–594. URL: `https://www.degruyter.com/view/journals/cclm/54/4/article-p585.xml` (cit. on p. 4).

[56] Matthias Menzel et al. “Experiences With Continuous Intra-Arterial Blood Gas Monitoring: Precision and Drift of a Pure Optode-System”. In: *Intensive Care Medicine* 29.12 (Dec. 2003), pp. 2180–2186. ISSN: 1432-1238. DOI: `10.1007/s00134-003-1962-1`. URL: `https://doi.org/10.1007/s00134-003-1962-1` (cit. on p. 4).

[57] Almir Badnjevic, Emir Beganovic, and Osman Music. “Facts About Solution Based and Cartridge Based Devices for Blood Gas Analysis”. In: *2011 18th International Conference on Systems, Signals and Image Processing*. 2011, pp. 1–5 (cit. on p. 4).

[58] J.S. Gravenstein et al. *Capnography, 2nd Edition*. Cambridge, UK: Cambridge University Press, 2011. DOI: `10.1017/CBO9780511933837` (cit. on pp. 4, 5).

[59] Bhavani Shankar Kodali. *Capnography, 11th Edition*. 2021. URL: `https://web.archive.org/web/20210928154254/https://www.capnography.com/` (visited on 09/28/2021) (cit. on p. 4).

[60] Mark S Siobal. “Monitoring Exhaled Carbon Dioxide”. In: *Respiratory Care* 61.10 (2016), pp. 1397–1416. ISSN: 0020-1324. DOI: `10.4187/respcare.04919`. eprint: `http://rc.rcjournal.com/content/61/10/1397.full.pdf`. URL: `http://rc.rcjournal.com/content/61/10/1397` (cit. on p. 5).

[61] Brit Long, Alex Koyfman, and Michael A. Vivirito. “Capnography in the Emergency Department: A Review of Uses, Waveforms, and Limitations”. In: *The Journal of Emergency Medicine* 53.6 (Dec. 2017), pp. 829–842. ISSN: 0736-4679. URL: `http://www.sciencedirect.com/science/article/pii/S0736467917307321` (cit. on p. 5).

[62] Alessandro Amaddeo and Brigitte Fauroux. “Oxygen and Carbon Dioxide Monitoring During Sleep”. In: *Paediatric Respiratory Reviews* 20 (Sept. 2016), pp. 42–44. ISSN: 1526-0542. URL: `http://www.sciencedirect.com/science/article/pii/S1526054215001487` (cit. on p. 5).

[63] Ori Hochwald et al. “Continuous Noninvasive Carbon Dioxide Monitoring in Neonates: From Theory to Standard of Care”. In: *Pediatrics* 144.1 (2019). ISSN: 0031-4005. DOI: `10.1542/peds.2018-3640`. eprint: `https://pediatrics.aappublications.org/content/144/1/e20183640.full.pdf`. URL: `https://pediatrics.aappublications.org/content/144/1/e20183640` (cit. on p. 5).

[64] M. B. Jaffe. “Mainstream or Sidestream Capnography?” In: *Respironics White Paper*. 2002 (cit. on p. 5).

[65] Linda S. Barter. “Capnography”. In: *Advanced Monitoring and Procedures for Small Animal Emergency and Critical Care*. John Wiley & Sons, Ltd, 2012. Chap. 26, pp. 340–348. ISBN: 9781118997246. DOI: `https://doi.org/10.1002/9781118997246.ch26`. eprint: `https://onlinelibrary.wiley.com/doi/pdf/10.1002/9781118997246.ch26`. URL: `https://onlinelibrary.wiley.com/doi/abs/10.1002/9781118997246.ch26` (cit. on p. 5).

[66] A. L. Balogh et al. “Capnogram Slope and Ventilation Dead Space Parameters: Comparison of Mainstream and Sidestream Techniques”. In: *British Journal of Anaesthesia* 117.1 (July 2016), pp. 109–117. ISSN: 0007-0912. DOI: `10.1093/bja/aew127`. URL: `https://doi.org/10.1093/bja/aew127` (cit. on p. 5).

[67] Keiji Nakatani et al. “Utility of Colorimetric End-Tidal Carbon Dioxide Detector for Monitoring During Prehospital Cardiopulmonary Resuscitation”. In: *The American Journal of Emergency Medicine* 17.2 (Mar. 1999), pp. 203–206. ISSN: 0735-6757. URL: `https://www.sciencedirect.com/science/article/pii/S0735675799900621` (cit. on p. 5).

[68] Arnaud Mari et al. “Transcutaneous PCO2 Monitoring in Critically Ill Patients: Update and Perspectives”. In: *Journal of thoracic disease* 11.Suppl 11 (July 2019), S1558–S1567. ISSN: 2072-1439. URL: `https://pubmed.ncbi.nlm.nih.gov/31388461` (cit. on pp. 5, 6, 58, 85).

[69] Aaron Conway et al. “Accuracy and Precision of Transcutaneous Carbon Dioxide Monitoring: A Systematic Review and Meta-Analysis”. In: *Thorax* 74 (Sept. 2018), pp. 157–163. DOI: `10.1136/thoraxjnl-2017-211466` (cit. on pp. 5, 46, 74, 75, 87, 146, 156, 174).

[70] Fabrice Vallée et al. “Variations of Cutaneous Capnometry and Perfusion Index During a Heating Challenge is Early Impaired in Septic Shock and Related to Prognostic in Non-Septic Shock”. In: *Shock* 51.5 (2019). ISSN: 1073-2322. URL: `https://journals.lww.com/shockjournal/Fulltext/2019/05000/Variations_of_Cutaneous_Capnometry_and_Perfusion.7.aspx` (cit. on pp. 5, 6).

[71] S. Fanconi, A. Tschupp, and L. Molinari. “Long-Term Transcutaneous Monitoring of Oxygen Tension and Carbon Dioxide at 42°C in Critically Ill Neonates: Improved Performance of the tcpo2 Monitor With Topical Metabolic Inhibition”. In: *European Journal of Pediatrics* 155.12 (1996), pp. 1043–1046. ISSN: 1432-1076. DOI: `10.1007/BF02532528` (cit. on p. 5).

[72] Ruben D Restrepo et al. “AARC Clinical Practice Guideline: Transcutaneous Monitoring of Carbon Dioxide and Oxygen: 2012”. In: *Respiratory Care* 57.11 (2012), pp. 1955–1962. ISSN: 0020-1324. DOI: `10.4187/respcare.02011`. eprint: `http://rc.rcjournal.com/content/57/11/1955.full.pdf`. URL: `http://rc.rcjournal.com/content/57/11/1955` (cit. on pp. 6, 57).

[73] Fabrice Vallée et al. “Cutaneous Ear Lobe PCO2 at 37C To Evaluate Microperfusion in Patients With Septic Shock”. In: *CHEST* 138.5 (Nov. 2010), pp. 1062–1070. ISSN: 0012-3692. DOI: `10.1378/chest.09-2690`. URL: `https://doi.org/10.1378/chest.09-2690` (cit. on p. 6).

[74] Adam Steventon et al. “Effect of Telehealth on Use of Secondary Care and Mortality: Findings From the Whole System Demonstrator Cluster Randomised Trial”. In: *BMJ* 344 (2012). DOI: `10.1136/bmj.e3874`. eprint: `https://www.bmj.com/content/344/bmj.e3874.full.pdf`. URL: `https://www.bmj.com/content/344/bmj.e3874` (cit. on pp. 6, 46).

[75] Clemens Kruse et al. “Telemonitoring to Manage Chronic Obstructive Pulmonary Disease: Systematic Literature Review”. In: *JMIR Med Inform* 7.1 (Mar. 2019), e11496. ISSN: 2291-9694. DOI: `10.2196/11496`. URL: `https://doi.org/10.2196/11496` (cit. on pp. 6, 46).

[76] Ji Eun Yun et al. “Comparative Effectiveness of Telemonitoring Versus Usual Care for Heart Failure: A Systematic Review and Meta-analysis”. In: *Journal of Cardiac Failure* 24.1 (Jan. 2018), pp. 19–28. ISSN: 1071-9164. URL: `https://www.sciencedirect.com/science/article/pii/S1071916417312113` (cit. on pp. 6, 46).

[77] Salem Garfan et al. “Telehealth Utilization During the Covid-19 Pandemic: A Systematic Review”. In: *Computers in Biology and Medicine* 138 (Nov. 2021), p. 104878. ISSN: 0010-4825. URL: `https://www.sciencedirect.com/science/article/pii/S0010482521006727` (cit. on pp. 6, 46).

[78] Jessilyn Dunn, Ryan Runge, and Michael Snyder. “Wearables and the Medical Revolution”. In: *Personalized Medicine* 15.5 (2018), pp. 429–448. DOI: `10.2217/pme-2018-0044`. eprint: `https://doi.org/10.2217/pme-2018-0044`. URL: `https://doi.org/10.2217/pme-2018-0044` (cit. on pp. 6, 46).

[79] Ali K. Yetisen et al. “Wearables in Medicine”. In: *Advanced Materials* 30.33 (2018), p. 1706910. DOI: `https://doi.org/10.1002/adma.201706910`. eprint: `https://onlinelibrary.wiley.com/doi/pdf/10.1002/adma.201706910`. URL: `https://onlinelibrary.wiley.com/doi/abs/10.1002/adma.201706910` (cit. on pp. 6, 46).

[80] Michael Chung, Giuseppino Fortunato, and Norbert Radacsi. “Wearable Flexible Sweat Sensors for Healthcare Monitoring: a Review”. In: *Journal of the Royal Society, Interface* 16.159 (Oct. 2019), pp. 20190217–20190217. ISSN: 1742-5662. DOI: `10.1098/rsif.2019.0217`. URL: `https://doi.org/10.1098/rsif.2019.0217` (cit. on pp. 6, 46).

[81] Lilas Dagher et al. “Wearables in Cardiology: Here to Stay”. In: *Heart Rhythm* 17.5 (May 2020), pp. 889–895. ISSN: 1547-5271. DOI: `10.1016/j.hrthm.2020.02.023`. URL: `https://doi.org/10.1016/j.hrthm.2020.02.023` (cit. on pp. 6, 46).

[82] John W. Severinghaus and Poul B. Astrup. “History of Blood Gas Analysis. III. Carbon Dioxide Tension”. In: *Journal of Clinical Monitoring* 2.1 (Jan. 1986), pp. 60–73. ISSN: 1573-2614. DOI: `10.1007/BF01619178`. URL: `https://doi.org/10.1007/BF01619178` (cit. on pp. 6, 69, 74, 85).

[83] J.W. Severinghaus and P.B. Astrup. “History of Blood Gas Analysis. VI. Oximetry”. In: *Journal of Clinical Monitoring* 2 (1986). severinghausreview1986. DOI: `10.1007/BF02851177` (cit. on pp. 6, 16).

[84] Sophie E. Huttmann, Wolfram Windisch, and Jan H. Storre. “Techniques for the Measurement and Monitoring of Carbon Dioxide in the Blood”. In: *Annals of the American Thoracic Society* 11.4 (2014), pp. 645–652. DOI: `10.1513/AnnalsATS.201311-387FR`. eprint: `https://doi.org/10.1513/AnnalsATS.201311-387FR`. URL: `https://doi.org/10.1513/AnnalsATS.201311-387FR` (cit. on p. 6).

[85] Scott Prahl. *Tabulated Molar Extinction Coefficient for Hemoglobin in Water.* 1998. URL: `http://web.archive.org/web/20190501180121/https://omlc.org/spectra/hemoglobin/summary.html` (visited on 05/01/2019) (cit. on pp. 6, 16, 17, 30, 171, 172).

[86] Emmanuel Dervieux et al. “Measuring Hemoglobin Spectra: Searching for Carbamino-Hemoglobin”. In: *Journal of Biomedical Optics* 25.10 (Oct. 2020), pp. 1–15. DOI: `10.1117/1.JBO.25.10.105001` (cit. on pp. 6, 17, 21, 30, 153, 154).

[87] Emmanuel Dervieux et al. “Skin Temperature Influence on Transcutaneous Carbon Dioxide (CO_2) Conductivity and Skin Blood Flow in Healthy Human Subjects at the Arm and Wrist”. In: *Frontiers in Physiology* 14 (2023). ISSN: 1664-042X. DOI: `10.3389/fphys.2023.1293752` (cit. on pp. 7, 42, 45, 63, 153, 154).

[88] Emmanuel Dervieux, Michaël Théron, and Wilfried Uhring. “Carbon Dioxide Sensing—Biomedical Applications to Human Subjects”. In: *Sensors* 22.1 (2022). ISSN: 1424-8220. DOI: `10.3390/s22010188` (cit. on pp. 7, 42, 69, 153, 154, 156).

[89] I. Klimant et al. “Dual Lifetime Referencing (DLR) — A New Scheme for Converting Fluorescence Intensity into a Frequency-Domain or Time-Domain Information”. In: *New Trends in Fluorescence Spectroscopy: Applications to Chemical and Life Sciences.* Berlin, Heidelberg: Springer Berlin Heidelberg, 2001, pp. 257–274. ISBN: 978-3-642-56853-4. DOI: `10.1007/978-3-642-56853-4\_13` (cit. on pp. 7, 76, 77, 98, 99, 103, 155).

[90] Emmanuel Dervieux et al. “On the Accuracy of Phase Extraction from a Known-Frequency Noisy Sinusoidal Signal”. In: *APSIPA Transactions on Signal and Information Processing* 13.1 (2024). DOI: `10.1561/116.20240042` (cit. on pp. 7, 69, 103, 153, 155).

[91] Emmanuel Dervieux and Wilfried Uhring. “Dual Lifetime Referencing for Accurate CO2 Sensing: An Experimental in vitro Validation”. In: *2024 22nd IEEE Interregional NEWCAS Conference (NEWCAS).* 2024 22nd IEEE Interregional NEWCAS Conference (NEWCAS). 2024, pp. 253–257. DOI: `10.1109/NewCAS58973.2024.10666315` (cit. on pp. 7, 121, 123, 144, 153, 155, 157).

[92] Laurence R. Fitzgerald. “Cutaneous Respiration in Man”. In: *Physiological Reviews* 37.3 (1957). PMID: 13465317, pp. 325–336. DOI: `10.1152/physrev.1957.37.3.325`. eprint: `https://doi.org/10.1152/physrev.1957.37.3.325`. URL: `https://doi.org/10.1152/physrev.1957.37.3.325` (cit. on pp. 9, 46, 67).

[93] N. J. Evans and N. Rutter. “Percutaneous Respiration in the Newborn Infant”. In: *The Journal of Pediatrics* 108.2 (1986), pp. 282–286. ISSN: 0022-3476 (cit. on p. 9).

[94] M.G. Levitzky. *Pulmonary Physiology.* Lange medical book. McGraw-Hill, 2003. ISBN: 9780071387651. URL: `https://books.google.fr/books?id=9d5qAAAAMAAJ` (cit. on pp. 10, 11, 13).

[95] William Henry and Joseph Banks. "III. Experiments on the Quantity of Gases Absorbed by Water, at Different Temperatures, and Under Different Pressures". In: *Philosophical Transactions of the Royal Society of London* 93 (1803), pp. 29–274. DOI: `10.1098/rstl.1803.0004`. eprint: `https://royalsocietypublishing.org/doi/pdf/10.1098/rstl.1803.0004`. URL: `https://royalsocietypublishing.org/doi/abs/10.1098/rstl.1803.0004` (cit. on p. 10).

[96] William V. Wojciechowski. *Respiratory Care Sciences: An Integrated Approach.* Delmar Cengage Learning, 2014. ISBN: 1133594778 (cit. on p. 10).

[97] G. Malatesha et al. "Comparison of Arterial and Venous pH, Bicarbonate, PCO2 and PO2 in Initial Emergency Department Assessment". In: *Emergency medicine journal : EMJ* 24 (Sept. 2007), pp. 569–571. DOI: `10.1136/emj.2007.046979` (cit. on p. 10).

[98] E Antonini and M Brunori. "Hemoglobin". In: *Annual Review of Biochemistry* 39 (1970), pp. 977–1042. ISSN: 1545-4509. DOI: `10.1146/annurev.bi.39.070170.004553` (cit. on pp. 10, 39).

[99] John Toffaletti and Willem G. Zijlstra. "Misconceptions in Reporting Oxygen Saturation". In: *Anesthesia & Analgesia* 105.6 (2007). ISSN: 0003-2999. DOI: `10.1213/01.ane.0000278741.29274.e1` (cit. on p. 11).

[100] Tatiana Souza do Nascimento. "Methemoglobinemia: From Diagnosis to Treatment". In: *Rev. Bras. Anestesiol. vol.58 no.6 Campinas* 58 (2008). methdiag (cit. on p. 11).

[101] Neil B. Hampson. "Carboxyhemoglobin: a Primer for Clinicians". In: *Journal of the Undersea and Hyperbaric Medical Society* 45.2 (2018), pp. 165–171. ISSN: 1066-2936 (cit. on p. 11).

[102] J. W. Severinghaus. "Blood Gas Calculator." In: *Journal of Applied Physiology* 21.3 (1966), pp. 1108–1116. ISSN: 8750-7587. DOI: `10.1152/jappl.1966.21.3.1108` (cit. on p. 11).

[103] Donald D. Van Slyke et al. "The Estimation of Plasma Protein Concentration From Plasma Specific Gravity". In: *Journal of Biological Chemistry* 183.1 (1950), pp. 331–347. ISSN: 0021-9258 (cit. on p. 12).

[104] J. Ditzel and J. Kampmann. "Whole-Blood Viscosity, Hematocrit and Plasma Protein in Normal Subjects at Different Ages". In: *Acta Physiologica Scandinavica* 81.2 (1971), pp. 264–268. ISSN: 0001-6772. DOI: `10.1111/j.1748-1716.1971.tb04899.x` (cit. on p. 12).

[105] U.S. Department of Health and Human Services. *Hematological and Iron Related Analytes: Reference Data for Persons Aged 1 Year and Older, United States, 1988-94.* DHHS publication. Centers for Disease Control and Prevention, National Center for Health Statistics, 2005. ISBN: 9780840605979 (cit. on pp. 12, 38).

[106] L.H.J. Van Kampen. "Estimation of Free and Hemoglobin-Bound CO2". PhD thesis. Katholieke Universiteit Nijmegen, 1972 (cit. on p. 12).

[107] G. Gros, H. S. Rollema, and R. E. Forster. "The Carbamate Equilibrium of alpha- and epsilon-Amino Groups of Human Hemoglobin at 37°C". In: *Journal of Biological Chemistry* 256.11 (1981), pp. 5471–5480. ISSN: 0021-9258 (cit. on p. 12).

[108] Lynsay I. Blake and Martin J. Cann. "Carbon Dioxide and the Carbamate Post-Translational Modification". In: *Frontiers in Molecular Biosciences* 9 (2022). ISSN: 2296-889X (cit. on pp. 12, 15).

[109] Robert A. Klocke. "Carbon dioxide transport". In: *Handbook of Physiology. The Respiratory System. Gas Exchange.* American Physiological Society, 1987. ISBN: 0683030396. DOI: `10.1002/cphy.cp030410` (cit. on p. 12).

[110] M. Perrella et al. "Identification of the High and Low Affinity CO2-Binding Sites of Human Haemoglobin". In: *Nature* 256.5520 (1975), pp. 759–761. ISSN: 1476-4687. DOI: `10.1038/256759a0` (cit. on pp. 12, 15).

[111] A.Baird Hastings and Julius Sendroy. "The Effect of Variation in Ionic Strength on the Apparent First and Second Dissociation Constants of Carbonic Acid". In: *Journal of Biological Chemistry* 65.2 (1925), pp. 445–455. ISSN: 0021-9258 (cit. on p. 13).

[112] Duncan A. MacInnes and Donald Belcher. “The Thermodynamic Ionization Constants of Carbonic Acid”. In: *Journal of the American Chemical Society* 55.7 (1933), pp. 2630–2646. DOI: `10.1021/ja01334a003`. eprint: `https://doi.org/10.1021/ja01334a003`. URL: `https://doi.org/10.1021/ja01334a003` (cit. on pp. 13, 76, 91).

[113] Arthur A. Messier. “First Apparent Dissociation Constant of Carbonic Acid, pK1’, of Plasma and Erythrocytes”. In: *Respiration Physiology* 24.1 (1975), pp. 51–68. ISSN: 0034-5687 (cit. on p. 13).

[114] Anne Waugh and Allison Grant. *Ross and Wilson Anatomy and Physiology in Health and Illness*. Elsevier, 2014. ISBN: 9780702053252 (cit. on p. 13).

[115] D Kummerow et al. “Variations of Intracellular pH in Human Erythrocytes via K+ (Na+) / H+ Exchange Under Low Ionic Strength Conditions”. In: *The Journal of membrane biology* 176 (Sept. 2000), pp. 207–216. DOI: `10.1007/s00232001089` (cit. on pp. 13, 29).

[116] F. B. Jensen. “Red Blood Cell pH, the Bohr Effect, and Other Oxygenation-Linked Phenomena in Blood O2 and CO2 Transport”. In: *Acta Physiologica Scandinavica* 182.3 (2004), pp. 215–227. DOI: `10.1111/j.1365-201X.2004.01361.x`. eprint: `https://onlinelibrary.wiley.com/doi/pdf/10.1111/j.1365-201X.2004.01361.x`. URL: `https://onlinelibrary.wiley.com/doi/abs/10.1111/j.1365-201X.2004.01361.x` (cit. on pp. 13, 29).

[117] H. D. Meen, P. H. Holter, and H. E. Refsum. “Changes in 2,3-Diphosphoglycerate (2,3-DPG) After Exercise”. In: *European Journal of Applied Physiology and Occupational Physiology* 46.2 (1981), pp. 177–184. ISSN: 1439-6327. DOI: `10.1007/BF00428869` (cit. on p. 13).

[118] O. Siggaard-Andersen. *The Acid-base Status of the Blood*. Scandinavian University books. Williams & Wilkins, 1974. ISBN: 9788716015679 (cit. on p. 14).

[119] P.A. Stewart. *How to Understand Acid-base: A Quantitative Acid-base Primer for Biology and Medicine*. Elsevier, 1981. ISBN: 9780444004062 (cit. on p. 14).

[120] Stephen Edward Rees et al. “Mathematical Modelling of the Acid-Base Chemistry and Oxygenation of Blood: a Mass Balance, Mass Action Approach Including Plasma and Red Blood Cells”. In: *European Journal of Applied Physiology* 108.3 (Feb. 2010), pp. 483–494. ISSN: 1439-6327. DOI: `10.1007/s00421-009-1244-x` (cit. on p. 14).

[121] David P. O’Neill and Peter A. Robbins. “A Mechanistic Physicochemical Model of Carbon Dioxide Transport in Blood”. In: *Journal of Applied Physiology* 122.2 (2017), pp. 283–295. ISSN: 8750-7587. DOI: `10.1152/japplphysiol.00318.2016` (cit. on pp. 14, 15).

[122] Filip Ježek and Jiří Kofránek. “Modern and Traditional Approaches Combined Into an Effective Gray-Box Mathematical Model of Full-Blood Acid-Base”. In: *Theoretical Biology and Medical Modelling* 15.1 (2018), p. 14. ISSN: 1742-4682. DOI: `10.1186/s12976-018-0086-9` (cit. on pp. 14, 15).

[123] H.W. Davenport. *The ABC of Acid-Base Chemistry: The Elements of Physiological Blood-Gas Chemistry for Medical Students and Physicians*. Biology - Medicine / Chicago. University of Chicago Press, 1974. ISBN: 9780226137032 (cit. on p. 14).

[124] Masaji Mochizuki, Hiroshi Tazawa, and Masakazu Tamura. “Mathematical Formulation of CO2 Dissociation Curve and Buffer Line of Human Blood at Rest”. In: *The Japanese journal of physiology* 32.2 (1982), pp. 231–244 (cit. on p. 14).

[125] Hiroshi Tazawa et al. “Quantitative Analyses of the CO2 Dissociation Curve of Oxygenated Blood and the Haldane Effect in Human Blood”. In: *The Japanese Journal of Physiology* 33.4 (1983), pp. 601–618 (cit. on p. 14).

[126] JA Loeppky, UC Luft, and ER Fletcher. “Quantitative Description of Whole Blood CO2 Dissociation Curve and Haldane Effect”. In: *Respiration physiology* 51.2 (1983), pp. 167–181 (cit. on p. 14).

[127] C. Bauer and E. Schröder. “Carbamino Compounds of Haemoglobin in Human Adult and Foetal Blood”. In: *The Journal of Physiology* 227.2 (1972), pp. 457–471. DOI: `10.1113/jphysiol.1972.sp010042`. eprint: `https://physoc.onlinelibrary.wiley.com/doi/pdf/10.1113/jphysiol.1972.sp010042`. URL: `https://physoc.onlinelibrary.wiley.com/doi/abs/10.1113/jphysiol.1972.sp010042` (cit. on p. 15).

[128] G. Gros, R. E. Forster, and L. Lin. “The Carbamate Reaction of Glycylglycine, Plasma, and Tissue Extracts Evaluated by a pH Stopped Flow Apparatus.” In: *Journal of Biological Chemistry* 251.14 (1976), pp. 4398–4407. ISSN: 0021-9258 (cit. on p. 15).

[129] Chr. Bohr, K. Hasselbalch, and August Krogh. “Ueber einen in biologischer Beziehung wichtigen Einfluss, den die Kohlensäurespannung des Blutes auf dessen Sauerstoffbindung übt”. In: *Acta Physiologica* 16 (1904) (cit. on p. 15).

[130] Johanne Christiansen, C.G. Douglas, and J.S. Haldane. “The Absorption and Dissociation of Carbon Dioxide by Human Blood”. In: *The Journal of Physiology* 48 (1914) (cit. on p. 15).

[131] Heimo Mairbäurl and Roy E. Weber. “Oxygen Transport by Hemoglobin”. In: Comprehensive Physiology. 2012, pp. 1463–1489. ISBN: 9780470650714. DOI: `10.1002/cphy.c080113` (cit. on p. 15).

[132] Willem Gerrit Zijlstra, Anneke Buursma, and Onno Willem van Assendelft. *Visible and Near Infrared Absorption Spectra of Human and Animal Haemoglobin: Determination and Application.* VSP, 2000 (cit. on pp. 16, 17, 21, 24, 28–30, 165).

[133] Carlo Fracassati. “An experiment of Signior Fracassati, Upon Blood Grown Cold”. In: *Philosophical Transactions of the Royal Society of London* 2.27 (1667), pp. 492–492. DOI: `10.1098/rstl.1666.0034` (cit. on p. 15).

[134] John Mayow. *Medico-Physical Works; Being a Translation of Tractatus Quinque Medico-Physici.* Alembic club reprints, no. 17. The Alembic Club, 1674. DOI: `10.5962/bhl.title.28895` (cit. on p. 15).

[135] Johannis Friderici Engelhart. “Commentatio de Vera Materiæ Sanguini Purpureum Colorem Impertientis Natura”. In: *Edinb Med Surg J* 27.90 (1827), pp. 95–102 (cit. on p. 15).

[136] O. W. van Assendelft. *Spectrophotometry of Haemoglobin Derivatives.* English. Summary in Spanish. Assen : Van Gorcum, 1970. ISBN: 902320560X (cit. on pp. 15–17, 28–31, 165).

[137] H. S. Newcomer. “Absorption Spectra of Acid Hematin, Oxyhemoglobin, and Carbon Monoxide Hemoglobin. A New Hemoglobinometer”. In: *Journal of Biological Chemistry* 37.3 (1919), pp. 465–496. ISSN: 0021-9258. DOI: `10.1016/S0021-9258(18)87408-7` (cit. on p. 17).

[138] A. E. Sidwell et al. “The Salf Effect on the Hemoglobin-Oxygen Equilibrium”. In: *Journal of Biological Chemistry* 123.1 (1938), pp. 335–350. ISSN: 0021-9258. DOI: `10.1016/S0021-9258(18)74182-3` (cit. on p. 17).

[139] B. L. Horecker. “The Absorption Spectra of Hemoglobin and its Derivatives in the Visible and Near Infra-Red Regions”. In: *Journal of Biological Chemistry* 148.1 (1943), pp. 173–183. eprint: `http://www.jbc.org/content/148/1/173.full.pdf+html`. URL: `http://www.jbc.org/content/148/1/173.short` (cit. on pp. 17, 28, 29).

[140] Robert B. Barlow and Michael L. Polanyi. “Absorption Measurements for Oxygenated and Reduced Hemoglobin in the Range 0.6—1.88 Microns”. In: *Clinical Chemistry* 8.1 (1962), pp. 67–71. ISSN: 0009-9147. eprint: `http://clinchem.aaccjnls.org/content/8/1/67.full.pdf`. URL: `http://clinchem.aaccjnls.org/content/8/1/67` (cit. on pp. 17, 28, 29).

[141] Yoshiki Sugita, Masako Nagai, and Yoshimasa Yoneyama. “Circular Dichroism of Hemoglobin in Relation to the Structure Surrounding the Heme”. In: *Journal of Biological Chemistry* 246.2 (1971), pp. 383–388. ISSN: 0021-9258. DOI: `10.1016/S0021-9258(18)62502-5` (cit. on p. 17).

[142] P. Dijkhuizen et al. “Sulfhaemoglobin. Absorption Spectrum, Millimolar Extinction Coefficient at $\lambda = 620$ nm, and Interference With the Determination of Haemiglobin and of Haemiglobincyanide”. In: *Clinica Chimica Acta* 78.3 (1977), pp. 479–487. ISSN: 0009-8981. DOI: `10.1016/0009-8981(77)90081-X` (cit. on p. 17).

[143] Michael R. Waterman. “Spectral Characterization of Human Hemoglobin and its Derivatives”. In: *Methods in Enzymology.* Vol. 52. Biomembranes - Part C: Biological Oxidations. Academic Press, 1978, pp. 456–463. DOI: `10.1016/S0076-6879(78)52050-8` (cit. on p. 17).

[144] G. A. Mook et al. “Spectrophotometric Determination of Oxygen Saturation of Blood Independent of the Presence of Indocyanine Green”. In: *Cardiovascular research* 13 (May 1979), pp. 233–237. DOI: `10.1093/cvr/13.4.233` (cit. on pp. 17, 28, 29).

[145] E.J. van Kampen and W.G. Zijlstra. "Spectrophotometry of Hemoglobin and Hemoglobin Derivatives". In: *Advances in Clinical Chemistry, Volume 23*. Ed. by A.L. Latner and Morton K. Schwartz. Elsevier, 1983, pp. 199–257. DOI: `https://doi.org/10.1016/S0065-2423(08)60401-1`. URL: `http://www.sciencedirect.com/science/article/pii/S0065242308604011` (cit. on pp. 16, 17).

[146] Susan Wray et al. "Characterization of the Near Infrared Absorption Spectra of Cytochrome aa3 and Haemoglobin for the Non-Invasive Monitoring of Cerebral Oxygenation". In: *Biochimica et Biophysica Acta (BBA) - Bioenergetics* 933.1 (1988), pp. 184–192. ISSN: 0005-2728. DOI: `https://doi.org/10.1016/0005-2728(88)90069-2`. URL: `http://www.sciencedirect.com/science/article/pii/0005272888900692` (cit. on pp. 17, 28, 29).

[147] Y. Mendelson and J. C. Kent. "Variations in Optical Absorption Spectra of Adult and Fetal Haemoglobins and its Effect on Pulse Oximetry". In: *IEEE Transactions on Biomedical Engineering* 36.8 (Aug. 1989), pp. 844–848. ISSN: 0018-9294. DOI: `10.1109/10.30810` (cit. on pp. 17, 28, 29).

[148] Mark Cope. "The Application of Near Infrared Spectroscopy to Non-Invasive Monitoring of Cerebral Oxygenation in the Newborn Infant". PhD thesis. University of London, Apr. 1991 (cit. on pp. 17, 28, 29).

[149] W.G. Zijlstra and W.P. Meeuwsenvanderroest. "Absorption Spectra of Human, Fetal and Adult Oxyhemoglobin, De-Oxyhemoglobin, Carboxyhemoglobin, and Methemoglobin". In: *Clinical Chemistry* 37 (1991), pp. 1633–1638. ISSN: 0009-9147 (cit. on pp. 17, 28, 29).

[150] J. Todd Kuenstner and Karl H. Norris. "Spectrophotometry of Human Hemoglobin in the near Infrared Region From 1000 to 2500 nm". In: *Journal of Near Infrared Spectroscopy* 2.2 (1994), pp. 59–65. ISSN: 0967-0335. DOI: `10.1255/jnirs.32` (cit. on p. 17).

[151] Deborah A. Grosenbaugh, James O. Alben, and William W. Muir. "Absorbance Spectra of Inter-Species Hemoglobins in the Visible and Near Infrared Regions". In: *Journal of Veterinary Emergency and Critical Care* 7.1 (1997), pp. 36–42. ISSN: 1479-3261. DOI: `10.1111/j.1476-4431.1997.tb00042.x` (cit. on p. 17).

[152] Moritz Friebel et al. "Determination of Optical Properties of Human Blood in the Spectral Range 250 to 1100 nm Using Monte Carlo Simulations with Hematocrit-Dependent Effective Scattering Phase Functions". In: *Journal of Biomedical Optics* 11.3 (2006), p. 034021. DOI: `10.1117/1.2203659` (cit. on p. 17).

[153] Christina Kolyva et al. "Systematic Investigation of Changes in Oxidized Cerebral Cytochrome C Oxidase Concentration During Frontal Lobe Activation in Healthy Adults". In: *Biomedical optics express* 3 (Oct. 2012), pp. 2550–2566. DOI: `10.1364/BOE.3.002550` (cit. on pp. 17, 30).

[154] Lynnette M. Neufeld et al. "Hemoglobin Concentration and Anemia Diagnosis in Venous and Capillary Blood: Biological Basis and Policy Implications". In: *Annals of the New York Academy of Sciences* 1450.1 (2019), pp. 172–189. ISSN: 0077-8923. DOI: `10.1111/nyas.14139` (cit. on p. 16).

[155] Katsuyuki Miyasaka et al. "Tribute to Dr. Takuo Aoyagi, Inventor of Pulse Oximetry". In: *Journal of Anesthesia* 35.5 (2021), pp. 671–709. ISSN: 1438-8359. DOI: `10.1007/s00540-021-02967-z` (cit. on p. 16).

[156] John W. Severinghaus and Yoshiyuki Honda. "History of Blood Gas Analysis. VII. Pulse Oximetry". In: *Journal of Clinical Monitoring* 3.2 (1987), pp. 135–138. ISSN: 1573-2614. DOI: `10.1007/BF00858362` (cit. on p. 16).

[157] Katja Urpalainen. "Development of a Fractional Multi-Wavelength Pulse Oximetry Algorithm". MA thesis. Aalto University, 2011 (cit. on pp. 17, 20, 21, 31).

[158] Steven L Jacques. "Optical Properties of Biological Tissues: A Review". In: *Physics in Medicine and Biology* 58.11 (May 2013), R37–R61. DOI: `10.1088/0031-9155/58/11/r37`. URL: `https://doi.org/10.1088/0031-9155/58/11/r37` (cit. on pp. 17, 20, 90).

[159] Camille Vazquez-Jaccaud, Gonzalo Paez, and Marija Strojnik. "Wavelength Selection Method with Standard Deviation: Application to Pulse Oximetry". In: *Annals of Biomedical Engineering* 39.7 (2011), pp. 1994–2009. ISSN: 1573-9686. DOI: `10.1007/s10439-011-0304-7` (cit. on pp. 19, 20).

[160] Hakan Tapar et al. "The Effect of Patient Positions on Perfusion Index". In: *BMC Anesthesiology* 18.1 (2018), p. 111. ISSN: 1471-2253. DOI: `10.1186/s12871-018-0571-z` (cit. on p. 20).

[161] Katharina J. Fodor et al. "The Perfusion Index as a Noninvasive Method for Continuous Monitoring of Peripheral Perfusion: A Baseline Study to Assess the Perfusion Index in Healthy Adult Volunteers". In: *Journal of Plastic, Reconstructive & Aesthetic Surgery* 75.6 (2022), pp. 2001–2018. ISSN: 1748-6815. DOI: `10.1016/j.bjps.2022.02.031` (cit. on p. 20).

[162] J. rathgeber et al. "Influence of Different Types of Recovery Positions on Perfusion Indices of the Forearm". In: *Resuscitation* 32.1 (1996), pp. 13–17. ISSN: 0300-9572. DOI: `10.1016/0300-9572(96)00952-5` (cit. on p. 20).

[163] P. Sivaprasath, Raja Mookka Gounder, and B. Mythili. "Prediction of Shock by Peripheral Perfusion Index". In: *The Indian Journal of Pediatrics* 86.10 (2019), pp. 903–908. ISSN: 0973-7693. DOI: `10.1007/s12098-019-02993-6` (cit. on p. 20).

[164] S. Chatterjee, J. P. Phillips, and P. A. Kyriacou. "Investigating Optical Path in Reflectance Pulse Oximetry Using a Multilayer Monte Carlo Model". In: *Clinical and Preclinical Optical Diagnostics*. Ed. by J. Brown. Vol. 10411. SPIE Proceedings. Munich: Optica Publishing Group, 2017, p. 1041106. DOI: `10.1117/12.2281612` (cit. on p. 20).

[165] Subhasri Chatterjee et al. "Investigating Optical Path and Differential Pathlength Factor in Reflectance Photoplethysmography for the Assessment of Perfusion". In: *Journal of Biomedical Optics* 23.7 (2018), p. 075005. DOI: `10.1117/1.JBO.23.7.075005` (cit. on p. 20).

[166] S. Chatterjee and P. A. Kyriacou. "Monte Carlo Model for Reflectance Pulse Oximetry Using Pulsatile Monolayer Perfused Skin Tissue". In: *Journal of Physics: Conference Series* 1151.1 (2019), p. 012005. ISSN: 1742-6596. DOI: `10.1088/1742-6596/1151/1/012005` (cit. on p. 20).

[167] Subhasri Chatterjee, Karthik Budidha, and Panayiotis A. Kyriacou. "Investigating the Origin of Photoplethysmography Using a Multiwavelength Monte Carlo Model". In: *Physiological Measurement* 41.8 (2020), p. 084001. ISSN: 0967-3334. DOI: `10.1088/1361-6579/aba008` (cit. on p. 20).

[168] Dale Nordenberg, Ray Yip, and Nancy J. Binkin. "The Effect of Cigarette Smoking on Hemoglobin Levels and Anemia Screening". In: *JAMA* 264.12 (1990), pp. 1556–1559. ISSN: 0098-7484. DOI: `10.1001/jama.1990.03450120068031` (cit. on p. 20).

[169] Rachel Ash-Bernal, Robert Wise, and Scott M. Wright. "Acquired Methemoglobinemia: A Retrospective Series of 138 Cases at 2 Teaching Hospitals". In: *Medicine* 83.5 (2004) (cit. on p. 20).

[170] Nathalia R. S. Remigio, Ligia C. A. Cardoso, and Tulio C. L. Lins. "Comparative Analysis of Methemoglobin, Oxygen Saturation and Hematological Parameters in Smokers and Non-Smokers: An Observational Analytical Cross-Sectional Study". In: *Brazilian Journal of Health and Biomedical Sciences* 20.2 (2022), pp. 144–150 (cit. on p. 20).

[171] Scott N. Beall and S. S. Moorthy. "Jaundice, Oximetry, and Spurious Hemoglobin Desaturation". In: *Anesthesia & Analgesia* 68.6 (1989). ISSN: 0003-2999 (cit. on p. 20).

[172] Francis Veyckemans and Philippe L. Baele. "More About Jaundice and Oximetry". In: *Anesthesia & Analgesia* 70.3 (1990). ISSN: 0003-2999 (cit. on p. 20).

[173] Martina C. Meinke et al. "Optical Properties of Platelets and Blood Plasma and Their Influence on the Optical Behavior of Whole Blood in the Visible to Near Infrared Wavelength Range". In: *Journal of Biomedical Optics* 12.1 (2007), pp. 1–9. DOI: `10.1117/1.2435177`. URL: `https://doi.org/10.1117/1.2435177` (cit. on pp. 20, 29).

[174] Nienke Bosschaart et al. "A Literature Review and Novel Theoretical Approach on the Optical Properties of Whole Blood". In: *Lasers in Medical Science* 29.2 (Mar. 2014), pp. 453–479. ISSN: 1435-604X. DOI: `10.1007/s10103-013-1446-7`. URL: `https://doi.org/10.1007/s10103-013-1446-7` (cit. on pp. 20, 162).

[175] J.G. Webster. *Design of Pulse Oximeters*. Series in Medical Physics and Biomedical Engineering. CRC Press, 1997. ISBN: 9781420050790 (cit. on pp. 20, 21).

[176] J. M. Schmitt. "Simple Photon Diffusion Analysis of the Effects of Multiple Scattering on Pulse Oximetry". In: *IEEE Transactions on Biomedical Engineering* 38.12 (1991), pp. 1194–1203. ISSN: 1558-2531. DOI: `10.1109/10.137285` (cit. on p. 20).

[177] P. D. Mannheimer, M. E. Fein, and J. R. Casciani. "Physio-optical Considerations in the Design of Fetal Pulse Oximetry Sensors". In: *European Journal of Obstetrics & Gynecology and Reproductive Biology* 72.1, Supplement 1 (1997), S9–S19. ISSN: 0301-2115. DOI: `10.1016/S0301-2115(97)02713-9` (cit. on p. 20).

[178] Nils J. Nilsson. "Oximetry". In: *Physiological Reviews* 40.1 (1960). PMID: 14427276, pp. 1–26. DOI: `10.1152/physrev.1960.40.1.1`. eprint: `https://doi.org/10.1152/physrev.1960.40.1.1`. URL: `https://doi.org/10.1152/physrev.1960.40.1.1` (cit. on p. 20).

[179] G.A. Mook, O.W. [van Assexdelft], and W.G. Zijlstra. "Wavelength Dependency of the Spectrophotometric Determination of Blood Oxygen Saturation". In: *Clinica Chimica Acta* 26.1 (1969), pp. 170–173. ISSN: 0009-8981. DOI: `https://doi.org/10.1016/0009-8981(69)90304-0`. URL: `http://www.sciencedirect.com/science/article/pii/0009898169903040` (cit. on pp. 20, 31).

[180] Damianos Damianou. "The Wavelength Dependence of the Photoplethysmogram and its Implication to Pulse Oximetry". PhD thesis. University of Nottingham, 1995 (cit. on p. 20).

[181] Wei Li, Ling Lin, and Gang Li. "Wavelength Selection Method Based on Test Analysis of Variance: Application to Oximetry". In: *Analytical Methods* 6.4 (2014), pp. 1082–1089. ISSN: 1759-9660. DOI: `10.1039/C3AY41601A` (cit. on p. 20).

[182] Michael W. Wukitsch et al. "Pulse oximetry: Analysis of Theory, Technology, and Practice". In: *Journal of Clinical Monitoring* 4 (Jan. 1987), pp. 290–301. DOI: `10.1007/BF01617328` (cit. on pp. 20, 21).

[183] A. C. Ralston, R. K. Webb, and W. B. Runciman. "Potential Errors in Pulse Oximetry III: Effects of Interference, Dyes, Dyshaemoglobins and Other Pigments". In: *Anaesthesia* 46.4 (1991), pp. 291–295. ISSN: 0003-2409. DOI: `10.1111/j.1365-2044.1991.tb11501.x` (cit. on pp. 20, 21).

[184] Jacques A. Brunelle et al. "Simultaneous Measurement of Total Hemoglobin and its Derivatives in Blood Using CO-Oximeters: Analytical Principles; Their Application in Selecting Analytical Wavelengths and Reference Methods; A Comparison of the Results of the Choices Made". In: *Scandinavian journal of clinical and laboratory investigation. Supplementum* 224 (Feb. 1996), pp. 47–69. DOI: `10.3109/00365519609088624` (cit. on pp. 20, 31).

[185] Bernd Manzke et al. "Multiwavelength Pulse Oximetry in the Measurement of Hemoglobin Fractions". In: vol. 2676. Proc.SPIE. 1996, pp. 332–340. DOI: `10.1117/12.238813` (cit. on p. 20).

[186] Hironori Suzaki et al. "Noninvasive Measurement of Total Hemoglobin and Hemoglobin Derivatives Using Multiwavelength Pulse spectrophotometry -In vitro study with a mock circulatory system". In: *2006 International Conference of the IEEE Engineering in Medicine and Biology Society.* 2006, pp. 799–802. DOI: `10.1109/IEMBS.2006.260273` (cit. on p. 20).

[187] Chunhu Shi et al. "The Accuracy of Pulse Oximetry in Measuring Oxygen Saturation by Levels of Skin Pigmentation: a Systematic Review and Meta-Analysis". In: *BMC Medicine* 20.1 (2022), p. 267. ISSN: 1741-7015. DOI: `10.1186/s12916-022-02452-8` (cit. on p. 21).

[188] Raghda Al-Halawani et al. "A Review of the Effect of Skin Pigmentation on Pulse Oximeter Accuracy". In: *Physiological Measurement* 44.5 (2023), 05TR01. ISSN: 0967-3334. DOI: `10.1088/1361-6579/acd51a` (cit. on p. 21).

[189] Mark S. Scheller M.D., Richard J. Unger M.D., and Michael J. Kelner M.D. "Effects of Intravenously Administered Dyes on Pulse Oximetry Readings". In: *Anesthesiology* 65.5 (1986), pp. 550–551 (cit. on p. 21).

[190] Yihang Jiang et al. "Investigating the Accuracy of Blood Oxygen Saturation Measurements in Common Consumer Smartwatches". In: *PLOS Digital Health* 2.7 (2023), e0000296. DOI: `10.1371/journal.pdig.0000296` (cit. on p. 21).

[191] Khalida Azudin et al. *The Principles of Hearable Photoplethysmography Analysis and Applications in Physiological Monitoring–A Review.* 2023. DOI: `10.3390/s23146484` (cit. on p. 21).

[192] Assim Boukhayma et al. “Ring-Embedded Micro-Power mm-Sized Optical Sensor for Accurate Heart Beat Monitoring”. In: *IEEE Access* 9 (2021), pp. 127217–127225. DOI: `10.1109/ACCESS.2021.3111956` (cit. on p. 21).

[193] Hendrana Tjahjadi et al. “A Review of Non-Invasive Monitoring of Blood Glucose Levels Based on Photoplethysmography Signals Using Artificial Intelligence”. In: *2022 International Conference on Advanced Computer Science and Information Systems (ICACSIS)*. 2022, pp. 111–116. DOI: `10.1109/ICACSIS56558.2022.9923513` (cit. on p. 21).

[194] Nikolaos Manetas-Stavrakakis et al. *Accuracy of Artificial Intelligence-Based Technologies for the Diagnosis of Atrial Fibrillation: A Systematic Review and Meta-Analysis.* 2023. DOI: `10.3390/jcm12206576` (cit. on p. 21).

[195] C. El-Hajj and P. A. Kyriacou. “A Review of Machine Learning Techniques in Photoplethysmography for the Non-Invasive Cuff-Less Measurement of Blood Pressure”. In: *Biomedical Signal Processing and Control* 58 (2020), p. 101870. ISSN: 1746-8094 (cit. on p. 21).

[196] Hooseok Lee et al. “Adaptive Scheduling of Acceleration and Gyroscope for Motion Artifact Cancelation in Photoplethysmography”. In: *Computer Methods and Programs in Biomedicine* 226 (2022), p. 107126. ISSN: 0169-2607 (cit. on p. 21).

[197] P.A. Kyriacou and J. Allen. *Photoplethysmography: Technology, Signal Analysis and Applications.* Elsevier Science, 2021. ISBN: 9780128235256 (cit. on p. 21).

[198] Peter H. Charlton et al. “The 2023 Wearable Photoplethysmography Roadmap”. In: *Physiological Measurement* 44.11 (2023), p. 111001. ISSN: 0967-3334. DOI: `10.1088/1361-6579/acead2` (cit. on p. 21).

[199] Alvin C. Rencher. *Methods of Multivariate Analysis, Second Edition.* John Wiley and Sons, 2002. ISBN: 9780471418894 (cit. on p. 23).

[200] Karim Bendjelid et al. “Transcutaneous pCO2 Monitoring in Critically Ill Adults: Clinical Evaluation of a New Sensor”. In: *Critical care medicine* 33 (Oct. 2005), pp. 2203–2206. DOI: `10.1097/01.CCM.0000181734.26070.26` (cit. on pp. 25, 57, 174).

[201] Ali Hadi. “Identifying Multiple Outliers in Multivariate Data”. In: *Journal of the Royal Statistical Society. Series B (Methodological)* 54 (Jan. 1992). DOI: `10.2307/2345856` (cit. on pp. 25, 166).

[202] Herman Aguinis, Ryan K. Gottfredson, and Harry Joo. “Best-Practice Recommendations for Defining, Identifying, and Handling Outliers”. In: *Organizational Research Methods* 16.2 (2013), pp. 270–301. DOI: `10.1177/1094428112470848`. eprint: `https://doi.org/10.1177/1094428112470848`. URL: `https://doi.org/10.1177/1094428112470848` (cit. on pp. 25, 166).

[203] Elzbieta Mieczkowska, Robert Koncki, and Lukasz Tymecki. “Hemoglobin Determination With Paired Emitter Detector Diode”. In: *Analytical and bioanalytical chemistry* 399 (Nov. 2010), pp. 3293–3297. DOI: `10.1007/s00216-010-4358-4` (cit. on pp. 28, 29).

[204] David L. Drabkin and J. Harold Austin. “Spectrophotometric Studies: V. A Technique for the Analysis of Undiluted Blood and Concentrated Hemoglobin Solutions”. In: *Journal of Biological Chemistry* 112.1 (1935), pp. 105–115. eprint: `http://www.jbc.org/content/112/1/105.full.pdf+html`. URL: `http://www.jbc.org/content/112/1/105.short` (cit. on pp. 28, 29).

[205] Keith A. Dalziel and John P. O’brien. “Side Reactions in the Deoxygenation of Dilute Oxyhaemoglobin Solutions by Sodium Dithionite.” In: *The Biochemical journal* 67 1 (1957), pp. 119–124 (cit. on pp. 28, 29).

[206] Francisco E. Robles, Shwetadwip Chowdhury, and Adam Wax. “Assessing Hemoglobin Concentration Using Spectroscopic Optical Coherence Tomography for Feasibility of Tissue Diagnostics”. In: *Biomed. Opt. Express* 1.1 (Aug. 2010), pp. 310–317. DOI: `10.1364/BOE.1.000310`. URL: `http://www.osapublishing.org/boe/abstract.cfm?URI=boe-1-1-310` (cit. on pp. 28, 29).

[207] Sigma-Aldrich. *Human haemoglobin lyophilised powder, H7379, product page.* 2020. URL: `https://web.archive.org/web/20200304080809/https://www.sigmaaldrich.com/catalog/product/sigma/h7379?lang=en&region=US` (visited on 03/04/2020) (cit. on p. 29).

[208] G. Schubart et al. “Spektralphotometrie von hämolysiertem Blut im nahen Infrarot”. In: *Pflüger’s Archiv für die gesamte Physiologie des Menschen und der Tiere* 265.1 (Aug. 1957), pp. 1–10. ISSN: 1432-2013. DOI: 10.1007/BF00364516. URL: https://doi.org/10.1007/BF00364516 (cit. on p. 29).

[209] P. D. Wimberley et al. “Effect of pH on the Absorption Spectrum of Human Oxyhemoglobin: A Potential Source of Error in Measuring the Oxygen Saturation of Hemoglobin.” In: *Clinical Chemistry* 34.4 (1988), pp. 750–754. ISSN: 0009-9147. eprint: http://clinchem.aaccjnls.org/content/34/4/750.full.pdf. URL: http://clinchem.aaccjnls.org/content/34/4/750 (cit. on p. 29).

[210] W.G. Zijlstra and A. Buursma. “Spectrophotometry of Hemoglobin: Absorption Spectra of Bovine Oxyhemoglobin, Deoxyhemoglobin, Carboxyhemoglobin, and Methemoglobin”. In: *Comparative Biochemistry and Physiology Part B: Biochemistry and Molecular Biology* 118.4 (1997), pp. 743–749. ISSN: 1096-4959. DOI: https://doi.org/10.1016/S0305-0491(97)00230-7. URL: http://www.sciencedirect.com/science/article/pii/S0305049197002307 (cit. on p. 29).

[211] Roy Weber. “Use of Ionic and Zwitterionic (Tris/BisTris and HEPES) Buffers in Studies on Hemoglobin Function”. In: *Journal of applied physiology (Bethesda, Md. : 1985)* 72 (May 1992), pp. 1611–1615. DOI: 10.1152/jappl.1992.72.4.1611 (cit. on p. 29).

[212] Paul M. Mcllvaine MS, William C. Nelson PhD, and Donald Bartlett Jr. MD. “Temporal Variation of Carboxyhemoglobin Concentrations”. In: *Archives of Environmental Health: An International Journal* 19.1 (1969). PMID: 4182162, pp. 83–91. DOI: 10.1080/00039896.1969.10666808. eprint: https://doi.org/10.1080/00039896.1969.10666808. URL: https://doi.org/10.1080/00039896.1969.10666808 (cit. on p. 30).

[213] N. J. Wald et al. “Carbon Monoxide in Breath in Relation to Smoking and Carboxyhaemoglobin Levels.” In: *Thorax* 36.5 (1981), pp. 366–369. ISSN: 0040-6376. DOI: 10.1136/thx.36.5.366. eprint: https://thorax.bmj.com/content/36/5/366.full.pdf. URL: https://thorax.bmj.com/content/36/5/366 (cit. on p. 30).

[214] Harvey Kravitz et al. “Methemoglobin Values in Premature and Mature Infants and Children”. In: *A.M.A. Journal of Diseases of Children* 91.1 (Jan. 1956), pp. 1–5. ISSN: 0096-6916. DOI: 10.1001/archpedi.1956.02060020003001. eprint: https://jamanetwork.com/journals/jamapediatrics/articlepdf/498276/archpedi_91_1_001.pdf. URL: https://doi.org/10.1001/archpedi.1956.02060020003001 (cit. on p. 30).

[215] E.J. van Kampen and W.G. Zijlstra. “Determination of Hemoglobin and Its Derivatives”. In: *Advances in Clinical Chemistry, Volume 8*. Ed. by Harry Sobotka and C.P. Stewart. Elsevier, 1966, pp. 141–187. DOI: https://doi.org/10.1016/S0065-2423(08)60414-X. URL: http://www.sciencedirect.com/science/article/pii/S006524230860414X (cit. on p. 30).

[216] Brian C. Wilson, W. Patrick Jeeves, and Diane M. Lowe. “In Vivo and Post Mortem Measurements of the Attenuation Spectra of Light in Mammalian Tissues”. In: *Photochemistry and Photobiology* 42.2 (1985), pp. 153–162. DOI: 10.1111/j.1751-1097.1985.tb01554.x. eprint: https://onlinelibrary.wiley.com/doi/pdf/10.1111/j.1751-1097.1985.tb01554.x. URL: https://onlinelibrary.wiley.com/doi/abs/10.1111/j.1751-1097.1985.tb01554.x (cit. on pp. 31, 37).

[217] C.A.S Melo et al. “Characterization of Light Penetration in Rat Tissues”. In: *Journal of clinical laser medicine and surgery* 19 (Sept. 2001), pp. 175–179. DOI: 10.1089/104454701316918925 (cit. on pp. 31, 37).

[218] Caerwyn Ash et al. “Effect of Wavelength and Beam Width on Penetration in Light-Tissue Interaction Using Computational Methods”. In: *Lasers in Medical Science* 32 (Sept. 2017). DOI: 10.1007/s10103-017-2317-4 (cit. on pp. 31, 37).

[219] Bernhard J. Brendel and Tim Nielsen. “Selection of Optimal Wavelengths for Spectral Reconstruction in Diffuse Optical Tomography”. In: *Journal of Biomedical Optics* 14.3 (2009), pp. 1–10. DOI: 10.1117/1.3156823. URL: https://doi.org/10.1117/1.3156823 (cit. on p. 31).

[220] Bernard Valeur and Mario N Berberan Santos. *Molecular Fluorescence: Principles and Applications, Second Edition*. May 2012. ISBN: 978-3-527-32837-6. DOI: 10.1002/9783527650002 (cit. on pp. 32, 124, 125, 132).

[221] Michiya Itoh et al. “Tryptophan Fluorescence of Human Hemoglobin. I. Significant Change of Fluorescence Intensity and Lifetimes in the T − R Transition”. In: *Biochemical and Biophysical Research Communications* 100.3 (1981), pp. 1259–1265. ISSN: 0006-291X. DOI: `https://doi.org/10.1016/0006-291X(81)91959-8`. URL: `http://www.sciencedirect.com/science/article/pii/0006291X81919598` (cit. on pp. 32, 33, 36).

[222] Rhoda Elison Hirsch. “Hemoglobin Fluorescence”. In: *Hemoglobin Disorders: Molecular Methods and Protocols.* Ed. by Ronald L. Nagel. Totowa, NJ: Humana Press, 2003, pp. 133–154. ISBN: 978-1-59259-373-6. DOI: `10.1385/1-59259-373-9:133`. URL: `https://doi.org/10.1385/1-59259-373-9:133` (cit. on p. 32).

[223] F. W. J. Teale and G. Weber. “Ultraviolet Fluorescence of the Aromatic Amino Acids”. In: *Biochemical Journal* 65.3 (Mar. 1957), pp. 476–482. ISSN: 0006-2936. DOI: `10.1042/bj0650476`. eprint: `https://portlandpress.com/biochemj/article-pdf/65/3/476/805651/bj0650476.pdf`. URL: `https://doi.org/10.1042/bj0650476` (cit. on p. 32).

[224] Mitchel Weissbluth. *Hemoglobin : Cooperativity and Electronic Properties.* English. Includes index. London : Chapman and Hall ; New York : Springer Verlag, 1974. ISBN: 0387065822 (cit. on p. 32).

[225] M. F. Perutz. “The Hemoglobin Molecule”. In: *Scientific American* 211.5 (1964), pp. 64–79 (cit. on pp. 32, 39).

[226] Rhoda Elison Hirsch. “[12] Front-Face Fluorescence Spectroscopy of Hemoglobins”. In: *Methods in Enzymology.* Vol. 232. Hemoglobins Part C: Biophysical Methods. Academic Press, 1994, pp. 231–246. DOI: `10.1016/0076-6879(94)32050-0` (cit. on pp. 32, 169).

[227] Rhoda Elison Hirsch, R. Suzanne Zukin, and Ronald L. Nagel. “Intrinsic Fluorescence Emission of Intact Oxy Hemoglobins”. English (US). In: *Biochemical and Biophysical Research Communications* 93.2 (Mar. 1980), pp. 432–439. ISSN: 0006-291X. DOI: `10.1016/0006-291X(80)91096-7` (cit. on pp. 32, 33, 38, 172).

[228] R E Hirsch and R L Nagel. “Conformational Studies of Hemoglobins Using Intrinsic Fluorescence Measurements.” In: *Journal of Biological Chemistry* 256.3 (1981), pp. 1080–1083. eprint: `http://www.jbc.org/content/256/3/1080.full.pdf+html`. URL: `http://www.jbc.org/content/256/3/1080.abstract` (cit. on pp. 32, 33, 36).

[229] Yue Yuan et al. “New Look at Hemoglobin Allostery”. In: *Chemical Reviews* 115.4 (2015), pp. 1702–1724. ISSN: 0009-2665. DOI: `10.1021/cr500495x` (cit. on pp. 33, 39).

[230] Bernard Alpert, David M. Jameson, and Gregorio Weber. “Tryptophan Emission From Human Hemoglobin and its Isolated Subunits”. In: *Photochemistry and Photobiology* 31.1 (1980), pp. 1–4. DOI: `10.1111/j.1751-1097.1980.tb03674.x`. eprint: `https://onlinelibrary.wiley.com/doi/pdf/10.1111/j.1751-1097.1980.tb03674.x`. URL: `https://onlinelibrary.wiley.com/doi/abs/10.1111/j.1751-1097.1980.tb03674.x` (cit. on pp. 33, 38).

[231] Wei Zheng et al. “Two-Photon Excited Hemoglobin Fluorescence”. In: *Biomed. Opt. Express* 2.1 (Jan. 2011), pp. 71–79. URL: `http://www.osapublishing.org/boe/abstract.cfm?URI=boe-2-1-71` (cit. on p. 33).

[232] Qiqi Sun et al. “Mechanism of Two-Photon Excited Hemoglobin Fluorescence Emission”. In: *Journal of Biomedical Optics* 20.10 (2015), pp. 1–6. DOI: `10.1117/1.JBO.20.10.105014`. URL: `https://doi.org/10.1117/1.JBO.20.10.105014` (cit. on p. 33).

[233] Sava Sakadžić et al. “Multi-photon Microscopy With a Low-Cost and Highly Efficient Cr:LiCAF Laser”. In: *Optics Express* 16.25 (Dec. 2008), pp. 20848–20863. DOI: `10.1364/OE.16.020848` (cit. on p. 33).

[234] Evan P. Perillo et al. “Deep In Vivo Two-Photon Microscopy With a Low Cost Custom Built Mode-Locked 1060 nm Fiber Laser”. In: *Biomedical Optics Express* 7.2 (Feb. 2016), pp. 324–334. DOI: `10.1364/BOE.7.000324` (cit. on p. 33).

[235] Georges A Wagnieres, Willem M Star, and Brian C Wilson. “In Vivo Fluorescence Spectroscopy and Imaging for Oncological Applications”. In: *Photochemistry and Photobiology* 68.5 (1998), pp. 603–632. ISSN: 1751-1097. DOI: `10.1111/j.1751-1097.1998.tb02521.x` (cit. on pp. 36, 38).

[236] Karthik Vishwanath and Nimmi Ramanujam. "Fluorescence Spectroscopy In Vivo". In: *Encyclopedia of Analytical Chemistry.* American Cancer Society, 2011. Chap. Biomedical Spectroscopy. ISBN: 9780470027318. DOI: `10.1002/9780470027318.a0102.pub2`. eprint: `https://onlinelibrary.wiley.com/doi/pdf/10.1002/9780470027318.a0102.pub2`. URL: `https://onlinelibrary.wiley.com/doi/abs/10.1002/9780470027318.a0102.pub2` (cit. on pp. 36, 38).

[237] Nikiforos Kollias, George Zonios, and Georgios Stamatas. "Fluorescence Spectroscopy of Skin". In: *Vibrational Spectroscopy* 28 (Feb. 2002), pp. 17–23. DOI: `10.1016/S0924-2031(01)00142-4` (cit. on pp. 36, 38).

[238] Otto S. Wolfbeis and Marc Leiner. "Mapping of the Total Fluorescence of Human Blood Serum as a New Method for its Characterization". In: *Analytica Chimica Acta* 167 (1985), pp. 203–215. ISSN: 0003-2670. DOI: `https://doi.org/10.1016/S0003-2670(00)84422-0`. URL: `http://www.sciencedirect.com/science/article/pii/S0003267000844220` (cit. on pp. 37, 38).

[239] Shumei Gao et al. "Characteristics of Blood Fluorescence Spectra Using Low-Level, 457.9 nm Excitation From Ar+ Laser". In: *Chin. Opt. Lett.* 2.3 (Mar. 2004), pp. 160–161. URL: `http://col.osa.org/abstract.cfm?URI=col-2-3-160` (cit. on p. 37).

[240] Ilyas Saytashev et al. "Multiphoton Excited Hemoglobin Fluorescence and Third Harmonic Generation for Non-Invasive Microscopy of Stored Blood". In: *Biomed. Opt. Express* 7.9 (Sept. 2016), pp. 3449–3460. DOI: `10.1364/BOE.7.003449`. URL: `http://www.osapublishing.org/boe/abstract.cfm?URI=boe-7-9-3449` (cit. on p. 37).

[241] Yang Yuanlong et al. "Characteristic Autofluorescence for Cancer Diagnosis and its Origin". In: *Lasers in Surgery and Medicine* 7.6 (1987), pp. 528–532. DOI: `10.1002/lsm.1900070617`. eprint: `https://onlinelibrary.wiley.com/doi/pdf/10.1002/lsm.1900070617`. URL: `https://onlinelibrary.wiley.com/doi/abs/10.1002/lsm.1900070617` (cit. on p. 37).

[242] Vadivel Masilamani et al. "Cancer diagnosis by autofluorescence of blood components". In: *Journal of Luminescence* 109 (Sept. 2004), pp. 143–154. DOI: `10.1016/S0022-2313(04)00117-6` (cit. on p. 37).

[243] Dr Manuela Lualdi et al. "Natural Fluorescence Spectroscopy of Human Blood Plasma in the Diagnosis of Colorectal Cancer: Feasibility Study and Preliminary Results". In: *Tumori Journal* 93.6 (2007). PMID: 18338491, pp. 567–571. DOI: `10.1177/030089160709300609`. eprint: `https://doi.org/10.1177/030089160709300609`. URL: `https://doi.org/10.1177/030089160709300609` (cit. on p. 37).

[244] Vadivel Masilamani et al. "Fluorescence Spectra of Blood and Urine for Cervical Cancer Detection". In: *Journal of Biomedical Optics* 17.9 (2012), pp. 1–6. DOI: `10.1117/1.JBO.17.9.098001`. URL: `https://doi.org/10.1117/1.JBO.17.9.098001` (cit. on p. 37).

[245] Wiel A. G. Bruls et al. "Transmission of Human Epidermis and Stratum Corneum as a Function of Thickness in the Ultraviolet and Visible Wavelengths". In: *Photochemistry and Photobiology* 40.4 (1984), pp. 485–494. DOI: `10.1111/j.1751-1097.1984.tb04622.x`. eprint: `https://onlinelibrary.wiley.com/doi/pdf/10.1111/j.1751-1097.1984.tb04622.x`. URL: `https://onlinelibrary.wiley.com/doi/abs/10.1111/j.1751-1097.1984.tb04622.x` (cit. on pp. 37, 38).

[246] Arthur F. Gmitro et al. "Measurement Depth of Laser-Induced Tissue Fluorescence With Application to Laser Angioplasty". In: *Appl. Opt.* 27.9 (May 1988), pp. 1844–1849. DOI: `10.1364/AO.27.001844`. URL: `http://ao.osa.org/abstract.cfm?URI=ao-27-9-1844` (cit. on pp. 37, 38).

[247] Frank Koenig et al. "Autofluorescence Guided Biopsy for the Early Diagnosis of Bladder Carcinoma". In: *The Journal of Urology* 159.6 (1998), pp. 1871–1875. ISSN: 0022-5347. DOI: `https://doi.org/10.1016/S0022-5347(01)63183-5`. URL: `http://www.sciencedirect.com/science/article/pii/S0022534701631835` (cit. on pp. 37, 38).

[248] V. V. Barun et al. "Absorption Spectra and Light Penetration Depth of Normal and Pathologically Altered Human Skin". In: *Journal of Applied Spectroscopy* 74.3 (May 2007), pp. 430–439. ISSN: 1573-8647. DOI: `10.1007/s10812-007-0071-2`. URL: `https://doi.org/10.1007/s10812-007-0071-2` (cit. on pp. 37, 38).

[249] Antony R Young. “Chromophores in Human Skin”. In: *Physics in Medicine and Biology* 42.5 (1997), pp. 789–802. DOI: `10.1088/0031-9155/42/5/004`. URL: `https://doi.org/10.1088%2F0031-9155%2F42%2F5%2F004` (cit. on pp. 37, 38).

[250] Yurii P. Sinichkin et al. “In Vivo Fluorescence Spectroscopy of the Human Skin: Experiments and Models”. In: *Journal of Biomedical Optics* 3.2 (1998), pp. 201–211. DOI: `10.1117/1.429876`. URL: `https://doi.org/10.1117/1.429876` (cit. on pp. 37, 38).

[251] Georgios N. Stamatas, Costas J. Balas, and Nikiforos Kollias. “Hyperspectral Image Acquisition and Analysis of Skin”. In: *Spectral Imaging: Instrumentation, Applications, and Analysis II*. Ed. by Richard M. Levenson, Gregory H. Bearman, and Anita Mahadevan-Jansen. Vol. 4959. International Society for Optics and Photonics. SPIE, 2003, pp. 77–82. DOI: `10.1117/12.479491`. URL: `https://doi.org/10.1117/12.479491` (cit. on pp. 37, 38).

[252] Massimo Paoli et al. “Crystal Structure of T State Haemoglobin with Oxygen Bound At All Four Haems”. In: *Journal of Molecular Biology* 256.4 (1996), pp. 775–792 (cit. on p. 39).

[253] Sam-Yong Park et al. “1.25 Å Resolution Crystal Structures of Human Haemoglobin in the Oxy, Deoxy and Carbonmonoxy Forms”. In: *Journal of Molecular Biology* 360.3 (2006), pp. 690–701. ISSN: 0022-2836 (cit. on p. 39).

[254] Mauro Bringas et al. “Tertiary and Quaternary Structural Basis of Oxygen Affinity in Human Hemoglobin as Revealed by Multiscale Simulations”. In: *Scientific Reports* 7.1 (2017), p. 10926. ISSN: 2045-2322. DOI: `10.1038/s41598-017-11259-0` (cit. on p. 39).

[255] A. Arnone, P. H. Rogers, and P. D. Briley. “The Binding of CO2 to Human Deoxyhemoglobin: An X-Ray Study Using Low-Salt Crystals”. In: *Biophysics and Physiology of Carbon Dioxide*. Ed. by Christian Bauer, Gerolf Gros, and Heinz Bartels. Berlin, Heidelberg: Springer Berlin Heidelberg, 1980, pp. 67–74. ISBN: 978-3-642-67572-0 (cit. on p. 39).

[256] R.F. Weiss. “Carbon Dioxide in Water and Seawater: the Solubility of a Non-Ideal Gas”. In: *Marine Chemistry* 2.3 (1974), pp. 203–215. ISSN: 0304-4203. DOI: `https://doi.org/10.1016/0304-4203(74)90015-2`. URL: `http://www.sciencedirect.com/science/article/pii/0304420374900152` (cit. on p. 43).

[257] Charles I. Wright. “The Diffusion of Carbon Dioxide in Tissues”. In: *Journal of General Physiology* 17.5 (May 1934), pp. 657–676. ISSN: 0022-1295. DOI: `10.1085/jgp.17.5.657`. URL: `https://doi.org/10.1085/jgp.17.5.657` (cit. on p. 44).

[258] George Nichols. “Solubility of Carbon Dioxide in Body Fat”. In: *Science* 126.3285 (1957), pp. 1244–1245. DOI: `10.1126/science.126.3285.1244`. eprint: `https://www.science.org/doi/pdf/10.1126/science.126.3285.1244`. URL: `https://www.science.org/doi/abs/10.1126/science.126.3285.1244` (cit. on p. 44).

[259] Robert J Scheuplein. “Permeability Of The Skin: A Review Of Major Concepts And Some New Developments”. In: *Journal of Investigative Dermatology* 67.5, Part 2 (1976), pp. 672–676. ISSN: 0022-202X. DOI: `https://doi.org/10.1111/1523-1747.ep12544513`. URL: `http://www.sciencedirect.com/science/article/pii/S0022202X1544923` (cit. on pp. 44, 58, 64, 85, 160).

[260] C.O. Gill. “The Solubility of Carbon Dioxide in Meat”. In: *Meat Science* 22.1 (1988), pp. 65–71. ISSN: 0309-1740. DOI: `https://doi.org/10.1016/0309-1740(88)90027-7`. URL: `https://www.sciencedirect.com/science/article/pii/0309174088900277` (cit. on p. 44).

[261] Madhubanti Chatterjee et al. “A Rate-Based Transcutaneous CO2 Sensor for Noninvasive Respiration Monitoring”. In: *Physiological measurement* 36 (Apr. 2015), pp. 883–894. DOI: `10.1088/0967-3334/36/5/883` (cit. on pp. 44, 85, 89).

[262] Louis A. Shaw and Anne C. Messer. “CUTANEOUS RESPIRATION IN MAN: I. Factors Affecting the Rate of Carbon Dioxide Elimination and Oxygen Absorption”. In: *American Journal of Physiology-Legacy Content* 95.1 (1930), pp. 107–118. DOI: `10.1152/ajplegacy.1930.95.1.13`. eprint: `https://doi.org/10.1152/ajplegacy.1930.95.1.13`. URL: `https://doi.org/10.1152/ajplegacy.1930.95.1.13` (cit. on pp. 45, 59, 67).

[263] Louis A. Shaw and Anne C. Messer. “CUTANEOUS RESPIRATION IN MAN: II. The Effect of Temperature and of Relative Humidity Upon the Rate of Carbon Dioxide Elimination and Oxygen Absorption”. In: *American Journal of Physiology-Legacy Content* 95.1 (1930), pp. 13–19. DOI: 10.1152/ajplegacy.1930.95.1.13. eprint: https://doi.org/10.1152/ajplegacy.1930.95.1.13. URL: https://doi.org/10.1152/ajplegacy.1930.95.1.13 (cit. on pp. 45, 59, 67, 85).

[264] A. G. R. Whitehouse, W. Hancock, and J. S. Haldane. “The Osmotic Passage of Water and Gases through the Human Skin”. In: *Proceedings of The Royal Society of London. Series B, Containing Papers of A Biological Character (1905-1934)* 111 (Jan. 1932), pp. 412–429. DOI: 10.1098/rspb.1932.0065 (cit. on pp. 45, 59).

[265] Ajándok Eöry. “In-Vivo Skin Respiration (CO2) Measurements in the Acupuncture Loci”. In: *Acupuncture & Electro-Therapeutics Research* 9.4 (1984), pp. 217–223. ISSN: 0360-1293. DOI: 10.3727/036012984816714668. URL: https://www.ingentaconnect.com/content/cog/aetr/1984/00000009/00000004/art00004 (cit. on pp. 46, 59, 62).

[266] A. I. Levshankov et al. “Determination of Local Gas Exchange on the Body Surface by the Method of Mass Spectrometry”. In: *Meditsinskaia tekhnika* 1 (Jan. 1983), pp. 21–26 (cit. on pp. 46, 56, 59, 62, 67, 85).

[267] Peter D. Wimberley et al. “Transcutaneous Carbon Dioxide and Oxygen Tension Measured at Different Temperatures in Healthy Adults.” In: *Clinical Chemistry* 31.10 (1985), pp. 1611–1615. ISSN: 0009-9147. eprint: http://clinchem.aaccjnls.org/content/31/10/1611.full.pdf. URL: http://clinchem.aaccjnls.org/content/31/10/1611 (cit. on pp. 46, 67, 87, 156, 174).

[268] Matthieu Roustit and Jean-Luc Cracowski. “Non-invasive Assessment of Skin Microvascular Function in Humans: An Insight Into Methods”. In: *Microcirculation* 19.1 (2012), pp. 47–64. DOI: https://doi.org/10.1111/j.1549-8719.2011.00129.x. eprint: https://onlinelibrary.wiley.com/doi/pdf/10.1111/j.1549-8719.2011.00129.x. URL: https://onlinelibrary.wiley.com/doi/abs/10.1111/j.1549-8719.2011.00129.x (cit. on pp. 46, 50, 51, 59).

[269] G. Koch. “Comparison of Carbon Dioxide Tension, pH and Standard Bicarbonate in Capillary Blood and in Arterial Blood with Special Respect to Relations in Patients with Impaired Cardiovascular and Pulmonary Function and During Exercise”. In: *Scandinavian Journal of Clinical and Laboratory Investigation* 17.3 (1965), pp. 223–229. DOI: 10.1080/00365516509075339. eprint: https://www.tandfonline.com/doi/pdf/10.1080/00365516509075339. URL: https://www.tandfonline.com/doi/abs/10.1080/00365516509075339 (cit. on p. 46).

[270] Gosta Rooth, Uwe W. Ewald, and F. Caligara. “Transcutaneous PO2 and PCO2 Monitoring at 37 degrees C. Cutaneous PO2 and PCO2.” In: *Advances in experimental medicine and biology* 220 (1987), pp. 23–32 (cit. on pp. 46, 60, 61, 63).

[271] Gary J. Hodges et al. “The Contribution of Sensory Nerves to the Onset Threshold for Cutaneous Vasodilatation During Gradual Local Skin Heating of the Forearm and Leg”. In: *Microvascular Research* 105 (May 2016), pp. 1–6. ISSN: 0026-2862. URL: https://www.sciencedirect.com/science/article/pii/S002628621530042X (cit. on pp. 46, 59, 60).

[272] S. Eletr et al. “Cutaneous Monitoring of Systemic Pco2 on Patients in the Respiratory Intensive Care Unit Being Weaned From the Ventilator”. In: *Acta Anaesthesiologica Scandinavica* 22.s68 (1978), pp. 123–127. DOI: 10.1111/j.1399-6576.1978.tb01406.x. eprint: https://onlinelibrary.wiley.com/doi/pdf/10.1111/j.1399-6576.1978.tb01406.x. URL: https://onlinelibrary.wiley.com/doi/abs/10.1111/j.1399-6576.1978.tb01406.x (cit. on pp. 46, 54, 58, 85).

[273] G.H. Greenspan et al. “Transcutaneous Noninvasive Monitoring of Carbon Dioxide Tension”. In: *Chest.* 80 (Oct. 1981) (cit. on pp. 46, 58, 85).

[274] Jane Hodgkinson and Ralph P Tatam. “Optical Gas Sensing: A Review”. In: *Measurement Science and Technology* 24.1 (Nov. 2012), p. 012004. DOI: 10.1088/0957-0233/24/1/012004. URL: https://doi.org/10.1088%2F0957-0233%2F24%2F1%2F012004 (cit. on pp. 47, 72).

[275] SenTec. *SenTec V-Sign Brochure, RF-007857-bm.* 2016. URL: https://archive.org/details/general-brochure-en-rf-007857-b (visited on 02/27/2023) (cit. on p. 49).

[276] Radiometer. *TCM CombiM, Continuous blood gas monitoring.* ALT. URL: `https://pdfhost.io/v/DaeEjvgEq_radiometer_combim`. 2020. URL: `https://archive.org/details/radiometer_combim` (visited on 02/16/2023) (cit. on p. 49).

[277] Robert F. Bonner and Ralph Nossal. “Principles of Laser-Doppler Flowmetry”. In: *Laser-Doppler Blood Flowmetry.* Ed. by A. P. Shepherd and P. Åke Öberg. Boston, MA: Springer US, 1990, pp. 17–45. ISBN: 978-1-4757-2083-9. DOI: `10.1007/978-1-4757-2083-9_2`. URL: `https://doi.org/10.1007/978-1-4757-2083-9_2` (cit. on p. 50).

[278] Christopher T. Minson. “Thermal Provocation to Evaluate Microvascular Reactivity in Human Skin”. In: *Journal of Applied Physiology* 109.4 (2010). PMID: 20507974, pp. 1239–1246. DOI: `10.1152/japplphysiol.00414.2010`. eprint: `https://doi.org/10.1152/japplphysiol.00414.2010`. URL: `https://doi.org/10.1152/japplphysiol.00414.2010` (cit. on pp. 50, 51, 59, 60).

[279] W Magerl and R D Treede. “Heat-Evoked Vasodilatation in Human Hairy Skin: Axon Reflexes Due to Low-Level Activity of Nociceptive Afferents”. In: *The Journal of Physiology* 497.3 (1996), pp. 837–848. DOI: `https://doi.org/10.1113/jphysiol.1996.sp021814`. eprint: `https://physoc.onlinelibrary.wiley.com/doi/pdf/10.1113/jphysiol.1996.sp021814`. URL: `https://physoc.onlinelibrary.wiley.com/doi/abs/10.1113/jphysiol.1996.sp021814` (cit. on pp. 50, 60).

[280] Andrew T. Del Pozzi, James T. Miller, and Gary J. Hodges. “The Effect of Heating Rate on the Cutaneous Vasomotion Responses of Forearm and Leg Skin in Humans”. In: *Microvascular Research* 105 (May 2016), pp. 77–84. ISSN: 0026-2862. URL: `https://www.sciencedirect.com/science/article/pii/S0026286216300048` (cit. on p. 50).

[281] Jean-Luc Cracowski et al. “Methodological Issues in the Assessment of Skin Microvascular Endothelial Function in Humans”. In: *Trends in Pharmacological Sciences* 27.9 (Sept. 2006), pp. 503–508. ISSN: 0165-6147. DOI: `10.1016/j.tips.2006.07.008`. URL: `https://doi.org/10.1016/j.tips.2006.07.008` (cit. on pp. 50, 51, 59, 60).

[282] Johanna Frantz et al. “Desensitization of Thermal Hyperemia in the Skin is Reproducible”. In: *Microcirculation* 19.1 (2012), pp. 78–85. DOI: `https://doi.org/10.1111/j.1549-8719.2011.00124.x`. eprint: `https://onlinelibrary.wiley.com/doi/pdf/10.1111/j.1549-8719.2011.00124.x`. URL: `https://onlinelibrary.wiley.com/doi/abs/10.1111/j.1549-8719.2011.00124.x` (cit. on pp. 50, 51, 59, 60).

[283] Christopher T. Minson, Latoya T. Berry, and Michael J. Joyner. “Nitric Oxide and Neurally Mediated Regulation of Skin Blood Flow During Local Heating”. In: *Journal of Applied Physiology* 91.4 (2001), pp. 1619–1626. DOI: `10.1152/jappl.2001.91.4.1619`. eprint: `https://doi.org/10.1152/jappl.2001.91.4.1619`. URL: `https://doi.org/10.1152/jappl.2001.91.4.1619` (cit. on pp. 50, 51, 59).

[284] H. Barcroft and O. G. Edholm. “The effect of Temperature on Blood Flow and Deep Temperature in the Human Forearm”. In: *The Journal of Physiology* 102.1 (1943), pp. 5–20. DOI: `10.1113/jphysiol.1943.sp004009`. eprint: `https://physoc.onlinelibrary.wiley.com/doi/pdf/10.1113/jphysiol.1943.sp004009`. URL: `https://physoc.onlinelibrary.wiley.com/doi/abs/10.1113/jphysiol.1943.sp004009` (cit. on pp. 50, 59, 63).

[285] W. F. Taylor et al. “Effect of High Local Temperature on Reflex Cutaneous Vasodilation”. In: *Journal of Applied Physiology* 57.1 (1984). PMID: 6469780, pp. 191–196. DOI: `10.1152/jappl.1984.57.1.191`. eprint: `https://doi.org/10.1152/jappl.1984.57.1.191`. URL: `https://doi.org/10.1152/jappl.1984.57.1.191` (cit. on pp. 50, 59, 60).

[286] D.C. Salter et al. “Skin Mechanics Measured In Vivo Using Torsion: a New and Accurate Model More Sensitive to Age, Sex and Moisturizing Treatment”. In: *International Journal of Cosmetic Science* 15.5 (Oct. 1993), pp. 200–218. ISSN: 0142-5463. DOI: `10.1111/j.1467-2494.1993.tb00075.x`. URL: `https://doi.org/10.1111/j.1467-2494.1993.tb00075.x` (cit. on p. 54).

[287] Manuel Held et al. “Changes in the Biomechanical Properties of Human Skin in Hyperthermic and Hypothermic Ranges”. In: *Wounds* 30.9 (Sept. 2018), pp. 257–262. ISSN: 1943-2704. URL: `https://www.ncbi.nlm.nih.gov/pubmed/30256752` (cit. on p. 54).

[288] M. B. McIlroy, G. Simbruner, and Y. Sonoda. “Transcutaneous Blood Gas Measurements Using a Mass Spectrometer”. In: *Acta Anaesthesiologica Scandinavica* 22.s68 (1978), pp. 128–130. DOI: `10.1111/j.1399-6576.1978.tb01407.x`. eprint: `https://onlinelibrary.wiley.com/doi/pdf/10.1111/j.1399-6576.1978.tb01407.x`. URL: `https://onlinelibrary.wiley.com/doi/abs/10.1111/j.1399-6576.1978.tb01407.x` (cit. on pp. 54, 85).

[289] T. N. Hansen, Y. Sonoda, and M. B. McIlroy. “Transfer of Oxygen, Nitrogen, and Carbon Dioxide through Normal Adult Human Skin”. In: *Journal of Applied Physiology* 49.3 (1980). PMID: 6782048, pp. 438–443. DOI: `10.1152/jappl.1980.49.3.438`. eprint: `https://doi.org/10.1152/jappl.1980.49.3.438`. URL: `https://doi.org/10.1152/jappl.1980.49.3.438` (cit. on pp. 54, 85, 87, 157).

[290] S. V. S. Rithalia, T. H. Clutton-Brock, and J. Tinker. “Characteristics of Transcutaneous Carbon Dioxide Tension Monitors in Normal Adults and Critically Ill Patients”. In: *Intensive Care Medicine* 10.3 (May 1984), pp. 149–153. ISSN: 1432-1238. DOI: `10.1007/BF00265805`. URL: `https://doi.org/10.1007/BF00265805` (cit. on p. 54).

[291] Mranvick. *What is the Influence of Humidity on NDIR* CO_2 *Measurements?* Physics Stack Exchange. 2024. URL: `https://web.archive.org/web/20240919060752/https://physics.stackexchange.com/questions/788798/what-is-the-influence-of-humidity-on-ndir-rm-co-2-measurements/788799#788799` (cit. on p. 55).

[292] Peer Fietzek et al. “In Situ Quality Assessment of a Novel Underwater pCO2 Sensor Based on Membrane Equilibration and NDIR Spectrometry”. In: *Journal of Atmospheric and Oceanic Technology* 31.1 (2014), pp. 181–196. DOI: `10.1175/JTECH-D-13-00083.1`. URL: `https://doi.org/10.1175/JTECH-D-13-00083.1` (cit. on pp. 55, 72).

[293] J. N. Wang et al. “Mid-Infrared Carbon Dioxide Sensor With Wireless and Anti-Condensation Capability for Use in Greenhouses”. In: *Spectroscopy Letters* 51.6 (July 2018), pp. 266–273. ISSN: 0038-7010. DOI: `10.1080/00387010.2018.1468785`. URL: `https://doi.org/10.1080/00387010.2018.1468785` (cit. on pp. 55, 72).

[294] George W. Frame, Walter G. Strauss, and Howard I. Maibach. “Carbon Dioxide Emission of the Human Arm and Hand”. In: *Journal of Investigative Dermatology* 59.2 (Aug. 1972), pp. 155–158. ISSN: 0022-202X. URL: `https://www.sciencedirect.com/science/article/pii/S0022202X15481941` (cit. on pp. 56, 59, 161).

[295] Robert King et al. “The Effect of Occlusion on Carbon Dioxide Emission From Human Skin”. In: *Acta dermato-venereologica* 58(2) (1978), pp. 135–8. URL: `https://api.semanticscholar.org/CorpusID:27418577` (cit. on pp. 56, 161).

[296] J. Faergemann et al. “Skin Occlusion: Effect on Pityrosporum Orbiculare, Skin PCO2, pH, Transepidermal Water Loss, and Water Content”. In: *Archives of Dermatological Research* 275.6 (Nov. 1983), pp. 383–387. ISSN: 1432-069X. DOI: `10.1007/BF00417338` (cit. on pp. 56, 161).

[297] Werner Schulze. “Untersuchungen über die Alkaliempfindlichkeit, das Alkalineutralisationsvermögen und die Kohlensäureabgabe der Haut”. In: *Archiv für Dermatologie und Syphilis* 185.1 (Dec. 1943), pp. 93–161. ISSN: 1432-069X. DOI: `10.1007/BF02714173` (cit. on pp. 56, 59, 62).

[298] B. Adamczyk, A. J. Boerboom, and J. Kistemaker. “A Mass Spectrometer for Continuous Analysis of Gaseous Compounds Excreted by Human Skin”. In: *Journal of Applied Physiology* 21.6 (1966). PMID: 5929324, pp. 1903–1906. DOI: `10.1152/jappl.1966.21.6.1903`. eprint: `https://doi.org/10.1152/jappl.1966.21.6.1903`. URL: `https://doi.org/10.1152/jappl.1966.21.6.1903` (cit. on pp. 56, 59, 85).

[299] Lindsay B. Baker. “Physiology of Sweat Gland Function: The Roles of Sweating and Sweat Composition in Human Health”. In: *Temperature* 6.3 (2019), pp. 211–259. DOI: `10.1080/23328940.2019.1632145`. eprint: `https://doi.org/10.1080/23328940.2019.1632145`. URL: `https://doi.org/10.1080/23328940.2019.1632145` (cit. on pp. 56, 68).

[300] D. Taylor et al. “Characterization of the Microflora of the Human Axilla”. In: *International Journal of Cosmetic Science* 25.3 (June 2003), pp. 137–145. ISSN: 0142-5463. DOI: `10.1046/j.1467-2494.2003.00181.x` (cit. on p. 56).

[301] H. H. Niu et al. “Thermal Symmetry of Skin Temperature: Normative Data of Normal Subjects in Taiwan”. In: *Chinese medical journal* 64.8 (2001), pp. 459–468. ISSN: 0578-1337. URL: `http://europepmc.org/abstract/MED/11720145` (cit. on p. 56).

[302] Märtha Sund-Levander, Christina Forsberg, and Lis Karin Wahren. "Normal Oral, Rectal, Tympanic and Axillary Body Temperature in Adult Men and Women: a Systematic Literature Review". In: *Scandinavian Journal of Caring Sciences* 16.2 (2002), pp. 122–128. ISSN: 0283-9318. DOI: `10.1046/j.1471-6712.2002.00069.x`. URL: `https://doi.org/10.1046/j.1471-6712.2002.00069.x` (cit. on p. 56).

[303] Rasha M. Al-Eidan, Hend Al-Khalifa, and Abdul Malik Al-Salman. "A Review of Wrist-Worn Wearable: Sensors, Models, and Challenges". In: *Journal of Sensors* 2018 (Dec. 2018), p. 5853917. ISSN: 1687-725X. DOI: `10.1155/2018/5853917`. URL: `https://doi.org/10.1155/2018/5853917` (cit. on p. 57).

[304] Stephanie Soon et al. "Wearable Devices for Remote Vital Signs Monitoring in the Outpatient Setting: an Overview of the Field". In: *BMJ Innovations* 6.2 (Apr. 2020), p. 55. DOI: `10.1136/bmjinnov-2019-000354`. URL: `https://doi.org/10.1136/bmjinnov-2019-000354` (cit. on p. 57).

[305] Gloria Cosoli, Susanna Spinsante, and Lorenzo Scalise. "Wrist-Worn and Chest-Strap Wearable Devices: Systematic Review on Accuracy and Metrological Characteristics". In: *Measurement* 159 (July 2020), p. 107789. ISSN: 0263-2241. URL: `https://www.sciencedirect.com/science/article/pii/S0263224120303274` (cit. on p. 57).

[306] Sujin Jang, Youngmee Kim, and Won-Kyung Cho. *A Systematic Review and Meta-Analysis of Telemonitoring Interventions on Severe COPD Exacerbations*. 2021. DOI: `10.3390/ijerph18136757`. URL: `https://doi.org/10.3390/ijerph18136757` (cit. on p. 57).

[307] Patrick Eberhard. "The Design, Use, and Results of Transcutaneous Carbon Dioxide Analysis: Current and Future Directions". In: *Anesthesia & Analgesia* 105.6 (2007). ISSN: 0003-2999. DOI: `10.1213/01.ane.0000278642.16117.f8` (cit. on p. 57).

[308] R. Carter and S.W Banham. "Use of Transcutaneous Oxygen and Carbon Dioxide Tensions for Assessing Indices of Gas Exchange During Exercise Testing". In: *Respiratory Medicine* 94.4 (Apr. 2000), pp. 350–355. ISSN: 0954-6111. DOI: `10.1053/rmed.1999.0714` (cit. on p. 57).

[309] Christian Domingo et al. "Optimal Clinical Time for Reliable Measurement of Transcutaneous CO2 with Ear Probes: Counterbalancing Overshoot and the Vasodilatation Effect". In: *Sensors* 10.1 (2010), pp. 491–500. ISSN: 1424-8220. DOI: `10.3390/s100100491` (cit. on p. 57).

[310] Steven Kesten, Kenneth R. Chapman, and Anthony S. Rebuck. "Response Characteristics of a Dual Transcutaneous Oxygen/Carbon Dioxide Monitoring System". In: *Chest* 99.5 (May 1991), pp. 1211–1215. ISSN: 0012-3692. DOI: `10.1378/chest.99.5.1211` (cit. on p. 57).

[311] Antoine Cuvelier et al. "Limitations of Transcutaneous Carbon Dioxide Measurements for Assessing Long-term Mechanical Ventilation". In: *Chest* 127.5 (May 2005), pp. 1744–1748. ISSN: 0012-3692. DOI: `10.1378/chest.127.5.1744` (cit. on p. 57).

[312] Jakub Rafl et al. "Response Time of Indirectly Accessed Gas Exchange Depends on Measurement Method". In: *Biomedical Engineering* 63.6 (2018), pp. 647–655. DOI: `10.1515/bmt-2017-0070` (cit. on p. 57).

[313] A. Carlton Ernstene and Marie C. Volk. "CUTANEOUS RESPIRATION IN MAN: IV. The Rate of Carbon Dioxide Elimination and Oxygen Absorption in Normal Subjects". In: *The Journal of Clinical Investigation* 11.2 (Mar. 1932), pp. 363–376. DOI: `10.1172/JCI100418`. URL: `https://doi.org/10.1172/JCI100418` (cit. on pp. 59, 62, 85).

[314] F. A. J. Thiele and L. H. J. Van Kempen. "A Micro Method for Measuring the Carbon Dioxide Release by Small Skin Areas". In: *British Journal of Dermatology* 86.5 (1972), pp. 463–471. DOI: `10.1111/j.1365-2133.1972.tb16098.x`. eprint: `https://onlinelibrary.wiley.com/doi/pdf/10.1111/j.1365-2133.1972.tb16098.x`. URL: `https://onlinelibrary.wiley.com/doi/abs/10.1111/j.1365-2133.1972.tb16098.x` (cit. on p. 59).

[315] J. M. Johnson et al. "Laser-Doppler Measurement of Skin Blood Flow: Comparison With Plethysmography". In: *Journal of Applied Physiology* 56.3 (1984). PMID: 6706783, pp. 798–803. DOI: `10.1152/jappl.1984.56.3.798`. eprint: `https://doi.org/10.1152/jappl.1984.56.3.798`. URL: `https://doi.org/10.1152/jappl.1984.56.3.798` (cit. on p. 59).

[316] Jean-Luc Cracowski and Matthieu Roustit. “Current Methods to Assess Human Cutaneous Blood Flow: An Updated Focus on Laser-Based-Techniques”. In: *Microcirculation* 23.5 (2016), pp. 337–344. ISSN: 1073-9688. DOI: `10.1111/micc.12257`. URL: `https://doi.org/10.1111/micc.12257` (cit. on p. 59).

[317] P. C. Johnson. “Autoregulation of Blood Flow.” In: *Circulation Research* 59.5 (1986), pp. 483–495. DOI: `10.1161/01.RES.59.5.483`. URL: `https://doi.org/10.1161/01.RES.59.5.483` (cit. on p. 59).

[318] W.Wayne Lautt. “Resistance or Conductance for Expression of Arterial Vascular Tone”. In: *Microvascular Research* 37.2 (1989), pp. 230–236. ISSN: 0026-2862. URL: `https://www.sciencedirect.com/science/article/pii/002628628990040X` (cit. on p. 59).

[319] Neil Herring and David J Paterson. “Haemodynamics: Flow, Pressure and Resistance”. In: *Levick’s Introduction to Cardiovascular Physiology*. CRC Press, 2018. Chap. 8, pp. 121–147. DOI: `10.1201/9781351107754` (cit. on p. 59).

[320] Dean L. Kellogg, Joan L. Zhao, and Yubo Wu. “Endothelial Nitric Oxide Synthase Control Mechanisms in the Cutaneous Vasculature of Humans in Vivo”. In: *American Journal of Physiology-Heart and Circulatory Physiology* 295.1 (2008). PMID: 18469149, H123–H129. DOI: `10.1152/ajpheart.00082.2008`. eprint: `https://doi.org/10.1152/ajpheart.00082.2008`. URL: `https://doi.org/10.1152/ajpheart.00082.2008` (cit. on pp. 59, 60).

[321] Julien Vionnet et al. “No Major Impact of Skin Aging on the Response of Skin Blood Flow to a Submaximal Local Thermal Stimulus”. In: *Microcirculation* 21.8 (2014), pp. 730–737. DOI: `https://doi.org/10.1111/micc.12154`. eprint: `https://onlinelibrary.wiley.com/doi/pdf/10.1111/micc.12154`. URL: `https://onlinelibrary.wiley.com/doi/abs/10.1111/micc.12154` (cit. on p. 60).

[322] Harvey N. Mayrovitz and Judith A. Leedham. “Laser–Doppler Imaging of Forearm Skin: Perfusion Features and Dependence of the Biological Zero on Heat-Induced Hyperemia”. In: *Microvascular Research* 62.1 (July 2001), pp. 74–78. ISSN: 0026-2862. URL: `https://www.sciencedirect.com/science/article/pii/S0026286201923143` (cit. on p. 60).

[323] Andreas Bircher et al. “Guidelines for Measurement of Cutaneous Blood Flow by Laser Doppler Flowmetry”. In: *Contact Dermatitis* 30.2 (1994), pp. 65–72. DOI: `https://doi.org/10.1111/j.1600-0536.1994.tb00565.x`. eprint: `https://onlinelibrary.wiley.com/doi/pdf/10.1111/j.1600-0536.1994.tb00565.x`. URL: `https://onlinelibrary.wiley.com/doi/abs/10.1111/j.1600-0536.1994.tb00565.x` (cit. on p. 60).

[324] Dan P. Stephens et al. “The Influence of Topical Capsaicin on the Local Thermal Control of Skin Blood Flow in Humans”. In: *American Journal of Physiology-Regulatory, Integrative and Comparative Physiology* 281.3 (Sept. 2001), R894–R901. ISSN: 0363-6119. DOI: `10.1152/ajpregu.2001.281.3.R894`. URL: `https://doi.org/10.1152/ajpregu.2001.281.3.R894` (cit. on p. 60).

[325] Food and Drug Administration. *Cutaneous Carbon Dioxide (PcCO2) and Oxygen (PcO2) Monitors - Class II Special Controls Guidance Document for Industry and FDA*. Tech. rep. U.S. Department Of Healsth and Human Services, 2002 (cit. on pp. 60, 174).

[326] W.T. Ambrosius. *Topics in Biostatistics*. Methods in Molecular Biology. Humana Press, 2007. ISBN: 9781588295316. URL: `https://books.google.fr/books?id=AfnJdwoZ2DEC` (cit. on pp. 60, 61).

[327] S.C. Chow et al. *Sample Size Calculations in Clinical Research*. Chapman & Hall / CRC Biostatistics Series. Taylor & Francis, 2017. ISBN: 9781138740983. URL: `https://books.google.fr/books?id=DkvSAQAACAAJ` (cit. on p. 60).

[328] Mun Jung Ko and Chi-Yeon Lim. “General Considerations for Sample Size Estimation in Animal Study”. In: *Korean journal of anesthesiology* 74.1 (Feb. 2021), pp. 23–29. ISSN: 2005-7563. DOI: `10.4097/kja.20662` (cit. on p. 60).

[329] F. G. Benedict, W. R. Miles, and A. Johnson. “The Temperature of the Human Skin”. In: *Proc Natl Acad Sci U.S.A.* 5.6 (June 1919), pp. 218–222. ISSN: 0027-8424. URL: `https://www.ncbi.nlm.nih.gov/pubmed/16576376` (cit. on p. 63).

[330] Wei-Ping Zhu and Xiang-Rong Xin. “Study on the Distribution Pattern of Skin Temperature in Normal Chinese and Detection of the Depth of Early Burn Wound by Infrared Thermography”. In: *Annals of the New York Academy of Sciences* 888 (Nov. 1999), pp. 300–313. DOI: `10.1111/j.1749-6632.1999.tb07964.x` (cit. on p. 63).

[331] J.A. Sarabia et al. “Circadian Rhythm of Wrist Temperature in Normal-Living Subjects: A Candidate of New Index of the Circadian System”. In: *Physiology and Behavior* 95 (Nov. 2008), pp. 570–580. DOI: `10.1016/j.physbeh.2008.08.005` (cit. on p. 63).

[332] A Blazquez et al. “Wrist Skin Temperature, Motor Activity, and Body Position as Determinants of the Circadian Pattern of Blood Pressure.” In: *Chronobiology international* 29 6 (2012), pp. 747–56 (cit. on p. 63).

[333] Antonio Martinez-Nicolas et al. “Uncovering Different Masking Factors on Wrist Skin Temperature Rhythm in Free-Living Subjects”. In: *PLOS ONE* 8.4 (Apr. 2013), pp. 1–10. DOI: `10.1371/journal.pone.0061142`. URL: `https://doi.org/10.1371/journal.pone.0061142` (cit. on p. 63).

[334] Ehrhardt Proksch, Johanna M. Brandner, and Jens-Michael Jensen. “The Skin: an Indispensable Barrier”. In: *Experimental Dermatology* 17.12 (2008), pp. 1063–1072. DOI: `https://doi.org/10.1111/j.1600-0625.2008.00786.x`. eprint: `https://onlinelibrary.wiley.com/doi/pdf/10.1111/j.1600-0625.2008.00786.x`. URL: `https://onlinelibrary.wiley.com/doi/abs/10.1111/j.1600-0625.2008.00786.x` (cit. on p. 64).

[335] H. Schaefer, A. Zesch, and G. Stüttgen. *Skin Permeability.* Berlin: Springer, 1982. ISBN: 978-3-540-11797-1. DOI: `10.1007/978-3-642-68734-1` (cit. on p. 64).

[336] Trinidad Montero-Vilchez et al. “Skin Barrier Function in Psoriasis and Atopic Dermatitis: Transepidermal Water Loss and Temperature as Useful Tools to Assess Disease Severity”. In: *Journal of Clinical Medicine* 10.2 (2021). ISSN: 2077-0383. DOI: `10.3390/jcm10020359`. URL: `https://www.mdpi.com/2077-0383/10/2/359` (cit. on pp. 64, 65).

[337] Jan Kottner, Andrea Lichterfeld, and Ulrike Blume-Peytavi. “Transepidermal Water Loss in Young and Aged Healthy Humans: a Systematic Review and Meta-Analysis”. In: *Archives of Dermatological Research* 305.4 (May 2013), pp. 315–323. ISSN: 1432-069X. DOI: `10.1007/s00403-012-1313-6`. URL: `https://doi.org/10.1007/s00403-012-1313-6` (cit. on pp. 64–66).

[338] M. Akdeniz et al. “Transepidermal Water Loss in Healthy Adults: a Systematic Review and Meta-Analysis Update”. In: *British Journal of Dermatology* 179.5 (Sept. 2018), pp. 1049–1055 (cit. on pp. 64–66).

[339] V. Rogiers. “EEMCO Guidance for the Assessment of Transepidermal Water Loss in Cosmetic Sciences”. In: *Skin Pharmacology and Physiology* 14.2 (2001), pp. 117–128. ISSN: 1660-5527. DOI: `10.1159/000056341`. URL: `https://doi.org/10.1159/000056341` (cit. on p. 64).

[340] J.W. Fluhr et al. *Bioengineering of the Skin: Water and the Stratum Corneum, 2nd Edition.* Dermatology: Clinical & Basic Science. CRC Press, 2004. ISBN: 9780849314438 (cit. on p. 64).

[341] Katherine Grice, H. Sattar, and Harvey Baker. “The Effect of Ambient Humidity on Transepidermal Water Loss”. In: *Journal of Investigative Dermatology* 58.6 (June 1972), pp. 343–346. ISSN: 0022-202X. URL: `https://www.sciencedirect.com/science/article/pii/S0022202X1548145X` (cit. on p. 64).

[342] Samuel N. Cheuvront et al. “A Simple and Valid Method to Determine Thermoregulatory Sweating Threshold and Sensitivity”. In: *Journal of Applied Physiology* 107.1 (July 2009), pp. 69–75. ISSN: 8750-7587. DOI: `10.1152/japplphysiol.00250.2009`. URL: `https://doi.org/10.1152/japplphysiol.00250.2009` (cit. on p. 64).

[343] Raza Aly et al. “Effect of Prolonged Occlusion on the Microbial Flora, pH, Carbon Dioxide and Transepidermal Water Loss on Human Skin”. In: *Journal of Investigative Dermatology* 71.6 (Dec. 1978), pp. 378–381. ISSN: 0022-202X. URL: `https://www.sciencedirect.com/science/article/pii/S0022202X15454090` (cit. on pp. 64, 65).

[344] Xin Li et al. “Dynamics of Water Transport and Swelling in Human Stratum Corneum”. In: *Chemical Engineering Science* 138 (Dec. 2015), pp. 164–172. ISSN: 0009-2509. URL: `https://www.sciencedirect.com/science/article/pii/S0009250915005497` (cit. on p. 64).

[345] Matthias Schmuth, Kenneth R. Feingold, and Peter M. Elias. “Stress Test of the Skin: The Cutaneous Permeability Barrier Treadmill”. In: *Experimental Dermatology* 29.1 (Jan. 2020), pp. 112–113. ISSN: 0906-6705. DOI: `10.1111/exd.14055`. URL: `https://doi.org/10.1111/exd.14055` (cit. on p. 64).

[346] Vera Rogiers. “Transepidermal Water Loss Measurements in Patch Test Assessment: the Need for Standardisation”. In: *Curr Probl Dermatol* 23 (1995), pp. 152–158 (cit. on pp. 64, 65).

[347] C.G Toby Mathias, Donald M. Wilson, and Howard I. Maibach. “Transepidermal Water Loss as a Function of Skin Surface Temperature”. In: *Journal of Investigative Dermatology* 77.2 (Aug. 1981), pp. 219–220. ISSN: 0022-202X. URL: `https://www.sciencedirect.com/science/article/pii/S0022202X15461640` (cit. on p. 64).

[348] Barbara Cravello and Ada Ferri. “Relationships Between Skin Properties and Environmental Parameters”. In: *Skin Research and Technology* 14.2 (May 2008), pp. 180–186. ISSN: 0909-752X. DOI: `10.1111/j.1600-0846.2007.00275.x`. URL: `https://doi.org/10.1111/j.1600-0846.2007.00275.x` (cit. on p. 64).

[349] Yujin Sunwoo et al. “Physiological and Subjective Responses to Low Relative Humidity”. In: *Journal of Physiological Anthropology* 25.1 (2006), pp. 7–14. DOI: `10.2114/jpa2.25.7`. URL: `https://doi.org/10.2114/jpa2.25.7` (cit. on p. 64).

[350] Nicholas Golda, John Koo, and Howard I. Maibach. “Effects and Uses of Occlusion on Human Skin: An Overview”. In: *Cutaneous and Ocular Toxicology* 24.2 (Jan. 2005), pp. 91–104. ISSN: 1556-9527. DOI: `10.1081/CUS-200059571`. URL: `https://doi.org/10.1081/CUS-200059571` (cit. on p. 65).

[351] Halina Laudanska, Teresa Reduta, and D Szmitkowska. “Evaluation of Skin Barrier Function in Allergic Contact Dermatitis and Atopic Dermatitis Using Method of the Continuous TEWL Measurement.” In: *Roczniki Akademii Medycznej w Bialymstoku* 48 (2003), pp. 123–7 (cit. on p. 65).

[352] Margaret Altemus et al. “Stress-Induced Changes in Skin Barrier Function in Healthy Women”. In: *Journal of Investigative Dermatology* 117.2 (Aug. 2001), pp. 309–317. ISSN: 0022-202X. URL: `https://www.sciencedirect.com/science/article/pii/S0022202X15413296` (cit. on p. 65).

[353] Neelam Muizzuddin et al. “Impact of Stress of Marital Dissolution on Skin Barrier Recovery: Tape Stripping and Measurement of Trans-Epidermal Water Loss (TEWL)”. In: *Skin Research and Technology* 9.1 (Feb. 2003), pp. 34–38. ISSN: 0909-752X. DOI: `10.1034/j.1600-0846.2003.00354.x`. URL: `https://doi.org/10.1034/j.1600-0846.2003.00354.x` (cit. on p. 65).

[354] Hitoshi Masaki et al. “The Simple Measuring Method of Water Evaporation Rate From the Skin Using Anhydrous Cobalt Chloride Paper”. In: *Journal of Society of Cosmetic Chemists of Japan* 20.3 (1986), pp. 206–209. DOI: `10.5107/sccj.20.206`. URL: `https://doi.org/10.5107/sccj.20.206` (cit. on p. 65).

[355] Kathryn A. Zug et al. “Patch-Test Results of the North American Contact Dermatitis Group 2005-2006”. In: *Dermatitis* 20.3 (2009). ISSN: 1710-3568. URL: `https://journals.lww.com/dermatitis/Fulltext/2009/05000/Patch_Test_Results_of_the_North_American_Contact.4.aspx` (cit. on p. 66).

[356] Jacob P. Thyssen. “Cobalt Sensitization and Dermatitis: Considerations for the Clinician”. In: *Dermatitis* 23.5 (2012). ISSN: 1710-3568. URL: `https://journals.lww.com/dermatitis/Fulltext/2012/09000/Cobalt_Sensitization_and_Dermatitis_.4.aspx` (cit. on p. 66).

[357] Richard Wm. Tock. “Permeabilities and Water Vapor Transmission Rates for Commercial Polymer Films”. In: *Advances in Polymer Technology* 3.3 (Sept. 1983), pp. 223–231. ISSN: 0730-6679. DOI: `10.1002/adv.1983.060030304`. URL: `https://doi.org/10.1002/adv.1983.060030304` (cit. on pp. 66, 137).

[358] Andrew Mills, Anne Lepre, and Lorraine Wild. “Breath-by-Breath Measurement of Carbon Dioxide Using a Plastic Film Optical Sensor”. In: *Sensors and Actuators B: Chemical* 39.1 (1997). 3rd European Conference on Optical Chemical Sensors and Biosensors, pp. 419–425. ISSN: 0925-4005. DOI: `https://doi.org/10.1016/S0925-4005(96)02116-8`. URL: `http://www.sciencedirect.com/science/article/pii/S0925400596021168` (cit. on pp. 67, 76, 86, 91, 138).

[359] C. Malins and B. D. MacCraith. “Dye-doped Organically Modified Silica Glass for Fluorescence Based Carbon Dioxide Gas Detection”. In: *Analyst* 123 (11 1998), pp. 2373–2376. DOI: `10.1039/A805803B`. URL: `http://dx.doi.org/10.1039/A805803B` (cit. on pp. 67, 76, 94, 132, 138, 158).

[360] Hiroyo Segawa et al. “Sensitivity of Fiber-Optic Carbon Dioxide Sensors Utilizing Indicator Dye”. In: *Sensors and Actuators B-chemical* 94 (Oct. 2003), pp. 276–281. DOI: `10.1016/S0925-4005(03)00372-1` (cit. on pp. 67, 76, 94, 95, 138).

[361] Xudong Ge, Yordan Kostov, and Govind Rao. “High-Stability Non-Invasive Autoclavable Naked Optical CO2 Sensor”. In: *Biosensors and Bioelectronics* 18.7 (2003), pp. 857–865. ISSN: 0956-5663. DOI: `https://doi.org/10.1016/S0956-5663(02)00159-8`. URL: `http://www.sciencedirect.com/science/article/pii/S0956566302001598` (cit. on pp. 67, 76, 95, 131, 138, 147).

[362] J. F. Fernández-Sánchez et al. “Optical CO2-Sensing Layers for Clinical Application Based on pH-Sensitive Indicators Incorporated into Nanoscopic Metal-Oxide Supports”. In: *Sensors and Actuators B: Chemical* 128.1 (Dec. 2007), pp. 145–153. ISSN: 0925-4005. URL: `http://www.sciencedirect.com/science/article/pii/S0925400507003978` (cit. on pp. 67, 76, 138, 158).

[363] Royce N. Dansby-Sparks et al. “Fluorescent-Dye-Doped Sol-Gel Sensor for Highly Sensitive Carbon Dioxide Gas Detection below Atmospheric Concentrations”. In: *Analytical Chemistry* 82.2 (2010). PMID: 20038093, pp. 593–600. DOI: `10.1021/ac901890r`. eprint: `https://doi.org/10.1021/ac901890r`. URL: `https://doi.org/10.1021/ac901890r` (cit. on pp. 67, 76, 77, 86, 94, 99, 138, 147).

[364] H. Matsumura et al. “Effect of Occlusion on Human Skin”. In: *Contact Dermatitis* 33.4 (Oct. 1995), pp. 231–235. ISSN: 0105-1873. DOI: `10.1111/j.1600-0536.1995.tb00472.x`. URL: `https://doi.org/10.1111/j.1600-0536.1995.tb00472.x` (cit. on p. 67).

[365] U. Ewald, G. Rooth, and T. Tuvemo. “Postischaemic Hyperaemia Studied With a Transcutaneous Oxygen Electrode Used at 33–37°C”. In: *Scandinavian Journal of Clinical and Laboratory Investigation* 41.7 (1981), pp. 641–645. DOI: `10.3109/00365518109090509`. eprint: `https://doi.org/10.3109/00365518109090509`. URL: `https://doi.org/10.3109/00365518109090509` (cit. on p. 67).

[366] A. C. Ernstene and M. C. Volk. “CUTANEOUS RESPIRATION IN MAN: V. The Rate of Carbon Dioxide Elimination and Oxygen Absorption in Subjects With Diseases of the Skin”. eng. In: *The Journal of Clinical Investigation* 11.2 (Mar. 1932), pp. 377–382. ISSN: 0021-9738. DOI: `10.1172/JCI100419` (cit. on p. 67).

[367] H. Lambers et al. “Natural Skin Surface pH is on Average Below 5, Which is Beneficial for its Resident Flora”. In: *International Journal of Cosmetic Science* 28.5 (2006), pp. 359–370. DOI: `10.1111/j.1467-2494.2006.00344.x`. eprint: `https://onlinelibrary.wiley.com/doi/pdf/10.1111/j.1467-2494.2006.00344.x`. URL: `https://onlinelibrary.wiley.com/doi/abs/10.1111/j.1467-2494.2006.00344.x` (cit. on p. 68).

[368] Pablo Martínez-Lozano and Juan Fernández de la Mora. “On-line Detection of Human Skin Vapors”. In: *Journal of the American Society for Mass Spectrometry* 20.6 (2009), pp. 1060–1063. ISSN: 1044-0305. DOI: `https://doi.org/10.1016/j.jasms.2009.01.012`. URL: `http://www.sciencedirect.com/science/article/pii/S1044030509000518` (cit. on p. 68).

[369] Asaf Stein and Shannon M. Bailey. “Redox Biology of Hydrogen Sulfide: Implications for Physiology, Pathophysiology, and Pharmacology”. In: *Redox Biology* 1.1 (2013), pp. 32–39. ISSN: 2213-2317. DOI: `https://doi.org/10.1016/j.redox.2012.11.006`. URL: `http://www.sciencedirect.com/science/article/pii/S2213231712000080` (cit. on p. 68).

[370] B de Lacy Costello et al. “A Review of the Volatiles From the Healthy Human Body”. In: *Journal of Breath Research* 8.1 (Jan. 2014), p. 014001. DOI: `10.1088/1752-7155/8/1/014001`. URL: `https://doi.org/10.1088%2F1752-7155%2F8%2F1%2F014001` (cit. on p. 68).

[371] Yaqian Huang et al. “Endogenous Sulfur Dioxide: A New Member of Gasotransmitter Family in the Cardiovascular System”. In: *Oxidative Medicine and Cellular Longevity* 2016 (Dec. 2015). ISSN: 1942-0900. DOI: `10.1155/2016/8961951`. URL: `https://doi.org/10.1155/2016/8961951` (cit. on p. 68).

[372] Basil Acock and Gerard W. Wall. "A Simple Conductimetric CO2 Analyzer With Automatic Recalibration: I. Design, Implementation, and Functionality". In: *Agronomy Journal* 87.1 (1995), pp. 70–75. DOI: `10.2134/agronj1995.00021962008700010012x`. eprint: `https://acsess.onlinelibrary.wiley.com/doi/pdf/10.2134/agronj1995.00021962008700010012x`. URL: `https://acsess.onlinelibrary.wiley.com/doi/abs/10.2134/agronj1995.00021962008700010012x` (cit. on pp. 69, 73).

[373] Kiminori Shitashima. "Evolution of Compact Electrochemical In-Situ pH-pCO2 Sensor Using ISFET-pH Electrode". In: *AGU Fall Meeting Abstracts* 1 (Sept. 2010). DOI: `10.1109/OCEANS.2010.5663782` (cit. on pp. 69, 75).

[374] S. Fanget et al. "Gas Sensors Based on Gravimetric Detection – A Review". In: *Sensors and Actuators B: Chemical* 160.1 (2011), pp. 804–821. ISSN: 0925-4005. DOI: `https://doi.org/10.1016/j.snb.2011.08.066`. URL: `http://www.sciencedirect.com/science/article/pii/S0925400511007891` (cit. on p. 69).

[375] J Zosel et al. "The Measurement of Dissolved and Gaseous Carbon Dioxide Concentration". In: *Measurement Science and Technology* 22 (May 2011). DOI: `10.1088/0957-0233/22/7/072001` (cit. on p. 69).

[376] Pradeep Puligundla, Junho Jung, and Sanghoon Ko. "Carbon Dioxide Sensors for Intelligent Food Packaging Applications". In: *Food Control* 25.1 (2012), pp. 328–333. ISSN: 0956-7135. DOI: `https://doi.org/10.1016/j.foodcont.2011.10.043`. URL: `http://www.sciencedirect.com/science/article/pii/S0956713511004610` (cit. on p. 69).

[377] Eduard Llobet. "Gas Sensors Using Carbon Nanomaterials: A Review". In: *Sensors and Actuators B: Chemical* 179 (2013). A Special Issue in Honour of Professor A. D'Amico, pp. 32–45. ISSN: 0925-4005. DOI: `https://doi.org/10.1016/j.snb.2012.11.014`. URL: `http://www.sciencedirect.com/science/article/pii/S0925400512011938` (cit. on p. 69).

[378] Suresh Neethirajan, D.S. Jayas, and Shashikant Sadistap. "Carbon Dioxide (CO2) Sensors for the Agri-food Industry—A Review". In: *Food and Bioprocess Technology* 2 (June 2009), pp. 115–121. DOI: `10.1007/s11947-008-0154-y` (cit. on p. 69).

[379] J. Barrington. "Design and Fabrication of Optical Fibre Long Period Gratings for CO2 Sensing". PhD thesis. Cranfield University, 2018. URL: `https://books.google.fr/books?id=sc8XzAEACAAJ` (cit. on pp. 69, 78).

[380] Matthias Rebber, Christoph Willa, and Dorota Koziej. "Organic–Inorganic Hybrids for CO2 Sensing, Separation and Conversion". In: *Nanoscale Horiz.* 5 (3 2020), pp. 431–453. DOI: `10.1039/C9NH00380K`. URL: `http://dx.doi.org/10.1039/C9NH00380K` (cit. on p. 69).

[381] Marwan Y. Rezk, Jyotsna Sharma, and Manas Ranjan Gartia. "Nanomaterial-Based CO2 Sensors". In: *Nanomaterials* 10.11 (2020). ISSN: 2079-4991. DOI: `10.3390/nano10112251`. URL: `https://www.mdpi.com/2079-4991/10/11/2251` (cit. on p. 69).

[382] Tynee Bhowmick et al. "Multilayered and Chemiresistive Thin and Thick Film Gas Sensors for Air Quality Monitoring". In: *Multilayer Thin Films*. Ed. by Sukumar Basu. Rijeka: IntechOpen, 2020. Chap. 8. DOI: `10.5772/intechopen.89710`. URL: `https://doi.org/10.5772/intechopen.89710` (cit. on pp. 69, 80).

[383] Manfred Decker, Wolfram Oelßner, and Jens Zosel. "Electrochemical CO2 Sensors With Liquid or Pasty Electrolyte". In: *Carbon Dioxide Sensing: Fundamentals, Principles, and Applications*. Wiley, Apr. 2019, pp. 87–116. ISBN: 9783527411825. DOI: `10.1002/9783527688302.ch4` (cit. on p. 69).

[384] D.A. Skoog et al. *Fundamentals of Analytical Chemistry*. Cengage Learning, 2013. ISBN: 9781285607191. URL: `https://books.google.fr/books?id=8bIWAAAAQBAJ` (cit. on p. 70).

[385] David T. Harvey. *Analytical Chemistry 2.1*. David T. Harvey, 2016. URL: `http://dpuadweb.depauw.edu/harvey_web/eTextProject/version_2.1.html` (cit. on p. 70).

[386] Peter F. Bernath. *Spectra of Atoms and Molecules (Topics in Physical Chemistry)*. Oxford, U.K.: Oxford University Press, 1995. ISBN: 9780195075984 (cit. on p. 70).

[387] I.E. Gordon et al. "The HITRAN2016 Molecular Spectroscopic Database". In: *Journal of Quantitative Spectroscopy and Radiative Transfer* 203 (2017). DOI: `10.1016/j.jqsrt.2017.06.038` (cit. on p. 71).

[388] J. Hodgkinson et al. “A Low Cost, Optically Efficient Carbon Dioxide Sensor Based on Nondispersive Infra-Red (NDIR) Measurement at 4.2 μm”. In: *Optical Sensing and Detection II.* Ed. by Francis Berghmans, Anna Grazia Mignani, and Piet De Moor. Vol. 8439. International Society for Optics and Photonics. SPIE, 2012, pp. 352–361. DOI: `10.1117/12.922258`. URL: `https://doi.org/10.1117/12.922258` (cit. on p. 70).

[389] Jane Hodgkinson et al. “Non-Dispersive Infra-Red (NDIR) Measurement of Carbon Dioxide at 4.2 μm in a Compact and Optically Efficient Sensor”. In: *Sensors and Actuators B: Chemical* 186 (2013), pp. 580–588. ISSN: 0925-4005. DOI: `https://doi.org/10.1016/j.snb.2013.06.006`. URL: `http://www.sciencedirect.com/science/article/pii/S0925400513006862` (cit. on pp. 70–72).

[390] W. Liu et al. “CMOS MEMS Infrared Source Based on Black Silicon”. In: *2016 IEEE 11th Annual International Conference on Nano/Micro Engineered and Molecular Systems (NEMS).* 2016, pp. 200–204. DOI: `10.1109/NEMS.2016.7758232` (cit. on pp. 70, 72).

[391] Daniel Popa and Florin Udrea. “Towards Integrated Mid-Infrared Gas Sensors”. In: *Sensors* 19 (May 2019), p. 2076. DOI: `10.3390/s19092076` (cit. on pp. 70, 72, 86).

[392] Guangjun Zhang, Yaping Li, and Qingbo Li. “A Miniaturized Carbon Dioxide Gas Sensor Based on Infrared Absorption”. In: *Optics and Lasers in Engineering* 48 (Dec. 2010), pp. 1206–1212. DOI: `10.1016/j.optlaseng.2010.06.012` (cit. on pp. 70, 72, 86).

[393] Yang Jing et al. “Design and Optimization of an Integrated MEMS Gas Chamber with High Transmissivity”. In: *Digital Communications and Networks* (2020). ISSN: 2352-8648. DOI: `https://doi.org/10.1016/j.dcan.2020.05.006`. URL: `http://www.sciencedirect.com/science/article/pii/S2352864820300250` (cit. on pp. 70, 86).

[394] William Kohsiek. “Fast-Response Water Vapor and Carbon Dioxide Sensor”. In: *Fiber Optic Sensors: Engineering and Applications.* Ed. by Anastasius J.A. Bruinsma and Brian Culshaw. Vol. 1511. International Society for Optics and Photonics. SPIE, 1991, pp. 114–119. DOI: `10.1117/12.45983`. URL: `https://doi.org/10.1117/12.45983` (cit. on pp. 70, 72).

[395] Desmond Gibson and Calum Macgregor. “A Novel Solid State Non-Dispersive Infrared CO2 Gas Sensor Compatible With Wireless and Portable Deployment”. In: *Sensors (Basel, Switzerland)* 13 (June 2013), pp. 7079–7103. DOI: `10.3390/s130607079` (cit. on pp. 70, 72, 85, 86).

[396] Dehui Xu et al. “MEMS-Based Thermoelectric Infrared Sensors: A Review”. In: *Frontiers of Mechanical Engineering* 12.4 (Dec. 2017), pp. 557–566. ISSN: 2095-0241. DOI: `10.1007/s11465-017-0441-2`. URL: `https://doi.org/10.1007/s11465-017-0441-2` (cit. on p. 72).

[397] Kook-Nyung Lee et al. “A High-Temperature MEMS Heater Using Suspended Silicon Structures”. In: *Journal of Micromechanics and Microengineering* 19.11 (Oct. 2009), p. 115011. DOI: `10.1088/0960-1317/19/11/115011`. URL: `https://doi.org/10.1088%2F0960-1317%2F19%2F11%2F115011` (cit. on p. 72).

[398] Tim Vincent and J.W. Gardner. “A Low Cost MEMS Based NDIR System for the Monitoring of Carbon Dioxide in Breath Analysis at ppm Levels”. In: *Sensors and Actuators B: Chemical* 236 (Apr. 2016), pp. 954–964. DOI: `10.1016/j.snb.2016.04.016` (cit. on p. 72).

[399] M. Müller et al. “Integration and Calibration of Non-Dispersive Infrared (NDIR) CO2 Low-Cost Sensors and Their Operation in a Sensor Network Covering Switzerland”. In: *Atmospheric Measurement Techniques* 13.7 (2020), pp. 3815–3834. DOI: `10.5194/amt-13-3815-2020`. URL: `https://amt.copernicus.org/articles/13/3815/2020/` (cit. on p. 72).

[400] Gas Sensing Solutions Ltd. *Reducing the Impact of Condensation on CO2 Sensor.* Tech. rep. AN008. Gas Sensing Solutions Ltd., 2020 (cit. on p. 72).

[401] Daehwan Jung et al. “Next Generation Mid-Infrared Sources”. In: *Journal of Optics* 19 (Oct. 2017). DOI: `10.1088/2040-8986/aa939b` (cit. on p. 72).

[402] Sarra Moumen et al. “Infrared Investigation of CO2 Sorption by Amine Based Materials for the Development of a NDIR CO2 Sensor”. In: *Sensors and Actuators B: Chemical* 236 (June 2016). DOI: `10.1016/j.snb.2016.06.014` (cit. on p. 72).

[403] S. Schaden et al. “Direct Determination of Carbon Dioxide in Aqueous Solution Using Mid-Infrared Quantum Cascade Lasers”. In: *Applied Spectroscopy* 58.6 (2004), pp. 667–670. DOI: `10.1366/000370204872971`. eprint: `https://doi.org/10.1366/000370204872971`. URL: `https://doi.org/10.1366/000370204872971` (cit. on pp. 72, 90, 162).

[404] Zoltán Bozóki, Andrea Pogány, and Gábor Szabó. “Photoacoustic Instruments for Practical Applications: Present, Potentials, and Future Challenges”. In: *Applied Spectroscopy Reviews* 46.1 (2011), pp. 1–37. DOI: `10.1080/05704928.2010.520178`. eprint: `https://doi.org/10.1080/05704928.2010.520178`. URL: `https://doi.org/10.1080/05704928.2010.520178` (cit. on p. 72).

[405] S. Borri et al. “Intracavity Quartz-Enhanced Photoacoustic Sensor”. In: *Applied Physics Letters* 104.9 (2014), p. 091114. DOI: `10.1063/1.4867268`. eprint: `https://doi.org/10.1063/1.4867268`. URL: `https://doi.org/10.1063/1.4867268` (cit. on p. 72).

[406] Roman Rousseau et al. “Quartz Tuning Fork Resonance Tracking and Application in Quartz Enhanced Photoacoustics Spectroscopy”. In: *Sensors (Basel, Switzerland)* 19.24 (Dec. 2019), p. 5565. ISSN: 1424-8220. DOI: `10.3390/s19245565`. URL: `https://doi.org/10.3390/s19245565` (cit. on p. 72).

[407] Louisa Scholz et al. “Miniature Low-Cost Carbon Dioxide Sensor for Mobile Devices”. In: *IEEE Sensors Journal* PP (Mar. 2017), pp. 2889–2895. DOI: `10.1109/JSEN.2017.2682638` (cit. on pp. 72, 86).

[408] J. Huber et al. “Miniaturized Photoacoustic CO2 Sensors for Consumer Applications”. In: *Proceedings SENSOR* E6 (May 2015), pp. 688–692. DOI: `10.5162/sensor2015/E6.3` (cit. on p. 72).

[409] Hans-Fridtjof Pernau et al. “Resonant Photoacoustic CO2 Spectroscopy With LED Light Source”. In: *Proceedings of the 30th anniversary Eurosensors Conference – Eurosensors 2016, 4-7. Sepember 2016, Budapest, Hungary.* Vol. 168. Dec. 2016, pp. 1325–1328. DOI: `10.1016/j.proeng.2016.11.362` (cit. on p. 72).

[410] Helene Lhermet et al. “Micro-Photoacoustic Cell With Integrated Microphone for Sub-Ppm Gas Sensing”. In: *2019 20th International Conference on Solid-State Sensors, Actuators and Microsystems & Eurosensors XXXIII (TRANSDUCERS & EUROSENSORS XXXIII).* June 2019, pp. 68–71. DOI: `10.1109/TRANSDUCERS.2019.8808295` (cit. on p. 72).

[411] M. A. Jensen and G. A. Rechnitz. “Response Time Characteristics of the pCO2 Electrode”. In: *Analytical Chemistry* 51.12 (1979), pp. 1972–1977. DOI: `10.1021/ac50048a019`. eprint: `https://doi.org/10.1021/ac50048a019`. URL: `https://doi.org/10.1021/ac50048a019` (cit. on pp. 73, 74, 91, 92).

[412] Andrew Mills. “Optical Sensors for Carbon Dioxide and Their Applications”. In: *Sensors for Environment, Health and Security.* Ed. by Marie-Isabelle Baraton. Dordrecht: Springer Netherlands, 2009, pp. 347–370. ISBN: 978-1-4020-9009-7 (cit. on pp. 73, 76, 86, 91, 93–95, 97, 131).

[413] Frank J. Millero et al. “Dissociation Constants of Carbonic Acid in Seawater as a Function of Salinity and Temperature”. In: *Marine Chemistry* 100.1 (2006), pp. 80–94. ISSN: 0304-4203. DOI: `https://doi.org/10.1016/j.marchem.2005.12.001`. URL: `https://www.sciencedirect.com/science/article/pii/S0304420305001921` (cit. on p. 73).

[414] Xiaoguang Wang et al. “Comprehensive Study of the Hydration and Dehydration Reactions of Carbon Dioxide in Aqueous Solution”. In: *The Journal of Physical Chemistry A* 114.4 (Feb. 2010), pp. 1734–1740. ISSN: 1089-5639. DOI: `10.1021/jp909019u`. URL: `https://doi.org/10.1021/jp909019u` (cit. on p. 73).

[415] John M. Baker, Egbert J. A. Spaans, and Clive F. Reece. “Conductimetric Measurement of CO2 Concentration: Theoretical Basis and Its Verification”. In: *Agronomy Journal* 88.4 (1996), pp. 675–682. DOI: `10.2134/agronj1996.00021962008800040029x`. eprint: `https://acsess.onlinelibrary.wiley.com/doi/pdf/10.2134/agronj1996.00021962008800040029x`. URL: `https://acsess.onlinelibrary.wiley.com/doi/abs/10.2134/agronj1996.00021962008800040029x` (cit. on p. 73).

[416] Anca Roxana Varlan and Willy Sansen. "Micromachined Conductometric p(CO2) Sensor". In: *Sensors and Actuators B: Chemical* 44.1 (Oct. 1997), pp. 309–315. ISSN: 0925-4005. URL: `http://www.sciencedirect.com/science/article/pii/S0925400597002232` (cit. on pp. 73, 86).

[417] Peyman Mirtaheri et al. "A New Biomedical Sensor for Measuring PCO2". In: *Physiological measurement* 25 (May 2004), pp. 421–436. DOI: `10.1088/0967-3334/25/2/002` (cit. on p. 73).

[418] Peyman Mirtaheri et al. "Miniaturization of a Biomedical Gas Sensor". In: *Physiological Measurement* 25.6 (Nov. 2004), pp. 1511–1522. DOI: `10.1088/0967-3334/25/6/015`. URL: `https://doi.org/10.1088/0967-3334/25/6/015` (cit. on pp. 73, 86).

[419] Christian Tronstad et al. "Early Detection of Cardiac Ischemia Using a Conductometric pCO2 Sensor: Real-Time Drift Correction and Parameterization". In: *Physiological measurement* 31 (Sept. 2010), pp. 1241–1255. DOI: `10.1088/0967-3334/31/9/013` (cit. on p. 73).

[420] Gerard W. Wall, Basil Acock, and G. A. Milliken. "A Simple Conductimetric CO2 Analyzer With Automatic Recalibration: II. Factors Affecting Calibration". In: *Agronomy Journal* 87.1 (1995), pp. 76–80. DOI: `https://doi.org/10.2134/agronj1995.00021962008700010013x`. eprint: `https://acsess.onlinelibrary.wiley.com/doi/pdf/10.2134/agronj1995.00021962008700010013x`. URL: `https://acsess.onlinelibrary.wiley.com/doi/abs/10.2134/agronj1995.00021962008700010013x` (cit. on p. 73).

[421] Karl Lis et al. "A PCO2 Surface Electrode Working on the Principle of Electrical Conductivity". In: *Pflügers Archiv : European journal of physiology* 381 (Oct. 1979), pp. 289–291. DOI: `10.1007/BF00583262` (cit. on p. 74).

[422] S. Neethirajan et al. "Development of Carbon Dioxide (CO2) Sensor for Grain Quality Monitoring". In: *Biosystems Engineering* 106.4 (2010), pp. 395–404. ISSN: 1537-5110. DOI: `https://doi.org/10.1016/j.biosystemseng.2010.05.002`. URL: `http://www.sciencedirect.com/science/article/pii/S1537511010000917` (cit. on p. 74).

[423] John W. Severinghaus and A. Freeman Bradley. "Electrodes for Blood pO2 and pCO2 Determination". In: *Journal of Applied Physiology* 13.3 (1958). PMID: 13587443, pp. 515–520. DOI: `10.1152/jappl.1958.13.3.515`. eprint: `https://doi.org/10.1152/jappl.1958.13.3.515`. URL: `https://doi.org/10.1152/jappl.1958.13.3.515` (cit. on pp. 74, 75, 86).

[424] A. V. Beran, R. F. Huxtable, and D. R. Sperling. "Electrochemical Sensor for Continuous Transcutaneous PCO2 Measurement". In: *Journal of Applied Physiology* 41.3 (1976). PMID: 965318, pp. 442–447. DOI: `10.1152/jappl.1976.41.3.442`. eprint: `https://doi.org/10.1152/jappl.1976.41.3.442`. URL: `https://doi.org/10.1152/jappl.1976.41.3.442` (cit. on p. 74).

[425] Jae Ho Shin et al. "A Planar pCO2 Sensor With Enhanced Electrochemical Properties". In: *Analytical Chemistry* 72.18 (2000), pp. 4468–4473. DOI: `10.1021/ac000427o`. eprint: `https://doi.org/10.1021/ac000427o`. URL: `https://doi.org/10.1021/ac000427o` (cit. on pp. 74, 75, 86).

[426] J. W. Severinghaus. "A Combined Transcutaneous P(O2)-P(CO2) Electrode With Electrochemical HCO3- Stabilization". In: *Journal of applied physiology: respiratory, environmental and exercise physiology* 51 (Nov. 1981), pp. 1027–1032. DOI: `10.1152/jappl.1981.51.4.1027` (cit. on p. 74).

[427] Pingsan Zhao and Wei-Jun Cai. "An Improved Potentiometric pCO2 Microelectrode". In: *Analytical Chemistry* 69.24 (Dec. 1997), pp. 5052–5058. ISSN: 0003-2700. DOI: `10.1021/ac970747g`. URL: `https://doi.org/10.1021/ac970747g` (cit. on pp. 74, 75).

[428] Hiroaki Suzuki et al. "Micromachined Severinghaus-Type Carbon Dioxide Electrode". In: *Analytical Chemistry* 71.9 (May 1999), pp. 1737–1743. ISSN: 0003-2700. DOI: `10.1021/ac9811468`. URL: `https://doi.org/10.1021/ac9811468` (cit. on p. 74).

[429] Haluk Beyenal, Catherine C. Davis, and Zbigniew Lewandowski. "An Improved Severinghaus-Type Carbon Dioxide Microelectrode for Use in Biofilms". In: *Sensors and Actuators B: Chemical* 97.2 (Feb. 2004), pp. 202–210. ISSN: 0925-4005. URL: `http://www.sciencedirect.com/science/article/pii/S0925400503007019` (cit. on pp. 74, 86).

[430] Terrence L. Donaldson and Harvey J. Palmer. “Dynamic Response of the Carbon Dioxide Electrode”. In: *AIChE Journal* 25.1 (1979), pp. 143–151. DOI: `https://doi.org/10.1002/aic.690250116`. eprint: `https://aiche.onlinelibrary.wiley.com/doi/pdf/10.1002/aic.690250116`. URL: `https://aiche.onlinelibrary.wiley.com/doi/abs/10.1002/aic.690250116` (cit. on p. 75).

[431] M. A. McGuire and R. O. Teskey. “Microelectrode Technique for In Situ Measurement of Carbon Dioxide Concentrations in Xylem Sap of Trees”. In: *Tree Physiology* 22.11 (Aug. 2002), pp. 807–811. ISSN: 0829-318X. DOI: `10.1093/treephys/22.11.807`. eprint: `https://academic.oup.com/treephys/article-pdf/22/11/807/4632535/22-11-807.pdf`. URL: `https://doi.org/10.1093/treephys/22.11.807` (cit. on p. 75).

[432] Wei-Jun Cai and Clare E. Reimers. “The Development of pH and pCO2 Microelectrodes for Studying the Carbonate Chemistry of Pore Waters Near the Sediment-Water Interface”. In: *Limnology and Oceanography* 38.8 (1993), pp. 1762–1773. DOI: `https://doi.org/10.4319/lo.1993.38.8.1762`. eprint: `https://aslopubs.onlinelibrary.wiley.com/doi/pdf/10.4319/lo.1993.38.8.1762`. URL: `https://aslopubs.onlinelibrary.wiley.com/doi/abs/10.4319/lo.1993.38.8.1762` (cit. on p. 75).

[433] Michelle D. Whitehead et al. “Transcutaneous Estimation of Arterial pO2 and pCO2 in Newborn Infants With a Single Electrochemical Sensor”. In: *The Lancet* 315.8178 (May 1980), pp. 1111–1114. ISSN: 0140-6736. URL: `http://www.sciencedirect.com/science/article/pii/S0140673680915561` (cit. on p. 75).

[434] P. Bergveld. “Development of an Ion-Sensitive Solid-State Device for Neurophysiological Measurements”. In: *IEEE Transactions on Biomedical Engineering* BME-17.1 (1970), pp. 70–71 (cit. on p. 75).

[435] B. Hu, H. H. Van Den Vlekkert, and N. F. De Rooij. “Carbon Dioxide Gas-Sensing Electrode Based on a pH-ISFET With Back-Side Contacts”. In: *Sensors and Actuators* 17.1 (May 1989), pp. 275–278. ISSN: 0250-6874. URL: `http://www.sciencedirect.com/science/article/pii/0250687489800915` (cit. on pp. 75, 86).

[436] P. Bergveld. “The Operation of an ISFET as an Electronic Device”. In: *Sensors and Actuators* 1 (1981), pp. 17–29. ISSN: 0250-6874. DOI: `https://doi.org/10.1016/0250-6874(81)80004-2`. URL: `http://www.sciencedirect.com/science/article/pii/0250687481800042` (cit. on p. 75).

[437] Shahriar Jamasb. “Continuous Monitoring of pH and Blood Gases Using Ion-Sensitive and Gas-Sensitive Field Effect Transistors Operating in the Amperometric Mode in Presence of Drift”. In: *Biosensors* 9.1 (Mar. 2019), p. 44. ISSN: 2079-6374. DOI: `10.3390/bios9010044`. URL: `https://doi.org/10.3390/bios9010044` (cit. on pp. 75, 76).

[438] A. Star et al. “Nanoelectronic Carbon Dioxide Sensors”. In: *Advanced Materials* 16.22 (2004), pp. 2049–2052. DOI: `10.1002/adma.200400322`. eprint: `https://onlinelibrary.wiley.com/doi/pdf/10.1002/adma.200400322`. URL: `https://onlinelibrary.wiley.com/doi/abs/10.1002/adma.200400322` (cit. on p. 75).

[439] Satoshi Mohri et al. “Measurements of CO2, Lactic Acid and Sodium Bicarbonate Secreted by Cultured Cells Using a Flow-Through Type pH/CO2 Sensor System Based on ISFET”. In: *Sensors and Actuators B: Chemical* 115.1 (2006), pp. 519–525. ISSN: 0925-4005. DOI: `https://doi.org/10.1016/j.snb.2005.10.029`. URL: `http://www.sciencedirect.com/science/article/pii/S0925400505008427` (cit. on p. 75).

[440] M. A. Ekwińska et al. “Transcutaneous Blood Capnometry Sensor Head Based on a Back-Side Contacted ISFET”. In: *Mechatronics: Recent Technological and Scientific Advances* (2012). Ed. by Ryszard Jabloński and Tomaš Březina. No volume number., pp. 607–614 (cit. on p. 75).

[441] Chao-Sung Lai et al. “Body Effect Minimization Using Single Layer Structure for pH-ISFET Applications”. In: *Sensors and Actuators B-chemical* 143 (Jan. 2010), pp. 494–499. DOI: `10.1016/j.snb.2009.09.037` (cit. on p. 75).

[442] Soumendu Sinha et al. “Temperature and Temporal Drift Compensation for Al2O3-Gate ISFET-Based pH Sensor Using Machine Learning Techniques”. In: *Microelectronics Journal* 97 (Mar. 2020), p. 104710. ISSN: 0026-2692. URL: `http://www.sciencedirect.com/science/article/pii/S0026269219307207` (cit. on p. 76).

[443] Kengo Shimanoe et al. “Development of FET-Type CO2 Sensor Operative at Room Temperature”. In: *Sensors and Actuators B: Chemical* 102 (Sept. 2004), pp. 14–19. DOI: `10.1016/j.snb.2003.11.037` (cit. on p. 76).

[444] Chia-Hsu Hsieh et al. “High-Performance Extended Gate Field-Effect-Transistor-Based Dissolved Carbon Dioxide Sensing System With a Packaged Microreference Electrode”. In: *Journal of Micro/Nanolithography, MEMS, and MOEMS* 13.3 (2014), pp. 1–8. DOI: `10.1117/1.JMM.13.3.033017`. URL: `https://doi.org/10.1117/1.JMM.13.3.033017` (cit. on pp. 76, 86).

[445] Mahesh Uttamlal and David R. Walt. “A Fiber-Optic Carbon Dioxide Sensor for Fermentation Monitoring”. In: *Bio/Technology* 13.6 (June 1995), pp. 597–601. ISSN: 1546-1696. DOI: `10.1038/nbt0695-597`. URL: `https://doi.org/10.1038/nbt0695-597` (cit. on pp. 76, 77, 92, 95, 131, 132).

[446] G. G. Vurek, P. J. Feustel, and J. W. Severinghaus. “A Fiber Optic PCO2 Sensor”. In: *Annals of Biomedical Engineering* 11.6 (Nov. 1983), pp. 499–510. ISSN: 1573-9686. DOI: `10.1007/BF02364081`. URL: `https://doi.org/10.1007/BF02364081` (cit. on pp. 76, 91, 92, 158).

[447] Michael D. DeGrandpre, Matthew M. Baehr, and Terence R. Hammar. “Calibration-Free Optical Chemical Sensors”. In: *Analytical Chemistry* 71.6 (1999), pp. 1152–1159. DOI: `10.1021/ac9805955`. eprint: `https://doi.org/10.1021/ac9805955`. URL: `https://doi.org/10.1021/ac9805955` (cit. on pp. 76, 78, 92, 158).

[448] Zhongming Lu et al. “A High Precision, Fast Response, and Low Power Consumption in situ Optical Fiber Chemical pCO2 Sensor”. In: *Talanta* 76.2 (2008), pp. 353–359. ISSN: 0039-9140. DOI: `https://doi.org/10.1016/j.talanta.2008.03.005`. URL: `http://www.sciencedirect.com/science/article/pii/S0039914008001847` (cit. on pp. 76, 78, 92).

[449] Aron Hakonen and Stefan Hulth. “A High-Precision Ratiometric Fluorosensor for pH: Implementing Time-Dependent Non-Linear Calibration Protocols for Drift Compensation”. In: *Analytica Chimica Acta* 606.1 (2008), pp. 63–71. ISSN: 0003-2670. DOI: `https://doi.org/10.1016/j.aca.2007.10.035`. URL: `http://www.sciencedirect.com/science/article/pii/S0003267007017795` (cit. on pp. 76, 131, 132, 138).

[450] Xudong Ge et al. “A Low-Cost Fluorescent Sensor for pCO2 Measurements”. In: *Chemosensors* 2 (June 2014), pp. 108–120. DOI: `10.3390/chemosensors2020108` (cit. on pp. 76, 95, 131).

[451] Hui Wang et al. “An Ultrasensitive Fluorescent Paper-Based CO2 Sensor”. In: *ACS Applied Materials & Interfaces* 12.18 (2020). PMID: 32320202, pp. 20507–20513. DOI: `10.1021/acsami.0c03405`. eprint: `https://doi.org/10.1021/acsami.0c03405`. URL: `https://doi.org/10.1021/acsami.0c03405` (cit. on pp. 76, 95, 138).

[452] N. Opitz and D. W. Lübbers. “Compact CO2 Gas Analyzer With Favourable Signal-to-Noise Ratio and Resolution Using Special Fluorescence Sensors (Optodes) Illuminated by Blue Led’s”. In: *Oxygen Transport to Tissue—VI*. Boston, MA: Springer, 1984, pp. 757–762. ISBN: 978-1-4684-4895-5. DOI: `10.1007/978-1-4684-4895-5_74`. URL: `https://doi.org/10.1007/978-1-4684-4895-5_74` (cit. on pp. 76, 91, 92, 94).

[453] Zhang Zhujun and W. Rudolf Seitz. “A Carbon Dioxide Sensor Based on Fluorescence”. In: *Analytica Chimica Acta - ANAL CHIM ACTA* 160 (Dec. 1984), pp. 305–309. DOI: `10.1016/S0003-2670(00)84536-5` (cit. on pp. 76, 91, 92, 94).

[454] Otto S. Wolfbeis et al. “Fiber-Optic Fluorosensor for Oxygen and Carbon Dioxide”. In: *Analytical Chemistry* 60.19 (1988), pp. 2028–2030. DOI: `10.1021/ac00170a009`. eprint: `https://doi.org/10.1021/ac00170a009`. URL: `https://doi.org/10.1021/ac00170a009` (cit. on pp. 76, 94, 138).

[455] Xiaoying. He and Garry A. Rechnitz. “Linear Response Function for Fluorescence-Based Fiber-Optic CO2 Sensors”. In: *Analytical Chemistry* 67.13 (1995), pp. 2264–2268. DOI: `10.1021/ac00109a054`. eprint: `https://doi.org/10.1021/ac00109a054`. URL: `https://doi.org/10.1021/ac00109a054` (cit. on pp. 76, 78, 94, 131, 158).

[456] M.D. Marazuela, M.C. Moreno Bondi, and G. Orellana. “Enhanced Performance of a Fibre-Optic Luminescence CO2 Sensor Using Carbonic Anhydrase”. In: *Sensors and Actuators B: Chemical* 29.1 (1995). Proceedings of the 2nd European Conference on Optical Chemical Sensors and Biosensors, pp. 126–131. ISSN: 0925-4005. DOI: `https://doi.org/10.1016/0925-4005(95)01673-2`. URL: `http://www.sciencedirect.com/science/article/pii/0925400595016732` (cit. on pp. 76, 94).

[457] Otto Wolfbeis et al. “Fiber-Optic Fluorescence Carbon Dioxide Sensor for Environmental Monitoring”. In: *Microchimica Acta* 129 (Jan. 1998), pp. 181–188. DOI: `10.1007/BF01244739` (cit. on pp. 76, 77, 94, 131, 133, 138).

[458] Ozlem Oter et al. “Emission-Based Optical Carbon Dioxide Sensing With HPTS in Green Chemistry Reagents: Room-Temperature Ionic Liquids”. In: *Analytical and Bioanalytical Chemistry* 386.5 (Nov. 2006), pp. 1225–1234. ISSN: 1618-2650. DOI: `10.1007/s00216-006-0659-z`. URL: `https://doi.org/10.1007/s00216-006-0659-z` (cit. on pp. 76, 131, 132).

[459] Ozlem Oter, Kadriye Ertekin, and Sibel Derinkuyu. “Ratiometric Sensing of CO2 in Ionic Liquid Modified Ethyl Cellulose Matrix”. In: *Talanta* 76.3 (July 2008), pp. 557–563. ISSN: 0039-9140. URL: `http://www.sciencedirect.com/science/article/pii/S0039914008002348` (cit. on pp. 76, 132, 138).

[460] Chen-Shane Chu and Yu-Lung Lo. “Fiber-Optic Carbon Dioxide Sensor Based on Fluorinated Xerogels Doped With HPTS”. In: *Sensors and Actuators B: Chemical* 129.1 (2008), pp. 120–125. ISSN: 0925-4005. DOI: `https://doi.org/10.1016/j.snb.2007.07.082`. URL: `http://www.sciencedirect.com/science/article/pii/S0925400507005552` (cit. on pp. 76, 77, 94, 131, 132, 138, 158).

[461] Chen-Shane Chu and Yu-Lung Lo. “Highly Sensitive and Linear Optical Fiber Carbon Dioxide Sensor Based on Sol-Gel Matrix Doped With Silica Particles and HPTS”. In: *Sensors and Actuators B: Chemical* 143.1 (2009), pp. 205–210. ISSN: 0925-4005. DOI: `https://doi.org/10.1016/j.snb.2009.09.019`. URL: `http://www.sciencedirect.com/science/article/pii/S0925400509007060` (cit. on pp. 76, 94, 131, 132, 138, 158).

[462] Cheng-Shane Chu and Jhih-Jheng Syu. “Optical Sensor for Dual Sensing of Oxygen and Carbon Dioxide Based on Sensing Films Coated on Filter Paper”. In: *Appl. Opt.* 56.4 (Feb. 2017), pp. 1225–1231. DOI: `10.1364/AO.56.001225`. URL: `http://ao.osa.org/abstract.cfm?URI=ao-56-4-1225` (cit. on pp. 76, 77, 94, 138).

[463] Isabel M. Perez de Vargas-Sansalvador et al. “Water Based-Ionic Liquid Carbon Dioxide Sensor for Applications in the Food Industry”. In: *Sensors and Actuators B: Chemical* 253 (2017), pp. 302–309. ISSN: 0925-4005. DOI: `https://doi.org/10.1016/j.snb.2017.06.047`. URL: `http://www.sciencedirect.com/science/article/pii/S0925400517310687` (cit. on p. 76).

[464] Jennifer S. Clarke et al. “Developments in Marine pCO2 Measurement Technology; towards Sustained in situ Observations”. In: *TrAC Trends in Analytical Chemistry* 88 (2017), pp. 53–61. ISSN: 0165–9936. DOI: `https://doi.org/10.1016/j.trac.2016.12.008`. URL: `http://www.sciencedirect.com/science/article/pii/S0165993616301868` (cit. on p. 76).

[465] Naoki Nakamura and Yutaka Amao. “Optical Sensor for Carbon Dioxide Combining Colorimetric Change of a pH Indicator and a Reference Luminescent Dye”. In: *Analytical and bioanalytical chemistry* 376 (Aug. 2003), pp. 642–646. DOI: `10.1007/s00216-003-1949-3` (cit. on pp. 76, 96, 138).

[466] Yutaka Amao and Naoki Nakamura. “Optical CO2 Sensor With the Combination of Colorimetric Change of α-naphtholphthalein and Internal Reference Fluorescent Porphyrin Dye”. In: *Sensors and Actuators B: Chemical* 100 (May 2004), pp. 347–351. DOI: `10.1016/j.snb.2004.02.003` (cit. on pp. 76, 93, 96, 138).

[467] Yutaka Amao and Naoki Nakamura. “An Optical Sensor With the Combination of Colorimetric Change of α-naphtholphthalein and Internal Reference Luminescent Dye for CO2 in Water”. In: *Sensors and Actuators B-chemical - SENSOR ACTUATOR B-CHEM* 107 (June 2005), pp. 861–865. DOI: `10.1016/j.snb.2004.12.028` (cit. on pp. 76, 96, 138).

[468] Yutaka Amao and Tasuku Komori. “Optical CO2 Sensor of the Combination of Colorimetric Change of α-naphtholphthalein in poly(isobutyl methacrylate) and Fluorescent Porphyrin in Polystyrene”. In: *Talanta* 66 (June 2005), pp. 976–981. DOI: `10.1016/j.talanta.2004.12.058` (cit. on pp. 76, 77, 93, 138, 142).

[469] I. M. Pérez de Vargas-Sansalvador et al. “Phosphorescent Sensing of Carbon Dioxide Based on Secondary Inner-Filter Quenching”. In: *Analytica Chimica Acta* 655.1 (Nov. 2009), pp. 66–74. ISSN: 0003-2670. URL: `http://www.sciencedirect.com/science/article/pii/S0003267009013051` (cit. on pp. 76, 77, 96, 125, 126, 138).

[470] M. L. Aguayo-López, L. F. Capitán-Vallvey, and M. D. Fernández-Ramos. “Optical Sensor for Carbon Dioxide Gas Determination, Characterization and Improvements”. In: *Talanta* 126 (Aug. 2014), pp. 196–201. ISSN: 0039-9140. URL: `http://www.sciencedirect.com/science/article/pii/S0039914014002409` (cit. on pp. 76, 77, 96, 97, 136, 138, 147).

[471] M. D. Fernández-Ramos et al. “Ionic Liquids on Optical Sensors for Gaseous Carbon Dioxide”. In: *Analytical and Bioanalytical Chemistry* 410.23 (Sept. 2018), pp. 5931–5939. ISSN: 1618-2650. DOI: `10.1007/s00216-018-1214-4`. URL: `https://doi.org/10.1007/s00216-018-1214-4` (cit. on pp. 76, 77, 86, 96, 125, 126, 138, 146, 158).

[472] M D Fernández-Ramos et al. “NIR Optical Carbon Dioxide Gas Sensor Based on Simple azaBODIPY pH Indicators”. In: *The Analyst* 144 (May 2019), pp. 3870–3877. DOI: `10.1039/C9AN00432G` (cit. on pp. 76, 77, 86, 137, 138, 142).

[473] Christoph von Bültzingslöwen et al. “Sol-gel Based Optical Carbon Dioxide Sensor Employing Dual Luminophore Referencing for Application in Food Packaging Technology”. In: *The Analyst* 127 (Dec. 2002), pp. 1478–1483. DOI: `10.1039/B207438A` (cit. on pp. 76, 77, 98, 100, 103, 125, 129, 131, 133, 138, 139).

[474] Conor S. Burke et al. “Development of an Optical Sensor Probe for the Detection of Dissolved Carbon Dioxide”. In: *Sensors and Actuators B: Chemical* 119.1 (2006), pp. 288–294. ISSN: 0925-4005. DOI: `https://doi.org/10.1016/j.snb.2005.12.022`. URL: `http://www.sciencedirect.com/science/article/pii/S0925400505009858` (cit. on pp. 76, 98, 100, 125, 133, 138, 158).

[475] Merima Cajlakovic, Alessandro Bizzarri, and Volker Ribitsch. “Luminescence Lifetime-Based Carbon Dioxide Optical Sensor for Clinical Applications”. In: *Analytica Chimica Acta* 573-574 (2006). Instrumental Methods of Analysis -IMA 2005, pp. 57–64. ISSN: 0003-2670. DOI: `https://doi.org/10.1016/j.aca.2006.05.085`. URL: `http://www.sciencedirect.com/science/article/pii/S0003267006011536` (cit. on pp. 76, 77, 98, 100, 101, 125, 126, 131, 133, 138, 147).

[476] Eva Fritzsche et al. “Highly Sensitive Poisoning-Resistant Optical Carbon Dioxide Sensors for Environmental Monitoring”. In: *Anal. Methods* 9 (1 2017), pp. 55–65. DOI: `10.1039/C6AY02949C`. URL: `http://dx.doi.org/10.1039/C6AY02949C` (cit. on pp. 76, 77, 98, 138, 142).

[477] Christoph Staudinger et al. “A Versatile Optode System for Oxygen, Carbon Dioxide, and pH Measurements in Seawater With Integrated Battery and Logger”. In: *Limnology and Oceanography: Methods* 16.7 (2018), pp. 459–473. DOI: `10.1002/lom3.10260` (cit. on pp. 76, 98, 103, 138).

[478] David Pfeifer et al. “Green to Red Emitting BODIPY Dyes for Fluorescent Sensing and Imaging of Carbon Dioxide”. In: *Sensors and Actuators B: Chemical* 304 (2020), p. 127312. ISSN: 0925–4005. DOI: `https://doi.org/10.1016/j.snb.2019.127312`. URL: `http://www.sciencedirect.com/science/article/pii/S0925400519315114` (cit. on pp. 76, 98, 99, 126, 138).

[479] Joseph R. Lakowicz, Henryk Szmacinski, and Mutlu Karakelle. “Optical Sensing of pH and pCO2 Using Phase-Modulation Fluorimetry and Resonance Energy Transfer”. In: *Analytica Chimica Acta* 272.2 (1993), pp. 179–186. ISSN: 0003-2670. DOI: `https://doi.org/10.1016/0003-2670(93)80567-5`. URL: `http://www.sciencedirect.com/science/article/pii/0003267093805675` (cit. on pp. 76, 95, 97).

[480] Gerhard Neurauter, Ingo Klimant, and Otto S. Wolfbeis. “Microsecond Lifetime-Based Optical Carbon Dioxide Sensor Using Luminescence Resonance Energy Transfer”. In: *Analytica Chimica Acta* 382.1 (1999), pp. 67–75. ISSN: 0003-2670. DOI: `https://doi.org/10.1016/S0003-2670(98)00748-X`. URL: `http://www.sciencedirect.com/science/article/pii/S000326709800748X` (cit. on pp. 76, 93, 97, 138, 147).

[481] Bernard Valeur. “Resonance Energy Transfer and Its Applications”. In: *Molecular Fluorescence*. John Wiley and Sons, Ltd, 2001. Chap. 9, pp. 247–272. ISBN: 9783527600243. DOI: `10.1002/3527600248.ch9`. eprint: `https://onlinelibrary.wiley.com/doi/pdf/10.1002/3527600248.ch9`. URL: `https://onlinelibrary.wiley.com/doi/abs/10.1002/3527600248.ch9` (cit. on pp. 76, 97).

[482] Christoph von Bültzingslöwen et al. "Lifetime-Based Optical Sensor for High-Level pCO2 Detection Employing Fluorescence Resonance Energy Transfer". In: *Analytica Chimica Acta* 480.2 (2003), pp. 275–283. ISSN: 0003-2670. DOI: `https://doi.org/10.1016/S0003-2670(02)01653-7`. URL: `http://www.sciencedirect.com/science/article/pii/S0003267002016537` (cit. on pp. 76, 97, 138).

[483] Otto S. Wolfbeis. "Materials for Fluorescence-Based Optical Chemical Sensors". In: *J. Mater. Chem.* 15 (27-28 2005), pp. 2657–2669. DOI: `10.1039/B501536G`. URL: `http://dx.doi.org/10.1039/B501536G` (cit. on pp. 76, 93, 131).

[484] Hans Kautsky. "Quenching of Luminescence by Oxygen". In: *Trans. Faraday Soc.* 35 (1939), pp. 216–219. DOI: `10.1039/TF9393500216`. URL: `http://dx.doi.org/10.1039/TF9393500216` (cit. on p. 77).

[485] J. R. Lakowicz and G. Weber. "Quenching of Fluorescence by Oxygen. A Probe for Structural Fluctuations in Macromolecules". In: *Biochemistry* 12.21 (Oct. 1973), pp. 4161–4170. ISSN: 0006-2960. DOI: `10.1021/bi00745a020`. URL: `https://doi.org/10.1021/bi00745a020` (cit. on p. 77).

[486] Christian Huber et al. "Optical Sensor for Seawater Salinity". In: *Fresenius' Journal of Analytical Chemistry* 368.2 (Sept. 2000), pp. 196–202. ISSN: 1432-1130. DOI: `10.1007/s002160000493`. URL: `https://doi.org/10.1007/s002160000493` (cit. on p. 77).

[487] Yangzi Zheng et al. "Miniature pH Optical Fiber Sensor Based on Fabry-Perot Interferometer". In: *IEEE Journal of Selected Topics in Quantum Electronics* 22 (Jan. 2015). DOI: `10.1109/JSTQE.2015.2497438` (cit. on p. 78).

[488] W. Ma et al. "Optical Fiber Fabry–Perot Interferometric CO2 Gas Sensor Using Guanidine Derivative Polymer Functionalized Layer". In: *IEEE Sensors Journal* 18.5 (2018), pp. 1924–1929. DOI: `10.1109/JSEN.2018.2790973` (cit. on p. 78).

[489] Sully Quintero et al. "Swelling and Morphological Properties of poly(vinyl alcohol) (PVA) and poly(acrylic acid) (PAA) Hydrogels in Solution With High Salt Concentration". In: *Polymer* 51 (Feb. 2010), pp. 953–958. DOI: `10.1016/j.polymer.2009.12.016` (cit. on p. 78).

[490] K. O. Hill and G. Meltz. "Fiber Bragg Grating Technology Fundamentals and Overview". In: *Journal of Lightwave Technology* 15.8 (1997), pp. 1263–1276. DOI: `10.1109/50.618320` (cit. on p. 78).

[491] S. Herber et al. "Exploitation of a pH-Sensitive Hydrogel Disk for CO2 Detection". In: *Sensors and Actuators B: Chemical* 103.1 (Sept. 2004), pp. 284–289. ISSN: 0925-4005. URL: `http://www.sciencedirect.com/science/article/pii/S0925400504002473` (cit. on p. 78).

[492] Pengbing Hu et al. "Photonic Crystal Fiber Interferometric pH Sensor Based on Polyvinyl Alcohol / Polyacrylic Acid Hydrogel Coating". In: *Applied Optics* 54 (Apr. 2015). DOI: `10.1364/AO.54.002647` (cit. on p. 78).

[493] Jiri Hromadka et al. "Carbon Dioxide Measurements Using Long Period Grating Optical Fibre Sensor Coated With Metal Organic Framework HKUST-1". In: *Sensors and Actuators B: Chemical* 255 (Feb. 2018), pp. 2483–2494. ISSN: 0925-4005. URL: `http://www.sciencedirect.com/science/article/pii/S0925400517317069` (cit. on pp. 78, 86).

[494] Luis Melo et al. "Highly Sensitive Coated Long Period Grating Sensor for CO2 Detection at Atmospheric Pressure". In: *Sensors and Actuators B: Chemical* 202 (Oct. 2014), pp. 294–300. DOI: `10.1016/j.snb.2014.05.062` (cit. on pp. 78, 86).

[495] X. Chong et al. "Ultrashort Near-Infrared Fiber-Optic Sensors for Carbon Dioxide Detection". In: *IEEE Sensors Journal* 15.9 (2015), pp. 5327–5332. DOI: `10.1109/JSEN.2015.2438063` (cit. on pp. 78, 86).

[496] Alan D. Kersey. "Multiplexed fiber optic sensors". In: *Distributed and Multiplexed Fiber Optic Sensors II.* Ed. by John P. Dakin and Alan D. Kersey. Vol. 1797. International Society for Optics and Photonics. SPIE, 1993, pp. 161–185. DOI: `10.1117/12.141286`. URL: `https://doi.org/10.1117/12.141286` (cit. on p. 79).

[497] R. A. Perez-Herrera and M. Lopez-Amo. "Fiber Optic Sensor Networks". In: *Optical Fiber Technology* 19.6, Part B (Dec. 2013), pp. 689–699. ISSN: 1068-5200. URL: `https://www.sciencedirect.com/science/article/pii/S1068520013000941` (cit. on p. 79).

[498] W. Hotan, W. Göpel, and R. Haul. "Interaction of CO2 and CO with Nonpolar Zinc Oxide Surfaces". In: *Surface Science* 83.1 (Apr. 1979), pp. 162–180. ISSN: 0039-6028. URL: `http://www.sciencedirect.com/science/article/pii/0039602879904862` (cit. on p. 79).

[499] C. T. Au, W. Hirsch, and W. Hirschwald. "Adsorption and Interaction of Carbon Dioxide, Formic Acid and Hydrogen/Carbon Dioxide Mixtures on (1010) Zinc Oxide Surfaces Studied by Photoelectron Spectroscopy (XPS and UPS)". In: *Surface Science* 199.3 (1988), pp. 507–517. ISSN: 0039-6028. URL: `http://www.sciencedirect.com/science/article/pii/0039602888909181` (cit. on p. 79).

[500] H.-J. Freund and M. W. Roberts. "Surface Chemistry of Carbon Dioxide". In: *Surface Science Reports* 25.8 (Jan. 1996), pp. 225–273. ISSN: 0167-5729. URL: `http://www.sciencedirect.com/science/article/pii/S0167572996000076` (cit. on p. 79).

[501] O. Seiferth et al. "IR Investigations of CO2 Adsorption on Chromia Surfaces: Cr2O3 (0001)/Cr(110) Versus Polycrystalline α-Cr2O3". In: *Surface Science* 421.1 (Feb. 1999), pp. 176–190. ISSN: 0039-6028. URL: `http://www.sciencedirect.com/science/article/pii/S0039602898008577` (cit. on p. 79).

[502] João Batista Lopes Martins et al. "The Interaction of H2, CO, CO2, H2O and NH3 on ZnO Surfaces: an Oniom Study". In: *Chemical Physics Letters* 400.4 (Dec. 2004), pp. 481–486. ISSN: 0009-2614. URL: `http://www.sciencedirect.com/science/article/pii/S000926140401704X` (cit. on p. 79).

[503] J. Herrán, G. G Mandayo, and E. Castaño. "Semiconducting BaTiO3-CuO Mixed Oxide Thin Films for CO2 Detection". In: *Thin Solid Films* 517.22 (Sept. 2009), pp. 6192–6197. ISSN: 0040-6090. URL: `http://www.sciencedirect.com/science/article/pii/S0040609009007275` (cit. on pp. 79, 86).

[504] Heshmat Noei et al. "Activation of Carbon Dioxide on ZnO Nanoparticles Studied by Vibrational Spectroscopy". In: *The Journal of Physical Chemistry C* 115.4 (Feb. 2011), pp. 908–914. ISSN: 1932-7447. DOI: `10.1021/jp102751t`. URL: `https://doi.org/10.1021/jp102751t` (cit. on p. 79).

[505] Qian-Lin Tang and Qing-Hong Luo. "Adsorption of CO2 at ZnO: A Surface Structure Effect From DFT+U Calculations". In: *The Journal of Physical Chemistry C* 117.44 (Nov. 2013), pp. 22954–22966. ISSN: 1932-7447. DOI: `10.1021/jp407970a`. URL: `https://doi.org/10.1021/jp407970a` (cit. on pp. 79, 162).

[506] A. B. Usseinov et al. "The First Principles Calculations of CO2 Adsorption on (1010) ZnO Surface". In: *AIP Conference Proceedings* 2174.1 (2019), p. 020181. DOI: `10.1063/1.5134332`. eprint: `https://aip.scitation.org/doi/pdf/10.1063/1.5134332`. URL: `https://aip.scitation.org/doi/abs/10.1063/1.5134332` (cit. on pp. 79, 162).

[507] Aruni Gankanda, David M. Cwiertny, and Vicki H. Grassian. "Role of Atmospheric CO2 and H2O Adsorption on ZnO and CuO Nanoparticle Aging: Formation of New Surface Phases and the Impact on Nanoparticle Dissolution". In: *The Journal of Physical Chemistry C* 120.34 (Sept. 2016), pp. 19195–19203. ISSN: 1932-7447. DOI: `10.1021/acs.jpcc.6b05931`. URL: `https://doi.org/10.1021/acs.jpcc.6b05931` (cit. on pp. 79, 80).

[508] Hakan Çolak and Ercan Karaköse. "Synthesis and Characterization of Different Dopant (Ge, Nd, W)-Doped ZnO Nanorods and Their CO2 Gas Sensing Applications". In: *Sensors and Actuators B: Chemical* 296 (Oct. 2019), p. 126629. ISSN: 0925-4005. URL: `http://www.sciencedirect.com/science/article/pii/S092540051930824X` (cit. on pp. 79, 80).

[509] Mario Enrique Álvarez-Ramos et al. "Room Temperature CO2 Sensing Using Au-Decorated ZnO Nanorods Deposited on an Optical Fiber". In: *Materials Science and Engineering: B* 262 (Dec. 2020), p. 114720. ISSN: 0921-5107. URL: `http://www.sciencedirect.com/science/article/pii/S0921510720302270` (cit. on pp. 79, 80).

[510] Padmanathan Karthick Kannan, Ramiah Saraswathi, and John Bosco Balaguru Rayappan. "CO2 Gas Sensing Properties of DC Reactive Magnetron Sputtered ZnO Thin Film". In: *Ceramics International* 40.8, Part B (Sept. 2014), pp. 13115–13122. ISSN: 0272-8842. URL: `http://www.sciencedirect.com/science/article/pii/S0272884214007342` (cit. on p. 79).

[511] Andrea Haeusler and Jörg-Uwe Meyer. "A Novel Thick Film Conductive Type CO2 Sensor". In: *Sensors and Actuators B: Chemical* 34.1 (1996), pp. 388–395. ISSN: 0925-4005. DOI: `https://doi.org/10.1016/S0925-4005(96)01847-3`. URL: `http://www.sciencedirect.com/science/article/pii/S0925400596018473` (cit. on pp. 79, 80, 86).

[512] Y.-J. Jeong, C. Balamurugan, and D.-W. Lee. "Enhanced CO2 Gas-Sensing Performance of ZnO Nanopowder by La Loaded During Simple Hydrothermal Method". In: *Sensors and Actuators B: Chemical* 229 (June 2016), pp. 288–296. ISSN: 0925-4005. URL: `http://www.sciencedirect.com/science/article/pii/S0925400515306754` (cit. on pp. 79, 86).

[513] R. Dhahri et al. "Enhanced Performance of Novel Calcium / Aluminum Co-Doped Zinc Oxide for CO2 Sensors". In: *Sensors and Actuators B: Chemical* 239 (Feb. 2017), pp. 36–44. ISSN: 0925-4005. URL: `http://www.sciencedirect.com/science/article/pii/S0925400516311996` (cit. on p. 79).

[514] Abhishek Ghosh et al. "CO2 Sensing Behavior of Calcium-Doped ZnO Thin Film: A Study To Address the Cross-Sensitivity of CO2 in H2 and CO Environment". In: *Langmuir* 35.32 (Aug. 2019), pp. 10267–10275. ISSN: 0743-7463. DOI: `10.1021/acs.langmuir.9b00724`. URL: `https://doi.org/10.1021/acs.langmuir.9b00724` (cit. on pp. 79, 80).

[515] Leon Cavanagh and Russell Binions. "BaSnO3 Thick Film as a Carbon Dioxide Sensor". In: *Journal of the Electrochemical Society* 159 (Oct. 2011), pp. 1006–1009. DOI: `10.1109/ICSENS.2011.6126930` (cit. on p. 79).

[516] Gang Chen et al. "Lanthanum Dioxide Carbonate La2O2CO3 Nanorods as a Sensing Material for Chemoresistive CO2 Gas Sensor". In: *Electrochimica Acta* 127 (May 2014), pp. 355–361. ISSN: 0013-4686. URL: `http://www.sciencedirect.com/science/article/pii/S0013468614003776` (cit. on p. 79).

[517] Mohamed A. Basyooni, Mohamed Shaban, and Adel M. El Sayed. "Enhanced Gas Sensing Properties of Spin-coated Na-doped ZnO Nanostructured Films". In: *Scientific Reports* 7.1 (Feb. 2017), p. 41716. ISSN: 2045-2322. DOI: `10.1038/srep41716`. URL: `https://doi.org/10.1038/srep41716` (cit. on pp. 79, 80).

[518] Boshra Ghanbari Shohany, Leili Motevalizadeh, and Majid Ebrahimizadeh Abrishami. "Investigation of ZnO Thin-Film Sensing Properties for CO2 Detection: Effect of Mn Doping". In: *Journal of Theoretical and Applied Physics* 12.3 (Sept. 2018), pp. 219–225. ISSN: 2251-7235. DOI: `10.1007/s40094-018-0302-3` (cit. on p. 79).

[519] Tatsumi Ishihara et al. "Capacitive-Type Gas Sensor for the Selective Detection of Carbon Dioxide". In: *Sensors and Actuators B: Chemical* 13.1 (May 1993), pp. 470–472. ISSN: 0925-4005. URL: `http://www.sciencedirect.com/science/article/pii/092540059385429E` (cit. on pp. 79, 80, 86).

[520] H. Shokry Hassan et al. "Synthesis, Characterization and Fabrication of Gas Sensor Devices Using ZnO and ZnO:In Nanomaterials". In: *Beni-Suef University Journal of Basic and Applied Sciences* 3.3 (Sept. 2014), pp. 216–221. ISSN: 2314-8535. URL: `http://www.sciencedirect.com/science/article/pii/S2314853514000572` (cit. on p. 79).

[521] Nauman Bin Tanvir et al. "Work Function Based CO2 Gas Sensing Using Metal Oxide Nanoparticles at Room Temperature". In: *Materials Today: Proceedings* 2.8 (Jan. 2015), pp. 4190–4195. ISSN: 2214-7853. URL: `http://www.sciencedirect.com/science/article/pii/S2214785315007865` (cit. on p. 80).

[522] N. B. Tanvir, O. Yurchenko, and G. Urban. "Optimization Study for Work Function Based CO2 Sensing Using CuO-nanoparticles in Respect to Humidity and Temperature". In: *Procedia Engineering* 120 (Jan. 2015), pp. 667–670. ISSN: 1877-7058. URL: `http://www.sciencedirect.com/science/article/pii/S1877705815023693` (cit. on p. 80).

[523] Tatsumi Ishihara et al. "Improved Sensitivity of CuO–BaTiO3 Capacitive-Type CO2 Sensor by Additives". In: *Sensors and Actuators B: Chemical* 28.1 (July 1995), pp. 49–54. ISSN: 0925-4005. URL: `http://www.sciencedirect.com/science/article/pii/092540059401539T` (cit. on pp. 80, 86).

[524] G. Heiland. "Homogeneous Semiconducting Gas Sensors". In: *Sensors and Actuators* 2 (Jan. 1981), pp. 343–361. ISSN: 0250-6874. URL: `https://www.sciencedirect.com/science/article/pii/0250687481800558` (cit. on p. 80).

[525] W. M. Sears, K. Colbow, and F. Consadori. "General Characteristics of Thermally Cycled Tin Oxide Gas Sensors". In: *Semiconductor Science and Technology* 4.5 (May 1989), pp. 351–359. DOI: `10.1088/0268-1242/4/5/004`. URL: `https://doi.org/10.1088/0268-1242/4/5/004` (cit. on p. 80).

[526] Satoshi Nakata et al. "Detection and Quantification of CO Gas Based on the Dynamic Response of a Ceramic Sensor". In: *Chemistry Letters* 20.9 (1991), pp. 1505–1508. DOI: `10.1246/cl.1991.1505`. eprint: `https://doi.org/10.1246/cl.1991.1505`. URL: `https://doi.org/10.1246/cl.1991.1505` (cit. on p. 80).

[527] Stanislaw Wlodek, Konrad Colbow, and Franco Consadori. "Signal-Shape Analysis of a Thermally Cycled Tin-Oxide Gas Sensor". In: *Sensors and Actuators B: Chemical* 3.1 (1991), pp. 63–68. ISSN: 0925-4005. URL: `https://www.sciencedirect.com/science/article/pii/0925400591850087` (cit. on p. 80).

[528] Yukio Hiranaka, T. Abe, and Hiroshi Murata. "Gas-Dependent Response in the Temperature Transient of SnO2 Gas Sensors". In: *Sensors and Actuators B-chemical* 9 (1992), pp. 177–182 (cit. on p. 80).

[529] Satoshi Nakata et al. "Gas Sensing Based on a Nonlinear Response: Discrimination Between Hydrocarbons and Quantification of Individual Components in a Gas Mixture". In: *Analytical Chemistry* 68.13 (July 1996), pp. 2067–2072. ISSN: 0003-2700. DOI: `10.1021/ac9510954`. URL: `https://doi.org/10.1021/ac9510954` (cit. on p. 80).

[530] Andrew P. Lee and Brian J. Reedy. "Temperature Modulation in Semiconductor Gas Sensing". In: *Sensors and Actuators B: Chemical* 60.1 (Nov. 1999), pp. 35–42. ISSN: 0925-4005. URL: `https://www.sciencedirect.com/science/article/pii/S0925400599002415` (cit. on p. 80).

[531] Alexander Vergara et al. "Optimized Feature Extraction for Temperature-Modulated Gas Sensors". In: *Journal of Sensors* 2009 (June 2009), p. 716316. ISSN: 1687-725X. DOI: `10.1155/2009/716316`. URL: `https://doi.org/10.1155/2009/716316` (cit. on p. 80).

[532] Rakesh Gosangi and Ricardo Gutierrez-Osuna. "Active Temperature Modulation of Metal-Oxide Sensors for Quantitative Analysis of Gas Mixtures". In: *Sensors and Actuators B: Chemical* 185 (Aug. 2013), pp. 201–210. ISSN: 0925-4005. URL: `https://www.sciencedirect.com/science/article/pii/S0925400513004899` (cit. on p. 80).

[533] A. Vergara et al. "Quantitative Gas Mixture Analysis Using Temperature-Modulated Micro-Hotplate Gas Sensors: Selection and Validation of the Optimal Modulating Frequencies". In: *Sensors and Actuators B: Chemical* 123.2 (May 2007), pp. 1002–1016. ISSN: 0925-4005. URL: `https://www.sciencedirect.com/science/article/pii/S0925400506007556` (cit. on p. 80).

[534] Stéphanie Madrolle, Pierre Grangeat, and Christian Jutten. "A Linear-Quadratic Model for the Quantification of a Mixture of Two Diluted Gases With a Single Metal Oxide Sensor". In: *Sensors* 18.6 (2018). ISSN: 1424-8220. DOI: `10.3390/s18061785`. URL: `https://www.mdpi.com/1424-8220/18/6/1785` (cit. on p. 80).

[535] Nak-Jin Choi et al. "Classification of Workplace Gases Using Temperature Modulation of Two SnO2 Sensing Films on Substrate". In: *Sensors and Actuators B: Chemical* 86.2 (Sept. 2002), pp. 251–258. ISSN: 0925-4005. URL: `https://www.sciencedirect.com/science/article/pii/S092540050200196X` (cit. on p. 80).

[536] J. K. Radhakrishnan, M. Kumara, and Geetika. "Effect of Temperature Modulation, on the Gas Sensing Characteristics of ZnO Nanostructures, for Gases O2, CO and CO2". In: *Sensors International* 2 (Jan. 2021), p. 100059. ISSN: 2666-3511. URL: `https://www.sciencedirect.com/science/article/pii/S2666351120300590` (cit. on p. 80).

[537] Noritaka Mizuno et al. "CO2-Sensing Characteristics of SnO2 Element Modified by La2O3". In: *Sensors and Actuators B: Chemical* 13.1 (May 1993), pp. 473–475. ISSN: 0925-4005. URL: `http://www.sciencedirect.com/science/article/pii/092540059385430I` (cit. on pp. 80, 86).

[538] Tatsumi Ishihara et al. "Application of Mixed Oxide Capacitor to the Selective Carbon Dioxide Sensor: I . Measurement of Carbon Dioxide Sensing Characteristics". In: *Journal of The Electrochemical Society* 138.1 (Jan. 1991), pp. 173–176. ISSN: 0013-4651. DOI: `10.1149/1.2085530`. URL: `https://doi.org/10.1149/1.2085530` (cit. on p. 80).

[539] G. Korotcenkov and B. K. Cho. “Metal Oxide Composites in Conductometric Gas Sensors: Achievements and Challenges”. In: *Sensors and Actuators B: Chemical* 244 (June 2017), pp. 182–210. ISSN: 0925-4005. URL: `https://www.sciencedirect.com/science/article/pii/S0925400516320895` (cit. on p. 80).

[540] Kazi Rafsanjani Amin and Aveek Bid. “Graphene as a Sensor”. In: *Current Science* 107.3 (2014), pp. 430–436. ISSN: 00113891. URL: `http://www.jstor.org/stable/24103495` (cit. on p. 80).

[541] Eric Singh, M. Meyyappan, and Hari Singh Nalwa. “Flexible Graphene-Based Wearable Gas and Chemical Sensors”. In: *ACS Applied Materials & Interfaces* 9.40 (Oct. 2017), pp. 34544–34586. ISSN: 1944-8244. DOI: `10.1021/acsami.7b07063`. URL: `https://doi.org/10.1021/acsami.7b07063` (cit. on p. 80).

[542] Hyeun Joong Yoon et al. “Carbon Dioxide Gas Sensor Using a Graphene Sheet”. In: *Sensors and Actuators B: Chemical* 157.1 (Sept. 2011), pp. 310–313. ISSN: 0925-4005. URL: `https://www.sciencedirect.com/science/article/pii/S0925400511002310` (cit. on pp. 80, 86).

[543] Yong Zhou et al. “Gas Sensors for CO2 Detection Based on RGO–PEI Films at Room Temperature”. In: *Chinese Science Bulletin* 59.17 (June 2014), pp. 1999–2005. ISSN: 1861-9541. DOI: `10.1007/s11434-014-0253-2`. URL: `https://doi.org/10.1007/s11434-014-0253-2` (cit. on p. 80).

[544] Fowzia Akhter et al. “Graphene Oxide (GO) Coated Impedimetric Gas Sensor for Selective Detection of Carbon Dioxide (CO₂) With Temperature and Humidity Compensation”. In: *IEEE Sensors Journal* 21.4 (2021), pp. 4241–4249. DOI: `10.1109/JSEN.2020.3035795` (cit. on pp. 80, 86, 88).

[545] Ganhua Lu, Leonidas E. Ocola, and Junhong Chen. “Reduced Graphene Oxide for Room-Temperature Gas Sensors”. In: *Nanotechnology* 20.44 (Oct. 2009), p. 445502. ISSN: 0957-4484. DOI: `10.1088/0957-4484/20/44/445502`. URL: `https://doi.org/10.1088/0957-4484/20/44/445502` (cit. on p. 80).

[546] Manoharan Muruganathan et al. “Electrically Tunable van der Waals Interaction in Graphene–Molecule Complex”. In: *Nano Letters* 15.12 (Dec. 2015), pp. 8176–8180. ISSN: 1530-6984. DOI: `10.1021/acs.nanolett.5b03653`. URL: `https://doi.org/10.1021/acs.nanolett.5b03653` (cit. on p. 80).

[547] Jian Sun, Manoharan Muruganathan, and Hiroshi Mizuta. “Room Temperature Detection of Individual Molecular Physisorption Using Suspended Bilayer Graphene”. In: *Science Advances* 2.4 (2016), e1501518. DOI: `10.1126/sciadv.1501518`. eprint: `https://www.science.org/doi/pdf/10.1126/sciadv.1501518`. URL: `https://www.science.org/doi/abs/10.1126/sciadv.1501518` (cit. on p. 80).

[548] Gugang Chen, Tereza M. Paronyan, and Avetik R. Harutyunyan. “Sub-ppt Gas Detection With Pristine Graphene”. In: *Applied Physics Letters* 101.5 (July 2012), p. 053119. ISSN: 0003-6951. DOI: `10.1063/1.4742327`. URL: `https://doi.org/10.1063/1.4742327` (cit. on p. 80).

[549] Anderson D. Smith et al. “Graphene-Based CO2 Sensing and its Cross-Sensitivity With Humidity”. In: *RSC Advances* 7.36 (2017), pp. 22329–22339. DOI: `10.1039/C7RA02821K`. URL: `https://doi.org/10.1039/C7RA02821K` (cit. on p. 80).

[550] Xuge Fan et al. “Humidity and CO2 Gas Sensing Properties of Double-Layer Graphene”. In: *Carbon* 127 (Feb. 2018), pp. 576–587. ISSN: 0008-6223. URL: `https://www.sciencedirect.com/science/article/pii/S0008622317311521` (cit. on p. 80).

[551] Shrouk E. Zaki et al. “Role of Oxygen Vacancies in Vanadium Oxide and Oxygen Functional Groups in Graphene Oxide for Room Temperature CO2 Gas Sensors”. In: *Sensors and Actuators A: Physical* 294 (Aug. 2019), pp. 17–24. ISSN: 0924-4247. URL: `https://www.sciencedirect.com/science/article/pii/S0924424719304819` (cit. on p. 80).

[552] K. R. Nemade and S. A. Waghuley. “Highly Responsive Carbon Dioxide Sensing by Graphene / Al2O3 Quantum Dots Composites at Low Operable Temperature”. In: *Indian Journal of Physics* 88.6 (June 2014), pp. 577–583. ISSN: 0974-9845. DOI: `10.1007/s12648-014-0454-1`. URL: `https://doi.org/10.1007/s12648-014-0454-1` (cit. on p. 80).

[553] K. R. Nemade and S. A. Waghuley. "Role of Defects Concentration on Optical and Carbon Dioxide Gas Sensing Properties of Sb2O3 / Graphene composites". In: *Optical Materials* 36.3 (Jan. 2014), pp. 712–716. ISSN: 0925-3467. URL: `https://www.sciencedirect.com/science/article/pii/S092534671300623X` (cit. on p. 80).

[554] M. Amarnath and K. Gurunathan. "Highly Selective CO2 Gas Sensor Using Stabilized NiO-In2O3 Nanospheres Coated Reduced Graphene Oxide Sensing Electrodes at Room Temperature". In: *Journal of Alloys and Compounds* 857 (Mar. 2021), p. 157584. ISSN: 0925-8388. URL: `https://www.sciencedirect.com/science/article/pii/S0925838820339487` (cit. on p. 80).

[555] Mohamed Shaban, Saber Ali, and Mohamed Rabia. "Design and Application of Nanoporous Graphene Oxide Film for CO2, H2, and C2H2 Gases Sensing". In: *Journal of Materials Research and Technology* 8.5 (Sept. 2019), pp. 4510–4520. ISSN: 2238-7854. URL: `https://www.sciencedirect.com/science/article/pii/S223878541831370X` (cit. on pp. 80, 86).

[556] Sergey Rumyantsev et al. "Selective Gas Sensing with a Single Pristine Graphene Transistor". In: *Nano Letters* 12.5 (May 2012), pp. 2294–2298. ISSN: 1530-6984. DOI: `10.1021/nl3001293`. URL: `https://doi.org/10.1021/nl3001293` (cit. on p. 80).

[557] M. Gauthier and A. Chamberland. "Solid-State Detectors for the Potentiometric Determination of Gaseous Oxides: I . Measurement in Air". In: *Journal of The Electrochemical Society* 124.10 (Oct. 1977), pp. 1579–1583. DOI: `10.1149/1.2133113`. URL: `https://doi.org/10.1149%2F1.2133113` (cit. on p. 81).

[558] Toshio Maruyama, Seihiro Sasaki, and Yasutoshi Saito. "Potentiometric Gas Sensor for Carbon Dioxide Using Solid Electrolytes". In: *Solid State Ionics* 23.1 (Mar. 1987), pp. 107–112. ISSN: 0167-2738. URL: `http://www.sciencedirect.com/science/article/pii/0167273887900889` (cit. on p. 81).

[559] Toshio Maruyama et al. "Potentiometric Sensor for Sulfur Oxides Using NASICON as a Solid Electrolyte". In: *Solid State Ionics* 17.4 (Nov. 1985), pp. 281–286. ISSN: 0167-2738. DOI: `10.1016/0167-2738(85)90072-4` (cit. on p. 81).

[560] Shotaro Kishi et al. "A Stable Solid-Reference Electrode of BiCuVOx/Perovskite-Oxide for Potentiometric Solid Electrolyte CO2 Sensor". In: *Journal of The Ceramic Society of Japan* 115 (Nov. 2007), pp. 706–711. DOI: `10.2109/jcersj2.115.706` (cit. on pp. 81, 82).

[561] Heng-Yao Dang and Xing-Min Guo. "Characteristics and Performance of NASICON-Based CO2 Sensor Using Bi8Nb2O17 plus Pt as Solid-Reference Electrode". In: *Sensors and Actuators B: Chemical* 178 (Mar. 2013), pp. 163–168. DOI: `10.1016/j.snb.2012.12.084` (cit. on p. 81).

[562] Inhee Lee, Sheikh A. Akbar, and Prabir K. Dutta. "High Temperature Potentiometric Carbon Dioxide Sensor With Minimal Interference to Humidity". In: *Sensors and Actuators B: Chemical* 142.1 (Oct. 2009), pp. 337–341. ISSN: 0925-4005. URL: `http://www.sciencedirect.com/science/article/pii/S092540050900584X` (cit. on pp. 81, 82, 86).

[563] Inhee Lee and Sheikh A. Akbar. "Potentiometric Carbon Dioxide Sensor Based on Thin Li3PO4 Electrolyte and Li2CO3 Sensing Electrode". In: *Ionics* 20.4 (Apr. 2014), pp. 563–569. ISSN: 1862-0760. DOI: `10.1007/s11581-013-1013-z`. URL: `https://doi.org/10.1007/s11581-013-1013-z` (cit. on pp. 81, 82, 86).

[564] Hyung Kun Lee et al. "Durability Improvement of Solid Electrolyte CO2 Sensor Against Humidity Variations". In: *Journal of Nanoscience and Nanotechnology* 15 (Sept. 2015), pp. 404–407. DOI: `10.1166/jnn.2015.8360` (cit. on pp. 81, 82).

[565] Kenji Obata et al. "Influences of Water Vapor on NASICON-Based CO2 Sensor Operative at Room Temperature". In: *Sensors and Actuators B-chemical - SENSOR ACTUATOR B-CHEM* 93 (Aug. 2003), pp. 243–249. DOI: `10.1016/S0925-4005(03)00177-1` (cit. on pp. 81, 82).

[566] Tetsuya Kida et al. "NASICON Thick Film-Based CO2 Sensor Prepared by a Sol–Gel Method". In: *Sensors and Actuators B: Chemical* 80.1 (Nov. 2001), pp. 28–32. ISSN: 0925-4005. URL: `http://www.sciencedirect.com/science/article/pii/S0925400501008784` (cit. on p. 81).

[567] Jun Liu and Werner Weppner. "Beta"-Alumina Solid Electrolytes for Solid State Electrochemical CO2 Gas Sensors". In: *Solid State Communications* 76.3 (Oct. 1990), pp. 311–313. ISSN: 0038-1098. URL: `http://www.sciencedirect.com/science/article/pii/0038109890908442` (cit. on p. 81).

[568] Nan Ma et al. "Novel Solid Electrolyte CO2 Gas Sensors Based on c-Axis-Oriented Y-Doped La9.66Si5.3B0.7O26.14". In: *ACS Applied Materials & Interfaces* 12.19 (May 2020), pp. 21515–21520. ISSN: 1944-8244. DOI: `10.1021/acsami.0c00454`. URL: `https://doi.org/10.1021/acsami.0c00454` (cit. on p. 81).

[569] Michal Struzik et al. "A Simple and Fast Electrochemical CO2 Sensor Based on Li7La3Zr2O12 for Environmental Monitoring". In: *Advanced Materials* 30.44 (2018), p. 1804098. DOI: `https://doi.org/10.1002/adma.201804098`. eprint: `https://onlinelibrary.wiley.com/doi/pdf/10.1002/adma.201804098`. URL: `https://onlinelibrary.wiley.com/doi/abs/10.1002/adma.201804098` (cit. on p. 81).

[570] Nak-Jin Choi et al. "Stacked-Type Potentiometric Solid-State CO2 Gas Sensor". In: *Sensors and Actuators B: Chemical* 187 (2013), pp. 340–346. ISSN: 0925-4005. DOI: `https://doi.org/10.1016/j.snb.2012.12.037`. URL: `https://www.sciencedirect.com/science/article/pii/S0925400512013469` (cit. on pp. 82, 86).

[571] L. E. Barrosse-Antle et al. "Voltammetry in Room Temperature Ionic Liquids: Comparisons and Contrasts with Conventional Electrochemical Solvents." In: *Chemistry – An Asian Journal* 5.2 (2010), pp. 202–230. DOI: `https://doi.org/10.1002/asia.200900191`. eprint: `https://onlinelibrary.wiley.com/doi/pdf/10.1002/asia.200900191`. URL: `https://onlinelibrary.wiley.com/doi/abs/10.1002/asia.200900191` (cit. on p. 82).

[572] Abdul Rehman and Xiangqun Zeng. "Methods and Approaches of Utilizing Ionic Liquids as Gas Sensing Materials". In: *RSC Adv.* 5 (72 2015), pp. 58371–58392. DOI: `10.1039/C5RA06754E`. URL: `http://dx.doi.org/10.1039/C5RA06754E` (cit. on p. 82).

[573] Kamalakanta Behera et al. "Ionic Liquid-Based Optical and Electrochemical Carbon Dioxide Sensors". In: *Sensors* 15.12 (2015), pp. 30487–30503. ISSN: 1424-8220. DOI: `10.3390/s151229813`. URL: `https://www.mdpi.com/1424-8220/15/12/29813` (cit. on p. 82).

[574] Tomasz Wasilewski. "Chapter 10 - Ionic Liquids in Gas Sensors and Biosensors". In: *Green Sustainable Process for Chemical and Environmental Engineering and Science*. Elsevier, Jan. 2020, pp. 287–318. ISBN: 978-0-12-817386-2. URL: `http://www.sciencedirect.com/science/article/pii/B978012817386200010X` (cit. on p. 82).

[575] Deby Fapyane and Niels Peter Revsbech. "Fast Responding Amperometric CO2 Microsensor with Ionic Liquid–Aprotic Solvent Electrolytes". In: *ACS Sensors* 5.8 (Aug. 2020), pp. 2604–2610. DOI: `10.1021/acssensors.0c01071`. URL: `https://doi.org/10.1021/acssensors.0c01071` (cit. on pp. 82, 83, 86, 88).

[576] B. A. Rosen, A. Salehi-Khojin, and R. I. Masel. "A Microfabricated Carbon Dioxide Sensor for Portable Applications". In: *SENSORS, 2010 IEEE*. 2010, pp. 365–368. DOI: `10.1109/ICSENS.2010.5690232` (cit. on pp. 82, 83).

[577] Yanxiang Li et al. "Poly(Ionic Liquid)-Wwrapped Single-Walled Carbon Nanotubes for Sub-ppb Detection of CO2". In: *Chemical Communications* 48.66 (2012), pp. 8222–8224. ISSN: 1359-7345. DOI: `10.1039/C2CC33365A`. URL: `https://doi.org/10.1039/C2CC33365A` (cit. on pp. 82, 83).

[578] M. Honda et al. "Low-Power-Consumption CO2 Gas Sensor Using Ionic Liquids for Green Energy Management". In: *SENSORS, 2012 IEEE*. 2012, pp. 1–4. DOI: `10.1109/ICSENS.2012.6411572` (cit. on p. 82).

[579] K. Ishizu et al. "Carbon Dioxide Gas Sensor With Ionic Gel". In: *2013 Transducers Eurosensors XXVII: The 17th International Conference on Solid-State Sensors, Actuators and Microsystems (TRANSDUCERS EUROSENSORS XXVII)*. 2013, pp. 1633–1636. DOI: `10.1109/Transducers.2013.6627097` (cit. on pp. 82, 83).

[580] Christoph Willa et al. "When Nanoparticles Meet Poly(Ionic Liquid)s: Chemoresistive CO2 Sensing at Room Temperature". In: *Advanced Functional Materials* 25.17 (2015), pp. 2537–2542. DOI: `https://doi.org/10.1002/adfm.201500314`. eprint: `https://onlinelibrary.wiley.com/doi/pdf/10.1002/adfm.201500314`. URL: `https://onlinelibrary.wiley.com/doi/abs/10.1002/adfm.201500314` (cit. on pp. 82, 83, 86).

[581] Christoph Willa et al. "Lightweight, Room-Temperature CO2 Gas Sensor Based on Rare-Earth Metal-Free Composites-An Impedance Study". In: *ACS applied materials and interfaces* 9.30 (Aug. 2017), pp. 25553–25558. ISSN: 1944-8252. DOI: `10.1021/acsami.7b07379`. URL: `https://doi.org/10.1021/acsami.7b07379` (cit. on pp. 82, 83, 88).

[582] Niels Peter Revsbech et al. "Amperometic Microsensor for Measurement of Gaseous and Dissolved CO2". In: *Sensors and Actuators B: Chemical* 283 (Mar. 2019), pp. 349–354. ISSN: 0925-4005. URL: `http://www.sciencedirect.com/science/article/pii/S0925400518321580` (cit. on pp. 82, 83, 86).

[583] Lichan Chen et al. "Carbon Dioxide Gas Sensor Based on Ionic Liquid-Induced Electrochemiluminescence". In: *Analytical Chemistry* 83.17 (Sept. 2011), pp. 6862–6867. ISSN: 0003-2700. DOI: `10.1021/ac201067u`. URL: `https://doi.org/10.1021/ac201067u` (cit. on pp. 82–84, 86).

[584] Marisa C. Buzzeo et al. "Kinetic Analysis of the Reaction between Electrogenerated Superoxide and Carbon Dioxide in the Room Temperature Ionic Liquids 1-Ethyl-3-methylimidazolium Bis(trifluoromethylsulfonyl)imide and Hexyltriethylammonium Bis(trifluoromethylsulfonyl)imide". In: *The Journal of Physical Chemistry B* 108.12 (Mar. 2004), pp. 3947–3954. ISSN: 1520-6106. DOI: `10.1021/jp031121z`. URL: `https://doi.org/10.1021/jp031121z` (cit. on p. 82).

[585] Chunhui Xiao and Xiangqun Zeng. "In Situ EQCM Evaluation of the Reaction between Carbon Dioxide and Electrogenerated Superoxide in Ionic Liquids". In: *Journal of The Electrochemical Society* 160.10 (2013), H749–H756. DOI: `10.1149/2.073310jes`. URL: `https://doi.org/10.1149%2F2.073310jes` (cit. on p. 82).

[586] Jushuai Wu et al. "In Situ μ-Printed Optical Fiber-Tip CO2 Sensor Using a Photocrosslinkable Poly(Ionic Liquid)". In: *Sensors and Actuators B: Chemical* 259 (Apr. 2018), pp. 833–839. ISSN: 0925-4005. URL: `http://www.sciencedirect.com/science/article/pii/S0925400517324589` (cit. on p. 82).

[587] Placido G. Mineo et al. "Fast and Reversible CO2 Quartz Crystal Microbalance Response of Vinylimidazolium-Based Poly(Ionic Liquid)s". In: *Polymers for Advanced Technologies* 23.11 (2012), pp. 1511–1519. DOI: `https://doi.org/10.1002/pat.2076`. eprint: `https://onlinelibrary.wiley.com/doi/pdf/10.1002/pat.2076`. URL: `https://onlinelibrary.wiley.com/doi/abs/10.1002/pat.2076` (cit. on pp. 82–84, 86).

[588] R. Zhou et al. "Reliable CO2 Sensors With Silicon-Based Polymers on Quartz Microbalance Transducers". In: *Sensors and Actuators B: Chemical* 19.1 (Apr. 1994), pp. 415–420. ISSN: 0925-4005. URL: `http://www.sciencedirect.com/science/article/pii/092540059301018Y` (cit. on p. 83).

[589] M.Teresa Gomes, Armando C. Duarte, and João P. Oliveira. "Detection of CO2 Using a Quartz Crystal Microbalance". In: *Sensors and Actuators B: Chemical* 26.1 (1995), pp. 191–194. ISSN: 0925-4005. DOI: `https://doi.org/10.1016/0925-4005(94)01584-5`. URL: `http://www.sciencedirect.com/science/article/pii/0925400594015845` (cit. on p. 83).

[590] Hyunjoo J. Lee et al. "Functionalization Layers for CO2 Sensing Using Capacitive Micromachined Ultrasonic Transducers". In: *Sensors and Actuators B: Chemical* 174 (Nov. 2012), pp. 87–93. ISSN: 0925-4005. URL: `http://www.sciencedirect.com/science/article/pii/S0925400512008398` (cit. on p. 83).

[591] R. Hoffmann, M. Schreiter, and J. Heitmann. "The Concept of Thin Film Bulk Acoustic Resonators as Selective CO_2 Gas Sensors". In: *Journal of Sensors and Sensor Systems* 6.1 (2017), pp. 87–96. DOI: `10.5194/jsss-6-87-2017`. URL: `https://jsss.copernicus.org/articles/6/87/2017/` (cit. on p. 83).

[592] Zachary A. Siefker et al. "Manipulating Polymer Composition to Create Low-Cost, High-Fidelity Sensors for Indoor CO2 Monitoring". In: *Scientific Reports* 11.1 (June 2021), p. 13237. ISSN: 2045-2322. DOI: `10.1038/s41598-021-92181-4`. URL: `https://doi.org/10.1038/s41598-021-92181-4` (cit. on p. 83).

[593] F. W. Giacobbe. "Precision Measurement of Acoustic Velocities in Pure Gases and Gas Mixtures". In: *The Journal of the Acoustical Society of America* 94.3 (Sept. 1993), pp. 1200–1210. ISSN: 0001-4966. DOI: `10.1121/1.408261` (cit. on p. 83).

[594] Markus Joos, Harald Müller, and Gerhard Lindner. “An Ultrasonic Sensor for the Analysis of Binary Gas Mixtures”. In: *Sensors and Actuators B: Chemical* 16.1 (Oct. 1993), pp. 413–419. ISSN: 0925-4005. URL: `http://www.sciencedirect.com/science/article/pii/0925400593852205` (cit. on pp. 83, 86).

[595] Ahmet Cicek et al. “Ultrasonic Gas Sensing by Two-Dimensional Surface Phononic Crystal Ring Resonators”. In: *ACS Sensors* 4.7 (July 2019), pp. 1761–1765. DOI: `10.1021/acssensors.9b00865`. URL: `https://doi.org/10.1021/acssensors.9b00865` (cit. on p. 83).

[596] Gerald Gerlach. “Acoustic CO2 Sensors”. In: *Carbon Dioxide Sensing.* John Wiley and Sons, Ltd, 2019. Chap. 9, pp. 215–245. ISBN: 9783527688302. DOI: `10.1002/9783527688302.ch9`. eprint: `https://onlinelibrary.wiley.com/doi/pdf/10.1002/9783527688302.ch9`. URL: `https://onlinelibrary.wiley.com/doi/abs/10.1002/9783527688302.ch9` (cit. on p. 83).

[597] L. B. Evans, H. E. Bass, and L. C. Sutherland. “Atmospheric Absorption of Sound: Theoretical Predictions”. In: *The Journal of the Acoustical Society of America* 51.5B (1972), pp. 1565–1575. DOI: `10.1121/1.1913000`. eprint: `https://doi.org/10.1121/1.1913000`. URL: `https://doi.org/10.1121/1.1913000` (cit. on p. 84).

[598] H E. Bass, Louis Sutherland, and A J. Zuckerwar. “Atmospheric Absorption of Sound - Update”. In: *The Journal of the Acoustical Society of America* 88 (Nov. 1990). DOI: `10.1121/1.400176` (cit. on p. 84).

[599] Andi Petculescu. “Future Trends in Acoustic Gas Monitoring and Sensing”. In: *Journal of Optoelectronics and Advanced Materials* 8 (Feb. 2006) (cit. on pp. 84, 86).

[600] Yefim Dain and Richard M. Lueptow. “Acoustic Attenuation in a Three-Gas Mixture: Results”. In: *The Journal of the Acoustical Society of America* 110.6 (2001), pp. 2974–2979. DOI: `10.1121/1.1413999`. eprint: `https://doi.org/10.1121/1.1413999`. URL: `https://doi.org/10.1121/1.1413999` (cit. on p. 84).

[601] Aurelien Cottet et al. “Acoustic Absorption Measurements for Characterization of Gas Mixing”. In: *Journal of The Acoustical Society of America - J ACOUST SOC AMER* 116 (Oct. 2004), pp. 2081–2088. DOI: `10.1121/1.1785631` (cit. on p. 84).

[602] Sally Ejakov et al. “Acoustic Attenuation in Gas Mixtures With Nitrogen: Experimental Data and Calculations”. In: *The Journal of the Acoustical Society of America* 113 (May 2003), pp. 1871–1879. DOI: `10.1121/1.1559177` (cit. on p. 84).

[603] Andi Petculescu et al. “A Prototype Acoustic Gas Sensor Based on Attenuation (L)”. In: *Journal of The Acoustical Society of America* 120 (Oct. 2006). DOI: `10.1121/1.2336758` (cit. on pp. 84, 86).

[604] Yaqiong Jia et al. “Gas Composition Recognition Based on Analyzing Acoustic Relaxation Absorption Spectra: Wavelet Decomposition and Support Vector Machine Classifier”. In: *Proceedings of the 2018 2nd International Conference on Electrical Engineering and Automation (ICEEA 2018).* Mar. 2018, pp. 126–130. DOI: `10.2991/iceea-18.2018.28` (cit. on p. 84).

[605] Allan J. Zuckerwar and William A. Griffin. “Effect of Water Vapor on Sound Absorption in Nitrogen at low Frequency/Pressure Ratios”. In: *The Journal of the Acoustical Society of America* 69.1 (1981), pp. 150–154. DOI: `10.1121/1.385359`. eprint: `https://doi.org/10.1121/1.385359`. URL: `https://doi.org/10.1121/1.385359` (cit. on p. 84).

[606] G. Wysocki, Anatoliy Kosterev, and Frank Tittel. “Influence of Molecular Relaxation Dynamics on Quartz-enhanced Photoacoustic Detection of CO2 at $\lambda = 2\ \mu$m”. In: *Appl. Phys. B Lasers Opt.* 85 (Nov. 2006), pp. 301–306. DOI: `10.1007/s00340-006-2369-9` (cit. on p. 86).

[607] M. Eberl et al. “Miniaturized Photoacoustic CO2 Gas Sensors - A New Approach for the Automotive Sector”. In: *AmE 2019 - Automotive meets Electronics; 10th GMM-Symposium.* 2019, pp. 1–5 (cit. on p. 86).

[608] C E W Hahn. “Techniques for Measuring the Partial Pressures of Gases in the Blood. I. In Vitro Measurements”. In: *Journal of Physics E: Scientific Instruments* 13.5 (May 1980), pp. 470–482. DOI: `10.1088/0022-3735/13/5/001`. URL: `https://doi.org/10.1088/0022-3735/13/5/001` (cit. on p. 86).

[609] Dariia Atamanchuk et al. “Performance of a Lifetime-Based Optode for Measuring Partial Pressure of Carbon Dioxide in Natural Waters”. In: *Limnology and Oceanography: Methods* 12.2 (2014), pp. 63–73. DOI: `10.4319/lom.2014.12.63` (cit. on pp. 86, 103).

[610] Shravanti Joshi et al. “Facile Conversion of Zinc Hydroxide Carbonate to CaO-ZnO for Selective CO2 Gas Detection”. In: *Journal of Colloid and Interface Science* 558 (2020), pp. 310–322. ISSN: 0021-9797. DOI: `https://doi.org/10.1016/j.jcis.2019.09.103`. URL: `https://www.sciencedirect.com/science/article/pii/S0021979719311488` (cit. on p. 86).

[611] K Kaneyasu et al. “A Carbon Dioxide Gas Sensor Based on Solid Electrolyte for Air Quality Control”. In: *Sensors and Actuators B: Chemical* 66.1 (2000), pp. 56–58. ISSN: 0925-4005. DOI: `https://doi.org/10.1016/S0925-4005(99)00411-6`. URL: `https://www.sciencedirect.com/science/article/pii/S0925400599004116` (cit. on p. 86).

[612] Madhubanti Chatterjee et al. “A Novel Approach Toward Noninvasive Monitoring of Transcutaneous CO2”. In: *Medical Engineering & Physics* 36.1 (Jan. 2014), pp. 136–139. ISSN: 1350-4533. URL: `https://www.sciencedirect.com/science/article/pii/S1350453313001483` (cit. on pp. 85, 89).

[613] Xudong Ge et al. “Development and Characterization of a Point-of Care Rate-Based Transcutaneous Respiratory Status Monitor”. In: *Medical Engineering and Physics* 56 (Apr. 2018). DOI: `10.1016/j.medengphy.2018.03.009` (cit. on pp. 85, 89).

[614] Kenta Iitani et al. “What do Masks Mask? A Study on Transdermal CO2 Monitoring”. In: *Medical Engineering & Physics* 98 (Dec. 2021), pp. 50–56. ISSN: 1350-4533. URL: `https://www.sciencedirect.com/science/article/pii/S1350453321001223` (cit. on pp. 85, 89).

[615] Pierre Grangeat et al. “First Evaluation of a Transcutaneous Carbon Dioxide Monitoring Wristband Device During a Cardiopulmonary Exercise Test”. In: *41st Annual International Conference of the IEEE Engineering in Medicine and Biology Society (EMBC).* 2019, pp. 3352–3355. DOI: `10.1109/EMBC.2019.8857020` (cit. on pp. 85, 89).

[616] Pierre Grangeat et al. “Evaluation in Healthy Subjects of a Transcutaneous Carbon Dioxide Monitoring Wristband During Hypo and Hypercapnia Conditions”. In: *42nd Annual International Conference of the IEEE Engineering in Medicine Biology Society (EMBC).* 2020, pp. 4640–4643. DOI: `10.1109/EMBC44109.2020.9175876` (cit. on pp. 85, 89).

[617] R. C. Targett et al. “Skin Gas Tensions and Resistances Measured by Mass Spectrometry in Adults”. In: *Journal of Applied Physiology* 56.5 (1984), pp. 1431–1435. DOI: `10.1152/jappl.1984.56.5.1431`. eprint: `https://doi.org/10.1152/jappl.1984.56.5.1431`. URL: `https://doi.org/10.1152/jappl.1984.56.5.1431` (cit. on pp. 85, 87, 89).

[618] Danick Briand et al. “Making Environmental Sensors on Plastic Foil”. In: *Materials Today* 14.9 (2011), pp. 416–423. ISSN: 1369-7021. DOI: `https://doi.org/10.1016/S1369-7021(11)70186-9`. URL: `https://www.sciencedirect.com/science/article/pii/S1369702111701869` (cit. on p. 88).

[619] Stefan Köstler et al. “C7.3 - From Optochemical Sensors for Industrial Processes to Large-Area Printing of Sensor Systems Integrated with Organic Electronics”. In: *SENSOR+TEST Conferences 2011.* 2011 (cit. on p. 88).

[620] Xiaoman Xing et al. “An Unobtrusive and Calibration-Free Blood Pressure Estimation Method Using Photoplethysmography and Biometrics”. In: *Scientific Reports* 9.1 (June 2019), p. 8611. ISSN: 2045-2322. DOI: `10.1038/s41598-019-45175-2`. URL: `https://doi.org/10.1038/s41598-019-45175-2` (cit. on p. 89).

[621] Jiang Shao et al. “A Revised Point-to-Point Calibration Approach With Adaptive Errors Correction to Weaken Initial Sensitivity of Cuff-Less Blood Pressure Estimation”. In: *Sensors* 20.8 (2020). ISSN: 1424-8220. DOI: `10.3390/s20082205`. URL: `https://www.mdpi.com/1424-8220/20/8/2205` (cit. on p. 89).

[622] Hye-Geum Kim et al. “Stress and Heart Rate Variability: A Meta-Analysis and Review of the Literature”. eng. In: *Psychiatry Investigation* 15.3 (Mar. 2018), pp. 235–245. ISSN: 1738-3684. URL: `https://pubmed.ncbi.nlm.nih.gov/29486547` (cit. on p. 89).

[623] Vicente Moret-Bonillo et al. “Intelligent Approach for Analysis of Respiratory Signals and Oxygen Saturation in the Sleep Apnea / Hypopnea Syndrome”. In: *The open medical informatics journal* 8 (June 2014), pp. 1–19. ISSN: 1874-4311. DOI: `10.2174/1874431101408010001`. URL: `https://doi.org/10.2174/1874431101408010001` (cit. on p. 89).

[624] M. Clarke et al. “Dynamic Threshold Analysis of Daily Oxygen Saturation for Improved Management of COPD Patients”. In: *IEEE Journal of Biomedical and Health Informatics* 20.5 (2016), pp. 1352–1360. ISSN: 2168-2208. DOI: `10.1109/JBHI.2015.2464275`. URL: `https://doi.org/10.1109/JBHI.2015.2464275` (cit. on p. 89).

[625] Gyula Domján et al. “Rapid Analysis of Whole Blood and Blood Serum Using Near Infrared Spectroscopy”. In: *Journal of Near Infrared Spectroscopy* 2.2 (Mar. 1994), pp. 67–78. ISSN: 0967-0335. DOI: `10.1255/jnirs.33`. URL: `https://doi.org/10.1255/jnirs.33` (cit. on pp. 90, 162).

[626] Christina Marasco et al. “Metabolic Rate Measurement Apparatus and Method Thereof”. US 2020/0113516 Al. 2020 (cit. on p. 90).

[627] Janet Freilich. “Prophetic patents”. In: *UC Davis L. Rev.* 53 (2019), p. 663 (cit. on p. 90).

[628] Linhong Kou, Daniel Labrie, and Petr Chylek. “Refractive Indices of Water and Ice in the 0.65- to 2.5-μm Spectral Range”. In: *Appl. Opt.* 32.19 (July 1993), pp. 3531–3540. DOI: `10.1364/AO.32.003531`. URL: `http://www.osapublishing.org/ao/abstract.cfm?URI=ao-32-19-3531` (cit. on pp. 90, 162).

[629] Zhang Zhujun and W. Rudolf Seitz. “A Fluorescence Sensor for Quantifying pH in the Range From 6.5 to 8.5”. In: *Analytica Chimica Acta - ANAL CHIM ACTA* 160 (Dec. 1984), pp. 47–55. DOI: `10.1016/S0003-2670(00)84507-9` (cit. on pp. 91, 131).

[630] Andrew Mills, Q. Chang, and N. McMurray. “Equilibrium Studies on Colorimetric Plastic Film Sensors for Carbon Dioxide”. In: *Analytical Chemistry* 64 (1992), pp. 1383–1389. ISSN: 0003-2700 (cit. on pp. 91, 93).

[631] Andrew Mills and Qing Chang. “Fluorescence Plastic Thin-Film Sensor for Carbon Dioxide”. In: *Analyst* 118 (7 1993), pp. 839–843. DOI: `10.1039/AN9931800839`. URL: `http://dx.doi.org/10.1039/AN9931800839` (cit. on p. 91).

[632] Karen Reynolds et al. “Temperature Dependence of LED and its Theoretical Effect on Pulse Oximetry”. In: *British journal of anaesthesia* 67 (Dec. 1991), pp. 638–643. DOI: `10.1093/bja/67.5.638` (cit. on p. 94).

[633] K. Ahmad and A.W. Mabbitt. “Gallium Indium Arsenide Photodiodes”. In: *Solid-State Electronics* 22.3 (1979), pp. 327–333. ISSN: 0038-1101. DOI: `https://doi.org/10.1016/0038-1101(79)90042-X`. URL: `http://www.sciencedirect.com/science/article/pii/003811017990042X` (cit. on p. 94).

[634] Irving J. Bigio and Sergio Fantini. *Quantitative Biomedical Optics: Theory, Methods, and Applications*. Cambridge Texts in Biomedical Engineering. Cambridge University Press, 2016. DOI: `10.1017/CBO9781139029797` (cit. on pp. 94, 170).

[635] Fabio Cenni. “High Level Modeling of Heterogeneous Systems, Analog / Digital Interfacing”. PhD thesis. Université de Grenoble, 2012. URL: `https://theses.hal.science/tel-00721972` (cit. on p. 94).

[636] Jesse H. Day. “Thermochromism”. In: *Chemical Reviews* 63.1 (Feb. 1963), pp. 65–80. ISSN: 0009-2665. DOI: `10.1021/cr60221a005` (cit. on p. 95).

[637] Usama El-Ayaan, Fumiko Murata, and Yutaka Fukuda. “Thermochromism and Solvatochromism in Solution”. In: *Monatshefte für Chemie / Chemical Monthly* 132.11 (Nov. 2001), pp. 1279–1294. ISSN: 1434-4475. DOI: `10.1007/s007060170018` (cit. on p. 95).

[638] Bernard Valeur. “Fluorescent Molecular Sensors of Ions and Molecules”. In: *Molecular Fluorescence*. John Wiley and Sons, Ltd, 2001. Chap. 10, pp. 273–350. ISBN: 9783527600243. DOI: `10.1002/3527600248.ch10`. eprint: `https://onlinelibrary.wiley.com/doi/pdf/10.1002/3527600248.ch10`. URL: `https://onlinelibrary.wiley.com/doi/abs/10.1002/3527600248.ch10` (cit. on p. 95).

[639] Th. Förster. “Zwischenmolekulare Energiewanderung und Fluoreszenz”. In: *Annalen der Physik* 437.1-2 (Jan. 1948), pp. 55–75. ISSN: 0003-3804. DOI: `10.1002/andp.19484370105` (cit. on p. 96).

[640] Jakub Włodarczyk and Borys Kierdaszuk. “Interpretation of Fluorescence Decays using a Power-like Model”. In: *Biophysical Journal* 85.1 (2003), pp. 589–598. ISSN: 0006-3495. DOI: `10.1016/S0006-3495(03)74503-2` (cit. on pp. 97, 124).

[641] Sergey M. Borisov et al. “Optical Carbon Dioxide Sensors Based on Silicone-Encapsulated Room-Temperature Ionic Liquids”. In: *Chemistry of Materials* 19.25 (2007), pp. 6187–6194. DOI: `10.1021/cm7019312`. eprint: `https://doi.org/10.1021/cm7019312`. URL: `https://doi.org/10.1021/cm7019312` (cit. on pp. 99, 133, 138, 158).

[642] Gerhard Neurauter. “Frequency Domain pCO2 Sensing”. PhD thesis. University of Regensburg, 2000 (cit. on pp. 99, 101–103, 126, 155).

[643] Hung Lam et al. “Dual Optical Sensor for Oxygen and Temperature Based on the Combination of Time Domain and Frequency Domain Techniques”. In: *Talanta* 84.1 (Mar. 2011), pp. 65–70. ISSN: 0039-9140. DOI: `10.1016/j.talanta.2010.12.016` (cit. on p. 102).

[644] Sergey M. Borisov et al. “Modified Dual Lifetime Referencing Method for Simultaneous Optical Determination and Sensing of Two Analytes”. In: *Applied Spectroscopy* 60.10 (2006), pp. 1167–1173. DOI: `10.1366/000370206778664590`. eprint: `https://doi.org/10.1366/000370206778664590`. URL: `https://doi.org/10.1366/000370206778664590` (cit. on p. 102).

[645] Anna S. Kocincova et al. “Fiber-Optic Microsensors for Simultaneous Sensing of Oxygen and pH, and of Oxygen and Temperature”. In: *Analytical Chemistry* 79.22 (Nov. 2007), pp. 8486–8493. ISSN: 0003-2700. DOI: `10.1021/ac070514h`. URL: `https://doi.org/10.1021/ac070514h` (cit. on p. 102).

[646] Sergey M. Borisov, Roman Seifner, and Ingo Klimant. “A Novel Planar Optical Sensor for Simultaneous Monitoring of Oxygen, Carbon Dioxide, pH and Temperature”. In: *Analytical and Bioanalytical Chemistry* 400.8 (June 2011), pp. 2463–2474. ISSN: 1618-2650. DOI: `10.1007/s00216-010-4617-4`. URL: `https://doi.org/10.1007/s00216-010-4617-4` (cit. on pp. 102, 146).

[647] Sergey M. Borisov and Ingo Klimant. “Ultrabright Oxygen Optodes Based on Cyclometalated Iridium(III) Coumarin Complexes”. In: *Analytical Chemistry* 79.19 (Oct. 2007), pp. 7501–7509. ISSN: 0003-2700. DOI: `10.1021/ac0710836`. URL: `https://doi.org/10.1021/ac0710836` (cit. on pp. 103, 129).

[648] S. L. Marple. “A Tutorial Overview of Modern Spectral Estimation”. In: *International Conference on Acoustics, Speech, and Signal Processing,* International Conference on Acoustics, Speech, and Signal Processing, 1989, 2152–2157 vol.4. DOI: `10.1109/ICASSP.1989.266889` (cit. on p. 103).

[649] L.L. Scharf and C. Demeure. *Statistical Signal Processing: Detection, Estimation, and Time Series Analysis.* Addison-Wesley series in electrical and computer engineering. Addison-Wesley Publishing Company, 1991. ISBN: 9780201190380 (cit. on p. 103).

[650] P. Stoica and R.L. Moses. *Spectral Analysis of Signals.* Pearson Prentice Hall, 2005. ISBN: 9780131139565 (cit. on p. 103).

[651] S.L. Marple. *Digital Spectral Analysis: Second Edition.* Dover Books on Electrical Engineering. Dover Publications, 2019. ISBN: 9780486780528 (cit. on p. 103).

[652] A. A. Girgis and F. M. Ham. “A Quantitative Study of Pitfalls in the FFT”. In: *IEEE Transactions on Aerospace and Electronic Systems* AES-16.4 (1980), pp. 434–439. ISSN: 1557-9603. DOI: `10.1109/TAES.1980.308971`. URL: `https://doi.org/10.1109/TAES.1980.308971` (cit. on p. 103).

[653] S. Schuster, S. Scheiblhofer, and A. Stelzer. “The Influence of Windowing on Bias and Variance of DFT-Based Frequency and Phase Estimation”. In: *IEEE Transactions on Instrumentation and Measurement* 58.6 (2009), pp. 1975–1990. ISSN: 1557-9662. DOI: `10.1109/TIM.2008.2006131`. URL: `https://doi.org/10.1109/TIM.2008.2006131` (cit. on p. 103).

[654] Huang Xiaohong, Wang Zhaohua, and Chou Guoqiang. “New Method of Estimation of Phase, Amplitude, and Frequency Based on all Phase FFT Spectrum Analysis”. In: *2007 International Symposium on Intelligent Signal Processing and Communication Systems.* 2007 International Symposium on Intelligent Signal Processing and Communication Systems. 2007, pp. 284–287. DOI: `10.1109/ISPACS.2007.4445879` (cit. on p. 103).

[655] Xiangdong Huang et al. "A Novel High-Accuracy Digitalized Measuring Phase Method". In: *2008 9th International Conference on Signal Processing*. 2008 9th International Conference on Signal Processing. 2008, pp. 120–123. DOI: `10.1109/ICOSP.2008.4697084` (cit. on p. 103).

[656] Taixin Su et al. "Power Harmonic and Interharmonic Detection Method in Renewable Power Based on Nuttall Double-Window All-Phase FFT Algorithm". In: *IET Renewable Power Generation* 12.8 (June 2018), pp. 953–961. ISSN: 1752-1416. DOI: `10.1049/iet-rpg.2017.0115`. URL: `https://doi.org/10.1049/iet-rpg.2017.0115` (cit. on p. 103).

[657] Tuna B. Tufan and Ulkuhan Guler. "A Miniaturized Transcutaneous Carbon Dioxide Monitor Based on Dual Lifetime Referencing". In: *2022 IEEE Biomedical Circuits and Systems Conference (BioCAS)*. 2022, pp. 144–148. DOI: `10.1109/BioCAS54905.2022.9948600` (cit. on pp. 103, 157).

[658] A. Ferrero and R. Ottoboni. "High-Accuracy Fourier Analysis Based on Synchronous Sampling Techniques". In: *IEEE Transactions on Instrumentation and Measurement* 41.6 (1992), pp. 780–785. ISSN: 1557-9662. DOI: `10.1109/19.199406`. URL: `https://doi.org/10.1109/19.199406` (cit. on p. 103).

[659] J. Cooley, P. Lewis, and P. Welch. "The Finite Fourier Transform". In: *IEEE Transactions on Audio and Electroacoustics* 17.2 (1969), pp. 77–85. DOI: `10.1109/TAU.1969.1162036` (cit. on p. 105).

[660] Joram Soch et al. *The Book of Statistical Proofs*. Version 2020. Dec. 2020. DOI: `10.5281/zenodo.4305950` (cit. on p. 106).

[661] A. van der Vaart and J.A. Wellner. *Weak Convergence and Empirical Processes: With Applications to Statistics*. Springer Series in Statistics. Springer, 1996. ISBN: 9780387946405 (cit. on p. 107).

[662] Amos Lapidoth. *A Foundation in Digital Communication*. 2nd ed. Cambridge: Cambridge University Press, 2017. ISBN: 9781107177321. DOI: `10.1017/9781316822708` (cit. on p. 107).

[663] Victor M. Panaretos and Shahin Tavakoli. "Fourier Analysis of Stationary Time Series in Function Space". In: *The Annals of Statistics* 41.2 (Apr. 2013), pp. 568–603. DOI: `10.1214/13-AOS1086`. URL: `https://doi.org/10.1214/13-AOS1086` (cit. on p. 107).

[664] Clément Cerovecki and Siegfried Hörmann. "On the CLT for Discrete Fourier Transforms of Functional Time Series". In: *Journal of Multivariate Analysis* 154 (Feb. 2017), pp. 282–295. ISSN: 0047-259X. URL: `https://www.sciencedirect.com/science/article/pii/S0047259X16301592` (cit. on p. 107).

[665] Dale Zimmerman Robert V. Hogg Elliot Tanis. *Probability and Statistical Inference*. 9th. Pearson, 2014. ISBN: 9781292062358 (cit. on pp. 109, 116).

[666] Abdul Alhazred. "Necronomicon". In: *R'lyeh University Archives* (730).

[667] N. Henze and B. Zirkler. "A Class of Invariant Consistent Tests for Multivariate Normality". In: *Communications in Statistics - Theory and Methods* 19.10 (Jan. 1990), pp. 3595–3617. ISSN: 0361-0926. DOI: `10.1080/03610929008830400`. URL: `https://doi.org/10.1080/03610929008830400` (cit. on p. 110).

[668] André Fujita et al. "Comparing Pearson, Spearman and Hoeffding's D Measure for Gene Expression Association Analysis". In: *Journal of Bioinformatics and Computational Biology* 07.04 (Aug. 2009), pp. 663–684. ISSN: 0219-7200. DOI: `10.1142/S0219720009004230`. URL: `https://doi.org/10.1142/S0219720009004230` (cit. on p. 110).

[669] Yoav Benjamini and Yosef Hochberg. "Controlling the False Discovery Rate: A Practical and Powerful Approach to Multiple Testing". In: *Journal of the Royal Statistical Society. Series B (Methodological)* 57.1 (1995), pp. 289–300. ISSN: 00359246. URL: `http://www.jstor.org/stable/2346101` (cit. on p. 110).

[670] D. Collett and T. Lewis. "Discriminating Between the Von Mises and Wrapped Normal Distributions". In: *Australian Journal of Statistics* 23.1 (Mar. 1981), pp. 73–79. ISSN: 0004-9581. DOI: `10.1111/j.1467-842X.1981.tb00763.x`. URL: `https://doi.org/10.1111/j.1467-842X.1981.tb00763.x` (cit. on p. 112).

[671] Kanti V. Mardia and Peter E. Jupp. *Directional Statistics*. Wiley Online Library, 1999. ISBN: 978-0-471-95333-3 (cit. on p. 112).

[672] Christophe Ley and Thomas Verdebout. *Modern Directional Statistics*. Chapman and Hall / CRC, 2017. ISBN: 9781315119472. DOI: `10.1201/9781315119472` (cit. on p. 112).

[673] Walter Kester. *Converting Oscillator Phase Noise to Time Jitter*. Tech. rep. MT-008. Analog Devices, 2010 (cit. on p. 115).

[674] C. E. Calosso, A. C. Cárdenas Olaya, and E. Rubiola. "Phase-Noise and Amplitude-Noise Measurement of DACs and DDSs". In: *2019 Joint Conference of the IEEE International Frequency Control Symposium and European Frequency and Time Forum (EFTF/IFC)*. 2019 Joint Conference of the IEEE International Frequency Control Symposium and European Frequency and Time Forum (EFTF/IFC). 2019, pp. 431–439. DOI: `10.1109/FCS.2019.8856100` (cit. on p. 115).

[675] T. Kailath. "The Divergence and Bhattacharyya Distance Measures in Signal Selection". In: *IEEE Transactions on Communication Technology* 15.1 (1967), pp. 52–60. DOI: `10.1109/TCOM.1967.1089532` (cit. on p. 119).

[676] D. B. Leeson. "Oscillator Phase Noise: A 50-Year Review". In: *IEEE Transactions on Ultrasonics, Ferroelectrics, and Frequency Control* 63.8 (2016), pp. 1208–1225. ISSN: 1525-8955. DOI: `10.1109/TUFFC.2016.2562663` (cit. on p. 121).

[677] Chee-Kian Ong et al. "Random Jitter Extraction Technique in a Multi-Gigahertz Signal". In: *Proceedings Design, Automation and Test in Europe Conference and Exhibition*. Vol. 1. Proceedings Design, Automation and Test in Europe Conference and Exhibition. 2004, pp. 286–291. DOI: `10.1109/DATE.2004.1268862` (cit. on p. 121).

[678] Nicola Da Dalt and Ali Sheikholeslami. *Understanding Jitter and Phase Noise: A Circuits and Systems Perspective*. Cambridge: Cambridge University Press, 2018. ISBN: 9781107188570. DOI: `10.1017/9781316981238` (cit. on p. 121).

[679] P. Lesage and C. Audoin. "Characterization of Frequency Stability: Uncertainty due to the Finite Number of Measurements". In: *IEEE Transactions on Instrumentation and Measurement* 22.2 (1973), pp. 157–161. ISSN: 1557-9662. DOI: `10.1109/TIM.1973.4314128` (cit. on p. 121).

[680] Carlos Nazareth et al. "New Jitter Measurement Technique Using TDC Principle in a FPGA Component". In: *Seminário Internacional de Metrologia Elétrica – VIII SEMETRO* (2009) (cit. on p. 121).

[681] Gabriele Ciarpi et al. "Asymmetric 5.5 GHz Three-Stage Voltage-Controlled Ring-Oscillator in 65 nm CMOS Technology". In: *Electronics* 12.3 (2023). ISSN: 2079-9292. DOI: `10.3390/electronics12030778` (cit. on p. 121).

[682] L. Song et al. "Photobleaching Kinetics of Fluorescein in Quantitative Fluorescence Microscopy". In: *Biophysical Journal* 68.6 (June 1995), pp. 2588–2600. ISSN: 0006-3495. DOI: `10.1016/S0006-3495(95)80442-X` (cit. on pp. 124, 125).

[683] Alexander P. Demchenko. "Photobleaching of Organic Fluorophores: Quantitative Characterization, Mechanisms, Protection". In: *Methods and Applications in Fluorescence* 8.2 (2020), p. 022001. ISSN: 2050-6120. DOI: `10.1088/2050-6120/ab7365` (cit. on pp. 124, 149).

[684] Guang S. He et al. "Multiphoton Absorbing Materials: Molecular Designs, Characterizations, and Applications". In: *Chemical Reviews* 108.4 (Apr. 2008), pp. 1245–1330. ISSN: 0009-2665. DOI: `10.1021/cr050054x` (cit. on p. 124).

[685] Mariacristina Rumi and Joseph W. Perry. "Two-Photon Absorption: an Overview of Measurements and principles". In: *Advances in Optics and Photonics* 2.4 (Dec. 2010), pp. 451–518. DOI: `10.1364/AOP.2.000451` (cit. on p. 124).

[686] Qinsi Zheng and Luke D. Lavis. "Development of Photostable Fluorophores for Molecular Imaging". In: *Current Opinion in Chemical Biology* 39 (Aug. 2017), pp. 32–38. ISSN: 1367-5931. DOI: `10.1016/j.cbpa.2017.04.017` (cit. on pp. 124, 125).

[687] Alberto Diaspro et al. "Photobleaching". In: *Handbook Of Biological Confocal Microscopy*. Ed. by James B. Pawley. Boston, MA: Springer US, 2006, pp. 690–702. ISBN: 978-0-387-45524-2. DOI: `10.1007/978-0-387-45524-2_39` (cit. on pp. 124, 125, 149).

[688] Babette Hinkeldey, Alexander Schmitt, and Gregor Jung. "Comparative Photostability Studies of BODIPY and Fluorescein Dyes by Using Fluorescence Correlation Spectroscopy". In: *ChemPhysChem* 9.14 (Oct. 2008), pp. 2019–2027. ISSN: 1439-4235. DOI: `10.1002/cphc.200800299` (cit. on p. 125).

[689] Loling Song et al. "Influence of Fluorochrome Labeling Density on the Photobleaching Kinetics of Fluorescein in Microscopy". In: *Cytometry* 27.3 (Mar. 1997), pp. 213–223. ISSN: 0196-4763. DOI: `10.1002/(SICI)1097-0320(19970301)27:3<213::AID-CYTO2>3.0.CO;2-F` (cit. on p. 125).

[690] Jerker Widengren and Rudolf Rigler. "Mechanisms of Photobleaching Investigated by Fluorescence Correlation Spectroscopy". In: *Bioimaging* 4.3 (Sept. 1996), pp. 149–157. ISSN: 0966-9051. DOI: `10.1002/1361-6374(199609)4:3<149::AID-BIO5>3.0.CO;2-D` (cit. on pp. 125, 149).

[691] Owen Woodford et al. "Dramatic Effect of Solvent on the Rate of Photobleaching of Organic Pyrrole-BF2 (BOPHY) Dyes". In: *ChemPhotoChem* 1.7 (July 2017), pp. 317–325. ISSN: 2367-0932. DOI: `10.1002/cptc.201600061` (cit. on p. 125).

[692] Joshua K. G. Karlsson et al. "Effects of Temperature and Concentration on the Rate of Photobleaching of Erythrosine in Water". In: *The Journal of Physical Chemistry A* 121.45 (Nov. 2017), pp. 8569–8576. ISSN: 1089-5639. DOI: `10.1021/acs.jpca.7b06440` (cit. on p. 125).

[693] D. A. Axelrod et al. "Mobility Measurement by Analysis of Fluorescence Photobleaching Recovery Kinetics". In: *Biophysical journal* 16 (Oct. 1976), pp. 1055–69. DOI: `10.1016/S0006-3495(76)85755-4` (cit. on p. 125).

[694] Gerald Donnert, Christian Eggeling, and Stefan W. Hell. "Major Signal Increase in Fluorescence Microscopy Through Dark-State Relaxation". In: *Nature Methods* 4.1 (Jan. 2007), pp. 81–86. ISSN: 1548-7105. DOI: `10.1038/nmeth986` (cit. on p. 125).

[695] Na Ji, Jeffrey C. Magee, and Eric Betzig. "High-Speed, Low-Photodamage Nonlinear Imaging Using Passive Pulse Splitters". In: *Nature Methods* 5.2 (Feb. 2008), pp. 197–202. ISSN: 1548-7105. DOI: `10.1038/nmeth.1175` (cit. on p. 125).

[696] Wei-Chuan Sun et al. "Synthesis of Fluorinated Fluoresceins". In: *The Journal of Organic Chemistry* 62.19 (Sept. 1997), pp. 6469–6475. ISSN: 0022-3263. DOI: `10.1021/jo9706178` (cit. on p. 125).

[697] Franco M. Cabrerizo et al. "Fluorescence Quenching by Oxygen: "Debunking" a Classic Rule". In: *ChemPhysChem* 11.4 (Mar. 2010), pp. 796–798. ISSN: 1439-4235. DOI: `10.1002/cphc.201000002` (cit. on p. 125).

[698] Yutaka Amao. "Probes and Polymers for Optical Sensing of Oxygen". In: *Microchimica Acta* 143.1 (Sept. 2003), pp. 1–12. ISSN: 1436-5073. DOI: `10.1007/s00604-003-0037-x` (cit. on p. 125).

[699] M. Cajlakovic et al. "Simultaneously Monitoring of Tissue O2 and CO2 Partial Pressures by Means of Miniaturized Implanted Fiber Optical Sensors". In: *SENSORS, 2009 IEEE*. SENSORS, 2009 IEEE. 2009, pp. 31–36. DOI: `10.1109/ICSENS.2009.5398126` (cit. on pp. 126, 158).

[700] Jens M. Kürner et al. "Inert Phosphorescent Nanospheres as Markers for Optical Assays". In: *Bioconjugate Chemistry* 12.6 (Nov. 2001), pp. 883–889. ISSN: 1043-1802. DOI: `10.1021/bc000130x` (cit. on p. 126).

[701] Christoph Alexander Johannes von von Bueltzingsloewen. "Development of Optical Sensors ("Optodes") for Carbon Dioxide and Their Application to Modified Atmosphere Packaging (MAP)". PhD thesis. University of Regensburg, Apr. 2004. URL: `https://epub.uni-regensburg.de/10190/` (cit. on p. 126).

[702] Edwards Angharad Naomi. "Development of Luminescent Labels for use in Miniaturised Diagnostic Devices". PhD thesis. Imperial College London, Sept. 2011. URL: `https://core.ac.uk/download/pdf/8767127.pdf` (cit. on p. 126).

[703] Ting-xiu Ye et al. "Preparation of Novel Core-Shell Silica Particles for pH Sensing Using Ratiometric Fluorescence Approach". In: *Analytical Methods* 4.4 (2012), pp. 1001–1004. ISSN: 1759-9660. DOI: `10.1039/C2AY25073J` (cit. on p. 126).

[704] Aamir A. Khan, Susan K. Fullerton-Shirey, and Scott S. Howard. "Easily Prepared Ruthenium-Complex Nanomicelle Probes for Two-Photon Quantitative Imaging of Oxygen in Aqueous Media". In: *RSC Advances* 5.1 (2015), pp. 291–300. DOI: `10.1039/C4RA11229F` (cit. on pp. 126, 134).

[705] Yanlong Feng et al. “Imaging and Simulation of Ruthenium Derivative Coating Microbeads at the Opaque Electrode with Electrogenerated Chemiluminescence”. In: *Chemical & Biomedical Imaging* 1.7 (Oct. 2023), pp. 648–658. DOI: `10.1021/cbmi.3c00042` (cit. on p. 126).

[706] Elise Villemin et al. “Polymer Encapsulation of Ruthenium Complexes for Biological and Medicinal Applications”. In: *Nature Reviews Chemistry* 3.4 (Apr. 2019), pp. 261–282. ISSN: 2397-3358. DOI: `10.1038/s41570-019-0088-0` (cit. on p. 126).

[707] Mikhail Y. Berezin and Samuel Achilefu. “Fluorescence Lifetime Measurements and Biological Imaging”. In: *Chemical Reviews* 110.5 (May 2010), pp. 2641–2684. ISSN: 0009-2665. DOI: `10.1021/cr900343z`. URL: `https://doi.org/10.1021/cr900343z` (cit. on p. 127).

[708] Masahiko Taniguchi, Hai Du, and Jonathan S. Lindsey. “PhotochemCAD 3: Diverse Modules for Photophysical Calculations with Multiple Spectral Databases”. In: *Photochemistry and Photobiology* 94.2 (Mar. 2018), pp. 277–289. ISSN: 0031-8655. DOI: `10.1111/php.12862`. URL: `https://doi.org/10.1111/php.12862` (cit. on p. 127).

[709] Masahiko Taniguchi and Jonathan S. Lindsey. “Database of Absorption and Fluorescence Spectra of >300 Common Compounds for use in PhotochemCAD”. In: *Photochemistry and Photobiology* 94.2 (Mar. 2018), pp. 290–327. ISSN: 0031-8655. DOI: `10.1111/php.12860`. URL: `https://doi.org/10.1111/php.12860` (cit. on pp. 127, 128).

[710] “Appendix: Characteristics of Fluorescent Organic Compounds”. In: *Molecular Fluorescence*. John Wiley & Sons, Ltd, 2012, pp. 521–550. ISBN: 9783527650002. DOI: `https://doi.org/10.1002/9783527650002.app1`. eprint: `https://onlinelibrary.wiley.com/doi/pdf/10.1002/9783527650002.app1`. URL: `https://onlinelibrary.wiley.com/doi/abs/10.1002/9783527650002.app1` (cit. on pp. 127–129).

[711] Technical University Graz. *Fluorophores.org Database*. 2022. URL: `https://web.archive.org/web/20220131100036/http://www.fluorophores.tugraz.at/substance/` (visited on 01/31/2022) (cit. on pp. 127–129).

[712] Max-Planck Institute for Brain Research. *Spectra Viewer*. 2022. URL: `https://web.archive.org/web/20220131101055/https://public.brain.mpg.de/shiny/apps/SpectraViewer/` (visited on 01/31/2022) (cit. on pp. 127–129).

[713] George McNamara. *PubSpectra - Open Data Access Fluorescence Spectra*. Tech. rep. 2012 (cit. on p. 127).

[714] Thermo Fisher Scientific. *Spectra Viewer*. 2022. URL: `https://web.archive.org/web/20220131101938/https://www.thermofisher.com/order/fluorescence-spectraviewer` (visited on 01/31/2022) (cit. on p. 127).

[715] Leica Microsystems. *Fluorescent Dyes, An Overview*. 2022. URL: `https://web.archive.org/web/20220131142705/https://www.leica-microsystems.com/science-lab/fluorescent-dyes/` (visited on 01/31/2022) (cit. on p. 127).

[716] Zeiss. *Filter Assistant - Dyes*. 2022. URL: `https://web.archive.org/web/20220131152345/https://www.micro-shop.zeiss.com/en/de/shop/filterAssistant/dyes/` (visited on 01/31/2022) (cit. on p. 127).

[717] FluoroFinder. *Spectra Viewer*. 2022. URL: `https://web.archive.org/web/20210117235922/https://app.fluorofinder.com/dyes` (visited on 01/17/2022) (cit. on p. 127).

[718] Dorota Wencel, Tobias Abel, and Colette McDonagh. “Optical Chemical pH Sensors”. In: *Analytical Chemistry* 86.1 (Jan. 2014), pp. 15–29. ISSN: 0003-2700. DOI: `10.1021/ac4035168`. URL: `https://doi.org/10.1021/ac4035168` (cit. on p. 127).

[719] Junyan Han and Kevin Burgess. “Fluorescent Indicators for Intracellular pH”. In: *Chemical Reviews* 110.5 (May 2010), pp. 2709–2728. ISSN: 0009-2665. DOI: `10.1021/cr900249z`. URL: `https://doi.org/10.1021/cr900249z` (cit. on p. 127).

[720] Noël Boens, Volker Leen, and Wim Dehaen. “Fluorescent Indicators Based on BODIPY”. In: *Chemical Society Reviews* 41.3 (2012), pp. 1130–1172. ISSN: 0306-0012. DOI: `10.1039/C1CS15132K`. URL: `https://doi.org/10.1039/C1CS15132K` (cit. on p. 127).

[721] Florent Le Guern et al. “Fluorescein Derivatives as Fluorescent Probes for pH Monitoring along Recent Biological Applications”. In: *International Journal of Molecular Sciences* 21.23 (2020). ISSN: 1422-0067. DOI: `10.3390/ijms21239217`. URL: `https://www.mdpi.com/1422-0067/21/23/9217` (cit. on p. 127).

[722] Luke D. Lavis, Thomas J. Rutkoski, and Ronald T. Raines. "Tuning the pKa of Fluorescein to Optimize Binding Assays". In: *Analytical Chemistry* 79.17 (Sept. 2007), pp. 6775–6782. ISSN: 0003-2700. DOI: `10.1021/ac070907g`. URL: `https://doi.org/10.1021/ac070907g` (cit. on p. 127).

[723] Otto S. Wolfbeis et al. "Fluorimetric Analysis 1. A Study on Fluorescent Indicators for Measuring Near Neutral ("Physiological") pH-Values". In: *Fresenius' Zeitschrift für analytische Chemie* 314.2 (1983), pp. 119–124. ISSN: 1618-2650. DOI: `10.1007/BF00482235`. URL: `https://doi.org/10.1007/BF00482235` (cit. on pp. 127, 131, 132, 139).

[724] T.-H. Tran-Thi et al. "Substituent and Solvent Effects on the Nature of the Transitions of Pyrenol and Pyranine. Identification of an Intermediate in the Excited-State Proton-Transfer Reaction". In: *The Journal of Physical Chemistry A* 106.10 (2002), pp. 2244–2255. DOI: `10.1021/jp0125606`. eprint: `https://doi.org/10.1021/jp0125606`. URL: `https://doi.org/10.1021/jp0125606` (cit. on pp. 127, 131, 132).

[725] "8-Hydroxypyrene-1,3,6-Trisulfonic Acid Trisodium Salt (HPTS) (Pyranine)". In: *Handbook of Fluorescent Dyes and Probes*. John Wiley & Sons, Ltd, 2015. Chap. 90, pp. 253–262. ISBN: 9781119007104. DOI: `https://doi.org/10.1002/9781119007104.ch90`. eprint: `https://onlinelibrary.wiley.com/doi/pdf/10.1002/9781119007104.ch90`. URL: `https://onlinelibrary.wiley.com/doi/abs/10.1002/9781119007104.ch90` (cit. on pp. 127, 131).

[726] Monique M. Martin and Lars Lindqvist. "The pH Dependence of Fluorescein Fluorescence". In: *Journal of Luminescence* 10.6 (July 1975), pp. 381–390. ISSN: 0022-2313. DOI: `10.1016/0022-2313(75)90003-4` (cit. on p. 128).

[727] Jessica P. Houston et al. "Overview of Fluorescence Lifetime Measurements in Flow Cytometry". In: *Flow Cytometry Protocols*. Ed. by Teresa S. Hawley and Robert G. Hawley. New York, NY: Springer New York, 2018, pp. 421–446. ISBN: 978-1-4939-7346-0. DOI: `10.1007/978-1-4939-7346-0_18`. URL: `https://doi.org/10.1007/978-1-4939-7346-0_18` (cit. on p. 127).

[728] Xu-dong Wang and Otto S. Wolfbeis. "Optical Methods for Sensing and Imaging Oxygen: Materials, Spectroscopies and Applications". In: *Chemical Society Reviews* 43.10 (2014), pp. 3666–3761. ISSN: 0306-0012. DOI: `10.1039/C4CS00039K` (cit. on pp. 128, 157).

[729] Joy E. Rogers et al. "Observation and Interpretation of Annulated Porphyrins: Studies on the Photophysical Properties of meso-Tetraphenylmetalloporphyrins". In: *The Journal of Physical Chemistry A* 107.51 (Dec. 2003), pp. 11331–11339. ISSN: 1089-5639. DOI: `10.1021/jp0354705`. URL: `https://doi.org/10.1021/jp0354705` (cit. on p. 129).

[730] Carsten Borek et al. "Highly Efficient, Near-Infrared Electrophosphorescence From a Pt–Metalloporphyrin Complex". In: *Angewandte Chemie International Edition* 46.7 (2007), pp. 1109–1112. DOI: `https://doi.org/10.1002/anie.200604240`. eprint: `https://onlinelibrary.wiley.com/doi/pdf/10.1002/anie.200604240`. URL: `https://onlinelibrary.wiley.com/doi/abs/10.1002/anie.200604240` (cit. on p. 129).

[731] Andrew Mills and Anne Lepre. "Controlling the Response Characteristics of Luminescent Porphyrin Plastic Film Sensors for Oxygen". In: *Analytical Chemistry* 69.22 (Nov. 1997), pp. 4653–4659. ISSN: 0003-2700. DOI: `10.1021/ac970430g`. URL: `https://doi.org/10.1021/ac970430g` (cit. on p. 129).

[732] J. Kalinowski et al. "Photophysics of an Electrophosphorescent Platinum (II) Porphyrin in Solid Films". In: *The Journal of Chemical Physics* 122.15 (Apr. 2005), p. 154710. ISSN: 0021-9606. DOI: `10.1063/1.1878612`. URL: `https://doi.org/10.1063/1.1878612` (cit. on p. 129).

[733] Dmitri B. Papkovsky et al. "Phosphorescent Complexes of Porphyrin Ketones: Optical Properties and Application to Oxygen Sensing". In: *Analytical Chemistry* 67.22 (Nov. 1995), pp. 4112–4117. ISSN: 0003-2700. DOI: `10.1021/ac00118a013`. URL: `https://doi.org/10.1021/ac00118a013` (cit. on p. 129).

[734] Peter C. Alford et al. "Luminescent Metal Complexes. Part 5. Luminescence Properties of Ring-Substituted 1,10-Phenanthroline Tris-Complexes of Ruthenium(II)". In: *Journal of the Chemical Society, Perkin Transactions 2* 5 (1985), pp. 705–709. ISSN: 0300-9580. DOI: `10.1039/P29850000705`. URL: `https://doi.org/10.1039/P29850000705` (cit. on pp. 129, 133, 134).

[735] J. Van Houten and R. J. Watts. “Temperature Dependence of the Photophysical and Photochemical Properties of the tris(2,2’-bipyridyl)ruthenium(II) Ion in Aqueous Solution”. In: *Journal of the American Chemical Society* 98.16 (Aug. 1976), pp. 4853–4858. ISSN: 0002-7863. DOI: 10.1021/ja00432a028. URL: https://doi.org/10.1021/ja00432a028 (cit. on p. 129).

[736] Pavel Müller and Klaus Brettel. “[Ru(bpy)3]2+ as a Reference in Transient Absorption Spectroscopy: Differential Absorption Coefficients for Formation of the Long-Lived 3MLCT Excited State”. In: *Photochemical & Photobiological Sciences* 11.4 (2012), pp. 632–636. ISSN: 1474-905X. DOI: 10.1039/C2PP05333K. URL: https://doi.org/10.1039/C2PP05333K (cit. on p. 129).

[737] Dervieux Emmanuel. “Dye-Based Transcutaneous Carbon Dioxide Sensing: a Review”. In: *Biosency Internal Publication* (2020) (cit. on p. 131).

[738] Stephen G. Schulman et al. “Dependence of the Fluorescence of Immobilized 1-Hydroxypyrene-3,6,8-Trisulfonate on Solution pH: Extension of the Range of Applicability of a pH Fluorosensor”. In: *Analytica Chimica Acta* 304.2 (Mar. 1995), pp. 165–170. ISSN: 0003-2670. URL: http://www.sciencedirect.com/science/article/pii/000326709400631U (cit. on pp. 131, 132).

[739] Rajnish Kumar et al. “8-Hydroxypyrene-1,3,6-Trisulfonic Acid Trisodium Salt (HPTS) Based High Fluorescent, pH Stimuli Waterborne Polyurethane Coatings”. In: *Polymer* 136 (Jan. 2018), pp. 157–165. ISSN: 0032-3861. URL: http://www.sciencedirect.com/science/article/pii/S0032386117312284 (cit. on pp. 131, 132).

[740] Noga Barrash-Shiftan, Brina (Beth) Brauer, and Ehud Pines. “Solvent Dependence of Pyranine Fluorescence and UV-Visible Absorption Spectra”. In: *Journal of Physical Organic Chemistry* 11.10 (1998), pp. 743–750. DOI: https://doi.org/10.1002/(SICI)1099-1395(1998100)11:10<743::AID-POC39>3.0.CO;2-H. eprint: https://onlinelibrary.wiley.com/doi/pdf/10.1002/%28SICI%291099-1395%281998100%2911%3A10%3C743%3A%3AAID-POC39%3E3.0.CO%3B2-H. URL: https://onlinelibrary.wiley.com/doi/abs/10.1002/%28SICI%291099-1395%281998100%2911%3A10%3C743%3A%3AAID-POC39%3E3.0.CO%3B2-H (cit. on pp. 132, 133).

[741] J.J. Nairn and W.A. Forster. “Photostability of Pyranine and Suitability as a Spray Drift Tracer”. In: *New Zealand Plant Protection* 68 (Jan. 2015), pp. 32–37. DOI: 10.30843/nzpp.2015.68.5795. URL: https://nzpps.org/_journal/index.php/nzpp/article/view/5795 (cit. on pp. 133, 148).

[742] Sharad R. Bobe et al. “Detection of Trace Amounts of Water in Organic Solvent by 8-Hydroxypyrene-1,3,6-Trisulfonic Acid Trisodium Salt”. In: *Australian Journal of Chemistry* 67.4 (2014), pp. 615–619. DOI: 10.1071/CH13381 (cit. on p. 133).

[743] Chemical Book. *Solvent Green 7*. 2024. URL: https://web.archive.org/web/20240216133151/https://www.chemicalbook.com/ChemicalProductProperty_EN_CB9402700.htm (visited on 02/16/2024) (cit. on p. 133).

[744] Wenying. Xu et al. “Oxygen Sensors Based on Luminescence Quenching: Interactions of Metal Complexes with the Polymer Supports”. In: *Analytical Chemistry* 66.23 (Dec. 1994), pp. 4133–4141. ISSN: 0003-2700. DOI: 10.1021/ac00095a004. URL: https://doi.org/10.1021/ac00095a004 (cit. on pp. 133, 134).

[745] J. R. Bacon and J. N. Demas. “Determination of Oxygen Concentrations by Luminescence Quenching of a Polymer-Immobilized Transition-Metal Complex”. In: *Analytical Chemistry* 59.23 (Dec. 1987), pp. 2780–2785. ISSN: 0003-2700. DOI: 10.1021/ac00150a012. URL: https://doi.org/10.1021/ac00150a012 (cit. on pp. 133, 134).

[746] G. Liebsch, I. Klimant, and O. S. Wolfbeis. “Luminescence Lifetime Temperature Sensing Based on Sol-Gels and Poly(acrylonitrile)s Dyed with Ruthenium Metal–Ligand Complexes”. In: *Advanced Materials* 11.15 (1999), pp. 1296–1299. DOI: https://doi.org/10.1002/(SICI)1521-4095(199910)11:15<1296::AID-ADMA1296>3.0.CO;2-B. eprint: https://onlinelibrary.wiley.com/doi/pdf/10.1002/%28SICI%291521-4095%28199910%2911%3A15%3C1296%3A%3AAID-ADMA1296%3E3.0.CO%3B2-B. URL: https://onlinelibrary.wiley.com/doi/abs/10.1002/%28SICI%291521-4095%28199910%2911%3A15%3C1296%3A%3AAID-ADMA1296%3E3.0.CO%3B2-B (cit. on pp. 133, 134).

[747] Gary A. Baker et al. “Effects of Processing Temperature on the Oxygen Quenching Behavior of Tris(4,7’-diphenyl-1,10’-phenanthroline) Ruthenium (II) Sequestered Within Sol-Gel-Derived Xerogel Films”. In: *Journal of Sol-Gel Science and Technology* 17.1 (2000), pp. 71–82. ISSN: 1573-4846. DOI: `10.1023/A:1008765106291`. URL: `https://doi.org/10.1023/A:1008765106291` (cit. on pp. 133, 134).

[748] Andrew Mills and Ashleigh Graham. “Extruded Polymer Films Pigmented With a Heterogeneous Ion-Pair Based Lumophore for O2 Sensing”. In: *Analyst* 138.21 (2013), pp. 6488–6493. ISSN: 0003-2654. DOI: `10.1039/C3AN01141K`. URL: `https://doi.org/10.1039/C3AN01141K` (cit. on pp. 133, 134).

[749] Andrzej Kapturkiewicz. “Electrogenerated Chemiluminescence From the Tris(4,7-Diphenyl-1,10-Phenanthroline)Ruthenium(II) complex”. In: *Chemical Physics Letters* 236.4 (Apr. 1995), pp. 389–394. ISSN: 0009-2614. URL: `http://www.sciencedirect.com/science/article/pii/000926149500232S` (cit. on p. 134).

[750] K Nakamaru, K Nishio, and H Nobe. “Reexamination of the Luminescence Quantum Yields of Tris (2, 2’-bipyridyl or 1, 10-phenanthroline and Their Derivatives) Ruthenium (II) Ions in Aqueous Solutions at Room Temperature (25C)”. In: *Sci. Rep. Hirosaki Univ* 26 (1979), pp. 57–62 (cit. on pp. 134, 191).

[751] J. N. Demas, E. W. Harris, and R. P. McBride. “Energy Transfer From Luminescent Transition Metal Complexes to Oxygen”. In: *Journal of the American Chemical Society* 99.11 (May 1977), pp. 3547–3551. ISSN: 0002-7863. DOI: `10.1021/ja00453a001`. URL: `https://doi.org/10.1021/ja00453a001` (cit. on p. 134).

[752] G. Korotcenkov. *Handbook of Gas Sensor Materials: Properties, Advantages and Shortcomings for Applications Volume 2: New Trends and Technologies*. Integrated Analytical Systems. Springer New York, 2014. ISBN: 9781461473879. DOI: `10.1007/978-1-4614-7388-6` (cit. on p. 134).

[753] H. Yasuda and William Stone JR. “Permeability of Polymer Membranes to Dissolved Oxygen”. In: *Journal of Polymer Science Part A-1: Polymer Chemistry* 4.5 (May 1966), pp. 1314–1316. ISSN: 0449-296X. DOI: `10.1002/pol.1966.150040529` (cit. on p. 135).

[754] Yuxin Wang, Mohit Gupta, and David A. Schiraldi. “Oxygen Permeability in Thermoplastic Polyurethanes”. In: *Journal of Polymer Science Part B: Polymer Physics* 50.10 (May 2012), pp. 681–693. ISSN: 0887-6266. DOI: `10.1002/polb.23053` (cit. on p. 135).

[755] Wu-Huang Yang, Victor F. Smolen, and Nikolaos A. Peppas. “Oxygen Permeability Coefficients of Polymers for Hard and Soft Contact Lens Applications”. In: *Journal of Membrane Science* 9.1 (Jan. 1981), pp. 53–67. ISSN: 0376-7388 (cit. on p. 135).

[756] Shuichi Aiba, Minoru Ohashi, and S.-Y. Huang. “Rapid Determination of Oxygen Permeability of Polymer Membranes”. In: *Industrial & Engineering Chemistry Fundamentals* 7.3 (Aug. 1968), pp. 497–502. ISSN: 0196-4313. DOI: `10.1021/i160027a022` (cit. on p. 135).

[757] Marion R. Surgi, A. J. Polak, and R. C. Sundahl. “Description of Oxygen Permeability in Various High Polymers Using a Graph Theoretical Approach”. In: *Journal of Polymer Science Part A: Polymer Chemistry* 27.8 (July 1989), pp. 2761–2776. ISSN: 0887-624X. DOI: `10.1002/pola.1989.080270821` (cit. on p. 135).

[758] W. J. Koros, M. R. Coleman, and D. R. B. Walker. “Controlled Permeability Polymer Membranes”. In: *Annual Review of Materials Science* 22.1 (Aug. 1992), pp. 47–89. ISSN: 0084-6600. DOI: `10.1146/annurev.ms.22.080192.000403` (cit. on p. 135).

[759] Shinji Kanehashi et al. “Analysis of Permeability; Solubility and Diffusivity of Carbon Dioxide; Oxygen; and Nitrogen in Crystalline and Liquid Crystalline Polymers”. In: *Journal of Membrane Science* 365.1 (Dec. 2010), pp. 40–51. ISSN: 0376-7388 (cit. on p. 135).

[760] Nivedita S. Sangaj and V. C. Malshe. “Permeability of Polymers in Protective Organic Coatings”. In: *Progress in Organic Coatings* 50.1 (June 2004), pp. 28–39. ISSN: 0300-9440 (cit. on p. 135).

[761] Laurence W. McKeen. *Permeability Properties of Plastics and Elastomers, 4th Edition*. Plastics Design Library. Elsevier, 2017. ISBN: 9780323508599 (cit. on pp. 134, 135, 137).

[762] Liesl K. Massey. *Permeability Properties of Plastics and Elastomers, 2nd Edition*. Plastics Design Library. William Andrew Inc., 2003. ISBN: 1884207979 (cit. on pp. 134, 135, 137).

[763] T. S. Sokolova et al. “Transparent and Mechanically Robust Poly (Para-Phenylene Terephthamide) PPTA Nanopaper Toward Electrical Insulation Based on Nanoscale Fibrillated Aramid-Fibers”. In: *Khimicheskie Volokna* 1 (1974), pp. 26–28 (cit. on p. 135).

[764] M. Arpin and C. Strazielle. “Characterization and Conformation of Aromatic Polyamides: Poly(1,4-Phenylene Terephthalamide) and Poly(p-Benzamide) in Sulphuric Acid”. In: *Polymer* 18.6 (June 1977), pp. 591–598. ISSN: 0032-3861 (cit. on p. 135).

[765] H. P. Westerhof. “On the Structure and Dissolution Properties of Poly(p-Phenylene Terephthalamide): Effect of Solvent Composition”. PhD thesis. Technische Universiteit Delft, 2009 (cit. on p. 135).

[766] John E. Flood, James L. White, and John F. Fellers. “Process for the Formation of Biaxially Oriented Films of Poly(p-Phenylene Terephthalamide) From Liquid Crystalline Solutions”. In: *Journal of Applied Polymer Science* 27.8 (Aug. 1982), pp. 2965–2985. ISSN: 0021-8995. DOI: `10.1002/app.1982.070270821` (cit. on p. 135).

[767] Tadahiro Fujita et al. “A Novel Process for the Formation of Poly(p-Phenylene Terephthalamide) Film From Liquid Crystalline Solutions”. In: *Polymer Engineering & Science* 29.18 (Sept. 1989), pp. 1237–1240. ISSN: 0032-3888. DOI: `10.1002/pen.760291805` (cit. on p. 135).

[768] D. H. Weinkauf, H. D. Kim, and D. R. Paul. “Gas Transport Properties of Liquid Crystalline Poly(p-Phenyleneterephthalamide)”. In: *Macromolecules* 25.2 (Jan. 1992), pp. 788–796. ISSN: 0024-9297. DOI: `10.1021/ma00028a044` (cit. on p. 135).

[769] Zhaoqing Lu et al. “Transparent and Mechanically Robust Poly (Para-Phenylene Terephthamide) PPTA Nanopaper Toward Electrical Insulation Based on Nanoscale Fibrillated Aramid-Fibers”. In: *Composites Part A: Applied Science and Manufacturing* 115 (Dec. 2018), pp. 321–330. ISSN: 1359-835X (cit. on p. 135).

[770] Ming Yang et al. “Aramid Nanofiber-Reinforced Transparent Nanocomposites”. In: *Journal of Composite Materials* 49.15 (June 2015), pp. 1873–1879. ISSN: 0021-9983. DOI: `10.1177/0021998315579230` (cit. on p. 135).

[771] Lynn Penn and Fred Larsen. “Physicochemical Properties of Kevlar 49 Fiber”. In: *Journal of Applied Polymer Science* 23.1 (1979), pp. 59–73. ISSN: 0021-8995. DOI: `10.1002/app.1979.070230106` (cit. on p. 135).

[772] S. M. Allen et al. “The Barrier Properties of Polyacrylonitrile”. In: *Journal of Membrane Science* 2 (Jan. 1977), pp. 153–163. ISSN: 0376-7388 (cit. on p. 135).

[773] H. C. Park and Charles R. Ashcraft. “The Use of Polyacrylonitrile Film in Barrier Food Packaging”. In: *Journal of Plastic Film & Sheeting* 1.2 (Apr. 1985), pp. 95–103. ISSN: 8756-0879. DOI: `10.1177/875608798500100203` (cit. on p. 135).

[774] Jean-Marie Prival. *Why is Mass Fraction Always Abbreviated wt% and not ma%?* Earth Science Stack Exchange. 2024. URL: `https://web.archive.org/web/20240919060623/https://earthscience.stackexchange.com/questions/18927/why-is-mass-fraction-always-abbreviated-wt-and-not-ma` (cit. on p. 135).

[775] Toru Kawai and Eizo Ida. “Analysis of Intrinsic Viscosity Data on Polyacrylonitrile in Various Solvents”. In: *Kolloid-Zeitschrift und Zeitschrift für Polymere* 194.1 (Jan. 1964), pp. 40–49. ISSN: 1435-1536. DOI: `10.1007/BF01499975` (cit. on p. 135).

[776] Makiko Hattori et al. “NMR Study on the Dissolved State of Polyacrylonitrile in Various Solvents”. In: *Polymer Journal* 28.7 (July 1996), pp. 594–600. ISSN: 1349-0540. DOI: `10.1295/polymj.28.594` (cit. on p. 135).

[777] M. M. Iovleva, V. N. Smirnova, and G. A. Budnitskii. “The Solubility of Polyacrylonitrile”. In: *Fibre Chemistry* 33.4 (July 2001), pp. 262–264. ISSN: 1573-8493. DOI: `10.1023/A:1012934313303` (cit. on p. 135).

[778] Lianjiang Tan, Ding Pan, and Ning Pan. “Thermodynamic Study of a Water–Dimethylformamide–Polyacrylonitrile Ternary System”. In: *Journal of Applied Polymer Science* 110.6 (Dec. 2008), pp. 3439–3447. ISSN: 0021-8995. DOI: `10.1002/app.28392` (cit. on p. 135).

[779] George E. Ham. “Polymerization of Acrylics”. In: *Textile Research Journal* 24.7 (1954), pp. 597–604. ISSN: 0040-5175. DOI: `10.1177/004051755402400701` (cit. on p. 135).

[780] Youngho Eom et al. “Effect of Dissolution Pathways of Polyacrylonitrile on the Solution Homogeneity: Thermodynamic- or Kinetic-Controlled Dissolution”. In: *Polymer* 205 (Sept. 2020), p. 122697. ISSN: 0032-3861 (cit. on pp. 135, 136).

[781] William M. Haynes. *CRC Handbook of Chemistry and Physics*. 95th. Physical Sciences. CRC, 2014. ISBN: 9780429170195. DOI: `10.1201/b17118` (cit. on p. 136).

[782] J. G. Cook. *Handbook of Textile Fibres: Man-Made Fibres*. Woodhead Publishing Series in Textiles. Elsevier Science, 1984. ISBN: 9781845693169 (cit. on p. 136).

[783] O. Olabisi and K. Adewale. *Handbook of Thermoplastics*. Plastics Engineering. CRC Press, 2016. ISBN: 9781466577237 (cit. on p. 136).

[784] H. Neil McMurray. “Novel Thin Optical Film Sensors for the Detection of Carbon Dioxide”. In: *Journal of Materials Chemistry* 2.4 (1992), pp. 401–406. ISSN: 0959-9428. DOI: `10.1039/JM9920200401` (cit. on p. 136).

[785] Dario Landini, Angelamaria Maia, and Fernando Montanari. “Phase-Transfer Catalysis. Nucleophilicity of Anions in Aqueous Organic Two-Phase Reactions Catalyzed by Onium Salts. A Comparison With Homogeneous Organic Systems”. In: *Journal of the American Chemical Society* 100.9 (1978), pp. 2796–2801. ISSN: 0002-7863. DOI: `10.1021/ja00477a036` (cit. on p. 136).

[786] Yuchuan Gong, David J.W. Grant, and Harry G. Brittain. “Principles of Solubility”. In: *Solvent Systems and Their Selection in Pharmaceutics and Biopharmaceutics*. Ed. by Patrick Augustijns and Marcus E. Brewster. New York, NY: Springer New York, 2007, pp. 1–27. ISBN: 978-0-387-69154-1. DOI: `10.1007/978-0-387-69154-1_1` (cit. on p. 136).

[787] N/A. “N/A”. In: *N/A*. N/A, 2002. Chap. Chapter 4. Permeability, Diffusivity, and Solubility of Gas and Solute Through Polymers. URL: `https://api.semanticscholar.org/CorpusID:2330176` (cit. on pp. 136, 137).

[788] Jaroslaw Drelich et al. “Hydrophilic and Superhydrophilic Surfaces and Materials”. In: *Soft Matter* 7.21 (2011), pp. 9804–9828. ISSN: 1744-683X. DOI: `10.1039/C1SM05849E` (cit. on p. 136).

[789] Carmelo Corsaro et al. “Hydrophilicity and Hydrophobicity: Key Aspects for Biomedical and Technological Purposes”. In: *Physica A: Statistical Mechanics and its Applications* 580 (2021), p. 126189. ISSN: 0378-4371. DOI: `10.1016/j.physa.2021.126189` (cit. on p. 136).

[790] Loreto M. Valenzuela, Bozena Michniak, and Joachim Kohn. “Variability of Water Uptake Studies of Biomedical Polymers”. In: *Journal of Applied Polymer Science* 121.3 (2011), pp. 1311–1320. ISSN: 0021-8995. DOI: `10.1002/app.33485` (cit. on pp. 136, 137).

[791] Elvira Vidović, Doris Klee, and Hartwig Höcker. “Evaluation of Water Uptake and Mechanical Properties of Biomedical Polymers”. In: *Journal of Applied Polymer Science* 130.5 (2013), pp. 3682–3688. ISSN: 0021-8995. DOI: `10.1002/app.39624` (cit. on p. 136).

[792] Michael Grossutti and John R. Dutcher. “Hydration Water Structure, Hydration Forces, and Mechanical Properties of Polysaccharide Films”. In: *Biomacromolecules* 21.12 (2020), pp. 4871–4877. ISSN: 1525-7797. DOI: `10.1021/acs.biomac.0c01098` (cit. on pp. 136, 147).

[793] Nirali G. Patel and Abu T.M. Serajuddin. “Moisture Sorption by Polymeric Excipients Commonly Used in Amorphous Solid Dispersion and its Effect on Glass Transition Temperature: I. Polyvinylpyrrolidone and Related Copolymers”. In: *International Journal of Pharmaceutics* 616 (2022), p. 121532. ISSN: 0378-5173. DOI: `10.1016/j.ijpharm.2022.121532` (cit. on pp. 136, 137, 146).

[794] Nirali G. Patel, Sabrina Banella, and Abu T.M. Serajuddin. “Moisture Sorption by Polymeric Excipients Commonly Used in Amorphous Solid Dispersions and its Effect on Glass Transition Temperature: II. Cellulosic Polymers”. In: *Journal of Pharmaceutical Sciences* 111.11 (2022), pp. 3114–3129. ISSN: 0022-3549. DOI: `10.1016/j.xphs.2022.07.020` (cit. on pp. 136, 137, 146, 147).

[795] Nirali G. Patel, Sabrina Banella, and Abu T.M. Serajuddin. “Moisture Sorption by Polymeric Excipients Commonly Used in Amorphous Solid Dispersions and its Effect on Glass Transition Temperature: III. Methacrylic Acid-Methyl Methacrylate and Related Copolymers (Eudragit)”. In: *International Journal of Pharmaceutics* 636 (2023), p. 122745. ISSN: 0378-5173. DOI: `10.1016/j.ijpharm.2023.122745` (cit. on pp. 136, 137, 146).

[796] G. K. van der Wel and O. C. G. Adan. “Moisture in Organic Coatings — A Review”. In: *Progress in Organic Coatings* 37.1 (Nov. 1999), pp. 1–14. ISSN: 0300-9440. DOI: `10.1016/S0300-9440(99)00058-2` (cit. on p. 137).

[797] Karol Kulasinski et al. “Impact of Moisture Adsorption on Structure and Physical Properties of Amorphous Biopolymers”. In: *Macromolecules* 48.8 (2015), pp. 2793–2800. ISSN: 0024-9297. DOI: `10.1021/acs.macromol.5b00248` (cit. on p. 137).

[798] Karol Kulasinski. “Polymer science : research advances , practical applications and educational aspects”. In: *Polymer science : research advances , practical applications and educational aspects*. Formatex Research Center S.L., 2016. Chap. Effects of Water Adsorption in Hydrophilic Polymers. ISBN: 8494213482 (cit. on p. 137).

[799] Roland Geyer, Jenna R. Jambeck, and Kara Lavender Law. “Production, Use, and Fate of All Plastics Ever Made”. In: *Science Advances* 3.7 (2017). DOI: `10.1126/sciadv.1700782` (cit. on p. 137).

[800] Nilofar Asim, Marzieh Badiei, and Masita Mohammad. “Recent Advances in Cellulose-Based Hydrophobic Food Packaging”. In: *Emergent Materials* 5.3 (June 2022), pp. 703–718. ISSN: 2522-574X. DOI: `10.1007/s42247-021-00314-2` (cit. on p. 137).

[801] B. Mishra et al. “Permeability of Edible Coatings”. In: *Journal of Food Science and Technology* 47.1 (2010), pp. 109–113. ISSN: 0975-8402. DOI: `10.1007/s13197-010-0003-7` (cit. on p. 137).

[802] True L. Rogers and Dave Wallick. “Reviewing the Use of Ethylcellulose, Methylcellulose and Hypromellose in Microencapsulation. Part 1: Materials Used to Formulate Microcapsules”. In: *Drug Development and Industrial Pharmacy* 38.2 (Feb. 2012), pp. 129–157. ISSN: 0363-9045. DOI: `10.3109/03639045.2011.590990` (cit. on p. 137).

[803] Ning Yang et al. “Moisture Sorption and Desorption Properties of Gelatin, HPMC and Pullulan Hard Capsules”. In: *International Journal of Biological Macromolecules* 159 (Sept. 2020), pp. 659–666. ISSN: 0141-8130. DOI: `10.1016/j.ijbiomac.2020.05.110` (cit. on pp. 137, 146).

[804] D. Rana and T. Matsuura. “Surface Modifications for Antifouling Membranes”. In: *Chemical Reviews* 110.4 (Apr. 2010), pp. 2448–2471. ISSN: 0009-2665. DOI: `10.1021/cr800208y` (cit. on p. 137).

[805] Youhong Guo et al. “Scalable Super Hygroscopic Polymer Films for Sustainable Moisture Harvesting in Arid Environments”. In: *Nature Communications* 13.1 (2022), p. 2761. ISSN: 2041-1723. DOI: `10.1038/s41467-022-30505-2` (cit. on p. 137).

[806] Hanneke M. L. Thijs et al. “Water Uptake of Hydrophilic Polymers Determined by a Thermal Gravimetric Analyzer With a Controlled Humidity Chamber”. In: *Journal of Materials Chemistry* 17.46 (2007), pp. 4864–4871. ISSN: 0959-9428. DOI: `10.1039/B711990A` (cit. on pp. 137, 146, 147).

[807] Hyoe Hatakeyama and Tatsuko Hatakeyama. “Interaction Between Water and Hydrophilic Polymers”. In: *Thermochimica Acta* 308.1 (Jan. 1998), pp. 3–22. ISSN: 0040-6031. DOI: `10.1016/S0040-6031(97)00325-0` (cit. on p. 137).

[808] Khaoula Khwaldia. “Physical and Mechanical Properties of Hydroxypropyl Methylcellulose-Coated Paper as Affected by Coating Weight and Coating Composition”. In: *BioResources* 8.3 (2013) (cit. on pp. 137, 146).

[809] Mahadevaiah et al. “Mechanical and Barrier Properties of Hydroxy Propyl Methyl Cellulose Edible Polymer Films with Plasticizer Combinations”. In: *Journal of Food Processing and Preservation* 41.4 (Aug. 2017), e13020. ISSN: 0145-8892. DOI: `10.1111/jfpp.13020` (cit. on p. 137).

[810] Meltem Aydinli and Mehmet Tutas. “Water Sorption and Water Vapour Permeability Properties of Polysaccharide (Locust Bean Gum) Based Edible Films”. In: *LWT - Food Science and Technology* 33.1 (Feb. 2000), pp. 63–67. ISSN: 0023-6438. DOI: `10.1006/fstl.1999.0617` (cit. on p. 137).

[811] Merve Zeyrek Ongun et al. “Tuning CO2 Sensing Properties of HPTS Along With Newly Synthesized Coordination Polymers (CPs)”. In: *Spectrochimica Acta Part A: Molecular and Biomolecular Spectroscopy* 263 (Dec. 2021), p. 120224. ISSN: 1386-1425. DOI: `10.1016/j.saa.2021.120224` (cit. on p. 138).

[812] Chi L. Li et al. “The Use of Hypromellose in Oral Drug Delivery”. In: *Journal of Pharmacy and Pharmacology* 57.5 (May 2005), pp. 533–546. ISSN: 0022-3573. DOI: `10.1211/0022357055957` (cit. on p. 137).

[813] Wesley L. Archer. “Determination of Hansen Solubility Parameters for Selected Cellulose Ether Derivatives”. In: *Industrial & Engineering Chemistry Research* 30.10 (Oct. 1991), pp. 2292–2298. ISSN: 0888-5885. DOI: `10.1021/ie00058a008` (cit. on p. 137).

[814] Nursel Pekel et al. “Radiation Crosslinking of Biodegradable Hydroxypropylmethylcellulose”. In: *Carbohydrate Polymers* 55.2 (Jan. 2004), pp. 139–147. ISSN: 0144-8617. DOI: `10.1016/j.carbpol.2003.08.015` (cit. on p. 137).

[815] James L. Ford. “Thermal Analysis of Hydroxypropylmethylcellulose and Methylcellulose: Powders, Gels and Matrix Tablets”. In: *International Journal of Pharmaceutics* 179.2 (1999), pp. 209–228. ISSN: 0378-5173. DOI: `10.1016/S0378-5173(98)00339-1` (cit. on p. 137).

[816] *Semiconductor Devices - Micro-Electromechanical Devices - Part 1: Terms and Definitions*. Standard. Geneva, CH: International Electrotechnical Comission, 2016 (cit. on p. 142).

[817] Frederik C. Krebs. “Fabrication and Processing of Polymer Solar Cells: A Review of Printing and Coating Techniques”. In: *Solar Energy Materials and Solar Cells* 93.4 (Apr. 2009), pp. 394–412. ISSN: 0927-0248. DOI: `10.1016/j.solmat.2008.10.004` (cit. on p. 142).

[818] Muhammad A. Butt. “Thin-Film Coating Methods: A Successful Marriage of High-Quality and Cost-Effectiveness—A Brief Exploration”. In: *Coatings* 12.8 (2022). ISSN: 2079-6412. DOI: `10.3390/coatings12081115` (cit. on p. 142).

[819] Jean Juillard. “Dimethylformamide: Purification, Tests for Purity and Physical Properties”. In: 49.6 (1977), pp. 885–892. DOI: `10.1351/pac197749060885` (cit. on p. 142).

[820] Z. Ebrahimi and B. Gosselin. “Ultralow-Power Photoplethysmography (PPG) Sensors: A Methodological Review”. In: *IEEE Sensors Journal* 23.15 (2023), pp. 16467–16480. ISSN: 1558-1748. DOI: `10.1109/JSEN.2023.3284818`. URL: `https://doi.org/10.1109/JSEN.2023.3284818` (cit. on p. 146).

[821] J. C. Callahan et al. “Equilibrium Moisture Content of Pharmaceutical Excipients”. In: *Drug Development and Industrial Pharmacy* 8.3 (1982), pp. 355–369. ISSN: 0363-9045. DOI: `10.3109/03639048209022105` (cit. on p. 146).

[822] Gulshan Kumar Malik, Anjali Khuntia, and Jayeeta Mitra. “Comparative Effect of Different Plasticizers on Barrier, Mechanical, Optical, and Sorption Properties of Hydroxypropyl Methylcellulose (HPMC)–Based Edible Film”. In: *Journal of Biosystems Engineering* 47.2 (June 2022), pp. 93–105. ISSN: 2234-1862. DOI: `10.1007/s42853-022-00132-2` (cit. on p. 146).

[823] Nugraha E. Suyatma et al. “Effects of Hydrophilic Plasticizers on Mechanical, Thermal, and Surface Properties of Chitosan Films”. In: *Journal of Agricultural and Food Chemistry* 53.10 (May 2005), pp. 3950–3957. ISSN: 0021-8561. DOI: `10.1021/jf048790+` (cit. on p. 146).

[824] C. Zeppa, F. Gouanvé, and E. Espuche. “Effect of a Plasticizer on the Structure of Biodegradable Starch/Clay Nanocomposites: Thermal, Water-Sorption, and Oxygen-Barrier Properties”. In: *Journal of Applied Polymer Science* 112.4 (May 2009), pp. 2044–2056. ISSN: 0021-8995. DOI: `10.1002/app.29588` (cit. on p. 146).

[825] Toshio Watanabe et al. “Influence of Humidity on Refractive Index of Polymers for Optical Waveguide and its Temperature Dependence”. In: *Applied Physics Letters* 72.13 (Mar. 1998), pp. 1533–1535. ISSN: 0003-6951. DOI: `10.1063/1.120574` (cit. on p. 147).

[826] Derya Gulsen and Anuj Chauhan. “Effect of Water Content on Transparency, Swelling, Lidocaine Diffusion in p-HEMA Gels”. In: *Journal of Membrane Science* 269.1 (2006), pp. 35–48. ISSN: 0376-7388. DOI: `10.1016/j.memsci.2005.06.024` (cit. on p. 147).

[827] T. A. Trezza and J. M. Krochta. “The Gloss of Edible Coatings as Affected by Surfactants, Lipids, Relative Humidity, and Time”. In: *Journal of Food Science* 65.4 (May 2000), pp. 658–662. ISSN: 0022-1147. DOI: `10.1111/j.1365-2621.2000.tb16068.x` (cit. on p. 147).

[828] Fesia L. Laksmana et al. "Using the Internal Stress Concept to Assess the Importance of Moisture Sorption-induced Swelling on the Moisture Transport through the Glassy HPMC Films". In: *AAPS PharmSciTech* 9.3 (Sept. 2008), pp. 891–898. ISSN: 1530-9932. DOI: `10.1208/s12249-008-9128-7` (cit. on p. 147).

[829] Ping Gao et al. "Swelling of Hydroxypropyl Methylcellulose Matrix Tablets. 2. Mechanistic Study of the Influence of Formulation Variables on Matrix Performance and Drug Release". In: *Journal of Pharmaceutical Sciences* 85.7 (July 1996), pp. 732–740. ISSN: 0022-3549. DOI: `10.1021/js9504595` (cit. on p. 147).

[830] Jianhua Huang. "A Simple Accurate Formula for Calculating Saturation Vapor Pressure of Water and Ice". In: *Journal of Applied Meteorology and Climatology* 57.6 (2018), pp. 1265–1272. DOI: `10.1175/JAMC-D-17-0334.1` (cit. on p. 148).

[831] J. Goicoechea et al. "Minimizing the Photobleaching of Self-Assembled Multilayers for Sensor Applications". In: *Sensors and Actuators B: Chemical* 126.1 (Sept. 2007), pp. 41–47. ISSN: 0925-4005. DOI: `10.1016/j.snb.2006.10.037` (cit. on p. 149).

[832] Hong Dinh Duong, Younsook Shin, and Jong Il Rhee. "Development of Fluorescent pH Sensors Based on a Sol-Gel Matrix for Acidic and Neutral pH Ranges in a Microtiter Plate". In: *Microchemical Journal* 147 (June 2019), pp. 286–295. ISSN: 0026-265X (cit. on p. 149).

[833] Merve Zeyrek Ongun et al. "Tuning CO2 Sensing Properties of HPTS Along With Newly Synthesized Coordination Polymers (CPs)". In: *Spectrochimica Acta Part A: Molecular and Biomolecular Spectroscopy* 263 (Dec. 2021), p. 120224 (cit. on p. 156).

[834] Merve Zeyrek Ongun and Sibel Oguzlar. "Improvement of the CO2 Sensitivity: HPTS-Based Sensors along with Zn@SnO2 and Sn@ZnO Additives". In: *ACS Omega* 8.32 (Aug. 2023), pp. 29635–29645. DOI: `10.1021/acsomega.3c03708` (cit. on p. 156).

[835] Sibel Oguzlar, Merve Zeyrek Ongun, and Aylin M. Deliormanlı. "Effect on Improving CO2 Sensor Properties: Combination of HPTS and γ-Fe2O3@ZnO Bioactive Glass". In: *ACS Omega* 8.43 (Oct. 2023), pp. 40561–40571. DOI: `10.1021/acsomega.3c05361` (cit. on p. 156).

[836] Ozan Yilmaz et al. "An Emission Based Optical CO2 Sensor Fabricated on Grating-Like TiO2 Substrates Using HPTS". In: *Spectrochimica Acta Part A: Molecular and Biomolecular Spectroscopy* 305 (Jan. 2024), p. 123502. ISSN: 1386-1425. DOI: `10.1016/j.saa.2023.123502` (cit. on p. 156).

[837] Ahmed Kotbi et al. "Gas Sensors Based on Exfoliated g-C3N4 for CO2 Detection". In: *Chemosensors* 10.11 (2022). ISSN: 2227-9040. DOI: `10.3390/chemosensors10110470` (cit. on p. 156).

[838] Ronil J. Rath et al. "Chemiresistive Sensor for Enhanced CO2 Gas Monitoring". In: *ACS Sensors* 9.4 (Apr. 2024), pp. 1735–1742. DOI: `10.1021/acssensors.3c01779` (cit. on p. 156).

[839] Shahina Shahid et al. "Highly Sensitive and Selective Colorimetric Sensing of CO_2 for Biomedical Applications". In: *3 Biotech* 12.12 (2022), p. 334. ISSN: 2190-5738. DOI: `10.1007/s13205-022-03396-9` (cit. on p. 156).

[840] Yupu Zhang et al. "A Tunable Colorimetric Carbon Dioxide Sensor Based on Ion-Exchanger- and Chromoionophore-Doped Hydrogel". In: *Analysis & Sensing* 3.6 (Nov. 2023), e202300002. ISSN: 2629-2742. DOI: `10.1002/anse.202300002` (cit. on p. 156).

[841] Seong-Soo Lee et al. "Turn Off–On Fluorescent CO2 Gas Detection Based on Amine-Functionalized Imidazole-Based Poly(ionic liquid)". In: *ACS Omega* 7.44 (Nov. 2022), pp. 40485–40492. DOI: `10.1021/acsomega.2c05695` (cit. on p. 156).

[842] Woo Jin Choi et al. "Bodipy-Based Dyes for Ionic-Liquid-Based Optical Carbon Dioxide Sensors". In: *Journal of Industrial and Engineering Chemistry* 138 (Oct. 2024), pp. 458–471. ISSN: 1226-086X. DOI: `10.1016/j.jiec.2024.04.025` (cit. on p. 156).

[843] Ori Green et al. "Activity-Based Approach for Selective Molecular CO2 Sensing". In: *Journal of the American Chemical Society* 144.19 (May 2022), pp. 8717–8724. ISSN: 0002-7863. DOI: `10.1021/jacs.2c02361` (cit. on p. 156).

[844] Zhong-Quan Zhu et al. "A Selective Fluorescent Probec Derived From Benzo[d]imidazole for Carbon Dioxide Detection and Bioimaging". In: *Journal of Photochemistry and Photobiology A: Chemistry* 454 (Sept. 2024), p. 115748. ISSN: 1010-6030. DOI: `10.1016/j.jphotochem.2024.115748` (cit. on p. 156).

[845] Ruyi Zhang, Liangliang Zhu, and Bingbing Yue. “Luminescent Properties and Recent Progress in Applications of Lanthanide Metal-Organic Frameworks”. In: *Chinese Chemical Letters* 34.2 (Feb. 2023), p. 108009. ISSN: 1001-8417. DOI: `10.1016/j.cclet.2022.108009` (cit. on p. 156).

[846] Sameera Sh. Mohammed Ameen and Khalid M. Omer. “Recent Advances of Bimetallic-Metal Organic Frameworks: Preparation, Properties, and Fluorescence-Based Biochemical Sensing Applications”. In: *ACS Applied Materials & Interfaces* 16.25 (June 2024), pp. 31895–31921. ISSN: 1944-8244. DOI: `10.1021/acsami.4c06931` (cit. on p. 156).

[847] Pierre Grangeat et al. *Dynamic Modeling of Carbon Dioxide Transport through the Skin Using a Capnometry Wristband*. 2023. DOI: `10.3390/s23136096` (cit. on p. 157).

[848] A. Persson and R. Seton. “Modeling and Evaluation of a Rate-Based Transcutaneous Blood Gas Monitor”. In: *IEEE Transactions on Biomedical Engineering* 70.11 (2023), pp. 3178–3186. ISSN: 1558-2531. DOI: `10.1109/TBME.2023.3279514` (cit. on p. 157).

[849] Juan Pedro Cascales et al. “A Patient-Ready Wearable Transcutaneous CO2 Sensor”. In: *Biosensors* 12.5 (2022). ISSN: 2079-6374. DOI: `10.3390/bios12050333`. URL: `https://www.mdpi.com/2079-6374/12/5/333` (cit. on p. 157).

[850] Juan Pedro Cascales et al. “Wearable Technology to Monitor Transcutaneous Oxygen and Carbon Dioxide Partial Pressure”. In: *Optica Sensing Congress 2023 (AIS, FTS, HISE, Sensors, ES)*. Technical Digest Series. Munich: Optica Publishing Group, July 2023, STu3C.7. DOI: `10.1364/SENSORS.2023.STu3C.7` (cit. on p. 157).

[851] T. B. Tufan and U. Guler. “A Transcutaneous Carbon Dioxide Monitor Based on Time-Domain Dual Lifetime Referencing”. In: *IEEE Transactions on Biomedical Circuits and Systems* 17.4 (2023), pp. 795–807. ISSN: 1940-9990. DOI: `10.1109/TBCAS.2023.3277398` (cit. on p. 157).

[852] T. B. Tufan et al. “Performance Analysis of a Flexible HPTS-Based Carbon Dioxide Sensor for Transcutaneous Blood Gas Monitoring”. In: *2023 IEEE Biomedical Circuits and Systems Conference (BioCAS)*. 2023 IEEE Biomedical Circuits and Systems Conference (BioCAS). 2023, pp. 1–5. DOI: `10.1109/BioCAS58349.2023.10389056` (cit. on p. 157).

[853] Yaoxuan Cui et al. “A Wearable Bracelet for Simultaneous Monitoring of Transcutaneous Carbon Dioxide and Pulse Rates”. In: *Advanced Electronic Materials* 10.5 (May 2024), p. 2300760. ISSN: 2199-160X. DOI: `10.1002/aelm.202300760` (cit. on p. 157).

[854] Preety Ahuja et al. “Air-Permeable Redox Mediated Transcutaneous CO2 Sensor”. In: *Chemical Engineering Journal* 457 (Feb. 2023), p. 141260. ISSN: 1385-8947. DOI: `10.1016/j.cej.2022.141260` (cit. on p. 157).

[855] Zhaoyuan Jia et al. “Development of a Transcutaneous Monitoring System for Carbon Dioxide Partial Pressure Measurement”. In: vol. 13208. Proc.SPIE. July 2024, 132081W. DOI: `10.1117/12.3036703` (cit. on p. 157).

[856] Biao Li et al. “Noninvasive Skin Respiration (CO2) Measurement Based on Quartz-Enhanced Photoacoustic Spectroscopy”. In: *Analytical Chemistry* 95.14 (Apr. 2023), pp. 6138–6144. ISSN: 0003-2700. DOI: `10.1021/acs.analchem.3c00536` (cit. on p. 157).

[857] A. Angelucci et al. “A Wearable Device to Monitor the Partial Pressure of Transcutaneous Carbon Dioxide”. In: *IEEE Transactions on Instrumentation and Measurement* 73 (2024), pp. 1–12. ISSN: 1557-9662. DOI: `10.1109/TIM.2024.3369136` (cit. on p. 157).

[858] Mahmoud El-Safoury et al. “Towards a Miniaturized Photoacoustic Sensor for Transcutaneous CO2 Monitoring”. In: *Sensors* 24.2 (2024). ISSN: 1424-8220. DOI: `10.3390/s24020457` (cit. on p. 157).

[859] T. B. Tufan, L. Rhein, and U. Guler. “Implementation Techniques for Transcutaneous Carbon Dioxide Monitoring: Approaches for Wearable Smart Health Applications”. In: *IEEE Transactions on Biomedical Engineering* 71.3 (2024), pp. 929–943. ISSN: 1558-2531. DOI: `10.1109/TBME.2023.3322871` (cit. on p. 157).

[860] Sara Bernasconi et al. “Recent Technologies for Transcutaneous Oxygen and Carbon Dioxide Monitoring”. In: *Diagnostics* 14.8 (2024). ISSN: 2075-4418. DOI: `10.3390/diagnostics14080785` (cit. on p. 157).

[861] I. Ouchi et al. “Features of Fluorescence Spectra of Polyethylene 2,6-naphthalate Films”. In: *Journal of Applied Polymer Science* 105.1 (2007), pp. 114–121. ISSN: 0021-8995. DOI: `10.1002/app.26085` (cit. on p. 158).

[862] M.C. Branchet et al. "Skin Thickness Changes in Normal Aging Skin". In: *Gerontology* 36.1 (1990), pp. 28–35. ISSN: 0304-324X. DOI: `10.1159/000213172` (cit. on p. 160).

[863] Hongbo Zhai and Howard I. Maibach. "Occlusion vs. Skin Barrier Function". In: *Skin Research and Technology* 8.1 (2002), pp. 1–6. ISSN: 0909-752X. DOI: `10.1046/j.0909-752x.2001.10311.x` (cit. on p. 161).

[864] Xinshu Niu, Weiping Du, and Weimin Du. "Preparation and Gas Sensing Properties of ZnM2O4 (M = Fe, Co, Cr)". In: *Sensors and Actuators B: Chemical* 99.2 (May 2004), pp. 405–409. ISSN: 0925-4005. DOI: `10.1016/j.snb.2003.12.007` (cit. on p. 162).

[865] Yukio Sato, Takahisa Yamamoto, and Yuichi Ikuhara. "Atomic Structures and Electrical Properties of ZnO Grain Boundaries". In: *Journal of the American Ceramic Society* 90.2 (2007), pp. 337–357. ISSN: 0002-7820. DOI: `10.1111/j.1551-2916.2006.01481.x` (cit. on p. 162).

[866] H.-W. Ra et al. "The Effect of Grain Boundaries Inside the Individual ZnO Nanowires in Gas Sensing". In: *Nanotechnology* 21.8 (2010), p. 085502. ISSN: 0957-4484. DOI: `10.1088/0957-4484/21/8/085502` (cit. on p. 162).

[867] Alexei A. Kamshilin and Nikita B. Margaryants. "Origin of Photoplethysmographic Waveform at Green Light". In: *Physics Procedia* 86 (2017), pp. 72–80. ISSN: 1875-3892. DOI: `10.1016/j.phpro.2017.01.024` (cit. on p. 162).

[868] Herbert C. Ward. "The Hourly Variations in the Quantity of Haemoglobin and in the Number of the Corpuscles in Human Blood". In: *American Journal of Physiology-Legacy Content* 11.4 (1904), pp. 394–403. DOI: `10.1152/ajplegacy.1904.11.4.394`. eprint: `https://doi.org/10.1152/ajplegacy.1904.11.4.394`. URL: `https://doi.org/10.1152/ajplegacy.1904.11.4.394` (cit. on p. 166).

[869] Angelika M. Stefan and Felix D. Schönbrodt. "Big Little Lies: a Compendium and Simulation of p-Hacking Strategies". In: *Royal Society Open Science* 10.2 (Feb. 2023), p. 220346. DOI: `10.1098/rsos.220346` (cit. on p. 166).

[870] Sigma-Aldrich. *1 M HEPES solution Datasheet*. Tech. rep. SRE0065. Sigma-Aldrich, 2015 (cit. on p. 166).

[871] P.C. Beadle and J.L. Burton. "Absorption of Ultraviolet Radiation by Skin Surface Lipid". In: *British Journal of Dermatology* 104.5 (1981), pp. 549–551. DOI: `10.1111/j.1365-2133.1981.tb08169.x`. eprint: `https://onlinelibrary.wiley.com/doi/pdf/10.1111/j.1365-2133.1981.tb08169.x`. URL: `https://onlinelibrary.wiley.com/doi/abs/10.1111/j.1365-2133.1981.tb08169.x` (cit. on p. 168).

[872] David M. Jameson, John C. Croney, and Pierre D.J. Moens. "Fluorescence: Basic concepts, Practical Aspects, and Some Anecdotes". In: *Methods in Enzymology*. Vol. 360. Biophotonics, Part A. Academic Press, Jan. 2003, pp. 1–43 (cit. on p. 169).

[873] Euralliage. *2017 A (AW-AlCu4MgSi (A))*. 2023. URL: `https://web.archive.org/web/20230214100923/https://www.euralliage.com/2017A.htm` (visited on 02/14/2023) (cit. on p. 173).

[874] J.R. (Eds.) Davis. *ASM Specialty Handbook - Copper and Copper Alloys*. ASM International, 2001. ISBN: 9781615834532 (cit. on p. 173).

[875] C. H. Daly et al. "The Effect Of Pressure Loading on the Blood Flow Rate in Human Skin". In: *Bed Sore Biomechanics: Proceedings of a seminar on Tissue Viability and Clinical Applications organised in association with the Department of Biomedical Engineering, the Institute of Orthopaedics (University of London), Royal National Orthopaedic Hospital, Stanmore, London, and held at the University of Strathclyde, Glasgow, in August, 1975*. Ed. by R. M. Kenedi and J. M. Cowden. London: Macmillan Education UK, 1976, pp. 69–77. ISBN: 978-1-349-02492-6. DOI: `10.1007/978-1-349-02492-6_10` (cit. on p. 173).

[876] Alvin H. Sacks et al. "Difficulties in Laser Doppler Measurement of Skin Blood Flow Under Applied External Pressure". In: *Journal of rehabilitation research and development* 25-3 (1988), pp. 19–24 (cit. on p. 173).

[877] A. A. Anosov et al. "Volumetric Quantification of Skin Microcirculation Disturbance Induced by Local Compression". In: *Laser Physics Letters* 17.8 (June 2020), p. 085601. ISSN: 1612-202X. DOI: `10.1088/1612-202X/ab9445` (cit. on p. 173).

[878] J. C. Lawrence and J. P. Bull. "Thermal Conditions which Cause Skin Burns". In: *Engineering in Medicine* 5.3 (1976), pp. 61–63. DOI: `10.1243/EMED_JOUR_1976_005_023_02` (cit. on p. 174).

[879] A. R. Moritz and F. C. Henriques. "Studies of Thermal Injury: II. The Relative Importance of Time and Surface Temperature in the Causation of Cutaneous Burns". In: *The American journal of pathology* 23.5 (Sept. 1947), pp. 695–720. ISSN: 0002-9440. URL: `https://pubmed.ncbi.nlm.nih.gov/19970955` (cit. on p. 174).

[880] G. N. Flint. "A Metallurgical Approach to Metal Contact Dermatitis". In: *Contact Dermatitis* 39.5 (Nov. 1998), pp. 213–221. ISSN: 0105-1873. DOI: `10.1111/j.1600-0536.1998.tb05912.x`. URL: `https://doi.org/10.1111/j.1600-0536.1998.tb05912.x` (cit. on p. 174).

[881] Monica Hindsén. "Metal Allergy: Aluminium". In: *Metal Allergy: From Dermatitis to Implant and Device Failure*. Ed. by Jennifer K Chen and Jacob P. Thyssen. Springer International Publishing, 2018, pp. 333–336. ISBN: 978-3-319-58503-1. DOI: `10.1007/978-3-319-58503-1_25`. URL: `https://doi.org/10.1007/978-3-319-58503-1_25` (cit. on p. 174).

[882] A. Fletcher Hall. "Occupational Contact Dermatitis among Aircraft Workers". In: *Journal of the American Medical Association* 125.3 (May 1944), pp. 179–185. ISSN: 0002-9955. DOI: `10.1001/jama.1944.02850210001001`. URL: `https://doi.org/10.1001/jama.1944.02850210001001` (cit. on p. 175).

[883] T. Peters et al. "Occupational Contact Sensitivity to Aluminium in a Machine Construction Plant Worker". In: *Contact Dermatitis* 39.6 (Dec. 1998), pp. 322–322. ISSN: 0105-1873. DOI: `10.1111/j.1600-0536.1998.tb05958.x`. URL: `https://doi.org/10.1111/j.1600-0536.1998.tb05958.x` (cit. on p. 175).

[884] Pauli Virtanen et al. "SciPy 1.0: Fundamental Algorithms for Scientific Computing in Python". In: *Nature Methods* 17 (2020), pp. 261–272. DOI: `10.1038/s41592-019-0686-2` (cit. on p. 187).

[885] Rainer Storn and Kenneth Price. "Differential Evolution—A Simple and Efficient Heuristic for global Optimization over Continuous Spaces". In: *Journal of Global Optimization* 11.4 (Dec. 1997), pp. 341–359. ISSN: 1573-2916. DOI: `10.1023/A:1008202821328`. URL: `https://doi.org/10.1023/A:1008202821328` (cit. on p. 187).

Additional Acknowledgments

TL;DR

This back-matter chapter includes additional acknowledgments for the graphical elements that were used throughout this manuscript, as well as for certain specific contributions that deserve recognition.

Previous chapter Main Table Of Content (TOC)

Graphical symbols were used for the following figures:

- Figure 2.5: photodiode by Marz Gallery†, LED by shashank singh† (also used in Figure 5.9 and Appendix E).
- Figure 2.6: sound symbol by kenzi mebius†, beaker by Icon Island†, gas cylinder by Eucalyp†, syringe and flask by Turkubb†.
- Figure 3.1: venous system by Mariana Ruiz Villarreal‡.
- Figure 3.3: computer by Whyakup†, power supply by Rflor†, USB logo by Mobius‡ (computer and USB logo also used in Figure 5.9).
- Figure 3.5: left arm drawing extracted from Pioneer plaque, from the NASA.
- Figure 3.11: male anatomy from Pixabay.
- Figure 4.2: original cloud picture by Ecem Afacan†, light bulb by Jeremie Sommet†.
- Figure 6.3: coil picture by Vectorstall†.

†: from the Noun Project, Creative Commons license (CC BY 3.0).
‡: from Wikipedia, Creative Commons license (CC BY 3.0).

Concerning the haemoglobin spectrophotometry study presented in Section 2.3, I would like to express my special thanks to Karine Pichavant for her technical and scientific support during the measurements, Céline Théron for her technical help, and Sylvain Gioux for his redacting advices.

Concerning the clinical study on transcutaneous CO_2 diffusion reported in Section 3.2, I wish to warmly thank Hervé Abitbol and the Tecmatel Engineering team for their design of the adhesive mounting jig, Julien Dolou for his help in the administrative formalities involved in conducting the clinical study, and Alexandre Desvaux, Mikaël Jamet (Cimtech) and Lucien Lecurieux Lafayette (Troisel) for their help in the design and manufacturing of the aluminium sensor body.

Concerning the theoretical developments on the accuracy of phase estimation developed in Section 4.4, I am particularly grateful to Yoshitate Takakura for his valuable insights in spectral estimation, and to Morgan Madec for his meticulous early review of this work.

Concerning the experimentations linked to the CO_2-sensing thin film's design presented in Section 5.5, I would like to thank Jeanne Beyrle, who did great during her six months internship, de-risking several avenues. I would also like to thank Stéphane Roques, Nicolas Zimmerman, and Damien Favier for their technical support.

Emmanuel DERVIEUX

Non-Invasive Transcutaneous Characterisation of Blood Carbon Dioxide (CO_2) Content

Thesis summary

This thesis aims to develop a non-invasive method for measuring arterial carbon dioxide (CO_2) content, which is crucial in clinical practice. Two main approaches are investigated: pulse carbametry, which extrapolates oximetry principles to carbaminohaemoglobin using spectrophotometric techniques, and the study of transcutaneous CO_2 diffusion, which provides insights into the CO_2 content of subcutaneous tissues. The first approach proved to be a dead-end, while the second shows greater potential.

In particular, the concept of a sensor in the form of a patch containing a pH-sensitive fluorophore appears especially promising. A preliminary clinical study was conducted to better characterize transcutaneous CO_2 diffusion, enabling the dimensioning of such a patch. An in-depth theoretical study followed, leading to the development of patch prototypes that exhibited a satisfactory response to CO_2. This thesis concludes that, despite the many improvements still needed for the patch to be usable in a real-life clinical context, this new measurement modality could pave the way for continuous and portable CO_2 monitoring in medical care.

Keywords: carbon dioxide (CO_2), biomedical, fluorescence, dual lifetime referencing, spectrometry, photobleaching, carbaminohaemoglobin.

Résumé en français

Cette thèse cherche à développer une méthode non-invasive de mesure du taux de dioxyde de carbone (CO_2) artériel, dont la connaissance est cruciale sur le plan clinique. Deux approches principales sont étudiées : la carbamétrie pulsée, qui extrapole les principes de l'oxymétrie à la carbamino-hémoglobine via des techniques spectrophotométriques, et l’étude de la diffusion transcutanée du CO_2, qui donne des indications sur le contenu en CO_2 des tissus sous-cutanés. La première approche s'est révélée être une impasse, tandis que la seconde montre un plus grand potentiel.

En particulier, la piste d’un capteur se présentant sous la forme d’un patch contenant un fluorophore sensible au pH semble particulièrement prometteuse. Une première étude clinique visant à mieux caractériser la diffusion transcutanée du CO_2 a été réalisée, permettant le dimensionnement d’un tel patch. Une étude théorique approfondie est ensuite menée, et des prototypes de patchs sont conçus, présentant une réponse au CO_2 satisfaisante. La thèse conclut que – malgré les nombreuses améliorations qui restent à apporter au patch ainsi conçu – cette nouvelle modalité de mesure pourrait permettre le suivi médical continu et portatif du CO_2.

Mots-clefs : dioxyde de carbone (CO2), biomédical, fluorescence, dual lifetime referencing, spectrophotométrie, photo-blanchiment, carbaminohémoglobine.

Résumé de thèse en Français

Emmanuel Dervieux

Sujet : Caractérisation non-invasive transcutanée de la teneur en dioxyde de carbone (CO2) du sang

Introduction à la surveillance du CO2

Dans le domaine médical, la mesure de la pression partielle de dioxyde de carbone (CO2) dans le sang artériel (paCO2) est essentielle pour évaluer l'état de santé respiratoire et métabolique des patients. La paCO2 est généralement mesurée de manière invasive, par ponction artérielle ou par intubation trachéale. Ces méthodes, bien qu'efficaces, sont coûteuses, inconfortables et présentent des risques, ce qui limite leur utilisation à des contextes hospitaliers. De plus, elles ne permettent pas un suivi continu ou à domicile, des besoins qui deviennent de plus en plus cruciaux avec l'essor de la télémédecine.

Cette thèse explore deux voies principales pour développer une méthode non-invasive, portable, voire « wearable » (portable sur le corps), permettant de mesurer la teneur en CO2 dans le sang :

1. **La méthode basée sur la Carbamino-hémoglobine (CO2Hb)**, qui utilise des techniques spectrophotométriques pour mesurer la concentration de CO2 dans le sang via l'absorption lumineuse.

2. **La méthode de diffusion transcutanée du CO2**, qui se concentre sur la mesure du CO2 diffusant à travers la peau, en utilisant des capteurs adaptés à ce phénomène.

Propriétés optiques de la CO2Hb et la carbamétrie de pouls

La première piste étudiée dans cette thèse repose sur les propriétés optiques de l'hémoglobine et de ses dérivés, notamment la CO2Hb. L'objectif était d'adapter le principe de l'oxymétrie de pouls – utilisé pour mesurer la saturation en oxygène dans le sang (spO2) – à la détection non-invasive de la CO2Hb, un processus surnommé « carbamétrie de pouls ».

Protocole expérimental

Des expériences ont été menées avec des spectrophotomètres pour analyser les spectres d'absorption du sang, en comparant l’hémoglobine oxygénée (O2Hb), désoxygénée (HHb), et liée au CO2 (CO2Hb). Toutefois, les résultats ont montré que les différences spectrales entre ces formes d'hémoglobine sont faibles, rendant difficile la distinction de la CO2Hb. En conséquence, la méthode de carbamétrie pulsée, bien qu’envisageable en théorie, s'est avérée être une impasse en pratique.

Mesure transcutanée du CO2

La seconde approche, plus prometteuse, repose sur la mesure de la diffusion du CO2 à travers la peau, un processus connu sous le nom de mesure transcutanée du CO2. Ce procédé consiste à utiliser des capteurs qui mesurent le CO2 diffusant à travers l’épiderme.

Modélisation et conception des capteurs

Le chapitre 3 de la thèse propose un modèle mathématique pour étudier la diffusion du CO2 à travers la peau, en tenant compte de divers paramètres tels que la température cutanée, l'épaisseur de la peau et le temps de réponse du capteur. Des capteurs transcutanés ont été conçus à partir de ce modèle, en créant des chambres fermées où le CO2 peut s’accumuler et être mesuré. Les résultats des expérimentations montrent une corrélation positive entre la température de la peau et les taux de diffusion du CO2. Plus la température de la peau est élevée, plus la diffusion est rapide.

Lorem ipsum dolor sit amet, consectetur adipiscing elit, sed do eiusmod tempor incididunt ut labore et dolore magna aliqua. Ut enim ad minim veniam, quis nostrud exercitation ullamco laboris nisi ut aliquip ex ea commodo consequat. Qui lira ça ? Duis aute irure dolor in reprehenderit in voluptate velit esse cillum dolore eu fugiat nulla pariatur. Excepteur sint occaecat cupidatat non proident, sunt in culpa qui officia deserunt mollit anim id est laborum.

Le travail aborde également des facteurs environnementaux comme l’**humidité** et la diffusion de l’oxygène, qui peuvent affecter la précision des capteurs transcutanés. Des stratégies pour minimiser ces interférences sont proposées, notamment l’utilisation de systèmes de chauffage contrôlé et une optimisation de l’emplacement du capteur sur le corps.

Revue des techniques de détection du CO2

Le chapitre suivant de la thèse propose une revue complète des technologies existantes pour la détection du CO2, en évaluant leur pertinence pour une utilisation transcutanée. Parmi les technologies analysées :

1. Absorption infrarouge (NDIR) : Une méthode courante pour la mesure du CO2 dans l'air expiré (capnographie), mais difficile à miniaturiser pour des dispositifs portables.

2. Capteurs électrochimiques : Les électrodes de Stow-Severinghaus sont utilisées pour les analyses des gaz sanguins, mais leur durabilité est limitée par l'usure du capteur au fil du temps.

3. Capteurs à base de colorants fluorescents : Ces capteurs changent de couleur en fonction de la concentration en CO2, une technologie prometteuse pour des dispositifs portables.

4. Capteurs acoustiques : Une technologie émergente qui mesure les propriétés acoustiques du CO2, mais qui en est encore à un stade expérimental pour les applications médicales.

Les technologies actuelles présentent des limitations liées à la sensibilité à la température, à l'humidité, ainsi qu'à la complexité de leur calibration. Cela complique leur intégration dans des capteurs transcutanés portables et utilisables à domicile.

Utilisation des films minces fluorescents pour la détection du CO2

La thèse explore ensuite l'utilisation de **films minces fluorescents** pour la mesure transcutanée du CO2. Ces films, qui modifient leurs propriétés optiques en fonction de la concentration de CO2, sont intégrés dans des capteurs pour une détection en temps réel.

Un travail approfondi est mené pour sélectionner les matériaux adéquats, en particulier les **polymères** et **luminophores** (substances fluorescentes). Un des défis majeurs est d'optimiser la stabilité et la durabilité des films minces, notamment face à des facteurs tels que la **photodégradation** (détérioration des matériaux sous l'effet de la lumière) et la sensibilité à l'**humidité**. Des stratégies d'encapsulation des luminophores sont testées pour protéger les capteurs et garantir leur fiabilité.

Prototype et validation de concept

Un prototype fonctionnel a été conçu, intégrant ces films minces dans un capteur optique. Les premiers résultats montrent une sensibilité encourageante à la concentration de CO2, bien que des améliorations soient encore nécessaires, notamment en termes de précision et de réponse à long terme.

Conclusion et perspectives

Dans la conclusion, l'auteur insiste sur le potentiel des capteurs transcutanés pour remplacer les méthodes invasives de mesure du CO2. Tandis que la piste spectrophotométrique de la CO2Hb a montré ses limites, la diffusion transcutanée du CO2 apparaît comme une alternative viable pour une utilisation non invasive, portable et continue.

Les prochaines étapes incluent l'**amélioration des capteurs**, notamment en termes de miniaturisation, de résistance et d'autonomie. L'auteur propose également d'étendre la recherche à d'autres applications biomédicales, telles que la détection d'autres gaz sanguins ou de paramètres physiologiques.

En résumé, cette thèse contribue de manière significative à l'avancement des technologies de mesure non invasive du CO2, avec des perspectives prometteuses pour la télémédecine et les dispositifs médicaux portables.